

✓ VOLUME 79

OCTOBER 9, 1975

NUMBER 21

JPCA X

THE JOURNAL OF
PHYSICAL
CHEMISTRY



PUBLISHED BIWEEKLY BY THE AMERICAN CHEMICAL SOCIETY

THE JOURNAL OF PHYSICAL CHEMISTRY

BRYCE CRAWFORD, Jr., *Editor*
STEPHEN PRAGER, *Associate Editor*
ROBERT W. CARR, Jr., **FREDERIC A. VAN-CATLEDGE**, *Assistant Editors*

EDITORIAL BOARD: C. A. ANGELL (1973-1977), F. C. ANSON (1974-1978), V. A. BLOOMFIELD (1974-1978), J. R. BOLTON (1971-1975), L. M. DORFMAN (1974-1978), H. L. FRIEDMAN (1975-1979), E. J. HART (1975-1979), W. J. KAUZMANN (1974-1978), R. L. KAY (1972-1976), D. W. McCLURE (1974-1978), R. M. NOYES (1973-1977), J. A. POPE (1971-1975), B. S. RABINOVITCH (1971-1975), S. A. RICE (1969-1975), F. S. ROWLAND (1973-1977), R. L. SCOTT (1973-1977), A. SILBERBERG (1971-1975), J. B. STOTHERS (1974-1978), W. A. ZISMAN (1972-1976)

AMERICAN CHEMICAL SOCIETY, 1155 Sixteenth St., N.W., Washington, D.C. 20036

Books and Journals Division

D. H. MICHAEL BOWEN *Director*

CHARLES R. BERTSCH *Head, Editorial Department*
BACIL GUILLEY *Head, Graphics and Production Department*
SELDON W. TERRANT *Head, Research and Development Department*

©Copyright, 1975, by the American Chemical Society. Published biweekly by the American Chemical Society at 20th and Northampton Sts., Easton, Pa. 18042. Second-class postage paid at Washington, D.C., and at additional mailing offices.

All manuscripts should be sent to *The Journal of Physical Chemistry*, Department of Chemistry, University of Minnesota, Minneapolis, Minn. 55455.

Additions and Corrections are published once yearly in the final issue. See Volume 78, Number 26 for the proper form.

Extensive or unusual alterations in an article after it has been set in type are made at the author's expense, and it is understood that by requesting such alterations the author agrees to defray the cost thereof.

The American Chemical Society and the Editor of *The Journal of Physical Chemistry* assume no responsibility for the statements and opinions advanced by contributors.

Correspondence regarding accepted copy, proofs, and reprints should be directed to Editorial Department, American Chemical Society, 20th and Northampton Sts., Easton, Pa. 18042. Department Head: CHARLES R. BERTSCH. Associate Department Head: MARIANNE C. BROGAN, Assistant Editors: CELIA B. MCFARLAND, JOSEPH E. YURVATI.

Advertising Office: Centcom, Ltd., 50 W. State St., Westport, Conn. 06880

Business and Subscription Information

Send all new and renewal subscriptions *with payment to:* Office of the Controller, 1155 16th Street, N.W., Washington, D.C. 20036. Subscriptions should be renewed promptly to avoid a break in your series. All correspondence and telephone calls regarding

changes of address, claims for missing issues, subscription service, the status of records, and accounts should be directed to Manager, Membership and Subscription Services, American Chemical Society, P.O. Box 3337, Columbus, Ohio 43210. Telephone (614) 421-7230. For microfiche service, contact ACS Microfiche Service, 1155 16th St. N.W., Washington, D.C. 20036. Telephone (202) 872-4444.

On changes of address, include both old and new addresses with ZIP code numbers, accompanied by mailing label from a recent issue. Allow four weeks for change to become effective.

Claims for missing numbers will not be allowed (1) if loss was due to failure of notice of change in address to be received before the date specified, (2) if received more than sixty days from date of issue plus time normally required for postal delivery of journal and claim, or (3) if the reason for the claim is "issue missing from files."

Subscription rates (hard copy or microfiche) in 1975: \$20.00 for 1 year to ACS members; \$80.00 to nonmembers. Extra postage \$4.50 in Canada and PUAS, \$5.00 other foreign. Supplementary material (on microfiche only) available on subscription basis, 1975 rates: \$15.00 in U.S., \$19.00 in Canada and PUAS, \$20.00 elsewhere. All microfiche airmailed to non-U.S. addresses; air freight rates for hard-copy subscriptions available on request.

Single copies for current year: \$4.00. Rates for back issues from Volume 56 to date are available from the Special Issues Sales Department, 1155 Sixteenth St., N.W., Washington, D.C. 20036.

Subscriptions to this and the other ACS periodical publications are available on microfilm. For information on microfilm write Special Issues Sales Department at the address above.

THE JOURNAL OF
PHYSICAL CHEMISTRY

Volume 79, Number 21 October 9, 1975

JPCHAx 79(21) 2203-2328 (1975)

ISSN 0022-3654

Thermal Dissociation of Carbon Disulfide Near 20 Torr	T. C. Peng* and H. V. Lilenfeld	2203
Rate for Energy Transfer from Excited Cyclohexane to Nitrous Oxide in the Liquid Phase	Toshinori Wada and Yoshihiko Hatano*	2210
Photochemistry of 2-Benzoyl-3-phenylquinoxaline 1,4-Dioxide	N. A. Masoud and J. Olmsted, III*	2214
On the Photochemistry of Radicals Trapped in Frozen Methanol-Water Mixtures	Johan Moan* and Bjørn Høvik	2220
Photochemistry in the Adsorbed Layer. IV. Effects of Oxygen upon the Photolysis of the Adsorbed Alkyl Ketones	Yutaka Kubokawa* and Masakazu Anpo	2225
Mechanisms Involving the Transient Absorptions of Cyanine Dyes in Gelatin. I. Temperature Dependence	S. H. Ehrlich	2228
Mechanisms Involving the Transient Absorptions of Cyanine Dyes Adsorbed to Silver Bromiodide Microcrystals in Gelatin. II. Temperature Dependence	S. H. Ehrlich	2234
Solubility of Nonelectrolytes in Polar Solvents. V. Estimation of the Solubility of Aliphatic Monofunctional Compounds in Water Using a Molecular Surface Area Approach	G. L. Amidon,* S. H. Yalkowsky, S. T. Anik, and S. C. Valvani	2239 ■
Aqueous Dissociation of Croconic Acid	Lowell M. Schwartz,* Robert I. Gelb, and Janet O. Yardley	2246
Small Anion Binding to Cycloamylose. Equilibrium Constants	J. F. Wojcik* and R. P. Rohrbach	2251 ■
Two-Dimensional Polymerization Processes in Mono- and Diacrylic Esters	A. Dubault,* C. Casagrande, and M. Veysse	2254
Backbending and Other Deviations from Ideality in Extraction Systems	J. J. Bucher* and R. M. Diamond	2259
Vibrational Spectra of $M^+NO_3^-$ Ion Pairs Variably Hydrated or Ammoniated in an Argon Matrix	Gary Ritzhaupt and J. Paul Devlin*	2265
Vibrational Spectra and Assignments for <i>cis</i> - and <i>trans</i> -1,2-Difluorocyclopropane and Three Deuterium Substituted Modifications of Each Isomer	Norman C. Craig,* T.-N. Hu Chao, Enrique Cuellar, Dan E. Hendriksen, and Jeffery W. Koepke	2270 ■
Electron Spin Resonance Studies of Anisotropic Ordering, Spin Relaxation, and Slow Tumbling in Liquid Crystalline Solvents	Carl F. Polnaszek and Jack H. Freed*	2283
Spin-Lattice Relaxation and Hydrogen Bonding in Methanol-Solvent Mixtures	Rush O. Inlow, Melvin D. Joesten,* and John R. Van Wazer*	2307
Electrochemical and Transport Properties of Lithium Chloride Solutions in Dimethyl Sulfoxide-Water and Dimethyl Sulfoxide-Methanol Mixtures	Melvin H. Miles,* L. Wayne McMahan, and Susan M. Nelson	2312 ■
Influence of the Formation of Ions on the Viscosity of Phenol-Amine Mixtures	Noel G. Felix and Pierre L. Huyskens*	2316 ■

THE JOURNAL OF PHYSICAL CHEMISTRY

Registered in U. S. Patent Office © Copyright, 1975, by the American Chemical Society

VOLUME 79, NUMBER 21 OCTOBER 9, 1975

Thermal Dissociation of Carbon Disulfide Near 20 Torr¹

T. C. Peng* and H. V. Lilienfeld

McDonnell Douglas Research Laboratories, McDonnell Douglas Corporation, St. Louis, Missouri 63166 (Received March 19, 1975)

Publication costs assisted by McDonnell Douglas Corporation

The thermal dissociation of CS₂ in CS₂-Ar gas mixtures was investigated in a resistively heated vitreous carbon oven for gas pressures between 10 and 40 Torr and oven temperatures up to 2400 K. The reaction products were mass spectrometrically analyzed using a modulated molecular-beam sampling technique. The results show the following. (1) Below 1850 K there is no dissociation of CS₂ into solid carbon and S₂ as predicted by equilibrium calculations, rather the main products are CS and S₂ as formed by the dissociation reaction, CS₂ → CS + ½S₂. (2) Above 1850 K the number of CS molecules generated is greater than the number of CS₂ molecules dissociated. This indicates that the vitreous carbon wall participates in the dissociation and that wall reactions of the type, C_{wall} + ½S₂ → CS, contribute significantly to the total CS production. (3) Above 2300 K the number of CS molecules generated is about 1.85 times the number of CS₂ molecules dissociated and the total CS production approaches that predicted by equilibrium calculations including the oven wall. In addition, the best fit for the CS₂ decomposition profile between theoretical and experimental data yields a value of 64 kcal/mol for the heat of formation of CS at 0 K.

Introduction

CS molecules are important intermediates in the operation of a CS₂-O fueled CO chemical laser.² Recently, it has been shown that a CO chemical laser with a CS-O fuel mixture produces a significant power increase over a CS₂-O fueled mixture.³ Present methods of producing CS such as flash photolysis⁴ and discharge⁵ techniques are limited in the partial pressure of CS that can be generated. The shock tube technique⁶ for generating CS is intermittent and the facility required is costly. An economical and simple way of generating CS is thermal dissociation as indicated by Blanchard and LeGoff.⁷ The present study investigated the feasibility of using a thermal source to generate CS at the elevated pressures needed to operate a high-power chemical laser system.

An initial study of thermal dissociation of CS₂ in a vitreous carbon oven at pressures of 10⁻³ to 10⁻² Torr indicated that CS concentrations comparable with those from gas-phase equilibrium calculations can be generated and that wall reactions producing additional CS molecules are present. The present work is an extension of this initial study to higher pressures and temperatures. In addition, the signal-to-noise ratio of the apparatus has been substantially improved.

Experimental Section

The general arrangement, shown in Figure 1, is similar to that previously described.⁸ However, because of the high gas pressures (20-40 Torr for an Ar-CS₂ gas mixture and the dissociated products) in the oven, a two-chamber, differentially pumped vacuum system was employed. Typical chamber pressures under a 29% Ar + 71% CS₂ gas load at a flow rate of ~2 × 10⁻⁴ g/sec were ~2 × 10⁻⁴ Torr in the expansion chamber and ~2 × 10⁻⁶ Torr in the mass spectrometer chamber. The oven assembly, shown in Figure 2, contains a cylindrical oven of 1.27-cm i.d. and 3.8-cm length. The oven, made of vitreous carbon, was resistively heated to a maximum temperature of 2400 K with an input power of 2.5 kW. The oven was protected from excessive heat loss by six layers of 0.0025-cm perforated Ta sheets used as radiative reflectors backed with 0.32-cm thick alumina insulation. The temperature of the oven was measured with an optical pyrometer (Pyro Micro Model 95) focused through a 1.2-cm thick quartz window on a row of indentations drilled about 75% through the oven wall. These indentations had a depth approximately equal to the opening diameters and were essentially blackbody cavities for temperature measurement. The longitudinal temperature profile of the oven, after correction for the quartz window,

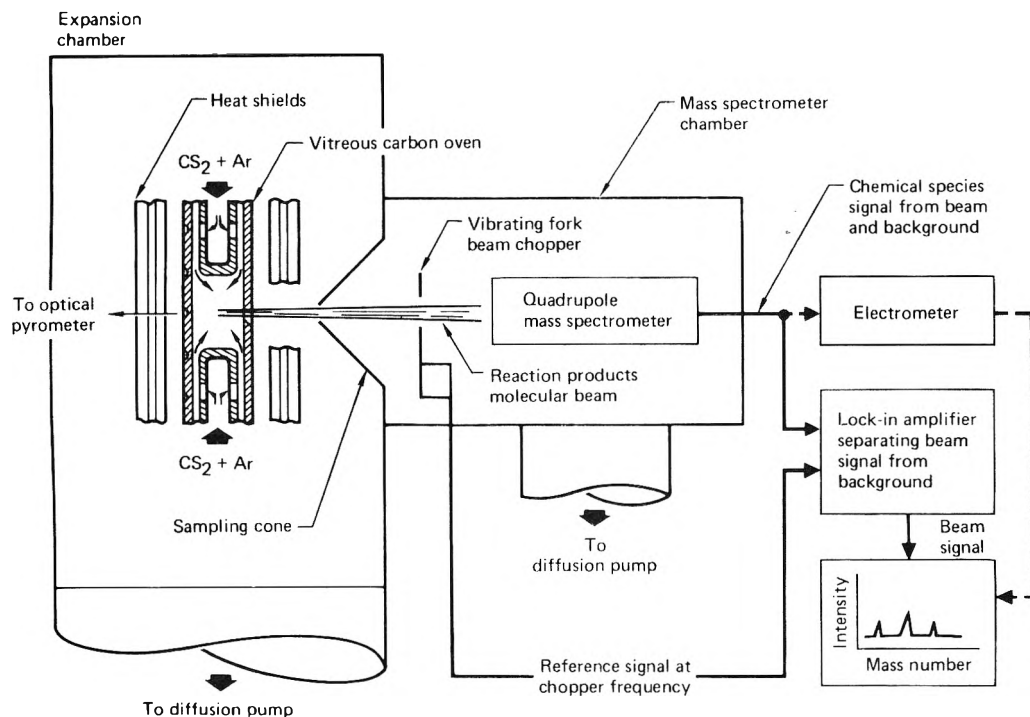


Figure 1. Experiment arrangement used for CS_2 dissociation studies near 20 Torr.

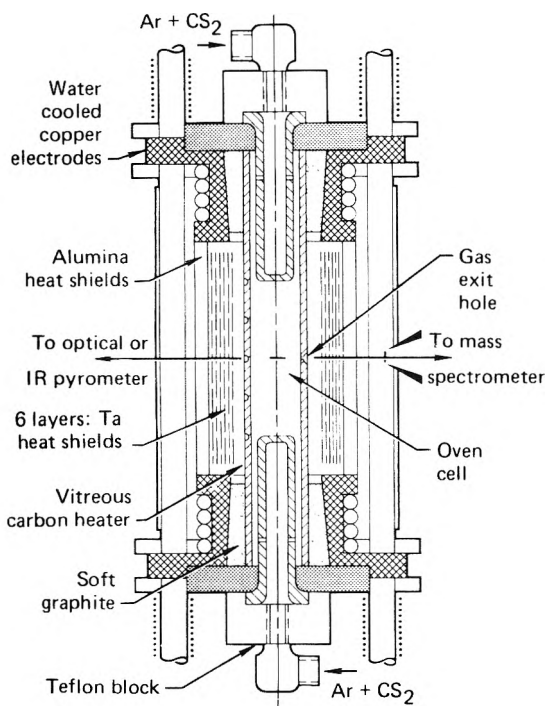


Figure 2. Vitreous carbon oven design.

was nearly symmetrical with respect to the oven center with a decreasing slope of ~ 10 K/cm at the center and ~ 50 K/cm near the edges of the oven.

The predetermined CS_2 -Ar gas mixture flowed into the oven through passages within the water-cooled electrodes (Figure 2). Calculations show (see Appendices A and B) that the gas mixture reached thermal equilibrium with the

wall in much less time than the flow transit time in the oven. This heating resulted in a partial dissociation of CS_2 molecules. Experimental data also suggested the occurrence of wall reactions between the hot vitreous carbon surface and various gas molecules in the oven. These reaction products and the undissociated CS_2 -Ar gas mixture emerged from the oven into the expansion chamber through an exit hole of $\sim 2 \times 10^{-2}$ cm diameter. Since the mean free path ($\sim 2 \times 10^{-3}$ cm, see Appendix A) in the oven was much smaller than the exit hole diameter, the exit flow formed a free jet expansion across a $\sim 10^5$ pressure ratio from ~ 20 Torr in the oven to $\sim 2 \times 10^{-4}$ Torr in the expansion chamber.

The flow fields of such free jet expansions have been described both theoretically and experimentally.^{9,10} These investigations have established the following important characteristics which are applicable to our experiment. The central core of the free jet contained only the gas species that were inside the oven. Furthermore, the flow was laminar and the expansion was isentropic within the core flow. The rapid expansion in the free jet converted most of the gas molecules' thermal energy into unidirectional kinetic energy. As a result, the chemical composition in the free jet remained essentially constant and was representative of the state of thermal dissociation of CS_2 within the vitreous carbon oven.

The core flow was extracted through the sampling cone. The presence of the sampling cone produced only small disturbances which would not significantly affect the sample composition or the species concentrations within the sample. This is because the low ambient pressure ($\sim 10^{-4}$ Torr) in the expansion chamber converted the free jet into a diffused flow around the sampling cone. The sampling cone and its supporting structure were utilized as a partition between the expansion chamber at $\sim 2 \times 10^{-4}$ Torr and the mass spectrometer chamber at $\sim 2 \times 10^{-6}$ Torr.

The sampling cone also served as a collimator after which the free jet became a molecular beam.

The molecular beam, modulated at a frequency of 435 Hz by a tuning fork chopper (Bulova, Model L 40 HH), traversed a quadrupole mass spectrometer (EAI Quad 150A) for chemical analysis. The modulated signal output from the mass spectrometer was amplified by a lock-in amplifier (PAR HR-8) and displayed on a X-Y recorder. This modulated-beam sampling technique was essential to separate the background gas signal from the beam gas signal to obtain an accurate measure of the CS₂ dissociation. For the study of CS₂ dissociation, the background gas in the mass spectrometer chamber contained not only the amount of CS₂ in the sampling beam but also the additional CS₂ molecules that resulted from the recombination of CS molecules on solid surfaces within the chamber.⁸ Hence, the true composition could not be determined by conventional residual gas analysis. This technique also eliminated interference from background gases such as N₂ and CO₂.

Although modulated-beam sampling usually has a low signal-to-noise ratio because of the low intensity of the sample beam relative to the background noise, the average signal-to-noise ratio of this experiment was 20:1, which was high enough to establish a CS temperature profile for evaluating the CS cracking pattern and the CS sensitivity factor of the mass spectrometer. The sensitivity factors of the stable species (CS₂ and Ar) were determined at room temperature by calibrating a known mass flow under steady-state conditions. The sensitivity factors of the unstable species (CS and S₂) were determined from the experimental data using material balance of sulfur atoms. The determinations of cracking patterns and sensitivities for CS and S₂ are discussed in the next section.

Data Analysis

The dissociation of CS₂ yields CS, S₂, and S as volatile reaction products. Because of the possible contributions from carbon wall reactions, it is important to determine the number of CS molecules generated for each CS₂ molecule dissociated. Hence, the CS signal ($m/e = 44$) at a given temperature, after correction for the CS₂ cracking pattern, was divided by the amount that the CS₂ signal ($m/e = 76$) decreased because of dissociation. This ratio, defined as $CS/(CS_2)_{diss}$, is proportional to the number of CS molecules generated for each CS₂ molecule dissociated. A plot of this ratio as a function of oven temperature is shown in Figure 3. Its value increased from ~ 0.45 at 1500 K to ~ 0.84 at 2400 K, indicating that there are ~ 1.85 times as many CS molecules generated at high temperatures as there are at low temperatures.

A probable explanation of this result would be the production of CS molecules from sulfur molecules (S₂ and S) reacting with the walls of the carbon oven at high oven temperatures. Another demonstration for sulfur-carbon wall reactions was found in a similar OCS dissociation experiment using the vitreous carbon oven. Analysis of this experiment indicated that at a temperature of 1800 K, both CS₂ and CO are formed; the amount of CS₂ and CO generated suggests $OCS \rightarrow CO + \frac{1}{2}S_2$ and $(S_2, 2S) + C_{wall} \rightarrow CS_2$ as the dominant reactions. Also, visual examination of the oven after the experiment gave evidence of erosion of the oven wall. Thus, the carbon wall must be participating in the formation reaction of CS molecules in the CS₂ dissociation.

There appeared to be little or no S-atom production. The

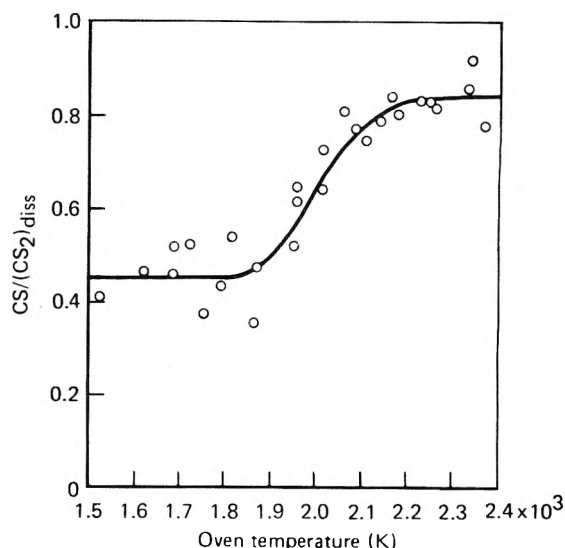


Figure 3. Temperature variations of $CS/(CS_2)_{diss}$.

signal at $m/e = 32$ was dominated by ions from cracking of CS₂, CS, and S₂. This conclusion is supported by following evidence. (1) The calculated S mole fractions are less than 10% of CS mole fractions from the equilibrium model excluding the carbon wall in the thermodynamic system, and are less than 1% of CS mole fractions from the equilibrium model including the carbon wall in the thermodynamic system. (2) According to the experimental data of Basco and Pearson,¹¹ the formation of S₂ from S under our experimental conditions would be virtually complete in a few milliseconds, much less than the flow transit time (0.36 to 0.46 s, Appendix A) of gas molecules within the oven. The S₂ signals at $m/e = 64$ indicate that the experimental amount of S₂ was generally a factor of 3 less than the maximum equilibrium predictions excluding the carbon wall for the temperatures from 2000 to 2400 K where a large amount of CS₂ dissociation occurs. Thus, the actual S mole fractions are expected to be 3% or less than those of CS mole fractions. Consequently, the signal intensity representing S atoms at $m/e = 32$ is expected to be negligibly small when compared with the signal intensity arising from the sum of cracking patterns of CS₂, S₂, and CS.

The cracking patterns of CS₂, S₂, and CS were determined as follows. (1) The cracking pattern of CS₂ was measured at room temperature. This cracking pattern was considered independent of oven temperature for this experiment. (The potential dependence of the cracking pattern on increasing oven temperature has been discussed in detail in a previous publication.⁸) (2) S₂ was generated during the release of adsorbed sulfur on the vitreous carbon wall at 550 K. The S₂ cracking pattern was obtained by measuring the increase in signal at both $m/e = 64$ (ΔI_{64}) and $m/e = 32$ (ΔI_{32}) during this release. The average value for the ratio of $\Delta I_{32}/\Delta I_{64}$, from the cracking pattern of S₂, was 0.175. (3) The cracking pattern of CS was then estimated by subtracting the CS₂ and S₂ cracking components from the total S signal at $m/e = 32$, assuming no contribution from S atoms. This was done for all high-temperature data where significant amounts of CS molecules were detected. The value for the ratio of the S signal from CS cracking at $m/e = 32$ (ΔI_{32}) to the CS signal at $m/e = 44$ (ΔI_{44}) was 0.17 ± 0.04 , which compares favorably with the value of 0.22 ± 0.03 from the mass spectrometric data analysis of the back-

ground gas for oven temperatures near 2400 K. The background gas signal should be devoid of S atoms because of the large sticking coefficient of sulfur atoms on solid surfaces.

Once the cracking patterns were determined, the sensitivity factors for CS and S₂ relative to CS₂ were derived from the sulfur atom balance between the input flow of CS₂ and the exit flow of CS₂, CS, and S₂ gas mixtures. From the values of cracking patterns and sensitivity factors, determinations of the composition of the sample beam, the amount of each component flux (Ar, CS₂, CS, and S₂) at the exit hole, and the component mole fractions were made using steady-state conditions and the measured input mass flow of an Ar-CS₂ gas mixture.

The component mole fractions, α_i , in the sample beam are also the component mole fractions of the reaction products in the vitreous carbon oven since there was little or no change in chemical composition throughout the exit flow molecular-beam sampling process. The component flux, ϕ_i , at the exit hole is related by gas dynamic expressions to the concentrations of that component, n_i , in the oven (Appendix A), namely

$$n_i = 1.57 \frac{\phi_i}{u_t A_t}$$

$$u_t = 1.08(R_m T_0)^{1/2}$$

where A_t , R_m , u_t , and T_0 are area of the exit hole, gas constant of the mixture in the oven, the flow velocity at the exit hole, and the oven temperature, respectively. With these formulae, the component concentrations representing the state of CS₂ dissociation in the oven at a given oven temperature can be calculated. Then, the partial pressure, P_i , and the total gas pressure, P_0 , in the oven can be calculated:

$$P_i = n_i k T_0 \quad P_0 = \sum P_i$$

where k = Boltzmann's constant. Based on the calculated gas pressure, P_0 , and the measured oven temperature, T_0 , equilibrium calculations were made to determine theoretical mole fractions for CS₂ dissociation at the experimental temperatures and pressures.

Even though chemical equilibrium is not always fully achieved, thermal equilibrium is readily achieved. This is demonstrated by the fact that the time required to reach thermal equilibrium in the oven (~0.03 sec, Appendix B) is much less than the flow transit time through the oven (0.36~0.46 sec, Appendix A). Thus, the measured data represent the results of chemical kinetics rather than those of fluid dynamics.

Results and Discussion

The mass spectrometric analyses of CS₂ dissociation after proper adjustment of cracking patterns and sensitivity factors are shown in Figures 4-6. The calculated compositions for two different thermodynamic models are also plotted in these figures. These models are (1) a system of gas species only, and (2) a system of gas species plus solid carbon. The standard thermodynamic data of graphite¹² were used in the equilibrium calculations for vitreous carbon. This substitution is reasonable because the complete data for vitreous carbon are not known at present, and the thermodynamic data of vitreous carbon are expected to differ only slightly with those of graphite.¹³ In addition, the heat of formation of CS at 0 K, $(\Delta H_f^\circ)_\text{CS}$, was taken to be

Gas mixture at room temperature:

71 mole% CS₂
29 mole% Ar

Total gas pressure:

18 Torr at 1000 K
35 Torr at 2370 K

Mass flow rate:

1.48×10^{-4} g/s for CS₂
 3.1×10^{-5} g/s for Ar

Equilibrium composition:

--- from model 1
— from model 2

○ Experimental data

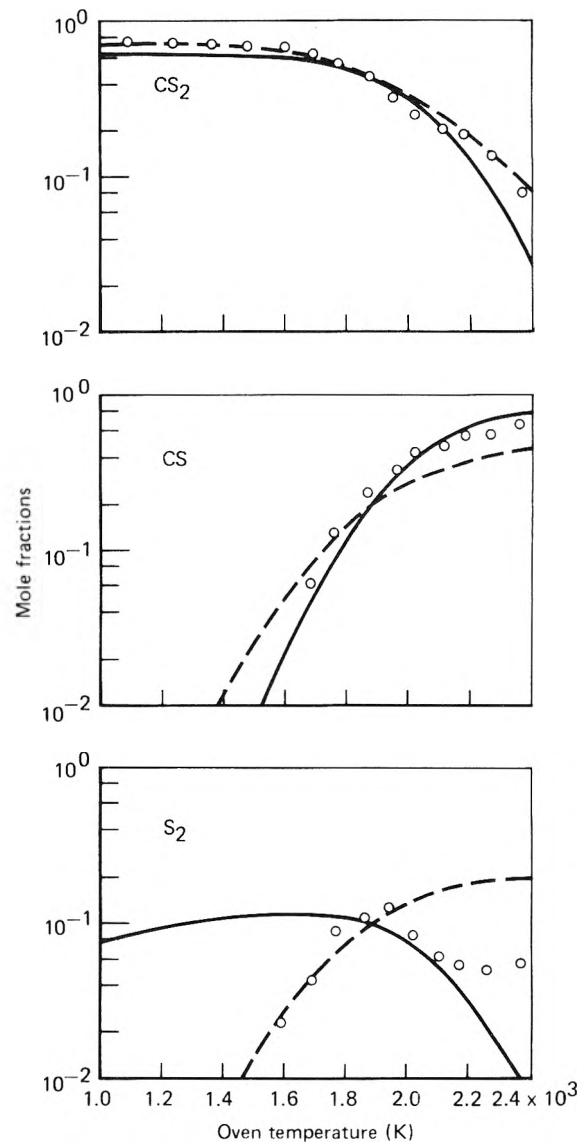


Figure 4. Species temperature profiles for CS₂ dissociation study (71 mol % CS₂, 29 mol % Ar).

64 kcal/mol. This value of $(\Delta H_f^\circ)_\text{CS}$ yielded a best fit for the CS₂ decomposition profile between the experimental data and the values obtained from equilibrium calculations excluding the carbon wall of the oven. A change of ± 1 kcal/mol would cause noticeable deviations. The reported value of $(\Delta H_f^\circ)_\text{CS}$ ranges from 55 to 69 kcal/mol.^{12,14} The more recent data^{15,16} indicate 65 kcal/mol as preferred. Thus, our finding, 64 kcal/mol for $(\Delta H_f^\circ)_\text{CS}$, compares favorably with recent data.

Of the two thermodynamic models mentioned, model 2 more closely represents the true equilibrium of our experimental system, whereas model 1 is a pseudo-equilibrium

Gas mixture at room temperature:

46 mole% CS₂
54 mole% Ar

Total gas pressure:

19 Torr at 1000 K
37 Torr at 2340 K

Mass flow rate:

1.07×10^{-4} g/s for CS₂
 6.6×10^{-5} g/s for Ar

Equilibrium composition:

— from model 1
- - - from model 2

○ Experimental data

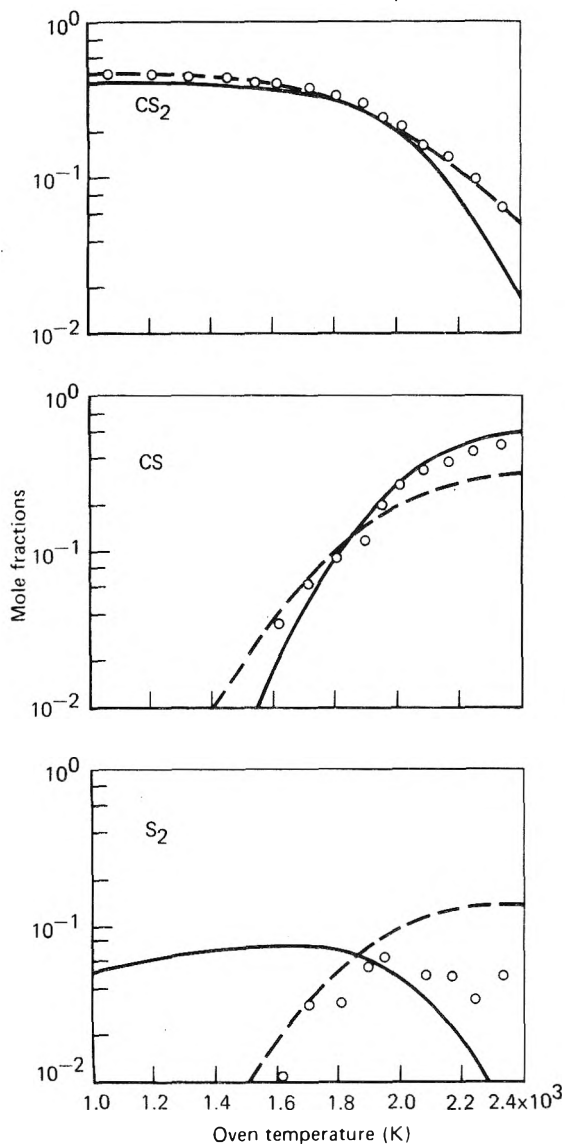


Figure 5. Species temperature profiles for CS₂ dissociation study (46 mol % CS₂, 54 mol % Ar).

used to illustrate the behavior pattern of our experimental system. The difference between models 1 and 2 below 1850 K represents the extent that the reaction $\text{CS}_2 \rightarrow \text{C}(\text{solid}) + \text{S}_2$ takes place. Above 1850 K, the difference between the models indicates the extent the carbon wall reacts with the CS₂ and dissociation products.

Below 1850 K, the experimental CS₂ data agree with the results of model 1. This agreement indicates that the partial dissociation of CS₂ into solid carbon and S₂, as predicted by the true equilibrium calculations (model 2), requires a much longer time than the gas flow transit time (0.36~0.46 sec) associated with our experiment. A check of

Gas mixture at room temperature:

51 mole% CS₂
49 mole% Ar

Total gas pressure:

10 Torr at 1000 K
19 Torr at 2340 K

Mass flow rate:

5.7×10^{-5} g/s for CS₂
 3.15×10^{-5} g/s for Ar

Equilibrium composition:

- - - from model 1
— from model 2

○ Experimental data

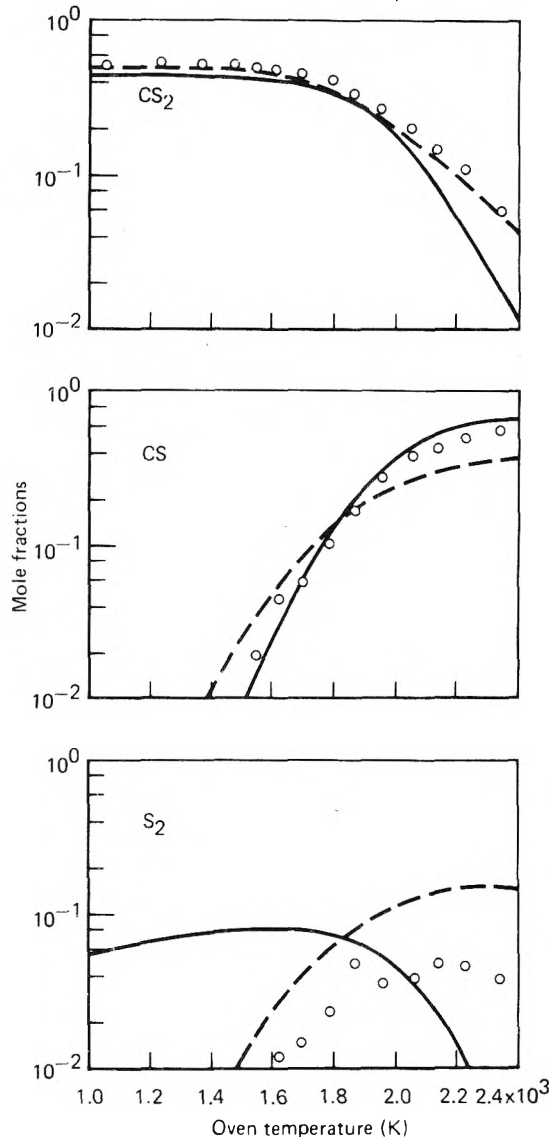


Figure 6. Species temperature profiles for CS₂ dissociation study (51 mol % CS₂, 49 mol % Ar).

S₂ data supports this view. At temperatures above 1850 K, the CS production exceeds the amount predicted by model 1 and approaches the limit of true equilibrium including wall reactions (model 2). Similarly, S₂ molecule profiles are much below the predictions of model 1. This observation strongly suggests that reactions such as $\text{C}_{\text{wall}} + \frac{1}{2}\text{S}_2 \rightarrow \text{CS}$ are operative. The conversion of S₂ into CS on a hot vitreous carbon wall was efficient above 1850 K and was ~85% complete at 2400 K.

The reaction $\text{C}_{\text{wall}} + \text{CS}_2 \rightarrow 2\text{CS}$ does not appear to play a significant role in CS production. This conclusion is supported by the observation that the CS₂ dissociation profile

does not approach the equilibrium prediction including the oven wall (model 2).

Conclusion

Thermal dissociation of CS₂ in 71% CS₂ + 29% Ar, 46% CS₂ + 54% Ar, and 51% CS₂ + 49% Ar gas mixtures at 20–40 Torr is about 85% complete at 2400 K. An equilibrium fit to experimental data yields 64 ± 1 kcal/mol as the heat of formation of CS at 0 K. This value compares favorably with the 65 kcal/mol recently determined.

The CS and S₂ production from CS₂ dissociation was evaluated. Comparison between the experimental and theoretical profiles of CS and S₂ indicated that (1) at 2400 K the number of CS molecules generated is about 1.85 times the number of CS₂ molecules dissociated, and the total CS production approaches that predicted by equilibrium calculations including the oven wall, and (2) wall reactions of the type C_{wall} + ½S₂ → CS contribute significantly to the total CS production.

Acknowledgment. The authors wish to express their thanks to Drs. C. J. Wolf and T. J. Menne for support and encouragement and to Dr. J. D. Kelley for useful discussions.

Appendix A. Gas Dynamics Calculations

For the analysis of CS₂ dissociation, it is necessary to calculate the species concentrations of reaction products, n_i (molecules/cm³); the total gas pressure, P_0 (Torr); the mean free path, λ (cm); and the flow transit time, τ_f (sec), within the oven. These gas dynamic properties are obtained using the expressions of isentropic expansion for the free jet exit flow and the mixing laws for gas mixtures.

The species concentration, n_i , is given by the flow relations for a gas mixture

$$n_i = \left(\frac{\gamma_m + 1}{2} \right)^{1/\gamma_m - 1} \frac{\phi_i}{u_t A_t} \quad (\text{A1})$$

where γ_m = the ratio of specific heats for the gas mixture, ϕ_i = molecular flow rate of the species in question, u_t = the gas flow at exit hole, A_t = the area of the exit hole, and

$$u_t = \left(\frac{2\gamma_m}{\gamma_m + 1} R_m T_0 \right)^{1/2} \quad (\text{A2})$$

where T_0 = oven temperature, and R_m = gas constant of the mixture

$$R_m = \sum_i \alpha_i \frac{R}{M_i} \quad (\text{A3})$$

where R is the universal gas constant, and M_i and α_i are the molecular weight and mole fraction of species i .

The molecular flow rate for each species, ϕ_i , was obtained from the calibrated mass spectrometric signals (see data analysis section). The mole fraction was calculated from

$$\alpha_i = \frac{n_i}{\sum n_i} = \frac{\phi_i}{\sum \phi_i} \quad (\text{A4})$$

since all species have the same exit velocity, u_t . Although γ_m varies from 5/3 to 11/9 for most gases and gas mixtures, $[(\gamma_m + 1)/2]^{1/(\gamma_m - 1)}$ and $2\gamma_m/(\gamma_m + 1)$ change only a few percent throughout the range of γ_m . Since the precise value of γ_m is difficult to calculate, approximate formulas for n_i and u_t are used.

$$n_i \approx 1.57 \frac{\phi_i}{u_t A_t} \quad (\text{A5})$$

$$u_t \approx 1.08 (R_m T_0)^{1/2} \quad (\text{A6})$$

Once n_i is known, the total and partial pressures (P_0 and P_i) are given by

$$P_0 = \sum P_i \quad P_i = n_i k T_0 \quad (\text{A7})$$

where k = the Boltzmann constant.

The mean free path, λ , between molecules in the oven is computed according to

$$\lambda = \frac{1}{\sqrt{2} n \pi \sigma^2} \quad (\text{A8})$$

where $\pi \sigma^2$ is the collision cross section between molecules. The collision cross sections for most neutral molecules at our experimental temperatures do not differ by more than a factor of 2. Thus, in the present study, an average cross section of 37×10^{-16} cm² was used for all species. The overall concentration, n ($= \sum n_i$), in the oven was nearly constant under our experimental conditions at $\sim 10^{17}$ molecules/cm³. Hence, the mean free path in the oven was $\sim 2 \times 10^{-3}$ cm.

The flow transit time, τ_f , of a steady flow system is given by

$$\tau_f = \frac{nV}{\phi} \quad (\text{A9})$$

where V , the oven volume, is 4.8 cm³. τ_f is the average time a molecule remains in the oven without chemical reactions or wall adsorption. Using eq A5 and A6

$$\tau_f = \frac{1.57V}{u_t A_t} = \frac{1.45V}{A_t (R_m T_0)^{1/2}} \quad (\text{A10})$$

Calculations for all temperatures and gas mixtures used in our experiment show that the flow transit time, τ_f , varies from 0.36 to 0.46 sec.

Appendix B. Temperature and Diffusion Transition Time within the Oven

To evaluate the state of thermodynamic equilibrium within the oven, the temperature and diffusion transition time of an incoming, cold gas flow must be estimated.

Temperature Transition Time, τ_T . Consider a core of cold gas that has an initial temperature, T_g , heated by the oven wall at a constant temperature, T_w , and a thermal boundary layer of $R - r$ as shown in Figure 7. The temperature transition time, τ_T , is defined as the time required to increase the gas core temperature, T_g , to $0.99T_w$ by conduction only. Convection is not significant because of the small gas velocity within the oven, and radiative transfer is not efficient because of low gas pressure (<40 Torr), although both convection and radiation tend to increase the heating process and therefore help to reduce the temperature transition time.

According to heat conduction

$$\frac{dQ(t)}{dt} = 2\pi r h \lambda \frac{dT}{dr} \quad (\text{B1})$$

where $Q(t)$ = the heat transferred from the oven wall to the gas core in time t .

$$\frac{dT}{dr} \approx \frac{T_w - T_t}{R - r} \quad T_g < T_t < T_w \quad (\text{B2})$$

and

$$T_t = T_g + \frac{Q(t)}{mc_v} \quad (\text{B3})$$

where T_t = the gas core temperature at time t , m is the gas core mass, and c_v is the specific heat of the gas core. Solving eq 11, 12, and 13 for T_t

$$\frac{T_t - T_g}{T_w - T_g} = 1 - \exp\left[-\left(\frac{2\pi rh\lambda}{mc_v(R-r)}\right)t\right] \quad (\text{B4})$$

Hence

$$\frac{T_t - T_g}{T_w - T_g} = 0.99 = 1 - \exp\left[-\left(\frac{\lambda}{mc_v}\right)\left(\frac{2\pi rh}{R-r}\right)\tau_T\right]$$

and

$$\tau_T = 23\left(\frac{mc_v}{\lambda}\right)\left(\frac{R-r}{2\pi rh}\right) \quad (\text{B5})$$

For our experimental gas mixture, $mc_v/\lambda \sim 0.132$ cm sec, $R = 0.64$ cm, $r = 0.49$ cm, and $h = 3.8$ cm. This yields $\tau_T = 0.031$ sec.

Diffusion Transition Time. Similarly, a molecule near the wall diffuses into the gas core region through molecular diffusion. A diffusion transit time, τ_D , is defined as the time required for 99% of the original molecules near the wall to diffuse into the gas core. Again referring to Figure 7, the concentration next to the oven wall maintains an equilibrium value, n_w . The concentration of these species in the gas core region at time t , is n_t . The amount of this species diffusing into the gas core region through a concentration profile, (dn/dr) , up to time, t , is N_t . Thus, the diffusive flux, dN_t/dt , is given by

$$\frac{dN_t}{dt} = 2\pi rhD \frac{dn}{dr} \quad (\text{B6})$$

where the concentration profile

$$\frac{dn}{dr} \approx \frac{n_w - n_t}{R - r} \quad (\text{B7})$$

and the gas core species concentration

$$n_t = \frac{N_t}{\pi r^2 h} \quad (\text{B8})$$

Substituting eq B7 and B8 into eq B6 and solving for n_t

$$\frac{n_t}{n_w} = 1 - \exp\left[-\left(\frac{2Dt}{(R-r)r}\right)\right]$$

For diffusion transit time, $n_t/n_w = 0.99$, $t = \tau_D$. Thus

$$\tau_D = 23[(R-r)r] \frac{1}{2D} \quad (\text{B9})$$

Using the average collision cross section of 37×10^{-16}

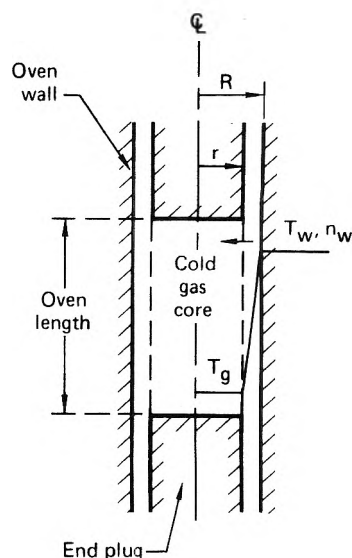


Figure 7. Physical model for calculating temperature and diffusion transit time.

cm² (Appendix A), the diffusion coefficients, D , for the CS₂-Ar gas mixture were estimated at an average temperature of 1500 K and an average pressure of 15 Torr. The values of R and r are the same as those used for calculating the temperature transition time, namely, $R = 0.64$ cm, and $r = 0.49$ cm thus, $\tau_D \sim 0.03$ sec.

References and Notes

- (1) This research was conducted under the McDonnell Douglas Independent Research and Development Program.
- (2) (a) S. J. Arnold and G. H. Kimball, *Appl. Phys. Lett.*, **15**, 351 (1969); (b) G. Hancock and I. W. M. Smith, *Chem. Phys. Lett.*, **3**, 573 (1969); (c) W. Q. Jeffers and C. E. Wiswall, *Appl. Phys. Lett.*, **17**, 67 (1970).
- (3) W. Q. Jeffers, C. E. Wiswall, J. D. Kelley, and R. J. Richardson, *Appl. Phys. Lett.*, **22**, 11 (1973).
- (4) P. J. Dyne and D. A. Ramsey, *J. Chem. Phys.*, **20**, 1055 (1952).
- (5) (a) J. Dewar and H. O. Jones, *Proc. R. Soc., Ser. A*, **83**, 526 (1909); (b) M. A. P. Hogg and J. E. Spice, *J. Chem. Soc.*, 4196 (1958); (c) R. J. Richardson, H. T. Powell, and J. D. Kelley, *J. Phys. Chem.*, **77**, 2601 (1973).
- (6) (a) A. G. Gaydon, G. H. Kimball, and H. B. Palmer, *Proc. R. Soc., Ser. A*, **279**, 313 (1964); (b) S. J. Arnold, W. G. Brownlee, and G. H. Kimball, *J. Phys. Chem.*, **74**, 8 (1970).
- (7) L. P. Blanchard and P. LeGoff, *Can. J. Chem.*, **35**, 89 (1957).
- (8) T. C. Peng, *J. Phys. Chem.*, **78**, 634 (1974).
- (9) J. B. Anderson, R. P. Andres, and J. B. Fenn, "Molecular Beams", J. Ross, Ed., Interscience, New York, N.Y., 1966, Chapter 8.
- (10) J. B. French, *AIAA J.*, **3**, 993 (1965).
- (11) N. Basco and A. E. Pearson, *Trans. Faraday Soc.*, **63**, 2684 (1967).
- (12) D. R. Stull and H. Prophet, *Natl. Stand. Ref. Data Ser., Natl. Bur. Stand., No. 37* (1971).
- (13) E. S. Bale, Third Conference on Industrial Carbon and Graphite, London, England, 1970.
- (14) D. L. Hildenbrand, *Chem. Phys. Lett.*, **15**, 379 (1972).
- (15) S. Bell, T. L. Ng, and C. Suggit, *J. Mol. Spectrosc.*, **44**, 267 (1972).
- (16) H. Okabe, *J. Chem. Phys.*, **56**, 4381 (1972).

Rate for Energy Transfer from Excited Cyclohexane to Nitrous Oxide in the Liquid Phase

Toshinori Wada and Yoshihiko Hatano*

Laboratory of Physical Chemistry, Tokyo Institute of Technology, Meguro-ku, Tokyo, Japan (Received April 29, 1975)

Pure liquid cyclohexane and cyclohexane solutions of nitrous oxide have been photolyzed at 163 nm. The quantum yield of the product hydrogen in the photolysis of pure cyclohexane is found to be 1.0. The addition of nitrous oxide results in the reduction in the yield of hydrogen and in the formation of nitrogen. The decrement of the hydrogen yield is approximately equal to the increment of the nitrogen yield. About 40% of the hydrogen yield in pure cyclohexane is found to be produced through a path which is not affected by the addition of nitrous oxide. The effect of the addition of nitrous oxide is attributed to energy transfer from excited cyclohexane to nitrous oxide with the rate constant of $k = 1.0 \times 10^{11} M^{-1} \text{sec}^{-1}$ (at 15°C). This value is about a factor of 10 larger than that expected as for diffusion-controlled rate. A contribution of the energy transfer process to the formation of nitrogen in the radiolysis of cyclohexane solutions of nitrous oxide has also been discussed.

I. Introduction

Photochemical studies of cyclohexane in the far-ultraviolet region indicate that excited cyclohexane molecules make important contributions in the formation of final products in both the gas phase¹ and the liquid phase.^{2a} However, the behavior of excited alkane molecules, especially in the liquid phase, formed by photons of energies near to, or slightly above, the ionization threshold is still not fully clarified.

Evidence has been reported that in liquid-phase photolysis neutral excited cyclohexane can transfer its excitation energy to various solutes.^{2,3} Further, it has been shown that a variety of liquid alkanes emit observable fluorescence when the alkanes are optically excited at 147 and 165 nm.⁴ An electronic energy transfer to aromatic solutes was confirmed to occur by observing the decrease of cyclohexane fluorescence and the development of aromatic fluorescence.⁵ The cyclohexane fluorescence is also quenched by typical electron scavengers.⁵ More recently, information about the lifetime of the excited cyclohexane has been given via the pulse radiolysis⁶ and X-ray⁷ excitation of liquid cyclohexane, pure and in the presence of solutes, and rate constants have been measured for energy transfer and for quenching of the excited cyclohexane. In the photolysis of liquid cyclohexane at 163 nm,⁸ it has also been reported that energy transfer from excited cyclohexane to a solute carbon tetrachloride or sulfur hexafluoride occurs in the liquid phase with the rate constant much larger than that expected as a diffusion-controlled rate.

The cyclohexane fluorescence spectrum and the energy transfer efficiencies obtained from photochemical experiments^{4,5,8} have been in good agreement with those obtained from X-ray excitation^{7,9} and pulse radiolysis,⁶ which indicates that a similar species (i.e., excited cyclohexane) is involved in both cases. Nitrous oxide has been widely used as an electron scavenger in radiolysis and the yield of nitrogen is related to the yield of electrons scavenged by nitrous oxide.¹⁰⁻¹² The mechanism of nitrogen formation has been discussed from various points of view. However, the mechanism is still not fully clarified. It has been shown by Holroyd^{2b} that nitrous oxide reacts with excited cyclohexane to form nitrogen in the liquid phase photolysis of cyclohexane solutions of nitrous oxide at 147 nm, which suggests an important contribution of this reaction to the formation of

the "excess" nitrogen. Recently, however, the possibility of this contribution has been critically discussed.¹²

Thus, further investigations of the photolysis of cyclohexane solutions of nitrous oxide to estimate the rate of electronic energy transfer from excited cyclohexane to nitrous oxide are necessitated, which has been undertaken in the present work. The effect of the addition of nitrous oxide is investigated in the photolysis of liquid cyclohexane at 163 nm.

II. Experimental Section

Cyclohexane^{8,11} (Phillips Research Grade, >99.99%) and nitrous oxide (Takachiho, >99.9%) were used without further purifications except for usual degassing and trap-to-trap distillations in a vacuum system. Ethylene (Takachiho, >99.9%) was used as received.

The 163-nm light source was an electrodeless discharge bromine lamp, which has been constructed in a manner similar to that described previously,⁸ except that bromine and 1 Torr of Ar as a carrier gas were introduced. The discharge was powered by a stabilized microwave generator (Ito Chotanpa Co.) operating at a power input of 75 W. During the operation a side arm of the lamp was immersed in a Dry Ice mixture and the lamp temperature was kept at a constant 200°C using a heating tape. As shown in Figure 1, the emission spectrum of the lamp, obtained with a vacuum-uv spectrometer (JASCO Model VUV-1 B), consisted of an intense line at 163 nm and very weak lines at 166 and 193 nm. The yield of hydrogen from ethylene photolysis was used as an actinometer. The lamp intensity was 2.1×10^{-8} einstein/sec and decreased gradually with a longer use.

After 8 ml of a degassed cyclohexane sample was distilled into the reaction cell, a known amount of nitrous oxide was added and thoroughly mixed. The concentration of nitrous oxide in the liquid phase was calculated from the Ostwald absorption coefficient of 3.3 in cyclohexane at 15°C.¹³ In the cell the window of the lamp was covered with the solution. Photolysis of the solution was carried out for 3 min. The solution was stirred during photolysis and cooled to 15 ± 1 °C by means of a water bath. Photolysis was repeated several times for cyclohexane solutions at various concentrations of nitrous oxide, and the total amount of conversion was less than 0.02%.

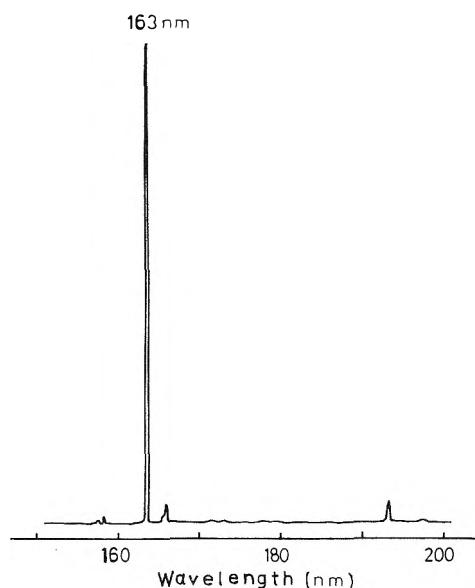


Figure 1. Emission spectrum of the Br lamp.

After a photolysis of a cyclohexane–nitrous oxide solution the noncondensable gas at 77 K was collected to a calibrated volume, and the pressure was measured. Hydrogen and nitrogen were identified by mass spectrometry. This gaseous mixture was analyzed by gas chromatography using a molecular sieve 5A column at room temperature, and the hydrogen yield was determined quantitatively. The liquid fraction was analyzed using a 6.0-m dimethylsulfolane column at 30°C for cyclohexene and a 0.75-m polyethylene glycol 600 column at 100°C for bicyclohexyl and cyclohexanol.

III. Results and Discussion

Pure Cyclohexane. Product distributions for photolysis of liquid cyclohexane, pure and in the presence of nitrous oxide, are given in Table I. The major photoproducts from pure liquid cyclohexane at 163 nm are hydrogen and cyclohexene; bicyclohexyl is a minor product. (The relative yield of bicyclohexyl in Table I is different from that previously reported.⁸ In the present experiment the yield of bicyclohexyl has been carefully measured again gas chromatographically and resulted in the value in Table I. The difference has been due to the gas chromatographically quantitative analysis of bicyclohexyl.) The product distribution shows the material balance between the yield of hydrogen and the sum of the yields of cyclohexene and bicyclohexyl produced in pure cyclohexane. Products other than those in Table I could not be observed in the gas chromatograms. Figure 2 shows the variations in the yields of hydrogen produced as a function of the irradiation time for the 163-nm photolysis of cyclohexane in the liquid phase and of ethylene in the gas phase (20 ~ 40 Torr). The linearities of these plots indicate that the secondary effects of products formed are not important in our reaction systems. The quantum yield of hydrogen formation $\Phi(\text{H}_2)_0 = 1.0 \pm 0.1$ for the liquid-phase photolysis of cyclohexane at 163 nm is obtained from the ratio of the slopes of these plots. Ethylene is used as an actinometer; $\Phi(\text{H}_2)$ for the gas-phase photolysis has been reported to be 0.42 at 163 nm.¹⁴ It is shown from the product distribution (Table I) that the main process for hydrogen formation is molecular detachment of hydrogen from the excited cyclohexane molecule leading to

TABLE I: Product Distributions from Photolysis of Cyclohexane in the Presence and Absence of Nitrous Oxide^a

Additive ^b	H ₂	N ₂	c-C ₆ -H ₁₀	(c-C ₆ -H ₁₁) ₂	c-C ₆ -H ₁₁ OH	H ₂ O
None	1		0.95	0.08		
N ₂ O (0.1 M)	1	0.40	1.24	0.04	0.13	nd

^a The maximum estimated error is $\pm 5\%$. ^b Maximum concentration at which the measurements were made.

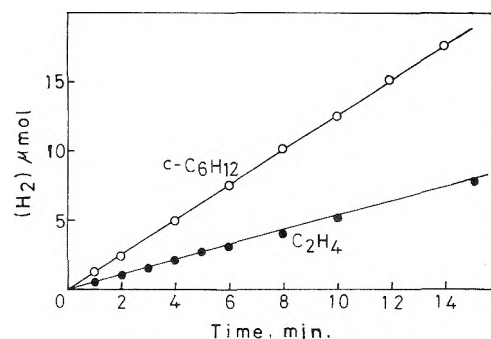


Figure 2. Variations in the amounts of hydrogen as a function of the irradiation time for the photolysis of cyclohexane in the liquid phase and of ethylene in the gas phase.

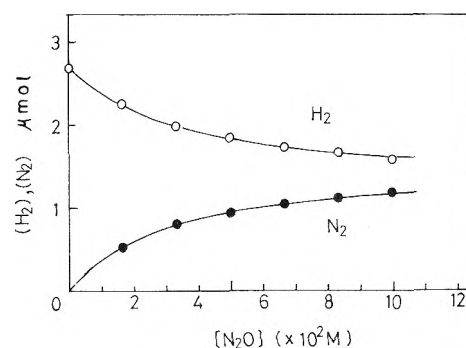


Figure 3. Variations in the amounts of hydrogen and nitrogen as a function of the concentration of N₂O.

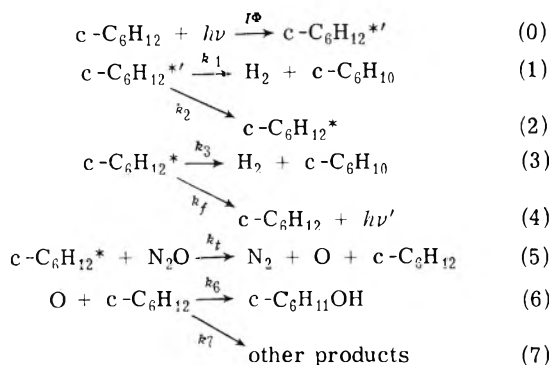
the formation of cyclohexene. The atomic detachment process leading to the formation of hydrogen atom and cyclohexyl radical is minor. Using an accepted value of 1.1¹⁵ for the disproportionation to recombination ratio of cyclohexyl radicals we can estimate, from the relative yield of bicyclohexyl, that the hydrogen atom quantum yield $\Phi(\text{H})_0$ is 0.17.

Cyclohexane in the Presence of Nitrous Oxide. Figure 3 shows the variations in the yields of hydrogen and nitrogen produced in the photolysis of cyclohexane–nitrous oxide solutions as a function of the concentration of N₂O. The addition of N₂O gradually increases the yield of nitrogen and complementarily decreases the yield of hydrogen to approach a constant value. In the process of hydrogen formation, there seems to be a path which is unaffected by the addition of N₂O. No changes in the results of the yields of hydrogen and nitrogen were observed using cyclohexane purified with a Na–K alloy. The ratio of the increment of the nitrogen yield to the decrement of the hydrogen yield is approximately unity, which is contrast to the result¹¹ in the radiolysis of cyclohexane–nitrous oxide solutions. As an

oxygen-containing product, $c\text{-C}_6\text{H}_{11}\text{OH}$ is observed and its yield is one-third that of nitrogen (Table I).

Since, in the gas phase at 163 nm, the photoabsorption coefficient of N_2O ¹⁶ is about a factor of 60 smaller than that of cyclohexane,¹⁷ the direct absorption of light with N_2O in liquid cyclohexane seems to be negligible even at the highest concentration of N_2O used in this experiment. It has been reported^{2b} that in the 147-nm photolysis of cyclohexane–nitrous oxide solutions nitrous oxide reacts with excited cyclohexane molecule to form nitrogen via dissociative energy transfer to nitrous oxide.

The following reaction scheme accounts adequately for the observed results.



where $c\text{-C}_6\text{H}_{12}^{*'}$ and $c\text{-C}_6\text{H}_{12}^*$ represent, respectively, a highly excited state and the first excited singlet state of cyclohexane. Although hydrogen formation is represented apparently as the molecular detachment process alone, the atomic detachment process is also involved effectively in reactions 1 and 3. The excited state $c\text{-C}_6\text{H}_{12}^{*'}$, which is not affected by N_2O , is the precursor of the lower excited state $c\text{-C}_6\text{H}_{12}^*$, both states being sources of hydrogen formation. The lower excited state is quenched by N_2O (reaction 5) and may be the one from which an observable fluorescence is emitted (reaction 4). A low yield of fluorescence, $\Phi_f = 10^{-2} \sim 10^{-3}$, has been observed by Lipsky et al.⁴ from liquid cyclohexane when excited at 147 or 165 nm and quenched by electron scavengers such as N_2O , CO_2 , and SF_6 in the photolysis at 147 nm.⁵ The efficiencies for quenching of the cyclohexane fluorescence by these solutes are similar to that for energy transfer from excited cyclohexane to CCl_4 or SF_6 reported previously in the photolysis at 163 nm.⁸ The oxygen atom generated by energy transfer to N_2O reacts with $c\text{-C}_6\text{H}_{12}$, via insertion reaction 6, to form $c\text{-C}_6\text{H}_{11}\text{OH}$. As another oxygen-containing product, H_2O would be formed by reaction 7 with a counterpart $c\text{-C}_6\text{H}_{10}$. Material balance is achieved between the amount of hydrogen plus nitrogen and the sum of the amounts of $c\text{-C}_6\text{H}_{10}$, $(c\text{-C}_6\text{H}_{11})_2$, and $c\text{-C}_6\text{H}_{11}\text{OH}$ (Table I).

From the steady-state treatment of the results in reactions 0–7, one obtains the following three equations relating the amount of hydrogen or nitrogen and the concentration of N_2O .

$$\frac{1}{(\text{N}_2)} = \frac{(k_1 + k_2)}{k_2 I \Phi} \left(1 + \frac{k_3}{k_t} \frac{1}{[\text{N}_2\text{O}]} \right) \quad (\text{I})$$

$$\frac{(\text{H}_2)}{(\text{N}_2)} = \frac{k_1}{k_2} + \frac{(k_1 + k_2) k_3}{k_2 k_t} \frac{1}{[\text{N}_2\text{O}]} \quad (\text{II})$$

$$\frac{1}{(\text{H}_2) - \{k_1 I \Phi / (k_1 + k_2)\}} = \frac{(k_1 + k_2)}{k_2 I \Phi} \left(1 + \frac{k_t}{k_3} [\text{N}_2\text{O}] \right) \quad (\text{III})$$

where k_t represents the rate constant of energy transfer to N_2O , I the amount of light absorbed, and Φ the quantum yield to form the highly excited cyclohexane $c\text{-C}_6\text{H}_{12}^{*'}$. In those equations reaction 4 is omitted because of a fluorescence yield much lower than unity. Linear plots of $1/(\text{N}_2)$ vs. $1/[\text{N}_2\text{O}]$ and of $(\text{H}_2)/(\text{N}_2)$ vs. $1/[\text{N}_2\text{O}]$ predicted by eq I and II are given in Figure 4. A rate constant ratio k_1/k_3 is obtained individually either from eq I or II; the values of the slope and the intercept of each linear plot give the value of k_1/k_3 as, respectively, 32 or 31 M^{-1} . They are in good agreement with each other. A ratio $k_1/k_2 = 0.77$ is obtained from a value of the intercept (eq II), which indicates about 60% of $c\text{-C}_6\text{H}_{12}^{*'}$ converts to $c\text{-C}_6\text{H}_{12}^*$. Thus the amount of hydrogen which is not quenched by N_2O , $k_1 I \Phi / (k_1 + k_2)$, is evaluated to be 1.20 μmol , which gives a plot of $1/(\text{H}_2) - 1.20$ vs. $[\text{N}_2\text{O}]$ as shown in Figure 5. As predicted by eq III a good linear relationship is observed with the same value of the intercept as that obtained for eq I. A ratio k_1/k_3 is obtained from this plot to be 29 M^{-1} , which is again in good agreement with those obtained for eq I and II. We therefore consider that the above reaction scheme described by reactions 0–7 accounts consistently for the observed results. In a previous study⁸ of the photolysis of cyclohexane in the presence of CCl_4 and SF_6 , the amount of hydrogen was the object of quenching and a good linear relationship of $1/(\text{H}_2)$ vs. $[\text{CCl}_4]$ or $[\text{SF}_6]$ was obtained, which is different from the result in this study. As a plausible explanation for this difference it may be offered that energy transfer can take place through a kind of complex between excited cyclohexane and additives and the detachment processes from this intermediate vary both with the energy states of cyclohexane molecule and with the properties of additives.

The value of the energy transfer efficiency $\alpha = k_t / (k_3 + k_f)$ obtained in this study is $31 \pm 2 M^{-1}$, which is in good agreement with $28 \pm 4 M^{-1}$ obtained by Holroyd^{2b} in the 147-nm photolysis. A reasonably agreed α value is also evaluated from a study for quenching of the cyclohexane fluorescence excited at 147 nm by N_2O .⁵ The lifetime of the excited state of cyclohexane was estimated by Henry and Helman⁷ from the fluorescence decay time measurements in the pulsed X-ray excitation as 0.3 nsec, and by Beck and Thomas⁶ from the measurements of growth of the fluorescence in the pulse radiolysis of aromatic solutes in cyclohexane as 0.28 nsec. The facts that photochemical excitation leads to the same fluorescence spectrum as X-ray excitation⁷ and the value of the energy transfer efficiency α obtained in photochemical experiments^{5,8} is in good agreement with the pulse radiolysis data⁶ indicate that the excited species formed in the radiolysis have properties similar to photoexcited molecules. Based on these facts we can consider $(k_3 + k_f)^{-1}$ to be equal to τ (0.3 nsec). With our value of α , $k_t = 1.0 \times 10^{11} M^{-1} \text{sec}^{-1}$ is obtained for the rate constant of energy transfer to N_2O at 15°C. This specific rate of energy transfer is about an order of magnitude greater than the expected rate $0.6 \times 10^{10} M^{-1} \text{sec}^{-1}$ (at 15°C), which is predicted by the Stokes–Einstein–Smoluchowski (SES) equation $k_{\text{SES}} = 8RT/3000\eta$ for a diffusion-controlled reaction in a solution with the viscosity η at an absolute temperature T . Previously we have reported similarly large rate constants for quenching of excited cyclohexane by CCl_4 and SF_6 with the values 2×10^{11} and $1 \times 10^{11} M^{-1} \text{sec}^{-1}$, respectively, at room temperature.⁸ Consistent with these results, Lipsky and his coworkers⁴ reported that fluorescence lifetimes estimated by fluorescence quenching or energy transfer measurements using the SES equation

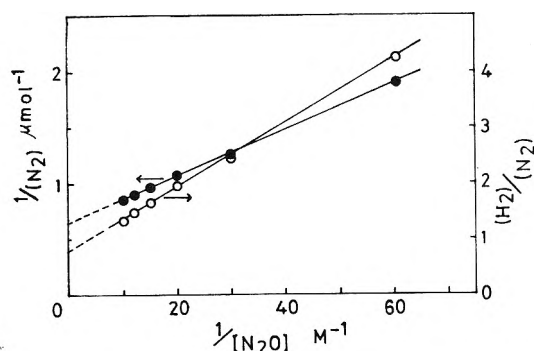


Figure 4. Plots of $1/(N_2)$ vs. $1/[N_2O]$ (●) and of $(H_2)/(N_2)$ vs. $1/[N_2O]$ (○).

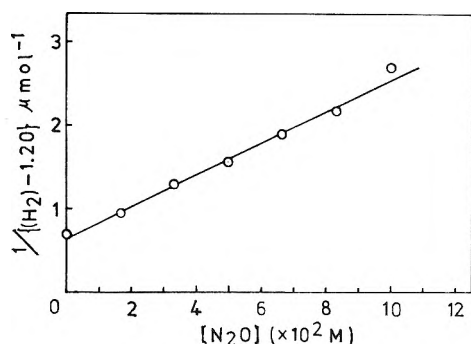


Figure 5. Plot of $1/[(H_2) - 1.20]$ as a function of the concentration of N_2O .

are about a factor of 10 longer than those⁷ directly measured. These results appear that the SES equation is inapplicable to reactions of excited alkane molecules. This is strikingly in contrast to its success when applied to reactions of excited aromatic molecules in a variety of solvents of different viscosity.¹⁸

The SES equation is derived from the Smoluchowski equation and the Stokes-Einstein equation under the assumptions that the interaction radii and the Stokes' radii of reactive molecules are each equal so that the two terms are cancelled. The fact that the Stokes-Einstein equation relating the diffusion coefficient, the Stokes radius, and the viscosity predicts a diffusion coefficient a factor of 2 or 3 smaller than the measured one for various solutes in cyclohexane¹⁹ is not enough to account for the large discrepancy between the observed rate of energy transfer and the expected diffusion-controlled rate. An efficient energy migration through alkane solvent has been negatively offered as an explanation.⁴ Helman⁹ has also reported higher values of specific rates (k_q) for the quenching of the fluorescence from the excited decalin and dodecane and showed that values of $k_q\eta/T$ are larger than expected from the SES equation but they are the same for both alkanes and are constant at several temperatures, suggesting that the quenching is controlled by diffusional motion. When an effective interaction distance within which energy transfer occurs between reactive molecules exceeds considerably a collisional distance between the stable solvent and solute molecules, i.e., the sum of geometrical radii, no cancellation holds between the interaction radius and the Stokes radius. Thus, the SES equation may be no more applicable to reactions of excited alkane molecules, and a constant and large value of $k_q\eta/T$ can be expected. A plausible explanation for

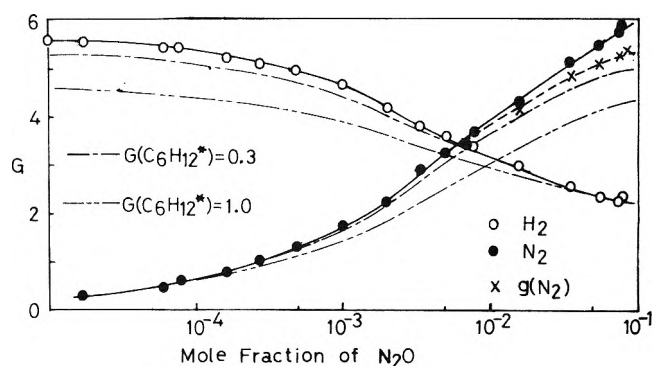


Figure 6. Yields of hydrogen and nitrogen produced in the radiolysis as a function of N_2O mole fraction. The corrected yields for the contribution from excited cyclohexane molecules are shown for $G(C_6H_{12}^*) = 0.3^{21}$ (---) and $G(C_6H_{12}^*) = 1.0^6$ (-.-.-).

the large value of the energy transfer rate constant may be offered as an excited alkane molecule has effectively a large interaction radius ($\sim 20 \text{ \AA}$) in liquid alkane, which is estimated from the Smoluchowski equation with the transient term. An expanded orbital or electrons in the excited alkane molecule would be imagined in liquid alkane. The fact reported by Lipsky et al.⁴ that the emission spectra of saturated hydrocarbons are displaced from their absorption spectra by unusually large energy gaps may support this view of an expanded molecule since large Stokes shifts imply severe nuclear distortion of the excited state. However, an expanded molecule may be somewhat speculative in view of that a considerably large expansion is required to account for the large rate constant. An expanded alkane excited state in the liquid phase, as described above, might not be differentiated essentially from the so-called geminate ion pair in liquid alkane. The exact state of affairs still remains obscure. Further work on this problem is clearly required.

Energy Transfer in the Radiolysis of Cyclohexane Solutions of Nitrous Oxide. Nitrous oxide has been widely used in the radiolysis of liquid hydrocarbons as an electron scavenger. The reaction of nitrous oxide with electron results in the formation of nitrogen and in the depression of the hydrogen yield from liquid cyclohexane. The yields of nitrogen and hydrogen¹¹ are shown as a function of the mole fraction of N_2O (Figure 6). The corrected yield of nitrogen, $g(N_2)$, for the direct radiolysis of N_2O at the higher N_2O concentration is also shown, taking $G(N_2)_0 = 10.4$ for pure N_2O .²⁰ It has been reported^{10,11} that the observed yield of nitrogen is greater than the expected yield of electron in the radiolysis of liquid cyclohexane and the decrease in the hydrogen yield corrected for the dose effect is smaller than the yield of nitrogen formed. Holroyd^{2b} has suggested that the "excess" nitrogen is attributed to energy transfer from excited cyclohexane to N_2O in the radiolysis. If the excited species formed in the radiolysis have properties similar to excited cyclohexane molecules formed in the photolysis, the possibility of which has already been discussed in the last section of this article, then an estimation of the yield of nitrogen, $G(N_2)_t$, formed by energy transfer in the radiolysis of cyclohexane solutions of N_2O is given by

$$G(N_2)_t = \frac{k_t[N_2O]}{k_t[N_2O] + \tau^{-1}} G(c-C_6H_{12}^*) \quad (IV)$$

$$= \frac{[N_2O]}{[N_2O] + \alpha^{-1}} G(c-C_6H_{12}^*)$$

where $G(c\text{-C}_6\text{H}_{12}^*)$ is the yield of the excited cyclohexane responsible for energy transfer to N_2O , τ is the lifetime of $c\text{-C}_6\text{H}_{12}^*$, and α is the energy transfer efficiency obtained from photolysis experiment to be $31 M^{-1}$. Thus, the amount of $G(\text{N}_2)_t$ is estimated from the yield of the excited cyclohexane in the radiolysis. Actually, it is not easy to experimentally determine the value of $G(c\text{-C}_6\text{H}_{12}^*)$. The value of $G(c\text{-C}_6\text{H}_{12}^*)$ has been tentatively estimated as 0.3²¹ or 1.0.⁶ The yields of hydrogen and nitrogen corrected for the contribution from the excited cyclohexane in each case are shown in Figure 6, where it is noted that the contribution of the energy transfer process to the yield of nitrogen, $G(\text{N}_2)_t$, predicted by eq IV appears at the low N_2O concentration (5×10^{-4} mole fraction of N_2O) and cannot be neglected at the higher concentrations. Generally, however, the excited states of alkanes in the liquid phase should be reconsidered.

References and Notes

- (1) (a) R. D. Doepker and P. Ausloos, *J. Chem. Phys.*, **42**, 3746 (1965); (b) R. R. Hentz and S. T. Rzad, *J. Phys. Chem.*, **71**, 4096 (1967).
- (2) (a) J. Y. Yang, F. M. Servadio, and R. A. Holroyd, *J. Chem. Phys.*, **48**, 1331 (1968); (b) R. A. Holroyd, *Adv. Chem. Ser.*, No. **82**, 488 (1968).
- (3) U. Laor and A. Weinreb, *J. Chem. Phys.*, **50**, 94 (1969).
- (4) F. Hirayama and S. Lipsky, *J. Chem. Phys.*, **51**, 3616 (1969); F. Hirayama, W. Rothman, and S. Lipsky, *Chem. Phys. Lett.*, **5**, 296 (1970); W. Rothman, F. Hirayama, and S. Lipsky, *J. Chem. Phys.*, **58**, 1300 (1973).
- (5) F. Hirayama and S. Lipsky in "Organic Scintillators", D. L. Horrocks, Ed., Academic Press, New York, N.Y., 1970, p 205.
- (6) G. Beck and J. K. Thomas, *J. Phys. Chem.*, **76**, 3856 (1972).
- (7) M. S. Henry and W. P. Helman, *J. Chem. Phys.*, **56**, 5734 (1972).
- (8) J. Nafisi-Movaghar and Y. Hatano, *J. Phys. Chem.*, **78**, 1899 (1974).
- (9) W. P. Helman, *Chem. Phys. Lett.*, **17**, 306 (1972).
- (10) (a) G. Scholes and M. Simic, *Nature (London)*, **202**, 895 (1964); (b) S. Sato, R. Yugeta, K. Shinsaka, and T. Terao, *Bull. Chem. Soc. Jpn.*, **39**, 156 (1966); (c) W. V. Sherman, *J. Chem. Soc. A*, 599 (1966); (d) N. H. Sagert and A. S. Blair, *Can. J. Chem.*, **45**, 1351 (1967); (e) J. M. Warman, K.-D. Asmus, and R. H. Schuler, *Adv. Chem. Ser.*, No. **82**, 25 (1968); (f) M. G. Robinson and G. R. Freeman, *J. Chem. Phys.*, **48**, 983 (1968); (g) P. O. Infelta and R. H. Schuler, *Int. J. Radiat. Phys. Chem.*, **5**, 41 (1973).
- (11) Y. Hatano, K. Takeuchi, and S. Takao, *J. Phys. Chem.*, **77**, 586 (1973).
- (12) G. R. Freeman and T. E. Sambrook, *J. Phys. Chem.*, **78**, 102 (1974).
- (13) T. Saito, K. Takahashi, and S. Sato, *Bull. Chem. Soc. Jpn.*, **41**, 2603 (1968).
- (14) L. C. Glasgow and P. Potzinger, *J. Phys. Chem.*, **76**, 138 (1972).
- (15) W. A. Cramer, *J. Phys. Chem.*, **71**, 1171 (1967).
- (16) J. R. McNesby and H. Okabe, *Adv. Photochem.*, **1**, 185 (1964).
- (17) J. W. Raymonda and W. T. Simpson, *J. Chem. Phys.*, **47**, 430 (1967).
- (18) (a) J. B. Birks, D. J. Dyson, and I. H. Munro, *Proc. R. Soc. London, Ser. A*, **275**, 575 (1963); (b) J. B. Birks "Photophysics of Aromatic Molecules", Wiley-Interscience, New York, N.Y., 1970.
- (19) A. H. Alwattar, M. D. Lumb, and J. B. Birks in "Organic Molecular Photo-physics", Vol. 1, Wiley-Interscience, New York, N.Y., 1973, p 403.
- (20) T. E. Sambrook and G. R. Freeman, *J. Phys. Chem.*, **78**, 32 (1974).
- (21) J. H. Baxendale and J. Mayer, *Chem. Phys. Lett.*, **17**, 458 (1972).

Photochemistry of 2-Benzoyl-3-phenylquinoxaline 1,4-Dioxide

N. A. Masoud and J. Olmsted, III*

Department of Chemistry, American University of Beirut, Beirut, Lebanon (Received December 26, 1974; Revised Manuscript Received June 9, 1975)

The basic photochemical and photophysical processes undergone by 2-benzoyl-3-phenylquinoxaline 1,4-dioxide (BPQO₂) have been studied in dilute ethanolic solutions under differing excitation and temperature conditions. Direct photolysis of BPQO₂ using 404-nm light at room temperature yields only one photoproduct, 1,3-dibenzoylbenzimidazolone (DBBI), formed monophotonically, with a quantum yield of 0.093. The remaining excited singlet BPQO₂ reverts to the ground state via internal conversion. At 313- and 254-nm excitation, fragmentation also occurs ($\phi = 0.03$), leading to ethyl benzoate. Quantum yields of BPQO₂ consumption are slightly temperature dependent ($E_a = 0.36$ kcal/mol), and in the glass at liquid nitrogen temperature an intermediate of lower conjugation than BPQO₂ can be observed. Triplet sensitization experiments show that the triplet state of BPQO₂, which is not populated by direct illumination, eliminates oxygen to yield 2-benzoyl-3-phenylquinoxaline. No DBBI is formed from the triplet state, and although the sensitized reaction is biphotonic, the monoxide is not formed in detectable amounts. Kinetic behavior of the triplet-sensitization experiments suggests a substrate-solvent complex which is thermally unstable as an intermediate in the two-photon deoxygenation.

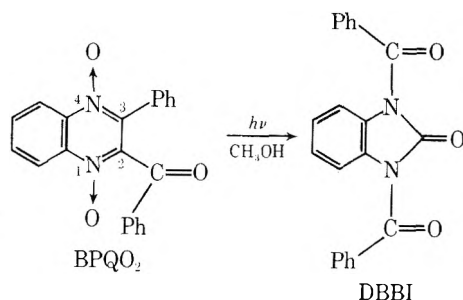
Introduction

Aromatic amine *N*-oxides can undergo a wide variety of primary and secondary photochemical reactions. Unlike in the case of aliphatic nitron photochemistry, where the three-membered oxaziridine intermediate has been identified, the nature of intermediates and the photophysical pathways of energy degradation for these compounds has remained a matter of uncertainty,¹ although the excited singlet state and an oxaziridine intermediate have usually been implicated in the reaction mechanism.^{1,2} However, recent work on isoquinoline *N*-oxides³ and on 1,2-diazine *N*-

oxides⁴ has failed to provide evidence for oxaziridines and elimination of NO from di- and triazine *N*-oxides has been interpreted as evidence for a C-N-N three-membered ring intermediate.^{5,6} The role of the triplet state in *N*-oxide photolysis has not been particularly examined, although Spence, Taylor, and Buchardt conclude in their review¹ that deoxygenation probably arises from a different excited state than does rearrangement.

Although quinoxaline 1,4-dioxides were the first of the aromatic amine *N*-oxides to be studied photochemically,⁷ 1,4-dioxides have received considerably less attention than monooxides. One reaction which has been reported to pro-

ceed in high yields⁸ is the extensive rearrangement of 2-benzoyl-3-phenylquinoxaline 1,4-dioxide (BPQO₂), upon irradiation in methanol, to give 1,3-dibenzoylbenzimidazolone (DBBI). In the present work we have undertaken to ex-



amine the photoprocesses involved in this reaction in greater detail and to relate the results to the photochemistry of other aromatic amine *N*-oxides. Ethanol was used as solvent rather than methanol because of its greater stability as a low-temperature glass.

Experimental Section

2-Benzoyl-3-phenylquinoxaline 1,4-dioxide (BPQO₂),⁹ 2-benzoyl-3-phenylquinoxaline (BPQ),¹⁰ and 1,3-dibenzoylbenzimidazolone (DBBI)¹¹ were prepared following techniques described in the literature. 2-Benzoyl-3-phenylquinoxaline 4-oxide was kindly provided by Professor M. J. Haddadin. Quinoline (K and K) was column chromatographed on alumina before use as a sensitizer. Other chemicals were of commercial purity, and all solvents were fractionally distilled to free them of possible luminescent impurities.

Photolyses were carried out using a 100-W Hg lamp and solution filters to isolate particular lines. Substrate disappearance was determined by measuring the attenuation of absorbance at 390 nm, or in low temperature glass by following luminescence decay. Low temperature photolyses were carried out utilizing unsilvered-tip Pyrex dewars in which the samples were immersed in organic solvent slush baths, liquid O₂, or liquid N₂. Light intensities were measured using standard ferrioxalate actinometry.

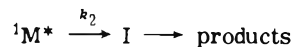
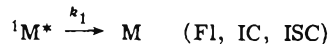
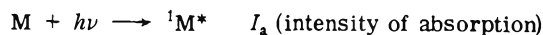
Product yields were determined from low-temperature luminescence intensities of photolyzed samples, to which, following photolyses, a measured amount of Rhodamin-B had been added as an internal standard. Product concentrations were found by comparing luminescence ratios for photolyzed solutions with those of standard solutions containing product and Rhodamin-B in known amounts. Yields were then calculated by comparing substrate disappearance, determined spectrophotometrically, with product appearance. Absorbance measurements were taken on a Perkin-Elmer Model 450 VIS-UV spectrophotometer.

Luminescence measurements were carried out on a Baird-Atomic SF-1 Fluorispec modified in its sample compartment to accept a cylindrical unsilvered-tip dewar flask in which samples were placed for low-temperature work. Luminescence lifetimes were measured using a Suntron-2 flash tube driven by a Xenon Corp. Model B micropulse unit. Decays were displayed and photographed on a Tektronix 551A oscilloscope.

Results

A. Direct Photolysis. The kinetic rate law for direct photolysis of BPQO₂ can be analyzed on the basis of a relative-

ly simple reaction scheme, utilizing the experimental observations (described below) that the reaction is monophotonic, involves the excited singlet state, and proceeds via an intermediate. We assume the following generalized reaction scheme:



where *M* represents the starting material and *I* represents the intermediate.

The rate of disappearance of *M* is given by

$$-d[M]/dt = I_a \phi_d$$

where $\phi_d = k_2/(k_1 + k_2)$ is the quantum yield of disappearance of the reactant. If *I*₀ represents the intensity of the incident light, *I*_T represents the intensity of the transmitted light, ϵ represents the extinction coefficient of the starting material, *M*, at the wavelength of the monochromatic light used for irradiation, and *l* is the path length of light, then

$$I_a = I_0(1 - 10^{-\epsilon l [M]}) \\ = I_0(1 - e^{-2.3 \epsilon l [M]})$$

$$d[M]/dt = -\phi_d I_0(1 - e^{-2.3 \epsilon l [M]}) \\ = n(1 - e^{-m [M]})$$

where $n = -\phi_d I_0$ and $m = 2.3 \epsilon l$. Rearrangement gives

$$\frac{m e^{m [M]} d[M]}{e^{m [M]} - 1} = n m dt$$

which integrates to

$$\ln(e^{m [M]} - 1) = n m t + \text{constant}$$

Resubstituting the values of *m* and *n* gives

$$\ln(e^{2.3 \epsilon l [M]} - 1) = -2.3 \epsilon l \phi_d I_0 t + \text{constant}$$

The above equation can be simplified further to

$$\log\left(\frac{1}{T} - 1\right) = -\epsilon l I_0 \phi_d t + \text{constant}$$

where *T* is the transmittance of the reactant at the wavelength of the monochromatic light used for irradiation at any photolysis time, *t*.

Plotting $\log [(1/T) - 1]$ vs. *t* should give a straight line the slope of which is $-\epsilon l I_0 \phi_d$.

Ethanol solutions of BPQO₂ of concentration $\sim 10^{-4}$ *M* were photolyzed using 405-nm light under differing conditions of incident light intensity, temperature, and oxygen concentration. The rate of disappearance of starting material was determined by monitoring the absorbance at the maximum of the S₀ → S₁ absorption band (λ 390 nm, ϵ 1.22 × 10⁴ M⁻¹ cm⁻¹). Linearity of $\log (T^{-1} - 1)$ vs. *t* plots was observed at temperatures where the solvent remained liquid as is illustrated in Figure 1. The quantum yields of BPQO₂ disappearance were computed from slopes of these plots.

Low-temperature luminescence spectra were used to identify the major photoproduct which was DBBI. Luminescence intensities, normalized to the fluorescence intensity of Rhodamine-B added to the samples as an internal standard and compared to the luminescence intensity of an authentic chemical sample of DBBI in ethanol, were used to compute the percent formation of the photoproduct fol-

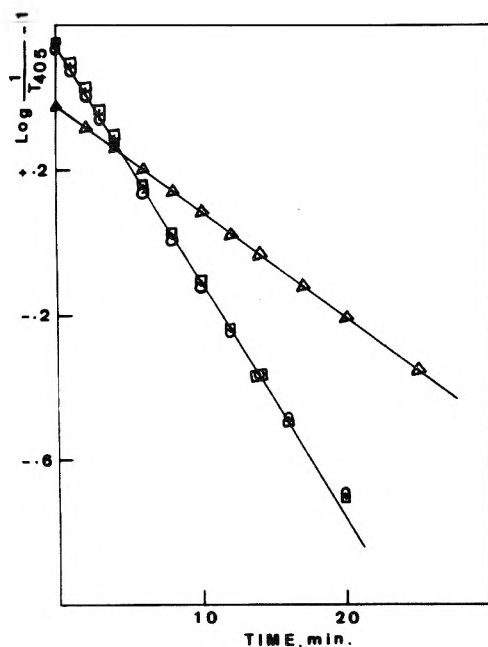


Figure 1. Variation with time of the rate of disappearance of BPQO₂ in ethanol at room temperature and 405-nm excitation: (○) de-gassed solution, $I_0 = 1.57 \times 10^{-6}$ einstein/l. sec; (□) O₂-saturated solution, $I_0 = 1.57 \times 10^{-6}$ einstein/l. sec; (△) air-saturated solution, $I_0 = 6.68 \times 10^{-7}$ einstein/l. sec.

lowing total photolysis (measured by disappearance of the BPQO₂ absorbance peak) of the substrate.

Quantum yields for BPQO₂ and yields of DBBI were found to be independent of incident light intensity, concentration of oxygen in the solution, and the presence of pyrene as a triplet quencher. A temperature dependence was, however, observed as was also a dependence on photolysis wavelength (see below).

When glassy solutions of BPQO₂ were photolyzed (liquid O₂ or liquid N₂ temperatures), qualitatively different behavior was observed. The rate of disappearance of substrate was no longer first order but instead showed a reduction with photolysis time, as illustrated in Figure 2. In addition, DBBI did not form (no luminescence was detected from the photolyzed glass) but instead a nonluminescent intermediate resulted whose absorption spectrum is shown in Figure 3. Storage of the sample in the dark at low temperature for up to 2 hr resulted in neither regeneration of substrate nor formation of products, indicating that the intermediate formed was stable in the glass. Upon warming to room temperature and then refreezing, the sample exhibited the characteristic emission spectrum of DBBI superimposed, however, upon emissions of an unidentified additional product or products. Although the rate of substrate disappearance was not constant, the ratio of quantum yields for liquid N₂ and liquid O₂ photolysis, for equal percent reaction from 0 to 40%, was a constant; moreover, the fraction of consumed substrate converted to DBBI was the same for total photolysis as for partial (28%) photolysis.

The appearance of an intermediate in low-temperature photolysis suggested the possibility of an observable intermediate at room temperature, which was searched for utilizing conventional flash photolytic techniques and monitoring the solution absorbance immediately after the flash. Although the low-temperature intermediate exhibited significant absorbance in the 300–350-nm range, no transient

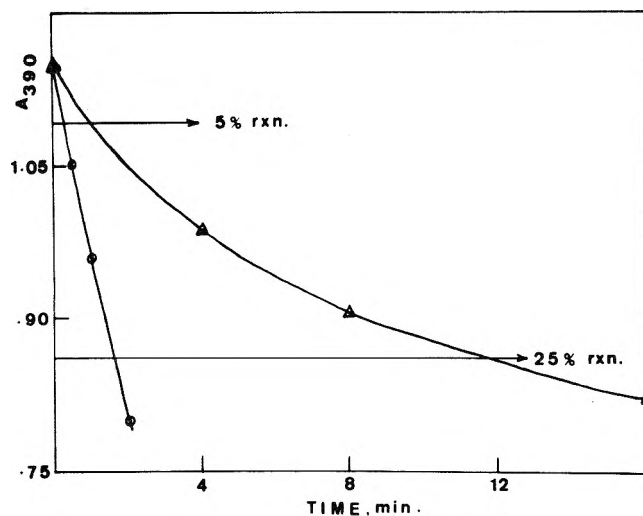


Figure 2. Comparison of photolysis of BPQO₂ in ethanol at room temperature (○) and at liquid oxygen temperature (△).

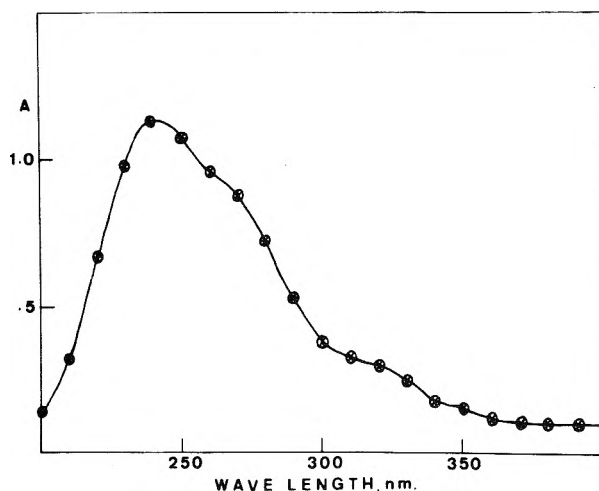


Figure 3. Absorption spectrum of intermediate formed upon irradiation of BPQO₂ in low-temperature ethanolic glass.

absorbance signal could be observed at room temperature between 300 and 700 nm (below 300 nm, substrate absorbance was too high to permit measurements).

In addition to photolysis in the S₁ manifold at 405 nm, BPQO₂ was also photolyzed utilizing higher energy photons (313 and 254 nm) which excited the system to higher singlet states. These photolyses were complicated somewhat by the fact that DBBI also significantly absorbs and itself undergoes photolysis at these wavelengths. Quantum yields and percent formation of DBBI therefore were determined under partial photolysis conditions (<35% consumption at 313 nm, <20% consumption at 254 nm). In addition to DBBI and a low-temperature emitter which was ascertained to be a photoproduct of DBBI by photolyzing a pure sample of DBBI, a third product exhibiting room-temperature fluorescence in the 330–380-nm range was formed. This new product, which was formed at both 313 and 254 nm, did not form in DBBI photolysis and must, therefore, arise from BPQO₂ itself. Its fluorescence spectrum (λ_{max} 360 nm, shoulders at 328, 343, and 375 nm) and the emission spectrum of ethyl benzoate in ethanol are closely similar, indicating that the new photoproduct is ethyl benzoate

TABLE I: Direct Photolysis of 2-Benzoyl-3-phenylquinoxaline 1,4-Dioxide^a

λ_{excit} , nm	Temp, K	ϕ_D^b	DBBI formed, ^c %	Notes
404	298	0.099	97	Air saturated
404	298	0.093	100	Degassed
404	298	0.093	96	O ₂ saturated
404	210	0.073	82	
404	178	0.063	73	
404	90	0.027		Glassy, initial rate
404	77	0.017	38	Rel. to 90 K rate
313	298	0.13	77	< 35% reaction
254	298	0.13	30 ^d	< 20% reaction

^a Ethanol solvent, substrate concentration $\sim 10^{-4}$ M, light intensity $\sim 10^{-6}$ einstein/l. sec. ^b Quantum yield for disappearance of substrate; ascertained to be independent of incident light intensity. ^c Percent of consumed substrate which appears as DBBI product. ^d Low owing to photolysis of DBBI by 254-nm light.

arising from reaction of highly excited substrate molecules with the ethanolic solvent. This observation is in agreement with the observation that methyl benzoate, identifiable both through its characteristic odor and by gas chromatographic analysis, forms upon irradiation of BPQO₂ solutions in methanol.^{12b}

Results of these experiments are summarized in Table I.

B. Sensitized Photolysis. Sensitized photolyses of BPQO₂ in ethanol at room temperature were carried out using two different triplet sensitizers: biacetyl and quinoline. When biacetyl sensitizer was used, 436-nm excitation was employed and the course of the reaction was followed by monitoring the solution absorption spectrum. As photolysis proceeded the BPQO₂ absorbance peak disappeared and a new absorbance developed with λ_{max} at around 335 nm, which is the wavelength at which both the quinoxaline monoxide (BPQO) and the deoxygenated compound (BPQ) absorb. Although BPQ is a strong luminescer at low temperature while BPQO luminesces only weakly, it was not possible to differentiate between these two possible products nor to search for the presence of DBBI owing to the strong interfering luminescence of biacetyl.

Further sensitization experiments were therefore undertaken using quinoline as sensitizer and 313-nm excitation, with quinoline concentrations sufficiently high ($>10^{-3}$ M) to ensure negligible absorption of exciting light by the substrate. Since quinoline absorbs negligibly at wavelengths greater than about 320 nm, it was possible in these experiments to follow both the disappearance of substrate and the appearance of product spectrophotometrically; and the product could also be identified by its low-temperature luminescence spectrum.

Substrate disappearance and product appearance were found to be directly correlated, with a well-defined isosbestic point occurring in the absorption spectra (Figure 4). However, the kinetics of substrate disappearance, which was determined using crossed-beam illumination to allow simultaneous continuous photolysis at 313 nm and monitoring of absorbance at 390 nm, was found to be complex. As illustrated in Figure 5, the rate of disappearance, initially rather slow, showed a distinct acceleration with time. Deliberate addition of BPQO or BPQ to the sample did not

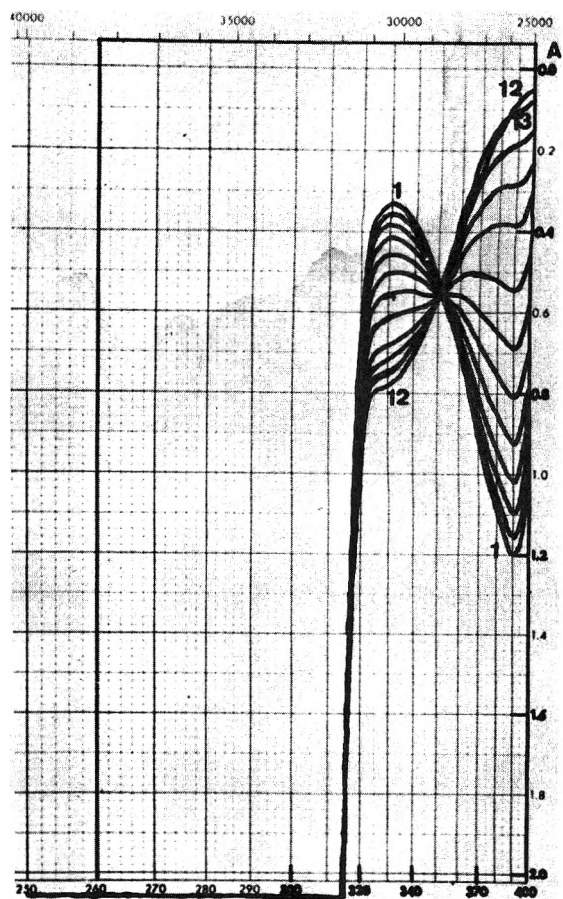


Figure 4. Absorption spectra of BPQO₂ undergoing triplet-sensitized photolysis in the presence of quinoline sensitizer: (curve 1) before photolysis; (curves 2-12) spectra after successive 2-min photolyses using 313-nm light; (curve 13) spectrum after an additional 22-min photolysis.

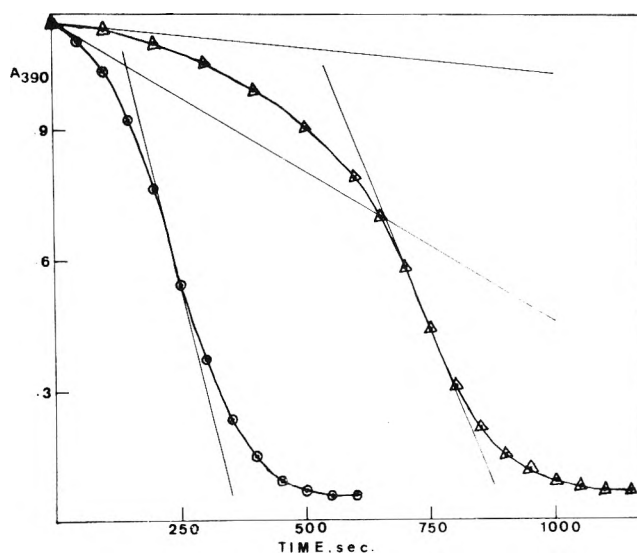


Figure 5. Disappearance of BPQO₂ during quinoline-sensitized photolysis in ethanol at room temperature. Tangents drawn to approximate initial and maximum rates: (O) $I_a = 6.53 \times 10^{-7}$ einstein/l. sec; (Δ) $I_a = 2.36 \times 10^{-7}$ einstein/l. sec.

result in any rate enhancement indicating that the phenomenon is not autocatalysis. On the other hand, interrup-

TABLE II: Summary of Triplet Photosensitized Reaction Rates^a

Starting conc of BPQO ₂ , 10 ⁻⁵ M	Light intensity, 10 ⁻¹ einstein/l. sec	Initial rate, 10 ⁻¹ ΔA/Δsec	Maximum rate, 10 ⁻³ ΔA/Δsec
6.24	6.53	-6.9	-4.1
9.36	6.53	-6.8	-4.9
12.5	6.53	-6.5	-5.8
9.36	2.63	-1.1	-2.8

^a Quinoline sensitizer, ethanol solvent, room temperature.

tion of photolysis for periods of 1–2 hr during which the sample was stored in the dark, while not effecting any change in the absorption spectrum, resulted in a distinct reduction in photolysis rate. Biacetyl-sensitized experiments also showed this effect, indicating that the phenomenon is not an artifact of the quinoline–BPQO₂ system.

Table II summarizes how the initial and maximum rates of BPQO₂ disappearance depend on substrate concentration and light intensity. The initial rate can be seen to be independent of substrate concentration and to vary with the square of light intensity, while maximum rate, qualitatively, depends on both concentration and intensity.

To ascertain which of the possible photoproducts, BPQO or BPQ, was being formed, quantitative comparisons were made between the low-temperature luminescence of photolyzed solutions and the luminescence of authentic chemically prepared samples of the two compounds. Although absorption and luminescence spectra of BPQO and BPQ are closely similar, the former has a very low luminescence efficiency while the latter emits relatively much more efficiently. Calculation of the percent yield of product from the luminescence intensity of either partially or totally photolyzed samples, assuming BPQ to be the sole photoproduct, gave yields of 100 ± 3%. Since the presence of the lower efficiency emitter would lead to an increase of yield over the calculated value, we conclude that only BPQ is formed in the triplet photosensitized reaction.

C. Luminescence Parameters. Luminescence spectra of BPQO₂ and the major possible photoproducts, DBBI, BPQ, and BPQO, were investigated both at room temperature and at low temperature. None of the compounds showed any significant emission at room temperature, and BPQO showed only faint luminescence at liquid air temperature which may have been due to the presence of some BPQ as impurity. The luminescence spectra of the other three compounds is shown in Figure 6. Lifetime measurements at liquid air temperature gave $\tau = 0.11$ sec for DBBI, $\tau = 0.40$ sec for BPQ, and $\tau < 0.1$ msec (the lifetime of the flash) for BPQO₂, indicating that the two photoproducts phosphoresce whereas the starting material is a low-temperature fluorescer.

Discussion

Information obtained in this work concerning the room-temperature photophysical and photochemical properties of BPQO₂ are summarized in Figure 7. The major observations are the following. (1) Excitation into S₁ at room temperature yields only DBBI with a quantum yield of 0.10. The reaction is monophotonic. (2) Excitation of higher singlet states yields both DBBI and another product, probably ethylbenzoate, with the quantum yield of substrate disap-

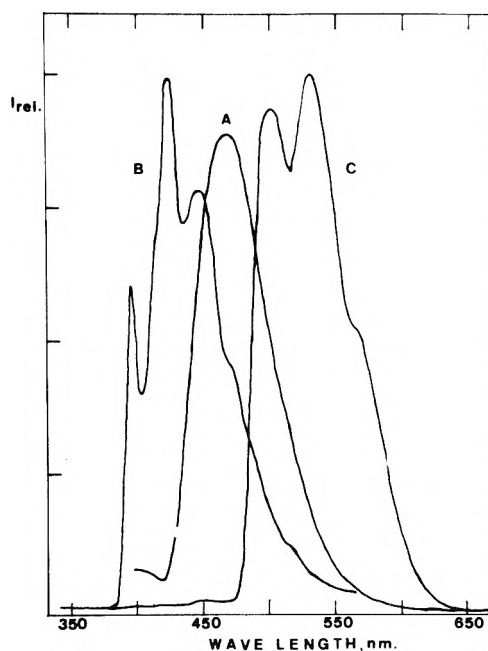


Figure 6. Emission spectra at liquid air temperature: (A) BPQO₂; (B) DBBI; (C) BPQ (not corrected for wavelength variation of photomultiplier tube response).

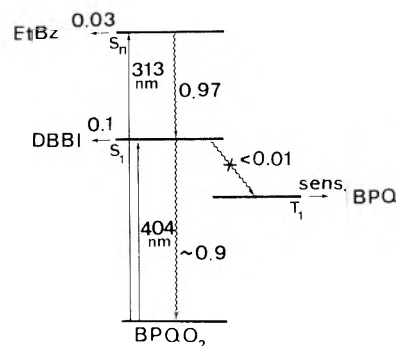


Figure 7. Summary of photophysical and photochemical processes of BPQO₂ (EtBz = ethyl benzoate).

pearance rising to 0.13. (3) Triplet-sensitized photochemistry yields only BPQ. (4) Phosphorescence is not observed, and fluorescence only occurs at temperatures where the solvent is glassy.

From these data, we conclude that, at room temperature, the first excited singlet state of BPQO₂ either rearranges to DBBI ($\phi = 0.10$) or internally converts back to the ground state. A higher excited singlet state S_n can undergo a different photochemical reaction, probably solvent attack ($\phi = 0.03$), in competition with internal conversion to S₁. The triplet state is not populated directly and thus plays no role in the direct photochemistry of the system.

As the temperature is reduced, the picture becomes more complex; the photochemical quantum yield is reduced, indicating an activation energy barrier for the photochemical primary process which is calculated from an Arrhenius plot of the relative rates to be 0.36 kcal/mol. Furthermore, not all of the consumed substrate converts to DBBI, indicating a competitive reaction, probably requiring substantial redistribution of excitation energy (i.e., occurring from a non-Franck-Condon configuration) and thus having a small

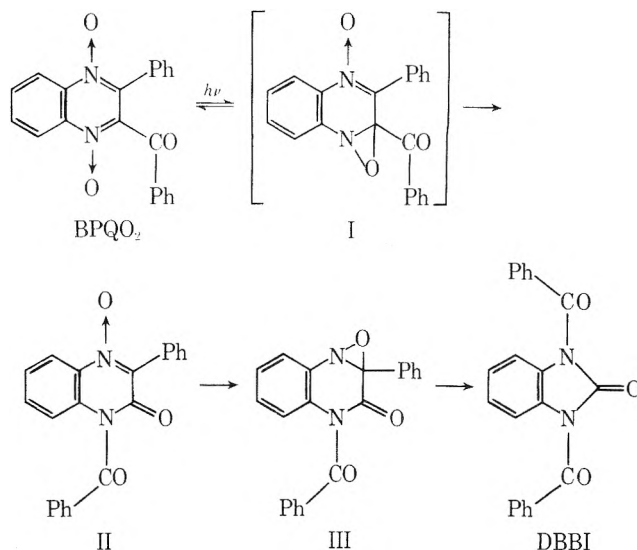
preexponential factor. At lower temperatures, this competing reaction becomes evident as the rate of the DBBI reaction is reduced. Finally, the appearance of fluorescence at low temperature indicates that the internal conversion rate is temperature dependent, or possibly that internal conversion occurs more readily from the equilibrated configuration than from the adiabatic (Franck-Condon) one, so that at high solvent viscosity (in the glass) fluorescence can occur.

The low-temperature observations show also that DBBI is not formed directly but through an intermediate which is stable in glassy solvent. Moreover, from the decrease in rate with percent photolysis observed in the glass, we infer that the intermediate itself has undergone steric changes which are hindered by certain conformations of the solvent cage; as those substrate molecules in more favored environments become photolyzed, the rate for the remaining molecules is reduced. From the absorbance spectrum of the low-temperature intermediate (Figure 3), it is evident that its structural alterations involve some loss of conjugation. Since warming of the intermediate yields less than quantitative conversion to DBBI, it is not certain that the same intermediate is involved in the low- and room-temperature reactions, especially since no transient absorption was observed at room temperature.

Nonetheless, the quantitative and monophotonic nature of the room-temperature reaction implies restrictions on the possible mechanisms. One can readily envisage only three possible initiating processes for the photochemical transformation: oxygen migration from the 1 to the 2 position (migration from the 4- to the 3-phenyl-substituted position is ruled out by observations that 2,3-diphenylquinoxaline di-*N*-oxide fails to undergo the ring-contraction reaction¹²); fragmentation, probably involving release of a benzoyl free radical; or ring opening, which would have to occur at the 2,3 bond to account for the absence of ring expansion. Fragmentation is ruled out by the nearly quantitative conversion to DBBI, which would not be expected if the molecule is fragmenting, especially in view of the formation of other products, including ethyl benzoate, using higher energy light that is more likely to cause bond cleavage. Ring opening seems extremely unlikely since the quinoxaline ring system is highly resonance stabilized; moreover, it is difficult to reconcile the observed quantitative conversion to DBBI with the highly reactive species which would result from ring opening.

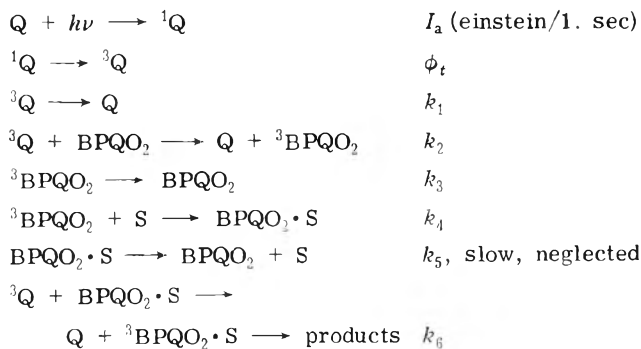
Oxygen migration, therefore, seems to be the only initiating step that is consistent with the experimental results; yet recent work on other *N*-oxides has cast some doubt on oxaziridine formation as the means of oxygen migration.^{3,4} We suggest that the reason for failure to observe the oxaziridine in aromatic systems arises out of the highly strained nature of the three-membered ring coupled to the planar aromatic nucleus, which favors rapid return to starting material or conversion by rearrangement. The following mechanism seems reasonable, although other possibilities, such as simultaneous formation of two oxaziridine three-membered rings followed by rearrangement, cannot be ruled out.

Intermediate I, an oxaziridine, is postulated as unstable with respect to either BPQO₂ (this could be the mechanism for internal conversion of BPQO₂) or intermediate II, and the reduced efficiency of photolysis at lower temperatures would be due to the activation energy for conversion from I to II. The apparent site effect in glassy solvent is also explained by solvent cage hindrance of the benzoyl migration



in going from I to II. Intermediate II, which was also proposed by Haddadin and Issidorides,⁸ might be the intermediate observed at low temperature if the absorbance tail observed in the 300–350-nm region represents the transition to first excited singlet. Failure to observe it at room temperature would be consistent with its apparent instability as evidenced by unsuccessful attempts to prepare it.⁹ Its transition to intermediate III and subsequently to DBBI is analogous to the BPQO₂ → II conversion and can be viewed as favored by the β-keto nitron configuration of II.

The most striking features of the triplet-sensitized deoxygenation reaction are its biphotonic nature and the intermediate which forms. The intermediate in this case has an absorption spectrum that is indistinguishable from starting material, and it reverts to starting material in the dark over a 1–2-hr period. Some kind of “loose” complex with solvent would be expected to have such characteristics,¹³ and could be either charge transfer or hydrogen bonding in nature. We propose the following scheme (Q = quinoline, S = solvent):



Applying the steady state approximation for [³Q] and [³BPQO₂] yields

$$\begin{aligned}
 \phi_t I_a &= \{k_1 + k_2[\text{BPQO}_2] + k_6[\text{BPQO}_2 \cdot S]\} [{}^3Q] \\
 [{}^3Q] &= \frac{\phi_t I_a}{k_1 + k_2[\text{BPQO}_2] + k_6[\text{BPQO}_2 \cdot S]} \approx \text{constant}
 \end{aligned}$$

and

$$\begin{aligned}
 k_2[\text{BPQO}_2][^3\text{Q}] &= (k_3 + k_4)[^3\text{BPQO}_2] \\
 [^3\text{BPQO}_2] &= \frac{k_2[\text{BPQO}_2][^3\text{Q}]}{k_3 + k_4} \\
 \frac{-d[\text{BPQO}_2]}{dt} &= k_4[^3\text{BPQO}_2] \\
 &= \frac{k_2k_4[^3\text{Q}][\text{BPQO}_2]}{k_3 + k_4} \\
 &= k_7[\text{BPQO}_2]
 \end{aligned}$$

where

$$k_7 = \frac{k_2k_4[^3\text{Q}]}{k_3 + k_4}$$

This is a first-order rate equation which, upon integration, gives

$$[\text{BPQO}_2] = X_0 e^{-k_7 t}$$

where X_0 is the initial concentration of BPQO_2 .

$$\begin{aligned}
 \frac{d[\text{BPQO}_2 \cdot \text{S}]}{dt} &= k_4[^3\text{BPQO}_2] - k_6[^3\text{Q}][\text{BPQO}_2 \cdot \text{S}] \\
 &= \frac{k_4k_2[^3\text{Q}][\text{BPQO}_2]}{k_3 + k_4} - k_6[^3\text{Q}][\text{BPQO}_2 \cdot \text{S}]
 \end{aligned}$$

The kinetic analysis from this point on is readily derived from analogous thermal reaction schemes;¹⁴ the progress curve expected for the reaction is exactly that observed ex-

perimentally (Figure 5). Whether the final step yields molecular oxygen or solvent oxidation products such as acetaldehyde is uncertain, but a stepwise deoxygenation by way of the monoxide is ruled out by our failure to observe any monoxide product even under partial deoxygenation conditions.

Acknowledgments. This work is derived from the Ph.D. dissertation of Mr. Masoud, AUB, June 1974. We are indebted to Professor M. J. Haddadin for many fruitful discussions and suggestions as well as for the gift of several chemicals.

References and Notes

- (1) G. G. Spence, L. C. Taylor, and O. Buchardt, *Chem. Rev.*, **70**, 231 (1970).
- (2) F. Bellamy, P. Martz, and J. Streith, *Tetrahedron Lett.*, 3189 (1974).
- (3) C. Lohse, *J. Chem. Soc., Perkin Trans. 2*, 229 (1972).
- (4) K. B. Tomer, N. Harrit, I. Rosenthal, O. Buchardt, P. L. Kumler, and D. Creed, *J. Am. Chem. Soc.*, **95**, 7402 (1973).
- (5) W. H. Horspool, J. R. Kershaw, and A. W. Murray, *J. Chem. Soc., Chem. Commun.*, 345 (1973).
- (6) W. H. Horspool, J. R. Kershaw, A. W. Murray, and G. M. Stevenson, *J. Am. Chem. Soc.*, **95**, 2390 (1973).
- (7) J. K. Landquist, *J. Chem. Soc.*, 2830 (1953).
- (8) M. J. Haddadin and C. H. Issidorides, *Tetrahedron Lett.*, 753 (1967).
- (9) M. J. Haddadin, G. Agopian, and C. H. Issidorides, *J. Org. Chem.*, **36**, 514 (1971).
- (10) C. H. Issidorides and M. J. Haddadin, *J. Org. Chem.*, **31**, 4067 (1966).
- (11) O. Christmann, *Chem. Ber.*, **98**, 1282 (1965).
- (12) (a) A. A. Jarrar, Ph.D. Dissertation, American University of Beirut, July 1971. (b) A. A. Jarrar and S. Halawi, unpublished observations.
- (13) P. R. Hammond and L. A. Burkardt, *J. Phys. Chem.*, **74**, 639 (1970).
- (14) A. A. Frost and R. G. Pearson, "Kinetics and Mechanisms", 2nd ed, Wiley, New York, N.Y., 1961, p 166.

On the Photochemistry of Radicals Trapped in Frozen Methanol–Water Mixtures

Johan Moan* and Bjørn Høvik

Norsk Hydro's Institute for Cancer Research, Montebello, Oslo 3, Norway (Received January 10, 1975;
Revised Manuscript Received May 27, 1975)

Publication costs assisted by the Norsk Hydro's Institute for Cancer Research

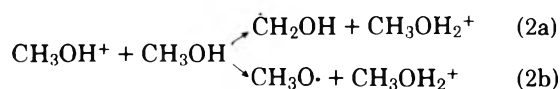
Methanol–water mixtures were exposed to X-rays at 77 K and the photochemistry and paths of conversion of the induced radicals were investigated by ESR methods. The main X-ray induced radical, the hydroxymethyl radical, is photolyzed by uv light to give $\dot{\text{C}}\text{H}_3$ and $\dot{\text{C}}\text{H}\text{O}$ radicals and H atoms. The $\dot{\text{C}}\text{H}\text{O}$ radicals give rise to $\dot{\text{C}}\text{H}_2\text{OH}$ and H atoms when bleached by visible light and to another radical, possibly the methoxy radical, when annealed. Uv irradiation of this radical gives back $\dot{\text{C}}\text{H}\text{O}$ radicals and $\dot{\text{C}}\text{H}_2\text{OH}$ radicals. The methyl radicals give rise to $\dot{\text{C}}\text{H}_2\text{OH}$ radicals, and possibly also $\dot{\text{C}}\text{H}\text{O}$ radicals when decaying at 77 K. The uv irradiation seems to cause photoionization of the hydroxymethyl radical. X-Irradiation gives rise to somewhat different spectra in glassy and polycrystalline matrices. In the latter case a narrow ($\Delta H = 3.4 \pm 0.6$ G) singlet spectrum is formed which is not seen in glassy matrices. This singlet may be due to electrons in shallow traps, since it is eliminated by the presence of an electron scavenger (H_2O_2).

Introduction

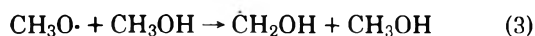
Methanol as well as other alcohol glasses are frequently used as trapping matrices in radiation and photochemical studies. Since the work of Alger et al.¹ on irradiation effects in frozen alcohols, this subject has received considerable at-

tention. Generally electrons and H-abstraction radicals $\dot{\text{R}}\text{CHOH}$ of the alcohols are formed by ionizing radiation. In the case of methanol this may be explained in the following:²⁻⁴

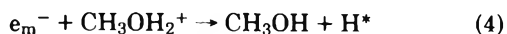




The work of Sargent et al.⁵ where 2-methyl-2-nitrosopropane was used as a spin trap seems to show that methoxy and hydroxymethyl radicals are formed in about equal amounts. Qualitatively, this is in accordance with the findings of Mao and Kevan⁶ who used phenyl *tert*-butyl nitron as a spin trap. Since methoxy radicals are not observed in X-irradiated frozen methanol matrices they probably give rise to hydroxymethyl radicals:



The trapped electrons, e_t^- , absorb in a broad band around 533 nm³ and when bleached they give rise to hydroxymethyl radicals with a probability close to unity supposedly by the reactions^{3,7}



The hydroxymethyl radical has an absorption spectrum extending into the ultraviolet³ and photolysis at 254 nm gives rise to the formyl radical:^{1,8}



The formyl radical may probably be photolyzed to give carbon monoxide and hydrogen atoms,⁸ the latter being able to abstract a hydrogen atom from methanol according to (5). Additionally it seems reasonable that photolysis of $\dot{\text{C}}\text{H}_2\text{OH}$ radicals give methyl radicals since the methane yield of an X-irradiated sample is enhanced by almost an order of magnitude if the sample is subjected to uv irradiation.⁸ Methyl radicals are found in uv-irradiated matrices of methanol.⁹

The role of H atoms in the photochemistry and radiation chemistry of frozen alcohols is poorly known, since these matrices do not trap H atoms either at 77 K or at 4 K. However, when water is added to the alcohol, H atoms may become stabilized at certain mole fractions. According to Hase and Kevan's work¹² hydrogen atoms are trapped when the mole fraction of methanol is between 0.2 and 0.5. By the use of such matrices we have tried to elucidate the role of the H atoms in the radiolysis of alcohols. We also present data which shed light on other photochemical reactions and paths of radical conversion in methanol-water matrices.

Experimental Section

Methanol, p.a. reagent from Merck, was mixed with doubly distilled water to the following volume ratios: M/H₂O = 96/4, 6/1, and 1/1 corresponding to the mole fractions 0.91, 0.73, and 0.31 of methanol. These mixtures gave transparent glasses at 77 K. Pellets of sample solution were prepared by allowing drops of 15- μ l volume to fall into liquid N₂. Because of this procedure the samples were not degassed. The pellets were kept in small plastic cups, irradiated with X-rays (220 keV, 3 krads/min) to a dose of 90 krads and transferred to quartz ESR tubes, all the time kept immersed in liquid N₂ and shielded from light. Annealing of the samples was carried out by placing the ESR tubes in a thermoregulated copper block kept at the appropriate temperature. The temperature in the pellets will probably be a few degrees lower than that in the copper block at the annealing times used in this work (1-5 min). The source of uv and visible light was a 200-W high-pres-

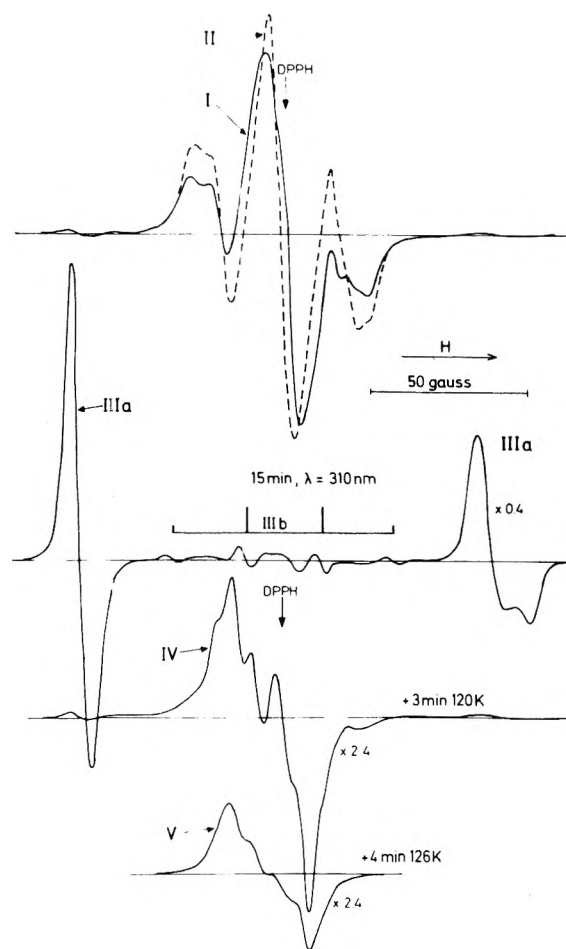


Figure 1. X-Ray induced ESR spectra of a glassy methanol-water mixture 6:1 by volume: (I) spectrum observed immediately after X-irradiation; (II) spectrum of the same sample after optical bleaching (λ 580 nm) for 1 min; (III) the same sample subjected to 15-min irradiation by 310-nm light. Annealing of the sample gives to the spectra IV and V. All the spectra are registered at 77 K.

sure mercury lamp fitted to a Bausch and Lomb grating monochromator. The light was focused on the sample by a 5-cm quartz lens, and the light intensity on the sample was of the order of 10^{-9} einstein/mm² sec as measured by a calibrated thermopile.

The ESR spectrometer was an X-band type with transmission cavity and 110-kHz field modulation.

Results

Figure 1 shows the initial X-ray induced spectrum of a glassy methanol-water mixture 6:1 by volume (M/H₂O = 6/1). Almost the same spectrum was found in matrices with M/H₂O = 1/1 and M/H₂O = 96/4. However, the central line of the spectrum was somewhat less intense in a sample with small water content, and the blue coloring of the sample was also less intense. If a sample with M/H₂O = 1/1 is annealed for a few minutes at 170 K it becomes white and polycrystalline. Such a sample has a different X-ray induced ESR spectrum as shown in Figure 2. The blue coloring is weak and the central line, part of which is bleachable with visible light λ \sim 700 nm is only 3.4 ± 0.6 G wide (Figure 2). The singlet is not found when 0.05 M of an electron scavenger is present (H₂O₂). In all cases when the samples are bleached with visible light the blue coloring disappears and the intensity of the triplet spectrum shown in Figures 1

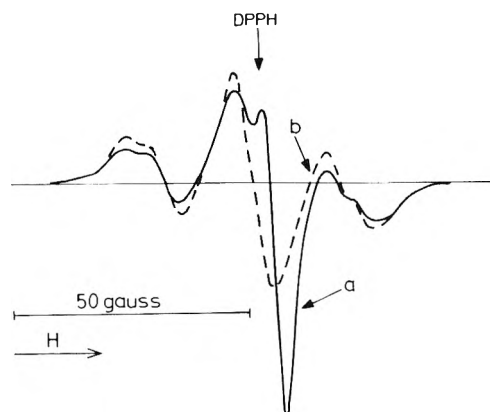


Figure 2. X-Ray induced ESR spectrum of a polycrystalline sample of methanol and water in volume ratio 1:1. The polycrystalline sample is obtained by annealing a glassy sample for 5 min at 170 K. (a) and (b) are the spectra before and after optical bleaching, respectively; recorded at 77 K.

and 2 increases. The total number of radicals was found to be unaffected by the bleaching. If the X-irradiated samples are annealed, until the coloring just disappears, the triplet is constant or decreases slightly in mixtures with low water content ($M/H_2O = 96/4$ or $6/1$). This is not the case in the matrix with $M/H_2O = 1/1$ where the triplet spectrum increased by about $20 \pm 5\%$ in the temperature region where the coloring disappears. It was found that all observed radicals were more stable on annealing in the matrix of the highest water content (1/1) than in the other matrices. Further annealing of the samples resulted in a uniform decay of the triplet spectra without giving rise to any new observable radicals.

A small yield of H atoms was seen in the sample with $M/H_2O = 1/1$. The H atoms signals showed satellite lines. The intensity of the H atom line increased by a factor ~ 2 when the sample was bleached with visible light.

When an X-irradiated sample ($M/H_2O = 6/1$ or $1/1$) which has been bleached with visible light is exposed to 254-nm uv light for 1 min a weak blue coloring reappears, and the central line of the spectrum increases slightly while the outer lines of the triplet decreases. These changes are reversed when the sample is bleached with visible light. If the sample is exposed to uv light for longer times the triplet ESR spectrum almost disappears and the new spectrum is like that shown in Figure 1, IIIa and IIIb. A sample treated in this way shows no color. The spectrum is the sum of the following resultant spectra: a doublet spectrum with asymmetric lines and a splitting of 133 G, IIIa on Figure 1; a quartet spectrum with a splitting of 23.5 G, IIIb; and a weak remainder of the triplet spectrum II. There is a loss of about 20–30% of the radicals in this process, but the H-atom yield is markedly enhanced. The ratio of the number of H atoms produced to the number of CHO radicals, which have the ESR spectrum IIIb (see Discussion), is dependent on the wavelength of photolysis as shown in Figure 3. The doublet spectrum IIIa is easily converted back to the triplet spectrum II by visible light. Also in this process H atoms are formed. On annealing for 3 min at 120 K spectrum III is changed to spectrum IV and on annealing for 4 min at 126 K spectrum V is obtained. Spectrum V is unaffected by visible light, but may be converted to spectra IIIa and II by uv light. It should be remarked that spectra IV and V are only obtained in the matrices with low water content. In the matrix $M/H_2O = 1/1$ spectrum IIIb decays first on an-

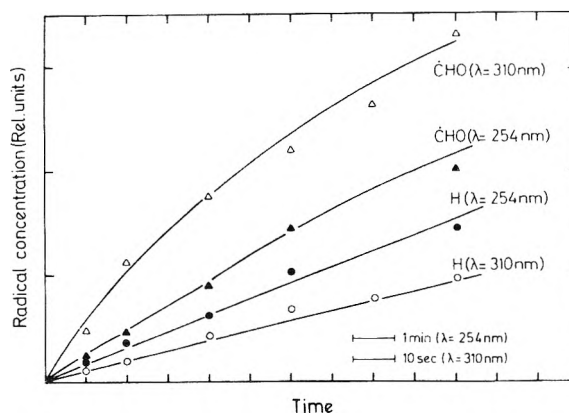


Figure 3. The formation kinetics of CHO radicals and H atoms observed when an X-irradiated sample ($M/H_2O = 1/1$) bleached with 580-nm light is exposed to uv light of wavelength 254 and 310 nm. The yields are given by peak measurements.

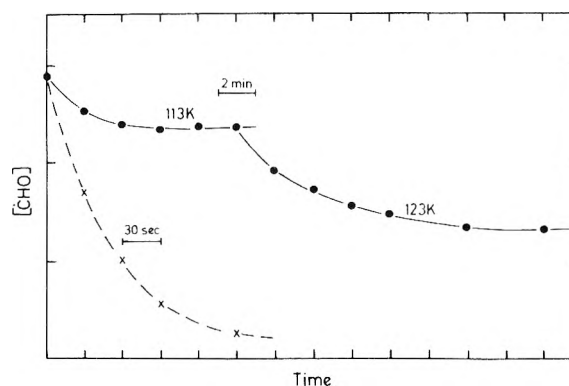


Figure 4. Decay kinetics of CHO radicals ($M/H_2O = 6/1$). (- X -) represents the decay during optical bleaching by light of wavelength 580 nm. (-●-) represents the thermal decay observed when the sample is annealed for 2 min between each recording at 77 K. The annealing temperatures are indicated on the curves.

nealing and then spectrum IIIa, no new radicals being observed.

The decay kinetics of the CHO radicals are shown on Figure 4. Optical bleaching results in an exponential decay. Annealing at a certain temperature results in decay to a plateau and no further decay is seen. Raising the temperature results in a new decay and a new plateau is reached. If a sample that has been annealed until a plateau is reached is stored for 1 day at 77 K and then annealed at the same temperature, additional decay is found and the decay proceeds evidently without reaching a new plateau.

If a sample ($M/H_2O = 1/1$) is exposed to the whole spectrum of the mercury lamp for 40 min a spectrum like that shown in Figure 5 is obtained. Annealing results in decay of the H atoms and of the quartet spectrum and increase in the doublet spectrum of CHO, and that of the triplet spectrum (Figure 5). A corresponding experiment was carried out with a sample with low methanol content where no H atoms were trapped, and Figure 6 shows the results. There is a decay of the quartet spectrum and an increase of the triplet spectrum. There is also a small increase in the doublet spectrum. Bleaching with 580-nm light does not affect the quartet spectrum but causes a decay of the doublet spectrum and a corresponding increase of the triplet spectrum.

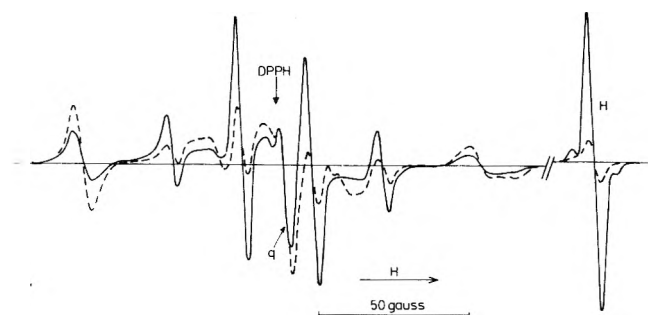


Figure 5. ESR spectrum observed when a glassy methanol-water sample (1:1) is exposed to the whole spectrum of the mercury lamp for 40 min at 77 K. The line marked q is a quartz signal from the ESR tube, and the line marked H is the high-field H-atom line. The stippled spectrum is obtained after annealing for 3 min at 103 K.

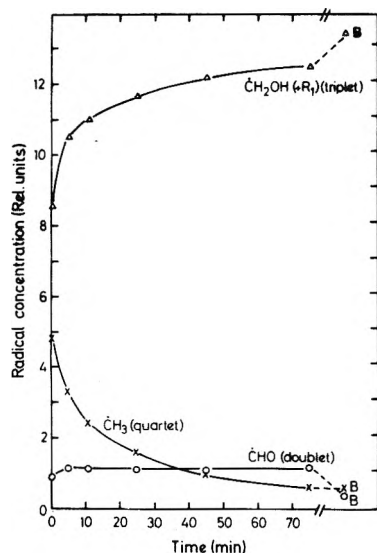


Figure 6. Radical conversion at 77 K in a uv-irradiated sample of methanol-water in volume ratio of 6:1. The sample was irradiated for 1 hr with the whole spectrum of the mercury lamp. The points marked B are obtained when the sample is bleached for 90 sec with 580-nm light.

Discussion

The photochemical reactions observed in this work are summarized in Figure 7. Several of the photochemical steps have been thoroughly discussed in the literature and will only be mentioned here. However, there are some new things that we wish to stress.

The triplet spectrum observed in X-irradiated samples of frozen methanol has been attributed to hydroxymethyl radicals $\dot{\text{C}}\text{H}_2\text{OH}$, and the blue coloring and part of the central line of the ESR spectrum may be attributed to trapped electrons e_t^- .³ However, the initial X-ray induced ESR spectrum is not solely the superposition of the $\dot{\text{C}}\text{H}_2\text{OH}$ triplet and a singlet spectrum. Dainton et al.³ attributed a sextet spectrum to e_t^- . In accordance with others,⁷ we found that decomposition of the initial spectrum is hard to perform unambiguously, so this point will not be further discussed here.

As seen in Figure 2 the bleachable part of the X-ray induced spectrum in a polycrystalline matrix is entirely different from that in a glassy matrix, being a singlet only 3.4-G wide. We propose that this singlet is due to electrons in shallow traps. The following observations seem to support this: (a) 0.05 M of an electron scavenger (H_2O_2) elimi-

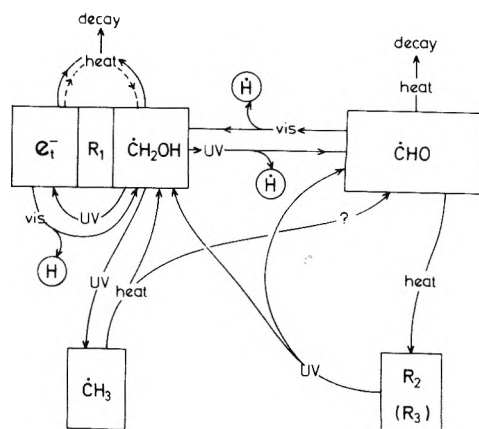


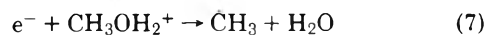
Figure 7. Schematic view of the radical conversion observed during annealing and irradiation with ultraviolet light and visible light.

nates the narrow singlet; (b) its width is typical for shallowly trapped electrons in alcohols at 4 K;^{10,11} (c) it is easily power saturated and bleachable by light of wavelength ~ 700 nm.

If this spectrum is due to shallowly trapped electrons the question arises why the molecules surrounding the electrons do not relax to make the traps deep as they do in a glassy matrix at 77 K. The explanation may be that within a crystal the molecules are more firmly bound together and less free to rotate than in the glassy state. The presence of water molecules in the crystals is obviously of importance since the narrow singlet was only observed in the 1:1 mixture of methanol and water. Further experiments are being carried out to elucidate this problem.

The conversion of e_t^- to $\dot{\text{C}}\text{H}_2\text{OH}$ radicals by bleaching with visible light is well known.^{3,7,13} The doubling of the yield of H_t observed in this work during optical bleaching is in accordance with eq 4.

Exposing the hydroxymethyl radicals to small doses of uv light seems to result in photoionization. This is indicated both by the coloring of the sample and by the ESR spectra. The coloring of the sample is not due to $\dot{\text{C}}\text{H}\text{O}$ radicals (which probably absorb in the same region of the spectrum as e_t^-),¹⁴ since samples containing a factor of 100 higher concentration of $\dot{\text{C}}\text{H}\text{O}$ radicals than the present one showed practically no coloring. Similar photoionization effects have been observed in an ethylene glycol-water glass.¹⁵ Photoionization of alcohol radicals was also proposed by Shiotani and Chachaty¹⁶ to explain the formation of $\dot{\text{C}}_2\text{H}_5$ radicals in the photolysis of γ -produced radicals in ethanol. The electrons released in the photoionization process may become trapped, or react according to eq 4. It is also possible that methyl radicals are produced in small yield in a way corresponding to the production of $\dot{\text{C}}_2\text{H}_5$ radicals in ethanol:¹⁶



If so, the probability of this reaction is small since the majority of the electrons obviously reacts according to eq 4.

In contrast with optical bleaching of e_t^- thermal annealing of X-irradiated methanol matrices of low water content results in a decay of e_t^- without any transformation to $\dot{\text{C}}\text{H}_2\text{OH}$ radicals. This is in correspondence with the findings of others^{3,13} and has been explained by the difference in energy of the H atoms formed in reaction 4 by optical bleaching and thermal annealing. i.e., the H atoms formed

during optical bleaching have enough energy to abstract other H atoms from methanol molecules while the H atoms formed from e_t^- during annealing are deficient of energy for such a reaction.^{3,13} However, we observed that in methanol-water mixtures of volume ratio 1/1 there is a reproducible increase by $20 \pm 5\%$ in the concentration of $\dot{C}H_2OH$ radicals in the temperature region where the trapped electrons disappear. Thus, this matrix behaves differently from the matrices with smaller water content. This is apparently but not necessarily in conflict with the above explanation. Thus it is possible that the H atoms liberated when the electrons react with H_2O^+ , the positive hole in the water moiety, have more energy than those liberated when the electrons react with $CH_3OH_2^+$. Another possibility would be that the energy required for H abstraction from methanol is smaller when water molecules are present, which probably could be explained by a different degree of hydrogen bonding. Thirdly, the independence of the concentration of $\dot{C}H_2OH$ radicals of the decay of trapped electrons in methanol matrices with small water content may be fortuitous, i.e., the electrons form hydroxymethyl radicals by reactions 4 and 5 but simultaneously there is a decay of such radicals. It should be remarked that the stability of all radicals was found to increase with the water content of the matrix.

The doublet spectrum IIIa in Figure 1 represents the main product when hydroxymethyl radicals are exposed to larger doses of uv light (~ 10 min in our case). This doublet is due to formyl radicals $\dot{C}HO$.^{3,17}

The quartet spectrum IIIb in Figure 1 is unambiguously due to $\dot{C}H_3$ radicals.¹⁸ Thus, photolysis of $\dot{C}H_2OH$ radicals with uv light gives both $\dot{C}HO$ and $\dot{C}H_3$ radicals. $\dot{C}H_3$ and $\dot{C}HO$ radicals are also formed when methanol matrices are exposed to the whole spectrum of a mercury lamp (Figure 5 and ref 9) but the ratio of formyl to methyl radicals is much smaller than after uv photolysis of hydroxymethyl radicals. (It should be remarked here that irradiation of methanol matrices with monochromatic uv light to the doses used in the rest of this work gave no detectable radicals.) This difference may be due to the high intensity of visible light from the mercury lamp which causes bleaching of the $\dot{C}HO$ radicals.

In view of the observation that the concentration of $\dot{C}HO$ radicals increases in the temperature region where the trapped hydrogen atoms decay (Figure 5 and ref 19) it seems reasonable that formyl radicals are formed either by reaction of H atoms with CO molecules which are produced by the uv light⁸ or by abstraction of H atoms from formaldehyde molecules. The $\dot{C}H_3$ radicals and the H atoms were found to decay parallelly in a matrix where $M/H_2O = 1/1$, so it cannot be excluded that $\dot{C}H_3$ radicals also play a role in the formation of $\dot{C}HO$ radicals during annealing in this matrix. However, in a matrix with small water content no H atoms are present. In such matrices the $\dot{C}H_3$ radicals produce mainly $\dot{C}H_2OH$ radicals and only a very small amount of $\dot{C}HO$ radicals when they decay (Figure 6).

In the photolysis of hydroxymethyl radicals by uv light we found that in addition to $\dot{C}HO$ and $\dot{C}H_3$ radicals and electrons, hydrogen atoms were also formed. Thus, it seems that the proposed reaction (6)³ for the formation of $\dot{C}HO$ radicals proceeds in two steps. It is also probable that some or all the observed hydrogen atoms stem from the electrons produced in the photoionization of $\dot{C}H_2OH$ radicals. This is the most likely explanation since the ratio of H atoms to

$\dot{C}HO$ radicals formed is much higher at 254 nm than at 310 nm (Figure 3). One would expect that 254-nm light is the more efficient of the two wavelengths in producing ionization.

The $\dot{C}HO$ radical is easily decomposed by visible light as already observed by Dainton and coworkers.³ According to the present work H atoms are formed in this process. The H atoms may in turn abstract H atoms from methanol whereby $\dot{C}H_2OH$ radicals are formed.

The thermal decay of $\dot{C}HO$ radicals is different from the decay during optical bleaching (Figure 4). Only a certain fraction was found to decay at a given temperature, the rest being practically stable. When such a sample was kept at 77 K for 1 day and then annealed at the same temperature a new decay was observed and the plateau was not as prominent as for a fresh sample. This may indicate that relaxation effects in the glass play a certain role in this decay. It seems that the thermal decay of the $\dot{C}HO$ radicals is due to a reaction with other radicals trapped nearby and that the radicals exist in spurs. Further experiments are needed to elucidate this point.

In the matrices of small water content ($M/H_2O = 96/4$ or $6/1$) one or possibly two types of radicals are formed when $\dot{C}HO$ radicals decay thermally (Figure 1). The most abundant and stable of these radicals, R_2 , has the ESR spectrum V in Figure 1. This spectrum is evidently composed of four lines, but the splitting ($a \sim 6.5$ G) is too small to make possible determination of the intensity ratio of the lines. It is tempting to attribute this spectrum to the $CH_3O\cdot$ radical.

Radical R_2 (Figure 1, V) may be photolyzed by light of wavelength 310 nm and hydroxymethyl radicals and formyl radicals are formed in comparable amounts without appreciable loss of spin. This observation may indicate that R_2 is the methoxy radical since both the $\dot{C}HO$ and $\dot{C}H_3OH$ radicals could be easily formed from this radical. However, this interpretation is in contrast with the observation that the methoxy radical seems to be unstable in methanol glass. Furthermore, Sullivan and Koski⁹ claim that this radical has an asymmetric singlet ESR spectrum. Further experimental data are needed to solve this problem.

References and Notes

- (1) R. S. Alger, T. H. Anderson, and L. A. Webb, *J. Chem. Phys.*, **30**, 695 (1959).
- (2) P. B. Ayscough, R. G. Collins, and F. S. Dainton, *Nature (London)*, **205**, 965 (1965).
- (3) F. S. Dainton, G. A. Salmon, and J. Tepley, *Proc. R. Soc. London, Ser. A*, **286**, 27 (1965).
- (4) F. S. Dainton, G. A. Salmon, and P. Wardman, *Proc. R. Soc. London, Ser. A*, **313**, 1 (1969).
- (5) F. P. Sargent, E. M. Gardy and H. R. Falle, *Chem. Phys. Lett.*, **24**, 120 (1974).
- (6) S. W. Mao and L. Kevan, *Chem. Phys. Lett.*, **24**, 505 (1974).
- (7) A. Habersbergerova, *Collect. Czech. Chem. Commun.*, **33**, 1925 (1968).
- (8) R. H. Johnsen, *J. Phys. Chem.*, **65**, 2144 (1961).
- (9) P. J. Sullivan and W. S. Koski, *J. Am. Chem. Soc.*, **85**, 384 (1963).
- (10) T. Higashimura, M. Noda, T. Warashina, and H. Yoshida, *J. Chem. Phys.*, **53**, 1152 (1970).
- (11) H. Hase, T. Warashina, M. Noda, A. Namiki, and T. Higashimura, *J. Chem. Phys.*, **57**, 1039 (1972).
- (12) H. Hase and L. Kevan, *J. Phys. Chem.*, **74**, 3355 (1970).
- (13) J. Tepley and I. Janovski, *Int. J. Radiat. Phys. Chem.*, **1**, 119 (1969).
- (14) F. S. Dainton, G. A. Salmon, and P. Wardman, *Chem. Commun.*, 1174 (1968).
- (15) J. Moan, *Int. J. Radiat. Phys. Chem.*, **5**, 293 (1973).
- (16) M. Shiotani and C. Chachaty, *Bull. Chem. Soc. Jpn.*, **47**, 28 (1974).
- (17) F. J. Adrian, E. L. Cochran, and V. A. Bowes, *J. Chem. Phys.*, **36**, 1661 (1962).
- (18) P. B. Ayscough in: "Electron Spin Resonance in Chemistry", Methuen, London, 1967, p 336.
- (19) C. V. Morgan, *J. Phys. Chem.*, **76**, 494 (1972).

Photochemistry in the Adsorbed Layer. IV. Effects of Oxygen upon the Photolysis of the Adsorbed Alkyl Ketones

Yutaka Kubokawa* and Masakazu Anpo

Department of Applied Chemistry, University of Osaka Prefecture, Sakai, Osaka, Japan 591 (Received February 13, 1975)

The effects of oxygen upon the photolysis of acetone- d_6 , methyl ethyl ketone, and 2-pentanone adsorbed on porous Vycor glass have been investigated. For all the ketones, with increasing oxygen pressure the rate of formation of each product passes through a maximum and then decreases. Such enhancements by oxygen of Norrish type II (2-pentanone) and type I reactions would be tentatively attributed to the interaction of oxygen with the triplet biradical intermediate and to suppression of the recombination of the acetyl-alkyl radical pairs, respectively. Applying the Stern-Volmer relationship to the rate decrease by oxygen, it has been concluded that in the adsorbed layer the lifetime of the alkyl radicals increases in the order methyl < ethyl < n -propyl radicals.

Introduction

In the previous paper¹ the present authors investigated the photochemistry of alkyl ketones adsorbed on porous Vycor glass and found that their photochemical reactivity was markedly different from that in the gas phase, leading to some general characteristics of the photochemistry in the adsorbed layer. Information on the nature and reactivity of the excited states as well as the free radicals in the adsorbed layer was obtained from the studies of the effect of nitric oxide upon the photolysis of adsorbed alkyl ketones. In the present work similar studies have been carried out using oxygen. During the course of those investigations, it has been found that a trace of oxygen enhances the photolysis of adsorbed alkyl ketones. Although the interpretation of such phenomena has not yet been settled, it seems worthwhile to report these results at the present stage, since there seems to be very few reports concerning such an oxygen effect.

Experimental Section

Details of the apparatus, procedures, and materials were described in the previous paper.¹ A conventional vacuum system was used. The specimen of porous Vycor glass (Corning, No. 7930) which had been heated in oxygen to remove carbonaceous impurities was introduced to the cell and degassed at 500°C for 7 hr. A small amount of ketone remaining in the gas phase after admission of the sample to the cell at room temperature was removed by a liquid nitrogen trap. Subsequently, oxygen was introduced into the cell, its pressure being adjusted in the range of 0.001–100 Torr. Then, photolysis was carried out using an ultra-high-pressure mercury lamp without filter. The products were analyzed by gas chromatography using a flame-ionization detector.

Results

In Figure 1 the rates of the ethylene and propane formation derived from the photolysis of adsorbed 2-pentanone are plotted against the oxygen pressure. As described previously,¹ the major gaseous products in this case are propane (Norrish type I reaction) and ethylene (Norrish type II reaction). It is seen in Figure 1 that for both types of pri-

mary steps the rate increases at first with increasing oxygen pressure, passes through a maximum, and then decreases at higher pressures of oxygen. It is to be noted that the pressure where the rate shows a maximum is higher for the ethylene than for the propane formation.

We have shown¹ that the rate of ethylene formation is decreased by added nitric oxide, which is attributed to quenching of the excited triplet state. Accordingly, the decrease in the rate of the ethylene formation observed at an oxygen pressure above 1×10^{-1} Torr is attributable to quenching of the triplet ketone molecules. In fact, it has been found that the phosphorescence of adsorbed 2-pentanone is quenched by oxygen. As regards to the propane formation, the decrease in the rate of formation observed above 1×10^{-2} Torr oxygen is attributable to quenching of the propyl radicals as well as their precursor, i.e., the triplet excited 2-pentanone molecules, as was done in the quenching studies by nitric oxide described in the previous paper.¹

Similar experiments were carried out with adsorbed acetone- d_6 and methyl ethyl ketone. In Figures 2 and 3 the rates of the methane and ethane formation from acetone- d_6 as well as the ethane formation from methyl ethyl ketone are plotted against oxygen pressure. It is seen that for all the plots the rate of formation passes through a maximum at a particular pressure of oxygen. The decrease in the rates of products formation with increasing oxygen pressure may be explicable on a similar basis to that in the case of the propane formation described above. In the gas-phase photolysis of acetone,² methane and ethane formation is completely quenched by oxygen at 6×10^{-2} Torr in contrast to the behavior of the photolysis in the adsorbed layer.

Discussion

(1) *Enhancement of the Rates of Products Formation by Oxygen.* As regards to the increase in the rates of products formation observed in the range of low pressures of oxygen, there seems some possibility that formation of a charge-transfer complex between molecules of oxygen and ketone would result in such a phenomenon. The absorption spectra of adsorbed 2-pentanone showed no change on addition of oxygen at high pressures. Furthermore, according to the work of Tsubomura and Mulliken,³ acetone shows no

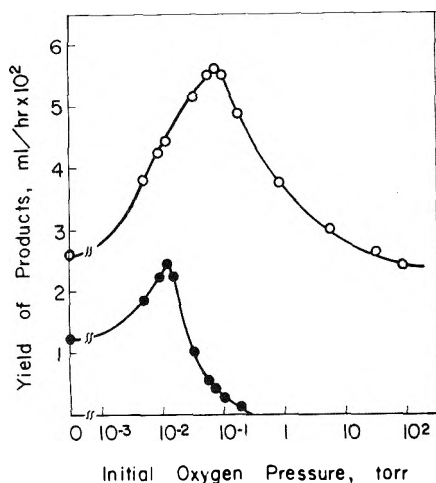


Figure 1. Effect of oxygen upon the yield of products of 2-pentanone photolysis at 25°C. The amount of 2-pentanone adsorbed was 1.65×10^{-5} mol/g. During the photolysis oxygen was somewhat consumed. It was confirmed, however, that the pressure decrease caused by it did not affect the values of τk_q and $\tau' k_q'$ in the Stern-Volmer equation: (O) ethylene; (●) propane.

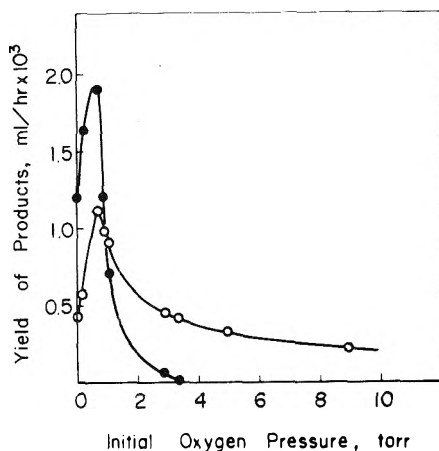


Figure 2. Effect of oxygen upon the yield of products of acetone- d_6 photolysis at 25°C. The amount of acetone- d_6 adsorbed was 1.83×10^{-4} mol/g: (O) methane; (●) ethane.

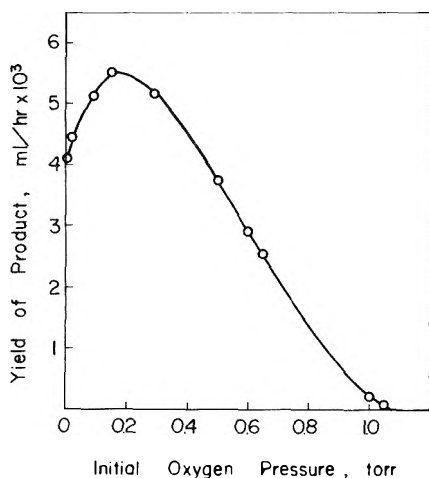
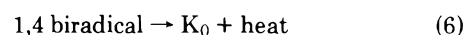
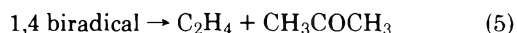
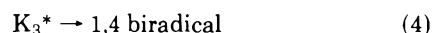
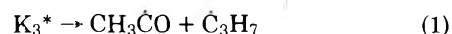


Figure 3. Effect of oxygen upon the yield of ethane in the photolysis of methyl ethyl ketone at 25°C. The amount of methyl ethyl ketone adsorbed was 3.86×10^{-5} mol/g.

charge-transfer absorption when it is saturated with oxygen. This suggests that such a possibility can be excluded.

As described in the previous paper,¹ the results of the type I reactions of adsorbed alkyl ketones can be explained by taking into consideration only the reaction from the triplet excited state. The type II reaction of adsorbed 2-pentanone occurs from both singlet and triplet excited states. Considering a marked difference in the reactivity of oxygen toward the singlet and triplet excited states, however, it may be allowed to assume that only the type II reactions from the triplet excited state are affected by oxygen. Thus, only reactions from the triplet state are included in the following scheme:



Reactions 4–6 are included, since there seems little or no doubt that the type II reaction proceeds via the 1,4 biradical generated by the intramolecular hydrogen abstraction reaction.⁴

It seems very difficult to expect that an interaction of oxygen with the excited triplet ketone molecules would result in an increase in the rate of products formation, since this interaction would probably lead to a rate decrease. Consequently, it seems probable that some kind of interaction of oxygen with the triplet biradical would result in an enhancement of the type II reaction. For example, the following possibility emerges: the triplet biradical is incapable of undergoing a bond-breaking process without spin conversion.⁵ It is well known that the singlet-triplet transition is enhanced by paramagnetic species such as oxygen and nitric oxide.⁶ Accordingly, reactions 5 and 6 would be expected to be accelerated by oxygen. In the case where reaction 5 is accelerated by oxygen more efficiently than reaction 6, such an increase in the ethylene formation would result. It has been shown by O'Neal et al.⁷ that in the gas phase the lifetime of the triplet 2-pentanone molecule is much shorter than the triplet 1,4 biradical lifetime. Furthermore, the more strongly hydrogen bonded to the surface a ketone molecules is, the longer the triplet 1,4 biradical lifetime becomes.⁸ This suggests that a similar situation would be expected for the adsorbed layer. Thus, the rate maximum such as shown in Figure 1 could be explained.

A similar enhancement of the type II reaction with oxygen has been found by Grotewold et al.,⁹ who investigated the photolysis of 4-methyl-1-phenylpentan-1-one and attributed it to an interaction of oxygen with the 1,4 biradical intermediate. As was described previously,¹ in the case of the nitric oxide quenching, no maximum in the rate of ethylene formation was observed. Such a different behavior may be ascribed to the fact that the excited triplet and/or biradical are deactivated to the ground state of 2-pentanone more efficiently by nitric oxide than by oxygen. Such a difference in the quenching efficiencies between nitric oxide and oxygen has already been found by Bäckström and Stenery¹⁰ and by Rebbert and Ausloos.¹¹

As for the increase in the rate of the type I reactions caused by a trace amount of oxygen, it seems unlikely that

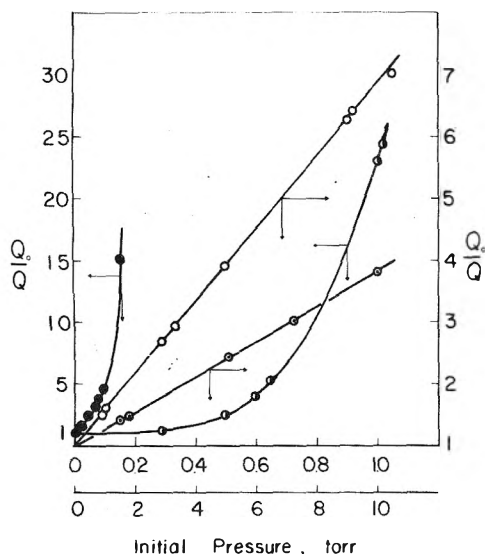


Figure 4. Stern-Volmer plots for products quenching in the photolyses of alkyl ketones adsorbed on Vycor glass. The upper abscissa refers to quenching of propane and ethane formation by oxygen and methane formation by nitric oxide. The lower abscissa refers to quenching of methane formation by oxygen: (●) propane; (○) ethane; (○) methane (oxygen quenching); (○) methane (nitric oxide quenching).

the possibility of α cleavage of alkyl ketones is enhanced in the presence of oxygen. This suggests that oxygen will affect the secondary reactions of the radicals produced by the α cleavage. According to the work of Hoare and Whytock,¹² in the gas phase the radical reactivity toward oxygen is much higher for acetyl than for alkyl radicals. Assuming a similar difference in the reactivities for the adsorbed layer, it is expected that only acetyl radicals are removed by oxygen at low pressure. As a result, recombination of the geminate radical pairs is suppressed, which results in enhancement of the formation of alkane. On increasing oxygen pressure, both alkyl and acetyl radicals are scavenged. Thus, the maximum rates for alkane formation would be explicable.

(2) *Lifetime of Adsorbed Radicals.* For quenching by oxygen of the methane formation from acetone- d_6 the following Stern-Volmer equation holds in the range below 10 Torr of oxygen (see Figure 4):

$$Q_0/Q = 1 + \tau k_q [O_2]$$

where Q_0 is not the rate of formation in the absence of oxygen but the maximum rate of formation. τ and k_q are the lifetime of the methyl radicals and the quenching rate constant, respectively. A similar Stern-Volmer plot holds for the quenching by nitric oxide of methane formation described in the previous paper¹ as shown in Figure 4. Such linear Stern-Volmer plots are in contrast with the photolysis of methyl ethyl ketone and 2-pentanone where the Stern-Volmer plots are concave upward, i.e., quadratic Stern-Volmer plots are applicable (Figure 4). This suggests that in the case of acetone little or no quenching of the excited triplet acetone molecules takes place, only scavenging of the radicals being observed. Such a short lifetime of the triplet acetone molecules is in agreement with the fact that no phosphorescence is observed for acetone adsorbed on porous Vycor glass.¹ Thus, it is confirmed that in the order 2-pentanone < methyl ethyl ketone < acetone radiationless decay becomes more efficient, i.e., the excited triplet lifetime becomes shorter.

TABLE I: Values of τk_q and $\tau' k'_q$ for NO and O_2 Quenching (M^{-1})

Quenchers	Methyl ethyl		
	2-Pentanone	ketone	Acetone- d_6
NO τk_q	4.9×10^5	2.4×10^5	5.4×10^4
$\tau' k'_q$	3.6×10^5	9.5×10^4	
O_2 τk_q	2.2×10^5	1.2×10^5	8.8×10^3
$\tau' k'_q$	1.2×10^5	3.2×10^4	

In the case of the quenching by nitric oxide of the ethane formation from methyl ethyl ketone and the propane formation from 2-pentanone, we have already obtained the τk_q values for the ethyl and propyl radicals using the Stern-Volmer quadratic equation.¹ Accordingly, in the case of quenching by oxygen, the same equation is expected to hold:

$$Q_0/Q = (1 + \tau k_q [O_2])(1 + \tau' k'_q [O_2])$$

where τ and k_q are the radical lifetime and the quenching rate constant for the radicals, respectively. τ' and k'_q are the corresponding values for the triplet ketone molecules. Q_0 is again the maximum rate of the products formation. As described in the previous paper,¹ the triplet excited state is quenched three times more efficiently by nitric oxide than by oxygen. Accordingly, using the $\tau' k'_q$ values for nitric oxide given previously,¹ the $\tau' k'_q$ values for oxygen is estimated at $1.2 \times 10^5 M^{-1}$ for 2-pentanone and $3.2 \times 10^4 M^{-1}$ for methyl ethyl ketone, respectively. From these $\tau' k'_q$ values the τk_q values are determined such that best fits to the experimental curves are obtained. The values of τk_q and $\tau' k'_q$, including the corresponding values determined from the nitric oxide quenching, are shown in Table I.

Although it is expected that in the adsorbed layer the reactivity of the radicals is different from that in the gas phase, it seems very difficult to attribute such a large difference in the τk_q values only to the difference in k_q . In other words, it can be concluded that the radical lifetime increases in the order methyl < ethyl < *n*-propyl radicals. By assuming that the relative reactivity of oxygen or nitric oxide toward these three radicals in the adsorbed layer is approximately equal to that in the gas phase,¹³ it is possible to estimate the relative lifetime of three radicals in the adsorbed layer as follows: $\tau_{\text{methyl}} : \tau_{\text{ethyl}} : \tau_{\text{n-propyl}} = 1:30:1000$.

From the investigation of the effect of surface pretreatments upon the rate of products formation, the authors have concluded that the lifetime of radicals formed on the solid surface is mainly determined by the probability of the recombination of the geminate radical pairs.³ It is therefore concluded that in the adsorbed layer efficiency of the recombination of geminate radical pairs increases in the order 2-pentanone < methyl ketone < acetone.

References and Notes

- (1) Y. Kubokawa and M. Anpo, *J. Phys. Chem.*, **78**, 2442 (1974).
- (2) G. S. Pearson, *J. Phys. Chem.*, **87**, 1686 (1963).
- (3) H. Tsubomura and R. S. Mulliken, *J. Am. Chem. Soc.*, **82**, 5960 (1960).
- (4) P. J. Wagner, *Tetrahedron Lett.*, 5385 (1968); 1753 (1967); J. A. Bartlett and J. D. Coyle, *ibid.*, 3235 (1968); N. J. Turro and P. A. Wriede, *J. Am. Chem. Soc.*, **92**, 321 (1970); N. C. Yang and S. P. Elliott, *ibid.*, **91**, 7550 (1969).
- (5) P. J. Wagner, *Acc. Chem. Res.*, **4**, 169 (1971); L. M. Stephenson and J. I. Brauman, *J. Am. Chem. Soc.*, **93**, 1988 (1971); P. D. Bartlett and N. A. Porter, *ibid.*, **90**, 5317 (1968).

- (6) G. Porter and F. Wright, *Discuss. Faraday Soc.*, **27**, 18 (1959).
 (7) H. E. O'Neal, R. G. Miller, and E. Gunderson, *J. Am. Chem. Soc.*, **96**, 3351 (1974).
 (8) M. Anpo, T. Wada, and Y. Kubokawa, *Bull. Chem. Soc. Jpn.*, in press.
 (9) J. Grotewold, C. M. Previtali, and D. Soria, *J. Chem. Soc., Chem. Commun.*, 207 (1973).
 (10) H. L. J. Bäckström and A. Stenery, *Acta Chem. Scand.*, **12**, 8 (1958).
 (11) R. E. Rebert and P. Ausloos, *J. Am. Chem. Soc.*, **87**, 1847 (1965).
 (12) D. E. Hoare and D. A. Whytock, *Can. J. Chem.*, **45**, 865 (1967).
 (13) M. I. Christie and J. S. Frost, *Trans. Faraday Soc.*, **61**, 468 (1965).

Mechanisms Involving the Transient Absorptions of Cyanine Dyes in Gelatin. I. Temperature Dependence

S. H. Ehrlich

Research Laboratories, Eastman Kodak Company, Rochester, New York 14650 (Received June 2, 1975)

Publication costs assisted by the Eastman Kodak Company

The temperature dependence of transient absorptions and steady-state spectral responses of four cyanine dyes dispersed in gelatin films was used to characterize two stereoisomers in 3,3'-diethyl-9-methylthiacarbocyanine bromide and anhydro-3-ethyl-9-methyl-3'-sulfobutylthiacarbocyanine hydroxide. The decay rates involving relaxation of the induced absorptions and rates of recovery to the ground state are interpreted in terms of kinetic reaction mechanisms, structural, and thermodynamic relationships.

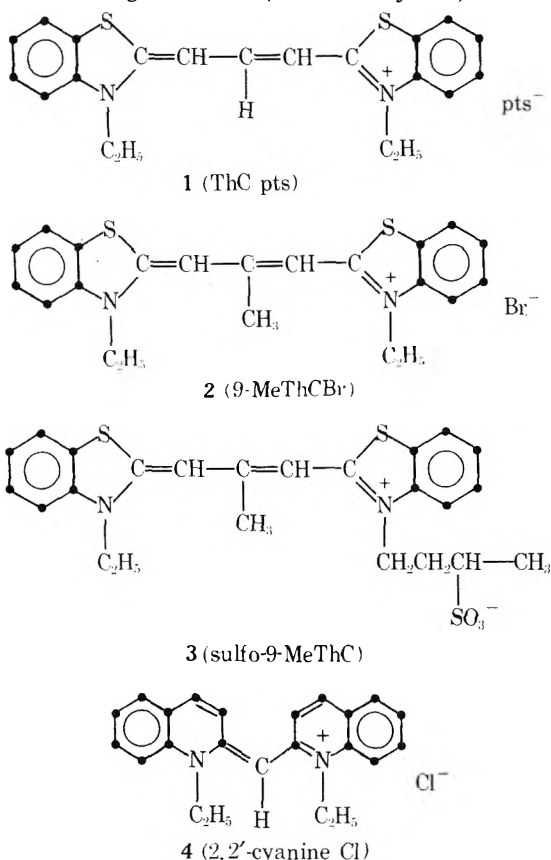
Introduction

Flash photolysis has enabled the detection of transient species formed during the exposure of photographic silver halide emulsion systems that might appear in the photographic process.^{1,2} The four cyanine dyes were previously studied at $2-4 \times 10^{-3} M$ in $\sim 30\text{-}\mu\text{m}$ thick gelatin films with and without AgBr(I) (0.05- μm microcrystals, sulfur and

gold [S + Au] surface treated):^{1,2} (1) ThC pts (3,3'-diethylthiacarbocyanine *p*-toluenesulfonate); (2) 9-MeThCBr (3,3'-diethyl-9-methylthiacarbocyanine bromide); (3) sulfo-9-MeThC (anhydro-3-ethyl-9-methyl-3'-sulfobutylthiacarbocyanine hydroxide); (4) 2,2'-cyanine (1,1'-diethyl-2,2'-cyanine chloride). In general,¹⁻⁴ pulsed irradiation within the visible absorption bands temporarily bleached the ground-state absorption bands and formed transient absorptions at longer wavelengths (Figures 1 and 2), which were assigned to triplets, free radicals, or metastable isomers. Several investigations monitored the short-wavelength transient absorption band formation and relaxation.⁵⁻⁷ Optical density changes after excitation of the dyes in gelatin (and adsorbed to silver halide crystals in gelatin) were described by

$$\Delta OD = A \exp(-k_2 t) + B \exp(-k_1 t) \quad (1)$$

where t is arbitrarily set equal to zero at the time the excitation pulse is interrupted. The complex decay curves were resolved into two exponential components: (1) a long-lived and (2) a short-lived process described by the specific rate constants k_1 and k_2 , respectively, or the reciprocal constants as lifetimes. The short-lived kinetics in regeneration and relaxation introduce the possibility of consecutive or concurrent reaction mechanisms from the excited state. The pulsed photolysis of all the cyanine dyes in gelatin and when adsorbed to silver halide microcrystals in gelatin showed apparent reversible transient processes on repeated flash excitation; however, approximately 1% of the dye in gelatin was irreversibly bleached after five flash excitations in air and at room temperature.^{1,2} A corresponding increase of 0.2% in transient density was observed in the dyed crystals dispersed in gelatin owing to silver formation. The excitation frequency/sample was, therefore, limited to three exposures.^{1,2} The rates of decay involving relaxation of the induced absorption and rates of recovering (regeneration) to the ground state were the same for the cyanine dyes in gel-



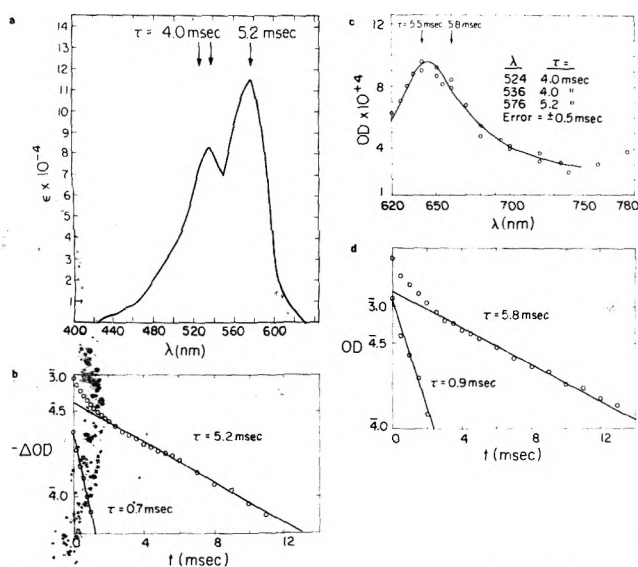


Figure 1. Absorption data for dye 1 in gel, concentration $2.7 \times 10^{-3} M$, sample thickness $19.6 \times 10^{-4} cm$: (a) absorption of ground state; (b) regeneration of the bleached ground-state absorption (576 nm); (c) transient absorption; (d) transient-absorption decay (660 nm).

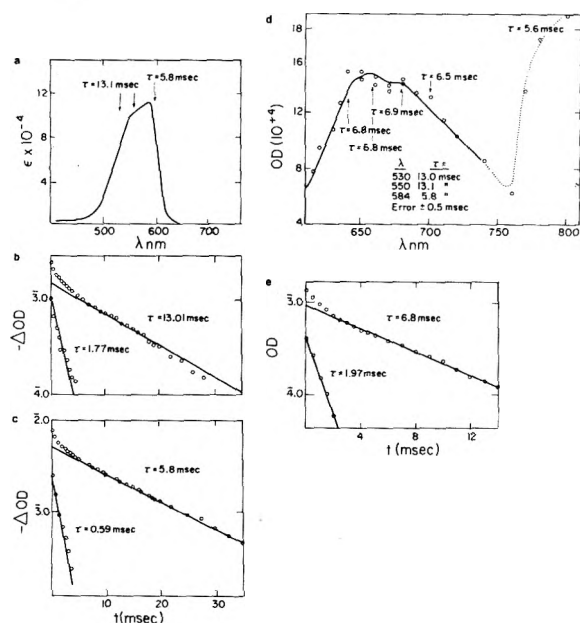


Figure 2. Absorption data for dye 3 in gel, concentration $3.08 \times 10^{-3} M$, sample thickness $20.8 \times 10^{-4} cm$: (a) absorption of the ground state; (b, c) regeneration of the bleached ground-state absorption (530, 584 nm); (d) transient absorption; (e) transient-absorption decay (640 nm).

atin films.^{1,2} 9-MeThCBr and sulfo-9-MeThC exhibited two long lifetimes in both the ground-state and induced spectra. Geometric isomers of the dyes were proposed.^{1,2}

In continuing our investigation of the sensitization mechanism of silver halide crystals and characterization of dye intermediates in gel and on silver bromide grains in gelatin, we have turned our attention to the temperature dependence of the relaxation processes occurring in the dyes in gelatin in order to compare the energetics of the recombination or loss mechanisms of dyes adsorbed to silver halide microcrystals dispersed in gelatin.

Cyanine Dyes Dispersed in Gelatin Films

Experimental Section. The general experimental arrangement has been described previously; therefore, the apparatus will be described briefly.¹⁻⁶ The 10–30- μm thick dispersions of dyes in gelatin were stripped from Estar (polyester film) base and mounted within a cryostat. The dyes were $2-4 \times 10^{-3} M$ in concentration. The change in optical density (10^{-3} to 10^{-5} OD unit) subsequent to filtered flash excitation was measured photometrically at selected wavelengths by a 0.75-m Jarrel-Ash Czerny-Turner scanning spectrometer and displayed on a Tektronix 585A oscilloscope with a modified solid-state 1A7A differential amplifier. The energy per flash was 129 J ($2.57 \mu F$, 10 kV). The filtered flash was triggered through a mercury ignitron with a hydrogen thyratron switch in series with the xenon-filled quartz flash lamp (Novatron 251, Xenon Corp.). The Novatron 251 lamp had a pulse half-width of 3 μsec with a tail dropping to 1% intensity in less than 10 μsec . The transient change in optical density in the flashed film was followed by measuring the transmitted light from a quartz-iodine 12-V, 100-W lamp which was collimated, filtered, passed through the film, and focused on the entrance slit of the monochromator to an EMI QB9558 photomultiplier. The phototube is sensitive from 300 to 850 nm and is coupled to the oscilloscope through an emitter follower. Each appropriately filtered flash of the photolysis lamp, 3 μsec at half-band width, triggered the oscilloscope and allowed direct observation and photographic recording of the transient by the kinetics of either the recovery of the original dye or the disappearance of the transient. The integrated radiation intensity, 440 to 800 nm, is 1.8×10^{15} quanta $sec^{-1} cm^{-2}$. Extrapolation of the decay curves to zero time provides both the action spectrum (ground state) of the original dye and the induced absorption spectrum of the transient species. The decay curves were resolved into two exponential components by drawing a straight line, on semilogarithmic plot, through the linear portion of the long component and subtracting the relative-intensity values on this line from the experimental points on the decay curve (Figures 1 and 2). The specific rate constants (k_1 and k_2) were determined from the slopes of the resolved components. A Hewlett-Packard 9864 digitizer, 9820A calculator, and 9862A plotter were programmed to gather, analyze, and process the large quantities of data from the analog signals generated from the oscilloscope traces. Only the long-lifetime specific rate constants, k_1 , were plotted as a function of temperature in order to determine the energy of activation, $E(act)$, and the frequency factor, A , from the simple Arrhenius equation

$$k_1 = Ae^{-E(act)/RT} \quad (2)$$

The ΔF^\ddagger , ΔH^\ddagger , and ΔS^\ddagger were calculated from transition-state theory⁸ assuming the transmission coefficient $t = 1$ by means of

$$k(T) = tKT/h \exp(-\Delta F^\ddagger/RT) = tKt/h \exp(\Delta S^\ddagger/R) \exp(-\Delta H^\ddagger/RT) \quad (3)$$

where the above symbols respectively represent the standard change in free energy, enthalpy, and entropy in producing a transition state during the relaxation process.

The steady-state visible absorption spectra of the dyes dispersed in gelatin films were measured with a Beckman Acta III spectrophotometer at temperatures from 23 to $-80^\circ C$. For measurements below room temperature, the

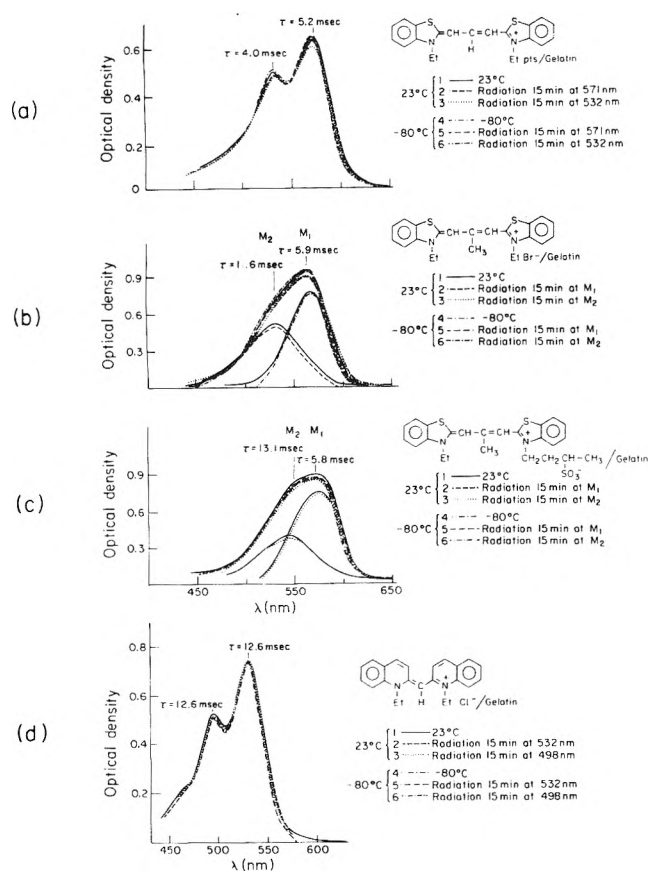


Figure 3. Temperature dependence of the ground-state absorption and regeneration lifetimes at 23°C (Table III): (a) dye 1 (trans), (b) dye 2 resolved absorption envelopes of the isomers (cis) 539 nm, radiation at M_2 (550 nm), (trans) 552 nm, radiation at M_1 (582 nm), (c) dye 3 resolved absorption envelopes of the isomers (cis) 550 nm, radiation at M_2 (530), (trans) 571 nm, radiation at M_1 (584 nm). (The underestimation of the vibronic components of C (dye 3), both the cis and trans become obvious in the 500-nm region.)

films were placed in a copper frame in the bottom of a steel-flanged, vacuum dewar and inserted into a three-windowed steel optical cell. The plane quartz windows provided for the passage of the photometric beam; the third window afforded an accessible view for alignment and an irradiation source. Temperatures were adjusted by a heating element placed within the dewar at the bottom, near the sample, and were measured with a copper-constantan thermocouple. Photolytic changes in the dyes were brought about at room and low temperatures by irradiation with monochromatic light of wavelengths near those of the maxima indicative of a mixture of geometrical isomers M_1 and M_2 , respectively, as illustrated in Figures 3b and 3c. A typical irradiation within band M_1 was accomplished by exposure for 900 sec to the light of a 150-W xenon lamp through a Bausch and Lomb 0.25-m Ebert monochromator. The radiation flux was measured with an International Light 600 photometer and calibrated assemblies 200A and C. The radiation intensities as a function of wavelength varied from 9.30×10^{13} (730 nm) to 4.59×10^{13} quanta $\text{sec}^{-1} \text{cm}^{-2}$ (430 nm). After irradiation, the absorption was diminished by approximately 5% owing to bleaching of the dye.

Steady-State Results for Dyes Dispersed in Gelatin Films

I. Absorption Spectra. The absorption spectra of four cyanine dyes at room temperature yield information on

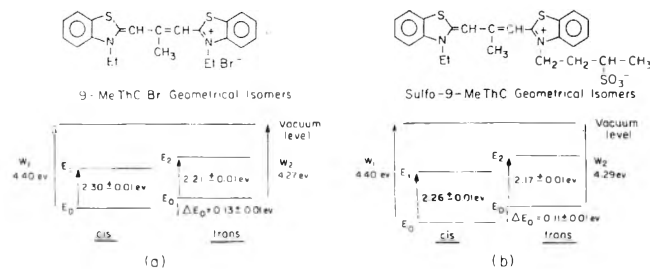


Figure 4. Energy-level diagram of the geometrical isomers of dyes 2 and 3 relative to the vacuum level.

several physical parameters as noted in Table I. The relationships between the oscillator strength (f), the experimentally determined integrated molar decadic extinction coefficient of an absorption band (ϵ), the transition dipole moment (R), and the amplitude (d) of the electronic displacement. The electronic charge (q , 4.8×10^{-10} esu), described in Table I, footnote b, allows the calculation of the electronic displacement (d).

West, Pearce, and Grum¹³ considered ThC pts to be a single isomer, whereas 9-alkyl analogs (e.g., 9-MeThCBr and sulfo-9-MeThC) exhibit two isomers, the trans configuration absorbing at longer wavelengths than the cis isomer. Their assignment has been reinforced in this study even though the geometrical isomers of sulfo-9-MeThC and 9-MeThCBr were not irreversibly photoconvertible by exciting either within the cis or the trans isomer absorption bands (–80 to 23°C).

9-MeThCBr and sulfo-9-MeThC exhibited two long lifetimes in both the ground-state and induced spectra. The complex absorption spectra of the geometric isomers as indicated in Figures 5b and 5c were resolved on a 310 Du Pont curve analyzer assuming skewed gaussian distributions. The long-wavelength electronic transition of highest intensity is assumed to be the all-trans isomer since the methine chain of that isomer has the longest configuration. The energy eigenvalues for the isomer transitions enable a determination of the length of the methine chain to be made by evaluating the dimension in the quantum model of "a particle in a box".¹⁴ The conjugate chain dimensions are listed in Table I, column a'. The transition dipole moments (R) and electronic displacement (d) are also slightly larger for the assigned trans isomers. The calculated equilibrium constant (Appendix) slightly favors the cis forms of sulfo-9-MeThC and 9-MeThCBr. Figures 4a and 4b are the energy-level diagrams of the geometrical isomers of dyes 2 and 3 relative to the vacuum level.

The metastable components of the mixtures of the isomers at lower temperatures are not irreversibly photoconvertible with excitation either within the M_1 or M_2 absorption bands. It is proposed that the rigid environment of the gelatin restricted the torsional movement of the heterocyclic nuclei about the methine bridge, e.g., 9–10 bond, Figures 5a and 5b in comparison to rigid ethanolic solvents.¹³ The all-trans structure as shown in Figure 5a would possibly be the most stable of the trans configurations because of less crowding and less deviation from coplanarity of the atoms within the methine chain. This structure is most likely to coexist in a metastable equilibrium with the mono-cis structure, Figure 5b, at room temperature.

II. Pulsed Photolysis. Kinetic Results for Dyes Dispersed in Gelatin Films. The flash kinetic spectrophotometry was the experimental technique employed for the measurement of rates of reversible torsional movement about a

TABLE I: Physical Parameters Determined from the 23°C Electronic Absorption Spectra of Four Cyanine Dyes

Dye	Assigned geometrical configuration	Concn (molar in gel)	a' , Å	$e(\text{max})$, $M^{-1} \text{cm}^{-1}$	f_{nm}	R, D	d , Å	τ_0 (calcd), nsec
1	Trans	2.7×10^{-3}	12.5	1.2×10^5 (576 nm)	0.91 ^a	10.5	2.2	9.7 ^b
2	Trans	$(8.0 \times 10^{-4})^c$	12.3	3.6×10^5 (552 nm) ^c	1.6 ^d	13.8	2.8	2.1
	Cis	$(1.3 \times 10^{-3})^c$	12.0	1.4×10^5 (539 nm) ^c	0.82	9.7	2.0	3.9
3	Trans	$(7.9 \times 10^{-4})^c$	12.4	4.4×10^5 (571 nm) ^c	2.0 ^d	15.5	3.2	1.7
	Cis	$(2.3 \times 10^{-3})^c$	12.2	1.0×10^5 (550 nm) ^c	0.62	8.5	1.7	5.3
4	Trans	2.6×10^{-3}	10.6	7.7×10^4 (536 nm)	0.53	7.8	1.6	12.5

^a The oscillator strength, f_{nm} , of an electronic or vibronic absorption transition is described by $f_{\text{nm}} = 4.319 \times 10^{-9} F \int_{\nu_0}^{\nu_2} e \, d\nu^2$; $F = 9n/(n^2 + 2)^2$ where n is the refractive index of gelatin;^{9,10} $f_{\text{nm}} = 4.7 \times 10^{29} \nu_0 |R|^2$ where ν_0 (cm^{-1}) is the wavelength at $e(\text{max})$ and $R = qd$.¹¹ The inherent radiative lifetime, $\tau_0 = 3.5 \times 10^8 / \nu_{\text{max}}^2 \int_{\nu_1}^{\nu_2} e \, d\nu$, is related to the transition probability of fluorescence.¹² ^b The lifetimes for dyes similar to these have been determined in gelatin films (cf. T. M. Kelly and D. F. O'Brien, *Photogr. Sci. Eng.*, 18, 68 (1974)). ^c Calculated values (Appendix). ^d Addition of a larger vibronic component to the short-wavelength shoulder of the cis isomers shifts the peak absorptions closer to each other; therefore, reducing the f_{nm} of the trans and increasing that of the cis. $\Delta E \pm 0.01$ eV will change the f_{nm} 23% of dye 2 and 40% of dye 3.

TABLE II: Temperature Dependence of Relaxation of the Cyanine Dyes^a

Dye ^b	Concn, M	Thick-ness, μm	Temp range, K	$E_{(\text{act})}$, cal	log A	$\Delta S_{(\text{act})}^\ddagger$, cal/deg	$\Delta F_{(\text{act})}^\ddagger$, cal
1 RGS (536, 576 nm.) IT (640, 660 nm)	2.7×10^{-3}	19.6	183.6–294.1	506	2.55	−46.6	14,500
			294.1–325.6	11,300	8.56	−19.3	17,500
2 RGS (582 nm)	2.1×10^{-3}	27.6	183.2–294.1	651	2.50	−46.8	14,100
			294.1–325.6	5,060	4.00	−40.0	17,100
3 RGS (530, 550 nm) RGS (584 nm)	3.1×10^{-3}	20.8	183.2–294.1	606	2.49	−46.8	14,600
			294.1–325.6	8,210	6.06	−30.7	17,400
			183.2–294.1	131	2.18	−48.3	14,600
4 IT (640 nm)	2.6×10^{-3}	27.8	294.1–325.6	6,730	5.14	−34.8	17,200
			183.2–296.1	888	1.91	−49.6	15,800

^a Uncorrected for spectral overlap. ^b RGS = regeneration of ground state; IT = induced transient.

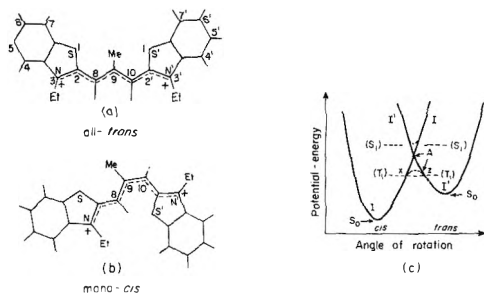


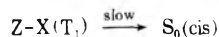
Figure 5. Generalized stable configurations of the 9-alkyl cyanine dyes: (a) all-trans; (b) mono-cis; (c) potential energy profile for cis \rightarrow trans isomerization or limited torsional motion through small angles; (d) potential energy profile for trans \rightarrow cis isomerization or limited torsional motion through small angles.

double bond. The generation of dye triplets by flash excitation (with subsequent monitoring of their rate of decay of the induced absorption and rates of recovery, regeneration, to the ground state) provides long-lived intermediates capable of being monitored. The filtered xenon source excites both isomers; each isomer relaxation has two lifetimes, but only the more reliable (long-lifetime) specific rate constant, k_1 , was used to determine the kinetic parameters. The dark relaxations of optically induced transients for dyes in gelatin are described, Table II, by two types of reactions having first-order rate constants described by the Arrhenius parameters of eq 2: (1) $k_1 = 10^{1.9-2.8} \exp(-500/RT)$ at -100 to 10°C with a low energy of activation (500–1000 cal) and low

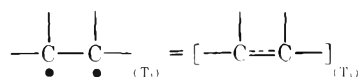
frequency factor $10^{1.9-2.8}$; (2) $k_1 = 10^{8.5-10.4} \exp(-5000/RT)$ at 10 to 55°C with a high energy of activation (5000–12000 cal) and “normal” frequency factor. Knudtson and Eyring⁵ studied the temperature dependence (-120 to 20°C) of the laser-induced transient absorptions involving photoisomerizations from 3,3'-dimethylthiacyanine iodide and 3,3'-dimethyl-9-ethylthiacyanine iodide in ethanolic solvents. The temperature dependence of the rates of cis-trans isomerism showed two regions of Arrhenius equation behavior similarly described by the specific rate constants k_1 in cases 1 and 2 above. Umberger⁷ studied the photoisomerization (trans \rightarrow cis) conversion and thermal isomerization (cis \rightarrow trans) of 3,3'-dimethylthiacyanine iodide in ethanolic solvents and determined the activation energy of the thermal process to be 15 kcal/mol, in agreement with McCartin's⁶ experimental value of 14.4 kcal/mol. The high energy of activation (Table II) for the thermal isomerization of ThC pts, cis \rightarrow trans, in gelatin is found to be 11.3 kcal/mol. Two distinct relaxation mechanisms are postulated for the reversible cis-trans conversions.

1. A Slight Reversible Torsional Movement about a Double Bond Resulting from a “Forbidden” Transition. A low frequency factor and low energy of activation are manifest at low temperatures (183–294 K). In the case of an unhindered gas-phase 180° rotation, isomerization could proceed via different reaction pathways along the hypersurfaces. One pathway would involve a photoexcitation of the double bond corresponding to the formation of a biradical

or triplet state with two unpaired electrons and thus free rotation about the resultant single bond. If a normal gaseous cis ethylenic molecule could make the transition from its normal excited singlet state to the triplet intermediate common to the ground state cis and trans isomers at X-Z, Figure 5c, and then back to the singlet state from Z for conversion to the trans ground-state form, the activation energy might be low. (The thermal isomerization, reverse process, is monitored spectrophotometrically



however, such transitions are "forbidden" by quantum-mechanical rules because they involve a change in multiplicity of the total electron spin of the molecule.) As a result of the small interaction between singlet and triplet states the probability of electronic transfer is small and hence the reaction will have a very low transmission coefficient with the result that the frequency factor will be small. It is to be noted that reactions involving the cyanine dyes rigidly dispersed in solid gelatin at low temperatures have a low energy of activation and high negative entropy of activation during the dark relaxation process. The energy of activation is the barrier height measured from the potential minima or saddle point, at X and at Z, to a transition state near point A. The transition state may be envisaged as the double-bond formation in the relaxation of the biradical (triplet) state; i.e.



The slight twisting of the molecule about a double bond, e.g., the C₉-C₁₀ axis, tends to minimize the overlap between π and π^* orbitals and the perpendicular configurations would be the most stable for the π - π^* excited configuration. The relaxation of this configuration, twisting through a small angle, allows the transition state, being more rigid than the excited state of the biradical, to provide the resultant large negative entropy.

If the properties of the rigid activated molecule are identical with those of the normal molecule, with the exception of the restricted torsional motion, which may be considered as a vibration, the translational, vibrational, and rotational contributions to the partition function cancel, leaving only a contribution due to the torsion; therefore, eq 4 can be reduced to eq 5 where ν_0 represents the torsional frequency of

$$k(T) = t \frac{KT}{h} \left/ \frac{F_1^\ddagger}{F_1} \right. e^{-E_a/RT} \quad (4)$$

$$k(T) = t \frac{KT}{h} (1 - e^{-h\nu_0/RT}) e^{-E_a/RT} \quad (5)$$

the rigid excited molecule. If ν_0 is assumed to be within the range of 10.0 cm⁻¹, a rotational quantum, then the transmission coefficient is calculated to be within the range of 10⁻⁹ sec⁻¹. It should be noted that butene-2, maleic ester, and stilbene have calculated transmission coefficients of 10⁻⁷ within the gas phase.⁸

2. *A Torsional Movement about a Double Bond Subsequent to an Allowed Transition.* A high frequency factor and high energy of action are observed at higher temperatures (294-325 K). The second pathway would also involve a torsional motion around a double bond (the triplet state thermal relaxation is again monitored). This mechanism would require large activation energies but should have "normal" frequency factors, $\sim 10^{12}$ sec⁻¹. The variation in

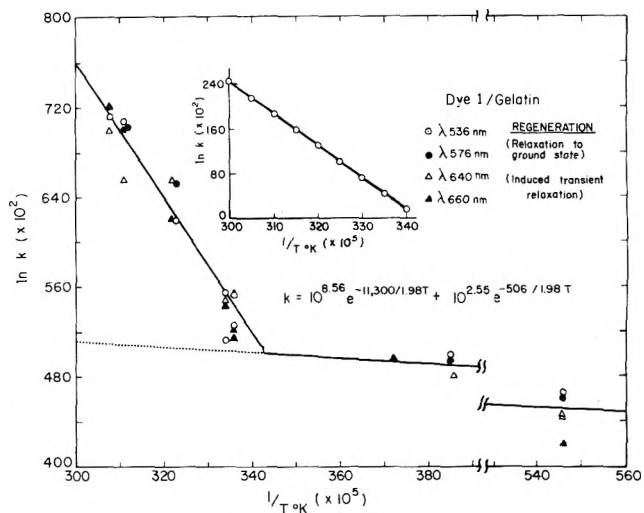
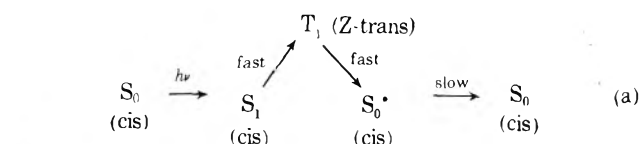
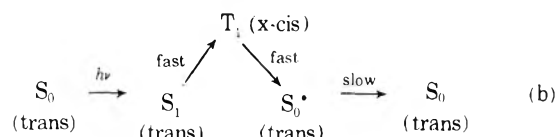


Figure 6. Representative temperature dependence of the dark relaxation of dyes in gelatin; resolution of two processes.

potential energy on thermal relaxation, rotation, about a double bond is represented by Figure 5c without change in multiplicity in the *slow* torsional movement



or



The considerable interaction between two equivalent structures in the activated state, A (S_0^*), results in a lowering of the potential energy at this crossing point as a direct result of greater opportunity for resonance.⁸

The main difference of the processes taking place at higher temperatures is the higher activation energy and larger transmission coefficient. The torsional motion is also no longer regarded as a strict vibrational mode but more as a rotation that can interact more strongly with the other vibrations owing to the mobility of the gelatin. The probability of the transfer of energy to vibrational modes within the molecule will be appreciable. This smearing out of the "discrete levels" owing to coupling with other motions of the molecule may be sufficient to permit the forbidden transition from X or Z to A. This latter reason would provide a transmission coefficient greater than the low-activation energy reaction. The resulting increase in the activation energy and increased transmission coefficient makes the singlet-to-singlet relaxations⁷ (high-temperature process) more favorable than triplet-to-singlet relaxations (low-temperature process). The frequency factors predicted for the former should be lower than those predicted for normal $\sim 10^{12}$ sec⁻¹ gas-phase reactions and activation energies should be higher than those of the low-temperature process. It is noted that the frequency factors are lower than 10^{12} sec⁻¹, i.e., 10^8 - 10^{10} sec⁻¹, and, therefore, the more favored relaxation mechanism occurs at higher temperatures. Figure 6, a plot of logarithm k vs. reciprocal of the temperature, describes the change in reaction path in a restricted

TABLE III: Lifetime Assignments for the Torsional Deactivation of the Triplet State

Dye	Dye in gelatin (regeneration of bleached ground state, msec)
1	cis not present trans 5.2 ± 0.3 (576 nm)
2	cis 18.2 ± 0.5 (550 nm) ^a trans 6.5 ± 0.3 (582 nm) ^a
3	cis 19.4 ± 0.5 (530 nm) ^a trans 6.5 ± 0.3 (584 nm) ^a
4	cis not present trans 12.5 ± 0.05 (536 nm)

^a Resolved lifetimes, corrected for overlapping absorptions.

torsional movement when the experimental conditions were altered. This behavior was also observed by Knudtson and Eyring⁵ for the dimethyl iodide derivative of ThC pts, dye 1. It is known from X-ray analysis that ThCBr displays one configuration within the crystalline state, the extended all-trans configuration.¹⁶ It is by analogy to the crystalline configuration that the relaxation lifetime of 5.2 msec is assigned to the trans configuration within the gelatin and longer lifetimes of the dye analogs to the mono-cis configuration at 23°C (Figures 3b and 3c). The lifetime assignments can be summarized in Table III. The substituents, 3-sulfobutyl in sulfo-9-MeThC vs. 3-ethyl in 9-MeThCBr or the anions (sulfo vs. bromide), do not significantly affect the relaxation lifetimes when comparing similar geometrical isomers. The larger, bulkier 3-sulfobutyl, dye 3, relative to the ethyl group of the cis configuration, dye 2, does not restrict the arrangements of the energy levels by crowding or displacing the planarity of the atoms in the methine chain. The deviation in planarity of the trans chromophoric chain, relative to the cis, makes available a larger density of states during the longitudinal electronic transition ($\delta\tau \cdot \delta E = h/2\pi$). It is postulated that the cis isomer is less hindered than the trans isomer in sulfo-9-MeThC and 9-MeThCBr.

The analytical data, including the delocalized transit distances for each isomer (particle in the box model), and calculations based upon spectroscopic evidence reinforce the kinetic observations by showing the equilibrium constant to favor the unhindered cis configuration.

Appendix

The equilibrium constants, cis \rightleftharpoons trans, and Gibbs standard free energies for 9-MeThCBr and sulfo-9-MeThC geometrical isomers at 23°C are $K' = 6.20 \pm 1.6 \times 10^{-1}$ ($\Delta G^\circ = 282 \pm 129$ cal), and $K' = 3.42 \pm 0.93 \times 10^{-1}$ ($\Delta G^\circ = 633 \pm 187$ cal), respectively, when calculated from¹⁷

$$K' = \exp(-\Delta E_s/KT) \frac{\sum_{i=0}^{\infty} g_i(\text{trans})e^{-\epsilon_i(\text{trans})/KT}}{\sum_{i=0}^{\infty} g_i(\text{cis})e^{-\epsilon_i(\text{cis})/KT}} \quad (6)$$

The extinction coefficients were calculated from eq 7 using

$$K' = \frac{[\text{trans}]}{[\text{cis}]} = \frac{\epsilon(\text{cis})\text{OD}(\text{trans})_{\text{max}}}{\epsilon(\text{trans})\text{OD}(\text{cis})_{\text{max}}} \quad (7)$$

Beer's law substitution. The concentrations of the metastable equilibrium components were calculated from eq 8 by substitution into eq 7.

$$C_{\text{Total}} = [\text{trans}] + [\text{cis}] \quad (8)$$

The equilibrium constant, K' , is a function of an energy term, ΔE_0 , the difference in the ground state of the cis and trans isomers, and an entropy term, the ratio of the partition function for the trans and cis isomers. ΔE_0 is calculated from the relationships

$$W_1/W_2 = E_1/E_2 = \lambda_2/\lambda_1 \quad (9)$$

$$W_2 + \Delta E_0 = W_1 \quad (10)$$

$$\Delta E = E_1 - E_2 = E_1(1 - \lambda_1/\lambda_2) \quad (11)$$

Therefore, from eq 7

$$\Delta E_0 = (1 - \lambda_1/\lambda_2)W_1 \quad (12)$$

or

$$\Delta E_0 = (\Delta E/E_1)W_1 \quad (13)$$

where W_1, W_2 = ionization potential of the assigned cis and trans configurations, respectively; E_1, E_2 = first electronic-state transition energy for the assigned cis and trans configuration, respectively; $\Delta E = E_1 - E_2$; ΔE_0 = difference in the ground-state energy of the assigned cis and trans isomers; $\Delta E_0(9\text{-MeThCBr}) = 0.13 \pm 0.01$ eV and $E_0(\text{sulfo-9-MeThC}) = 0.11 \pm 0.01$ eV (Figure 6). The basic assumptions involved in the calculations are that the wave shapes of the isomers are similar, the vibronic contributions are not pronounced, and the relative lifetime variations as a function of wavelength are determined by the overlap ratio of the isomer absorption bands; an equilibrium is involved between two ground-state species having different regeneration lifetimes, e.g., $\tau(\lambda) = \sum_i 1/k_i(\lambda)$.

The polarographic anodic potentials for sulfo-9-MeThC and 9-MeThCBr were 0.73 and 0.76 V, respectively, when the dyes were dissolved in acetonitrile and the potentials were measured with respect to a reference 1 N calomel electrode. The ionization potentials were determined from a plot of ionization potentials vs. polarographic potentials and adjusted to a gelatin matrix.¹⁸ The cis ionization potential, therefore, was assigned the value of 4.40 eV for both dyes under investigation. The threshold photoionizations are difficult to determine experimentally; the presence of geometrical isomers and a distribution of energies, 1 eV, within the samples should lead one to exercise caution in the use of these data.¹⁹

References and Notes

- (1) S. H. Ehrlich, the Vogel Centennial Symposium, Dye Sensitization Past and Future, Putney, Vt., Aug 26-30, 1973; *Photogr. Sci. Eng.*, **18**, 179 (1974).
- (2) S. H. Ehrlich, Eleventh Informal Conference on Photochemistry, Vanderbilt University, June 16-20, 1974; *J. Photochem.*, **3**, 403 (1974-1975).
- (3) A. V. Buettner, *J. Chem. Phys.*, **46**, 1348 (1967).
- (4) R. A. Berg and R. A. Pierce, *J. Chem. Phys.*, **51**, 1267 (1969).
- (5) J. T. Knudtson and E. M. Eyring, *J. Phys. Chem.*, **78**, 2355 (1974).
- (6) R. J. McCartin, *J. Chem. Phys.*, **42**, 2980 (1965).
- (7) J. Q. Umberger, *Photogr. Sci. Eng.*, **11**, 392 (1967).
- (8) J. L. Magee, W. Shand, Jr., and H. Eyring, *J. Am. Chem. Soc.*, **63**, 677 (1941).
- (9) A. Rabinowicz, *Rep. Prog. Phys.*, **12**, 233 (1948-1949).
- (10) D. C. Skillman and C. R. Berry, *J. Opt. Soc. Am.*, **63**, 707 (1973).
- (11) W. Kauzmann, "Quantum Chemistry", Academic Press, New York, N.Y., 1957, p. 651.
- (12) T. Förster, "Fluoreszenz Organischer Verbindungen", Vandenhoeck and Ruprecht, Göttingen, 1951.
- (13) W. West, S. Pearce, and F. Grum, *J. Phys. Chem.*, **71**, 1316 (1967).
- (14) S. M. Blinder, "Advanced Physical Chemistry", Macmillan, Toronto, 1969, p. 93.
- (15) Thermal relaxation of the photoexcited trans isomer is monitored by the decay of the transient absorption of the $Z \rightarrow X(T_1) \rightarrow$ (slow) $S_0(\text{trans})$ transition.
- (16) P. J. Wheatley, *J. Chem. Soc.* 4096 (1959).
- (17) P. Yanoulis and R. C. Nelson, *Photogr. Sci. Eng.*, **18**, 94 (1974).
- (18) T. H. James, *Photogr. Sci. Eng.*, **16**, 120 (1972).
- (19) S. Glasstone, K. J. Laidler, and H. Eyring, "The Theory of Rate Processes", McGraw-Hill, New York, N.Y., 1941, p. 183.

Mechanisms Involving the Transient Absorptions of Cyanine Dyes Adsorbed to Silver Bromiodide Microcrystals in Gelatin. II. Temperature Dependence

S. H. Ehrlich

Research Laboratories, Eastman Kodak Company, Rochester, New York 14650 (Received November 18, 1974; Revised Manuscript Received June 2, 1975)

Publication costs assisted by the Eastman Kodak Company

Flash photolysis techniques were used to characterize the transient absorption of the chemically treated (sulfur and gold) microcrystallites of AgBr(I) dispersed in gelatin. The pulsed irradiated microcrystallites exhibited apparent reversible transient absorption processes attributed to the trapped halide and sulfide holes near the silver, Ag_n^0 , centers. An overall electron transfer mechanism is proposed when adsorbed dyes are irradiated on chemically treated microcrystallites of AgBr(I) dispersed in gelatin. The relaxation rates were measured as a function of temperature and interpreted with specific reference to the following: (1) electron injection from the adsorbed dye into the conduction band of the silver halide substrate with the resultant formation of a radical cation (doublet), (2) recombination distances (conduction-band model) from parent adsorbed dye, and (3) trap-depth determinations.

Introduction

The flash spectrophotometric technique was used to detect transient species, formed during the exposure of photographic silver halide emulsion systems, that might appear in the photographic process.^{1,2} In the application of flash-photolysis techniques to the photographic processes, the basic objectives are to identify the transient chemical intermediates and relate their properties to the formation of silver (Ag_n^0) centers subsequent to irradiation. Heretofore,¹⁻³ the temperature dependence of the relaxation processes occurring in the dyes in gelatin and steady-state spectral responses were interpreted in terms of kinetic, structural, and thermodynamic relationships. The studies described in this paper are directed toward the following: (1) identification of the transient absorptions relating to the chemical treatment (sulfur and gold) of AgBr(I) microcrystallites dispersed in gelatin, and (2) mechanistic interpretation of the temperature-dependent transient absorption relaxations for AgBr(I) (S + Au) and dye adsorbed to the surface of AgBr(I) (S + Au) microcrystallites dispersed in gelatin.

Experimental Section

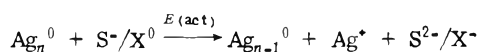
1. *Apparatus.* The flash spectrophotometer was described previously.¹⁻³

2. *Materials.* The film coatings consisted of 0.05- μ m silver bromiodide (2.5 mol % iodide) octahedral microcrystallites dispersed in gelatin which were surface sulfur-plus-gold (S + Au) treated by heating for 40 min at 70°C (pH 6.2, pAg 8.2) with 176 mg of $Na_2S_2O_3 \cdot 5H_2O$ and 88 mg of $KAuCl_4$ per silver mole. The sample films were coated at 4.89×10^{-4} g silver/cm² plus 2.91 mg of gelatin/cm² to give a dry thickness of $31\text{--}32 \times 10^{-4}$ cm for dyes 1-3 and 35×10^{-4} cm for dye 4.³ The dyes 1 (1.31×10^{-2} mol/silver mol), 2 (1.43×10^{-2} mol/silver mol), 3, and 4 (1.63×10^{-2} mol/silver mol) correspond to a grain surface monolayer coverage of 0.91, 0.94, 0.99, and 0.77, respectively, assuming a surface occupancy of 50 Å²/molecule. The dispersions were adjusted to pH 5.9 and pAg 7.9 prior to the addition of the dyes. The untreated grains required 16,000 erg/cm² where-

as the (S + Au) and adsorbed dye increase the sensitivity to 1000 erg/cm², to achieve a density of 0.3 above fog level. The unfiltered xenon excitation flash lamp radiates/flash 2191 erg/cm² (400-570 nm) and 1700 erg/cm² (520-600 nm). Excitation frequency/sample was limited to one exposure.

Transient Absorption Spectra of 0.5- μ m AgBr(I) (S + Au) Dispersed in Gelatin

Figure 1 shows the 23°C transient absorption spectra produced by pulsed irradiation of nonchemically treated, undyed AgBr(I) with peak absorptions at 520 and 640 nm. The peak absorptions are significantly shifted and the intensity is enhanced by surface chemical treatment with sulfur and gold. The contribution of sulfur and gold to the overall transient absorption is described by the subtractive spectra, AgBr(I) (S + Au) minus AgBr(I) absorption coefficients (cm⁻¹)⁴ vs. wavelength. Prominent shifted new absorptions are observed at 490 and 700 nm. These are a direct result of crystal-surface chemical treatment and are assigned to either a sulfur hole (S⁻) or differences in the size of silver aggregation, Ag_n^0 , due to the presence of sulfur and gold.⁵ The size of the aggregate should manifest a different transient absorption spectrum but have little effect upon the lifetime of the transient relaxation. The sulfur-hole complements the halogen hole (X⁰) of the AgBr(I) which is assigned to 520- and 620-nm spectral regions. A possible mechanism is discussed in the next section with regard to the temperature dependence of the relaxation for the transient responses. The long lifetime of 92 msec,⁶ Figure 1, describes S⁻ or X⁰ with Ag⁺ in the competitive annihilation of Ag_n^0 centers



An activation energy, 0.033 ± 0.002 eV (760 ± 30 cal) at 490 and 680 nm of AgBr(I) (S + Au) is assigned to the dissociation of Ag_n^0 , Figure 2. Beutel¹³ found 0.0145-eV activation energies (40-160 K) for first light pulsed photoconductivity responses of 0.42- μ m AgBr microcrystals in gelatin.

Saturation irradiation increased the activation energy to 0.062 eV (60–300 K).

Cyanine Dyes Adsorbed to AgBr(I) (S + Au) Crystals Dispersed in Gelatin

I. Initial Observations. In the accompanying paper,³ we described the temperature dependence and structural and thermodynamic relationships of the photoinduced transient response of four cyanine dyes in gelatin; in the previous section, pulsed irradiation of surface chemical treat-

ment of sulfur and gold showed apparent reversible transient processes of trapped halide and sulfide holes near the silver, Ag_n^0 , centers. In this section our attention will be focused upon the electron-transfer mechanisms involving the excited cyanine dyes adsorbed to the crystals of AgBr(I) (S + Au) dispersed in gelatin.

A summary of the relaxation rates of each dye in gelatin and adsorbed to AgBr(I) grains dispersed in gelatin appears in Table I. Different transient species were formed when the dyes were adsorbed upon the grains compared to dyed gel samples (Table I). The induced transient absorptions observed for the dye adsorbed to the silver halide grain are most likely radicals or charge-transfer complexes, e.g., dye complexed with the grain (Figures 3 and 4).^{1,2}

The relaxation lifetimes of induced absorptions (30–50 msec) for cyanine dyes adsorbed to the grain surface are not the same as lifetimes for regeneration of the ground state (5–16 msec) (Figure 5).¹⁴ This observation may be

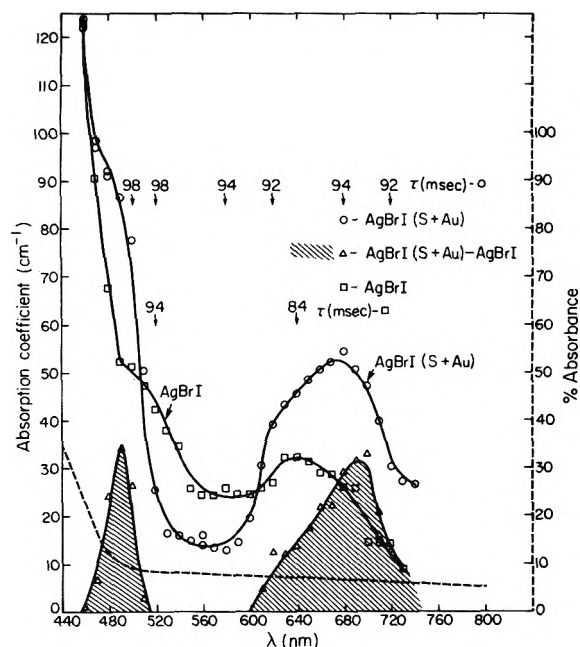


Figure 1. Transient effective absorption coefficients vs. wavelength; absorbance vs. wavelength after single exposure. Undyed 0.05- μ m AgBr(I) emulsion (S + Au), 2.5% iodide, silver ion concentration 4.89×10^{-1} mg/cm², sample thickness 18.0×10^{-4} cm.

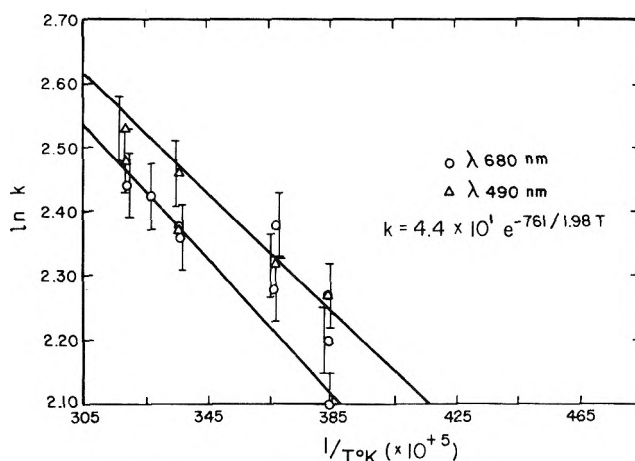


Figure 2. Temperature dependence involving annihilation of silver centers, Ag_n^0 , at 490 and 680 nm [$E_{\text{act}} = 0.033 \pm 0.002$ eV].

TABLE I: Comparison of the Relaxation Lifetimes of Dyes in Gelatin and the Dyes Adsorbed on the 0.05- μ m AgBr(I) (S + Au) Emulsions^a

Dye	Gelatin		Emulsion	
	Regeneration of bleached ground state, msec	Relaxation of induced absorption, msec	Regeneration of bleached ground state, msec	Relaxation of induced transient absorption, msec
1. ThC pts	5.2 (576 nm)	5.5 (640 nm)	9.4 (594 nm) 4.6 (565 nm)	32.3 (710 nm) 14.0 (780 nm)
2. 9-MeThCBr	5.9 (582 nm)	5.6 (640 nm)	15.0 (592 nm) 16.2 (518 nm)	52.6 (650 nm)
3. sulfo-9-MeThC	11.6 (530 nm)	8.0 (690 nm)	11.0 (582 nm) 5.5 (536 nm)	4.5 (710 nm) 29.3 (780 nm)
	13.1 (530 nm)	6.8 (660 nm)	10.5 (522 nm)	35.3 (660–800 nm)
	13.1 (550 nm) 5.8 (584 nm)	5.8 (770 nm)	14.9 (594 nm) 24.5 (622 nm)	24.3 (830 nm)
4. 2,2'-cyanine Cl	12.5 (536 nm)	14.2 (620 nm)	(522 nm) (560–580)	85.5 (640 nm) ^b 64.1 (730 nm) ^b
5. undyed emulsion AgBr(I) (S + Au)				92.0 (500–740 nm)

^a The long-lifetime component of the relaxation process is used unless specified. (Unresolved lifetimes not corrected for overlapping absorption bands.)¹⁻³ ^b The lifetimes are associated with the 0.05- μ m AgBr(I) (S + Au) grains. 2,2'-Cyanine chloride does not exhibit a detectable lifetime due to a J-aggregate recombination lifetime $\leq 10^{-6}$ sec.¹

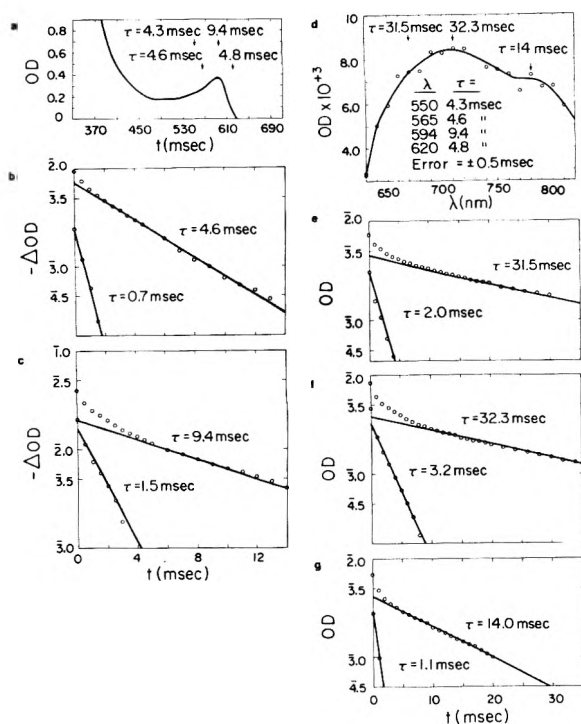
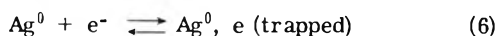
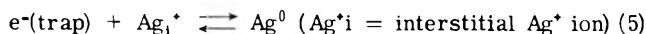
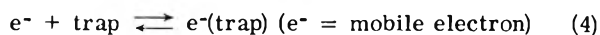
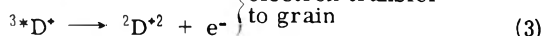
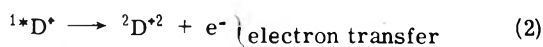
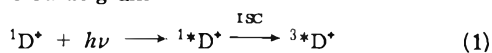


Figure 3. Absorption data for dye 1 adsorbed on grains dispersed in gelatin, concentration $1.68 \times 10^{-3} M$, sample thickness $32.0 \times 10^{-4} \text{ cm}$: (a) adsorption of the ground state; (b, c) regeneration of the bleached ground-state absorption (565, 594 nm); (d) transient absorption; (e, f, g) transient-absorption decay (670, 710, 780 nm).

due to the formation of the sulfur, S^- , or halide, X^0 , hole (eq 7 and 9) absorptions, 600–700 nm, overlapping the induced transient absorptions from the dye–grain complex. The regeneration of the ground state may be described by three concurrent reactions involving surface sites, electron traps, and latent image sites, Ag_n^0 (eq 9–11). The observed lifetime is $\tau = 1/\sum_i k_i(C_i)$, where C_i is the concentration of the i species reacting with the radical center $^2D^{2+}$. The lifetime for the decay of the induced transient and the regeneration of the ground state would be controlled by the slow detrapping of the electron (eq 10) or annihilation of the silver center, Ag_n^0 (eq 11). The overall review of the proposed mechanisms, consistent with observed transient absorptions for dyes adsorbed to $AgBr(I)$ ($S + Au$) grains, can be described by eq 1–13. Reactions 2–6 and 8 lead to latent image formation, whereas reactions 9–13 and the reverse of 4–6 are sources of inefficiency.^{15–17}

(A) The excitation and electron-transfer process of the dye on silver bromide grain¹⁸



(B) Alternative process leading to transient species and growth of latent image, Ag_n^0

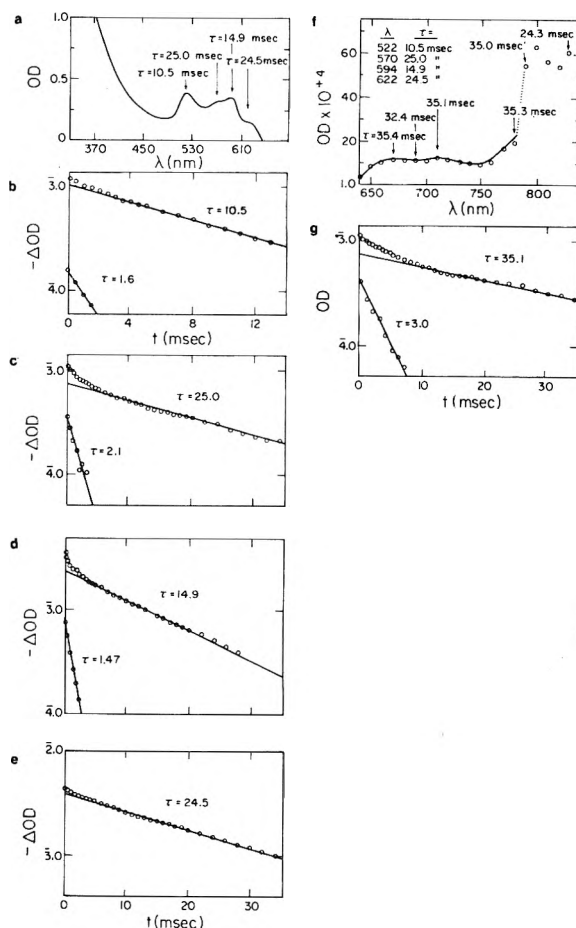
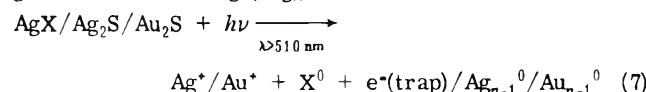


Figure 4. Absorption data for dye 3 adsorbed on grains dispersed in gelatin, concentration $2.08 \times 10^{-3} M$, sample thickness $30.8 \times 10^{-4} \text{ cm}$: (a) absorption of the ground state; (b, c, d, e) regeneration of the bleached ground state (522, 570, 594, 622 nm); (f) transient absorption; (g) transient-absorption decay (710 nm).

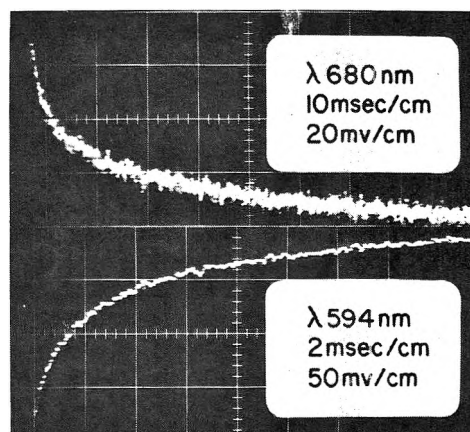
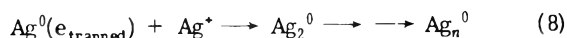


Figure 5. Representative oscilloscope traces of dye 1 adsorbed to $0.05\text{-}\mu\text{m}$ $AgBr(I)$ ($S + Au$) grain: lower trace, regeneration of the bleached ground state; upper trace, induced transient decay.



Let $X^0 = I, Br, S^-(\text{holes}); X^- = I^-, Br^-, S^{2-}(\text{anions})$.

(C) A simple model for the regeneration of the dye ground state via concurrent reactions (5–16 msec)

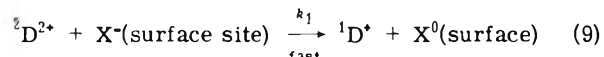
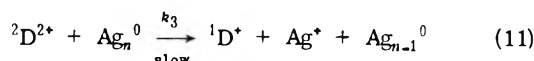
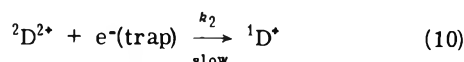
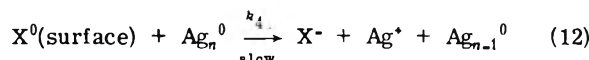


TABLE II: Activation Energies (275.4–323.6 K) of Regeneration of Dye Adsorbed to 0.05- μm AgBr(I) (S + Au) Dispersed in Gelatin Films

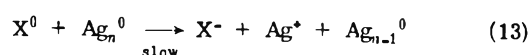
Dye	Regeneration to ground state, nm	Life-time, msec	E_{act} , kcal	W ($E_{\infty} = 1.2$ eV), \AA	W ($E_{\infty} = 0.56$ eV), \AA	$\Delta S_{\text{act}}^{\ddagger}$, cal/deg
ThC pts	565	4.3	3.7	4.4	11.4	-37
	594	9.4	2.5	4.2	9.9	-41
9-MeThCBr	518	16.2	0.73	3.9	8.6	-49
	536	5.5	5.7	4.8	14.6	-30
	592	15.9	0.73	3.9	8.6	-49
Sulfo-9-MeThC	522	10.5	3.3	4.3	10.9	-38
	570	25.0	2.7	4.2	10.3	-42
	594	14.9	2.4	4.1	9.9	-42
	622	24.5	2.3	4.1	9.9	-44
AgBr(I) (S + Au) (no dye)	490	92	0.76			-51
	680	92	0.86			-51



(D) Relaxation model for the induced transient spectrally overlapping the dye radical complex absorption. Annihilation of latent image center, Ag_n^0 (30–50 msec) [X^0 (surface) formed from reaction 9]



(E) Relaxation model for the induced (S + Au)-sensitized grain transient (92 msec) (X^0 formed from reaction 7)



II. Temperature Dependence. The activation energies relating to the temperature dependence for regeneration of the ground state, Table II, were divided into two categories. (1) Relatively high activation energies corresponding to thermal detrapping of the electron (eq 10) (2.3–5.7 kcal) or annihilation of the latent image, Ag_n^0 , via dissociation and electron transfer to the recombination site (eq 11) (Figure 6). (2) Low activation energies attributed to capture of the electron by the halogen or sulfide hole or dissociation of Ag_n^0 (eq 13) (0.60–0.80 kcal), and followed by rapid regeneration of the ground state (eq 9). Since regeneration of the ground state and the decay of the induced transient exhibit different lifetimes, additional transients were formed (eq 7–9 and 12) absorbing primarily in the 600–700- and 440–520-nm regions.

The different activation energies for the regeneration of the dye are related to the additional transients formed. This is particularly true near 520 and 595 nm, where 9-MeThCBr shows the low activation energies attributed to trapped halogen or sulfide holes.

III. A Possible Trapped Electron Model. The very large negative values for the $\Delta S^{\ddagger}(\text{act})$, Table II, described a more random arrangement in the transition state (${}^2\text{D}^{2+}\text{X}^- \rightarrow e^-(\text{trapped}) \rightarrow \text{Ag}_n^+\text{X}_n^-$) compared to the ground state (${}^1\text{D}^+\text{X}^- \rightarrow \text{Ag}_n^+\text{X}_n^-$) suggesting localization

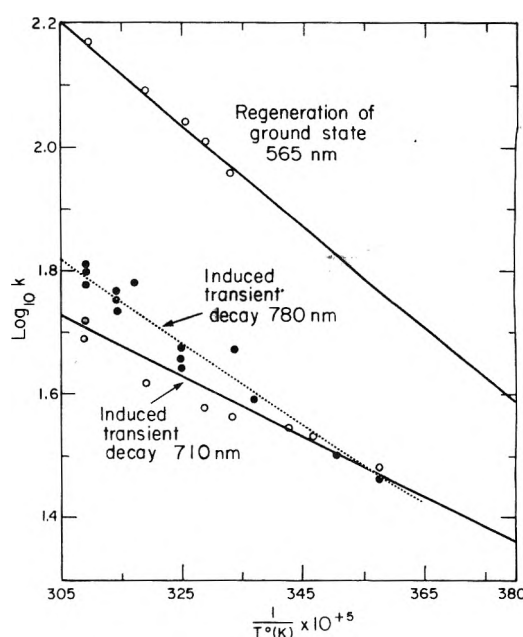


Figure 6. Representative temperature dependence of the dye 1 relaxation process at 565, 710, and 780 nm when adsorbed to 0.05- μm AgBr(I) (S + Au) grains.

of the electron near the recombination center of the ${}^2\text{D}^{2+}\text{X}^-$ (e.g., eq 10).¹⁹ It is, therefore, the object of this section to establish an estimate of the injection distance (range) of an electron emitted by the sensitizing dye radical cation. This range is of interest because the developed images are surface images and not internal grain images. A model may now be derived. In electrostatic theory, the magnitude of the barrier between two traps may be described as a simple function of the distance, W , between them, by assuming simple coulombic potentials (Figure 7).

$$E(\text{total}) = \frac{(-e)(Z'e)}{K(W-X)} + \frac{(-e)(Ze)}{KX} + C \quad (14)$$

where $E(\text{total})$ is the electrostatic interaction energy between electron-recombination center and electron trap as measured from the bottom of the conduction band of the grain.

$$\frac{dE(\text{total})}{dX} = -\frac{Z'e^2}{K} \frac{1}{(W-X)^2} + \frac{Ze^2}{KX^2} = 0 \quad (15)$$

therefore

$$X = L_m \quad (16)$$

$$L_m = \frac{W}{1 + (Z'/Z)^{1/2}}$$

The distance W (eq 25) from ${}^2\text{D}^{2+}$ is described as a function of activation energies, E_{act} , dielectric constant, K ($n_D^2 = 5.062$), where $1 > Z > 0$, $Z \approx 0.1$, the charge of the traps, neglecting screening constants (independent of electron approach), $Z' = 1 - Z$, the charge of the dye recombination center, ${}^2\text{D}^{2+}\text{X}^-$, L_m , the distance from the center of the electron trap to the maximum of the potential barrier, and E_{∞} , the energy of an electron in an isolated trap (representing bulk trapping parameters).

$$E_{\text{act}} = E_{\infty} + E_{\text{total}} \quad (\text{when } X = L_m) \quad (17)$$

$$E_{\text{act}} = E_{\infty} - \frac{e^2}{WK} \left\{ 1 + \left(\frac{Z'}{Z} \right)^{1/2} \right\} \left\{ \frac{Z'}{(Z'/Z)^{1/2}} + Z \right\} \quad (18)$$

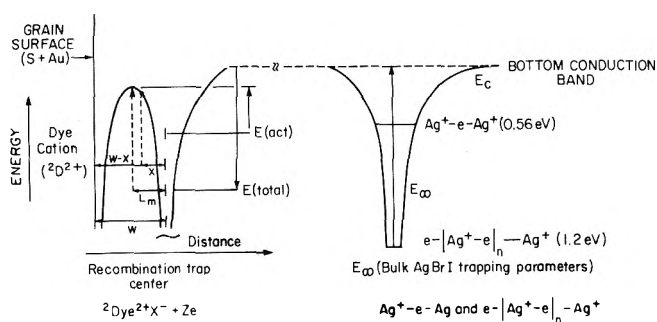


Figure 7. Simple isolated electrostatic trap model for describing relaxation mechanisms.

$$E_{(act)} = E_{\infty} - \frac{e^2}{WK} \left\{ \left(\frac{Z}{Z'} \right)^{1/2} + 1 \right\} \{ Z' + (Z'Z)^{1/2} \} \quad (19)$$

$$W = \frac{e^2}{(E_{\infty} - E_{act})K} \left\{ \left(\frac{Z}{Z'} \right)^{1/2} + 1 \right\} \{ Z' + (Z'Z)^{1/2} \} \quad (20)$$

Appropriate E_{∞} values²⁰ range between 0.56 eV for the latent image center, $Ag^+ - e - Ag^+$, and 1.2 eV (stable latent image) $e^- / Ag^+ - e / n - Ag^+$.²⁰ The following values of W ($E_{(act)}$, E_{∞}) were calculated: 3.9–4.8 Å (0.7–5.7 kcal, 1.2 eV) and 8.6–14.5 Å (0.70–5.7 kcal, 0.56 eV), assuming $Z \approx 0.1$. The values of $W(E_{(act)}, E_{\infty})$ when $Z \approx 0.9$ were also calculated and found to be 6.2–7.6 Å (0.7–5.7 kcal, 1.2 eV), and 13.8–23.2 Å (0.70–5.7 kcal, 0.56 eV). The stable latent image should be identical with the Fermi level for metallic silver and provides minimal distances for W . Detrapping wavelengths as long as 2.2 μ in pure unsensitized silver bromide yield the minimal value for E_{∞} , 0.56 eV, from Herschel-effect measurements and maximum distances of W . The Poole-Frenkel effect in insulators^{21–23} is analogous to the model proposed. The field lowering of the barrier, the activation energy maximum, is caused by a charge localized on the surface by the dye radical cation. A plausible recombination mechanism, via the conduction band, involving the activation energy is the field assistance by the charged dye radical cation. The same field-assisted recombination applies to the sulfide/halide hole and the latent image center, eq 12. The larger values of W , with E_{∞} constant, may be due to the diminished overlap of the coulomb potential walls or small $E_{(act)}$. W is relatively insensitive to the activation energy changes but is dominated by the isolated trap depth E_{∞} and charge of the silver sites within the grain (Table II).

The two relaxation phenomena described in Table II (dye-grain complex) and Table II of the accompanying paper (dye-gelatin) are different, as indicated by the activation-energy comparisons. Initial TSC (thermally stimulated current/conductivity) and ionic thermocurrent (ITC) measurements imply that the induced transient relaxations within dye adsorbed to grain surfaces are due to charge-

transfer complex (radical) formation via an injection mechanism into the conduction band of the grain rather than excited species within gelatin films. Specifically, AgBr(I) (S + Au) grains and ThC pts adsorbed on grains yield activation energies of 760 ± 30 cal (0.033 ± 0.002 eV) and 2300 ± 200 cal (0.10 ± 0.01 eV) for both ITC and optical relaxation processes, respectively. A deeper trap has also been observed optically, 3700 ± 200 cal (0.16 ± 0.01 eV) and with ITC 3500 ± 200 cal (0.155 ± 0.002 eV) for ThC pts adsorbed to grain surfaces. The energy to depolarize the impurity ion-cation vacancy dipole (ITC) is at present tentatively assumed to be equal to a trapped electron near the impurity ion site as required by the electron injection from the ${}^2D^{2+}X^-$. Experiments are in progress to further elucidate the proposed mechanisms.

Acknowledgments. It gives me great pleasure to acknowledge the stimulating discussions with Dr. J. May of the Eastman Kodak Research Laboratories. The tedious initial TSC and ITC measurements were undertaken by Dr. A. R. Vaala of the Eastman Kodak Research Laboratories.

References and Notes

- (1) S. H. Ehrlich, the Vogel Centennial Symposium, Dye Sensitization Past and Future, Putney, Vt., Aug 26–30, 1973; *Photogr. Sci. Eng.*, **18**, 179 (1974).
- (2) S. H. Ehrlich, Eleventh Informal Conference on Photochemistry, Vanderbilt University, June 16–20, 1974; *J. Photochem.*, **3**, 403 (1974–1975).
- (3) S. H. Ehrlich, *J. Phys. Chem.*, preceding article in this issue.
- (4) The effective transient absorption coefficient in units of cm^{-1} is defined: $(\Delta OD/coverage)$ density = cm^{-1} .
- (5) D. C. Skillman and C. R. Berry, *J. Chem. Phys.*, **48**, 3297 (1968).
- (6) Long lifetime decay times of photoexcited holes in silver halide crystals have been reported by several authors: (1) greater than several milliseconds,⁷ (2) 10^{-2} sec,^{8–11} and (3) minutes.¹²
- (7) M. Georgiev, *Phys. Status Solidi*, **15**, 193 (1966).
- (8) J. Malinowski and P. Suptitz, *Z. Wiss. Photogr., Photophys. Photochem.*, **57**, 4 (1963).
- (9) J. Malinowski and W. Platanikowa, *Phys. Status Solidi*, **6**, 885 (1964).
- (10) J. Malinowski, *Contemp. Phys.*, **8**, 285 (1967).
- (11) V. I. Saunders, Twenty-eighth Annual Conference, Society of Photographic Scientists and Engineers, Denver, Colo., May 11–16, 1975.
- (12) T. Tani, Twenty-eighth Annual Conference, Society of Photographic Scientists and Engineers, Denver, Colo., May 11–16, 1975.
- (13) J. Beutel, *Photogr. Sci. Eng.*, **19**, 95 (1975).
- (14) The short-lived induced transient may be due to the competing reactions of the ${}^2dye^{2+}$, but the resolution of the lifetimes due to the amplitude of the long-lived species, at present, precludes a definitive conclusion in the comparison of the regeneration of the ground state and the relaxation of the induced transient. The existence of several long-lived induced transients indicates the presence of different types of recombination centers, i.e., hole annihilation by electron traps.
- (15) (a) R. W. Gurney and N. F. Mott, *Proc. R. Soc. London, Ser. A*, **164**, 151 (1938); (b) N. F. Mott and R. W. Gurney, "Electronic Processes in Ionic Crystals", Oxford University Press, London, 1948.
- (16) W. West and P. B. Gilman, *Photogr. Sci. Eng.*, **13**, 221 (1969).
- (17) (a) T. Tani, S. Kikuchi, and K. Honda, *ibid.*, **12**, 80 (1968); (b) T. Tani, *ibid.*, **13**, 231 (1969); (c) T. Tani, *ibid.*, **14**, 63, 72, 237 (1970); (d) T. Tani, *ibid.*, **15**, 21 (1971).
- (18) The simplified notation refers to an isolated dye molecule, but in reality there is mixing of wave functions of adsorbed dye on grain surfaces.
- (19) S. Benson, "The Foundations of Chemical Kinetics", McGraw-Hill, New York, N.Y., 1960, p 493.
- (20) C. R. Berry, *J. Photogr. Sci.*, **18**, 169 (1970).
- (21) W. Vollmann, *Phys. Status Solidi*, (a) **22**, 195 (1974).
- (22) R. M. Hill, *Phil. Mag.*, **23**, 59 (1971).
- (23) J. L. Hartke, *J. Appl. Phys.*, **39**, 4871 (1968).

Solubility of Nonelectrolytes in Polar Solvents. V. Estimation of the Solubility of Aliphatic Monofunctional Compounds in Water Using a Molecular Surface Area Approach

G. L. Amidon,*¹ S. H. Yalkowsky, S. T. Anik, and S. C. Valvani

Center for Health Sciences, School of Pharmacy, University of Wisconsin, Madison, Wisconsin 53706 and The Upjohn Company, Kalamazoo, Michigan 49001 (Received April 11, 1975)

Publication costs assisted by The Upjohn Company

The molecular surface areas for 158 aliphatic hydrocarbons, olefins, alcohols, ethers, ketones, aldehydes, esters, and fatty acids have been computed and correlated with their aqueous solubilities. The hydrocarbon and functional group contributions to the free energy of solution are compared and discussed with particular regard to the chosen standard state. The results indicate that the functional group contributions to the free energy of solution in water are nearly equivalent from the pure liquid standard state while being significantly different when the gas phase (1 mmHg) standard state is chosen. The interpretation of the differing hydrocarbon surface area slopes is shown to be complicated by mutual miscibility considerations (water solubility in the pure liquid) and by the presence of curvature for the longer chain length (greater than C₁₀) compounds. The curvature in the alcohol and fatty acid data is shown to become very evident when correction is made to the pure (supercooled) liquid standard state for the solid compounds. Finally the surface area method is shown to hold considerable promise in its extension to the solubility estimation of complex organic molecules with limited aqueous solubilities.

Introduction

Recently, increasing attention has been directed to the use of a cavity or interfacial tension model and corresponding molecular surface areas for the calculation of the transfer (solvent) free energy contributions to solubility,²⁻⁴ partitioning,^{4,5} complexation,⁵⁻⁹ and solution conformational equilibria^{6,10} processes. Historically, Langmuir¹¹ was the first to suggest the use of the molecular surface area in the estimation of solution free energies and it has subsequently been employed or discussed by numerous investigators in a variety of contexts.²⁻¹⁵ In this report we extend the surface area method of estimating aqueous solubilities, previously shown to be successful in estimating the solubilities of alcohols³ and hydrocarbons.^{2,3} The following additional aliphatic (cyclic and acyclic) monofunctional compounds are considered: ethers, ketones, aldehydes, carboxylic acids, esters, and olefins. The objective of this investigation is to assess the following: (i) the degree to which molecular surface area is a useful parameter in the estimation of aqueous solubilities; (ii) is the hydrocarbon contribution the same for all functional groups; (iii) the relative functional group contributions to the solubility process; (iv) the evidence for curvature in the log (solubility) vs. surface area (or chain length) graphs above C₁₀; and (v) how the choice of standard state, i.e., pure (supercooled) liquid, affects the interpretation of the results.

Method

The surface area approach to solubility is suggested by considering the following three steps in the transfer of a solute from pure liquid to aqueous solution to be proportional to the molecular surface area:³ (i) removal of solute from its pure liquid; (ii) creation of a cavity in water; and (iii) placement of solute into the cavity. Adding on the entropy of mixing (cratic contribution) gives the following result: $\Delta\bar{G} = \theta \cdot \text{TSA} + RT \ln x$ where TSA is total molecular surface area. At equilibrium $-RT \ln X_s = \theta \cdot \text{TSA}$ where X_s is

the mole fraction solubility of the pure liquid in water.³ For monofunctional aliphatic compounds the total surface area (TSA) can be further divided into hydrocarbon (HYSA) and functional group (FGSA) contributions

$$\text{TSA} = \text{HYSA} + \text{FGSA}$$

Assuming that the hydrocarbon and functional group portions contribute independently suggests the following generalized equation for use in solubility correlations

$$\log S = \theta_1 \cdot \text{HYSA} + \theta_2 \cdot \text{FGSA} + \theta_3 \cdot \text{IFG} + \theta_0 \quad (1)$$

where S is the aqueous solubility in molal concentration units, θ_0 the intercept, HYSA and FGSA are the hydrocarbon and functional groups surface areas, respectively, and IFG is the functional group index, being zero for hydrocarbons and one for a monofunctional compound.

Molecular surface areas were calculated by the method reported by Hermann² including a solvent radius of 1.5 Å. The pure liquid form of the solute is chosen as the standard state with the appropriate correction (to the supercooled liquid) being made for the few solids in the study.^{3,16} The parameters in eq 1 were determined by regression analysis using the experimental solubilities and the computed molecular surface area. The data set for each group of monofunctional compounds included the solubilities of 17 hydrocarbons¹⁷ to allow determination of the IFG coefficient for that functional group.

Solubilities were taken from ref 17-25 and multiple determinations were included.²⁶

Results

The results of the regression analysis using eq 1 are presented in Table I. The overall statistics are excellent with an average standard error of 0.167 and an average correlation coefficient of 0.991. Two features of Table I are particularly interesting. The first is the very similar values of the IFG term for all functional groups except olefins and the second is the negative value of the FGSA term. The simi-

TABLE I: Results of Regression Analysis on the Solubility of Monofunctional Aliphatic Compounds^a

Compd	θ_1	θ_2	θ_3	θ_0	r	s	n
Hydrocarbons	-0.0195(0.001)			2.21	0.977	0.165	18
Alcohols	-0.184(0.003)	3.37(0.10)	-0.023(0.002)	1.84	0.993	0.180	91
Ethers	-0.0201(0.0006)	3.46(0.09)	-0.060(0.008)	2.38	0.997	0.130	45
Ketones/ aldehydes	-0.0186(0.0005)	3.61(0.11)	-0.034(0.003)	1.93	0.996	0.158	53
Esters	-0.0166(0.0004)	3.66(0.14)	-0.030(0.003)	1.30	0.992	0.190	76
Carboxylic acids	-0.0175(0.004)	3.66(0.51)	-0.024(0.007)	1.59	0.995	0.193	34
Olefins	-0.0200(0.0007)	0.47(0.19)	-0.018(0.006)	2.35	0.987	0.155	30

^a The model is $\log(\text{sol}) = \theta_1 \cdot \text{HYSA} + \theta_2 \cdot \text{IFG} + \theta_3 \cdot \text{FGSA} + \theta_0$ (the values in parentheses are standard errors). The significance level of the overall regression equation in each case was greater than 99.99%.

larity of the HYSA and FGSA coefficients suggest the use of the simpler equation

$$\log(S) = \theta_1' \cdot \text{TSA} + \theta_2' \cdot \text{IFG} + \theta_0' \quad (2)$$

The results using this model are presented in Table II. The average standard error and correlation coefficient are only slightly poorer for this more restricted model and the IFG terms are again very similar except for the olefins. The results in Table II suggest that, excluding the olefins, an equation including only TSA and a constant may give a reasonable correlation. The result is

$$\log(\text{sol}) = -0.0168\text{TSA} + 4.44 \quad (3)$$

(0.002)

with ($r = 0.988$, $s = 0.216$, $n = 227$). This is a surprisingly good correlation considering its simplicity and the variety of compounds covered.

Hydrocarbons Surface Area Coefficients. The coefficients for the HYSA term in eq 1 can be compared either on an energy/unit area or a energy/CH₂ group basis.³ For the hydrocarbons these values are 18.5 erg/cm² and 846 cal/CH₂ group (using 31.8 Å² as the area/CH₂ group), respectively. The value of 18.5 erg/cm² may be compared with the value of about 50 erg/cm² for a bulk hydrocarbon-water interface.²⁷ Part of this difference is due to the definition of surface area, having included a solvent radius ($R = 1.5$ Å) in this study. The incremental increase in surface area per -CH₂- group with solvent radius 1.5 Å is 31.8 Å² while that with solvent radius zero is 22.7 Å². Allowing for this difference the slope becomes 26 erg/cm². The factor of two that remains is well within the range of what is expected for a curvature correction, undoubtedly important at a molecular interface.^{3,28,29} For the seven groups of compounds included in this study the general trend is for the more polar compounds to show smaller (in absolute value) slopes and intercepts (Table I and II). This suggests a smaller methylene group hydrophobic effect for the polar compounds. This may be due to the differing effect of a methylene unit on solute-solvent interactions in the aqueous phase or solute-solute, solute-solvent interactions in the "solute" phase (vide infra).

IFG Coefficient. The IFG coefficient can be interpreted as the logarithmic solubility increase of the (mono) substituted compound over that of its hydrocarbon homomorph.³⁰ For example, 1-butanol is 1.9×10^3 times more soluble than *n*-pentane, while $10^{3.37} = 2.34 \times 10^3$ is the average solubility increase for all alcohols studied. Excluding the olefins, the IFG coefficients are not significantly different, though the esters and carboxylic acids have the largest

numerical values. The average IFG coefficient is 3.55 (excluding olefins) and corresponds to a -4.84 kcal/mol contribution of the functional group to the free energy of transfer (compared to its hydrocarbon homomorph). The olefinic group contributes -641 cal/mol to the free energy of transfer. The fact that the IFG coefficients are not significantly different suggests that a considerable amount of compensation must be occurring. That is, while some of the groups can interact more strongly with water than others, they also interact with themselves more strongly, with the net difference being nearly the same for all functional groups (except olefins) considered (vide infra).

FGSA Coefficient. The FGSA coefficient indicates the effect of the surface area variation of the functional group (through structural isomerization) on solubility. This, for example, is one of the terms which distinguishes between primary, secondary, and tertiary alcohols.³ In all cases it is negative indicating that reducing the functional group surface area increases the solubility of the compound. Aside from possible electronic effects which are presumed to be small³ three factors determine the magnitude of this term: (1) the surface area dependence of the ability of the functional group to interact with water, (2) the cavity size in water, and (3) the surface area dependence of the ability of the functional group to interact with itself in the pure liquid phase. While factor 1 would be expected to give a positive contribution to the FGSA coefficient factors 2 and 3 would make negative contributions, and on the basis of these results must be larger in magnitude than factor 1. If factor 3 was important it should be observable in some of the properties of the pure liquids. This has been shown to be true in the case of the alcohols where a reduction in the hydroxyl group surface area decreases its boiling point (increases vapor pressure) leading to an increase in solubility.³ This seems to be generally true for the compounds included in this study. Thus the increase in solubility due to branching is due in part to the effect of branching on the properties of the pure liquid (vide infra).

Intercept. Three factors influence the value of the intercept of eq 1. (i) the solubility units employed (molal in this study), (ii) the definition of surface area³¹ (includes a 1.5-Å solvent radius in this study, and (iii) the solubility of water in the "solute" phase (vide infra).

The considerations leading to eq 1 suggest that on a mole fraction and a natural log scale basis the intercept should be zero. Converting this to log and a molality concentration scale gives an expected intercept of 1.74.

The solvent radius effect, as noted by Reynolds et al.,⁴ results from the fact that with a solvent radius, a solute

TABLE II: Results of Regression Analysis Using the Model $\log(\text{sol}) = \theta_1 \cdot \text{TSA} + \theta_2 \cdot \text{IFG} + \theta_0^a$

Compd	θ_1	θ_2	θ_0	r	s
Hydrocarbons	-0.0195(0.001)		2.21	0.977	0.165
Alcohols	-0.0185(0.0003)	3.16(0.05)	1.90	0.992	0.184
Ethers	-0.0184(0.0007)	3.00(0.05)	1.87	0.995	0.168
Ketones/aldehydes	-0.0177(0.0006)	3.06(0.06)	1.64	0.993	0.196
Esters	-0.0152(0.0004)	3.00(0.06)	0.882	0.989	0.219
Carboxylic acids	-0.0173(0.0004)	3.16(0.07)	1.52	0.995	0.193
Olefins	-0.0200(0.0008)	0.520(0.06)	2.35	0.987	0.153

^a Values in parentheses are standard errors. The significance level of the overall regression equation in every case was greater than 99.99%.

with zero radius ("no particle") would have a nonzero surface area dependant on the solvent radius used in the computations. Using a solvent radius of 1.5 Å results in a surface area of 28.3 Å² for this particle of zero radius. This, however, is not the appropriate area to use for the intercept considerations in this study. The reason for this is evident from Figure 1, which is a graph of surface area with zero solvent radius vs. surface area with a 1.5-Å solvent radius for normal hydrocarbons methane through decane as well as some arbitrary point particles of radius 0.5, 1.0, and 1.5 Å (the surface area of methane is equivalent to that of a point particle radius of 1.98 Å). The graph is nonlinear, however, since all compounds in this study are larger than methane the nonlinearity can be neglected. Hence the solvent radius effect on the intercept should be taken from the extrapolated intercept of the linear segment. For the normal hydrocarbons³² the equation of the line is

$$\text{TSA}(1.5) = 1.41\text{TSA}(0) + 91.8$$

where $\text{TSA}(a)$ is the total surface with solvent radius a . The slope of 1.41 is just the ratio of methylene unit increments to the TSA with and without a solvent radius (31.8/22.6). The solubility model is

$$\log(\text{sol}) = \theta_1 \cdot \text{TSA}(1.5) + \theta_0$$

Assuming that a molecular surface area with zero solvent radius is a more "natural" choice³³ and using the results in Table I for hydrocarbons we obtain

$$\begin{aligned} \log(\text{sol}) &= -0.0195 \cdot \text{TSA}(1.5) + 2.21 \\ &= -0.0275 \cdot \text{TSA}(0) + 0.42 \end{aligned}$$

Thus the observed intercept is smaller than the expected intercept of 1.74 on a molal scale. The intercept on this basis for the monofunctional compounds would be appropriately smaller. This result for the intercept indicates that, for example, from the results for hydrocarbons, a "hydrocarbon" molecule with a surface area of about 105 Å² (including solvent radius) would have a 1 *m* solubility (methane has a surface area of 152 Å²). This result is quite consistent with, for example, graphs of $\log(\text{sol})$ vs. chain lengths, which extrapolate to a 1 *m* solubility for $n \approx 0.5$. This indicates that, solvent radius considerations aside, the extrapolation from large (four carbons and above) surface area molecules to smaller molecules (e.g., inert gases) is not plausible.^{3,34}

Discussion

The conventional standard state chosen in solubility studies, the pure (supercooled) liquid, while convenient in many respects,¹⁶ complicates the interpretation of the structural effects on the solution process in three ways. The first is that the effect of the structural change on the properties of the pure liquid must be considered, the second is

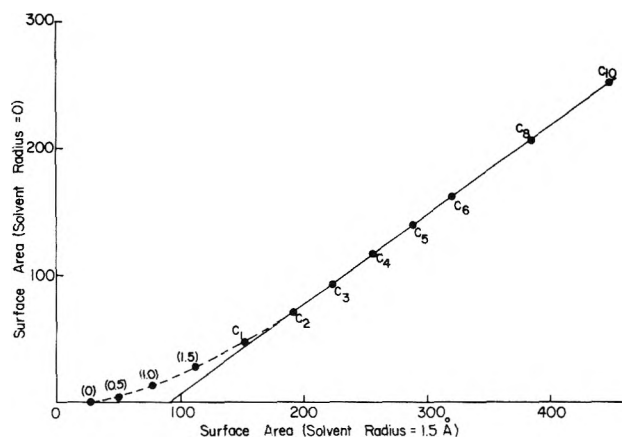


Figure 1. Relationship between surface area with zero solvent radius and that with a 1.5-Å solvent radius for the C₁-C₁₀ hydrocarbons and several point particles of radii 0, 0.5, 1.0, and 1.5 Å.

the solubility of water in the pure solute and the consequent lowering of the solute activity, and the third is that if in the course of studying a homologous series, at some point the compounds become solids at the temperature of interest a correction must be made to the pure supercooled liquid using thermal data.^{3,15}

Vapor Phase Standard State. Hildebrand³⁵ has suggested that the use of a vapor phase standard state, e.g., solubility at 1 mmHg, would facilitate the analysis of solute-solvent interactions since solute-solute interactions can generally be neglected. This standard state is the usual one for gases.

The solubility of a liquid based on the pure liquid standard state can be converted to the gas-phase standard state by assuming that Henry's law holds for the solute and dividing the solubility by the vapor pressure of the pure liquid.³⁵ Since the solubilities in this study are less than about 1 *M* (<0.02 mole fraction) and from the fact that the results of the previous study³ on the solubility of alcohols gave good estimates for the activity coefficients of the miscible alcohols suggests that Henry's law is a reasonable approximation.

The comparison of the alcohol and hydrocarbon solubilities at 1 mmHg is chosen due to the availability of solubility³ and vapor pressure³⁵ data for the normal compounds as well as a significant number of the isomers. Table III presents the results of regression analysis according to the model:

$$\log(X) = \theta_1 \cdot \text{TSA} + \theta_0$$

where X is the aqueous solubility (sol), vapor pressure at 25°C (vp), or solubility at 1 mmHg (sol/vp). TSA refers to the total molecular surface area and for the normal com-

TABLE III: Results of Regression Analysis for the Normal Alcohols and Hydrocarbons (C₄-C₁₀) Using the Model $\log(X) = \theta_1 \cdot \text{TSA} + \theta_0$ ^a

X	Alcohols ^b		Hydrocarbons ^b	
	θ_1	θ_0	θ_1	θ_0
sol	-0.0192 (±0.0007)	5.27(±0.25)	-0.0203 (±0.0010)	2.54(±0.31)
vp	-(0.0149 (±0.0007)	4.90(±0.26)	-0.0164 (±0.0011)	7.39(±0.36)
sol/vp	-(0.0043 (±0.0006)	0.37(±0.21)	-0.0038 (±0.0015)	-4.85(±0.48)

^a X = molal solubility (sol), vapor pressure at 25°C (vp), and solubility at 1 mmHg (sol/vp). Values in parentheses are 95% confidence limits. ^b The significance level in all cases was greater than 99.9%.

pounds is equivalent to using chain length. The coefficients for θ_1 in Table III suggest that the aqueous solubility and vapor pressure of the alcohols decrease less rapidly than those for hydrocarbons, while the solubility at 1 mmHg decreases more rapidly for alcohols than for hydrocarbons. This latter result is due to the less rapidly decreasing vapor pressure as a function of chain length for the alcohols. Thus the lower slope of the aqueous solubility vs. TSA (or chain length) for the normal alcohols appears to be due to the choice of standard states and not on any effects in the aqueous phase. The confidence intervals for the θ_1 coefficients for vapor pressure just overlap at the 95% level (Table III) and do not overlap at the 90% confidence level, while the θ_1 coefficient for the aqueous solubility just overlap at the 90% level. The confidence intervals for the aqueous solubility at 1 mmHg overlap at the 60% level. Hence some (~90%) confidence may be placed in the slope difference for solubility and vapor pressure vs. TSA, while very little can be placed in the solubility at 1 mmHg.

Table IV presents similar results where branched isomers have also been included. From Table IV it can be observed that the slopes for the aqueous solubilities do not change significantly from those of the normal compounds (the branched compounds outnumber the normal compounds in these studies) while the slopes for vapor pressure become steeper (more negative). This increase in slope of the vapor pressure TSA dependence is due to the fact that branching increase the vapor pressure (particularly for the alcohols) and since there are more branched C₅ and C₆ alcohols included in the study, the intercept increases and there is a corresponding increase in the slope. There is a consequent reduction in the slopes of the solubility at 1 mmHg vs. TSA graph and the alcohol and hydrocarbon slopes are virtually identical. However the correlations in this case are not particularly good as can be observed in Figure 2. This graph shows the somewhat surprising result that the normal compounds are *more* soluble (at equivalent partial pressures) than the corresponding branched (lower surface area) compounds of the same carbon number. This is true for both alcohols and hydrocarbons with the effect being more pronounced for the alcohols. While this result is difficult to explain, the interpretation is complicated by the mutual miscibility problem and is discussed below. (While there is a potential for considerable experimental error, the systematic trend in the data makes this explanation less probable.)

Mutual Miscibility Considerations. As noted previously,

TABLE IV: Results of Regression Analysis for the Normal and Branched Alcohols and Hydrocarbons (C₄-C₁₀) Using the Same Model as in Table III^a

X	Alcohols ^b		Hydrocarbons ^b	
	θ_1	θ_0	θ_1	θ_0
sol	-0.0192 (±0.001)	5.29(±0.41)	-0.0203 (±0.002)	2.42(±0.80)
vp	-0.0164 (±0.002)	5.60(±0.68)	-0.0176 (±0.002)	7.70(±0.74)
sol/vp	-0.0027 (±0.001)	-0.31(±0.43)	-0.0027 (±0.002)	-5.28(±0.66)

^a Values in parentheses are the 95% confidence limits. ^b Significance level for sol and vp equations greater than 99.99%, and for sol/vp greater than 98.8%.

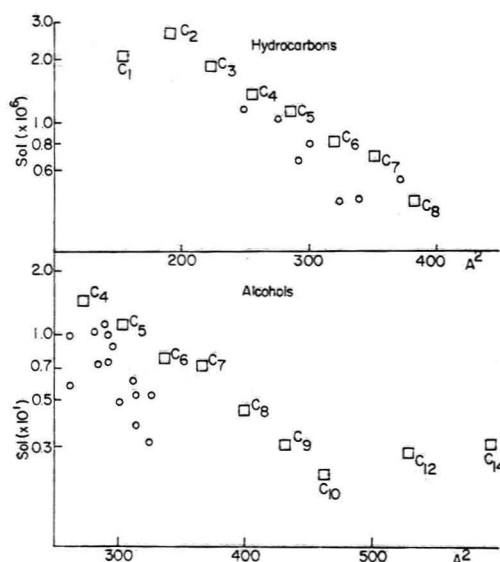


Figure 2. Solubilities of hydrocarbons and alcohols in water at equivalent partial pressures (1 mmHg); (□) normal compounds; (○) branched compounds.

the implied standard state in solubility studies is the pure liquid where as most studies involve the equilibration of the two phases. For the smaller molecular weight polar compounds the solubility of water in the "solute" phase is considerable. (See Table V.) This lowers the activity of the solute from that in its pure state. Since in general the water solubility in the solute phase decreases as the hydrocarbon segment becomes longer (except possibly for hydrocarbons) the short chain solutes will exhibit an "artificially" low solubility. This has the effect of lowering the slope of a log (sol) vs. surface area graph and reducing its intercept compared to that for the hydrocarbons. This is evident in Table I, where the hydrocarbons and olefins exhibit larger slopes and intercepts than the polar compounds and is also consistent with the polar carboxylic acids and esters, exhibiting the smallest slopes and intercepts.

Returning to the previous observation that at equivalent partial pressures, the branched compounds are less soluble than the normal compounds (Figure 2) we can note from Table V that for the alcohols, branching significantly increases the water solubility in the alcohol phase. This would cause a larger relative reduction in the activity of the branched isomer when compared to the corresponding nor-

TABLE V: Solubility of Water in Various Solvents

Compound	$T, ^\circ\text{C}$	TSA, \AA^2	Mole fraction solubility ^a
1-Butanol	25	272.1	0.515
1-Pentanol	25	303.9	0.283
3-Methyl-1-butanol	25	291.4	0.342
2-Pentanol	25	295.9	0.396
3-Methyl-2-butanol	25	284.3	0.399
2-Methyl-2-butanol	25	282.5	0.600
1-Hexanol	20	335.7	3.88×10^{-2}
<i>n</i> -Butane	20	255.2	2.1×10^{-1}
Isobutane	20	249.1	2.4×10^{-1}
<i>n</i> -Pentane	20	287.0	3.6×10^{-1}
Isopentane	20	274.6	3.6×10^{-1}
<i>n</i> -Hexane	20	319	5.3×10^{-1}
Valeric acid	20	303.4	0.459
Ethyl formate	20	242.1	0.457
Methyl acetate	20	244.9	0.264
Butyl acetate	20	344.6	0.109
Ethyl propionate	20	312.5	0.066
1-Butene	20	246.6	1.24×10^{-3}
2-Butene	20		1.4×10^{-3}
1-Heptene	20	342.1	5.7×10^{-3}
Ethyl ether	25	281.1	5.78×10^{-2}
Propyl ether	25	344.8	2.61×10^{-2}
Isopropyl ether	20		3.15×10^{-2}
Propionaldehyde	25	224.0	0.33
Butyraldehyde	25	255.8	0.11
2-Butanone	20	258.0	0.31
3-Pentanone	20	289.4	0.11
4-Methyl-2-pentanone	25	308.7	9.7×10^{-2}

^a Hydrocarbon and olefin data were taken from ref 54. The remaining solubilities are from ref 55.

mal compound. Thus the branched compounds would show an "artificially" lower solubility in water. For the branched C₄ and C₅ alcohols we have corrected the solubility for this activity effect by dividing the experimental solubility by the vapor pressure of the pure alcohol times the mole fraction of alcohol in the alcohol phase (i.e., assuming Raoult's law). The result is that while the general trend is still the same, the deviations are considerably reduced, i.e., several of the branched compounds show the expected increase in solubility (at equivalent partial pressures) over the corresponding normal compound. Due to the potential experimental error, the small differences involved in these derived values and the assumption of Raoult's law we have not reported these values. However, we may conclude that the solubility of water in the solute phase has a significant effect on the solute activity and that the lower slopes (and intercepts) of the log (sol) vs. chain length or surface area graphs for polar compounds is due in part to this effect. This is consistent with the observation in the previous study³ that extrapolation from the solubility data to the activity coefficients for the alcohols generally leads to an overestimate of the activity coefficient for the smaller alcohols. This is expected since the reduced activity of the alcohol in the alcohol phase is artificially ascribed to a higher activity coefficient in the water phase.

Due to the limited availability of experimental data for the water solubility in branched hydrocarbons, no conclusion can be made at the present time as to whether this ef-

TABLE VI: Results of Regression Analysis on the log (solubility) Surface Area Relationship for the Normal Alcohols and Carboxylic Acids Using the Model $\log(\text{sol}) = \theta_0 + \theta_1 \cdot \text{TSA} + \theta_2 \cdot (\text{TSA})^2$

Compd	Parameter values ^a			
	θ_0	$\theta_1 (\times 10^2)$	$\theta_2 (\times 10^6)$	$P, \%$
Alcohols C ₁ -C ₁₀	4.6(0.6)	-1.5(0.3)	-4.9(4.1)	30
Alcohols C ₄ -C ₁₆ (uncorrected)	6.0(0.3)	-2.3(0.1)	6.1(0.1)	0.43
Alcohols C ₄ -C ₁₆ (corrected)	6.8(0.3)	-2.8(0.2)	12(2)	0.02
Carboxylic acids C ₅ -C ₁₀	9.4(3.1)	-4.2(1.6)	30(21)	30
Carboxylic acids C ₅ -C ₁₆ (uncorrected)	6.6(1.0)	-2.5(0.4)	7.9(4.4)	13
Carboxylic acids C ₅ -C ₁₆ (corrected)	7.87(0.8)	-3.4(0.4)	19(4)	0.33

^a Values in parentheses are the standard errors of the coefficient. ^b The probability of assigning a value of zero to the (TSA)² coefficient times 100.

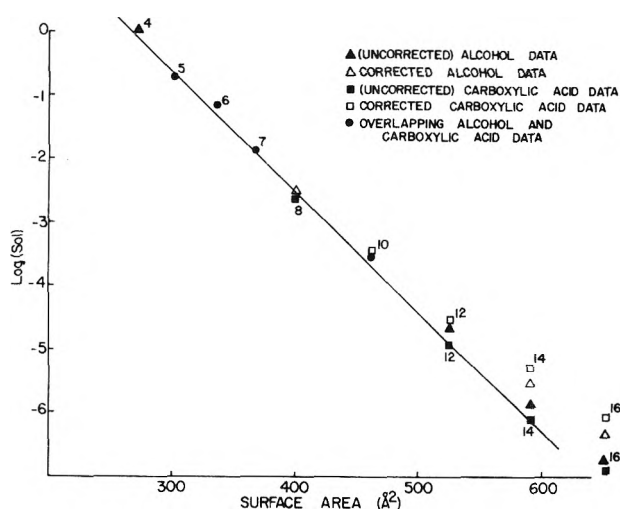


Figure 3. Log molal solubility, corrected and uncorrected, for alcohols and carboxylic acids vs. surface area (with 1.5- \AA solvent radius).

fect can account for the deviations in the case of hydrocarbons. However, since the solubilities are expected to be very low (Table V), it seems unlikely that this correction will have a significant effect.³⁷

Activity Correction for Solids. The activity correction for solids (to the supercooled liquid) is of interest due to its effect on the slope of log (sol) vs. chain length graphs (i.e., the hydrophobic contribution per $-\text{CH}_2-$ group) as well as its bearing on the question of the presence of curvature in such graphs.^{3,4,38} Figure 3 presents a graph on which both the corrected and uncorrected solubilities are shown for the normal alcohols and carboxylic acids. The heats of fusion required for this correction were taken from ref 36 for the alcohols and ref 39 for the carboxylic acids. The significant curvature of the corrected data in Figure 3 is very evident. The results of regression analysis using a model with a (TSA)² term are presented in Table VI. These results indicate that the curvature is significant for the C₁₂-

TABLE VII: Regression Results for the Normal Compounds Using a Linear Model $\log(\text{sol}) = \theta_0 + \theta_1 \cdot \text{TSA}^a$

Compd	θ_1	θ_0	n	r	s
Alcohols (C ₄ -C ₁₀)	-0.0193(±0.0006)	5.30(±0.23)	7	1.00	0.04
Alcohols (C ₄ -C ₁₀) (uncorrected)	-0.0180(±0.0006)	4.82(±0.29)	10	1.00	0.107
Alcohols (C ₄ -C ₁₀) (corrected)	-0.0170(±0.001)	4.46(±0.50)	10	1.00	0.19
Carboxylic acids (C ₅ -C ₁₆)	-0.0188(±0.004)	5.05(±1.46)	5	0.99	0.15
Carboxylic acids (C ₅ -C ₁₆) (uncorrected)	-0.0184(±0.001)	4.87(±0.56)	8	1.00	0.16
Carboxylic acids (C ₅ -C ₁₆) (corrected)	-0.0153(±0.002)	3.75(±0.93)	8	0.99	0.27

^a Values in parentheses are the 95% confidence limits.

TABLE VIII: Functional Group Contribution to the Free Energy of Solution from the Gas Phase

Compd	Sol, m/mmHg	Homomorph	Sol, m/mmHg	$\delta\Delta G$, kcal/mol
<i>n</i> -Hexane	8.35×10^{-7}			0
<i>n</i> -Hexene	3.53×10^{-6}	<i>n</i> -Hexane	8.35×10^{-7}	-0.854
Ethyl propyl ether	1.07×10^{-3}	<i>n</i> -Hexane	8.35×10^{-7}	-4.24
Diethyl ketone	3.6×10^{-2}	3-Methylpentane	7.97×10^{-7}	-6.35
Propyl acetate	4.73×10^{-3}	3-Methylpentane	7.97×10^{-7}	-5.14
Pentanoic acid	8.16×10^{-1}	2-Methylhexane	$(7.02 \times 10^{-7})^a$	$(-8.27)^a$
Pentanol	1.11×10^{-1}	<i>n</i> -Hexane	8.35×10^{-7}	-6.99

^a The solubility of *n*-heptane was used in place of the unavailable 2-methylhexane. If the comparison is made between propanoic acid (using an extrapolated aqueous solubility) and 2-methylbutane the $\delta\Delta G$ is -7.96 kcal/mol.

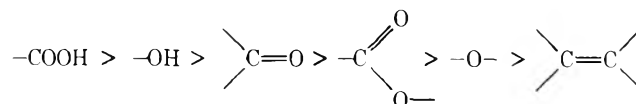
C₁₆ compounds and, particularly for the carboxylic acids, may be overlooked using uncorrected data, but must be accepted when using corrected data.

Table VII presents the results of a similar analysis using a linear model. The reduction in the slope and intercept for the corrected data compared with the C₄ (C₅ for carboxylic acids) to C₁₀ compounds is very evident. The basic regression statistics for all sets of data in Table VII are reasonably satisfactory and it is only in a more detailed analysis that the curvature becomes evident (Table VI).⁴⁰ Thus the presence of curvature on going to longer chain length may account in part for some of the observed differences in slopes and hence the differing hydrophobic effect per -CH₂- group for the various functional groups (the deviations for the longer chain length compounds is also evident in Figure 2 for the alcohols).

The most reasonable cause of this curvature seems to be some type of self-association (dimers, trimers, etc.).⁴² It was previously shown that a reasonable estimate of a "dimerization" constant by Mukerjee⁴⁴ for hexadecanoic acid accounts for about half of the observed increase in the (corrected) solubility over the predicted solubility for 1-hexadecanol.³ A similar factor is estimated for hexadecanoic acid. A further point to note is that the corrected solubility of dodecanoic acid (a solid at room temperature) lies considerably closer to the experimental solubility of dodecanol, a liquid. This is more consistent with the nearly identical solubilities of the acids and alcohols up to C₁₀ and further supports the necessity of including the correction for solids. Thus the increased curvature for acids and alcohols above C₁₀ is consistent with the observed curvature for alkanes¹⁸ above C₁₀ and supports arguments for some type of association for the longer chain length compounds.⁴⁵

Functional Group Contribution to Solubility. In the

previous discussion of the results of Tables I and II it was noted that all the functional groups (except the double bond in olefins) seemed to make approximately equivalent contributions to the free energy of solution from the pure liquid state. The success of eq 3 is apparently due to this result. That this is due to a balancing of interactions in the two phases is shown by the data in Table VIII. This table gives the group contribution to the free energy of transfer for the process gas (1 mmHg, 298) → solution (*x*, 298). While the surface areas are not identical for the various compounds this correction is small since the gas phase solubilities have a relatively small dependence on surface area (=18 kcal/32 Å², see Figure 2). The differing abilities of the various functional groups to interact with water are apparent from Table VIII with the order being



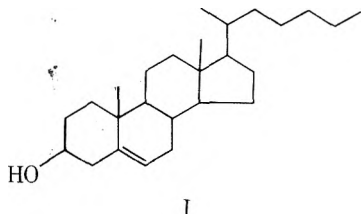
While these values may more nearly approximate the interaction free energy,⁴⁶ for the more polar compounds that have a strong tendency to dissolve water these values probably underestimate the interaction free energy for the reasons discussed above.

Cavity Model for Solvent Contribution to Conformation Free Energy. The desire to include solvent contributions in theoretical calculations of conformational equilibria has led to the use of a cavity type model in a number of cases. Based on the results of this investigation the following points can be made: (i) the slope of the log (solubility) at 1 mmHg vs. surface area curve is considerably smaller than would be expected on the basis of surface or interfacial tension data, and (ii) while an overall decrease in solubility

with surface area is observed, it is not certain that small changes in surface area (e.g., branching) go in the predicted direction. The results of Table IV (see also Figure 2) indicate that of the 833 cal contribution to the free energy of transfer per CH₂ group (for alcohols) 646 cal result from the pure liquid → vapor phase transfer and only 187 cal from the vapor phase → water transfer.⁴⁷ Thus a reduction of surface area equivalent to the loss of one methylene group will contribute less than 0.2 kcal/mol to the preference for the lower surface area state, the major portion of the free energy resulting from the hydrocarbon-hydrocarbon interactions.

Extrapolation of the Surface Area Results. As noted previously the utility of the surface area method probably lies in its extension to larger and more complex molecules. Two examples are chosen to illustrate this point: tetrahydropyran and cholesterol. Tetrahydropyran is a cyclic ether with a computed surface area of 268.3 Å². The estimated solubility using eq 3 is 0.83 *m* compared to the experimental value of 0.93 *m*.⁴⁹ This result is of interest since no cyclic ethers were included in the study and of the 158 compounds (238 data points) only eight were cyclic compounds (five hydrocarbons, two olefins, and one alcohol). This result and those for the cyclic compounds included in the study indicates that cyclic compounds are easily handled by the surface area method.

Cholesterol (I) represents a complex structure whose sol-



ubility cannot be estimated by any of the current methods. The experimental solubility is $7 \times 10^{-8} M$.⁵⁰ Correcting to the pure supercooled liquid using known thermal data $\Delta H_f = 6.625$ kcal/mol, $T_m = 149.5^\circ C$, $\Delta H_T = 0.550$ kcal/mol, $T_T = 40^\circ C$,⁵¹ gives a value of $3.4 \times 10^{-6} M$. The estimated solubility is computed from eq 3 and adding on the IFG term for olefins. An extended conformation of the side chain gives a TSA equal to 699 Å² while a folded conformation gives 655 Å². The resulting estimates for the solubility are 1.6×10^{-7} and $1 \times 10^{-6} M$. Both values are somewhat lower than the experimental value.⁵² Correcting the estimated solubility to that of the solid gives 3.3×10^{-9} to 2×10^{-8} , cf. $7 \times 10^{-8} M$ experimental. While further testing and evaluation of this extrapolation must be considered, the result indicates that the surface area method may be a very useful method for estimating the aqueous (monomer) solubilities of relatively complex molecules with low aqueous solubilities.

Summary and Conclusions

An investigation into the relationship between molecular surface area and aqueous solubilities for a large number of aliphatic monofunctional compounds shows the computed molecular surface area to be a very reliable estimator of aqueous solubility. Structural isomerization and cyclization are conveniently handled without any additional factors. While extension of the method to small surface area compounds is questionable, the extension to larger and more complex compounds with limited aqueous solubilities appears to be very promising.

A detailed analysis of the solubility data in view of the assumed (pure liquid) standard state indicates that the interpretation of log (solubility) vs. chain length (or more generally surface area) graph is complicated by the changing properties of the pure liquid solute (especially at the liquid → solid transition point) and by mutual miscibility considerations. In light of these considerations, little significance can be attributed to differing log (sol) vs. surface area slopes for the various compounds with the present data. Furthermore curvature in the log (solubility) vs. surface area graphs above C₁₀ is shown to be very significant for alcohols and fatty acids. Neglecting this effect results in lower slopes, i.e., a lower hydrophobic effect, that is actually the case.

Finally, converting the experimental solubilities to those at equivalent partial pressures indicates that the transfer free energy is only mildly dependent on surface area (~170 cal/CH₂ group) and further that branched (lower surface area) compounds are less soluble than expected.

Acknowledgments. Part of this work was carried out while one of the authors (G.L.A.) was a Visiting Professor at the Upjohn Company. Their support, and the support of the Graduate School of the University of Wisconsin, is gratefully acknowledged.

Supplementary Material Available. A listing of the solubilities and molecular surface areas used in this study will appear following these pages in the microfilm edition of this volume of the journal. Photocopies of the supplementary material from this paper only or microfiche (105 × 148 mm, 24× reduction, negatives) containing all of the supplementary material for the papers in this issue may be obtained from the Business Office, Book and Journals Division, American Chemical Society, 1155 16th St., N.W., Washington, D.C. 20036. Remit check or money order for \$4.00 for photocopy or \$2.50 for microfiche, referring to code number JPC-75-2239.

References and Notes

- (1) Author to whom correspondence should be addressed at the Center for Health Sciences, School of Pharmacy, University of Wisconsin, Madison, Wisc. 53706.
- (2) R. B. Hermann, *J. Phys. Chem.*, **76**, 2754 (1972).
- (3) G. L. Amidon, S. H. Yalkowsky, and S. Leung, *J. Pharm. Sci.*, **63**, 1858 (1974).
- (4) J. A. Reynolds, D. B. Gilbert, and C. Tanford, *Proc. Natl. Acad. Sci. U.S.A.*, **71**, 2925 (1974).
- (5) M. H. Harris, T. Higuchi, J. H. Rytting, *J. Phys. Chem.*, **77**, 2694 (1973).
- (6) O. Sinanoglu in "Molecular Associations in Biology", B. Pullman, Ed., Academic Press, New York, N.Y., 1968, p 427.
- (7) R. E. Moser and H. G. Cassidy, *J. Am. Chem. Soc.*, **87**, 3463 (1965).
- (8) J. L. Cohen and K. A. Connors, *J. Pharm. Sci.*, **59**, 1271 (1970).
- (9) G. L. Amidon, *J. Pharm. Sci.*, **63**, 1520 (1974).
- (10) D. L. Beveridge, M. M. Kelly, and R. I. Radua, *J. Am. Chem. Soc.*, **96**, 3769 (1974).
- (11) I. Langmuir, "Third Colloid Symposium Monograph", Chemical Catalog Co., New York, N.Y., 1925, p 3.
- (12) H. H. Uhlig, *J. Phys. Chem.*, **41**, 1215 (1937).
- (13) D. D. Eley, *Trans. Faraday Soc.*, **35**, 1421 (1939).
- (14) R. A. Pierotti, *J. Phys. Chem.*, **69**, 281 (1965).
- (15) R. B. Hermann, *J. Phys. Chem.*, **75**, 363 (1971).
- (16) J. H. Hildebrand, J. M. Prausnitz, and R. L. Scott, "Regular and Related Solutions", Van Nostrand-Reinhold, New York, N.Y., 1970.
- (17) C. McAuliffe, *J. Phys. Chem.*, **70**, 1267 (1966).
- (18) G. H. Bell, *Chem. Phys. Lipid*, **10**, 1 (1973).
- (19) J. R. Hommelen, *J. Colloid Sci.*, **14**, 385 (1959).
- (20) R. Vochten and G. Petre, *J. Colloid Interface Sci.*, **42**, 320 (1973).
- (21) C. Hansch, J. E. Quimlar, and G. L. Lawrence, *J. Org. Chem.*, **33**, 347 (1968).
- (22) R. Irmann, *Chem. Ing. Tech.*, **37**, 789 (1965).
- (23) N. C. Deno and H. E. Berkheimer, *J. Chem. Eng. Data*, **5**, 1 (1960).
- (24) I. D. Robb, *Aust. J. Chem.*, **19**, 2281 (1966).
- (25) R. A. Pierotti, C. H. Deal, and E. L. Derr, *Ind. Eng. Chem.*, **51**, 95 (1959), and supplementary tables.

- (26) See paragraph at end of text regarding supplementary material.
- (27) R. H. Rowkes, *Ind. Eng. Chem.*, **56**, 40 (1964).
- (28) R. C. Tolman, *J. Chem. Phys.*, **17**, 333 (1949).
- (29) H. Wakeshima, *J. Phys. Soc. (Jpn.)*, **16**, 6 (1961).
- (30) Assuming that the compound and its homomorph have the same total surface area. This is usually correct to within about 5% (e.g., TSA (*n*-hexane) = 319 Å, TSA (1-pentanol) = 304 Å).
- (31) This contribution to the intercept pointed out by Reynolds et al.⁴ was overlooked in the previous study on the aliphatic alcohols.³
- (32) In general, the relationship between TSA (1.5) and TSA (0) cannot be described by a linear equation. This equation is quite satisfactory for "cylindrical" molecules but somewhat less satisfactory for "spherical" molecules.
- (33) Implicit in this approach is that the solute molecule is significantly larger than the solvent molecule, otherwise free volume effects arise. The use of a solvent radius is convenient from the point of view of calculating the number of solvent molecules around a given solute molecule. The use of such a number would certainly emphasize the packing considerations and associated problems.
- (34) The utility of the surface area approach is more likely to reside in the extrapolation to larger and more complex molecules.
- (35) J. H. Hildebrand, *J. Phys. Colloid Chem.*, **53**, 973 (1949).
- (36) R. C. Wilhoit and B. J. Zwolinski, *J. Phys. Chem., Ref. Data*, **2**, Suppl. 1 (1973).
- (37) It has been suggested that cavity shape effects may be important.⁴ From a cavity (or "interfacial") model point of view, the smaller radius of curvature for a branched (more spherical) molecule would lead to a higher surface (or interfacial) tension and hence require more energy/unit area to create a cavity of a given size, thus lowering the solubility. While this is consistent with the observations, the situation in water is undoubtedly more complex.
- (38) R. Smith and C. Tanford, *Proc. Natl. Acad. Sci. U.S.A.*, **70**, 289 (1973).
- (39) A. Bondi, "Physical Properties of Molecular Crystals, Liquids and Gases", Wiley, New York, N.Y., 1968, p 161.
- (40) Residual plots for both the uncorrected and corrected data sets in Table VII show trends indicative of the omission of a quadratic term.⁴¹
- (41) N. R. Draper and H. Smith, "Applied Regression Analysis", Wiley, New York, N.Y., 1966, p 86.
- (42) However, the possibility of a contribution of some intramolecular effects (e.g., coiling) cannot be ruled out.⁴³
- (43) R. H. Aronow and L. Witten, *J. Phys. Chem.*, **64**, 1843 (1960).
- (44) P. Mukerjee, *Adv. Colloid Interface Sci.*, **1**, 241 (1967).
- (45) We can further note that if the solubilities of the shorter length alcohols and carboxylic acids were correct for the solubility of water in the pure liquid phase, the solubilities of these compounds would be somewhat increased and further accentuate the curvature in Figure 3.
- (46) The comparison is made to the homomorph in order to reduce the strictly cavity effect of adding a functional group to the hydrocarbon. If, for example, the comparison were made between pentanol and pentane the $\delta\Delta G$ in Table VII would be about 0.2 kcal/mol more positive.
- (47) Similar results have been noted by Butler⁴⁸ and Mukerjee.⁴⁴
- (48) J. A. V. Butler, C. N. Ramchandani, and D. W. Thomson, *J. Chem. Soc.*, 952 (1935).
- (49) G. M. Bennett and W. G. Philip, *J. Chem. Soc.*, 1937 (1928).
- (50) H. Y. Saad and W. I. Higuchi, *J. Pharm. Sci.*, **54**, 1205 (1965).
- (51) J. L. Sheumaker and J. K. Guillory, Abstracts, 15th Annual Academy Pharmaceutical Sciences Meeting, San Diego, 1973.
- (52) The estimated solubility is that of a monomer; in addition to impurities, other factors such as self-association and solvation of the cholesterol crystal could be responsible for this result.⁵³
- (53) G. L. Flynn, personal communication.
- (54) C. Black, G. G. Joris, and H. S. Taylor, *J. Chem. Phys.*, **16**, 537 (1948).
- (55) J. A. Riddick and W. B. Bunger, "Organic Solvents", 3rd ed, Wiley-Interscience, New York, N.Y., 1970.

Aqueous Dissociation of Croconic Acid

Lowell M. Schwartz,* Robert I. Gelb, and Janet O. Yardley

Department of Chemistry, University of Massachusetts, Boston, Massachusetts 02125 (Received March 10, 1975)

The dissociation constants of croconic acid $\text{H}_2\text{C}_5\text{O}_5$ have been measured in aqueous solution and are found to be $\text{p}K_1 = 0.80 \pm 0.08$ and $\text{p}K_2 = 2.24 \pm 0.01$ at 25°C. These measurements were done spectrophotometrically and corroborating values were determined by pH potentiometry. The temperature dependencies of the dissociation constants yield the standard thermodynamic parameters $\Delta H_1^\circ = +3.9 \text{ kcal mol}^{-1}$ and $\Delta S_1^\circ = +9.5 \text{ cal mol}^{-1} \text{ deg}^{-1}$ for the primary dissociation and $\Delta H_2^\circ = -3.0 \text{ kcal mol}^{-1}$ and $\Delta S_2^\circ = -20.2 \text{ cal mol}^{-1} \text{ deg}^{-1}$ for the secondary dissociation. Both ΔH_1° and ΔS_1° are unusually large positive values for dissociation of an uncharged acid and lead to the conclusion that the relatively high acid strength of croconic acid is attributable to entropy considerations.

Introduction

1,2-Dihydroxycyclopentenetrione, $\text{H}_2\text{C}_5\text{O}_5$, commonly known as "croconic acid" is a member of the series of oxo-carbon ring systems which has been under extensive study by West and coworkers.¹ The dianions of these acids are strongly stabilized by π -electron delocalization² which has been proposed to account for the unusually high acid strengths of the parent compounds. On the other hand, we have proposed an alternative explanation for the strength of aqueous squaric acid $\text{H}_2\text{C}_4\text{O}_4$ based on considerations of entropy of solvation.³ Since a comparison of oxocarbon acid $\text{p}K$ values⁴ shows croconic acid about as strong as squaric acid, we would like to investigate croconic acid in a similar way but enthalpies and entropies of dissociation are unknown. Reported measurements of aqueous dissociation constants are for $\text{H}_2\text{C}_5\text{O}_5$, $\text{p}K_{1c} = 0.32$ and $\text{p}K_{2c} = 1.51$;⁵

for $\text{H}_2\text{C}_4\text{O}_4$, $\text{p}K_1 = 0.54 \pm 0.006$ ^{3,6} and $\text{p}K_2 = 3.48 \pm 0.02$.⁷ These sets of numbers, however, are not directly comparable because the squaric acid constants are "thermodynamic" values in the sense of relating species activities but the croconic acid measurements were made in constant ionic strength media of 2M NaCl + HCl and no attempt was made to apply activity coefficients. We can make a rough activity coefficient correction to the croconic acid dissociation constants by noting that the activity coefficient of HCl in 2M NaCl + HCl is approximately 0.88.⁸ If we denote the activity coefficients of ionic species HC_5O_5^- by γ_1 and of $\text{C}_5\text{O}_5^{2-}$ by γ_2 and if we assume in a given solution that $\gamma_{\text{HCl}} = \gamma_{\text{H}^+} = \gamma_1 = \gamma_2^{1/4}$, then the estimated dissociation constants are $\text{p}K_1 = \text{p}K_{1c} - \log \gamma_{\text{H}^+\gamma_1} = 0.43$ and $\text{p}K_2 = \text{p}K_{2c} - \log \gamma_{\text{H}^+\gamma_2/\gamma_1} = 1.73$. By this estimate the acid strength of $\text{H}_2\text{C}_5\text{O}_5$ is somewhat greater than $\text{H}_2\text{C}_4\text{O}_4$ but the crude nature of the estimation leaves the relative acidities very

much in doubt. The work reported here represents attempts (1) to measure the aqueous dissociation constants of croconic acid in lesser ionic strength solution so that activity coefficients can be estimated with greater certainty, (2) to obtain individual spectra of the three croconate species in aqueous solutions, (3) to measure the temperature dependence of the dissociation constants in order to separate enthalpy and entropy contributions to the dissociation reactions, and (4) to compare all these results with corresponding determinations on squaric acid seeking to establish trends in the oxocarbon ring series.

Methods

To measure the aqueous dissociation constants we have employed both spectrophotometric and pH potentiometric methods. Spectrophotometry is particularly well suited to the croconic acid-croconate system because there is a substantial change in the solution uv absorption as the equilibrium composition is shifted from principally $\text{H}_2\text{C}_5\text{O}_5$ to HC_5O_5^- to $\text{C}_5\text{O}_5^{2-}$ by increasing the pH. Both dissociation constants K_1 and K_2 are determined with relatively high degrees of confidence. The pH potentiometric method can be used to measure K_2 accurately but is less suitable for K_1 because the determination is quite sensitive to reagent purity and to the response of the glass electrode and these factors introduce a relatively large uncertainty.

The spectrophotometric method has been described by Carlqvist and Dyrssen⁵ and others. Briefly, if $\epsilon_0(\lambda)$, $\epsilon_1(\lambda)$, and $\epsilon_2(\lambda)$ are the molar extinction coefficient spectra of $\text{H}_2\text{C}_5\text{O}_5$, HC_5O_5^- , and $\text{C}_5\text{O}_5^{2-}$, respectively, then the absorbance $A(\lambda)$ spectrum of a 1.00-cm path through a given solution is, assuming Beer's law for each species

$$A(\lambda) = [\text{H}_2\text{C}_5\text{O}_5]\epsilon_0(\lambda) + [\text{HC}_5\text{O}_5^-]\epsilon_1(\lambda) + [\text{C}_5\text{O}_5^{2-}]\epsilon_2(\lambda) \quad (1)$$

The species concentrations and therefore $A(\lambda)$ are pH dependent. After writing the two dissociation reactions in terms of activities

$$K_1 = \frac{\gamma_{\text{H}^+}\gamma_1 [\text{H}^+][\text{HC}_5\text{O}_5^-]}{\gamma_0 [\text{H}_2\text{C}_5\text{O}_5]} \quad (2)$$

and

$$K_2 = \frac{\gamma_{\text{H}^+}\gamma_2 [\text{H}^+][\text{C}_5\text{O}_5^{2-}]}{\gamma_1 [\text{HC}_5\text{O}_5^-]} \quad (3)$$

The croconate species concentrations can be eliminated from eq 1, with the result being

$$A = \left[\epsilon_0 + \frac{\epsilon_1 K_1}{[\text{H}^+]G_1} + \frac{\epsilon_2 K_1 K_2}{[\text{H}^+]^2 G_1 G_2} \right] \frac{F}{P} \quad (4)$$

or

$$\frac{AP}{F} - \epsilon_2 \frac{K_1 K_2}{[\text{H}^+]^2 G_1 G_2} = \epsilon_0 + \epsilon_1 \frac{K_1}{[\text{H}^+]G_1} \quad (5)$$

In these equations, we denote molar concentrations by [], molar activity coefficients by γ , $\gamma_{\text{H}^+}\gamma_1/\gamma_0$ by G_1 , $\gamma_{\text{H}^+}\gamma_2/\gamma_1$ by G_2 , croconate formality (analytical concentration) by F , and

$$\left[1 + \frac{K_1}{[\text{H}^+]G_1} + \frac{K_1 K_2}{[\text{H}^+]^2 G_1 G_2} \right]$$

by P . The strategy is to make up a series of solutions ranging in pH values from below $\text{p}K_1$ to above $\text{p}K_2$ with each solution containing the same croconate formality F and to measure the uv spectra of these solutions from about 400 to

250 nm, in which region the absorption of the individual species is most intense and different. This work gives us $A(\lambda)$, $[\text{H}^+]$, and F , and if K_1 , K_2 , G_1 , G_2 , and $\epsilon_2(\lambda)$ were known then the only unknowns remaining in eq 5 would be $\epsilon_0(\lambda)$ and $\epsilon_1(\lambda)$. Conveniently, we find that for any given λ these parameters are the intercept and slope, respectively, of a predicted straight line on cartesian coordinates with an abscissa of $K_1/[\text{H}^+]G_1$ and with an ordinate of the left-hand side of eq 5. A series of such lines, each representing a distinct wavelength, is required to determine the species spectra $\epsilon_0(\lambda)$ and $\epsilon_1(\lambda)$. The other necessary parameters are determined as follows: $\epsilon_2(\lambda)$ is found by measuring the spectrum of croconate solution at $\text{pH} > 5$. Since $\text{p}K_2$ is near 2, this spectrum is due solely to absorption by $\text{C}_5\text{O}_5^{2-}$. G_1 and G_2 are composites of activity coefficients. We assume that $\gamma_c = 1$ for the undissociated $\text{H}_2\text{C}_5\text{O}_5$, that the mean activity coefficient γ_{\pm} of $\text{H}^+(\text{HC}_5\text{O}_5^-)$ is the same as that of the acid (H^+Cl^- or H^+ClO_4^-) employed in setting the desired pH of the medium, and that for HCl the activity coefficients are those measured by Harned and Ehlers⁹ and for HClO_4 , those tabulated in Robinson and Stokes^{10a} for $[\text{H}^+] \geq 0.1 m$ and those predicted by the Debye-Hückel equation^{10b} with ion-size parameter $a = 6.7 \text{ \AA}$ for $[\text{H}^+] < 0.1 m$. Furthermore, we take $G_2 = \gamma_2 = \gamma_{\pm}^4$, which in effect assumes $\gamma_{\text{H}^+} = \gamma_1$. K_1 and K_2 are determined by a systematic digital computer scan seeking those two values which yield the closest least-squares fit of the calculated spectra (A of eq 4) to the experimental spectra of all solutions.

As mentioned above, ϵ_0 and ϵ_1 are calculated at each wavelength from the intercept and slope, respectively, of straight lines in accordance with eq 5. We see that to extract ϵ_0 and ϵ_1 by conventional least-squares analysis of lines of the form $y = b + mx$ would be inappropriate as conventional least-squares requires each y data value to have equal a priori statistical uncertainty δy , i.e., δy must be independent of x . Statistical uncertainty enters the left-hand side of eq 5 principally in the absorbance values which are all approximately ± 0.005 , and these measurements appear as A and as $\epsilon_2 = A_2/F$, where A_2 are the $\text{C}_5\text{O}_5^{2-}$ absorbances. Since both A and A_2 are multiplied by functions of $[\text{H}^+]$ and $x = K_1/G_1[\text{H}^+]^2$ is also a function of $[\text{H}^+]$, the uncertainties δy are functions of x and so a weighted least-squares procedure is necessary. Each data point must be multiplied by a weighting factor inversely proportional to the variance δy^2 of the y value.^{18a} Assuming that only A and A_2 parameters in y carry significant variance (0.005² units each), we find the variance

$$\delta y^2 = 0.005^2 \left[\frac{P^2}{F^2} + \left(\frac{K_1 K_2}{F[\text{H}^+]^2 G_1 G_2} \right)^2 \right]$$

and so an appropriate weighting factor is

$$\left[P^2 + \left(\frac{K_1 K_2}{[\text{H}^+]^2 G_1 G_2} \right)^2 \right]^{-1}$$

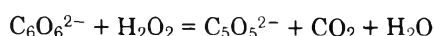
The physical reasoning for this weighting factor is as follows. In solutions where $K_2/[\text{H}^+]$ is high enough, the second dissociation is complete, all the croconate is dianion, and no $\text{H}_2\text{C}_5\text{O}_5$ or HC_5O_5^- exists. Since eq 5 expresses nothing but the sum of the absorbances of these two species, a data point from a solution not containing these is meaningless and must be discarded from the analysis by a small weighting factor. To fail to do this would introduce erroneous points with $y = 0$ but ϵ_0 and ϵ_1 perhaps not zero. The weighting factor approaches unity in highly acidic solutions when all the croconate is in the form $\text{H}_2\text{C}_5\text{O}_5$ and

decreases with increasing pH as $[C_5O_5^{2-}]$ increases. In our solutions, the weighting factors ranged from 0.58 in 0.75 *M* H^+ to 0.00 below 0.006 *M* H^+ .

The pH potentiometric method is an aqueous titration of potassium croconate $K_2C_5O_5$ salt with HCl solution and measurements of the pH and volumes of the solutions. The equations defining the equilibria and stoichiometry during an acid-base titration of this sort are well known. From any given solution of known volume, croconate formality, and pH, a single dissociation constant can be calculated. We regard the titration data from the start of the titration to the first equivalence point as determining K_2 and so in this region K_1 is treated as a known quantity estimated from data points beyond the first equivalence point. K_2 is calculated for each recorded solution in this region (excluding values within 10 volume % of the start and the equivalence point) and the mean of these is computed. In the region between the two equivalence points K_1 is calculated at each recorded solution and K_2 is regarded as an estimated known, the mean K_2 just mentioned. Again excluding points within 10% of the equivalence points, the mean of the K_1 values is computed and this serves as the estimate for the K_1 in the first region. The calculation alternates from one region to the other until the mean K_1 and the mean K_2 cease to change on further refinement, which invariably occurs within four cycles. A subsidiary set of iterations is also required because, in any given solution, the coupled nonlinear set of equations defining the dissociation constants, species concentrations, activity coefficients, and ionic strength cannot be solved explicitly in terms of the input quantities: pH, formalities, and solution volume. However, by starting with reasonable estimates of activity coefficients, convergence is very rapid. The assumptions with regard to activity coefficients used in this calculation are the same as used in the spectrophotometric calculations described above. Typical titration calculations were free from trends in either K_1 or K_2 values, which lends a degree of confidence both to the experimental technique and the validity of the model equations used.

Experimental Section

Croconic acid was prepared as the dipotassium salt starting from dipotassium rhodizonate, $K_2C_6O_6$, purchased from Aldrich Chemical Co., Milwaukee, Wisc. Two procedures were used, one reported by Fatiadi and coworkers¹¹ utilizing MnO_2 as oxidizing agent, the other developed in this laboratory using H_2O_2 according to the equation



0.1 mol of $K_2C_6O_6$ and 0.25 mol of KOH are dissolved in about 50 ml of warm water. 3% H_2O_2 is added slowly with stirring up to a slight excess of 0.1 mol. When the dark green rhodizonate has changed to the yellow-orange croconate, the solution is cooled to 0°C and the product crystallizes spontaneously. The crystals are collected and washed with cold water-ethanol. The crude product is recrystallized from water-ethanol and dried under vacuum at 60°C. Before extended drying the crystals analyze to formula weight near 272 corresponding to the trihydrate $K_2C_5O_5 \cdot 3H_2O$ in accordance with Fatiadi et al.¹¹ but with even slight heating, the crystals become more yellow and opaque and with loss of weight, the formula weight approaches 236 indicating conversion to a monohydrate. Both the ir and the aqueous uv spectra of the materials prepared by MnO_2 and H_2O_2 oxidation are identical and the aqueous uv spec-

trum is identical with that reported by Carlqvist and Dyrsen.⁵

We analyzed the potassium croconate crystals by reaction with excess Ce(IV) in dilute HCl according to $C_5O_5^{2-} + 12Ce(IV) + 5H_2O = 5CO_2 + 12Ce(III) + 10H^+$ followed by back titration of the excess cerium with Fe(II) to a potentiometric endpoint using a platinum indicator electrode. Since no melting of the $K_2C_5O_5 \cdot H_2O$ is observed below 300°C, and no detectable spurious uv-visible absorption is observed, we assume that any deviation of an analysis from FW 236 (typically 2%) is attributable to extraneous water of hydration, which effect is easily compensated in the calculations.

The spectrophotometric determinations were made of freshly prepared aqueous solutions of croconate in HCl or $HClO_4$ ranging in $[H^+]$ from 0.75 to 0.0025 *M*. Since aqueous croconic acid decomposes slowly in HCl and more rapidly in $HClO_4$ (half-life about 1 day), most of the spectra of these solutions were measured within minutes of their preparation and if temperature equilibration necessitated a longer delay, the possible decay of absorption was checked against a fresh solution. One series of determinations was made at 25°C using several separately prepared croconate samples in each acid and another series was made from a single sample in HCl at temperatures ranging from 10 to 40°. Measurements were made with a Beckman Acta C III spectrophotometer using thermostatted ($\pm 0.1^\circ C$) silica cuvetts, the reference cuvet containing aqueous acid with $[H^+]$ identical with the sample.

The pH measurements were made during titration of croconate solutions 0.05 to 0.08 *M* with 1.000 *M* HCl and employing an Orion Model 801 digital pH meter with glass and Ag|AgCl reference electrodes. The pH meter was standardized with both 0.1000 *M* HCl and NBS standard 1:1 phosphate buffer whose pH as a function of temperature is given by Bates.¹² The titrated solutions were thermostatted to $\pm 0.1^\circ C$.

Results

The results of both spectrophotometric and potentiometric measurements are given in Table I. In the column headed Solution is a code which describes the source of the croconate sample and the acid medium: F denotes croconate by MnO_2 oxidation, G by H_2O_2 oxidation, H denotes HCl, and P denotes $HClO_4$. In the Rms deviation column are listed the average deviation (in absorbance units) of the calculated from the experimental spectral values. The average rms deviation of about 0.007 is to be compared to recorded absorbance values typically 0.2 to 2.0 which indicates an acceptable fit of the model equations to the experimental data.

The pH potentiometric results are given in the lower part of Table I. The several values at 25°C reflect the variability of results from different batches of synthesized potassium croconate. The uncertainties quoted with each pK value indicate the standard deviation of pK values obtained from about ten measurements made during a single titration. In one titration of type GH at 25°C a substantial trend was observed in pK₁ values and this is reflected in the anomalously large uncertainty of pK₁ in this case.

We have attempted to estimate the degree of uncertainty of the dissociation constant determinations both as a result of determinate and of random errors. The effect of determinate error on the calculated pK values is found by repeating the pK calculations in turn with each input param-

TABLE I: Croconic Acid pK Determinations

t, °C	Solution ^a	pK ₁	pK ₂	Rms deviation
Spectrophotometric Method				
10.0	FH	0.90	2.13	0.007
15.0	FH	0.85	2.16	0.007
20.0	FH	0.80	2.19	0.006
25.0	FH	0.76	2.23	0.006
25.0	FP	0.94	2.26	0.007
25.0	GH	0.86	2.24	0.003
30.0	FH	0.72	2.27	0.006
35.0	FH	0.64	2.30	0.008
40.0	FH	0.62	2.35	0.007
pH Potentiometric Method				
14.6	GH	0.76 ± 0.009	2.21 ± 0.010	
17.1	FH	0.78 ± 0.010	2.24 ± 0.009	
25.0	FH	0.76 ± 0.012	2.28 ± 0.012	
25.0	GH	0.69 ± 0.005	2.26 ± 0.012	
25.0	GH	0.45 ± 0.11	2.28 ± 0.005	
35.6	FH	0.70 ± 0.004	2.34 ± 0.010	
44.4	FH	0.66 ± 0.010	2.40 ± 0.012	
54.5	FH	0.57 ± 0.004	2.47 ± 0.009	

^a FH means HCl medium and K₂C₅O₅ prepared with MnO₂. FP means HClO₄ medium and K₂C₅O₅ prepared with MnO₂. GH means HCl medium and K₂C₅O₅ prepared with H₂O₂.

eter incremented by its estimated determinate error. The random errors are propagated into the resultant pK values by a Monte Carlo computer simulation¹³ of repeated experimentation with each input parameter in turn subjected to random fluctuation consonant with its estimated standard deviation. The results of these uncertainty estimates are shown in Table II. Clearly, the pK values are less sensitive to uncertainties by the spectrophotometric method. The sums of the uncertainties of both determinate and random nature represent conservative estimates of the overall uncertainty in pK values and these are by spectrophotometry, ±0.08 and ±0.01 for pK₁ and pK₂, respectively, and by potentiometry ±0.34 and ±0.14 for pK₁ and pK₂, respectively. Appending these estimates to the results at 25°C in Table I we conclude that by spectrophotometry pK₁ = 0.80 ± 0.08 and pK₂ = 2.24 ± 0.01 and by potentiometry pK₁ = 0.7 ± 0.3 and pK₂ = 2.28 ± 0.14. The pK₁ = 0.80 cited is the average of two values as explained in Table IV.

The spectrophotometric method yields extinction coefficient spectra of each of the three croconic acid species. Our results here agree very well with those of Carlqvist and Dyrssen⁵ as shown in their Figure 8. Each species spectrum appears to be the sum of two overlapping peaks. The peak absorption shifts to longer wavelength and to greater intensity as protons are successively removed from H₂C₅O₅. We have resolved each spectrum into two component gaussians¹⁴ and have shown the results in Table III together with similar results with squaric acid and its anions. In this table, ε_{max} is the molar extinction coefficient at the center of a component peak, λ_{max} is its position, δ is the half-width of the peak, and the rms deviation is the degree of discrepancy between the spectrum and the sum of the two component gaussians as expressed as a percentage of the maximum extinction coefficient.

The temperature dependencies of pK₁ and pK₂ have been fitted to linear equations by the method of least-squares with the following results:

TABLE II: Computed Effects of Uncertainties on pK Determinations

Est uncertainty	Approximate effect on	
	pK ₁	pK ₂
Spectrophotometric Method		
I. Determinate errors		
A. [H ⁺] of medium	0.5%	0.001 0.002
B. K ₂ C ₅ O ₅ formality	2%	nil nil
C. Photometric accuracy	0.4%	nil nil
D. Activity coefficients as reflected in ion-size parameter	3 Å	0.068 0.001
II. Random errors		
A. Absorbance readings	0.005	0.013 0.010
B. K ₂ C ₅ O ₅ formality	0.2%	nil nil
C. [H ⁺] of medium	0.1%	nil nil
Potentiometric Method		
I. Determinate errors		
A. K ₂ C ₅ O ₅ formality	2%	0.050 0.008
B. HCl concentration	0.1%	0.005 nil
C. Volumetric calibration	0.2%	nil nil
D. pH meter calibration	0.003	0.020 0.003
E. Activity coefficients as reflected in ion-size parameter	3 Å	0.13 0.08
II. Random errors		
A. K ₂ C ₅ O ₅ formality	0.4%	0.010 nil
B. pH meter readings	0.002	0.007 nil
C. Volumetric readings	0.01 ml	0.12 0.052

TABLE III: Spectra of Croconic and Squaric^a Acids and their Anions in Aqueous Solution at 25°C Resolved into Two Component Gaussian Peaks

	Peak 1			Peak 2			% rms deviation
	10 ⁻⁴ ε _{max}	λ _{max} , nm	δ, nm	10 ⁻⁴ ε _{max}	λ _{max} , nm	δ, nm	
H ₂ C ₅ O ₅	1.46	286	19.5	0.31	341	33.1	1.6
HC ₅ O ₅ ⁻	1.93	309	14.5	1.88	355	34.0	3.2
C ₅ O ₅ ²⁻	2.48	334	15.7	3.61	365	15.5	0.9
H ₂ C ₄ O ₄	1.34	230	10.4	1.90	251	12.8	1.7
HC ₄ O ₄ ⁻	2.08	241	13.5	1.81	263	10.5	1.7
C ₄ O ₄ ²⁻	2.27	251	14.6	2.31	272	10.1	0.9

^a Reference 15.

$$pK_1 = -2.08(\pm 0.15) + \frac{845(\pm 45)}{T} \quad (6)$$

$$pK_2 = 4.39(\pm 0.08) - \frac{644(\pm 24)}{T} \quad (7)$$

with the temperature *T* in Kelvin. The data points contributing to these empirical equations are those measured spectrophotometrically on samples only of the same type, code FH in Table I, and between 10 and 40°C. The figures in parentheses in eq 6 and 7 are standard deviations of the least-squares parameters and these uncertainties reflect the extent of statistical scatter of the data points about the correlations. The pK₁ and pK₂ experimental results of the FH series are plotted in Figure 1 with the overall predicted

TABLE IV: Summary of Standard Thermodynamic Properties of Dissociation at 25°C

	Croconic acid			Squaric acid ^e
		Statistical uncertainty ^c	Maximum uncertainty ^d	
pK_1	0.85 ^a 0.76 ^b		± 0.08	0.54 ± 0.06
ΔG_1° , kcal mol ⁻¹	1.025 ^b	± 0.007	± 0.11	0.74 ± 0.08
ΔH_1° , kcal mol ⁻¹	+3.87 ^b	± 0.21	± 2.2	-1.49 ± 0.12
ΔS_1° , cal deg ⁻¹ mol ⁻¹	+9.54 ^b	± 0.73	± 7.7	-7.5 ± 0.7
pK_2	2.24 ^a 2.23 ^b		± 0.01	3.48 ± 0.02
ΔG_2° , kcal mol ⁻¹	3.051 ^b	± 0.003	± 0.01	4.75 ± 0.03
ΔH_2° , kcal mol ⁻¹	-2.95 ^b	± 0.11	± 0.32	-3.0 ± 0.5
ΔS_2° , cal deg ⁻¹ mol ⁻¹	-20.1 ^b	± 0.4	± 1.1	-26.1 ± 1.6

^a Average of spectrophotometric determinations listed in Table I. ^b Evaluated from the empirical eq 6 or 7 at 298.15 K. ^c Derived from standard error of estimate and statistical uncertainties in the slope and intercept values in empirical eq 6 on 7. ^d Derived from extreme slopes through error bounds based on error from sources listed in Table II. ^e References 3 and 7.

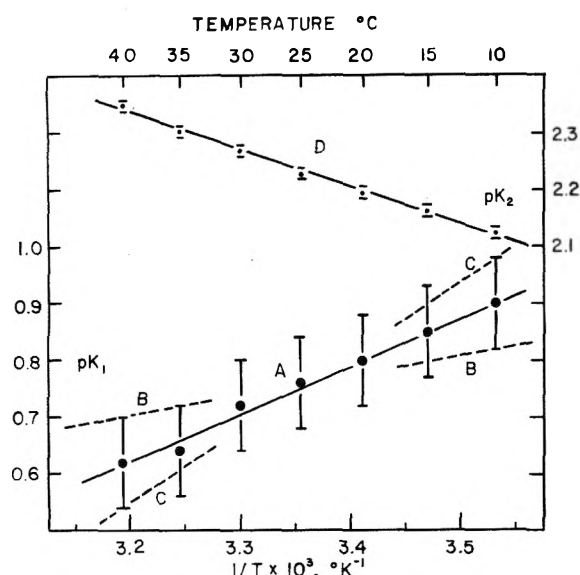


Figure 1. pK_1 and pK_2 vs. temperature. Data points are the results of spectrophotometric series FH. Error flags are uncertainty estimates of ± 0.08 for pK_1 and ± 0.01 for pK_2 from Table II. Lines A and D are plots of eq 6 and 7, respectively. Lines B and C are the extreme slopes through all the pK_1 error bounds.

uncertainties of ± 0.08 and ± 0.01 drawn as error flags about the pK_1 and pK_2 points, respectively.

Discussion

By comparing croconic acid $pK_1 = 0.80 \pm 0.08$ with squaric acid $pK_1 = 0.54 \pm 0.06$, it is clear that squaric acid is the stronger of the two, yet the relative acid strengths of the monoanions are reversed, $pK_2 = 2.24 \pm 0.01$ for croconic vs. $pK_2 = 3.48 \pm 0.02$ for squaric. The measured temperature variations of pK serves as a means of calculating ΔH° , ΔS° , and ΔG° , the standard enthalpy, entropy, and Gibbs free energy, respectively, of each dissociation reaction from the well-known thermodynamic relationships. By differentiating eq 6 and 7 at 25°C, we find $\Delta H_1^\circ = +3.87 \pm 0.21$ kcal mol⁻¹ and $\Delta H_2^\circ = -2.95 \pm 0.11$ kcal mol⁻¹. The uncertainties quoted here are estimates of the precisions of the slope and are calculated from the standard deviations of the coefficients of $1/T$ in the two empirical equations.

Similarly, these equations predict $\Delta G_1^\circ = 1.025 \pm 0.007$ kcal mol⁻¹ and $\Delta G_2^\circ = 3.051 \pm 0.003$ kcal mol⁻¹, where the statistical uncertainties here are calculated as the standard errors of the linear regression estimates.^{18b} By combining the standard enthalpies and Gibbs free energies, we find $\Delta S_1^\circ = +9.54 \pm 0.73$ cal deg⁻¹ mol⁻¹ and $\Delta S_2^\circ = -20.1 \pm 0.4$ cal deg⁻¹ mol⁻¹ at 25°C. These values and their statistical uncertainties are listed in Table IV. The most surprising results are the ΔH_1° and ΔS_1° values for the primary dissociation of croconic acid. Both these values are unusually positive when compared to dissociation reactions of other acids in aqueous solution, at least of those acids surveyed by Larson and Hepler.¹⁶ That survey unfortunately did not include ene-diol acids which presumably would provide the most valuable comparisons with croconic acid. In the absence of such data comparisons are more difficult but some general conclusions seem reasonable. The first concerns the value of $\Delta H_1^\circ = +3.9$ kcal mol⁻¹ for croconic acid compared with $\Delta H_1^\circ = 0 \pm 1$ kcal mol⁻¹ for typical uncharged acids. This result is difficult to reconcile with the picture of croconic acid dissociating to hydrogen croconate ion accompanied by increased resonance or π -electron delocalized stabilization. Indeed, hydrogen croconate ion seems to be energetically less stable than undissociated croconic acid. On the other hand, since $\Delta H_2^\circ = -3.0$ kcal mol⁻¹, the unprotonated croconate ion plus H^+ is energetically more stable than $HC_5O_5^-$. The complete dissociation of $H_2C_5O_5$ into $2H^+$ and $C_5O_5^{2-}$ in aqueous solution has a net positive ΔH° and considering the fact that hydration of the two protons must be energetically favorable, it is difficult to see how π -electron stabilization even in $C_5O_5^{2-}$ can be playing an important role in explaining the high acid strength of croconic acid. Our data do not seem to indicate any substantial increase in energetic stabilization going from $H_2C_5O_5$ to $HC_5O_5^-$ to $C_5O_5^{2-}$. The acid strength is attributable to the high positive entropy change of the primary dissociation. Considering that uncharged carboxylic acids dissociate with ΔS° values of -20 to -30 cal mol⁻¹ deg⁻¹, that squaric acid and other moderately strong acids¹⁷ dissociate with ΔS° values of -1 to -13 cal mol⁻¹ deg⁻¹, the value of $\Delta S_1^\circ = +9.5$ cal mol⁻¹ deg⁻¹ measured here for croconic acid seems abnormally large. It is difficult for us to offer a plausible microscopic interpretation of structural and solvent interactive phenomena accompanying this dissociation which could explain such a large

positive ΔS_1° . We can repeat the interpretations offered earlier for the relatively positive ΔS_1° of squaric acid;³ either (1) the uncharged $\text{H}_2\text{C}_5\text{O}_5$ molecule imparts an unusually high degree of structuring to the surrounding water such that relatively little structuring or, in fact, some de-structuring occurs on dissociation to ions, or (2) the HC_5O_5^- ion imparts an unusually small degree of structuring on the water perhaps due to a delocalization of its negative charge. We feel that the first of these two possibilities is more consistent with the large positive ΔH_1° measured here.

In any case, both anomalously large ΔH_1° and ΔS_1° values stem directly from the observed decrease in $\text{p}K_1$ with increasing temperature. In Figure 1, we have plotted $\text{p}K_1$ vs. $1/T$ and have drawn ± 0.08 $\text{p}K$ unit error flags on the data points to show our conservative uncertainty estimates. Also, we have drawn the empirical line of eq 6, and two other slopes which seem to represent extreme divergences from this and still be within plausible range of the error flags. These divergent slopes yield a maximum uncertainty estimate of ± 2.2 kcal mol^{-1} for ΔH_1° which leads to a maximum uncertainty of ± 7.7 eu mol^{-1} for ΔS_1° . The minimum ΔS_1° we can justify, therefore, is $+1.8$ eu mol^{-1} which value would not change the conclusion that ΔS_1° for $\text{H}_2\text{C}_5\text{O}_5$ dissociation is anomalous. One further point of evidence on this conclusion is that the decreasing temperature dependence of $\text{p}K_1$ was observed also in our pH potentiometric experiments. The $\text{p}K_1$ values at 14.6 and 17.1° in Table I are clearly greater than at 44.4 and 54.5°. Even though the large uncertainties associate with these measurements makes any further calculations of doubtful value, the fact that the temperature dependence trend is

the same as found by spectrophotometry lends credibility to the latter results.

We note that $\text{p}K_2$ for croconic acid is substantially less than for squaric acid and observe that the enthalpy changes accompanying these second dissociations are virtually the same at -3.0 kcal mol^{-1} . The difference in acid strength of the monoanions, therefore, is due to entropy considerations again. There appears to be somewhat less additional water structuring upon the dissociation of HC_5O_5^- than upon the dissociation of HC_4O_4^- .

References and Notes

- (1) E. Patton and R. West, *J. Am. Chem. Soc.*, **95**, 8073 (1973), and previous papers in this series.
- (2) R. West and D. L. Powell, *J. Am. Chem. Soc.*, **85**, 2577 (1963).
- (3) L. M. Schwartz and L. O. Howard, *J. Phys. Chem.*, **75**, 1798 (1971).
- (4) E. Patton and R. West, *J. Phys. Chem.*, **74**, 2512 (1970).
- (5) B. Carlqvist and D. Dyrssen, *Acta Chem. Scand.*, **16**, 94 (1962).
- (6) R. I. Gelb, *Anal. Chem.*, **43**, 1110 (1971).
- (7) L. M. Schwartz and L. O. Howard, *J. Phys. Chem.*, **74**, 4347 (1970).
- (8) H. S. Harned, *J. Am. Chem. Soc.*, **57**, 1865 (1935).
- (9) H. S. Harned and R. W. Ehlers, *J. Am. Chem. Soc.*, **55**, 2179 (1933).
- (10) R. A. Robinson and R. H. Stokes, "Electrolyte Solutions", 2nd ed, Revised, Butterworths, London, 1965: (a) Appendix 8.10, Table 9; (b) Chapter 9.
- (11) A. J. Fatiadi, H. S. Isbell, and W. F. Sager, *J. Res. Natl. Bur. Stand., Sect. A*, **67**, 153 (1963).
- (12) R. G. Bates, "Determination of pH Theory and Practice", 2nd ed, Wiley, New York, N.Y., 1973.
- (13) L. M. Schwartz, *Anal. Chem.*, **47**, 963 (1975).
- (14) L. M. Schwartz, *Anal. Chem.*, **43**, 1336 (1971).
- (15) L. M. Schwartz and L. O. Howard, *J. Phys. Chem.*, **77**, 314 (1973).
- (16) J. W. Larson and L. G. Hepler, "Heat and Entropies of Ionization", in "Solute-Solvent Interactions", J. F. Coetzee and C. D. Ritchie, Ed., Marcel Dekker, New York, N.Y., 1969.
- (17) J. L. Kurz and J. M. Farrar, *J. Am. Chem. Soc.*, **91**, 6057 (1969).
- (18) O. L. Davies and P. L. Goldsmith, "Statistical Methods in Research and Production", 4th ed, Revised, Oliver and Boyd, Edinburgh, 1972: (a) Section 7.5, (b) Section 7.28.

Small Anion Binding to Cycloamylose. Equilibrium Constants

J. F. Wojcik* and R. P. Rohrbach

Department of Chemistry, Villanova University, Villanova, Pennsylvania 19085 (Received April 7, 1975)

Publication costs assisted by Villanova University

The equilibrium constants for the formation of inclusion complexes of α - and β -cycloamylose with small anions were measured using conductance methods. For the series of anions, ClO_4^- , SCN^- , I^- , Br^- , and NO_3^- , the association constants for complexes with α -cycloamylose are 28.9, 18.7, 12.4, 3.5, and 1.4 M^{-1} . The association constant for SCN^- with β -cycloamylose is 9.9 M^{-1} . Cl^- , SO_4^{2-} , and acetate do not bind with α -cycloamylose.

Introduction

The cycloamyloses are well known for their ability to form inclusion complexes in which a guest molecule resides in the cavity of the macrocyclic sugar.¹ The nature of the "forces" causing the binding still remain obscure although hydrophobic binding has been invoked in most cases.^{1,2} However, crystalline inclusion complexes with ionic guest molecules have been studied³ and there is a small amount of evidence for the existence of inclusion complexes in which small anions are guests in aqueous solution.^{4,5} Any

explanation of the nature of binding must thus account for the diversity of guest molecules. The work presented here confirms the earlier work on the small anion binding and gives data for anions not previously studied. A possible rationalization for this binding is given using the results of recent crystallographic studies as a guide.

Experimental Section

Association constants for binding the cycloamyloses were measured by conductance methods. A Jones Bridge was

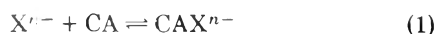
constructed in our labs⁶ using a Leeds and Northrup precision ac decade resistance box. The ac source was a Hewlett-Packard 200DC oscillator and the detector was a Tektronix oscilloscope with appropriate plug in units. The conductivity cell has a cell constant of 0.20602 and was suspended in a 25° constant temperature oil bath which had temperature fluctuations limited to $\pm 0.002^\circ$. The bridge was shown to be sensitive to changes in resistance of the order of 1 part in 10^5 . All measurements were made at 6000 Hz. The water used in the experiments was deionized and redistilled in a long-path glass column and had a residual conductivity of $2 \times 10^{-6} \text{ ohm}^{-1} \text{ cm}^{-1}$, adequate for the work done here.

α - and β -cycloamylose were obtained from Aldrich chemicals and purified by literature methods.⁷ The salts used were reagent grade and were dried at about 110° for a few hours. Volumetric methods were used in preparing the solutions for study. Because of this, the uncertainties in the resistance readings were larger than the readability of the bridge and were of the order of 1.0%.

Results

Conductance measurements were made on solutions of the potassium salts of SCN^- , Cl^- , ClO_4^- , Br^- , NO_3^- , and I^- and the sodium salts of acetate and SO_4^{2-} all in the presence of α -cycloamylose. Measurements were also made on the β -cycloamylose-KSCN system. In all cases, the resistance of a solution maintained at constant salt concentration increased as the concentration of cycloamylose increased. For a 0.02 *M* α -cycloamylose solution, the increase varied from about 3% for Cl^- , SO_4^{2-} , and acetate to 22% in the case of ClO_4^- . It was found that at 25° , the viscosity of a 0.01 *M* solution of α -cycloamylose relative to water was 1.0191 while for a 0.02 *M* solution the relative viscosity was 1.0400. Using data for sucrose as a guide,⁸ a 3.2% increase in resistance is predicted for a salt solution with 0.02 *M* α -cycloamylose over that for a solution with no α -cycloamylose. Any additional increase in resistance over the 3% value was assumed to be due to inclusion complex formation.

If an equilibrium of the form



is assumed and if α is defined as the fraction of the anion existing in an uncomplexed state, then it is easily shown that

$$K_A = \frac{(1 - \alpha)\gamma_{\text{MCAX}}}{\alpha[C_{\text{CA}}^0 - (1 - \alpha)C_{\text{X}}^0]\gamma_{\text{MX}}\gamma_{\text{CA}}} \quad (2)$$

where K_A is the association constant (in units of molarity), C_{CA}^0 is the total concentration of cycloamylose, C_{X}^0 is the total salt concentration (both in moles per liter), and the γ 's are the appropriate activity coefficients. Defining κ by

$$\kappa = K_c/R \quad (3)$$

where K_c is the conductance cell constant and R is the resistance of the solution, α is given by

$$\alpha = \frac{(\kappa 1000/C_{\text{X}}^0) - \Lambda_{\text{MCAX}}}{\Lambda_{\text{MX}} - \Lambda_{\text{MCAX}}} \quad (4)$$

In eq 4 Λ_{MX} is the equivalent conductance of the free salt and Λ_{MCAX} is the analogous quantity for the complex. Both equivalent conductances are a function of the salt concentration. Λ_{MX} is obtained from a resistance measurement of a solution of the salt in the absence of cycloamylose. Λ_{MCAX} is assumed to be given by⁹

$$\Lambda_{\text{MCAX}} = \Lambda_{\text{MCAX}} - BC_{\text{X}}^{1/2} \quad (5)$$

where B is a constant.

In treating the data it was assumed that Cl^- , SO_4^{2-} , and acetate did not bind under the conditions of the experiment (i.e., had K_A values less than 1). This assumption is supported by the fact that cycloamylose affects the resistance of solutions of these salts in the same fashion within the experimental error and is completely accounted for by the increase in the viscosity of the solutions (see below). In addition, a correlation based on the other anions and presented below predicts values for the formation constants for these anions well below 1. Spectroscopic studies for SO_4^{2-} ⁴ and kinetic inhibition studies for the acetate¹⁰ also agree with the results presented here. Our measurements on these three ions were used to correct for viscosity results for the other anions.

In order to obtain equilibrium constants for the remaining cases, it is necessary to evaluate Λ_{MCAX}^0 , B (eq 5), and the ratio of the activity coefficients. Now the diffusion coefficient of β -cycloamylose has been determined.¹¹

Assuming that the diffusion coefficient of the small anion complexes of the α - and β -cycloamyloses are the same as that of β -cycloamylose, a value of $80.3 \text{ ohm}^{-1} \text{ cm}^2 \text{ equiv}^{-1}$ is calculated¹⁷ for the equivalent conductivity of the potassium salt of the cycloamylose complexes, yielding a value of $6.8 \text{ ohm}^{-1} \text{ cm}^2 \text{ equiv}^{-1}$ for the single ion equivalent conductance of the cycloamylose-anion complex.

Since the ratio of the activity coefficients involves the activity coefficient of a neutral species and the ratio of activity coefficients of electrolytes of the same charge type, and since all of the solutions are relatively dilute (less than 0.03 *M* in salt and less than 0.02 *M* in cycloamylose) this ratio is taken to be unity.

The coefficient B can be evaluated using the value of Λ_{MCAX}^0 and the theory of conductivity⁹ and it turns out to be 79.1.

With these assumptions, the association constants for binding were calculated. The results are given in Table I. The fit of the data was checked by recalculating the resistances expected for each solution using the parameters and equations given above. Table II (available in the microfilm edition, see paragraph at end of text regarding supplementary material) gives the experimental data and the calculated resistances along with the standard deviations in the resistances. The latter are consistent with the experimental error. The association constants agree with limited data available in the literature. For the ClO_4^- - α -cycloamylose system, a K of 29.4 M^{-1} was found by a spectrophotometric displacement technique.⁴ A value of 13.5 M^{-1} for K_A for the I^- - α -cycloamylose system has been given.⁵ For Cl^- , SO_4^{2-} , and acetate, the resistance of solutions of constant salt concentration simply increased according to the following equation: $R = R_0(1 + 1.55C_{\text{CA}}^0)$, where R_0 is the resistance of the solution in the absence of cycloamylose.

Discussion

As the results show, anion binding by cycloamyloses is a fact. Based on the results of X-ray studies of crystalline cycloamylose^{3,13,14} the anion is probably located in the hydrophilic plane roughly defined by the primary hydroxyl groups. Any explanation of binding should therefore be given in terms of these hydroxyl groups and the hydrophobic cavity. The driving force for the binding is probably a combination of effects. The order of stability parallels the

TABLE I: Equilibrium Constants^a

Complex	Obsd	Calcd ^b
KSCN- α -CA	18.7	15.0
KClO ₄ - α -CA	28.9	38.7
KNO ₃ - α -CA	1.4	4.2
KBr- α -CA	3.5	2.2
KI- α -CA	12.4	28.2
KSCN- β -CA	9.9	

^aDetermined at 25° and with ionic strength between 0.01 and 0.03. Units are M^{-1} . ^bCalculated on the basis of the correlation noted in the text.

structure breaking properties of the anions (i.e., the better "structure breakers" bind tighter) and so the properties of the free anions are probably important. However the same factors which determine which anion is a better "structure breaker" (ion size, electric field, etc.) could also be invoked to explain the nature of the interactions at the primary hydroxyl groups. No clear cut deductions can thus be drawn from the parallel of stabilities with solvation properties.

The small differences in the association constants for the complexes of SCN⁻ with α - and β -cycloamylose suggest that relief of torsion angle strain need not be invoked to explain the driving force for anion binding.¹⁵ It is expected that such torsion angle strain should be more important in the α -cycloamylose (six glucose residues) than in the β -cycloamylose (seven glucose residues).

The parallel of the association constants with the structure breaking properties of the anions suggested that a quantitative correlation with some water structure sensitive parameter might exist. Such a correlation was found to exist between the log of the association constant and the coefficient of the linear term of the concentration dependence of proton relaxation rates in aqueous salt solutions, B^- . (See ref 16 for a full discussion of these B^- values and an extensive table.) In fact it was found that $\log K_A = -0.75 - 26.5B^-$ with a correlation coefficient of 0.9 (95% probability that the correlation is real). Without trying to interpret this in terms of molecular structure, one can use

it to predict equilibrium constants for other anions. Thus for Cl⁻, SO₄²⁻, and acetate, one obtains values of K_A equal to 0.3, 9×10^{-5} , and $2 \times 10^{-6} M^{-1}$. These values are consistent with the absence of binding noted above. This correlation also predicts that no other anion will bind to α -cycloamylose more tightly than does ClO₄⁻. The association constants calculated from the correlation are given in Table I along with the observed constants.

Supplementary Material Available. Table II will appear following these pages in the microfilm edition of this volume of the journal. Photocopies of the supplementary material from this paper only or microfiche (105 × 148 mm, 24× reduction, negatives) containing all of the supplementary material for the papers in this issue may be obtained from the Business Office, Books and Journals Division, American Chemical Society, 1155 16th St., N.W., Washington, D.C. 20036. Remit check or money order for \$4.00 for photocopy or \$2.50 for microfiche, referring to code number JPC-75-2251.

References and Notes

- (1) D. W. Griffiths and M. L. Bender, *Adv. Catal.*, **23**, 209 (1973).
- (2) W. P. Jencks, "Catalysis in Chemistry and Enzymology", McGraw-Hill, New York, N.Y., 1969, p 409.
- (3) A. Hybl, R. W. Rundle, and D. E. Williams, *J. Am. Chem. Soc.*, **87**, 2779 (1965).
- (4) F. Cramer, W. Saenger, and H.-Ch. Spatz, *J. Am. Chem. Soc.*, **89**, 14 (1967).
- (5) D. French, *Adv. Carbohydrate Chem.*, **12**, 189 (1957).
- (6) G. Jones and R. C. Josephs, *J. Am. Chem. Soc.*, **50**, 1049 (1928).
- (7) D. French, M. L. Levine, J. H. Pazur, and E. Norbery, *J. Am. Chem. Soc.*, **71**, 353 (1949).
- (8) R. A. Robinson and R. H. Stokes, "Electrolyte Solutions", 2nd ed, Butterworths, London, 1959, p 308.
- (9) Reference 8, p 143.
- (10) R. L. Van Etten, J. F. Sebastian, G. A. Clowes, and M. L. Bender, *J. Am. Chem. Soc.*, **89**, 3242 (1967).
- (11) H. Uedaira and H. Uedaira, *J. Phys. Chem.*, **74**, 2211 (1970).
- (12) R. A. Robinson and R. H. Stokes, ref 8, p 124.
- (13) R. K. McMullan, W. Saenger, J. Fayos, and D. Mootz, *Carbohydrate Res.*, **31**, 37 (1973).
- (14) P. C. Manor and W. Saenger, *J. Am. Chem. Soc.*, **96**, 3630 (1974).
- (15) D. A. Rees, *J. Chem. Soc. B*, 377 (1970).
- (16) H. G. Hertz in "Water, A Comprehensive Treatise", F. Franks, Ed., Vol. 3, Plenum Press, New York, N.Y., 1973, p 368.
- (17) R. A. Robinson and R. H. Stokes, ref 8, p 288.

Two-Dimensional Polymerization Processes in Mono- and Diacrylic Esters

A. Dubault,* C. Casagrande, and M. Veyssie

Laboratoire de Physique de la Matière Condensée, Collège de France, 75231 Paris Cedex 05, France (Received April 21, 1975)

Publication costs assisted by Collège de France Physique de la Matière Condensée

The uv induced polymerization of monolayers of *n*-octadecyl methacrylate and 1-*n*-octadecyloxy-2,3-diacryloyloxypropane at water-gas interface has been studied. In each case, the compressibility and the surface viscosity of the film at different stages of irradiation were measured. The main difference between mono- and diacrylic esters is the occurrence of a divergence of the viscosity coefficient during the polymerization process for the second compound. In the light of our experimental results, we discuss the mechanism of the photochemical reaction, the role played by chain entanglements, and the specific effects of cross linking in the diacrylic ester.

Introduction

In a previous letter,¹ we have shown the possibility of obtaining cross-linking polymerization in a monolayer of a diacrylic ester, namely 1-*n*-octadecyloxy-2,3-diacryloyloxypropane, at a water-gas interface by uv irradiation. We report here the results of a quantitative study of the polymerization process with a view to determining the mechanism and the kinetics of the reaction, as well as the properties of the partially and totally polymerized film. We were led to undertake a parallel study of the linear polymerization of a similar monoacrylic ester, namely, octadecyl methacrylate, in order to discern the specific effect of cross-linking polymerization. The experimental methods used in this work are essentially isothermal compressibility and surface viscosity measurements.

After a brief description of the materials used as monomers in the polymerizations, we shall describe the experimental procedure which allows us to follow the course of the polymerization. We then report the results obtained for the monoacrylic and diacrylic compound, respectively, and finally, we discuss these data and try to interpret their common features and differences.

Experimental Section

Materials. The monomers used as starting materials in these polymerization studies were synthesized by Strzelecki. *n*-Octadecyl methacrylate, $\text{CH}_3(\text{CH}_2)_{17}\text{O}-\text{C}(=\text{O})-\text{C}(\text{CH}_3)=\text{CH}_2$, was obtained by allowing octadecanol to react with methacrylic acid chloride. 1-*n*-Octadecyloxy-2,3-diacryloyloxypropane, $\text{CH}_3(\text{CH}_2)_{17}-\text{O}-\text{CH}_2-\text{CH}(\text{O}-\text{C}(=\text{O})-\text{CH}=\text{CH}_2)-\text{CH}_2(\text{O}-\text{C}(=\text{O})-\text{CH}=\text{CH}_2)$, was obtained by allowing *n*-octadecyloxy-2,3-dihydroxypropane to react with acrylic acid chloride. Both were purified on alumina, the purity being checked by infrared spectroscopy and high-resolution NMR. We shall refer to the first and second compounds as respectively the "monoacrylic ester" and the "diacrylic ester".

Surface Pressure. Area Measurements. For compressibility measurements we used a commercial Lauda film balance, in which the surface pressure π is directly measured by an induction dynamometer, with a sensibility of 0.1 dyn/cm. In all our experiments, the monolayer was continuously compressed at the lowest available speed, 15 cm²/min. The temperature of the trough was regulated by circulation of water, and measured by a copper-constantan

thermocouple with wires of 0.13 mm diameter, located just at the water surface. The temperature was kept constant with an accuracy of 0.5°C; in general, experiments were done at 20.5°C.

Viscosity Measurements. The compression barrier was modified to allow the measurement of monolayer viscosity by the "canal method":² slits of various width in the range 1–5 mm were mounted in a Teflon barrier of 3 cm width. We measure the rate of flow of the monolayer through the canal, moving the barrier to keep the surface pressure of the film constant.

Polymerization by Uv Irradiation. The monolayer was irradiated by a 5654A Hanovia mercury vapor lamp (2500–3500 Å) through a quartz window fitted in the top of the film balance, the distance between the lamp and the water surface being adjustable to change the radiation intensity at the film. During irradiation the apparatus was flushed with a temperature controlled nitrogen flow. The oxygen content of the atmosphere above the monolayer was measured to be less than 0.2% in volume, using a Beckman oxygen analyzer.

Experimental Procedure. For both the mono- and diacrylic monomer we first recorded the pressure-area isotherm $\pi(A)$, at 20.5°C, where π is the surface pressure (dyne/cm) and A the area per monomer molecule (Å²) (Figures 1a and 2a). Then, starting from different equilibrium points on the isotherm, we irradiated the monolayer, keeping the pressure constant, and recording the variation of the area A as function of time (t), we obtained the $A(t)$ curves shown on Figure 3. A decreases monotonously to a constant value. In subsequent experiments, to investigate the polymerization process, we stopped the irradiation at different points on the $A(t)$ curve, and measured the properties of the monolayer corresponding to each of these stages of irradiation. Previously we made sure that the area does not change when the uv radiation is stopped. For each stage of irradiation, we make the following measurements. (a) A complete pressure-area isothermal curve shortly after stopping the irradiation; this means a delay period of about 30 min, corresponding to the time necessary to decompress the film and wait 10 min at null pressure before recompression. (b) A pressure-area curve after several (≈ 3) hours of relaxation of the irradiated monolayer at null pressure. (c) Surface viscosity determined at the pressure at which the irradiation occurred, and isothermal compressibility after flowing through the canal viscosimeter. The viscosity mea-

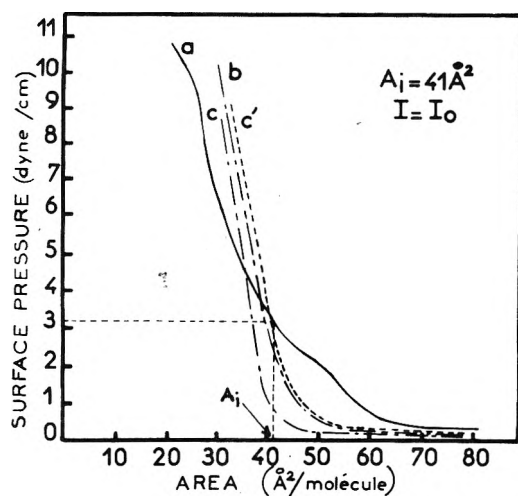


Figure 1. Surface pressure–area curves of monoacrylic ester at various stages of uv irradiation: curve a, monomer; curve b, irradiated until $A(t) = 36 \text{ \AA}^2$ (after waiting 10 min); curve c, irradiated until $A(t) = A_i = 31 \text{ \AA}^2$ (after waiting 10 min); curve c', irradiated until $A(t) = A_i = 31 \text{ \AA}^2$ (after waiting 2.5 hr).

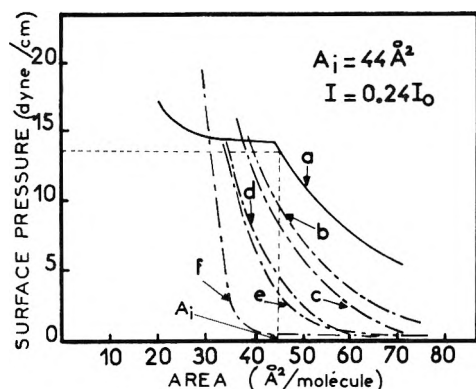


Figure 2. Surface pressure–area curves of diacrylic ester at various stages of uv irradiation and after waiting 10 min at null pressure: curve a, monomer; curve b, irradiated until $A(t) = 37 \text{ \AA}^2$; curve c, irradiated until 35 \AA^2 ; curve d, irradiated until 34 \AA^2 ; curve e, irradiated until 33 \AA^2 ; curve f, irradiated until $A(t) = A_i = 30 \text{ \AA}^2$.

measurements were very crude and we do not claim to get absolute values of the viscosity coefficient for the following reasons. (i) The difference, $\pi_2 - \pi_1$, between the two sides of the slit can be very high (of the order of several dyne/cm) because the flow takes place between the compressed monolayer at π_2 and the clean water surface behind the compression barrier. (ii) If π_2 is kept constant during flow, π_1 slightly changes with time but this effect is probably less serious than (i). In spite of these restrictions, this single canal technique is convenient, and gives a qualitative idea of the evolution of the surface viscosity during the polymerization process. (d) Solubility tests: the film was recovered by slowly sweeping the surface with a glass plate. After drying, we tried to dissolve this deposit in different solvents. We have checked that, under these conditions, the deposits collected from monomer monolayers are entirely soluble in their spreading solvents.

Experimental Results

(1) *Monoacrylic Ester.* Other authors have previously studied irradiation induced surface polymerization for this

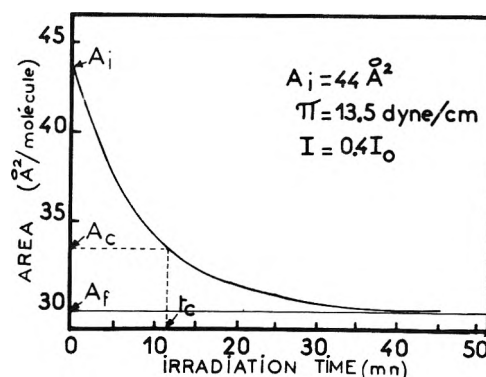


Figure 3. Surface change of the diacrylic monolayer during irradiation at constant surface pressure π . A_c corresponds to the anomaly of the viscosity (cf. text and Figure 5).

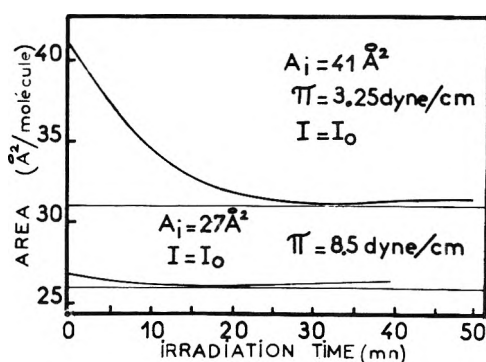


Figure 4. Surface change of the monoacrylic monolayer during irradiation at constant surface pressure π for two different initial areas.

monomer^{3,4} or a very similar one,⁵ but their experimental conditions and measurements differed from ours, in particular they generally irradiated at constant area. It appears therefore necessary to perform exactly the same experiments on this compound as on the diacrylic ester, in order to clearly distinguish the behavior specific to linear polymerization from cross-linking effects.

(a) *Isothermal Curves.* The monoacrylic ester was spread from a benzene solution. It exhibited a liquid-like pressure area isotherm (Figure 1a) with a bump near $A = 50 \text{ \AA}^2$ ($\pi = 2.0 \text{ dyn/cm}$) and a second accident for $A = 25 \text{ \AA}^2$ ($\pi = 9 \text{ dyn/cm}$). We interpret the latter as the collapse of the film. This general behavior is similar to that observed by Beredjick and Burlant,³ but is quite different from that of Ackermann and coworkers.⁴ We note that the monoacrylic ester is difficult to spread, which is why we have used benzene instead of the generally preferred cyclohexane and have had to wait 0.5 hr for complete evaporation before compression. Moreover, the shape of the isotherm is extremely sensitive to temperature around 20.5°C . In conclusion, great care is necessary to get reproducible results, which may explain the discrepancies between previously published results.^{3,4}

(b) *Irradiation. Effects on the Area.* We irradiated the monolayer starting from two different points on the compression isotherm, one just after the bump at $A_i = 41 \text{ \AA}^2$, and the other just before the collapse, at $A_i = 27 \text{ \AA}^2$. In the first case, the area decreases significantly during irradiation, and reaches a plateau at 31 \AA^2 , in the second case this contraction is much smaller (Figure 4). In both cases, after

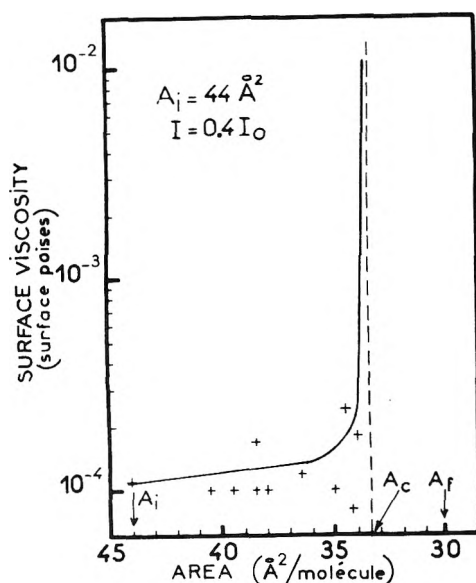


Figure 5. Surface viscosity of the diacrylic ester monolayer during irradiation.

long irradiation times we observed a slight increase of A , which may be due to a further degradation of the polymer.

(c) *Irradiation Effects on the Viscosity.* Measuring the viscosity along the $A(t)$ curve, we find a continuous increase from 10^{-5} surface poise for the monomer to 10^{-4} surface poise at the plateau. Finally we find a slight decrease in the viscosity accompanying the rise of the area that we have attributed to long time degradation effects.

(d) *Irradiation. Solubility Test of the Final Product.* The collected deposit appears to be almost completely soluble in cyclohexane and largely insoluble in methanol. This is in agreement with the solubility of polyoctadecyl methacrylate which can be prepared in benzene and precipitated by methanol.^{3,4}

(e) *Discussion.* From (c) and (d) we conclude that linear polymerization occurs during uv irradiation; this process is associated with a significant shrinkage of the film at constant pressure, if the initial state has a large area A per monomer.

(f) *Equation of State of the Partly Polymerized Film.* We have also studied the compressibility of the monolayer at different degrees of polymerization. The isotherm continuously evolves from an expanded liquid-like isotherm to a solid-like one at the end of the process (Figure 1). We must emphasize that the post-polymerization isotherms change significantly if we make several cycles of decompression and compression allowing the film to relax several hours at null pressure (curves c and c' in Figure 1).

This nonequilibrium behavior does not appear for the monomer curves, and thus cannot be attributed to surface contamination under our experimental conditions. Similar effects have previously been noticed by Hatada et al.⁵ for octadecyl acrylate.

(2) *Diacrylic Ester.* In sharp contrast to the monoacrylic ester, the diester can easily be spread from a cyclohexane solution. It gives fairly reproducible $\pi(A)$ curves.

(a) *Isothermal Curves.* At the same temperature (20.5°C) the diacrylic monomer also exhibits a liquid-like $\pi(A)$ curve with no inflections up to a pressure of 14 dyn/cm at $A = 42 \text{ \AA}^2$ (Figure 2a). The singularity observed at this point could indicate a transition to a condensed liquid

TABLE I: Experimental Results for Diacrylic Ester Polymerization^a

I	$A_i, \text{ \AA}^2$	$A_f, \text{ \AA}^2$	$\Delta A/A_i$	$A_c, \text{ \AA}^2$	θ_c	$\tau = k_p^{-1} [\text{M}\cdot]^{-1} \text{ sec}$ (extreme values)
I_0	44	30	0.32	33.5	0.75	36 \longleftrightarrow 60
$0.4I_0$	44	30	0.32	33.5	0.75	72 \longleftrightarrow 168
$0.24I_0$	44	30	0.32	33.5	0.75	116 \longleftrightarrow 174
$0.4I_0$	55	32.5	0.41	39	0.71	60 \longleftrightarrow 114
$0.24I_0$	55	32.5	0.41	39	0.71	162
$0.4I_0$	66	37.5	0.43	43.5	0.79	60 \longleftrightarrow 126
$0.24I_0$	66	37.5	0.43	43.5	0.79	162

^a I is the intensity of the uv irradiation in arbitrary units, A_i the area per molecule at the beginning of the polymerization process, A_f the area per molecule at the end of the polymerization process, A_c the area per molecule at the critical point where the viscosity diverges, θ_c the conversion parameter for $A = A_c$, and τ the time constant of the polymerization reaction.

state; this is supported by the fact that the singular point shifts smoothly toward higher pressures as the temperature is increased. However, there remains the possibility that this point corresponds to a collapse, as we do not observe any other inflections after this point even at small areas.

(b) *Irradiation Effects.* We repeat on this substance the polymerization experiments as described above for varying initial conditions and uv intensity at the monolayer surface. The main changes during irradiation are (i) a decrease of the area at constant pressure from an initial value A_i to final area A_f (Figure 3). (In contrast with the previous case, we do not observe any increase of A after the plateau, even for several hours. Previously we reported a slight increase in A after reaching the plateau; this has however been eliminated in our present experiments by improved control of temperature and oxygen content.); (ii) a sharp rise of the surface viscosity at a certain level of irradiation: the surface viscosity becomes practically infinite when A reaches a value $A_c < A_f$ (Figure 5). The values of A_i , A_c , and A_f are collected in Table I for different experimental conditions. Note that A_c and A_f depends on the initial area, but are independent of radiation intensity. For all stages of irradiation, the collected monolayer always shows an insoluble component (in tetrahydrofuran and in dimethylformamide) which is a direct proof of the existence of cross linkages in the polymerized product.

(c) *Isotherms for Partially Polymerized Films.* The recompression curves of the partially polymerized product show that the monolayer becomes less compressible and tends to a solid-like behavior at the end of the process (Figure 2). The film has then a compressibility of $10^{-2} \text{ dyn}^{-1} \text{ cm}$ compared to $2.9 \times 10^{-2} \text{ dyn}^{-1} \text{ cm}$ for the monoacrylic ester under similar conditions, which seems reasonable due to the cross-linking effects. We observe on these recompression curves the hysteresis effect described earlier for the monoacrylic compound (Figure 6). This effect can be obtained either by waiting several hours at zero pressure before recompressing, or by flowing the film through the viscosimeter canal; it tends to diminish as the polymerization level increases.

Discussion

Let us compare the results of the uv induced polymerization of mono- and diacrylic ester monolayers: (i) both es-

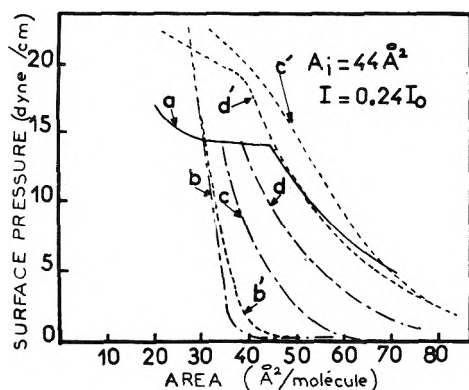


Figure 6. Surface pressure-area curves of diacrylic ester at various stages of uv irradiation, and after various times of waiting at null pressure: curve a, monomer; curve b, irradiated until $A(t) = A_i = 30 \text{ \AA}^2$ and after waiting 10 min; curve b', irradiated until 30 \AA^2 and after 2.5 hr; curve c, irradiated until 34 \AA^2 and after 10 min; curve c', irradiated until 34 \AA^2 and after 2.5 hr; curve d, irradiated until 37 \AA^2 and after 10 min; curve d', irradiated until 37 \AA^2 and after 2.5 hr.

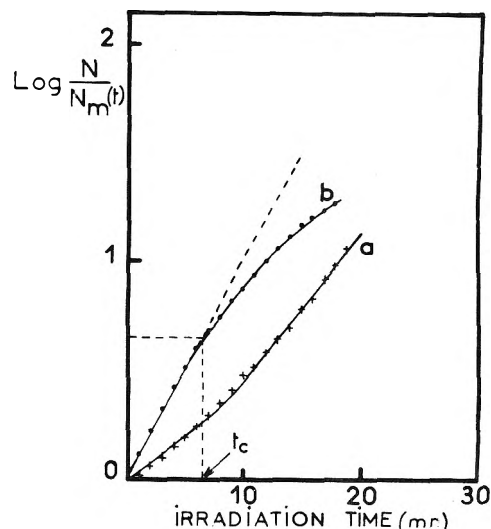


Figure 7. Kinetics of the polymerization reaction: curve a, monoacrylic ester $A_i = 41 \text{ \AA}^2$, $I = I_0$; curve b, diacrylic ester $A_i = 44 \text{ \AA}^2$, $I = 0.4I_0$; N is the initial number of monomers units, $N_m(t)$ the number of monomer units at time t .

ters show a decrease of the area per molecule when irradiated at constant pressure; (ii) the changes of the viscosity and of the solubility occurring during the polymerization are very different for the two species.

(a) *Relation between Shrinkage and the Polymerization Kinetics.* The shrinkage of the film during the irradiation can be attributed to the well-known contraction of vinylic compounds when polymerized. This effect is greatest when the monolayer is in an expanded state before irradiation (for instance, $\Delta A/A_i = 0.43$ for $A_i = 66 \text{ \AA}^2$, cf. Table I). The values of $\Delta A/A_i$ (cf. Table I) were quite reproducible in our experiments. However, the compressibility of the rigid film obtained at the end of irradiation cannot explain the differences in the final areas A_f for different initial areas A_i . For instance, the difference between the final areas for $A_i = 66 \text{ \AA}^2$ ($\pi = 6.5 \text{ dyn/cm}$) and $A_i = 44 \text{ \AA}^2$ ($\pi = 14 \text{ dyn/cm}$), equal to 7.5 \AA^2 (cf. Table I), is twice as large as the variation of A between $\pi = 6.5 \text{ \AA}^2 \text{ dyn/cm}$ and $\pi = 14 \text{ dyn/cm}$ measured on the compressibility curve of the completely polymerized film (cf. Figure 2f). This is probably related to the hysteresis effects on the compressibility curves for the irradiated monolayers. This leads us to think that the observed contraction of the monolayer may be due not only to the creation of covalent bonds between monomeric units, but partly to mechanical entanglements occurring between the growing chains; these entanglements might disappear after long time rearrangement or by flow. Velasco has calculated the effect of such entanglements on the equation of state for a linear polymer film.⁶ The predicted evolution of the isotherms, which shift to larger areas as the number of entanglements decreases, is in qualitative agreement with our experimental results.

In spite of these remarks, we have tried to correlate the relative contraction of the film with the progress of the polymerization reaction. We make two assumptions. (i) When $A(t)$ is constant, there is a total conversion from monomer to polymer; in consequence, we consider A_f as the specific area for the repetitive unit when it is engaged in a polymer chain as compared to A_i for the same unit in the monomer state. (ii) During the course of polymerization, we assume that areas are additive, so that

$$A(t) = \frac{N_m(t)A_i + N_p(t)A_p}{N_m(t) + N_p(t)}$$

$N_m(t)$ and $N_p(t)$ are respectively the number of units in the monomeric and polymeric state for an irradiation time t , and $N = N_m(t) + N_p(t)$ the initial number of monomeric units. From this, we can calculate the conversion parameter $\theta(t) = N_p(t)/N$.

We are aware of the limitations of the first assumption since an apparent stopping of the reaction can correspond to phenomena other than total conversion of the monomer, such as, for example, the quenching of the diffusion process for a certain stage of the polymerized monolayer.

Unfortunately, the extremely small quantity of matter present in each film (about $50 \times 10^{-6} \text{ g}$) forbids any conventional chemical analysis, such as titrating the remaining double bonds or measurements of molecular weights.

In the light of assumptions (i) and (ii) we determine $\theta(t)$ for both mono- and diacrylic compounds, and plot $\log [1 - \theta(t)]^{-1} = \log N/N_m(t)$ vs. t to get an idea of the kinetic laws of the reaction (Figure 7).

With the diacrylic compound we get a fairly linear behavior up to an irradiation time which coincides with that for an infinite viscosity. Before this time, the polymerization appears to be a first-order reaction; this suggests that the free-radical concentration $[M\cdot]$ remains constant during irradiation as one would expect if the uv radiation is absorbed by a photosensitizer which decomposes into radicals, and not directly by the diacrylic monomer (cf. ref 7 chapter IV, p 14). We might suspect, for instance, the role played by the fraction of oxygen remaining in the atmosphere or in the water subphase. This last remark could explain the observed dispersion of the values of the reaction time constant τ , for different experiments with identical conditions for the temperature, initial area, and uv intensity (cf. Table I). The observed slowing of the reaction rate after the critical point must probably be related to some slackening of a diffusion process accompanying the increase of the viscosity. In the case of the monoacrylic ester, the reaction rates are lower (Figure 7); this is in agreement with the significant difference between the rate constants of methacrylate and acrylate compounds determined in bulk polymerization (cf. ref 7, p 158), but the fact that we

do not observe a linear law in the monoacrylic case has no evident interpretation.

(b) *Discussion of the Surface Viscosity.* The most striking feature is the divergence of η_s observed in diacrylic ester polymerization (Figure 5); this effect is specific to the bifunctional monomer and, as a consequence, is clearly related to the occurrence of cross-linking effects. We may attempt to interpret this as a "gel-point" as introduced by Flory⁷ in cross-linked polymer chains: gelation occurs when the number of cross links is sufficient to form an infinite network, which appears in a bulk polymerization as an insoluble fraction of the system. In the frame of this model, and following Flory's analysis, we estimate the conversion factor θ_g at the gel point, taking into account the experimental fact that, during the initial period, the reaction follows first-order kinetics.

We start from the following equations

$$\begin{aligned}\frac{d[M]}{dt} &= -k_p[M\cdot][M] \\ \frac{d[C_2]}{dt} &= 2k_{p,P}[C_1][M\cdot] \\ \frac{d[C_1]}{dt} &= k_p[M\cdot][M] - 2k_{p,P}[C_1][M\cdot] \approx k_p[M\cdot][M]\end{aligned}$$

where all the quantities in brackets refer to a number of units per unit area (we do not take into account the variation of these quantities due to the shrinkage of the film during irradiation): $[M]$ is the number of monomer units, $[C_1]$ the number of units engaged in one chain, $[C_2]$ the number of units engaged in two chains, and $[M\cdot]$ the number of free radicals.

k_p and $k_{p,P}$ are propagation and cross-linking rate constants as introduced by Flory.⁷

Integrating these equations with $[M\cdot]$ independent of t , we express the gelation condition as

$$\rho_g = \frac{[C_2]}{[C_1]} = \frac{1}{\bar{y}_w}$$

with $\bar{y}_w = B(k_p/k_t)[M][M\cdot]^{-1}$ when k_t is the determination rate constant, and B a numerical factor which depends on the type of termination process. This gives

$$\frac{1 - e^{-k_p[M\cdot]t_g}}{2k_p k_{p,P}[M\cdot]t_g - 2k_{p,P}(1 - e^{-k_p[M\cdot]t_g})} = \frac{B[M_0]}{k_t[M\cdot]} e^{-k_p[M\cdot]t_g}$$

where $[M_0]$ is the initial monomer concentration. In a crude first-order approximation, we obtain for the gelation time

$$t_g = \frac{2k_t}{2k_{p,P}k_p[M_0] + k_t k_p[M\cdot]}$$

and for the conversion parameter at gelation

$$\theta_g = \frac{[C_1(t_g)]}{[M_0]} = 2 \left/ \left(1 + \frac{2k_{p,P}[M_0]}{Bk_t[M\cdot]} \right) \right.$$

From our experimental results on $\tau = k_p^{-1}[M\cdot]^{-1}$, it appears that $[M\cdot]$ changes significantly with the uv intensity I , but is not dependent on the initial monomer concentration $[M_0]$ (cf. Table I). With these conditions, θ_g would be dependent on both I and $[M_0]$, which is in disagreement with our experimental measurements of the conversion parameter θ_c at the critical point (cf. Table I). In spite of the drastic approximations used in this simple model, the discrepancy between the predicted and observed behavior of

θ_c casts doubt on the interpretation of this anomaly as a gelation point. This is reinforced by the fact, previously noticed, that the partially polymerized monolayer seems to have an insoluble fraction even before reaching θ_c .

Another possible interpretation for the anomaly of the viscosity has been suggested to us by Chapiro; this phenomena could be associated with a glass transition. If the monomer is considered as a solvent of the polymer, the temperature of the glass transition T_g is expected to increase as relative concentration of the monomer diminishes, i.e., when the conversion parameter increases, thus attaining the temperature of our experiments for the concentration of the polymer relative to the monomer obtained at θ_c . This concentration effect could be expected to occur in the monoacrylic compound as well as the diacrylic one. In order to interpret our experimental results, we have to suppose that T_g remains below 20.5°C for poly(octadecylmethacrylate) even at the end of the reaction, while T_g reaches 20.5°C at $\theta = \theta_c$ in the case of the diacrylic compound, due to the well-known^{8,9} effect of cross linking on the glass temperature. In this interpretation the divergence of the viscosity appears as an indirect consequence of the cross-linking polymerization. It seems difficult to go further in this analysis due to the absence of data relative to glass transition in two-dimensional polymerization. We can just notice that on this hypothesis one would expect a very pronounced slowing of the reaction at the critical point.

Conclusion

We must emphasize once more the difficulties of these kinds of experiments. The very small quantities of matter involved in monolayer studies makes the experiments extremely sensitive to impurities and other experimental parameters. We have had to repeat each measurement several times to get reliable data. Moreover, all or nearly all classical techniques used in the physical chemistry of polymers being excluded, we have been forced to rely on indirect determinations of the reacted fraction. However, bearing these remarks in mind, we have found a simple law for the kinetics of the diacrylic ester polymerization, which gives some indications of the free-radical creation process; we have also shown that mechanical entanglements probably take place during chain growth. Last, but not least, we have found a divergence of the surface viscosity which occurs at a well-defined stage of irradiation in the diacrylic ester only. The interpretation of this critical point as a gelation point or a glass transition remains ambiguous. Further experiments are necessary to clarify this point; studies of the polymerization as a function of temperature and studies of mixtures of mono- and diacrylic molecules are being considered.

Acknowledgments. We thank L. Strzelecki and L. Liebert for the synthesis of monomer molecules and numerous chemical advice, and L. Lacombe for NMR analysis.

We have had fruitful discussions with A. Chapiro, P. G. de Gennes, and R. M. Velasco.

References and Notes

- (1) A. Dubault, M. Veysie, L. Liebert, and L. Strzelecki, *Nature (London)*, **245**, 94 (1973).
- (2) G. L. Gaines, "Insoluble Monolayers at Liquid-Gas Interfaces", Wiley, New York, N.Y., 1966, p 91.

- (3) N. Beredjick and W. J. Burlant, *J. Polym. Sci., Part A1*, **8**, 2807 (1970).
(4) R. Ackermann, O. Inacker, and H. Ringsdorf, *Kolloid-Z. Z. Polym.*, **249**, 1118 (1971).
(5) M. Hatada, M. Nishii, and K. Hirota, *J. Colloid Interface Sci.*, **45**, 502 (1973).
(6) R. M. Velasco, to be submitted for publication.
(7) P. J. Flory, 'Principles of Polymer Chemistry', Cornell University Press, Ithaca, N.Y.
(8) T. G. Fox and S. Loshaek, *J. Polym. Sci.*, **XV**, 371 (1955).
(9) S. Loshaek, *J. Polym. Sci.*, **XV**, 391 (1955).

Backbending and Other Deviations from Ideality in Extraction Systems¹

J. J. Bucher* and R. M. Diamond

Lawrence Berkeley Laboratory, University of California, Berkeley, California 94720 (Received March 14, 1975)

Publication costs assisted by the U.S. Energy Research and Development Agency

The use of slope analysis for interpreting extraction data is usually coupled with the assumption that the activity coefficients of the new chemical species that yield the changes in slope are ideal. This assumption is shown to be wrong in several extraction systems that are described. In particular, the phenomenon of "backbending" in certain tertiary ammonium salt systems is completely inexplicable under such an assumption, and incorrect extractant coordination numbers are obtained for trioctylphosphine oxide-strong acid species in poor solvents. As a result of this assumption literature values for aggregation numbers determined for alkylammonium salts in poor solvents may be too large.

Introduction

Slope analysis is an often-used method for interpreting and analyzing data from extraction equilibria in order to obtain information on the nature of the extracting species.² Central to the application of this method is the assumption that any deviation from the law of mass action is due to the formation of a new chemical species, e.g., a higher complex of the extraction reagent, if the latter's concentration is being increased, or a higher ion association or aggregate, if the concentration of an extracted ionic species is being increased. However, as has been pointed out,³⁻⁷ it is unreasonable to ignore all nonspecific nonidealities of the extracted species and blame all deviations on new chemical species. For example, with amine salt systems, the strong electrical interactions between ions in low dielectric-constant media that cause association to ion pairs and ion quadrupoles, etc., surely lead to nonconstant activity coefficients for these same ion aggregates. The importance of the analog of the solubility parameter term of regular solution theory has been described in the literature for these same systems,^{3b} and use of such an activity-coefficient correction was shown to lead to more "chemically sensible" results than unrestricted computer fitting to a large number of oligomers.⁸⁻¹¹

Some years ago one of the present authors⁴ described extraction behavior of a half-dozen amine-salt systems that was clearly incompatible with the usual slope analysis procedure of ignoring the activity coefficients of the amine-salt aggregates and blaming all deviations from ideal (ion-pair) behavior on higher ion aggregation. In these examples the log-log plots of $[\text{TLA}\cdot\text{HX}]_0$ vs. $[\text{TLA}]_0(\text{H}^+\text{X}^-)$ not only deviated upward away from the ion-pair slope of unity observed at low concentration, but went beyond the limiting asymptote of mass-action law theory for aggregation into a colloid, namely, a vertical line. They actually bent backward so that $[\text{TLA}\cdot\text{HX}]_0$ became a double-valued function

of the product $[\text{TLA}]_0(\text{H}^+\text{X}^-)$, Figure 1. Since this indicated a complete breakdown of the assumptions usually used for slope analysis, and because it posed an interesting problem to explain in its own right, we have examined the origin and generality of such behavior further in this work. We have also considered another type of organic-phase activity coefficient variation arising in certain trioctylphosphine oxide-strong acid extraction systems.

Experimental Section

Reagents. The tri-laurylamine (TLA), Rhône-Poulenc, qualité nucléaire-99% pure tertiary amine, was used as received. A comparison using this material and TLA that was further purified (by repeated recrystallization of the TLA-HCl salt from petroleum ether, bp 30-65°C) indicated no significant difference in the equilibrium data. Trioctylphosphine oxide (TOPO) was obtained from the Carlisle Chemical Corp., Reading, Ohio. The technical grade TOPO was washed with mild base and distilled water and recrystallized five times from pentane. The HClO₄ solutions were prepared by diluting a stock solution of reagent grade acid (G. F. Smith) with distilled water. Standardization of the stock HClO₄ solution was by titration with sodium hydroxide, using Bromothymol Blue as an endpoint indicator. Reagent grade 57% hydroiodic acid (Merck, without the usual 1.5% H₃PO₂ as a preservative) was further purified by saturation with H₂S gas and subsequent distillation. The stock solution of HI was stored in amber-glass bottles. Iodide tracer, Na¹³¹I in 0.1 M NaOH solution, was obtained from New England Nuclear Corp. and used as received. HReO₄ solutions were made by dilution from a stock prepared by dissolving Re₂O₇ (Varlacoid Corp. 99.5% purity) in distilled water. The isooctane and cyclohexane were "spectro grade" reagents from Matheson Coleman and Bell. CCl₄ and 1-

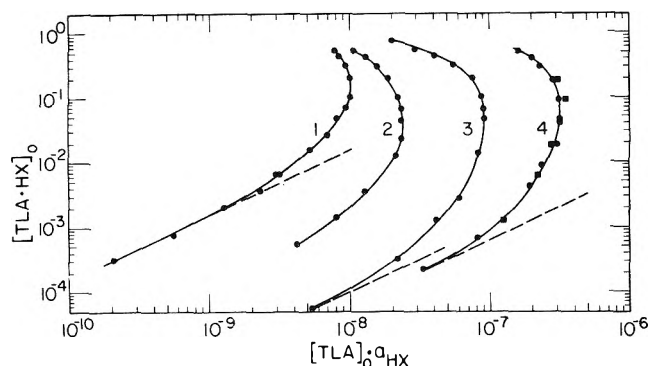


Figure 1. Total ammonium salt concentration $[\text{TLA}\cdot\text{HX}]_0$ vs. $[\text{TLA}]_0(\text{H}^+\text{X}^-)$ for various diluents. Curve 1 is the $\text{TLA}\cdot\text{HClO}_4$ -1-bromooctane system; curve 2 is the $\text{TLA}\cdot\text{HClO}_4$ - CCl_4 system; curve 3 is the $\text{TLA}\cdot\text{HClO}_4$ -cyclohexane system; and curve 4 is the $\text{TLA}\cdot\text{HI}$ -cyclohexane system. The dashed lines indicate unit slope. The square symbols, ■ (curve 4), indicate acid-base titration data from ref 4.

bromooctane were obtained from J. T. Baker. The 1-bromooctane was purified to a colorless reagent by distillation.

Solutions of the particular ammonium salt were prepared by taking ~ 0.5 M TLA in a diluent and shaking it fairly vigorously with ~ 0.6 M HX for several hours. After separation with the aid of centrifugation, the organic layer was washed with ~ 0.01 M HX to remove, or to prevent any possibility of having, excess acid in the amine salt (i.e., ratio of TLA/HX < 1.0). For CCl_4 solutions two methods of preparation were attempted: the one outlined above and another in which a solution of TLA-HCl in CCl_4 was repeatedly washed with an aqueous solution of 0.01 M HClO_4 (to prevent premature hydrolysis) and ~ 2 M NaClO_4 . Complete conversion to the amine perchlorate salt was judged by testing for the lack of a visual precipitate with AgNO_3 . It is known that aliphatic amines may react with CCl_4 or nearly any halocarbon,¹² but in this instance the amine salt from either procedure gave the same extraction results.

The amine-HI salt was made as described above. However because of the sensitivity of acidic iodide to air oxidation, both the organic and aqueous solutions were carefully purged with argon. This removal of oxygen gave amine-HI solutions that were stable for > 1 week (no visual formation of brownish I_3^- , etc. observed) instead of < 1 hr with exposure to air. Details for the preparation of the TOPO solutions can be found elsewhere.¹³

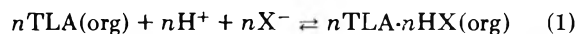
Procedures. The amine extraction systems were studied by a back-extraction or hydrolysis technique. Starting from standardized ~ 0.5 M trilaurylammonium salt solutions in the organic solvent, a series of solutions was prepared by dilution. These salt solutions (5 or 10 ml) were then shaken for > 18 hr with 50 ml of distilled water for the $\text{TLA}\cdot\text{HClO}_4$ systems and with an equal aqueous volume (10 ml) for the $\text{TLA}\cdot\text{HI}$ systems. Before equilibration of the $\text{TLA}\cdot\text{HI}$ systems, radioactive iodide ($< 10^{-5}$ M) was added to the aqueous phase. After equilibration, phase separation was accelerated by centrifugation. (If the shaking during the equilibration process is done too vigorously, at least for the most concentrated salt solutions, a cloudy aqueous layer is obtained. This phase is then quite resistant to clearing even with prolonged centrifugation.) For the counting of the tracer iodide in a $\text{Na}(\text{Tl})\text{I}$ well-type crystal, 3-ml samples of each phase were taken, or smaller samples of a particular

phase adjusted to 3 ml if the count rate was too high. Conventional acid-base titrations were made to analyze the aqueous equilibrium acid content. Except for the lowest initial amine-salt concentrations, the aqueous acid concentration is by far the most sensitive parameter to be determined. This is due to the relatively small amount of amine salt that is hydrolyzed over most of the concentration range considered. Subtraction of this quantity from the well-established initial amine salt concentration is, in most instances, a minor perturbation upon the latter. That is, the equilibrium organic-phase salt concentration is little different from the initial value.

Procedures that were used to obtain the distribution data for the $\text{TOPO}\cdot\text{HReO}_4$ system are similar to those already outlined elsewhere.¹³ Distribution measurements for all systems were at room temperature, $24 \pm 2^\circ\text{C}$.

Results and Discussion

The extraction of a strong acid, H^+X^- , by a solution of trilaurylamine, TLA, in a low dielectric-constant medium that induces association of the resulting salt to an ion pair or higher aggregate can be described by the reaction



with an equilibrium constant

$$K = \frac{[n\text{TLA}\cdot n\text{HX}]_0 y_{n\text{TLA}\cdot n\text{HX}}}{(\text{H}^+\text{X}^-)^n [\text{TLA}]_0^n y_{\text{TLA}}^n} \quad (2)$$

Brackets indicate concentrations, parentheses are activities, and y is a molar activity coefficient. Taking logarithms, eq 2 can be written

$$\log [n\text{TLA}\cdot n\text{HX}]_0 = \log K + n \log [\text{TLA}]_0(\text{H}^+\text{X}^-) + \log \frac{y_{\text{TLA}}^n}{y_{n\text{TLA}\cdot n\text{HX}}} \quad (3)$$

Thus, a log-log plot of the stoichiometric concentration of the organic-phase amine salt $[\text{TLA}\cdot\text{HX}]_0$ vs. the product $[\text{TLA}]_0(\text{H}^+\text{X}^-)$ should yield a curve whose tangent is the value of n at that point, if the activity coefficient ratio is a constant. This condition is usually assumed in slope analysis work.

The results of the present study of the extraction by TLA of HClO_4 into 1-bromooctane and into CCl_4 and HClO_4 and HI into cyclohexane are shown as log-log plots of $[\text{TLA}\cdot\text{HX}]_0$ vs. $[\text{TLA}]_0(\text{HX})$ in Figure 1, curves 1-4, respectively. Where determined to low amine-salt concentrations, as for curve 1 (and other examples not shown), the log-log plots are straight lines with unit slope, indicating predominantly ion pairs for the salt in this region and the validity of the assumption that the organic-phase activity coefficient ratio is constant. This constancy is due to the very low concentrations of the salt and of the amine in the organic diluent, so that the nature of the organic phase is essentially unchanged.

However at higher concentrations, the curves deviate upward from a line of unit slope. This is the region that has been of most interest in the literature,¹⁴ and this behavior has almost always been ascribed to a further association of the ion pairs to higher ion aggregates in the low dielectric-constant medium.¹⁵ As just described, the average value of this aggregation, \bar{n} , at any point can be determined by the tangent of the curve, or the whole curve can be fitted to a small number of oligomers, by hand or by computer, to yield the changing nature of the amine-salt species, if the

activity coefficient ratio of the various oligomers are assumed constant. As the concentration is increased, the slopes become steeper, indicating the predominance of still higher and higher species. The limiting slope for such a system of ideal amine-salt aggregates is a vertical asymptote, corresponding to infinite aggregation, the formation of a colloid. However as can be seen in Figure 1, and less conclusively in the earlier work,⁴ with "poor" diluents the curves for these TLA salts actually "backbend" for concentrations above $\sim 0.1 M$, yielding negative values for the slope.

This behavior is completely unexplainable in the context of an aggregation model with ideal activity coefficients for the salt associations. It does not appear to be a nonequilibrium effect. In the TLA-HReO₄ system in CCl₄ (not shown), for instance, the same results are obtained either by starting with HReO₄ tracer in the aqueous phase or by titrating the macroconcentrations of HReO₄ in the aqueous phase which is hydrolyzed from the salt. The simplest, and we believe the correct, explanation is still that given earlier,^{4,5} namely, that at these large concentrations of amine salt we are dealing with a new diluent. Instead of the original solvent phase, we now have a more polar phase consisting of the amine salt (25-30% by volume at 0.4 M TLA-HClO₄) in the solvent. This new organic phase has properties more favorable for extraction of the salt; for example, it has a higher dielectric constant, due to the presence of the ion aggregates themselves. In an earlier paper the origin of the backbend was similarly stated as being due to a change in the nature of the diluent leading to enhanced extraction; the increase in dielectric constant was measured⁴ but explicitly stated as being only one example of the type of change occurring, rather than the sole cause of the increased extraction as quoted in the English translation of ref 6. As a result, the value of the organic-phase-coefficient $y_{n\text{TLA-nHX}}$ decreases with the increase in amine-salt concentration. However there are thermodynamic limits to the rate of decrease of $y_{n\text{TLA-nHX}}$ (ref 16 and 17). Considering a three-component system of diluent, amine salt, and amine, the condition $\partial\mu_{(n\text{TLA-nHX})}/\partial n_{(n\text{TLA-nHX})} > 0$ must be satisfied. This limitation of the decrease of $y_{n\text{TLA-nHX}}$ led the authors of ref 6 to state that to explain the backbending behavior one must take into account the activity of other components of the system, and, in particular, the water in the organic phase.¹⁸

Indeed, no amount of tinkering with the amine-salt activity coefficient alone can yield the results of Figure 1, and we, too, believe that one must take into account another component. However we think it is the amine that is important, and not the water. For just as the introduction of macro amounts of the amine salt ($\geq 0.1 M$) changes the nature of the solvent from the original diluent to a mixed one whose properties (more polar nature, higher dielectric constant,¹⁹ etc.) should lower the activity coefficient of the amine salt,^{21,20} these changes in the diluent make it less suitable for the nonpolar and relatively inert trilaurylamine itself. That is, the activity coefficient of the TLA should increase with increasing salt concentration in the mixed diluent, and both activity coefficient changes should cause a very marked lowering in the ratio $y_{n\text{TLA-nHX}}/y_{\text{TLA}}^n$. In fact by inspecting eq 2 or 3, it can be seen that for backbending to occur, the value of y_{TLA} must increase sufficiently to overcome the decrease in the product $[\text{TLA}]_0(\text{H}^+\text{X}^-)$ with increasing amine-salt concentration. Even though the concentration of amine in the organic phase is small (10^{-2} to $10^{-3} M$) so that one might think its activity coefficient

would not vary much, the change in the nature of the diluent from a pure hydrocarbon or halogenated hydrocarbon to an amine-salt solution can cause large changes in the amine activity. Some support for the suggested amine activity coefficient behavior appears in the solubility pattern of tertiary amines.²² In general they are completely miscible with nonpolar diluents, but only sparingly soluble in alcohols and other polar solvents. Since the concentrated amine-salt solutions are certainly more polar than the initial diluent,^{4,19,23} an increase in the amine coefficient is thus suggested.

While it is not possible to determine the changes in the individual organic-phase activity coefficients in the backbending region (only the change in the ratio of the coefficients is measured), limits can be set on the change in y_{TLA} using eq 1 and the experimental data shown in Figure 1. For even if $y_{n\text{TLA-nHX}}$ falls as steeply as permitted by thermodynamics without third-phase formation, the value of y_{TLA} must increase with increasing amine-salt concentration at least enough to account for the decrease in $[\text{TLA}]_0(\text{H}^+\text{X}^-)$ from its maximum value. For a change in the amine-salt concentration from 0.1 to 0.5 M, the four curves in Figure 1 suggest a minimum increase in y_{TLA} of 1.3-4.5, a reasonable set of lower limits.

We have described how it is impossible to explain the backbending behavior of a number of concentrated amine-salt systems using the usual slope analysis method which attributes all deviations from simple ion-pair behavior to the formation of higher ion associations, all of which behave ideally (have activity coefficients = 1). Instead we suggest that the increasing proportion of amine salt in the organic phase changes the nature of that phase so much that the activity coefficients of various ion aggregates of the amine salt decrease and that of the amine increases. To a smaller degree this behavior is also true below the concentration of amine salt at which backbending commences, so that all of the deviation from a straight line of unit slope (pure ion-pair behavior) in that region may not be due to the formation of higher ion associations. Some of the increased extraction is because of the change in the solvent, and so the true degree of aggregation is smaller than that determined by the usual slope analysis methods, whether graphical or by computer. This feature probably explains the rather unusual series of oligomers usually determined by slope analysis of amine-salt systems in "poor" diluents, in which the ion pair is followed by a dimer and then a much higher oligomer, or where even the dimer is skipped and the next smallest ion association is a trimer.⁸⁻¹¹ The irregularities are probably false; the true aggregation is less than the apparent value, and the appearance of high oligomers or of a trimer without passing through a dimer species is likely due to the neglect of the nonidealities of the ion dipoles and quadrupoles, in particular of their (attractive) electrostatic interactions with each other in the increasingly concentrated organic phase. If the ideas presented are correct, the irregularities in the series and the degree of aggregation would become more marked, the more inert and less polar the initial diluent and the higher the charge on the anion, for then the changes in the activity coefficients of the salt species and of the amine would be the larger.

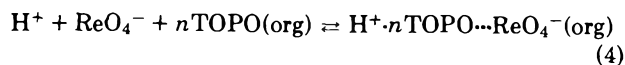
Actually one of the early examples in the literature where simple slope analysis of an amine-salt system led to completely unexplainable results was the extraction of H₂SO₄ by trioctylamine in benzene.²⁴ Although the extraction of the normal sulfate salt appeared well behaved at low

salt concentrations and followed the mass-action expression for an ion triplet, $(\text{TOAH}^+)_2\text{SO}_4^{2-}$, the extraction increasingly deviated upward from an ideal slope above a salt concentration of $\sim 0.025 M$. The explanation given at that time was that the salt was aggregating to a colloid.²⁴ However later light-scattering studies by the same author²⁵ showed that the sulfate salt remained essentially monomeric, leaving the extraction behavior unexplained. We wish to suggest that the enhanced extraction of the amine sulfate in concentrated benzene solution is due, not to ion association, but to a more nonspecific interaction of the salt with itself through changing the nature of the medium from the original benzene to a mixture of salt in benzene (a more polar, better-extracting solvent).

Other than by light-scattering studies, it is not easy to unambiguously determine the state of aggregation of an amine salt in the range of concentrations being considered. The (nonspecific) interaction of the amine-salt species with themselves brings into question the accuracy of the determination of aggregation numbers of amine-salt solutions by osmometric methods, as again ideal activity coefficients are usually assumed for the associated species. In this case the effect of the change in the amine activity coefficient is not important, but the changes in the salt species activity coefficients still play a role and would again make the true aggregation smaller than that derived assuming all deviation from ideality comes from association alone. Marcus has discussed a rough quantitative way to take part of the nonidealities into account,³ and has shown that his treatment does lead to simpler, more chemically reasonable aggregation behavior. The effect is noticeable in the examples he uses of aromatic solvent solutions of triaurylammonium salts from $0.010 \rightarrow 0.10 M$ in concentration, but the differences with simple association calculations would become much larger with less polar diluents and more concentrated salt solutions.

A variation of this process where the presence of an amine salt decreases its own activity coefficient is the solubilization of an amine salt, which is difficult to dissolve even in a relatively polar solvent, by the addition of a more soluble amine salt. For example, the salt $(\text{R}_3\text{NH}^+)_2(\text{CoCl}_4^{2-})$ in *p*-xylene is solubilized by appreciable concentrations of the extractant salt, $\text{R}_3\text{NH}^+\text{Cl}^-$,²⁶ and there are other examples in the literature.²⁷ In fact, the activity coefficient of $(\text{R}_3\text{NH}^+)(\text{FeCl}_4^-)$ has been shown to decrease with an increase in $\text{R}_3\text{NH}^+\text{Cl}^-$ concentration,²⁸ exactly as expected from the present discussion.

Are there other types of extraction systems that do not allow for simple slope analysis, and, if so treated, lead to wrong conclusions? The answer appears to be yes. Consider the extraction of HReO_4 by trioctylphosphine oxide (TOPO) solutions in isooctane. The extraction to an ion-paired product can be expressed



with the corresponding equilibrium constant

$$K_n^a = \frac{[\text{H}^+ \cdot n\text{TOPO} \cdots \text{ReO}_4^-]_{\text{org}} y_{n\text{TOPO-HReO}_4}}{(\text{H}^+\text{ReO}_4^-)[\text{TOPO}]^n y_{\text{TOPO}}^n} \quad (5)$$

Thus a log-log plot of the organic-phase HReO_4 concentration vs. the aqueous-phase acid activity for a constant TOPO concentration should yield a straight line of unit slope if the organic-phase species is an ion pair and the ratio of activity coefficients is constant. This result is in-

deed obtained for fixed TOPO concentrations from 0.0020 to $0.10 M$ and for aqueous HReO_4 activities ranging from 10^{-8} to $10^{-1} M$ (except at the highest HReO_4 activities and lowest TOPO concentrations). Then to determine the value of n , the number of TOPO molecules coordinated to the extracted acid, one can study the dependence of the extracted acid on the TOPO concentration. To exclude the possibility of aggregation beyond the ion pair, tracer concentrations of HReO_4 can be used. Figure 2 shows the distribution of $1 \times 10^{-6} M \text{HReO}_4$ in $1.0 M \text{HCl}$ with TOPO in isooctane. The initial slope drawn is two ($n = 2$), but the raw data show deviations from this line even at TOPO concentrations as low as $2-3 \times 10^{-3} M$. The organic-phase HReO_4 concentration at these TOPO concentrations is $\sim 10^{-8} M$, so no aggregation beyond the ion pair is expected. Extension of the line of slope two is shown by a dashed line, and the subtraction of this line from the raw data is indicated by the dashed line connecting the filled triangles. This resultant line has a slope three. By all the normal rules of slope analysis this indicates that at the initial low TOPO concentrations there are two TOPO molecules coordinated per extracted acid, but that over most of the TOPO concentration range studied the slope of three indicates a three-to-one complex.

Figure 3 shows the extraction of 0.10 and $0.010 M \text{HReO}_4$ (macro amounts of perrhenic acid) as a function of TOPO concentration. Curve 2, for $0.010 M \text{HReO}_4$, is almost a duplicate of the tracer distribution study in Figure 2. A dashed line of slope two is drawn in to match the apparent concentration quotient, K_2^a , obtained from line 1. The open triangles are the result of subtracting the slope-two line from the raw data, and they give a line with a slope of three. The upper end of these data must be corrected for TOPO complexed by acid. Square symbols indicate correction assuming a 2TOPO complex, but there is little difference between a choice of 2TOPO or 3TOPO for curve 2. However, in the set of data illustrated in curve 1, for $0.10 M$ aqueous HReO_4 , the choice of two or three TOPO molecules in the complex leads to much more divergent results after subtraction of the slope-two line. If one assumes a 2TOPO- HReO_4 complex, the points indicated by squares are obtained, and fall surprisingly upon a line of slope three. If one assumes a 3TOPO per acid correction (the inverted triangles), a line with a slope considerably steeper than three is obtained. The result for a 3:1 complex would be possible if aggregation were occurring, but a similar degree of aggregation ought to have been observed in the set of data for $0.010 M \text{HReO}_4$ curve 2, where a similar range of $[\text{HReO}_4]_0$ concentrations was examined. It is not; nor is there any indication for a large degree of aggregation from the log-log plots of organic-phase HReO_4 vs. aqueous acid described earlier.

Thus there is a problem. Is the extracted species at the top of curve 1 a 2:1 or a 3:1 complex, and, whichever it is, why is it not well behaved? In an earlier publication we took this type of extraction results at higher TOPO concentration to indicate a 3:1 complex.²⁹ However infrared spectroscopic results³⁰ over the whole TOPO range studied indicate that the species is a 2TOPO- HReO_4 complex like the one known in other diluents, and water analyses show that it is essentially anhydrous and so not based on a hydronium cation³¹ (which has three possible positive sites for a 3:1 complex), but on a bare proton, which is unlikely to permit coordination to more than two close TOPO molecules.^{13,30}

So in this case, dependence on simple slope analysis

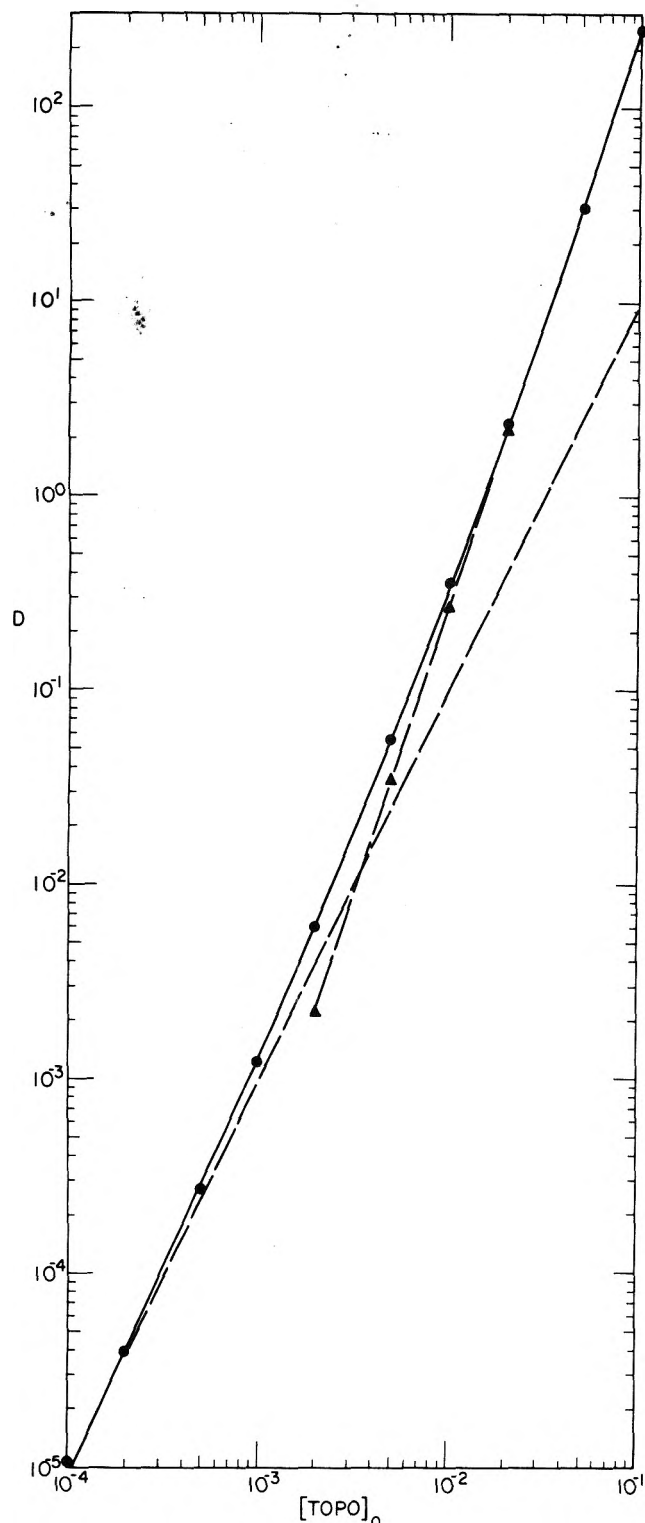


Figure 2. Variation of distribution ratio, D , with TOPO in isooctane for 1×10^{-6} M HReO_4 in 1.0 M HCl . The dashed lines are drawn with either slope two or three (Δ).

leads to the wrong result (although there are warning inconsistencies); the $\text{TOPO} \cdot \text{HReO}_4$ species in isooctane is only a $2\text{TOPO} \cdot \text{HReO}_4$ species with no evidence for the 3:1 complex suggested by the log-log plots in Figures 2 and 3. What can be the cause of this error in the simple mass-law analysis, especially since deviations from the line of slope two appear at extremely low values of the HReO_4 concen-

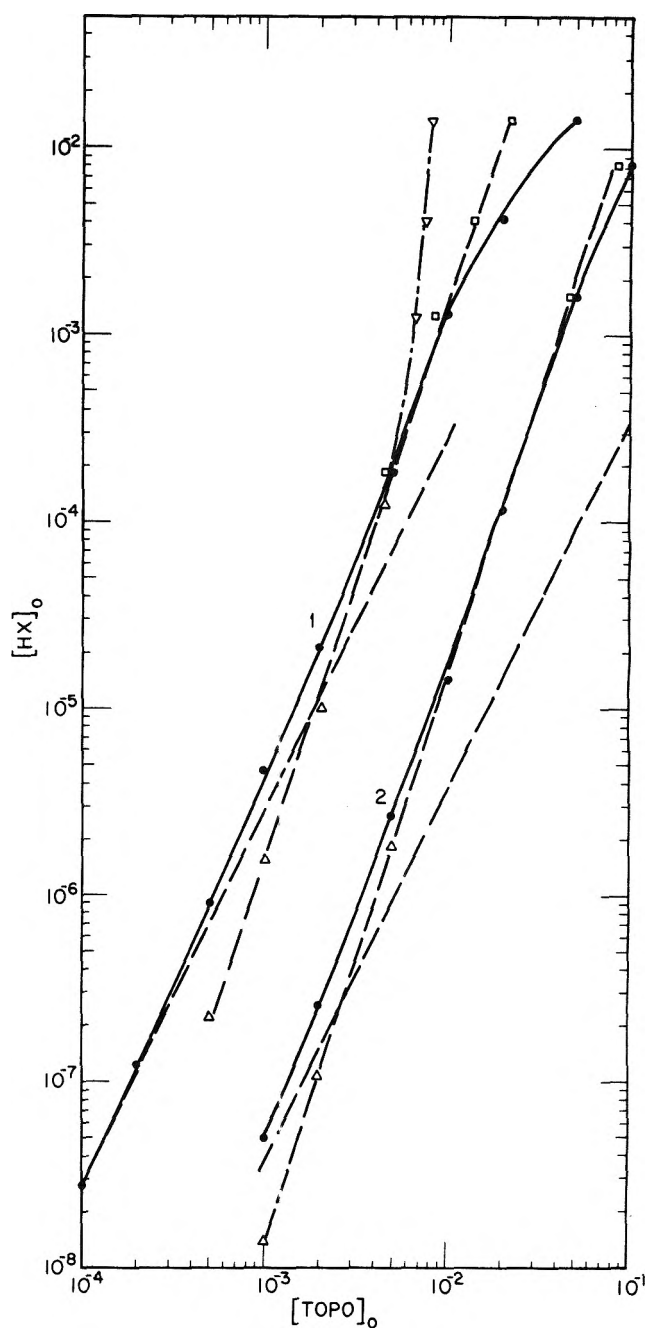


Figure 3. Variation of acid content of the organic-phase with TOPO in isooctane for aqueous HReO_4 concentrations of 0.10 M (line 1) and for 0.010 M (line 2): \bullet , uncorrected data; Δ , result of subtracting slope two component from raw data; \square , data corrected for assuming 2:1 $\text{TOPO}:\text{H}^+$ complex; ∇ , data corrected for used-up TOPO assuming a 3:1 $\text{TOPO}:\text{H}^+$ complex. Dashed lines are drawn with either slope two or three.

tration in the organic phase (10^{-8} M in Figure 2 and $<10^{-6}$ M in Figure 3)? These concentrations are too low to suppose that the presence of the $\text{TOPO} \cdot \text{HReO}_4$ species changes the nature of the solvent, so that, in contrast to the amine situation, we must look elsewhere for the origin of the deviations. It is certainly an organic-phase effect, as this behavior does not occur under the same aqueous conditions but with other "better" diluents.¹³ We believe it is due to the presence of the polar TOPO molecules when dissolved in very inert ("poor") diluents. That is, the addition of the very polar TOPO molecules makes the inert diluent

isooctane into a new and more polar solvent, a mixture of isooctane and TOPO. This explains why the deviations occur similarly for both tracer and macro amounts of acid (Figures 2 and 3) but at the same TOPO concentration. It is surprising, however, at least to us, what a small amount of TOPO is necessary to cause deviations from the line of slope two. Figures 2 and 3 show significantly enhanced extraction at as low as $2-3 \times 10^{-3} M$ TOPO. At such a concentration there is only one TOPO for approximately 4000 isooctane molecules; to have any marked effect the TOPO must selectively solvate (be in the vicinity of) the even rarer $H^+(TOPO)_2ReO_4^-$ species. This process leads to a lowering of the activity coefficient of the extracted acid but not the formation of a higher TOPO complex or aggregation of the $H^+(TOPO)_2ReO_4^-$ species.

Summary

In this paper we have described several examples of systems that do not follow the behavior expected for extraction models based on the simple application of mass action to stepwise equilibria. In the usual application of slope analysis to extraction systems, all deviations from the behavior at low concentrations are considered to be due to the stepwise formation of higher complexes but with ideal activity coefficients for all of the species involved. Types of studies included are the formation of higher complexes with the extractant molecule, as the extractant concentration is increased, and stepwise aggregation of the extracted amine salt, as the salt concentration is increased. In the former case, neglect of possible organic-phase activity coefficient variations in applying slope analysis leads to the suggestion of higher complexes than actually exist or make sense chemically. In the latter case, ignoring possible activity coefficient variations in the analysis yields a greater degree of ion aggregation and higher types of ion aggregates than really exist. This leads us to question the accuracy of the determinations of such ion aggregation properties in the literature from extraction studies or even osmometric methods, when all deviation from ideal behavior are blamed on aggregation alone, especially with "poor" solvents.⁸⁻¹¹ For tertiary amine salts in such solvents, there may appear the very interesting phenomenon of "back-bending" in the log-log plot of extracted acid concentration vs. the product of aqueous acid activity and amine concentration. This result is completely inexplicable in the simple slope analysis formulation, and is excellent proof that the

activity coefficients of both the amine salt and the amine are changing with amine-salt concentration. We believe that the origin of this change comes from the change in properties of the diluent as it goes from the initially pure solvent to a mixture of amine salt and solvent.

References and Notes

- (1) Work performed under the auspices of the U.S. Atomic Energy Commission.
- (2) Y. Marcus and A. S. Kertes, "Ion Exchange and Solvent Extraction of Metal Complexes", Wiley-Interscience, New York, N.Y., 1969; many references to using slope analysis are noted therein.
- (3) (a) Y. Marcus, *Pure Appl. Chem.*, **20**, 85 (1969); (b) *J. Phys. Chem.*, **77**, 516 (1973).
- (4) W. Müller and R. M. Diamond, *J. Phys. Chem.*, **70**, 3469 (1966).
- (5) R. M. Diamond in "Solvent Extraction Chemistry", D. Dryssen, J. O. Liljenzin, and J. Rydberg, Eds., North Holland Publishing Co., Amsterdam, 1967, p 349.
- (6) Yu. G. Frolov, A. V. Ochkin, and V. V. Sergievsky, *Russ. At. Energy Rev.*, **7**, 71 (1969). See in particular p 108 and references therein.
- (7) V. S. Shmidt, V. N. Shesterikov, and E. A. Mezhev, *Russ. Chem. Rev.*, **36**, 94f (1967).
- (8) O. Levy, G. Markovits, and A. S. Kertes, *J. Inorg. Nucl. Chem.*, **33**, 551 (1971); A. S. Kertes, O. Levy, and G. Markovits, *J. Phys. Chem.*, **74**, 3568 (1970).
- (9) P. R. Canesi, F. Orlandini, and G. Scibona, *J. Inorg. Nucl. Chem.*, **30**, 2513 (1968).
- (10) E. Hogfeldt in "Solvent Extraction Research", A. S. Kertes and Y. Marcus, Eds., Wiley-Interscience, New York, N.Y., 1969, p 157.
- (11) R. W. Cattrall and S. J. E. Slater, *J. Inorg. Nucl. Chem.*, **36**, 841 (1974).
- (12) R. Foster, *Chem. Ind. (London)*, 1354 (1960).
- (13) J. J. Bucher, M. Zirin, R. C. Laugen, and R. M. Diamond, *J. Inorg. Nucl. Chem.*, **33**, 3869 (1971).
- (14) See, for example, the references in ref 2, p 737; and ref 5.
- (15) C. A. Kraus, *Science*, **90**, 281 (1939); C. A. Kraus, *J. Phys. Chem.*, **58**, 673 (1954); also the review article, ref 6.
- (16) I. Prigogine and R. Defay, "Chemical Thermodynamics", Longmans, London, 1954, p 225.
- (17) H. L. Friedman, *J. Phys. Chem.*, **66**, 1595 (1962).
- (18) Reference 6, p 104.
- (19) O. Levy, G. Markovits, and A. S. Kertes, *J. Phys. Chem.*, **75**, 542 (1971).
- (20) Reference 7, p 955.
- (21) A. S. Kertes and G. Markovits, *J. Phys. Chem.*, **72**, 4202 (1968).
- (22) C. W. Hoerr and H. J. Harwood, *J. Org. Chem.*, **16**, 779 (1951); A. W. Ralston, C. W. Hoerr, and P. L. DuBrow, *ibid.*, **9**, 259 (1944); ref 2, p 741.
- (23) J. A. Geddes and C. A. Kraus, *Trans. Faraday Soc.*, **32**, 585 (1936).
- (24) K. A. Allen, *J. Phys. Chem.*, **60**, 239 (1956).
- (25) K. A. Allen, *J. Phys. Chem.*, **62**, 1119 (1958).
- (26) V. S. Shmidt, E. A. Mezhev, and V. N. Shesterikov, *Russ. J. Inorg. Chem.*, **11**, 1495 (1966).
- (27) A. Nelson, J. Fasching, and R. McDonald, *J. Inorg. Nucl. Chem.*, **27**, 439 (1965); P. J. Lloyd and E. A. Mason, *J. Phys. Chem.*, **68**, 3120 (1964).
- (28) W. Smulek and S. Siekierski, *J. Inorg. Nucl. Chem.*, **24**, 1651 (1962).
- (29) T. J. Conocchioli, M. I. Tocher, and R. M. Diamond, *J. Phys. Chem.*, **69**, 1106 (1965).
- (30) J. J. Bucher and R. M. Diamond, *J. Inorg. Nucl. Chem.*, **34**, 3531 (1972).
- (31) For example, D. C. Whitney and R. M. Diamond, *J. Phys. Chem.*, **67**, 209 (1963); J. J. Bucher and R. M. Diamond, *ibid.*, **73**, 675, 1494 (1969).

Vibrational Spectra of $M^+NO_3^-$ Ion Pairs Variably Hydrated or Ammoniated in an Argon Matrix

Gary Ritzhaupt and J. Paul Devlin*

Department of Chemistry, Oklahoma State University, Stillwater, Oklahoma 74074 (Received May 21, 1975)

Publication costs assisted by the National Science Foundation

Studies of the vibrational spectra of $M^+NO_3^-$ ion pairs have been extended by matrix isolation of the vapors of the molten salts in the 400–450°C range in mixed matrices of argon–water and argon–ammonia at 10 K. These vapors are known to be composed of largely monomer ion pairs which in the mixed matrices are observed to associate strongly with the H_2O and NH_3 molecules. The dominant spectroscopic effect of this association is a progressive reduction in the cation distortion of NO_3^- as measured by the splitting, $\Delta\nu_3$, of the asymmetric stretching mode. This splitting, which, for example, decreases from 260 cm^{-1} for $Li^+NO_3^-$ in argon to 65 cm^{-1} in a pure H_2O matrix, is observed to decrease sharply to 168 cm^{-1} for single hydration of the cation and, then, gradually to the pure water matrix value as the percent water in the matrix is increased. This behavior, as well as that for $Li^+NO_3^-$ in mixed argon–ammonia matrices and for $K^+NO_3^-$ in argon matrices mixed with H_2O and NH_3 , is firm evidence that the overall reduction in $\Delta\nu_3$ is primarily the result of cation coordination with the H_2O (NH_3) molecules with a resultant diffusion of the cation charge density and thus of its polarizing power as reflected in the $\Delta\nu_3$ values. The new data support previous conclusions, based on residual cation effects in the pure H_2O and NH_3 matrices, that the $M^+NO_3^-$ ion pair retains a contact character for all matrix compositions. Thus the ion pair data for glassy H_2O and NH_3 matrices can be used with considerable confidence to identify contact ion pair features in aqueous and ammonia liquid solution vibrational spectra of nitrates. The matrix data are consistent with recent interpretations of ammonia solution spectra but suggest a new approach to the existing aqueous solution results.

Introduction

The use of vibrational spectra to characterize ionic solutions by identifying the nature and relative amounts of species present and, in some instances, to yield insights regarding the structure of the particular species has been a practice for many years. With the ease and accuracy of laser Raman methods that have evolved in the last decade this practice has increased and been considerably refined.¹ Nevertheless, there are severe problems associated with such studies the most formidable being that, in general, there are several different but related species present in such systems and the individual species spectra and structures for the particular solution environment have not all been determined in independent studies.

Thus, for example, if one considers an aqueous solution containing a moderate concentration ($\sim 5 M$) of $LiNO_3$ it is usually assumed that the nitrate spectrum is a composite of that of the completely solvated NO_3^- ion and the solvated contact ion pair ($Li^+NO_3^-$),^{1a} while at higher concentrations the nitrate ion environment progressively approaches that of the molten salt. The spectra for the two extreme cases are accessible through studies of highly dilute solutions² and the molten salt,³ but independent data for the individual contact ion pairs have not been available.

Recent matrix isolation studies that have confirmed that the dominant species in the vapors of many heated salt crystals and molten salts are the monomeric ion pairs, such as $Li^+NO_3^-$, have presented the possibility for such independent studies of the ion pairs. Thus, extensive data have been reported for nitrate, chlorate, and perchlorate alkali metal ion pairs in argon matrices.^{4–6} These data have emphasized the extreme degree of distortion that an anion ex-

periences when polarized by a contacting cation in an inert medium. Thus the 260- cm^{-1} splitting of the nitrate ν_3 degenerate stretching mode translates into a bonding scheme wherein one N–O bond has roughly one-third the strength of the other two N–O bonds.⁴ This represents unique quantitative information about the nitrate ion for a well-defined, noncrystalline case. The relationship of this contact ion pair spectra for a solid argon medium to spectra for nitrate aqueous solutions was not immediately apparent, but that relationship has since been displayed by substituting water for argon as the matrix medium.⁷ Since recent studies have shown that water deposited at 10 K forms a glassy film, with X-ray diffraction patterns similar to those for liquid water,⁸ it can be assumed that the ion-pair environment in the water matrices closely resembles that for the aqueous solutions and should thus permit identification of the contact ion-pair components of the spectra for aqueous solutions. Similar data and reasoning have been presented for ammonia solutions as well.

The glassy water and ammonia data have both been marked by evidence for a dramatic reduction in the anion polarization by the contacting cation.⁷ For example, the 170- cm^{-1} ν_3 splitting for $K^+NO_3^-$ (argon) is reduced to 20 cm^{-1} in NH_3 . Such reductions have been related to an effective neutralization (or diffusion) of the cation charge densities through donation of lone pair solvent electrons to the cation during the solvation process. However, the magnitude of the reduction of the anion distortion has raised the possibility that solvent molecules are actually inserting themselves between the ion-pair components as the matrices form. Arguments, such as the one based on the sizable cation effect still evident in the glassy water and ammonia matrices, have been presented to discount this possibility.⁷

but additional evidence was sought to confirm the contact nature of the $\text{H}_2\text{O}(\text{NH}_3)$ matrix ion pairs before proceeding to apply the new data to the interpretation of solution spectra.

If the reduction in anion distortion in a $\text{H}_2\text{O}(\text{NH}_3)$ matrix occurs through diffusion of the cation charge, the stepwise removal of water (ammonia) with substitution of argon as solvent should result in a gradual increase in the anion distortion. However, the insertion of a solvent molecule between the cation and anion would seem to occur in a single step so that a sharp, rather than gradual variation in anion distortion would occur during the stepwise replacement of water (ammonia) molecules by argon atoms. Thus, following a suggestion by Hester,⁹ we have measured the vibrational spectra for Li^+NO_3^- and K^+NO_3^- deposited at high dilution in matrices that vary in composition from pure argon to pure water (ammonia). In this paper we describe the new data obtained from such mixed matrices and consider the implications for the interpretation of liquid solution spectra.

Experimental Section

The volatilization of the metal nitrates was from the melts in resistance heated Pyrex glass Knudsen cells at temperatures in the 400–500°C range. The matrix gases, mixtures of argon with NH_3 and H_2O vapors, were metered through a Fisher-Porter $\frac{1}{16}$ -in. glass flowmeter and condensed with the nitrate molecular beam within a standard low-temperature infrared cell fitted to an Air Products CS-202 closed-cycle helium refrigerator. Matrix to sample ratios were chosen to give complete isolation of the nitrate species by setting the Knudsen cell temperatures and gas flow rates at values previously found to give dominantly monomer ion-pair spectra in argon matrices.^{4,7} The substrate deposition temperature was 10 K which suggests that the water-rich films were glassy in nature.⁸

The infrared spectra were recorded using a Beckman IR-7 infrared spectrometer. Spectra were routinely scanned from 600 to 4000 cm^{-1} to monitor the degree of isolation of the water (ammonia) in the argon at the various water-argon compositions. However, the nitrate data were restricted to the 800- and 1400- cm^{-1} regions corresponding to the $\text{NO}_3^- \nu_2$ and ν_3 regions, respectively.

Results and Discussion

The complete set of observed ν_{3a} and ν_{3b} infrared curves for matrix compositions ranging from pure argon to pure H_2O , or pure NH_3 , are presented in Figures 1–4 for LiNO_3 and KNO_3 . The top and bottom curves of each figure have previously been published but are presented here for comparison with the mixed matrix results. In addition to the large magnitude of $\Delta\nu_3$ ($\Delta\nu_3 = \nu_{3a} - \nu_{3b}$) of 170 cm^{-1} for KNO_3 and 260 cm^{-1} for LiNO_3 , a noteworthy aspect of the pure argon matrix data is the corresponding values of 85 and $\sim 150 \text{ cm}^{-1}$ for the weak features of dimeric (M^+NO_3^-)₂ species. As already noted the $\Delta\nu_3$ values for the pure glassy water and pure NH_3 matrices (top curves Figures 1–4) are drastically reduced relative to the argon matrix data.

The data for Li^+NO_3^- in the mixed H_2O -argon matrices are most easily discussed since, after an initial relatively sharp reduction in the splitting (6% cases), the $\Delta\nu_3$ value decreases in a gradual uniform manner throughout the composition range. For example, Figure 1 shows that in the range 0–6% H_2O the $\Delta\nu_3$ value for Li^+NO_3^- reduces, in es-

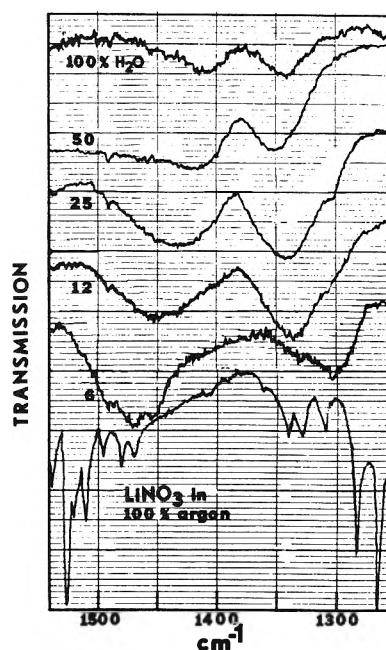


Figure 1. Infrared bands for the ν_3 nitrate mode for Li^+NO_3^- ion pairs isolated in matrices with composition varying from pure argon to pure H_2O . The numbers indicate the percent water in the mixed water-argon matrices.

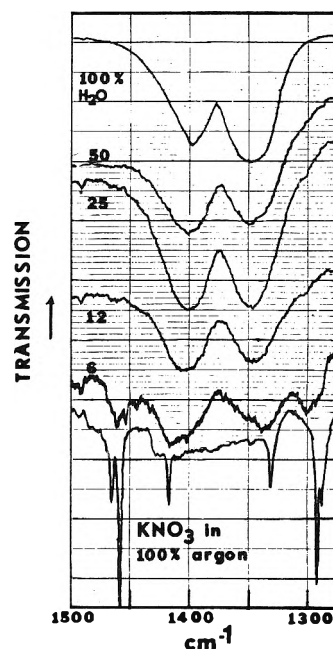


Figure 2. Infrared bands for the ν_3 nitrate mode for K^+NO_3^- ion pairs isolated in matrices with composition varying from pure argon to pure water. The numbers indicate the percent water in the mixed water-argon matrices.

entially a single step, from 260 to 168 cm^{-1} . As justified in the next paragraph, we relate this reduction to the coordination of one H_2O molecule with each Li^+ cation. Addition of further water to the matrix reduces $\Delta\nu_3$ to 115 cm^{-1} (12%), 90 cm^{-1} (25%), 70 cm^{-1} (50%), and finally 65 cm^{-1} for the pure H_2O case. The definite peaking of the ν_3 components at different values for the various percent compositions, plus the realization that a cation associated with

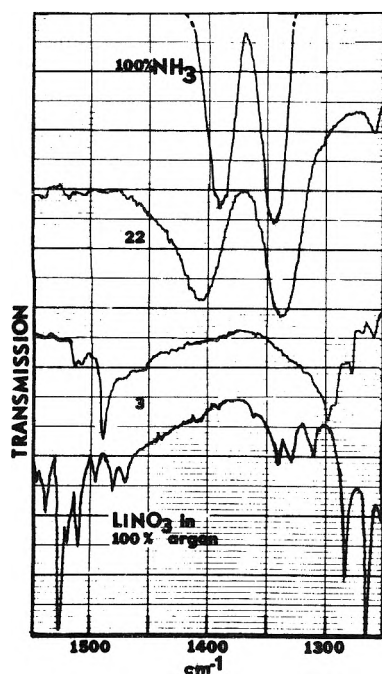


Figure 3. Infrared bands for the ν_3 nitrate mode for $Li^+NO_3^-$ ion pairs isolated in matrices with composition varying from pure argon to pure NH_3 . The numbers indicate the percent ammonia in the mixed ammonia-argon matrices.

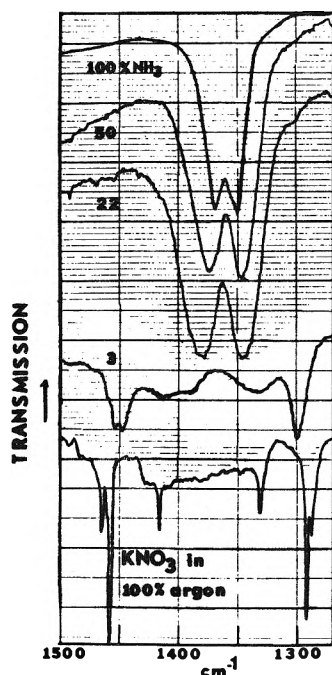


Figure 4. Infrared bands for the ν_3 nitrate mode for $K^+NO_3^-$ ion pairs isolated in matrices with composition varying from pure argon to pure ammonia. The numbers indicate the percent ammonia in the mixed ammonia-argon matrices.

NO_3^- is unlikely to coordinate with more than four or five solvent molecules, tempts one to relate the $Li(H_2O)_2^+ \cdot NO_3^-$ species to the 120-cm^{-1} splitting and the 90-cm^{-1} splitting to the $Li(H_2O)_3^+ \cdot NO_3^-$ molecules. Unfortunately, the mobility of the water molecules in the fluid surface of the matrix as it forms permits the H_2O molecules to seek

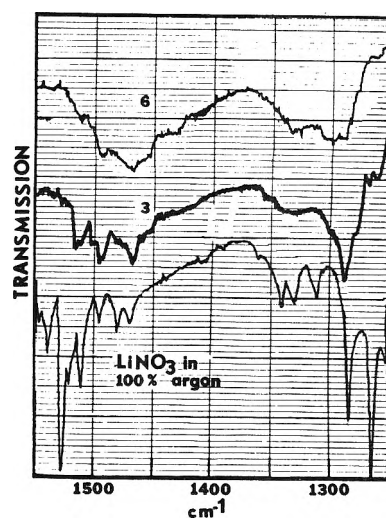


Figure 5. Infrared spectra of the ν_3 nitrate mode for $Li^+NO_3^-$ ion pairs isolated in water-argon mixed matrices with low percent H_2O content as indicated by the numbers.

out the cation to a limited degree, and thus prevents any rigorous use of the known H_2O :argon ratios in assigning the $\Delta\nu_3$ values. For example, at 6% H_2O the statistically most probable environment for the Li^+ ion in a $Li^+NO_3^-$ ion pair would be with " n " near neighbor argon ions (where " n " is the coordination number for Li^+ reduced to account for the contact paired NO_3^- ion). However, the $\sim 100\text{-cm}^{-1}$ reduction in $\Delta\nu_3$ at this matrix composition very strongly suggests that, on the average, one H_2O has entered the cation inner solvent shell.

Figure 5 compares the pure argon $Li^+NO_3^-$ spectrum to that for 3 and 6% H_2O -argon matrices and thereby shows the growth of the singly hydrated ion pair bands to dominance. In the 3% case the components that dominate in the 6% H_2O case ($\Delta\nu_3 = 168\text{ cm}^{-1}$) are observable, but there are also (a) bands that are nearly superimposable on the pure argon matrix features ($\Delta\nu_3 \approx 260\text{ cm}^{-1}$) and (b) a pair of bands at 1290 and 1495 cm^{-1} with only $\sim 50\text{ cm}^{-1}$ reduction for $\Delta\nu_3$. The latter bands are believed to reflect the influence of outer shell coordinated water molecules but could result from water- NO_3^- interaction at the anion end of the $Li^+NO_3^-$ contact ion pairs or from different matrix sites such as are responsible for multiplet structure in the pure argon matrices.

An equivalent discussion could be given for the $K^+NO_3^-$ species in NH_3 -argon mixed matrices based on the data of Figure 4. The major point regarding both of these cases is that the behavior of the $\Delta\nu_3$ splitting is precisely what one would predict provided the cation-anion contact is retained throughout: namely, the first associating solvent molecule to enter the cation inner coordination sphere has a sizeable effect on the cation polarizing power as reflected in a sharp drop in $\Delta\nu_3$. Subsequent inner shell solvent molecules have a progressively smaller effect so the $\Delta\nu_3$ value tends to approach the pure H_2O (or NH_3) value in a gradual monotonic manner. This behavior is demonstrated in the plots of $\Delta\nu_3$ vs. percent $H_2O(NH_3)$ in Figure 6.

The spectra of Figure 2, the data of Table I, and the corresponding plots of Figure 6 suggest, at first glance, a considerably different behavior for $K^+NO_3^-$ in H_2O . A naive consideration of the data might prompt the conclusion that the $\Delta\nu_3$ value produced by anion distortion by the K^+ ion is

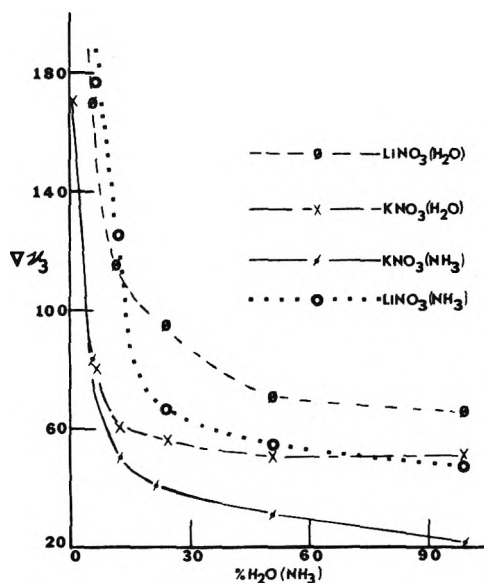


Figure 6. Plots of the splitting, $\Delta\nu_3$, in cm^{-1} for the dominant infrared features as a function of matrix composition.

reduced in two large steps from 170 cm^{-1} to the pure H_2O matrix value of $\sim 50 \text{ cm}^{-1}$. This view, however, ignores the fact that the NO_3^- ion, in dilute aqueous solutions, has a $\Delta\nu_3$ value of $\sim 50 \text{ cm}^{-1}$ ² such that, regardless of the magnitude of the cation distortion of the anion, the ν_3 splitting in a pure glassy H_2O matrix cannot be reduced below 50 cm^{-1} . With this in mind, it becomes reasonable to propose a much closer analogy for the solvation of the K^+NO_3^- in NH_3 -argon and K^+NO_3^- in mixed H_2O -argon matrices than is suggested by comparison of Figures 2 and 4 alone. That is, in the absence of the H_2O - NO_3^- interaction splitting of 50 cm^{-1} , it is easy to imagine that the series of $\Delta\nu_3$ values for K^+NO_3^- in H_2O -argon mixed matrices would go as 79 cm^{-1} (6%), $\sim 60 \text{ cm}^{-1}$ (12%), $\sim 40 \text{ cm}^{-1}$ (25%), $\sim 30 \text{ cm}^{-1}$ (50%), and $\sim 20 \text{ cm}^{-1}$ (100%) as for the NH_3 -argon case. It is clear from a comparison of Figures 2 and 4, as well as the plots of Figure 6, that the first two H_2O molecules to enter the K^+ inner shell have nearly the identical effect on $\Delta\nu_3$ as do the first two NH_3 molecules. At higher $\text{H}_2\text{O}(\text{NH}_3)$ ratios spectral differences arise primarily because the H_2O distortion of the NO_3^- ion prevents $\Delta\nu_3$ from dropping below 50 cm^{-1} . Thus the difference between Figures 2 and 4 arise from the much larger distortion of NO_3^- ($\Delta\nu = 50 \text{ cm}^{-1}$) by H_2O than by NH_3 ($\Delta\nu_3 \leq 20 \text{ cm}^{-1}$), rather than any strong difference in the ability of NH_3 and H_2O to diffuse the cation charge.

The foregoing is affirmed to a large extent by comparison of Figures 1 and 3 and Tables I and II. The Li^+NO_3^- in NH_3 -argon matrix ν_3 spectra (Figure 3) compare closely to the corresponding H_2O -argon cases. Since the limiting pure H_2O and pure NH_3 $\Delta\nu_3$ values, 65 and 47 cm^{-1} , are both significantly greater than for the K^+NO_3^- cases, it is obvious that the $\Delta\nu_3$ values for Li^+NO_3^- for all matrix compositions are determined primarily by the lithium distortion of the anion. For these cases, where the direct solvent-anion distortion is of secondary importance, the H_2O and NH_3 coordination with Li^+ are seen to have basically the same effect on cation charge density, just as presumed for the K^+NO_3^- discussion in the preceding paragraph.

The behavior of the ν_2 mode has been found to be predictable, and of little interest throughout these studies but

TABLE I: Frequencies in cm^{-1} for the Dominant ν_3 Band Components, as well as ν_2 and $\Delta\nu_3$ Values, for Li^+NO_3^- and K^+NO_3^- Ion Pairs Isolated in Mixed Argon-Water Matrices

	Argon	6% H ₂ O	12% H ₂ O	25% H ₂ O	50% H ₂ O	100% H ₂ O
			LiNO₃			
ν_2	817	820	820	823		827
ν_{3a}	1264	1302	1335	1342	1350	1347
ν_{3b}	1524	1470	1450	1432	1420	1412
$\Delta\nu_3$	260	168	115	90	70	65
			KNO₃			
ν_2	830	826	828			
ν_{3a}	1291	1337	1345	1347	1350	1348
ν_{3b}	1462	1416	1405	1401	1400	1498
$\Delta\nu_3$	171	79	60	54	50	50

TABLE II: Frequencies in cm^{-1} for the Dominant ν_3 Band Components, as well as ν_2 and $\Delta\nu_3$ Values, for Li^+NO_3^- and K^+NO_3^- Ion Pairs Isolated in Mixed Argon-Ammonia Matrices

	Argon	6% NH ₃	10% NH ₃	25% NH ₃	50% NH ₃	100% NH ₃
			LiNO₃			
ν_2	817	826	827 ^a	827	828	828
ν_{3a}	1264	1300	(1335) ^a	1338	1343	1345
ν_{3b}	1524	1478	(1450) ^a	1405	1399	1392
$\Delta\nu_3$	260	178	(125) ^a	67	56	47
			KNO₃			
ν_2	830	830	830	830	830	830
ν_{3a}	1291	1335	1345	1346	1347	1350
ν_{3b}	1462	1412	1400	1380	1374	1370
$\Delta\nu_3$	171	77	55	34	27	20

^a Estimated from 8% ND_3 in argon spectrum.

frequencies are tabulated for completeness in Tables I and II. Thus ν_2 retains a value of 830 cm^{-1} for all K^+NO_3^- in H_2O -argon mixtures while shifting slowly from the pure argon matrix value of 817 cm^{-1} to the pure H_2O matrix value of 827 for Li^+NO_3^- . The Li^+NO_3^- value similarly shifts from 817 to 828 cm^{-1} through the series pure argon to pure NH_3 .

Conclusions

The major conclusion of this study has already been indicated: namely, that the data are consistent with and confirm the view that the contact ion pairs, M^+NO_3^- , are the dominant species regardless of matrix composition and that the reduction previously reported for the $\Delta\nu_3$ value, in changing from an inert to associating matrices, is primarily the result of decreased cation polarizing powers produced by coordination of the associating matrix molecules with the cation. However, with these facts established there are several additional significant conclusions to be drawn. For example it is clear that the effect of a H_2O molecule in the cation inner coordination shell on the cation polarizing power is quite similar to that of an NH_3 molecule. Further, a comparison of the $(\text{H}_2\text{O})\text{M}^+\text{NO}_3^-$ ν_3 values with those noted earlier for the dimers, $(\text{M}^+\text{NO}_3^-)_2$, suggests that a

second NO_3^- ion in the M^+ coordination shell also has a similar attenuating effect on the M^+ polarizing power. Thus the $\Delta\nu_3$ values for the three cases, where M^+ is K^+ , are seen to be 79 (H_2O), 77 (NH_3), and 85 (NO_3^-) whereas for $M^+ = Li^+$ the $\Delta\nu_3$ values are 168 (H_2O), 178 (NH_3), and ~ 150 (NO_3^-). In view of the observed effect on the M^+ polarizing power from additional inner shell $H_2O(NH_3)$ molecules, an extension of this comparison to molten or glassy $LiNO_3$, where each Li^+ is coordinated to several NO_3^- species, makes it difficult to accept the $\Delta\nu_3$ value for that case (110 cm^{-1})¹⁰ as resulting from distortion of the anion by the cation alone. In fact, dilution of molten $LiNO_3$ with $LiClO_3$ has shown that only $\sim 70\text{ cm}^{-1}$ of that splitting is from anion distortion,¹⁰ a value that is close to the $\Delta\nu_3$ values for the $Li^+NO_3^-$ ion pair in pure glassy H_2O and NH_3 . Thus, a consistent picture is beginning to emerge. A similar dilution study for glassy KNO_3 in $KClO_3$, via codeposition methods, indicates that $\Delta\nu_3$ for K^+ polarization is 33 cm^{-1} , also reasonably close to the value for $K^+NO_3^-$ in pure glassy NH_3 ¹¹ (but not in pure H_2O where the H-bond solvent effect is dominant).

The principal conclusion, cited above, also strongly suggests that published ν_{3a} and ν_{3b} values for $Li^+NO_3^-$ contact ion pairs in aqueous solutions (1389 and 1464 cm^{-1}),^{1a} as estimated by curve resolution techniques, are in serious error. This observation in turn challenges the validity of the procedure (i.e., curve resolution) by which these values were estimated. The 1464-cm^{-1} value is 42 cm^{-1} above the $Li^+NO_3^-$ value of 1412 cm^{-1} for the glassy H_2O matrix. This difference seems to be too great to be attributed to any basic differences between the glassy H_2O and liquid H_2O environments, particularly considering that the corresponding band positions for NH_3 solutions, determined without the need for curve resolution, agree within 5 cm^{-1} (1392 cm^{-1} from Table II and $\sim 1396\text{ cm}^{-1}$ from ref 1b and 1c). It seems apparent that curve resolution is not a viable procedure where cooperative effects contribute significantly to a spectrum as is apparently the case for intensely infrared active modes of molten salts and concentrated salt solutions.^{1e,10} On the other hand, the ν_{3a} and ν_{3b} values reported for $LiNO_3$ in NH_3 for the 6:1 mole ratio concentration range have been correctly assigned to the contact ion pair.^{1b,c} Reduction of this splitting to values less than 50 cm^{-1} (the glassy NH_3 matrix ion pair value) for more dilute solutions apparently is the result of overlap of the ion pair doublet with the ν_3 band of the completely solvated NO_3^- . On the other hand, reduction of the NH_3 -nitrate mole ratio below 4:1 causes $\Delta\nu_3$ to approach the 110-cm^{-1} molten salt value as cooperative effects based on dipole-dipole coupling take over.^{1b,10} As indicated, we agree with the basic NH_3 solution assignments of Lemly and Lagowski^{1c} but one relevant inconsistency in their arguments should be noted. They report that for a 16:1 $LiNO_3$ mole ratio $\Delta\nu_3$ is 33 cm^{-1} , which thus becomes an upper limit on the NO_3^- distortion splitting via H bonding with NH_3 . However, they subsequently assign a 49-cm^{-1} splitting for concentrated NH_4NO_3 in NH_3 to just such a distortion splitting; a clear

inconsistency. Our results show that, in fact, the NH_3 H-bonding distortion splitting must be less than or equal to 20 cm^{-1} , the $K^+NO_3^-$ in glassy NH_3 value. We have also observed $\Delta\nu_3$ for $ND_4^+NO_3^-$ contact ion pairs in pure glassy ND_3 and found $\Delta\nu_3$ to be 23 cm^{-1} . The origin of the 49-cm^{-1} splitting for NH_4NO_3 in NH_3 ^{1c} may be a combination of distortion splitting of the NO_3^- by $\sim 23\text{ cm}^{-1}$ (via either NH_4^+ or NH_3 association, or both) together with dipole-dipole coupling.

Other conclusions suggested by the new data include one based on the recognition that $\Delta\nu_3$ produced by cation distortion for $K^+NO_3^-$ ion pairs in an H_2O solution is less than the $\Delta\nu_3$ splitting resulting from NO_3^- association with H_2O molecules. Thus, the $\Delta\nu_3$ value is the same for contact ion paired and solvent separated NO_3^- ions so that the ν_3 spectra are not distinguishable. Although, the emphasis of this paper has been on cation-anion interaction, clearly the matrix-anion interactions are large and must not be ignored. This situation is further emphasized by the observation that NO_3^- is dynamically, as well as statically, coupled to the matrixes. Thus, although it has not been pointed out in our presentation of results, the absolute values of ν_{3a} and ν_{3b} increase $\sim 5\text{ cm}^{-1}$ when D_2O (ND_3) is substituted for H_2O (NH_3). Since the direction of this shift is opposite to that expected on a mass basis, it is likely a result of resonant interaction with the nearby matrix molecule bending modes which are above ν_3 for the protonated cases but below ν_3 for the deuterated solvents.

Finally, from this study vibrational frequencies are now available for the species $(H_2O)M^+NO_3^-$ and $(NH_3)M^+NO_3^-$ (i.e., 6% columns of Tables I and II). Such data are of particular interest since they provide a potential test of ab initio quantum chemical calculations such as have recently been reported for hydrated ions.¹²

Acknowledgment. This research has been supported by the National Science Foundation under Grant No. MPS 74-17689.

References and Notes

- (1) See, for example: (a) D. E. Irish, D. L. Nelson, and M. H. Brooker, *J. Chem. Phys.*, **54**, 654 (1971); (b) D. J. Gardiner, R. E. Hester, and W. E. L. Grossman, *ibid.*, **59**, 175 (1973); (c) A. T. Lemly and J. J. Lagowski, *J. Phys. Chem.*, **78**, 708 (1974); (d) J. D. Riddell, D. J. Lockwood, and D. E. Irish, *Can. J. Chem.*, **50**, 2951 (1972); and (e) D. J. Gardiner, R. B. Girling, and R. E. Hester, *J. Phys. Chem.*, **77**, 640 (1973).
- (2) D. E. Irish and A. R. Davis, *Can. J. Chem.*, **46**, 943 (1968).
- (3) J. P. Devlin, P. C. Li, and G. Pollard, *J. Chem. Phys.*, **52**, 2267 (1970).
- (4) D. Smith, D. W. James, and J. P. Devlin, *J. Chem. Phys.*, **54**, 4437 (1971).
- (5) N. Smyrl and J. P. Devlin, *J. Chem. Phys.*, **60**, 2540 (1974).
- (6) G. Ritzhaupt and J. P. Devlin, *J. Chem. Phys.*, in press.
- (7) N. Smyrl and J. P. Devlin, *J. Phys. Chem.*, **77**, 3067 (1973).
- (8) C. G. Verkatash, S. A. Rice, and A. H. Narten, *Science*, **186**, 928 (1974).
- (9) R. E. Hester, private communication.
- (10) J. P. Devlin, G. Ritzhaupt, and T. Hudson, *J. Chem. Phys.*, **58**, 817 (1973).
- (11) G. Ritzhaupt and J. P. Devlin, unpublished data.
- (12) H. Kistenmacher, H. Popkie, and E. Clemente, *J. Chem. Phys.*, **59**, 5842 (1973).

Vibrational Spectra and Assignments for *cis*- and *trans*-1,2-Difluorocyclopropane and Three Deuterium Substituted Modifications of Each Isomer

Norman C. Craig,* T.-N. Hu Chao, Enrique Cuellar, Dan E. Hendriksen, and Jeffery W. Koepke

Department of Chemistry, Oberlin College, Oberlin, Ohio 44074 (Received March 31, 1975)

Publication costs assisted by the Petroleum Research Fund

Infrared spectra under a variety of experimental conditions and Raman spectra for the liquid phase have been recorded for the *cis* and *trans* isomers of 1,2-difluorocyclopropane and the 1,2-*d*₂, 3,3-*d*₂, and *d*₄ deuterated modifications. Almost all of the 168 fundamentals of this set of eight molecules have been observed and assigned convincingly. For *cis*-1,2-difluorocyclopropane-*d*₀ the fundamentals are (a') 3105, 3063, 3023, 1450, 1365, 1224, 1135, 1047, 862, 784, 468, 209 cm⁻¹; (a'') 3055, 1346, 1150, 1089, 1060, 993, 739, 621, 319 cm⁻¹. For *trans*-1,2-difluorocyclopropane-*d*₀ the fundamentals are (a) 3070, 3021, 1457, 1380, 1203, 1132, 1068, 961, 842, 415, 279 cm⁻¹; (b) 3110, 3070, 1304, 1161, 1072, 1005, 937, 783, 452, 303 cm⁻¹. Only the 1089-cm⁻¹ mode in the *cis* and the 937-cm⁻¹ mode in the *trans* are in doubt. Group frequency descriptions are discussed qualitatively, and attention is drawn to the fundamentals near 1450 cm⁻¹ which are characteristic of fluorocyclopropanes and appear to be largely due to ring stretching. From previously published equilibrium data for the *cis*-to-*trans* isomerization and the fundamental frequencies of the two isomers, an electronic energy difference of -2800 ± 200 cal/mol has been calculated. In contrast, the *trans* isomer of 1,2-difluoroethylene has an energy 1100 cal/mol greater than the *cis*, and the *trans* rotamer of 1,2-difluoroethane has an energy about 600 cal/mol greater than the *gauche*.

Introduction

The *cis* and *trans* isomers of 1,2-difluorocyclopropane were selected originally for vibrational spectroscopy as part of a study of the "cis effect". 1,2-Difluoroethylene, 1-chloro-2-fluoroethylene, 1,2-dichloroethylene, and difluorodiazene (FN=NF) are examples of this effect, in which the *cis* isomer has the lower electronic energy.^{1,2} Because the *cis*-*trans* energy differences are at most a few kilocalories per mole, it is desirable to have complete assignments of the vibrational fundamentals of such molecules in order to extract differences in electronic energies alone from thermodynamic data. Force constants, derived from normal coordinate calculations, have also yielded several correlations with the *cis* effect.^{3,4} For saturated compounds such as 1,2-difluoroethane, a related "gauche effect" has been discussed.^{2,5} However, such molecules in which facile internal rotation occurs are more difficult to study^{6,7} than *cis*-*trans* isomers which have locked geometries. *cis*- and *trans*-1,2-difluorocyclopropanes provide an example of locked geometries in a molecular pair which does not have a double bond. A preliminary study of the thermal isomerization of difluorocyclopropane has indicated that the *trans* isomer predominates at equilibrium at about 200°C and is of lower energy.¹

Our earlier interest in the difluorocyclopropanes as potential examples of the *cis* effect has led us into a comprehensive study of the vibrational spectroscopy of partly fluorinated cyclopropanes. The literature does not appear to contain any work on the vibrational spectroscopy of 1,2-difluorocyclopropanes or any other 1,2-dihalocyclopropanes. Cyclopropane itself is, of course, a well-studied molecule,⁸ and the vibrational spectra of perfluorocyclopropane have been assigned.⁹ We have recently completed an assignment of 1,1,2,2-tetrafluorocyclopropane,¹⁰ which, in conjunction with the present study, has made it possible to identify some group frequencies for the fluorocyclopro-

panes. Most important of these is a frequency in the 1450–1550-cm⁻¹ region, which appears to have a large component of ring stretching. An investigation of 1,1-difluorocyclopropane is also nearing completion in our laboratory.

Interest in fluorocyclopropanes has also been stimulated by Hoffmann's discussion of the effect of halogens and other substituents on bond strengths in the cyclopropane ring.¹¹ Structural investigations in the microwave have revealed significant effects on CC bond lengths due to fluoro and cyano substituents.¹² Well-defined force constants derived from vibrational spectra should also reflect these changes in CC bonds.

In the present paper, we report vibrational assignments for *cis*- and *trans*-difluorocyclopropane and three, symmetrically deuterated modifications of each molecule. From infrared and Raman spectra of this set of eight molecules, it has been possible to obtain a convincing assignment of the 21 fundamentals of the two undeuterated molecules and a qualitative description of the normal modes. The overall set of more than 160 directly observed fundamentals for the two closely related isomers provides a promising basis for normal coordinate calculations. However, our preliminary calculations have shown that the motions of the nonhydrogen parts of the molecule are not sufficiently well defined to permit a straightforward refinement of a minimum set of force constants. It appears that such a result must await an overlay calculation involving additional fluorocyclopropanes and possibly ¹³C-substituted rings.

Experimental Section

Syntheses. *cis*- and *trans*-1,2-difluorocyclopropane were prepared by photolysis of mixtures of diazomethane and 1,2-difluoroethylene in the liquid phase at -80°C .¹³ During the photolysis with uv light from a medium-pressure mercury arc the liquid was held in a small tube immersed in a Dry Ice-ethanol mixture in an unsilvered Pyrex dewar. The

system was vented through an atmosphere of gaseous nitrogen. Purification consisted of removal of the olefin fraction by bulb-to-bulb distillation at toluene slush temperature (-95°C) followed by repeated gas chromatographic fractionation on 4-m dibutylphthalate (DBP)-on-firebrick and 4-m DBP-on-Teflon columns at temperatures between 60 and 0°C . Relative elution times on the firebrick-packed column at 25°C were for air, 1.0; for the *trans* isomer, 12; for the *cis* isomer, 61. Carbon dioxide and water were removed by first passing the fluorocyclopropane through Ascarite and then through phosphorus pentoxide. Final purity (GC result) of each isomer was greater than 99 mol %. Identities of these new compounds were established by 60-MHz proton NMR ($\sim 30\%$ solutions in CFCl_3 , TMS reference) and mass spectrometry. In the NMR, the *cis* isomer had one complex and unsymmetrical pattern spreading out from 1.1 ppm and a second, symmetrical and less complex, doublet-like pattern with a spacing of ~ 65 Hz centered at 4.3 ppm. The *trans* isomer had one complex, symmetrical pattern centered at 1.2 ppm and a complex, symmetrical doublet system with a spacing of ~ 62 Hz centered at 4.7 ppm. The mass spectrum of the *cis* isomer gave the parent peak at 78 with 0.23 of the intensity of the base peak at 77. For the *trans* isomer the peak at 78 had 0.31 the intensity of the peak at 77. Boiling point of the *cis* isomer, 53°C ; of the *trans*, 11.5°C .

Cis and *trans* isomers of 1,2-difluorocyclopropane-1,2- d_2 were synthesized and purified in the same manner as the undeuterated compounds except that 1,2-difluoroethylene- d_2 was used.¹⁴ Final purity (GC result) was greater than 99%. Isotopic purity was also in the 99% range as judged from the ir and NMR spectra. Isotopic impurities would be the species with a single deuterium atom as formed from the residual $\text{HFC}=\text{CFD}$ in the starting material. The proton NMR spectra confirmed the identities of these isomers. The absorptions due to the CFH group with $\delta \sim 4.5$ ppm were gone, and the patterns in the 1.0-ppm region were simplified. Moreover, the spectrum of the *trans* isomer with $\delta = 1.2$ ppm retained symmetry (~ 8 - and ~ 37 -Hz separations for principal features) while that of the *cis* with $\delta \sim 1.1$ ppm remained too unsymmetrical to characterize simply.

Cis and *trans* isomers of 1,2-difluorocyclopropane-3,3- d_2 were synthesized by the photolysis of mixtures of ketene- d_2 , which was made by pyrolysis of perdeuterioacetone, and 1,2-difluoroethylene in the gas phase.¹⁰ Unfortunately, this reaction gave a very complex mixture of products including a number of fluoropropenes and a low yield of the desired cyclopropanes. In general, purification was as described above except that the 4-m DBP-on-firebrick column was supplemented with a halocarbon-oil-on-firebrick column. Although acetyl fluoride (presumably a $\text{DF} + \text{CD}_2\text{CO}$ product) was not resolved from the *trans* isomer, the Ascarite step took it out. Final GC purity on the 4-m DBP column was greater than 99%, and the isotopic purity was also in this range. Chromatography of the d_4 material (vide infra) on a longer column revealed a few percent of impurities in both isomers, thus making the analysis of the 3,3- d_2 material on the 4-m column doubtful. In the proton NMR spectra absorption due to methylene protons in the 1.0-ppm region was gone, and symmetrical patterns were observed for both isomers in the 4.5-ppm region. For the *cis* isomer a pair of broad triplets was centered at 4.5 ppm with the two strong peaks separated by ~ 62 Hz. For the *trans* isomer, two pairs of broad doublets were centered at 4.7 ppm and separated by 50 and 74 Hz, respectively.

Cis and *trans* isomers of 1,2-difluorocyclopropane- d_4 were prepared in the same manner as the 3,3- d_2 material except for the substitution of 1,2-difluoroethylene- d_2 in the synthesis. In addition to the 4-m GC DBP column an 8-m DBP-on-firebrick column was employed in the final purification steps. Final purity (GC analysis) was greater than 99% for the samples used for the infrared spectra. However, those samples used for the Raman spectra contained totals of about 5% of several impurities, which were not thought to contribute significant intensity to these spectra.

Spectroscopy. All mid-infrared spectra were recorded on a Perkin-Elmer 621 spectrometer, and cesium iodide windows were used throughout except in liquid-phase work. The far-infrared spectrum of the undeuterated *cis* isomer, Figure 1c, was recorded on a Beckman IR-11 in a cell equipped with polyethylene windows. For all gas-phase spectra, Figures 1a-8a, a 10-cm cell length was used. For liquid-phase spectra 1.0- and 0.1-mm cells with potassium bromide windows were used. Spectra of annealed solid films were run in a conventional cold cell at liquid nitrogen temperature. Matrix spectra were obtained at 20 K with a Cryogenics Technology, Inc., Model 20 system. Matheson research grade nitrogen was used as the diluent. In all of the infrared spectra important features were examined under high resolution, expanded scale conditions and measured to ± 2 cm^{-1} .

Liquid-phase Raman spectra were obtained in several ways. Originally, spectra of the d_0 and 1,2- d_2 isomers were recorded photographically on a Hilger EG12 with mercury 4358- \AA excitation, from which spectra tabulated frequencies and intensities were obtained. Subsequently, the spectra of the d_0 isomers were recorded again under survey conditions on a Spex Ramalog instrument with 6471- \AA excitation from a helium-neon laser. These two spectra are shown in Figures 1b and 5b. Spectra of the 3,3- d_2 isomers, Figures 3b and 7b (microfilm edition), were also recorded on a Ramalog with 6471- \AA excitation. However, the spectra of the d_4 isomers, Figures 4b and 8b (microfilm edition), were recorded with 4880- \AA excitation of an argon-ion laser. For the laser excited spectra samples of a few tenths of a millimole were sealed in melting point capillaries. Frequencies of Raman bands are believed to be accurate to ± 5 cm^{-1} . Details of infrared and Raman spectra and the assignments are given in Tables II-V and VIII-XI.

The NMR spectra were recorded on a Varian A-60 spectrometer, and the mass spectra were recorded on a Hitachi RMS4 with an ionization potential of 70-80 V.

Results and Discussion

Configurational Assignments. NMR. The proton NMR spectra provide an unambiguous assignment of the *cis* and *trans* configurations of the 1,2-difluorocyclopropanes. In the *trans* isomer the CH_2 protons are symmetrically equivalent, whereas in the *cis* isomer they are not. Thus, in the *trans* spectrum the pattern at high field is symmetrical, while the corresponding pattern in the *cis* isomer is obviously asymmetrical. That the high-field pattern is due to methylene protons is confirmed in the spectra of the partially deuterated molecules. The 3,3- d_2 species shows no absorption due to CH_2 protons.

No NMR spectra were obtained for the perdeuterio molecules. Nonetheless, the method of synthesis, the GC elution times, and the vibrational spectra leave no doubt about the identities of these molecules.

Vibrational Assignments for the *Cis* Isomer. *cis*-1,2-Difluorocyclopropane and the series of three deuterated mod-

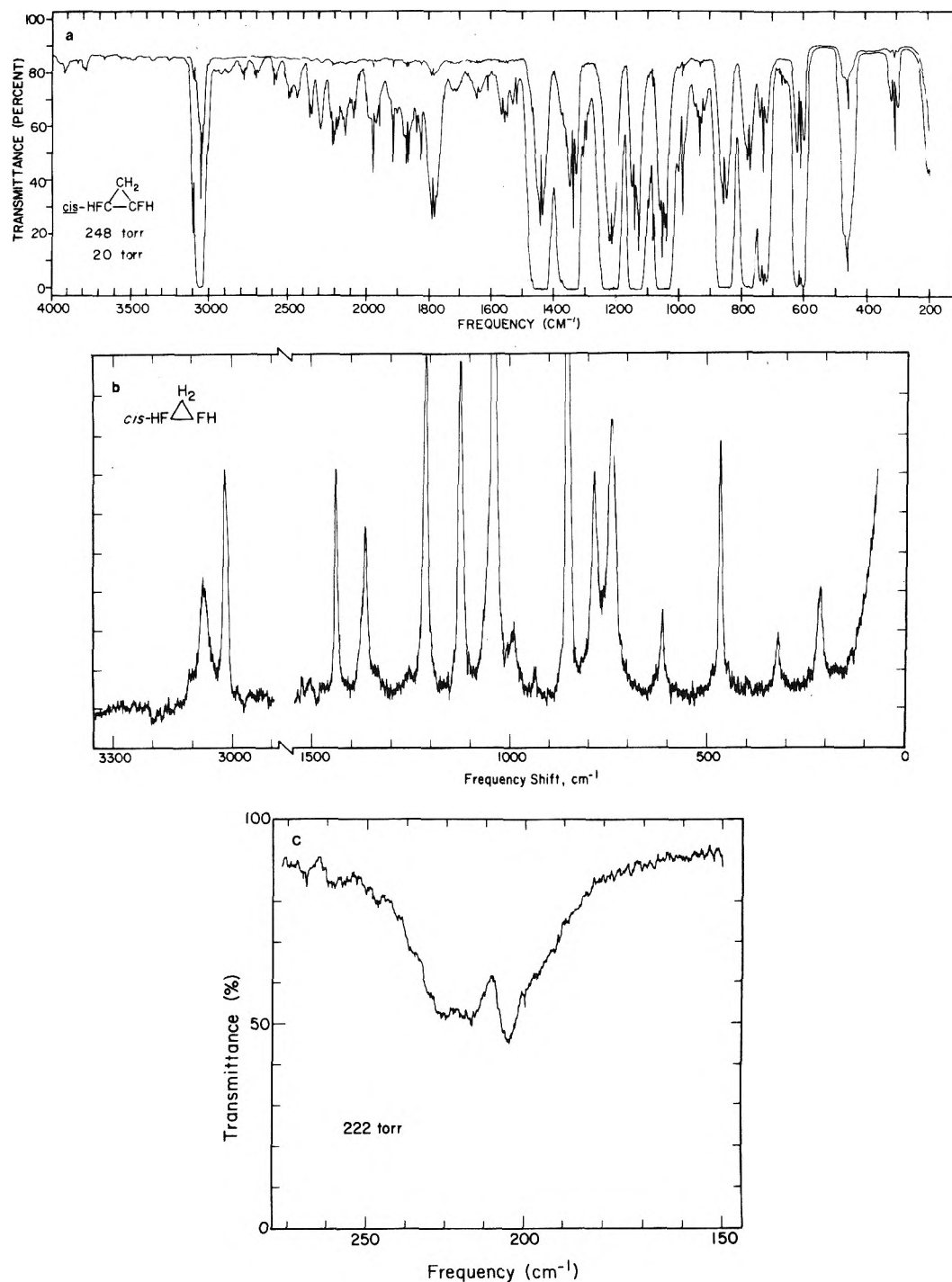


Figure 1. Gas-phase infrared spectrum (a), liquid-phase Raman spectrum (b) (helium–neon excitation), and far-infrared, gas-phase spectrum (c) of *cis*-1,2-difluorocyclopropane.

ifications investigated in this work have single planes of symmetry and thus belong to the C_s point group. These molecules have twelve fundamentals of symmetry species a' , which should give polarized bands in the Raman, and nine fundamentals of species a'' , which will have depolarized Raman bands. Since the axis of least moment of inertia, I_a , is perpendicular to the plane of symmetry, the a'' modes, which have dipole moment changes along this axis, have A-type band shapes in the gas-phase infrared. The I_b and I_c axes lie in the plane of symmetry, and consequently band shapes ranging from B type to C type are indicative of

a' modes. The direction of the I_c axis is essentially parallel to the plane containing the two fluorines and attached carbon atoms. *cis*-Difluorocyclopropane is a rather asymmetric top with $\kappa = -0.48$ and $\rho = 0.96$, as calculated from the principal moments of inertia (Table I) which are based on assumed structural parameters. With these moments of inertia, computed gas-phase infrared band shapes have the following characteristic spacings: PR for A type, 20 cm⁻¹; PR for C type, 30 cm⁻¹; QQ for B type, 9 cm⁻¹.¹⁵

cis-1,2-Difluorocyclopropane. The undeuterated *cis* isomer was the most thoroughly studied of the four *cis* species.

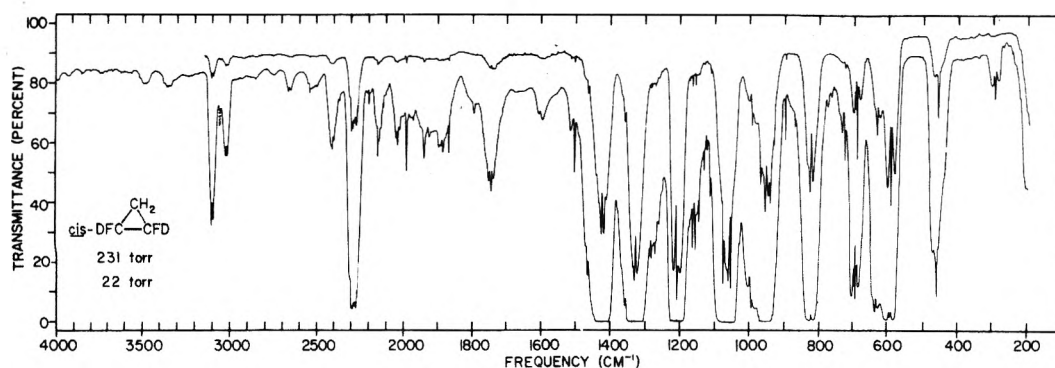


Figure 2. Gas-phase infrared spectrum of *cis*-1,2-difluorocyclopropane-1,2- d_2 .

TABLE I: Principal Moments of Inertia (amu \AA^2) and Assumed Geometric Parameters^a

		H_2		D_2	
		HF \triangle FH	DF \triangle FD	HF \triangle FH	DF \triangle FD
Cis	I_a	61.8	66.0	70.5	74.8
	I_b	105.6	112.0	107.8	114.5
	I_c	140.9	145.1	147.5	151.3
Trans	I_a	43.4	47.9	51.0	55.6
	I_b	141.4	146.3	143.1	148.0
	I_c	164.2	164.9	171.2	172.0

^a $r_{\text{CC}} = 1.514 \text{ \AA}$, $r_{\text{CH}} = 1.082 \text{ \AA}$, $r_{\text{CF}} = 1.330 \text{ \AA}$; all $\alpha_{\text{CC}} = 60^\circ$, $\alpha_{\text{HC}} = 116.5^\circ$, $\alpha_{\text{HCF}} = 113.8^\circ$, $\alpha_{\text{CCH}} = 117.1^\circ$, $\alpha_{\text{CCF}} = 119.4^\circ$. See ref 10 and 12.

In addition to gas-phase infrared spectra (Figures 1a and 1c) and liquid phase Raman spectra (Figure 1b), infrared spectra of solutions in carbon disulfide and carbon tetrachloride, of dilute nitrogen matrices at 20 K, and of solid films at 77 K were recorded. Principal features of these latter spectra are presented in Table II along with the assignments for the various spectral features shown in the figures.

For six of the twelve a' fundamentals, bands of approximately B-type shape are easily found in the gas-phase infrared spectrum. These bands are at 3105, 1450, 1224, 862, 784, and 209 cm^{-1} . Q branches are sharp and spaced by 8–9 cm^{-1} in agreement with the calculated band shapes. Although the 3105-, 784-, and 209- cm^{-1} bands have Raman counterparts which are apparently depolarized and hence due to modes of uncertain symmetry, the infrared band shapes leave no doubt about assigning these three, as well as the other three, to a' symmetry. C-type contours are at 3063, 1135, 1047, and 468 cm^{-1} , and polarized Raman bands confirm each of these frequencies as belonging to a' modes. Due to overlapping bands, the PR spacing cannot be measured for the 1136- and 1047- cm^{-1} bands, but the spacings of 28–29 cm^{-1} for 3063- and 468- cm^{-1} bands check with the predictions. Polarized Raman bands at 3017 and 1365 cm^{-1} and infrared features which are more obvious in solid and matrix phases reveal the remaining two a' fundamentals. Further, strong support for the 1365- cm^{-1} assignment is found in the infrared spectrum of the 1,2- d_2 species (Figure 2) which has a convincing B-type contour at 1334 cm^{-1} .

Six of the nine a'' fundamentals are indicated by well-formed A-type bands at 1346, 1150, 1060, 739, 621, and 319 cm^{-1} . PR spacings of 19–21 cm^{-1} are in agreement with

predictions. All but the 1150- cm^{-1} frequency also appear as depolarized bands in the Raman spectrum. One of the remaining three a'' fundamentals must be in the CH stretching region. A doublet structure in the infrared spectrum of the matrix reinforces the selection of the weaker Q-branch feature in the gas-phase spectrum at 3055 cm^{-1} for this mode. The distorted band at 993 cm^{-1} in the gas-phase infrared spectrum appears to be another a'' fundamental. Solution, solid phase, and matrix infrared spectra also have a band here as does the Raman spectrum. The remaining a'' fundamental is not an obvious feature in either the gas-phase infrared or liquid-phase Raman spectra. However, clear features of medium intensity occur near 1100 cm^{-1} in the solution, solid, and matrix-phase infrared spectra. The Q branch at 1089 cm^{-1} in the gas phase is taken as the frequency of this fundamental. Strongest support for this assignment comes from the well-formed A-type band at 1086 cm^{-1} in the spectrum of the 3,3- d_2 species. Placing a fundamental of this type (antisymmetric CH rock) near 1100 cm^{-1} is also consistent with the assignments for *trans*- d_0 and *trans*-3,3- d_2 species (vide infra).

In Table VII the assignments of all 21 fundamentals of *cis*-1,2-difluorocyclopropane are presented and compared with the results for the other three isotopic modifications of the *cis* isomer. The approximate characterizations of the normal coordinates in terms of symmetry coordinates, which are also given in this table, are considered below after presentation of all of the assignments.

Three Deuterated cis-1,2-Difluorocyclopropanes. Discussion of the assignments for *cis*-1,2- d_2 , *cis*-3,3- d_2 , and *cis*- d_4 molecules are included in the microfilm edition along with Raman spectra of the 3,3- d_2 and d_4 species. No photometric trace of the Raman spectrum of the 1,2- d_2 species is available. Infrared spectra are given in Figures 2, 3a, and 4a, and the details of the assignments are in Tables III–V.

Summary. Cis Assignments. Table VII summarizes all of the fundamentals of the four *cis* molecules. Less certain assignments are set in italics. In this table, the frequencies have been arranged by group frequency to emphasize correlations between the isotopic species. However, in Tables III–V, where the assignments for the deuterated species are given in detail, the numbering follows the customary pattern of decreasing frequency. The overall assignment is consistent with the Rayleigh rule¹⁶ as well as with the isotope product rules (Table VI). In order to save space, omitted from Tables II–V are most of the weaker spectral features and their generally satisfactory explanations as binary combinations. Supported by the largely successful assignments for the whole set of isotopically substituted *cis*

molecules, we are confident of all of the fundamentals of the key, undeuterated cis molecule with the possible exception of the ν_{16} (a'') mode. The approximate descriptions of the normal modes in terms of symmetry coordinates have been derived from generally accepted group frequencies, intensities, and band shapes within the four isotopically substituted cis species and from specific group frequency comparisons with the trans isomers, 1,1,2,2-tetrafluorocyclopropane, and *cis*-1,2-difluoroethylene. A discussion of these descriptions is deferred until the trans assignments have been developed in the next few sections.

Vibrational Assignments for the Trans Isomers. *trans*-1,2-Difluorocyclopropane and its symmetrically deuterated modifications have a single symmetry element, a twofold rotation axis which lies in the plane of the ring and passes through the methylene carbon atom. For this C_2 symmetry there are eleven fundamentals of symmetry species a and ten of species b. Only the totally symmetric a species have

polarized Raman transitions. In the gas-phase infrared spectra the a species are expected to have B-type band shapes since the I_b moment of inertia axis is coincident with the symmetry axis. The modes of b symmetry give rise to band shapes ranging from A to C type. The I_a axis passes close to the two fluorine atoms. With the moments of inertia given in Table I, the calculated band shapes give PR separations of 17 and 22 cm^{-1} for A and C type bands, respectively. In the calculated B-type bands, Q branches are not well differentiated and the apparent PR separation is about 14 cm^{-1} . The molecule approximates a prolate symmetric top with $\kappa = -0.88$ and $\rho = 2.5$. Since I_b and I_c differ by only 15% for the assumed structure, one might wonder if I_b and I_c could be interchanged in the actual molecule and thus make the association of B-type bands with a symmetry species unreliable. Of necessity the symmetry axis passes through the methylene carbon and thus will have fewer heavy atoms off it than does the I_c axis. Thus, the predic-

Table II. Assignments of Infrared and Raman Spectra of *cis*-1,2-Difluorocyclopropane-d₀ (Frequencies in cm^{-1})

Infrared		Raman		Assignment	
freq. ^a	band shape ^b	solid ^c	intense polariz. ^d	freq.	symmetry species ^e
3105(9)	0.2 B	3116 wv	3091 w	3102 w,d	fund. ν_1 a'
3065(29)	0.76 C	3075 w	3087 w 3052 w	3070 w,p	fund. ν_2 a'
3055	a AT	3070 wv	3081 wv		fund. ν_{13} a''
3032(8)	0.08 B	3034 wv	3021 wv <3010 w	3017 w,p	fund. ν_3 a'
1983(25)	0.04 CT		<1982 wv <1975 wv		1998 $\nu_{13}\nu_{14}$ A'
				1986 ν_{12} A'	
1793(8)	0.16 B	<1800 wv	<1793 w <1790 w	1799 $\nu_{12}\nu_{13}$ A'	
1450(9)	2.1 B	1451 w	1444 w 1441 w	1437 w,p	fund. ν_4 a'
1381(8)	w BT	1375 w	1379 w 1375 w	1378 w,7	1379 $\nu_{12}\nu_{13}$ A'
1369	w CT	1364 w	1366 w 1365 w	1365 w,p	fund. ν_5 a'
1348(21)	1.3 A	1344 w	1340 w 1337 w	1339 w,v,d	fund. ν_{14} a'
1218(8)	2.8 B	1221 wv	1207 wv 1213 wv	1215 w,p	fund. ν_6 a'
1150(20)	1.5 A	1144 w	1129 w 1135 w		fund. ν_7 a'
1135	w C	1135 w	1122 w 1128 w	1124 w,p	fund. ν_8 a'
1104	w A-C	1107 w	1112 w 1105 w	1103 w	$\nu_{10}\nu_{21}$ A'
1089	w A-C		1091 w		fund. ν_9 a'
				1089 $\nu_{11}\nu_{20}$ A'	
1060(19)	2.0 A	1062 wv	1054 wv 1054 w	1059 w,d	fund. ν_{17} a'
1047	w C	1047 w	1046 w 1041 w	1044 w,v,z	fund. ν_8 a'
992(21)	0.1 A	995 wv	998 w	993 w,d	fund. ν_{18} a'
945	wv A			948 $\nu_{11}\nu_{19}$ A'	
939	wv C		<940 wv	940 $\nu_{10}\nu_{21}$ A'	
928(7)	w B			936 ν_{12} A'	
				923 $\nu_{12}\nu_{13}$ A'	
862(7)	1.7 B	862 w	858 w 855 wv	854 w,v,p	fund. ν_9 a'
784(8)	1.1 B	793 w	792 w 783 w	789 w,d	fund. ν_{10} a'
739(21)	0.56 A	748 w	741 w 738 w	744 w,d	fund. ν_{19} a'
621(22)	0.92 A	621 w	614 w 622 w	616 w,v,d	fund. ν_{20} a'
448(28)	0.27 C	474 w	475 w 466 w	468 w,p	fund. ν_{11} a'
319(21)	0.04 A	325 wv		324 w,d	fund. ν_{21} a'
209(9)	0.08 B	224 w		218 w,v,d	fund. ν_{12} a'

^a Frequencies include PD scatterings for A- and C-type bands and QQ scatterings for B-type.

^b μ is absorption coefficient in $cm^{-1} \text{ atm}^{-1}$.

^c B and C designations are approximate for this molecule of C_2 symmetry.

^d HCFMD(12) where multiplet structure is observed, freq. of strongest or average peak is given.

^e Solid at 77°K; strongest or average of multiplet given.

^f 10 mol. percent solution.

^g From CCl_4 solution; all others from CCl_2 solution.

Table III. Assignments of Infrared and Raman Spectra of *cis*-1,2-Difluorocyclopropane-1,2-d₂ (Frequencies in cm^{-1})

Infrared, gas		Raman, liquid		Assignment	
freq. ^a	band shape ^b	freq.	intense polariz. ^d	freq.	symmetry species
3105(8)	0.13 B	3098	w,d	fund. ν_1	a'
3064	w T			1-d ₂ impurity	a'
3059				fund. ν_2	a'
3023(8)	0.06 B	3018	w,p	fund. ν_3	a'
2367	0.1 CT	2330	w,t	fund. ν_4	a''
2298	T	2294		fund. ν_5	a'
2281				fund. ν_6	a'
2278		2273		fund. ν_7	a'
2270				fund. ν_8	a'
1993	w C			fund. ν_9	a'
1429(7)	1.8 B	<1438	w,v,p	fund. ν_{10}	a'
1334(9)	2.5 B	1330	w,p	fund. ν_{11}	a'
1218(19)	2.6 A			fund. ν_{12}	a'
1082	w C	1067	w,v,p	fund. ν_{13}	a'
1060	w A			fund. ν_{14}	a'
1000(19)	0.2 A			fund. ν_{15}	a'
975	C	972	w,d	fund. ν_{16}	a'
957(8)	1.3 B	951	w,v,d	fund. ν_{17}	a'
947				fund. ν_{18}	a'
936	w A			fund. ν_{19}	a'
875	wv A	875	w,d	fund. ν_{20}	a'
829(8)	1.0 B	826	w,v,p	fund. ν_{21}	a'
696(21)	0.32 A	700	w,p	fund. ν_{22}	a'
637(8)	0.35 B	641	w,p	fund. ν_{23}	a'
600(21)	0.96 A	597	w,v,d	fund. ν_{24}	a'
465(24)	0.21 C	466	w,p	fund. ν_{25}	a'
302(20)	0.02 A	303	w,v,d	fund. ν_{26}	a'
<300	w	215	w,v,d	fund. ν_{27}	a'

^{a-c} See footnotes to Table II.

Table IV. Assignments of Infrared and Raman Spectra of *cis*-1,2-Difluorocyclopropane-1,3-d₂ (Frequencies in cm^{-1})

Infrared, gas		Raman, liquid		Assignment	
freq. ^a	band shape ^b	freq.	intense polariz. ^d	freq.	symmetry species ^e
3063(26)	0.62 C	3079	w,p	fund. ν_1	a'
3053	AT			fund. ν_2	a'
2342(7)	0.10 B	2348	w,d,t	fund. ν_3	a'
2245	0.05 A-C			2242 ν_4 A'	
				2224 $\nu_4\nu_{16}$ A'	
				Perm. resonance with ν_3 ?	
2221	w	2224	w,p	fund. ν_5	a'
1419(6)	2.4 B	1417	w,p	fund. ν_6	a'
1335(20)	1.3 A	<1330	w	fund. ν_7	a'
1233(7)	2.4 B	1230	w,p	fund. ν_8	a'
1139(18)	1.7 A			fund. ν_9	a'
1121	w CT	<1120	w,p	fund. ν_{10}	a'
1110	w T	1110	w,p	1109 $\nu_{10}\nu_{11}$ A'	
				Perm. resonance with ν_6	
1084(20)	1.0 A	<1090	w,v,d,t	fund. ν_{16}	a''
1054(24)	3.25 C	1064	w,p	fund. ν_7	a'
974(24)	3.14 C			fund. ν_8	a'
949(19)	3.19 A	952	w,d	fund. ν_9	a'
819(7)	2.4 B	822	w,p	fund. ν_{17}	a'
791(22)	3.02 A			fund. ν_{18}	a'
707(28)	3.04 C	713	w,p	fund. ν_{19}	a'
648(20)	1.4 A	645	w,v,d	fund. ν_{20}	a'
574(20)	0.13 A			fund. ν_{21}	a'
401(24)	0.17 C	407	w,p	fund. ν_{22}	a'
292(19)	0.94 A	<300	wv	fund. ν_{23}	a'
<200(19)		319	w,p,t	fund. ν_{24}	a'

^{a-c} See footnotes to Table II.

Table V. Assignments of Infrared and Raman Spectra of *cis*-1,2-Difluorocyclopropane-d₂ (Frequencies in cm^{-1})

Infrared		Raman		Assignment		
freq. ^a	band shape ^b	solid ^c	intense polariz. ^d	freq.	symmetry species	
3058	wv	A-C		3070	w,v,-	1,1,3-d ₃ impurity?
2351(8)	w	BT	2342 w	2345	w,p	fund. ν_1 a'
2305	0.4 CT	CT	2293 wv	2301	w,p	fund. ν_2 a'
2289	0.4 CT	CT	2284 wv	2290	w,p	2291 $\nu_3\nu_4$ a'
						Perm. resonance with ν_2
2275	w	AT	2260 wv	2272	w,d,p?	fund. ν_{13} a''
				2220 w	w,p	fund. ν_5 a'
1383(6)	w	BT	1378 w	1382	w,p	1377 $\nu_6\nu_{10}$ A'
						Perm. resonance with ν_6
1365(5)	3.8 B	B	1354 wv	1356	w,p	fund. ν_6 a'
1195(20)	3.0 A	A	1154 w	1168	w,v,d?	fund. ν_{15} a''
1092(23)	1.0 C	C	1082 wv	1085	w,p	fund. ν_5 a'
1065(7)	1.0 B	B	994 wv	998	w,p	fund. ν_6 a'
				974 w	w,p	965 $\nu_6\nu_{12}$ A'
						Perm. resonance with ν_7
944(7)	0.69 B	B	940 w	948	w,p	fund. ν_7 a'
927	w	C	925 w	923	w,p	fund. ν_8 a'
				918 w	w,-	fund. ν_{16} a'
877(23)	0.14 A	A	867 w	855	w,-	fund. ν_{16} a'
760(14)	w	A	752 w	765	w,-	fund. ν_{17} a'
758(6)	w	B	755 w	760	w,v,p	fund. ν_{18} a'
628(21)	1.1 A	A	627 w	630	w,p	fund. ν_9 a'
618(26)	w	C	618 w	same	w,p	fund. ν_{19} a'
541(19)	0.19 A	A	543 w	575	w,d,t	fund. ν_{20} a'
397(24)	0.14 C	C	403 w	401	w,p	fund. ν_{21} a'
281(21)	0.04 A	A	288 w	291	w,d,t	fund. ν_{22} a'
<200	w		221 w	214	w,p,t	fund. ν_{23} a'

^{a-c} See footnotes to Table II.

^d Solid at 77°K; strongest or average of multiplet given.

tions of the assumed geometry seem secure, and these expectations are borne out by the nearly perfect correlation between B-type bands in the infrared and polarized bands in the Raman spectrum. In principle all 21 fundamentals are both infrared and Raman active for this C2 molecule. In practice we expect a rough rule of mutual exclusion to hold between centrosymmetric and antisymmetric CH and CF motions in the HFCCFH part of the molecule. Thus, the g-like modes will be strong in the Raman and weak in the infrared spectrum. The reverse will be true for the u-like ones.

trans-1,2-Difluorocyclopropane. In parallel to the study of the cis isomers, the undeuterated trans-1,2-difluorocyclopropane was the most thoroughly investigated in the trans series. In addition to the standard gas-phase infrared and liquid-phase Raman spectra (Figure 5a and 5b, respectively), solutions, solid films at 77 K, and dilute nitrogen matrices at 20 K were examined in the infrared. All of these

data are assembled in Table VIII.

For the 11 modes of a symmetry three obvious B-type bands are seen in the gas-phase infrared spectrum in Figure 6a at 961, 842, and 415 cm-1. PR spacings in these bands are about 11 cm-1, somewhat smaller than the calculated one of about 14 cm-1. It should also be noted that in contrast to the calculated band envelopes, Q branches do appear to be distinguishable in some of the B-type bands of the various isotopically substituted trans species. Nonetheless, only estimates of PR separations are given in Tables VIII-XI. Corresponding to the three B-type bands are intense, polarized Raman lines. Gas-phase infrared band shapes also suggest three more fundamentals in that distorted B-type bands are found at 1457, 1203, and 279 cm-1. The 1457-cm-1 band has an apparent PR spacing of 11 cm-1 and is coincident with a polarized Raman band. The 1203-cm-1 band has a PR spacing of 12 cm-1 and a strongly polarized Raman counterpart. The complex feature near

Table VIII. Assignments of Infrared and Raman Spectra of trans-1,2-Difluorocyclopropane-d0 (Frequencies in cm-1)

Table with columns for Infrared gas (Freq. a, b, Band shape c) and Raman liquid (Freq., Intens., polariz.). Includes assignments and symmetry species for various modes like 3110(45), 3070(181), 3029(102), etc.

a Parentheses enclose PR spacings. b a is absorption coefficient in cm-1 atm-1. c a- and c-type designations are approximate for this molecule of C2 symmetry. d w/2000/1; strongest or average of multiplets given. e Solid at 77K; strongest or average of multiplets given. f 10 wt. percent solution. g From CCl4 solution; all others from C52 solution.

Table IX. Assignments of Infrared and Raman Spectra of trans-1,2-Difluorocyclopropane-1,2-d2 (Frequencies in cm-1)

Table with columns for Infrared gas (Freq. a, b, Band shape c) and Raman liquid (Freq., Intens., polariz.). Includes assignments and symmetry species for various modes like 3109(16), 3070, 3027(8), etc.

a-c See footnotes to Table VIII.

Table X. Assignments of Infrared and Raman Spectra of trans-1,2-Difluorocyclopropane-1,2-d2 (Frequencies in cm-1)

Table with columns for Infrared gas (Freq. a, b, Band shape c) and Raman liquid (Freq., Intens., polariz.). Includes assignments and symmetry species for various modes like 3070(15), 2340(19), 2255, etc.

a-c See footnotes to Table VIII.

Table XI. Assignments of Infrared and Raman Spectra of trans-1,2-Difluorocyclopropane-d4 (Frequencies in cm-1)

Table with columns for Infrared gas (Freq. a, b, Band shape c) and Raman liquid (Freq., Intens., polariz.). Includes assignments and symmetry species for various modes like 3059, 2340(16), 2280(17), etc.

a-c See footnotes to Table VIII.

d Solid at 77K; strongest or average of multiplets given.

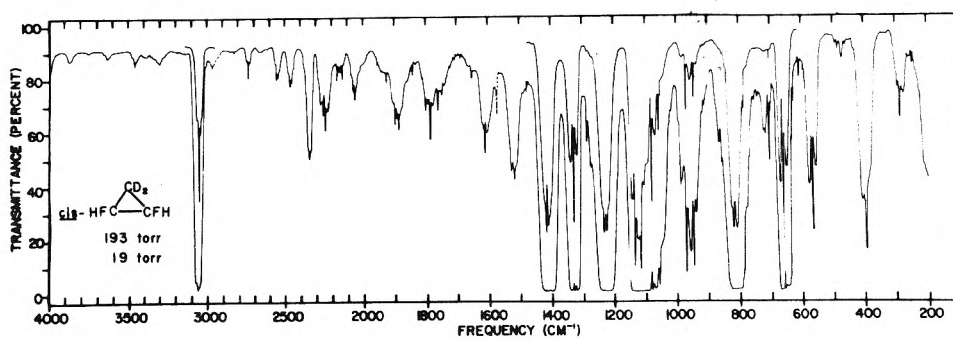


Figure 3. (a) Gas-phase infrared spectrum of *cis*-1,2-difluorocyclopropane-3,3- d_2 .

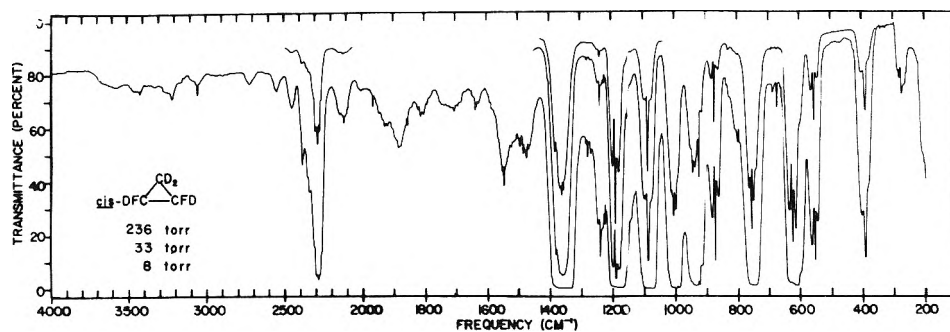


Figure 4. (a) Gas-phase infrared spectrum of *cis*-1,2-difluorocyclopropane- d_4 .

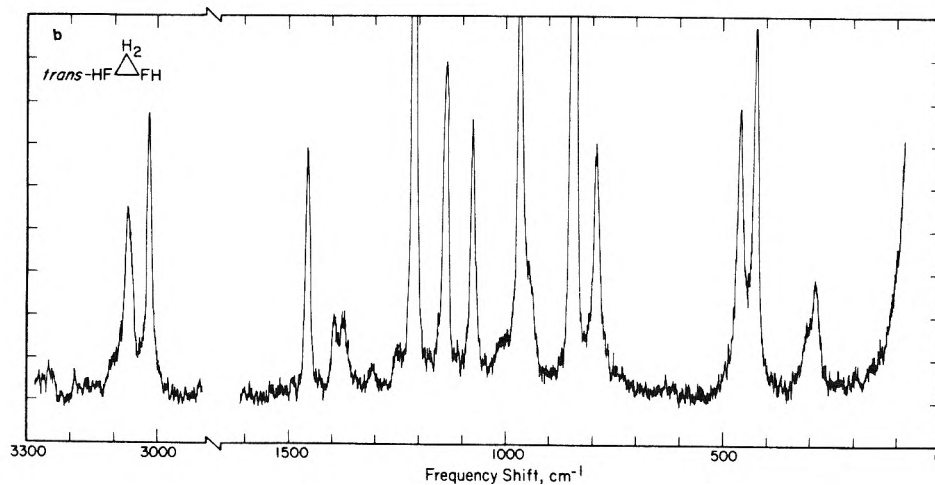
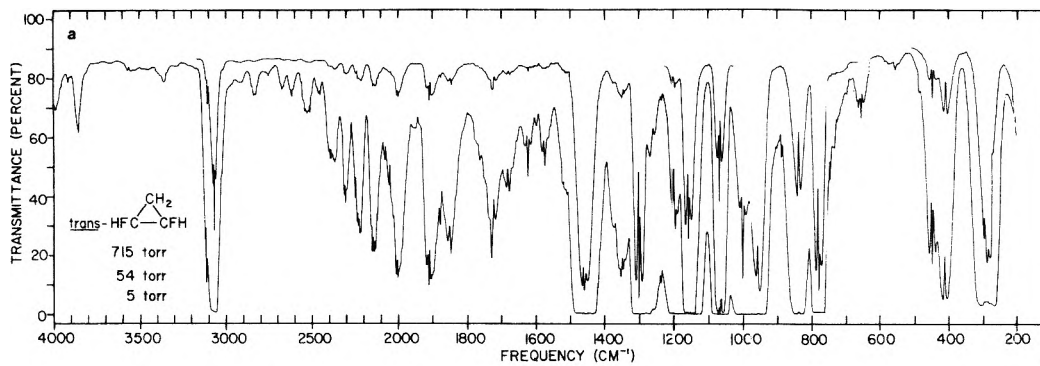


Figure 5. Gas-phase infrared spectrum (a) and liquid-phase Raman spectrum (b) of *trans*-1,2-difluorocyclopropane (helium-neon excitation).

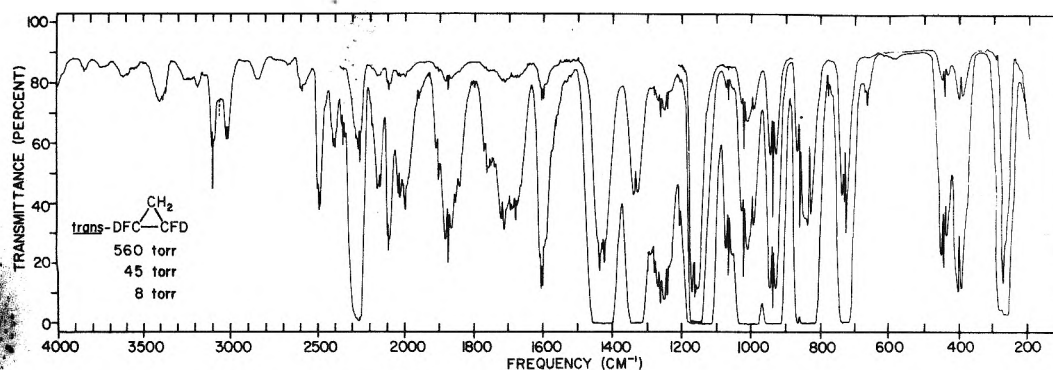


Figure 6. Gas-phase infrared spectrum of *trans*-1,2-difluorocyclopropane-1,2- d_2 .

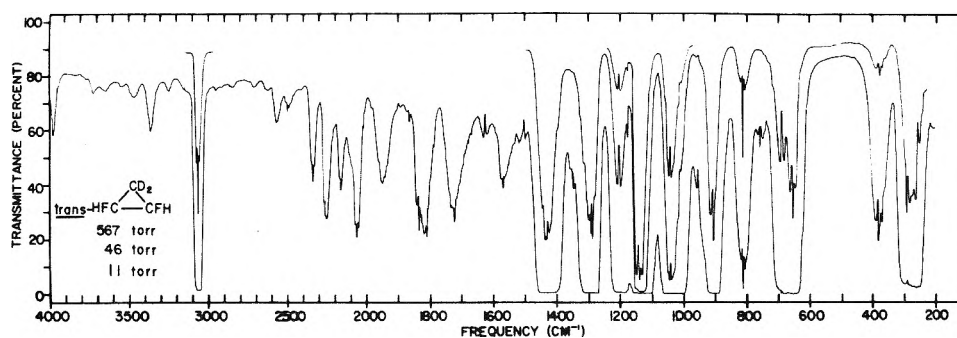


Figure 7. (a) Gas-phase infrared spectrum of *trans*-1,2-difluorocyclopropane-3,3- d_2 .

TABLE VI: Product Rule Ratios^a

		H_2	D_2	D_4	
		DF \triangle FD	HF \triangle FH	DF \triangle FD	
Cis	a'	calcd	0.375	0.274	0.102
		obsd	0.385	0.287	0.109
		diff	+2.6%	+4.6%	+7.0%
	a''	calcd	0.375	0.524	0.196
		obsd	0.387	0.534	
		diff	+3.3%	+2.0%	
Trans	a	calcd	0.365	0.361	0.131
		obsd	0.383	0.355	0.141
		diff	+4.9%	-1.7%	+7.6%
	b	calcd	0.382	0.402	0.153
		obsd		0.399	0.159
		diff		-0.8%	+3.9%

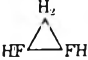

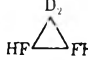
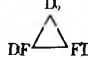
^a Each ratio has the product of frequencies for HF \triangle FH in the denominator.

300 cm^{-1} in the gas-phase infrared spectrum is broad enough to contain two partly overlapped bands. That two fundamentals are in this region is clearly seen in the spectra of various condensed phases. Under expanded scale, high-resolution conditions it appears that the B-type band is centered near 279 cm^{-1} and a distorted C type is at 303 cm^{-1} . This band shape pattern is seen more clearly in the spectrum of the 3,3- d_2 species (Figure 7a), where the two fundamentals are separated by an additional 10 cm^{-1} . The spectra of the 1,2- d_2 and d_4 species do not help because the two low-frequency fundamentals are essentially coincident in these molecules. In the Raman spectra of both the d_0 and 3,3- d_2 species the lower frequency band is more in-

tense, and its depolarization ratio may be somewhat less than 0.75 in the 3,3- d_2 case. Based on these observations, we have tentatively associated a symmetry with the lower frequency component. This assignment of the two low-frequency fundamentals gives acceptable product rule checks (Table VI) throughout the series. Reversing the assignment improves the agreement of the ratios for the a modes but introduces a difference of 11% in the d_4/d_0 ratio for the b modes. We have examined the combination bands in search of further support for the present assignment of the higher frequency to the b mode. The critical bands and their interpretations are included in Table VIII. Although each can be accounted for satisfactorily in frequency and band shape with the present assignment, they can also be explained with the reversed assignment and thus do not prove helpful.

The Raman spectrum leads the way to the remaining five a modes at 3070, 3021, \sim 1380, 1132, and 1068 cm^{-1} . Although several are expected to be weak in the infrared due to being vibrations with approximate centers of symmetry, all but the 3070- cm^{-1} one were observed in the nitrogen matrix or in the polycrystalline film. A strongly polarized Raman band is at 3070 cm^{-1} and must be due to an a mode even though the gas-phase infrared spectrum in this region is dominated by an A- to C-type band. The 3021- cm^{-1} band, which is a shoulder in the gas phase, shows clearly in the solid film. In the 1380- cm^{-1} region of the Raman spectrum a pair of low intensity but definitely polarized bands appears which are undoubtedly a Fermi resonance doublet. The average frequency is used for the fundamental. The matrix infrared has a weak feature at 1395 cm^{-1} , and the gas-phase infrared has a probable B-type band at 1364 cm^{-1} . Any doubts about assigning a fundamental in this region are dispelled by the infrared spectrum of the 1,2- d_2

TABLE VII: Summary of the Fundamentals of the *cis*-1,2-Difluorocyclopropanes (Frequencies in cm^{-1})^e

Approx descriptions ^d	H_2 	H_1 	D_2 	D_0 
	HF \triangle FH	DF \triangle FD	HF \triangle FH	DF \triangle FD
a'				
ν_1 asym CH(D) ₂ str	3105	3105	2342	2345 ^a
ν_2 sym CH(D) str	3063	2310 ^a	3063	2295 ^{a,b}
ν_3 sym CH(D) ₂ str	3023	3023	2224 ^a	2227 ^a
ν_4 sym CCC str	1450	1429	1419	1363
ν_5 sym CH(D) ₂ bend	1365 ^a	1334	974	927
ν_6 sym CH(D) bend	1224	957	1233	944
ν_7 sym CF str	1135	1082	1121 ^b	1092
ν_8 CC str	1047	975	1064	1005
ν_9 asym CH(D) ₂ bend	862	829	707	758
ν_{10} sym CH(D) rock	784	637	819	618
ν_{11} sym CF rock	468	465	402	397
ν_{12} sym CF bend	209	206 ^c	208 ^c	205 ^c
a''				
ν_{13} asym CH(D) str	3055	2282	3053	2275 ^a
ν_{14} asym CH(D) bend	1346	947	1335	[949]
ν_{15} asym CF str	1150	1216	1139	1195
ν_{16} asym CH(D) rock	1089	875	1086	877
ν_{17} CH(D) ₂ rock	1060	1060	949	916
ν_{18} CH(D) ₂ twist	993	1000	791	760
ν_{19} asym CCC str	739	696	668	628
ν_{20} asym CF bend	621	600	574	561
ν_{21} asym CF rock	319	302	292	281

^a From liquid-phase Raman. ^b Perturbed by Fermi resonance. ^c Estimated from Raman. See text. ^d sym = symmetric; asym = antisymmetric with respect to plane of symmetry or plane of ring for CH₂ group. ^e Uncertain assignments in italics; value calculated from isotopic product rule in brackets.

molecule (Figure 6) in which a fine B-type band appears at 1339 cm^{-1} . Also, a similar pattern of a definite Raman band but weak infrared band for a CH₂ scissors mode in this region was found for the *cis* isomer and for 1,1,2,2-tetrafluorocyclopropane.¹⁰ Clearly polarized Raman bands at 1132 and 1068 cm^{-1} are the remaining two a modes. In the gas-phase infrared, the only bands in these two regions are definitely of A-type shape and thus due to fundamentals of b symmetry. However, in the infrared of the matrix and the solid phase, sharp features at about 1132 cm^{-1} give further support to one of these assignments. A shoulder is also found in the liquid-phase infrared spectrum in this region. In both the matrix and the solid a weaker, sharp feature is found just above the intense band due to the b mode at 1068 cm^{-1} . This may be the infrared counterpart of the Raman band at 1068 cm^{-1} .

Eight of the ten fundamentals of b symmetry give well-defined A- to C-type bands in the gas-phase infrared spectrum. A C-type band is at 1005 cm^{-1} , and intermediate, A- to C-type bands are at 3110 and 3070 cm^{-1} . A-type bands are at 1304, 1161, 1072, 783, and 452 cm^{-1} . The PR spacing in the C type is 18 cm^{-1} , and PR spacings in the A-type bands range from 15 to 18 cm^{-1} in rough agreement with the predictions. Supporting, depolarized Raman bands are found for five of these fundamentals. The remaining three, 3070, 1161, and 1072 cm^{-1} , presumably correspond to modes which have near-u symmetry and thus low Raman intensity. We have already considered the problem of the two overlapping bands in the 300- cm^{-1} region and have placed ν_{21} at 303 cm^{-1} . The remaining b fundamental possibly appears as an enhanced P branch of the B-type band

which is centered at 961 cm^{-1} in the gas-phase infrared spectrum. A sharp though weak feature at 941 cm^{-1} in the matrix and a corresponding band in the crystal support the choice of the depolarized Raman band at 937 cm^{-1} for this assignment. In the Raman spectrum in Figure 5b only a shoulder is seen, but when the intensity of the neighboring band is reduced by rotating the analyzer, the 937- cm^{-1} band stands out more clearly. This same feature is observed as a shoulder in the liquid-phase infrared spectrum.

In Table XII the assignments of all the fundamentals of the *trans*- d_0 molecule are summarized and correlated with those of the other three *trans* species.

Three Deuterated trans-1,2-Difluorocyclopropanes. The discussions of the assignments of the spectra of the *trans*-1,2- d_2 , *trans*-3,3- d_2 , and *trans*- d_4 molecules are included in the supplement to this paper in the microfilm edition. Figures 6, 7a, and 8a give the infrared spectra. The Raman spectra of the 3,3- d_2 and d_4 species are also in the supplementary edition; no photometric trace of the Raman spectrum of the 1,2- d_2 is available. Spectral features and assignments for these three molecules are given in Tables IX–XI.

Summary. Trans Assignments. In Table XII the fundamentals of all four of the *trans* molecules are listed. The numbering of the frequencies is correct for the d_0 species only. Entries for the deuterated species are arranged to reflect group frequency patterns. In Tables IX–XI the frequencies of the deuterated species follow the customary pattern of decreasing numerical order. To facilitate group frequency comparisons the fundamentals of the *cis*- d_0 molecule and the pertinent ones for 1,1,2,2-tetrafluorocyclo-

TABLE XII: Summary of the Fundamentals of the *trans*-1,2-Difluorocyclopropanes and Group Frequency Comparisons with Related Molecules (Frequencies in cm^{-1})^f

Approx descriptions ^f	Trans						Cis			<i>trans</i> - HFC=CFH ^b	<i>cis</i> - HFC=CFH ^b
	H ₂ DF	H ₂ FD	H ₂ FH	D ₂ FH	D ₂ FD	H ₂ FD	H ₂ FH	H ₂ F ₂	D ₂ F ₂		
ν_1 sym CH(D) str	3070 ^c	3070 ^c	3070 ^c	3078 ^c	3078 ^c	3063	3063	3022	2237	3111	3122
ν_2 sym CH(D) ₂ str	3021 ^c	3027	3027	2218 ^{c,d}	2218 ^{c,d}	3023	3023	3022	2237	3111	3122
ν_3 sym CCC str	1457	1434 ^d	1437	1437	1437 ^d	1450	1450	1526	1518	1286	1263
ν_4 sym CH(D) ₂ bend	1380 ^{c,d}	1339	1339	967	967	1365	1365	1366	982	1123	1015
ν_5 sym CH(D) bend	1203	939 ^c	939 ^c	1210	1210	1224	1224	1076	1087	875	756
ν_6 sym CF str	1132 ^c	1125 ^c	1125 ^c	1120 ^c	1120 ^c	1136	1136	1076	1087	548	237
ν_7 sym CC str	1068 ^c	1002	1002	1048	1048	1047	1047	913	709	329	
ν_8 sym CH(D) rock	961	742 ^c	742 ^c	917	917	784	784	913	709		
ν_9 CH(D) ₂ twist	842	836	836	697	697	993	993	209	748		
ν_{10} sym CF bend	415	403	403	393	393	209	209	468			
ν_{11} sym CF rock	279	273 ^c	273 ^c	268	268	468	468				
ν_{12} asym CH(D) ₂ str	3110	3109	3109	2346	2346	3105	3105	3115	2340	3114	3136
ν_{13} asym CH(D) str	3070	2267 ^{c,d}	2267 ^{c,d}	3070	3070	3055	3055			1274	1374
ν_{14} asym CH(D) bend	1304	942	942	1299 ^d	1299 ^d	1346	1346			1159	1130
ν_{15} asym CF str	1161	1168	1168	1146	1146	1150	1150			788	839
ν_{16} asym CH(D) rock	1072	864	864	1023	1023	1089	1089				
ν_{17} CH(D) ₂ rock	1005	1026	1026	819	819	1060	1060				
ν_{18} asym CCC str	937 ^e	[972]	[972]	912	912	739	739				
ν_{19} asym CH(D) ₂ bend	783	734	734	662	662	862	862				
ν_{20} asym CF rock	452	448	448	381	381	319	319				
ν_{21} asym CF bend	303	272	272	302	302	621	621			341	495

^a Reference 10. ^b Reference 14. ^c From liquid-phase Raman. ^d Perturbed by Fermi resonance. ^e Uncertain assignments are in italics; value in brackets calculated from isotope product rule. ^f Infrared of solid phase. / sym = symmetric; asym = antisymmetric with respect to C₂ axis.

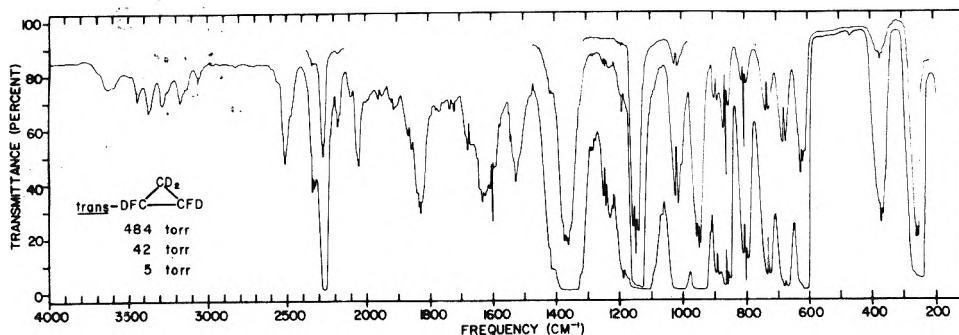


Figure 8. (a) Gas-phase infrared spectrum of *trans*-1,2-difluorocyclopropane- d_4 .

propane- d_0 and - d_2 ¹⁰ and *cis*- and *trans*-1,2-difluoroethylenes¹⁴ are also included in this table. Less certain assignments of the *trans* species are given in italics. As shown in Table VI, the *trans* assignments are generally supported by the product rules. With minor exceptions, the overall *trans* assignment is consistent with the Rayleigh rule. In general, weaker features in the spectra have been omitted from Tables VIII–XI but have been assigned satisfactorily to binary combinations. Due to the extensive spectral data for the d_0 molecule as well as the general pattern in the assignments for the whole set of *trans* molecules, we have considerable confidence in the assignment for the d_0 species. However, it is possible that $\nu_{11}(a)$ and $\nu_{21}(b)$ might have to be interchanged, and $\nu_{18}(b)$ at 937 cm^{-1} might not be definitive. More doubt attends some of the assignments of the deuterated species as is indicated by giving those frequencies in italics in Table XII.

Normal Coordinate Calculations. We had hoped that a normal coordinate calculation in which a single set of force constants was fitted simultaneously to all the frequencies of the *cis* and *trans* species would be straightforward. Such a calculation was attempted using a nonredundant set of stretching and bending coordinates, 10 diagonal force constants, and 10 off-diagonal force constants.¹⁷ In refining the diagonal force constants alone, the CF stretching constant went to an unacceptably low value of 3.7 mdyn/\AA , and CF stretching then made substantial contributions to the lowest frequency modes. By holding the CF stretching constant at 5.9 mdyn/\AA while refining the other diagonal constants and then refining the 10 off-diagonal constants, progress was made. Finally, the CF constant was released and the whole set of 20 force constants polished. The final CF value was 5.7 mdyn/\AA . Average errors in the frequency fit ranged from 3.3 to 4.5%, and some of the normal coordinate descriptions were unconvincing in view of the qualitative descriptions discussed below, which are derived from the spectra. Two problems hamper these calculations. First, few well suited force constants are available for the zero-order approximation and to aid in assessing the refined ones. Extensive calculations have been performed on cyclopropane itself,⁸ but none, other than zero-order calculations, have been done on a fluorocyclopropane.¹⁸ In particular, no estimates of off-diagonal values are available, and a value for CF stretching force constant is especially puzzling. Second, the crowding of many modes into the $1400\text{--}600\text{-cm}^{-1}$ region and the rather tight kinetic coupling in the compact cyclopropane molecules opens alleys leading to erroneous solutions. We have decided to defer further exploration of the normal coordinate calculations until our spectroscopic study of 1,1-difluorocyclopropane is complete.

Group Frequencies. When the observed fundamental frequencies of the 1,2-difluorocyclopropanes are organized and compared with the appropriate fundamentals of 1,1,2,2-tetrafluorocyclopropane and the *cis*- and *trans*-1,2-difluoroethylenes, a number of approximate group frequency descriptions can be recognized. Table VII summarizes the assignments and descriptions of the four *cis* molecules. Table XII not only summarizes the assignments for the four *trans* molecules but also includes for comparison assignments for the *cis*- d_0 isomer and the other molecules. The previously noted parallel between the frequencies of tetrafluorocyclopropane and tetrafluoroethylene¹⁰ is also found between the 1,2-difluorocyclopropanes and the 1,2-difluoroethylenes. It must be emphasized that, in the absence of convincing normal coordinate calculations, the group frequency descriptions in the following discussion are approximate. There is undoubtedly considerable mixing of symmetry coordinates, as has been shown to be true, for example, for the difluoroethylenes.^{4,14}

CH Stretching. The pattern of frequency shifts which accompany deuteration leaves no doubt about the descriptions of the frequencies observed for CH stretching. In both *cis* and *trans* isomers symmetric and antisymmetric CH_2 stretching are split by about 100 cm^{-1} with the frequency of the antisymmetric mode the higher as chosen in accord with normal coordinate calculations. In contrast, coupling between the two FC–H stretching modes is small and results in a splitting of less than 20 cm^{-1} . Stretching force constants are essentially the same (5.1 mdyn/\AA) for the two kinds of CH bonds, notwithstanding the influence of the fluorine atom. CD stretching modes which are located in the $2220\text{--}2350\text{-cm}^{-1}$ region have a similar frequency pattern.

CC and CF Stretching. As has been pointed out before,¹⁰ a good group frequency for fluorocyclopropanes occurs in the $1450\text{--}1550\text{-cm}^{-1}$ region. The persistence of a frequency in this region as tetrafluorocyclopropane and the *cis*- and *trans*-1,2-difluorocyclopropanes are deuterated shows that this mode has little, if any, CH bending character. That the 1450-cm^{-1} mode in the 1,2-difluorocyclopropanes is largely CC stretching with a moderate admixture of CF stretching is strongly implied by the present difluorocyclopropane assignments. The most compelling evidence is the observation of near mutual exclusion between infrared and Raman bands that must be due to CF stretching. As in *trans*-1,2-difluoroethylene, the band due to antisymmetric CF stretching dominates the infrared spectrum in intensity and shifts very little with deuteration. In addition, this frequency undergoes a relatively large shift to lower frequency between gas and solid phases as is common for antisymmetric CF stretching modes. The symmetric CF stretch gives a

nearly constant feature in the various Raman spectra. In the *cis* molecules a set of bands with weak-to-unobserved Raman features and large shifts between gas and solid phases are also assigned to antisymmetric CF stretching. Symmetric CF stretching modes are nearby.

Assigning the other symmetric CC stretching mode to the 1000–1100-cm⁻¹ region fits the overall pattern of the difluorocyclopropanes and the tetrafluorocyclopropane rather well. The identification of the antisymmetric CCC stretch is unsatisfactory. Since this mode cannot involve the bond between the fluorine bearing carbons, one might expect it to be reasonably constant throughout the series. However, it apparently spans a range of 200 cm⁻¹.

Tuazon, Fateley, and Bentley have argued that modes in fluoroalkanes which are predominantly symmetric C–C stretching occur at relatively high frequencies (1200–1300 cm⁻¹) while modes that are principally symmetric CF stretching occur at relatively low frequencies (750–900 cm⁻¹).¹⁹ On the other hand, symmetric CF stretching modes for fluoroethylenes fall in the 1000–1100-cm⁻¹ region in most cases. The effect is pronounced when a carbon atom bears more than one fluorine atom. Fluorocyclopropanes are probably intermediate cases, their inherently higher CC stretching frequencies being shifted to higher values by some admixture of CF stretching.

CF Bending and Rocking. There is no doubt that CF bending and rocking coordinates are concentrated in the two lowest frequency modes in the two symmetry species of each isomer. Bending is taken as a bending motion perpendicular to the plane of the ring and rocking parallel to the plane of the ring. The choice of descriptions given in Tables VII and XII for these fundamentals is based on the preliminary normal coordinate calculations and is consistent with the difluoroethylene assignments.

CH₂ Bending. The totally symmetric mode in the 1350-cm⁻¹ region must be largely CH₂ scissoring. It is present in all of the cyclopropanes containing the CH₂ group including the 1,2-*d*₂ species. Upon deuteration this mode drops into the 900–1000-cm⁻¹ range. Less confidently we place the antisymmetric CH₂ bending in the 780–870-cm⁻¹ region.

CH Bending. One expects a much smaller splitting between the symmetric and antisymmetric CH bending modes for the HFC–CFH framework than for the corresponding CH₂ modes. Persistent bands in the 1200–1370-cm⁻¹ region in the *d*₀ and 3,3-*d*₂ molecules are obvious choices for these assignments. Deuteration appears to shift these into the vicinity of 900 cm⁻¹. In the *trans* molecule the symmetric mode is strong in the Raman and relatively weak in the infrared in accord with mutual exclusion for a near center of symmetry.

Other CH Modes. We have less confidence in the descriptions of CH rocking, CH₂ rocking, and CH₂ twisting. A mode which can be ascribed to CH₂ rocking does fall in the 1000–1150-cm⁻¹ region. The range of about 150 cm⁻¹ for CH₂ twisting in the several molecules suggests that this symmetry coordinate has not been properly localized. Revising the symmetric CH rocking and CH₂ twisting modes in the *trans* molecule fits the data almost as well as the present assignment. On the other hand, an antisymmetric CH rocking mode does seem to be localized in the 1050-cm⁻¹ region.

Thermodynamic Functions. Statistical thermodynamic calculations were carried out for the two isomers of difluorocyclopropane using the rigid rotor, harmonic oscillator, ideal gas model. The moments of inertia were those given

in Table I. For the *cis* isomer, $S^{\circ}_{298} = 69.94$ gibbs/mol and $H^{\circ}_{298} - H^{\circ}_0 = 3500$ cal/mol. For the *trans* isomer, $S^{\circ}_{298} = 70.01$ gibbs/mol and $H^{\circ}_{298} - H^{\circ}_0 = 3522$ cal/mol.²⁰ Tables of thermodynamic functions at 100° intervals from 100 to 2000 K are on file. From earlier observations of equilibrium for the *cis*-to-*trans* reaction in the gas phase at 585 K, $\Delta G^{\circ}_{585} = -2900 \pm 200$ cal/mol.¹ This must be viewed as a preliminary value due to the limited temperature range over which the isomerization reaction was observed. From this ΔG° and the present work we can calculate $\Delta E(\text{elect})$, the difference between the *electronic* energies of the two isomers. $\Delta G^{\circ}_{585} = \Delta H^{\circ}_{585} - (585 \text{ K}) \Delta S^{\circ}_{585}$ and $\Delta H^{\circ}_{585} = \Delta E(\text{elect}) + \Delta E(\text{zero point vibration}) + \Delta H^{\circ}_{585}(\text{thermal})$. $\Delta S^{\circ}_{585} = 0.14$ gibbs/mol, $\Delta H^{\circ}_{585} = -2818$ cal/mol, $\Delta E(\text{zero point vibration}) = -67$ cal/mol, and $\Delta H^{\circ}_{585}(\text{thermal}) = 51$ cal/mol. Thus, $\Delta E(\text{elect}) = -2800 \pm 200$ cal/mol, where the error estimate comes from the equilibrium constant measurement and does not include contributions from uncertainties in molecular parameters and vibrational fundamentals or from the limitations of the rigid rotor, harmonic oscillator, ideal gas model. However, it is to be expected that these latter effects are small and also tend to cancel for *cis* and *trans* isomers. The electronic energy difference for *cis*-*trans* isomerization is less than 200 cal/mol different from ΔH° at 585 K, the energy contributions from translation and rotation exactly cancel and those from vibration nearly cancel.

The finding that the *electronic* energy of *trans*-difluorocyclopropane is nearly 3000 cal/mol *lower* than that of its *cis* isomer contrasts sharply with the known energy difference for *cis*- and *trans*-difluoroethylene. In this instance the electronic energy of the *trans* isomer is higher by 1086 cal/mol.¹ An even more striking case of this "cis effect" is the 3050 cal/mol difference for *cis*- and *trans*-difluorodiazene (FN=NF).^{1,21} The electronic energy difference for the difluorocyclopropanes also has an opposite sign from that for the *gauche*-to-*trans* conversion of 1,2-difluoroethane, where a difference of 600 cal/mol has been calculated from the ΔH° for the corresponding change in the liquid phase.^{6a,22}

Structural data for the various isomer pairs should be of value in assessing theories of the "cis and *gauche* effects". Such data are now available for both the *cis* and *trans* isomers of difluorodiazene²³ and 1,2-difluoroethylene.²⁴ For both pairs the most significant difference is that the angle between the double bond and the bond to fluorine is somewhat larger in the *cis* isomer. Geometric parameters have also been obtained recently from both microwave and electron diffraction studies for the *gauche* rotamer of 1,2-difluoroethane.^{22,25} The dihedral angle between the two CCF planes of about 73° is substantially larger than the "unperturbed" angle of 60°. The *cis* and *trans* isomers of 1,2-difluorocyclopropane are currently under investigation by microwave spectroscopy in Professor V. W. Laurie's laboratory.

Acknowledgments. We gratefully acknowledge the donors of the Petroleum Research Fund, administered by the American Chemical Society, for support of this research. Richard J. Buss assisted in the normal coordinate calculations. E.C., D.E.H., and J.W.K. were National Science Foundation Undergraduate Research Participants. We are also grateful to Drs. R. O. Kagel and G. Y.-S. Lo of the Dow Chemical Co. who obtained the Raman spectra for us and to the Department of Chemistry at Princeton University

where N.C.C. completed this paper while serving as a Visiting Professor.

Supplementary and Miniprint Material Available. Figures 3b, 4b, 7b, and 8b, which are Raman spectra of the deuterated species, Tables II-V and VIII-XI, and discussions of the assignments of the six deuterated species will appear following these pages in the microfilm edition of this volume of the journal. Photocopies of the supplementary material and full-size photocopies of the miniprinted material from this paper only or microfiche (105 × 148 mm, 24× reduction, negatives) containing all of the supplementary material for the papers in this issue may be obtained from the Business Office, Books and Journal Division, American Chemical Society, 1155 16th St., N.W., Washington, D.C. 20036. Remit check or money order for \$4.50 for photocopy or \$2.50 for microfiche, referring to code number JPC-75-2270.

References and Notes

- (1) N. C. Craig, L. G. Piper, and V. L. Wheeler, *J. Phys. Chem.*, **75**, 1453 (1971).
- (2) N. D. Epiotis, *J. Am. Chem. Soc.*, **95**, 3087 (1973).
- (3) N. C. Craig, Y.-S. Lo, L. G. Piper, and J. C. Wheeler, *J. Phys. Chem.*, **74**, 1712 (1970). Subsequently, we calculated the torsional force constants for *cis*- and *trans*-FN=NF (see references in ref 1) and found them to be nearly the same. This has caused us to question the assignment of the torsional mode for *cis*-N₂F₂, which is based on a weak spectral feature in the Raman.
- (4) R. A. R. Pearce and I. W. Levin, *J. Chem. Phys.*, **59**, 2698 (1973).
- (5) S. Wolfe, *Accounts Chem. Res.*, **5**, 102 (1972).
- (6) (a) P. Klaboe and J. R. Nielsen, *J. Chem. Phys.*, **33**, 1764 (1960); (b) R. J. Abraham and R. H. Kemp, *J. Chem. Soc. B*, 1240 (1971); (c) P. Huber, H. Frei, R. Meyer, and H. H. Gunthard, Symposium on Molecular Spectroscopy and Structure, Columbus, Ohio, June 1974, Paper RE'3.
- (8) J. L. Duncan and G. R. Burns, *J. Mol. Spectrosc.*, **30**, 253 (1969), and references cited therein.
- (9) F. A. Miller and K. O. Hartman, *Spectrochim. Acta, Part A*, **23**, 1609 (1967).
- (10) N. C. Craig, G. J. Anderson, E. Cuellar-Ferreira, J. W. Koepke, and P. H. Martyn, *Spectrochim. Acta, Part A*, **28**, 1175 (1972).
- (11) R. Hoffmann, *Tetrahedron Lett.*, 2907 (1970); R. Hoffmann, Symposium on Molecular Spectroscopy and Structure, Columbus, Ohio, June 1973, Paper A2.
- (12) (a) A. T. Perretta and V. W. Laurie, *J. Chem. Phys.*, **62**, 2469 (1975); (b) R. Pearson, A. Choplin, V. Laurie, and J. Schwartz, *ibid.*, **62**, 2949 (1975).
- (13) See ref 1. This report omitted mention of the methanol impurity, which through tailing interferes with gas chromatographic fractionation on firebrick supports. Presumably methanol arises through CH₂ insertion into the OH bond of water swept over from the diazomethane generator.
- (14) N. C. Craig and J. Overend, *J. Chem. Phys.*, **51**, 1127 (1969).
- (15) Computer program written by Dr. I. Haller, IBM, and supplied in a Fortran IV version by Professor J. C. Durig, University of South Carolina.
- (16) D. Steele, "Theory of Vibrational Spectroscopy", W. B. Saunders, Philadelphia, Pa., 1971, p 109.
- (17) Internal coordinates: three CC stretching, two CF stretching, four CH stretching, four CCH bending for the CH₂ part, four CCH bending for the CHF part, and four CCF bending. Ten diagonal force constants: two CC stretching, two CH stretching, one CF stretching, three CH bending, and two CF bending. Ten off-diagonals: two F_{CC,CC}; two F_{CC,CF}; two F_{CF,CH} for the CFH group; F_{CC,CCH} for CH₂-CFH; two F_{CCH,CCH} for CH₂ groups.
- (18) After completion of this present work, the paper by K. Venkateswarlu and M. K. Rudra Warriar, *Ind. J. Pure Appl. Phys.*, 319 (1973), was found. These authors have done normal coordinate calculations on hexafluorocyclopropane alone with a 25 parameter force field. With a CF stretching constant of 6.65 mdyn/Å, they find that the 1557-cm⁻¹ mode is largely CF stretching.
- (19) E. C. Tuazon, W. G. Fateley, and F. F. Bentley, *J. Appl. Spectrosc.*, **25**, 374 (1971).
- (20) For the equimolar *d-l* mixture of *trans* isomers. The entropy includes an *R* ln 2 contribution for mixing.
- (21) V. I. Vedenev, A. A. Kibkalo, and G. G. Chervyakov, *Dokl. Akad. Nauk SSR*, **216**, 1084 (1974), report $\Delta H = 2070 \pm 145$ cal/mol and $\Delta S = 1.55 \pm 0.37$ gibbs/mol from a study of the *cis*-to-*trans* isomerization equilibrium between 373 and 423 K. While the enthalpy change is in general agreement with the value of 3000 ± 300 cal/mol observed from enthalpies of reaction by G. T. Armstrong and S. Marantz, *J. Chem. Phys.*, **38**, 169 (1963), the entropy change is inconsistent with the calculated entropy change of -0.25 ± 0.2 gibbs/mole (ref 1). Thus, it is doubtful that true equilibrium was achieved in these recent experiments.
- (22) E. J. M. Van Schaick, H. J. Geise, F. C. Mijlhoff, and G. Renes, *J. Mol. Struct.*, **16**, 23 (1973), have estimated an energy difference of 1700 cal/mol from electron diffraction patterns to which the *trans* rotamer made no detectable contribution.
- (23) (a) R. L. Kuczkowski and E. B. Wilson, *J. Chem. Phys.*, **39**, 1030 (1963); (b) R. K. Bohn and S. H. Bauer, *Inorg. Chem.*, **6**, 309, (1967).
- (24) (a) V. W. Laurie and D. T. Pence, *J. Chem. Phys.*, **38**, 2693 (1963); (b) E. J. M. Van Schaick, F. C. Mijlhoff, G. Renes, and H. J. Geise, *J. Mol. Struct.*, **21**, 17 (1974); (c) J. L. Carlos, Jr., R. R. Karl, Jr., and S. H. Bauer, *J. Chem. Soc., Faraday Trans. 2*, 177 (1974).
- (25) S. S. Butcher, R. A. Cohen, and T. C. Rounds, *J. Chem. Phys.*, **54**, 4123 (1971).

Electron Spin Resonance Studies of Anisotropic Ordering, Spin Relaxation, and Slow Tumbling in Liquid Crystalline Solvents¹

Carl F. Polnaszek

Division of Biological Sciences, National Research Council of Canada, Ottawa, Canada K1A 0R6

and Jack H. Freed*

Department of Chemistry, Cornell University, Ithaca, New York 14853 (Received May 9, 1975)

Publication costs assisted by the Petroleum Research Fund

A detailed study of anisotropic ordering, line shapes, and relaxation is reported for the perdeuterated 2,2,6,6-tetramethyl-4-piperidone *N*-oxide (PD-Tempone) nitroxide radical in several liquid crystal solvents. The line width results are analyzed in terms of the Polnaszek, Bruno, and Freed (PBF) theory appropriately modified for anisotropic ordering both in the motional narrowing and slow tumbling region. The motional narrowing results are usually consistent with isotropic rotational diffusion, but under a weak (asymmetric) ordering potential, $\langle D_{00}^2 \rangle \approx -0.1$, and activation energies characteristic of the twist viscous properties of the liquid crystal. Anomalous line shape behavior in the incipient slow tumbling region is observed, which is not explained by the extrapolation of the appropriate parameters from the motional narrowing region. This anomaly is discussed in terms of anisotropic viscosity and director fluctuations. The latter is predicted to be of negligible importance for the weakly ordered spin probe, as well as qualitatively of the wrong behavior. Anisotropic viscosity, while apparently able to "explain" the anomaly, leads to physically untenable conclusions. The anomaly is then discussed in terms of slowly fluctuating intermolecular torques, leading to a frequency-dependent diffusion coefficient. While this latter may in part offer an explanation (when one distinguishes between torque components parallel and perpendicular to the director), the implied slowness of the fluctuating torques suggests, from general theory, a new model based upon a local solvent structure around the spin probe which may persist over longer periods than the reorientation time of the spin probe. A simple model calculation of the effects on the ESR relaxation is given. This limiting model is also appropriate for highly structured isotropic liquids. It is shown that such a model could have the same formal spectral effects as anisotropic rotational diffusion, and it would yield non-Debye-like spectral densities of the type that could potentially "explain" the observed incipient slow tumbling anomaly. More general theoretical approaches for the analysis of these effects are briefly discussed.

I. Introduction

In a recent series of papers we have shown the wide range of information that one is able to obtain from ESR relaxation studies about rotational reorientation in liquid and frozen media, when careful studies are made of ESR spectra over the full range from the very fast motional region to the rigid limit.²⁻⁴ These studies, from which estimates could be made of (1) anisotropic rotational diffusion coefficients; (2) frequency dependence of the rotational reorientational correlation functions; (3) the non-Brownian nature of the reorientational process (e.g., large angle jump diffusion); (4) spin-rotational and angular momentum relaxation, were all performed on isotropic liquids containing spin probes. There is currently great interest in the dynamical reorientational properties of liquid crystals which may also be studied by ESR, and this has been reviewed in several places.⁵⁻⁸ There have been several recent studies of the dynamics of nitroxide free radicals in oriented systems such as nematic liquid crystals and lyotropic liquid crystals.⁹⁻¹² However, these studies have been based upon analyses appropriate when the probe motion is rapid, an assumption, we shall see, which is not always justified. Nordio and coworkers have presented a useful analysis of motional narrowing ESR line widths in liquid crystals for Brownian reorientation¹³ which is appropriate for such studies. Polnaszek, Bruno, and Freed (PBF)¹⁴ have generalized this approach to cover the slow tumbling region based on the slow tumbling theory of Freed et al.¹⁵ In that

work PBF also developed improved methods for analyzing the motional narrowing widths; they considered other models for rotational reorientation; and they obtained solutions for rotational diffusion with very strong restoring potentials.

The present work was undertaken to attempt to perform an extensive study of relaxation of nitroxide spin probes in liquid crystal solvents in the spirit of I and II (i.e., to obtain detailed information on rotational anisotropy and the deviations from Brownian motion in ordered fluids) utilizing the PBF theory for the analysis.

It was shown in II that the need for a high degree of spectral resolution for accurate spin relaxation studies could be fulfilled by the use of a perdeuterated spin label 2,2,6,6-tetramethyl-4-piperidone *N*-oxide (PD-Tempone), for which inhomogeneous broadening due to unresolved intramolecular proton or deuteron interactions is minimized. Thus, this probe was used in our most extensive studies, although other nitroxide probes were also used for comparison purposes. Another advantage of using the PD-Tempone probe is the fact that careful and extensive results on isotropic liquids given in II are available for comparison purposes, so that those results in liquid crystals, which are peculiar to these solvents, could be readily distinguished. In fact, as will be seen, such studies proved useful in shedding further light on molecular dynamics in liquids in general, as studied by ESR.

Actually, it was found at an early stage of this work, that

the PBF theory required some generalization before it could be applied to the experiments described here. This is because the ordering of the spin probes is, in general, not axially symmetric. In section II we give the appropriate analysis for rotational diffusion under more general mean field restoring potentials. Also, a more complete discussion of motional narrowing line widths is given, and the importance of frequency-dependent spectral densities, usually ignored by other workers, is stressed. The experimental procedures including analysis of any non-Lorentzian line shapes (in the motional narrowing region) are summarized in section III. The rigid limit spectra and magnetic parameters are discussed in section IV. A detailed discussion of the motional narrowing results including the asymmetric ordering and line width analyses appears in section V. The limitations of the motional narrowing analysis as the motion slows is also discussed there. It was possible, with the small spin probes, to obtain results in the incipient slow tumbling region, and the analysis of these spectra in terms of the PBF theory is discussed in section VI. It is shown there that these spectra have distinctly anomalous behavior.

We have in II and in a recent theoretical study¹⁶ undertaken a detailed statistical mechanical analysis of molecular reorientation to serve as the basis for analyzing unusual relaxation behavior not predicted by simple models of rotational reorientation. This general theory and its applicability to ordered fluids is summarized in section VII. The concept of relatively slowly fluctuating torques is then first discussed from the viewpoint of its effects on a frequency-dependent diffusion coefficient in a manner analogous to that given in II for isotropic liquids. However, because these results imply the existence of torque components fluctuating significantly more slowly than the molecular reorientation, one has, from the general theory,¹⁶ that it is probably more accurate to treat these components as persistent torques (by analogy with the mean field director), against which rotational reorientation takes place, but these torques then relax on a slower time scale. A simple "local structure" model is given in section VII for analyzing such effects, where it is shown that such a mechanism may (1) contribute to "apparent" anisotropic diffusion observations; (2) yield non-Debye-like spectral densities; and (3) possibly explain in part the experimental slow tumbling anomalies. An analysis of ESR effects of hydrodynamic fluctuations in the director based on the approach used in recent discussions of NMR relaxation¹⁷⁻²¹ is given in the Appendix. It is related to, but different from, the nonhydrodynamic "local structure" model of section VII.

Further discussion of the spin relaxation results appears in section VIII and a summary of the conclusions appears in section IX.

II. Rotational Diffusion in Anisotropic Liquids and ESR Line Shapes

The theory for analyzing slow tumbling as well as motional narrowing ESR spectra in liquid crystals has been discussed in detail by PBF. For purposes of the present work, it is necessary to generalize their methods to cases where the ordering of the solute molecule is of lower symmetry than cylindrical, since this was, in general, found to be the case in our current work. Also we give more explicit expressions for line widths in the motional-narrowing region.

Following PBF we may write the perturbing hamiltonian

$$\mathcal{H}_1(\Omega, \Psi) = \sum_{L, K, M} (-1)^K D_{-KM}^L(\Omega) D_{M^*}^L(\Psi) F'_{\mu, i}{}^{(L, K)} A_{\mu, i}{}^{(L, M)} \quad (2.1)$$

where the $F'_{\mu, i}{}^{(L, K)}$ and $A_{\mu, i}{}^{(L, M)}$ are irreducible tensor components of rank L , with F' in molecule-fixed coordinates, while A is a spin operator in the laboratory axes (whose z axis coincides with the applied dc field). Equation 2.1 is based upon two sets of rotations of the coordinate systems: first from the molecular axis system (x', y', z') into the director axis system (x'', y'', z'') with Euler angles $\Omega = (\alpha, \beta, \gamma)$; and then into the laboratory axis system x, y, z with Euler angles Ψ . The orientation of the director relative to the laboratory frame can be specified by the two polar angles θ and φ such that $\Psi = (0, \theta, \varphi)$. More precisely, we mean by the molecular coordinate system (x', y', z') the principal axis system for the orientation of the molecule in the mesophase. It may be necessary to transform from the principal axis system of the magnetic interactions (x''', y''', z''') to the (x', y', z') system with Euler angles Θ , according to

$$F'_{\mu, i}{}^{(L, K)} = \sum_{K'} D_{K, K'}^L(\Theta) F''''_{\mu, i}{}^{(L, K')} \quad (2.2)$$

where $\Theta = (\alpha', \beta', \gamma')$.

A. Rotational Diffusion. The problem of rotational diffusion in nematic solvents has been studied^{13,14} by means of adding the effects of an orienting potential to the rotational diffusion equation for isotropic liquids. The previous authors considered a cylindrically symmetric potential in the diffusion equation, but our results and that of other workers^{22,23} have shown that the ordering tensors for several different free radicals dissolved in various liquid crystals are not axially symmetric. These latter observations imply that the ordering potential is not axially symmetric, and an asymmetric potential should in general be included in the diffusion equation to explain ESR relaxation in the mesophase of liquid crystals. The diffusion equation for a particle undergoing Brownian rotational diffusion in the presence of a potential U is given by^{16,24}

$$\frac{\partial P(\Omega, t)}{\partial t} = -\mathbf{M} \cdot \left[\mathbf{R} \cdot \frac{MU(\Omega)}{kT} + \mathbf{R} \cdot \mathbf{M} \right] P(\Omega, t) - \Gamma_{\Omega} P(\Omega, t) \quad (2.3)$$

where $U(\Omega)$ can be taken to be the orienting pseudopotential for a liquid crystal, \mathbf{M} is the vector operator which generates an infinitesimal rotation, and is identified with the quantum mechanical angular momentum operator for a rigid rotator, while \mathbf{R} is the diffusion tensor of the molecule. Both \mathbf{R} and \mathbf{M} are defined in the (x', y', z') molecular coordinate system. The angular momentum operator \mathbf{M}^{24-26} is defined by

$$M^2 \varphi_{KM}^L(\Omega) = L(L+1) \varphi_{KM}^L(\Omega) \quad (2.4a)$$

$$M_{\pm} \varphi_{KM}^L(\Omega) = [(L \mp K)(L \pm K + 1)]^{1/2} \varphi_{K \pm 1, M}^L(\Omega) \quad (2.4b)$$

$$M_{z'} \varphi_{KM}^L(\Omega) = K \varphi_{KM}^L(\Omega) \quad (2.4c)$$

where $\varphi_{KM}^L(\Omega)$ are the eigenfunctions of M^2 and $M_{z'}$, L is the "angular momentum quantum number", and K is its component along the z' axis and

$$M_{\pm} = M_{z'} \pm iM_{y'} \quad (2.4d)$$

Then $\varphi_{KM}^L(\Omega)$ are the normalized generalized spherical harmonics, i.e., eigenfunctions of the rigid rotor:

$$\varphi_{KM}^L(\Omega) = \left(\frac{2L+1}{8\pi^2} \right)^{1/2} D_{KM}^L(\Omega) \quad (2.5)$$

When $U = 0$, eq 2.3 is simply the equation for (asymmetric) Brownian rotational diffusion in isotropic liquids. Equation 2.3 is based on the assumption that the external torque \mathbf{T} is derived from the potential $U(\Omega)$.^{16,24,27}

$$\mathbf{T} = iM U(\Omega) \quad (2.6)$$

The equilibrium solution to eq 2.3 is given by

$$P_0(\Omega) = \exp(-U(\Omega)/kT) / \int d\Omega \exp(-U(\Omega)/kT) \quad (2.7)$$

It is convenient to transform the Markov operator Γ_0 defined in eq 2.3 to a symmetrized form:

$$\tilde{\Gamma}_\Omega = P_0(\Omega)^{-1/2} \Gamma_0 P_0(\Omega)^{1/2} \quad (2.8a)$$

and

$$\tilde{P}(\Omega, t) = P_0(\Omega)^{-1/2} P(\Omega, t) \quad (2.8b)$$

Then one obtains the diffusion equation

$$\frac{\partial \tilde{P}(\Omega, t)}{\partial t} = -\tilde{\Gamma}_\Omega \tilde{P}(\Omega, t) \quad (2.9a)$$

where

$$\tilde{\Gamma}_\Omega = \mathbf{M} \cdot \mathbf{R} \cdot \mathbf{M} + \frac{(\mathbf{M} \cdot \mathbf{R} \cdot \mathbf{M} U)}{2kT} + \frac{\mathbf{T} \cdot \mathbf{R} \cdot \mathbf{T}}{(2kT)^2} \quad (2.9b)$$

The restoring potential for liquid crystals can be written in its most general form as

$$U(\Omega) = \sum_{L, K, M} \epsilon_{KM}^L D_{KM}^L(\alpha, \beta, \gamma) \quad (2.10)$$

The assumption of cylindrical symmetry about the director axis, \hat{n} , implies that all averages taken over the angle γ vanish unless $M = 0$.²⁸ The uniaxial property of nematic liquid crystals (i.e., $\hat{n} \equiv -\hat{n}$) implies that L must be even. It is useful to use the linear combinations of the D_{K0}^L which are of definite parity, i.e., the real linear combinations:

$$U(\Omega) = \sum_{\text{even } L} \left(\epsilon_0^L D_{00}^L(\Omega) + \sum_{K > 0} \epsilon_{K\pm}^L [D_{K0}^L(\Omega) \pm D_{-K0}^L(\Omega)] \right) \quad (2.11)$$

These have simpler properties for molecular symmetries less than cylindrical.

Usually one considers only the leading term $\epsilon_0^2 D_{00}^2(\Omega)$, i.e., the Maier-Saupe potential.²⁹ We¹⁴ have already considered the cylindrically symmetric case when $\epsilon_0^4 \neq 0$ as well, but we have shown that typical ESR spectral predictions are not very sensitive to having $\epsilon_0^4 \neq 0$. In general, however, one expects the terms for $L > 2$ to be less important than those for $L = 2$, and we may approximate

$$U(\Omega) \cong \epsilon_0^2 D_{00}^2(\Omega) + \sum_{K > 0} \epsilon_{K\pm}^2 [D_{K0}^2(\Omega) \pm D_{-K0}^2(\Omega)] \quad (2.12)$$

The $\epsilon_0^2, \epsilon_{K\pm}^2 = \epsilon_K^2 \pm \epsilon_{-K}^2$ (with K positive) are themselves second rank irreducible tensor components, so that, in the principal axis of molecular orientation system (x', y', z') their cartesian components ϵ_{ij}^2 are diagonalized, with $\text{Tr}_i \epsilon_{ij}^2 = 0$, and complete specification is given by just ϵ_0^2 and ϵ_{2+}^2 . (Equation 2.12 may be thought of as the scalar product of second rank irreducible tensors.)

TABLE I: Comparison of the Different Schemes of Ordering Parameters^a

Wigner rotation matrices	Saupe's ordering tensor ^b	Snyder's motional constants ^c
$\langle D_{00}^2 \rangle$	O_{zz}	$(5)^{-1/2} C_{3z^2-r^2}$
$\langle D_{20}^2 + D_{-20}^2 \rangle$	$(6)^{1/2}/2(O_{yy} - O_{xx})$	$-(2/5)^{1/2} C_{x^2-y^2}$
$\langle D_{10}^2 - D_{-10}^2 \rangle$	$(8/3)^{1/2} O_{xz}$	$(2/5)^{1/2} C_{xz}$
$\langle D_{10}^2 + D_{-10}^2 \rangle$	$i(8/3)^{1/2} O_{yz}$	$i(2/5) C_{yz}$
$\langle D_{20}^2 - D_{-20}^2 \rangle$	$-i(8/3)^{1/2} O_{xy}$	$-i(2/5) C_{xy}$

^a Luz and Meiboom, *J. Chem. Phys.*, 59, 275 (1973), use a set of orientation parameters, C_{qn}^L , which are simply related to our ordering parameter: $\langle D_{kn}^2 \rangle = C_{kn}^2$. ^b Reference 29. ^c Reference 30.

The ordering tensor is defined by

$$\langle D_{KM}^L(\Omega) \rangle = \int d\Omega P_0(\Omega) D_{KM}^L(\Omega) \quad (2.13)$$

where $L = 2$ and $M = 0$. It is also a second rank irreducible tensor whose symmetry properties are related to those of the $\epsilon_{K\pm}^2$. Thus from eq 2.7 and 2.12 and the orthogonality of the $D_{KM}^L(\Omega)$ terms it follows that in the (x', y', z') system only $\langle D_{00}^2(\Omega) \rangle$ and $\langle D_{20}^2 + D_{-20}^2 \rangle$ are nonzero, i.e. $\langle D_{KM}^L(\Omega) \rangle$ is also diagonalized. The correspondence between the ordering tensor $\langle D_{KM}^L(\Omega) \rangle$ and those of Saupe²⁹ and Snyder³⁰ is given in Table I. Thus the "diagonalized" potential (retaining only $L = 2$ terms) becomes

$$U(\Omega) = \epsilon_0^2 D_{00}^2(\Omega) + \epsilon_{2\pm}^2 (D_{20}^2(\Omega) + D_{-20}^2(\Omega)) \quad (2.14)$$

or equivalently

$$U(\alpha, \beta) = \gamma_2 \cos^2 \beta + \epsilon \sin^2 \beta \cos 2\alpha \quad (2.14')$$

where $\epsilon_0^2 = 2\gamma_2/3$ and $\epsilon_{2\pm}^2 = 2\epsilon(6)^{-1/2}$. For molecules in which the molecular x' and y' axes are aligned to different extents, ϵ is nonzero. If one chooses the orientation coordinate system such that the z' axis tends to align to a greater degree either parallel or perpendicular to the director than both the x' or y' axes, one should have $|\gamma_2| > |\epsilon|$. From Table I it is seen that ϵ is proportional to the difference in the ordering parameters for the y' and x' axes, and the case $\epsilon < 0$ corresponds to the y' axis being ordered preferential to the x' axis along the direction of \hat{n} and/or to the x' axis being ordered to a greater degree perpendicular to the \hat{n} than the y' axis. Note that, if the director is not parallel to the magnetic field, but is rotated by $\Psi = (0, \theta, \varphi)$, the potential parameters for the orientation of the molecule relative to the director are not affected. [Note also that the two-parameter potential enables one to permute the labeling of the principal axes, i.e., if we have $\gamma_{2,z}, \epsilon_z$ as the potential terms when the magnetic z axis corresponds to the z axis defining the generalized spherical harmonic, then one can write the potential terms with respect to y alignment as $\gamma_{2,y} = -(\gamma_{2,z} - 3\epsilon_z)/2$ and $\epsilon_y = -(\gamma_{2,z} + \epsilon_z)/2$; similarly $\gamma_{2,x} = -(\gamma_{2,z} + 3\epsilon_z)/2$ and $\epsilon_x = (\gamma_{2,z} - \epsilon_z)/2$ (cf. discussion below eq 2.12). It is sometimes true, as will be seen in section V, that such a relabeling of axes can reduce the specification of the potential to just the one parameter γ_2 , or else it may still succeed in keeping ϵ small.]

We may utilize eq 2.6 and 2.4b,c to obtain \mathbf{T} from the potential in eq 2.14²⁶ in terms of its components in the (x', y', z') coordinate system

$$\mathbf{T}_\pm = T_{x'} \pm iT_{y'} = \pm i \sin 2\beta [\epsilon e^{i\alpha} - \gamma_2 e^{i\alpha}] \quad (2.15a)$$

$$T_{z'} = -2\epsilon \sin^2 \beta \sin 2\alpha \quad (2.15b)$$

This permits the determination of the last term on the right-hand side in eq 2.9b once \mathbf{R} is given in the (x', y', z') coordinate system. We shall assume axially symmetric rotation about z' , such that $R_{x'x'} = R_{y'y'} = R_{\perp}$ and $R_{z'z'} = R_{\parallel}$. The second term on the right-hand side of eq 2.9b is found from the well-known form of the operator $\mathbf{M} \cdot \mathbf{R} \cdot \mathbf{M}$.²⁴⁻²⁶ We introduce the definitions

$$\lambda = -\gamma_2/kT \quad (2.16a)$$

and

$$\rho = -\epsilon/kT \quad (2.16b)$$

and obtain for the symmetrized Markov operator defined in eq 2.9

$$\tilde{\Gamma} = \mathbf{M} \cdot \mathbf{R} \cdot \mathbf{M} - f(R_{\perp}, R_{\parallel}, \lambda, \rho, \Omega) \quad (2.17a)$$

where

$$f(R_{\perp}, R_{\parallel}, \lambda, \rho, \Omega) =$$

$$\sum_{L=0,2,4} \left[X_{00}^L D_{00}^L + \sum_{0 < K \leq L} X_{K0}^L (D_{K0}^L + D_{-K0}^L) \right] \quad (2.17b)$$

with

$$X_{00}^0 = -(2/15)[R_{\perp}(\lambda^2 + \rho^2) + 2R_{\parallel}\rho^2] \quad (2.18a)$$

$$X_{00}^2 = 2[R_{\perp}\lambda - [R_{\perp}(\lambda^2 + \rho^2) - 4R_{\parallel}\rho^2]/21] \quad (2.18b)$$

$$X_{00}^4 = 4[2R_{\perp}(\lambda^2 + \rho^2) - R_{\parallel}\rho^2]/35 \quad (2.18c)$$

$$X_{20}^2 = (6)^{1/2}\rho[(R_{\perp} + 2R_{\parallel})/3 + 2R_{\parallel}\lambda/7] \quad (2.18d)$$

$$X_{20}^4 = 4(10)^{1/2}R_{\perp}\rho\lambda/35 \quad (2.18e)$$

$$X_{40}^4 = (8/35)^{1/2}R_{\parallel}\rho^2 \quad (2.18f)$$

One may also write the diffusion equation in terms of the general angular momentum operator \mathbf{N} referred to the director frame.²⁴ This is appropriate when \mathbf{R} is diagonal in this frame, i.e., anisotropic viscosity. One then generates an analogous set of expressions.^{24,31} In particular we assume $R_{xx} = R_{yy} = \hat{R}_{\perp}$, $R_{zz} = \hat{R}_{\parallel}$, and one finds for the components of \mathbf{T} in the (x, y, z) coordinates:

$$\begin{aligned} T_x \pm iT_y &= [2\epsilon \sin \beta \sin 2\alpha \mp \\ &\quad i \sin 2\beta(\gamma_2 - \epsilon \cos 2\alpha)]e^{i\alpha} \quad (2.19a) \\ T_z &= 0 \end{aligned}$$

and

$$\Gamma_{\Omega} = \mathbf{N} \cdot \mathbf{R}_{\Omega} \cdot \mathbf{N} - \hat{R}_{\perp} \hat{f}(\lambda, \rho, \Omega) \quad (2.20a)$$

where

$$\hat{f}(\lambda, \rho, \Omega) = \sum_{L=0,2,4} (\hat{X}_{00}^L D_{00}^L(\Omega) + \sum_{0 < K \leq L} \hat{X}_{K0}^L (D_{K0}^L(\Omega) + D_{-K0}^L(\Omega))) \quad (2.20b)$$

with

$$\hat{X}_{00}^0 = -2(\lambda^2 + 3\rho^2)/15 \quad (2.21a)$$

$$\hat{X}_{00}^2 = 2[\lambda - (\lambda^2 - 3\rho^2)/21] \quad (2.21b)$$

$$\hat{X}_{00}^4 = 4(2\lambda^2 + \rho^2)/35 \quad (2.21c)$$

$$\hat{X}_{20}^2 + 6^{1/2}\rho[1 + 2\lambda/7] \quad (2.21d)$$

$$\hat{X}_{20}^4 = 4(10)^{1/2}\lambda\rho/35 \quad (2.21e)$$

$$\hat{X}_{40}^4 = (8/35)^{1/2}\rho^2 \quad (2.21f)$$

The procedure for solution now follows the general approach of PBF, utilizing the normalized generalized spheri-

cal harmonics of eq 2.5 as an orthonormal basis set. Actually, it is more convenient, as seen from the above discussions, to use the real functions of definite parity:

$$D_{K\pm, M}^L(\Omega) = N_L^{-1/2} \frac{1}{\sqrt{2}} [D_{K, M}^L(\Omega) \pm (-1)^K D_{-K, M}^L(\Omega)] \quad \text{for } K \neq 0 \quad (2.22)$$

Computer programs based on the PBF theory were written for calculating nitroxide line shapes when (1) the asymmetric potential defined by eq 2.14' describes the orientation of a nitroxide radical for which the principal magnetic (x''', y''', z''') and orientation (x', y', z') axes are coincident and (a) eq 2.17 and 2.18 apply or (b) eq 2.20 and 2.21 apply; (2) a Maier-Saupe potential is used, but the z' and z''' axes are tilted by angle β' ; (3) different reorientational models are used for a Maier-Saupe potential with either an axial nitroxide or asymmetric nitroxide. All these programs contain the correction terms for nonsecular contributions to the resonant frequency shifts. Further details, as well as computer-program listings, appear in Polnaszek's thesis.³¹

B. Motional Narrowing Region. Many of the special simplifying features which may be applied to spectra in the motional narrowing region have been discussed by PBF. We extend and apply that discussion to the problems of interest here.

(1) *Effective Spin Hamiltonian and Ordering Parameters.* Here one uses an effective spin hamiltonian

$$\mathcal{H} = \mathcal{H}_{0'} + \mathcal{H}_{1'}(\Omega) \quad (2.23a)$$

where

$$\mathcal{H}_{0'} = \mathcal{H}_0 + \langle \mathcal{H}_1(\Omega) \rangle \quad (2.23b)$$

and

$$\mathcal{H}_{1'}(\Omega) = \mathcal{H}_1(\Omega) - \langle \mathcal{H}_1(\Omega) \rangle \quad (2.23c)$$

where the averaging implied by the angular brackets is according to the prescription of eq 2.13. When nuclear Zeeman terms are neglected the static spin hamiltonian in the high field approximation is

$$\hbar \mathcal{H}_0 = \langle g \rangle \beta_e B_0 S_z - \hbar \gamma_n \sum_i \langle a_i \rangle S_z I_z \quad (2.24)$$

The apparent g and a values, i.e. $\langle g \rangle$ and $\langle a \rangle$, must be corrected for nonsecular static and dynamic frequency shifts according to the methods discussed by PBF. Thus, for example, for the potential of eq 2.14 and for a molecule in which the (x''', y''', z''') coordinates are the same as the (x', y', z') coordinates, i.e., the magnetic tensor principal axes coincide with the orientational principal axes, one obtains the following equation (for a single nucleus of spin I) for these nonsecular frequency shifts:

$$\begin{aligned} \omega_{\text{corr}} - \omega_{\text{order}} &= \Delta\omega(m) = \frac{1}{\omega_0} [(I(I+1) - m^2)2b^2] - \\ &\quad \left\{ \frac{3}{20} (F_0^2 + 2F_2^2) + \frac{3m}{10} (F_0 D_0' + 2F_2 D_2') + \right. \\ &\quad \left. \frac{1}{15} (7I(I+1) - m^2)(D_0^2 + 2D_2^2) + \right. \\ &\quad \left. \left[\frac{3}{28} (F_0^2 - 2F_2^2) + \frac{3m}{14} (F_0 D_0' - 2F_2 D_2') - \right. \right. \\ &\quad \left. \left. \frac{2}{21} (5I(I+1) - 8m^2)(D_0^2 - 2D_2^2) + bD'[I(I+1) - \right. \right. \\ &\quad \left. \left. m^2] \langle D_{00}^2 \rangle + \left(-\frac{3}{14} [F_0 F_2 + m(F_0 D_2' + F_2 D_0')] + \right. \right. \\ &\quad \left. \left. \frac{4}{21} [5I(I+1) - 8m^2] D_0 D_2 \right) \langle D_{20}^2 + D_{-20}^2 \rangle \right\} \frac{\omega_0 \tau_R^2}{1 + \omega_0^2 \tau_R^2} \quad (2.25) \end{aligned}$$

where we are using the notation of I (except that F_2 and D_2 used here have opposite sign than the use in I for the consistent set of conventions needed for anisotropic liquids, cf. Polnaszek's thesis³¹). In principle, terms including $\langle D_{00}^2 \rangle$ and $\langle D_{20}^2 \rangle + \langle D_{-20}^2 \rangle$ can be included but they are negligible (<1% of the sum of the terms retained).

If the magnetic tensors are known, eq 2.13 can then be used to calculate the ordering parameters. For the case in which the asymmetric potential of eq 2.14 is applicable and $\Psi = 0$, the following equations result:

$$\langle D_{00}^2 \rangle = \frac{(\langle a \rangle - a)(g_x - g_y) - (\langle g \rangle - g)(a_x - a_y)}{(a_z - a)(g_x - g_y) - (g_z - g)(a_x - a_y)} \quad (2.26a)$$

$$\langle D_{20}^2 + D_{-20}^2 \rangle = \frac{\sqrt{6}[(\langle a \rangle - a)(g_z - g) - (\langle g \rangle - g)(a_z - a)]}{(g_x - g_y)(a_z - a) - (g_z - g)(a_x - a_y)} \quad (2.26b)$$

[In eq 2.26 and hereafter we shall refer to magnetic tensor components in the x''', y''', z''' axes as the x, y, z components, or else some cyclic permutation of the (x''', y''', z''') axes provided there is no confusion with the laboratory axes.]

With the ordering parameters known, eq 2.13 can be expressed as a system of two integral equations and the potential parameters λ and ρ obtained. Note that, because there are only two experimental observables, viz. $\langle g \rangle$ and $\langle a \rangle$, obtained from a motional-narrowing nematic ESR spectrum of a nitroxide, one can have at most two adjustable parameters, and one must then assume some knowledge of the x', y', z' axis system.³²

For many compounds of appropriate molecular geometry, the one-parameter Maier-Saupe potential may prove sufficient to describe its orientation, and a second parameter, which may then be determined, is the tilt angle of the magnetic z axis with respect to the z' axis. For this case, one obtains the set of equations

$$\cos^2 \beta' = \frac{(a_x - a)(\langle g \rangle - g) - (g_x - g)(\langle a \rangle - a)}{(g_z - g_x)(\langle a \rangle - a) - (\langle g \rangle - g)(a_z - a_x)} \quad (2.27)$$

$$\langle D_{00}^2(\Omega) \rangle = \frac{\langle a \rangle - a}{(a_z - a_x) \cos^2 \beta' + (a_x - a)} \quad (2.27a)$$

where the magnetic tensor components are in their principal axis system.

Note that the possible solutions of eq 2.27 for β' are $\pm\beta' \pm n\pi$ ($n = 0, 1, 2, \dots$) but, because of the uniaxial property of nematics, they are equivalent.

If there is a static distribution of directors around the laboratory axis, then one would have to use eq 2.1 and average the spectrum over the distribution in Ψ (e.g., a potential such as $V(\Psi) = \mu \cos^2 \theta$).^{3,31}

(2) *Relaxation*. If we define, as in PBF, the correlation function

$$C(L, L'; m, m', q, q'; \tau) = \langle D'_{-m, q}^{(L)}(t) D'_{-m', q'}^{(L')}*(t + \tau) \rangle$$

[where the prime on a function is defined by $f'_a(\Omega) = f_a(\Omega) - \langle f_a(\Omega) \rangle$], and its Fourier-Laplace transform (the spectral density function):

$$K(LL', mm', q, q', i\omega) = \int_0^\infty d\tau \exp(-i\omega\tau) C(L, L'; m, m'; q, q'; \tau)$$

then the line widths and other relaxation behavior may be

described in terms of these functions, according to the methods outlined by PBF. In particular one has

$$\text{Re } K(LL', KK', MM'; i\omega) = \sum_n \frac{E_n}{E_n^2 + \omega^2} \times \langle G_0(\Omega) | D_{KM}^L(\Omega) | G_n(\Omega) \rangle \langle G_n(\Omega) | D_{K'M'}^{L'*}(\Omega) | G_0(\Omega) \rangle \quad (2.28)$$

where the $G_n(\Omega)$ are the eigenfunctions of $\bar{\Gamma}_0$ of eq 2.9b with eigenvalues E_n . Equation 2.28 may be simplified by noting that for general potentials of form eq 2.11 or 2.12, only those K for which $M' = M$ are nonzero, so

$$K(L, L', K, K', M, M', i\omega) = K(L, L', K, K', M, i\omega) \delta_{MM'} \quad (2.29a)$$

We note further that the usual terms of $\mathcal{H}_1(\Omega)$ only require $L = L' = 2$. Also it can be shown for the potential of eq 2.14 that

$$\begin{aligned} K(2, K, K', M, i\omega) &= K(2, -K, -K', M, i\omega) = \\ K(2, K, K', -M, i\omega) &= K(2, -K, -K', -M, i\omega) = \\ K(2, K', K, M, i\omega) & \quad (2.29b) \end{aligned}$$

[For a cylindrically symmetric potential one also has $K = K'$ for nonzero values of K .]¹⁴ Thus, for the asymmetric potential of eq 2.14, the line widths are given

$$T_2^{-1} = \text{Re} \sum_{\substack{K, K', M \\ \alpha, \alpha', \beta, \beta'}} K(2, K, K', M, i\omega) F_{\mu_i}^{(2, K)} F_{\nu_j}^{(2, K')} * \times [A_{\mu_i}^{(2, M)}]_{\alpha\beta} [A_{\nu_j}^{(2, M')}]_{\alpha'\beta'} * \quad (2.30a)$$

For a single nuclear spin of I , one has the usual dependence of the line width upon the z component of the nuclear spin quantum number, m_I

$$T_2^{-1}(m_I) = A + Bm_I + Cm_I^2 \quad (2.30b)$$

where

$$\begin{aligned} (A - A') &= \\ \text{Re} \left\{ \frac{I(I+1)}{3} \gamma_e^2 \sum_{K, K'} D_K D_{-K'} [K(2, K, K', 0, \omega_0) + \right. & \\ 3K(2, K, K', 1, \omega_0) + 6K(2, K, K', 2, \omega_0)] + & \\ \left. \frac{\hbar^2 \gamma_e^2}{16\beta_e^2} \sum_{K, K'} F_K F_{-K'} [4K(2, K, K', 0, 0) + \right. & \\ \left. 3K(2, K, K', 1, \omega_0) \right\} & \quad (2.31a) \end{aligned}$$

$$\begin{aligned} B &= -\text{Re} \left\{ \frac{\hbar \gamma_e^2}{\sqrt{6}\beta_e} \sum_{K, K'} D_K F_{-K'} [4K(2, K, K', 0, 0) + \right. \\ \left. 3K(2, K, K', 1, \omega_0) \right\} & \quad (2.31b) \end{aligned}$$

$$\begin{aligned} C &= \text{Re} \left\{ \frac{\gamma_e^2}{3} \sum_{K, K'} D_K D_{-K'} [8K(2, K, K', 0, 0) - \right. \\ K(2, K, K', 0, \omega_0) + 6K(2, K, K', 1, \omega_0) - & \\ \left. 3K(2, K, K', 1, \omega_0) - 6K(2, K, K', 2, \omega_0) \right\} & \quad (2.31c) \end{aligned}$$

where the D_K and F_K are defined as in I; also $\omega_a \approx \omega_\pm = \pm\omega_n + \frac{1}{2}a|\gamma_d|$. Note A' , the residual width, includes all other nuclear-spin independent line-broadening mechanisms. [The units of A, B , and C are sec^{-1} ; for comparison with experimental results, they are multiplied by $2(3)^{-1/2}/|\gamma_d|$ to give values which correspond to peak-to-peak line widths in gauss.] Note that nonsecular terms are readily included in this treatment of ESR line widths in the motional narrowing region of the nematic mesophase. In previous

work nonsecular terms were either neglected or considerably complicated the method.^{9-13,28}

In the isotropic limit, the spectral densities are

$$K(2, K, K', M, \omega) =$$

$$(1/5) \delta_{KK'} \frac{\tau_{LK}^{-1}}{(\tau_{LK}^{-1})^2 + \omega^2} = \frac{1}{5} j_{LK}(\omega) \quad (2.32)$$

and then eq 2.31 corresponds to the equation given for axially symmetric rotational diffusion in I.

For an axially symmetric potential, eq 2.31 can be used to calculate motional narrowing line widths by the substitution of $K_{KM}^{(2)} \delta_{KK'}$ for the $K(2, K, K', M, \omega)$. In this case the $K_{KM}^{(2)}$ for $|\lambda| \leq 1$ may be obtained by a perturbation theory approach and are given by PBF. (Their equations for $K_{KM}^{(2)}$ allow for the K and M to be permuted throughout, to obtain all the needed expressions.)^{33,34}

Programs for the analysis of the motional-narrowing relaxation of a nitroxide with asymmetric magnetic parameters oriented by the asymmetric potential of eq 2.14 are given in Polnaszek's thesis.³¹

III. Experimental Section

A. Sample Preparation. The nitroxide free radical 2,2,6,6-tetramethyl-4-piperidone *N*-oxide (Tempone) and its totally perdeuterated analog (PD-Tempone) were synthesized by Dr. R. P. Mason using the method of Rozantsev.³⁵ The bromoacetamide spin label, 3[[2-[2-(bromoacetamido)ethyl]ethyl]carbamoyl]-5,5-tetramethyl-1-pyrrolidinyloxy (BASL), was purchased from Syva Associates. The α -phenylnitroxyl nitroxide (PNN) was a gift of Dr. G. Rist. The di-*tert*-butyl nitroxide (DTBN) was synthesized by B. Kaplan using the method of Hoffmann et al.³⁶ All free radical nitroxides were used without further purification.

The liquid crystal bis(4'-*n*-octyloxybenzyl)-2-chloro-1,4-phenylenediamine (BOCP) was purchased from Aldrich Chemical Corp. and used without further purification. The nematic compounds butyl-*p*-(*p*-ethoxyphenoxy-carbonyl)phenyl carbonate (BEPC), *p*-(*p*-ethoxyphenyl-azo)phenyl hexanoate (PEPH), and *p*-[*N*-(*p*-methoxybenzylideneamino)-*n*-butylbenzene (MBBA) were obtained from Eastman Kodak. BEPC was purified by several recrystallizations from methanol, PEPH was recrystallized from absolute alcohol, and MBBA was purified by vacuum distillation.³⁷ The *p*-ethoxy-*p*'-hexyloxyazoxybenzene (EHAB) and its nematic precursor *p*-ethoxy-*p*-hexyloxyazoxybenzene were synthesized as described by Koch³⁸ and recrystallized from ethanol-water mixtures and then from absolute ethanol. The nematic compound *p*-[*N*-(σ -hydroxy-*p*-methoxybenzylidene)amino]-*n*-butylbenzene (OH-MBBA)³⁹ was synthesized by refluxing *p*-*n*-butylaniline (Aldrich) and *p*-methoxy- σ -hydroxybenzaldehyde prepared by the method of Zemlen et al.⁴⁰ in absolute alcohol. Upon recrystallization from methanol, OH-MBBA melted at 42°C. Nematic phase IV, a low melting nematic eutectic, was synthesized by the methods of Steinstrasser and Pohl^{41a} and recrystallized from a methanol-hexane mixture; it was also purchased from EM Laboratories. Nematic phase V,^{41b} a lower melting nematic eutectic composed of 65% phase IV and 35% of another mixture, was obtained from EM Laboratories and used without further purification. The dimethoxyethane (DME) was Eastman White Label and was purified by the methods of Bolton and Fraenkel.⁴² Deoxygenated samples were prepared by

standard methods, and further details may be found in Polnaszek's thesis.³¹

B. ESR Spectrometer. Most of the ESR measurements were performed on a Varian E-12 spectrometer using 10-kHz field modulation, cf. I and II. The temperature in the active region of the cavity was controlled by a Varian E-257 variable temperature control unit and was stable to $\pm 1^\circ\text{C}$. The temperature gradient over the active region of the cavity relative to the center was found to vary with temperature. At room temperature the value was $\pm 0.5^\circ\text{C}$, while at 150°C the gradient increased to $\pm 2^\circ\text{C}$. Other techniques are as described in I and II.

C. Line Width Measurements. All line width measurements were performed with the modulation amplitude set at a value of less than one-tenth of the line width and with the microwave power set well below that required to maximize the signal amplitude. All the spin labels studied had unresolved proton or deuteron hyperfine structure in each of three principal ESR lines. This inhomogeneous broadening causes the line shapes to be non-Lorentzian and to appear to be broader than the true peak-to-peak line width $2|\gamma_e| T_2^{-1} (3)^{-1/2}$. The correct line widths can be obtained as was done in II. One measures the line shape by noting the variation of the derivative half-amplitude as a function of the distance from resonance. This line shape is then compared to a theoretical line shape calculated using a peak-to-peak line width and hyperfine splitting (hfs) constants for the nuclei causing the inhomogeneous broadening. Kreilick using an NMR technique has determined these hyperfine splitting constants in the isotropic phase for Tempone to be $a_{\beta^H} = -0.11$ G and $a_{\gamma^H} = -0.01$ G.⁴³ Because there are 12 β protons and 4 γ protons and a_{γ^H} is so small, the effect of the γ protons was neglected in the line shape simulations.

For Tempone in the isotropic phase of BEPC, a β proton coupling constant of 0.125 ± 0.003 G is needed to fit the observed line shape. In the nematic phase of BEPC the β -proton coupling was found to vary with the temperature as a result of the increase of $\langle D_{K0}^2 \rangle$ with decreasing temperature. If one assumes an axially symmetric potential, the ordering parameter can be determined from the nitrogen hfs using eq 2.27a with $\beta' = 0$. Then one may use this ordering parameter and the isotropic β proton coupling to calculate the z component of the methyl proton hyperfine tensor in the principal axis of the nitrogen magnetic tensors (from eq 2.27a). One obtains $a_z^{H\beta} = -0.739 \pm 0.008$ G and $a_{\perp}^{H\beta} = \frac{1}{2}(a_x + a_y) = 0.182$ G, if one assumes axial symmetry of the methyl proton hyperfine tensor. For PD-Tempone in phase V a similar analysis applied to the β deuteron splittings yields $a_D^{\text{iso}} = -0.0215 \pm 0.0005$ G and $a_z^D = -0.093 \pm 0.007$ G. Since the isotropic splittings, a_N and the a_z^N determined for the rigid limit were nearly identical for PD-Tempone in all the liquid crystal solvents, it was assumed that the a_D and a_z^D were the same for all systems in the liquid and nematic regions. Then, after one has obtained $\langle D_{00}^2 \rangle$ relative to the molecular z axis, this can be used to calculate the $\langle a_D \rangle$ needed for the line shape analysis. The intrinsic peak-to-peak line width for PD-Tempone, or any radical in which the inhomogeneous broadening is due to 12 equivalent deuterons, can be obtained from Figure 1 and knowledge of the deuteron hfs.

In the motional narrowing region, when the variation in the line width among the three nitrogen lines is small compared to the line widths, it is usually more accurate to determine one line width and use the relative amplitude of

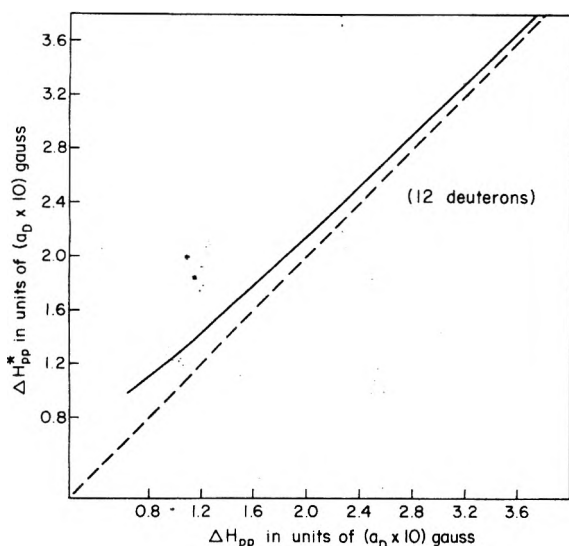


Figure 1. Calibration curve for obtaining the intrinsic derivative line width ΔH_{pp}^* from the observed (inhomogeneous) derivative line width ΔH_{pp} for PD-Tempone involving 12 equivalent deuterons.

the lines to calculate the relative line width of all the lines. This procedure can be readily modified to the case of inhomogeneously broadened lines. After determining $\langle a_D \rangle$ and one line width as described above, one can use that value of $\langle a_D \rangle$ and vary the intrinsic line widths in the line shape program until one obtains the correct intensity ratios. This procedure was applied to all spectra in which the line widths were 1 G or less. For widths >1 G the corrections were less than 1%. [Magnetic field inhomogeneity will not cause serious inhomogeneous broadening of the lines, since it is ~ 5 mG,² whereas the minimum intrinsic line width observed for PD-Tempone in phase V was 134 mG at 67°C.]

Another factor which can affect the observed line shapes in the nematic mesophase is the possibility of the director \hat{n} not being parallel to the dc magnetic field. deGennes has predicted that due to thermal fluctuations the director can have components which are not parallel to the field.⁴⁴ One notes that the resonant positions of the lines will be different for each orientation of the director. If the motion of the director is taken as being slow on the ESR time scale,^{17,44} then each observed line will be a superposition of resonances from different director orientations and any modulation by the motion of the director may be neglected, i.e., one has a static distribution of directors. The total line shape for a distribution of lorentzians with the director distribution also of a Maier-Saupe form is given by

$$I(B_0) = \int_{-\pi/2}^{\pi/2} \frac{T_2^{-1}(B(\theta) - B_0)}{[(T_2^{-1})^2 + (B(\theta) - B_0)^2]^2} \times \exp(\alpha \sin^2 \theta) \sin \theta d\theta \quad (3.1)$$

where

$$B(\theta) = \{B + m_I[a + D_{00}^2(\theta)\langle D_{00}^2(\Omega) \rangle(a_z - a)] - [I(I + 1) - m_I^2][a - \frac{1}{2}D_{00}^2(\theta)\langle D_{00}^2(\Omega) \rangle(a_z - a)]^2/2B_0\} [1 - D_{00}^2(\theta)\langle D_{00}^2(\Omega) \rangle(g_z - g)/g] \quad (3.2)$$

where the $\langle D_{00}^2(\Omega) \rangle$ are the experimentally determined ordering parameters, θ is the angle between \mathbf{B}_0 and \hat{n} , B_0 is the resonant field of the center line in the absence of a potential $= (\omega_0/\gamma_d)$, and $\alpha = -(kT\theta_0^2)^{-1}$ where θ_0 is the root mean square fluctuation in θ ^{6a} and we have assumed small

TABLE II: Magnetic Parameters for Nitroxides in Liquid Crystals^a

(A) PD-Tempone in Phase V			
g_x	2.0097 ± 0.0002	A_y, G	5.01 ± 0.2
g_y	2.0062 ± 0.0002	A_z, G	33.7 ± 0.3
g_z	2.00215 ± 0.0001	$\langle A \rangle, G$	14.77 ± 0.3
$\langle g \rangle$	2.0060 ± 0.00017	a_N, G	14.78 ± 0.02
g_s	2.00601 ± 0.00005	A, G	2.2
A_x, G	5.61 ± 0.2	B, G	0.2

(B) Other Systems

System	A_z	a_N	g
PD-Tempone in Phase IV	33.5	14.75	2.00602
PD-Tempone in BOCF	33.9	14.74	
PD-Tempone in BEPC	33.8	14.79	2.00600
PNN in BEPC	18.1	7.62	
Bromoacetamide spin label in BEPC	33.2	14.62	2.0058

^a Polycrystalline matrices.

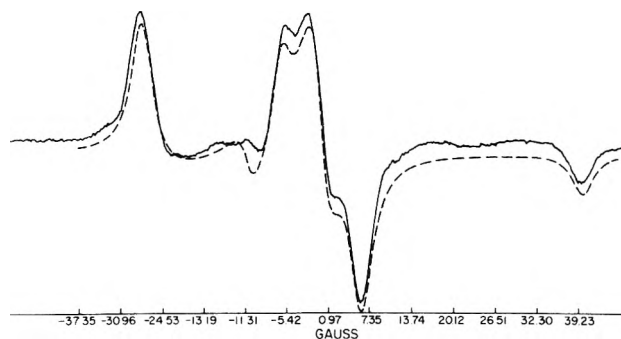


Figure 2. Rigid limit spectrum for PD-Tempone in phase V and simulation based on magnetic parameters given in Table II.

ordering parameters to get a simple result in eq 3.2. [In general, T_2^{-1} will depend on θ , a matter to be discussed in section VII. However for small values of θ_0 expected for this mechanism, it is reasonable to neglect this effect.]

We have observed in our work with PD-Tempone in phases IV and V, marginal asymmetries of the hyperfine lines, which would require values of $\alpha > 100$ (i.e., let R be the ratio of the low-field to high-field extremum intensity of a hyperfine line, then we see $R \sim 0.94$ to 1.0). These values for α are very much larger than those used by Brooks et al.⁴⁵ for VAAC in PAA. Furthermore (1) our observed asymmetries increase with decreasing temperature, or the opposite direction expected for director fluctuations, but in the correct direction if due to slowing of the rate of molecular reorientation; also (2) the high-field line is predicted to have $R > 1$ while we observe $R < 1$, etc. Thus, within experimental error it does not appear that we observe any effects from a static distribution of directors.⁴⁶ Dynamic effects of fluctuations in the director are discussed in section VII and the Appendix.

IV. Determination of Magnetic Tensor Components. Rigid Limit

In order to simulate slow motional spectra and to analyze the data in the motional narrowing region, one must know

the components of the g and A tensors which occur in the spin hamiltonian $\mathcal{H}_1(\Omega)$. We have made our measurements on polycrystalline samples in the manner given in I and II. All of the liquid crystals used froze into amorphous solids when cooled slowly below their nematic range. However, to prevent some residual ordering from being frozen in, the samples were frozen outside the magnet gap or inside the cavity with the magnetic field turned off. MBBA and OH-MBBA, if quick-frozen in liquid nitrogen, formed rigid glasses. However the spectra of PD-Tempone in all the frozen nematics was virtually identical and independent of whether the sample was amorphous or glassy. Also the isotropic a and g values for PD-Tempone in all the liquid crystals studied were nearly equal as shown in Table II. Thus, it was decided to determine accurately the magnetic tensors for PD-Tempone in one system and use these values for all systems and also for Tempone.

The rigid limit spectrum of PD-Tempone in frozen phase V at -190°C is shown in Figure 2. Note the resolution in the central region. For Tempone in the rigid limit, the center region is not resolved because of inhomogeneous broadening due to unresolved proton hyperfine structure. Thus deuteration of the nitroxide spin label is seen to aid in the analysis of the rigid limit spectrum as well as the motional narrowing and slow motional spectra. Further resolution can be obtained by deuteration of the solvent (cf. I and II). The parameters which gave the best fit are given in Table II. A lorentzian line shape gave the best overall fit, although a gaussian shape function appears to fit the extrema better. Note that the theoretical spectrum is slightly lowered from the experimental one, so that the fit in the region -24.53 to -13.19 G is an artifact of the drawing; it is this region for which a gaussian gives a better fit. [We note that rigid limit spectra for PD-Tempone in toluene solvent were more successfully fit with a lorentzian shape, although some features of the spectrum in 85% glycerol were better fit with a gaussian (cf. II).] The form for the orientationally dependent intrinsic line width was assumed to be²

$$T_2^{-1} = A + B \cos^2 \beta \quad (4.1)$$

It was found that the values of A and B of 2.2 ± 0.1 and 0.2 ± 0.1 G, respectively, gave the best fit to the experimental spectrum. It was shown in II that the magnetic parameters and intrinsic line widths for PD-Tempone vary with solvent in nonliquid-crystalline solvents. The near equivalence of these quantities for all the liquid crystals is probably due to chemical similarity of these compounds. Also these results are very similar to the magnetic parameters obtained in II for nonhydrogen-bonding isotropic solvents (e.g., toluene) as one might expect.

There are some differences between the theoretical and experimental spectra. One of the possible causes, which was discussed above, is the residual motion present. It was not experimentally convenient to reduce the temperature further; however the observed spectra changed very little with temperature in this region. The deuterium inhomogeneous broadening is expected to be negligible, since the largest component of the methyl deuterium hyperfine tensor is -0.09 G. Quadrupole terms were neglected in the theoretical hamiltonian used. Dinse et al.³² have measured the quadrupole splitting of a chemically similar nitroxide to be -0.9 G, but the effect of the quadrupole splitting will be to shift the lines corresponding to the x and y orientations by⁴⁷

$$\frac{9}{32} \left(\frac{1}{a_1} \right) \left(\frac{e^2 q Q}{\hbar \gamma_e} \right)^2 \approx 0.04 \text{ G} \quad (4.2)$$

which is negligible; also there will be no shift in the lines from the z orientations. Spectra simulated with nuclear Zeeman terms included did not differ from those in which these terms were neglected. It was thought that the small bump appearing near -13 G might be due to the presence of a spectrum arising from ^{15}N ($I = \frac{1}{2}$). However, simulation performed with parameters appropriate for the ^{15}N species, that was added to the line shape calculated for ^{14}N using the correct isotropic abundances, did not show such a bump nor was the rest of the spectrum affected. Another source of error is the assumption used in the hamiltonian to simulate the spectra that the principal axes of the g and hyperfine tensors coincide. It has been reported that the xy planes differ by 6° for DTBN.⁴⁸ If this were true for PD-Tempone the values for the x and y components may be changed somewhat, but it would be within our error limits. Thus one can be confident that the magnetic parameters given in Table II are fairly accurate.

The spin parameters determined from the rigid limit simulations give the same isotropic values (obtained at temperatures 300° higher) when one averages the values of the principal components. Thus, it is reasonable to believe that the magnetic tensors are temperature independent, so they may be used for all the line shape analyses.

V. Motional Narrowing Results

A. Preliminary Observations. The motional narrowing ESR spectra of all nitroxides consisted of three sharp lines in the isotropic and nematic phases in all liquid crystals studied. If one refers to PBF, one finds that this observation need not in itself be indicative of motional narrowing. The analyses will be given for only the nematic mesophase. [Several of the liquid crystals had underlying smectic mesophases. All the smectic solvents gave spectra which had splitting constants nearly identical with the isotropic splittings and thus were indicative of randomization of the director in the smectic phase. The lines were much broader than the nematic phase and in some cases were asymmetric. This is indicative of the local ordering present in the macroscopically disordered smectic phases.¹⁸ The nematic compounds which did not have underlying smectic phases all froze to amorphous randomly oriented solid phases. All mesophases could be supercooled considerably below their melting points, and no sudden changes (or discontinuities) were observed in the ESR spectra in this region until the samples froze. Below the freezing point in all systems, the spectra varied continuously with temperature until the rigid limit was reached.

The nematic-isotropic transition point, T_K , was determined to be the temperature at which the observed splitting constant changed from its isotropic value to a smaller value indicative of the ordering in the nematic phase. Because of the temperature gradient in the cavity as well as impurities in the liquid crystal solvent, it was possible to observe spectra from both phases simultaneously if one was at or near T_K . These transition points and freezing points were dependent upon the concentration of the radical and also upon the specific radical which was dissolved in the nematic solvent. Thus the values of the transition points and freezing points could vary by several degrees from sample to sample.

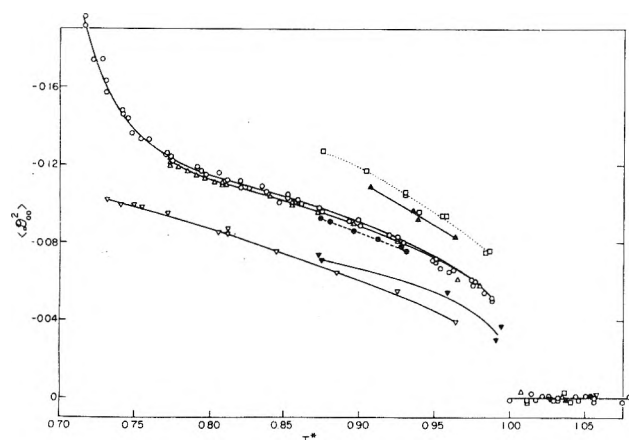


Figure 3. Ordering parameter $\langle D_{00}^2 \rangle_z$ vs. reduced temperature $T^* = T/T_K$ for PD-Tempone in several liquid crystals: (O) phase V; (Δ) phase IV; (\bullet) MBBA; (\blacktriangledown) OHMBBA; (∇) BOCP; (\blacktriangle) BEPC; (\square) Tempone in BEPC.

One finds that phase V and BOCP should be the best liquid crystals in which to do an ESR relaxation study, since they have nematic ranges of over 100° . However phase V freezes at least 80° below BOCP and thus would be a more suitable solvent in which to look for slow-motional effects. When the experimental study was performed, phase V was the lowest melting nematic compound readily available. Radical stability is another factor to be considered in the choice of lower temperature liquid crystals. If the radical is volatile, it may distill out of the liquid crystal when heated in the evacuated sample tubes. Also, as noted previously the temperature gradients in the cavity are much greater at the higher temperatures.

The radical chosen for most of the motional narrowing studies was PD-Tempone. As we have shown, the contribution from inhomogeneous broadening can be completely neglected for spectra having all lines of width 1 G or greater, and the contribution is quite small for narrower lines. The accuracy of the line width measurements is considerably increased compared to proton inhomogeneously broadened lines. The only apparent disadvantage in using PD-Tempone is that, because of its size and geometry, it is not ordered to a large extent in the nematic phase.

B. Order Parameters and Potential Expansion Coefficients. In order to perform relaxation studies, one must know the coefficients in the potential (cf. eq 2.14) which determines the distribution function for the orientation of the radical in the nematic phase. These coefficients can be determined from the ordering parameters calculated in the motional narrowing region.

The ordering parameters $\langle D_{00}^2 \rangle_z$ determined for PD-Tempone in several liquid crystals for the Maier-Saue potential are plotted vs. T^* in Figure 3 where $T^* = T/T_K$. The magnetic parameters used are those given in Table II for PD-Tempone in phase V. The ordering parameters for a solute molecule in different solvents might be expected to lie on nearly the same line when plotted against T^* . The fact that they do not in all cases shows $\lambda = -\gamma_2/kT$ is a function of the solvent to some extent as well as the radical. In general, it is found that liquid crystals of nearly the same geometry but with different chemical groups in the center orient PD-Tempone to the same amount. For instance, phase V, phase IV, and MBBA have similar alkyl end groups and OH-MBBA and BOCP are laterally substituted liquid crystals with an atom or group on a benzene

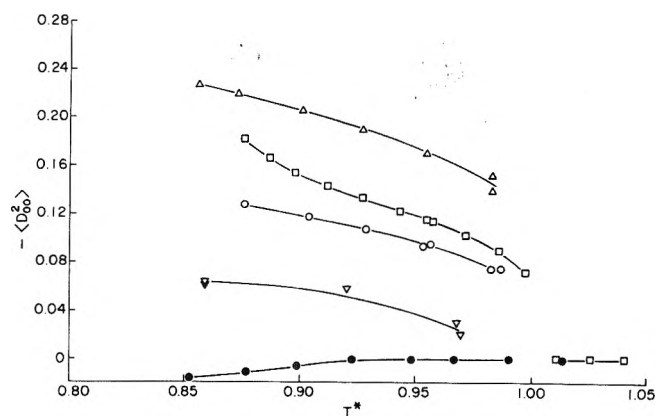


Figure 4. Ordering parameter $\langle D_{00}^2 \rangle_z$ vs. reduced temperature $T^* = T/T_K$ for several nitroxide radicals: (Δ) PNN in BEPC; (\square) BASL in BEPC; (O) Tempone in BEPC; (∇) DTBN in EHAB; (\bullet) MSL in PEPH.

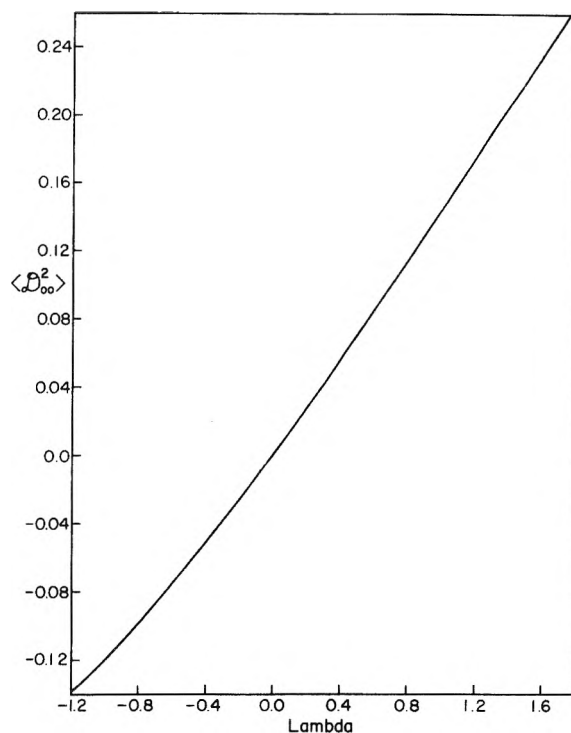


Figure 5. Calibration curve of ordering parameter $\langle D_{00}^2 \rangle_z$ vs. λ for the Maier-Saue potential.

ring ortho to the center group. The discontinuity in the ordering at the transition point is indicative of a first-order phase transition, whereas the deviation of the observed $\langle D_{00}^2 \rangle_z$ vs. T^* from near linearity for phase V and to a lesser extent phase IV at low T^* is a result of the breakdown of the assumption of motional narrowing upon which eq 2.26 is based.

Further results of $\langle D_{00}^2 \rangle_z$ for different radicals are given in Figure 4. The relationship between λ and $\langle D_{00}^2 \rangle_z$ according to eq 2.13 is given in graphical form in Figure 5 for the range of values of interest. The most ordered system in Figure 3, Tempone in BEPC, is included for comparison. [Also note in Figure 3 that Tempone and PD-Tempone appear to order to a slightly different degree in BEPC. We have not determined whether this is a true effect or whether it reflects differences in sample preparation.]⁶⁴ The radical PNN oriented the largest amount, but was found to decom-

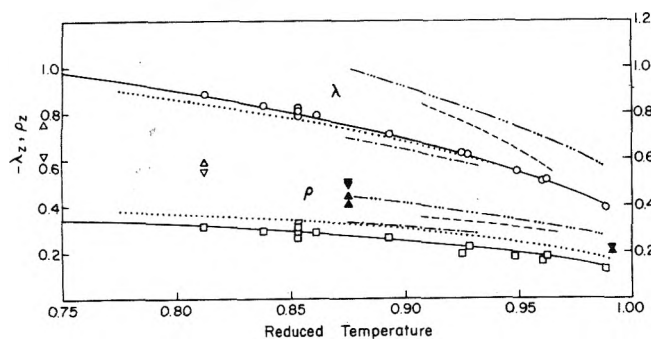


Figure 6. Asymmetric ordering parameters vs. reduced temperature for PD-Tempone in various solvents. The ordering parameters are defined with respect to the z -molecular axis (see text). Solvents are denoted by (—) phase V; (· · · · ·) phase IV; (- · - · -) MBBA; (- - - -) BEPC; (- · · · -) Tempone in BEPC; (Δ) for λ_z and (▽) for ρ_z in BOCF; (▲) for λ_z and (▼) for ρ_z in OH-MBBA.

pose to another radical after 1 hr or more in the liquid crystals used. The larger bromoacetamide spin label orients to a lesser degree, but it is beginning to show slow motional effects at much more elevated temperatures than PD-Tempone. The curves for DTBN and the maleamide spin label (MSL) are representative of nitroxides which are very weakly ordered and almost not ordered, respectively. However, for MSL this may be due to a tilt of the z axis with respect to the z' axis such that β' is close to the magic angle. [The DTBN reacted to give another spectrum after 1 hr in the isotropic phase of PEPH.]

We now recall that the magnetic tensors of PD-Tempone are not axially symmetric. An examination of a molecular model of PD-Tempone indicates that there is no particular axis in the molecule about which it would prefer to align in a nematic phase. Because of these two reasons, one should be able to determine an ordering tensor for PD-Tempone that need not be axially symmetric. In fact an asymmetric potential (cf. eq 2.12, 2.14) is needed to describe the ordering of PD-Tempone in the mesophase. The second potential parameter is determined utilizing the g values measured for the nematic and isotropic phases. These measured g values were corrected for the static and dynamic nonsecular shifts using eq 2.25. The corrected g and hyperfine values permit the calculation of the two ordering parameters from eq 2.13. It is found that PD-Tempone in phase V orients weakly with the magnetic z axis tending to be perpendicular to the director, the y axis tending to be parallel to the director, and the x axis tending to be oriented nearly at the magic angle. [This implies that if there is a single axis of cylindrical symmetry, it is not one of the magnetic principal axes.¹⁴⁹ The values of the two ordering parameters were then used to calculate the potential parameters λ and ρ from eq 2.13. The results are shown in Figure 6 for the z -axis parameters for PD-Tempone and Tempone in several liquid crystals. It can be seen that $|\lambda| > |\rho|$ for all solvents except BOCF and OH-MBBA. However, if one calculates λ and ρ with respect to the y magnetic axis as the primary axis of PD-Tempone from the known values with respect to the z axis, one obtains the result that $\rho_y \approx 0$ for these two solvents. Thus for BOCF and OH-MBBA, the orientation can be described by a Maier-Saupe potential with respect to the y axis. Therefore (by a proper choice of labeling of the magnetic principal axes) it is the first term, i.e., the Maier-Saupe potential, which predominates in the potential expansion for all systems studied. This encourages us in the belief that the two-parameter potential of eq

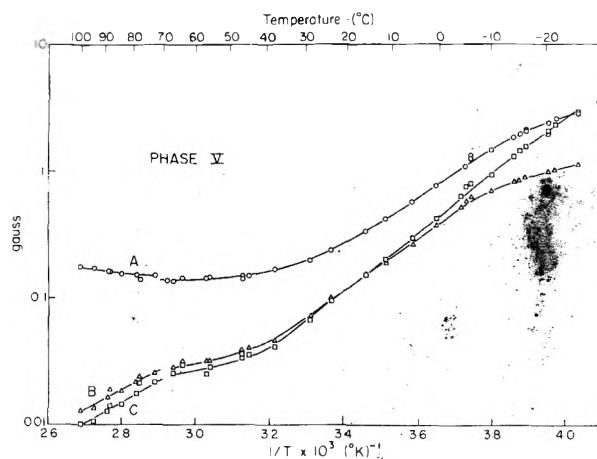


Figure 7. A, B, and C vs. $1/T$ for PD-Tempone in phase V.

2.14 is adequate for dealing with the molecular dynamics. For phase IV and phase V the λ and ρ curves were extrapolated for those values of T^* corresponding to the slow motional region. These values of λ and ρ were used for simulating slow motional spectra.

C. Line Width Analysis. The ESR spectra of PD-Tempone in the nematic phase of a liquid crystal are now analyzed in the motional narrowing region. Because all observed spectra consisted of three lines, one might think that the motional narrowing limit will apply for all temperatures. However, the lines become asymmetric at lower temperatures and the two hyperfine splittings become considerably different. It is in this region that one must use the slow-tumbling theory to simulate the observed spectra. The slow motional spectra of the weakly ordered PD-Tempone are expected to be sensitive to model dependence, anisotropic viscosity, asymmetric molecular reorientation, and the type of liquid crystalline potential used as is readily seen from the examples in PBF. A thorough analysis of the motional narrowing region should help to show which of the above-mentioned processes are important. It is expected that in the absence of any second-order phase transition, the same sort of diffusion process will occur at all temperatures, and one should be able to extrapolate the results of the motional narrowing region into the slow motional region.

The first case to be discussed will be that of PD-Tempone in phase V, a system which exhibits slow motional effects, but, nevertheless, has a long mesomorphic range over which one can observe motional narrowing behavior. The other systems will be analyzed in terms of their similarities or differences to this system. All line widths were measured by the method of relative amplitudes (cf. I and II) and corrected for deuterium inhomogeneous broadening using the ordering parameters given in Figure 3 to calculate the deuterium hfs (cf. section III). All line width data can be expressed as coefficients A, B, and C of eq 2.30b.

(1) *Isotropic Phase.* The line width results for PD-Tempone in the isotropic phase of phase V are shown in Figure 7. Our analysis of the line widths in the isotropic region is identical with that given in I and II. For PD-Tempone in the isotropic phase of phase V, one is in the region $\omega_0^2 \tau_R^2 \sim 1$ where nonsecular terms are expected to be important. If nonsecular terms are included in the calculation of τ_R , one gets the result that τ_R determined from B does not equal τ_R from C for isotropic rotation. In fact τ_R^C / τ_R^B varies from 1.3 near T_K to 1.5 at 99°. If nonsecular terms are neglected,

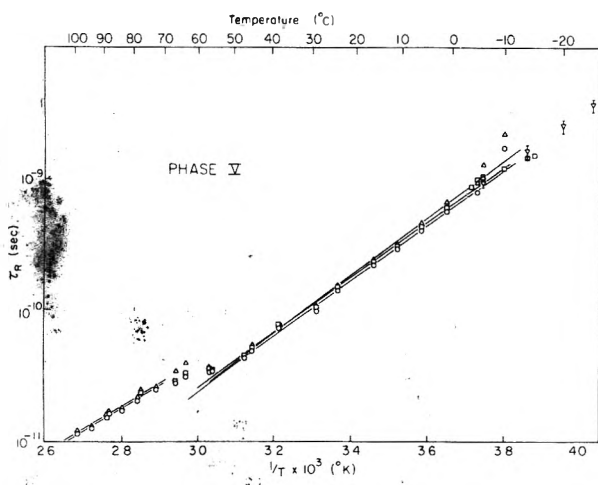


Figure 8. τ_R vs. $1/T$ for PD-Tempone in phase V. The points given by \circ represent the best fit obtainable for an axial potential allowing for anisotropic viscosity. The results for asymmetric potential with (Δ) anisotropic rotation and with (\square) anisotropic viscosity. For anisotropic viscosity, $\tau_R = \tau_{R\perp} = (6R_{\perp})^{-1}$, while for anisotropic rotation, $\tau_R = (6\sqrt{R_{\parallel}R_{\perp}})^{-1}$. The best results for an $\epsilon' \neq 1$ are also the same as \square except for the lower temperatures where they are given by ∇ .

the ratio varies from 0.9 to 0.8. The same sort of behavior was found in I and II in the region where $\omega_0^2\tau_R^2 \sim 1$ and was fit in an ad-hoc manner by changing the spectral density function for the nonsecular terms only. That is, the quantity $E_n(E_n^2 + \omega_0^2)^{-1}$ in eq 2.28 is changed to $E_n/(E_n^2 + \epsilon\omega_0^2) = \tau_R/(1 + \epsilon^2\tau_R^2\omega_0^2)$ where ϵ is an adjustable parameter. Calculated rotational correlation times are shown in Figure 8. The standard deviations for the calculated τ_R are $\leq 3\%$ whereas the average value of ϵ is found to be 4.6 ± 1.7 . The parameter ϵ is believed to be indicative of deviations from the assumption of simple Brownian rotational diffusion due to relatively slowly fluctuating torques that induce the reorientation (cf. section VII). This value of ϵ is comparable to the values found in II for the same radical in several isotropic solvents. Another effect which can cause τ_R^B to be unequal to τ_R^C is anisotropic rotational diffusion. In fact, one may analyze for this in the usual way (I, II) to obtain an $N_y = 3.2 \pm 0.5$, which would imply rotation about the y axis (in the magnetic tensor principal axis system). This alternate explanation conflicts with the observations in II that the motion is virtually isotropic in a variety of isotropic solvents. Thus by comparison with the results in I and II, we favor an $\epsilon = 4.6$ and isotropic motion for PD-Tempone in phase V. [One cannot distinguish between the contributions from the two sources from our present data in the isotropic phase, as there are always contributions from nonsecular terms in the range of τ_R 's available. It was possible, however, to make such a distinction in I and II.]

The isotropic-phase results for the other liquid crystals are similar to those for phase V. Results are plotted in Figures 9–12. Again the τ_R 's are all in the range where nonsecular terms will contribute to the line widths. For the case of Tempone in BEPC the data could only be fit by assuming anisotropic rotation about the y axis and one obtains $N_y = 2.3 \pm 0.6$ for $\epsilon = 4.6$. For the other samples N_y is equal to one within the experimental error for $\epsilon = 4.6$. [It is, of course, possible that the magnetic parameters have been sufficiently altered in BEPC to cause an apparent $N_y \neq 1$, cf. II, but it is not likely since a and a_z are essentially the same for BEPC as for the other solutes, cf. Table I.] In the

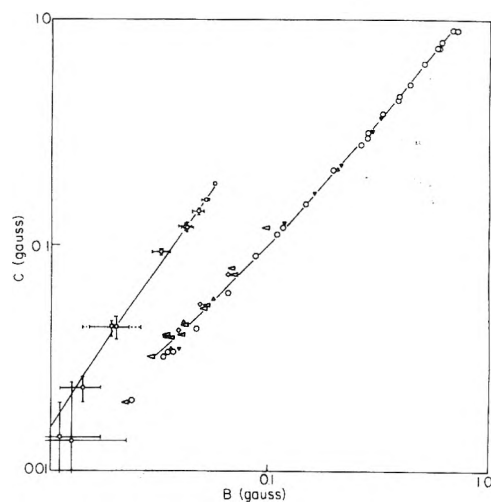


Figure 9. C vs. B for PD-Tempone in several liquid crystals: (\circ) phase IV; (∇) MBBA; (Δ) OH-MBBA; (\square) BOCP; (\diamond) BEPC; (Δ) Tempone in BEPC.

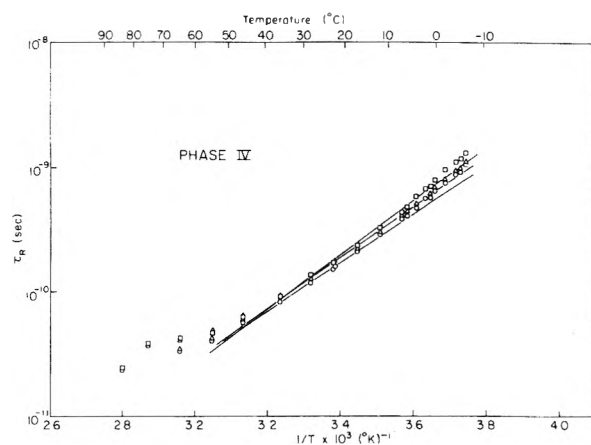


Figure 10. τ_R vs. $1/T$ for PD-Tempone in phase IV. The points given by \circ , Δ , and \square are as given in Figure 8.

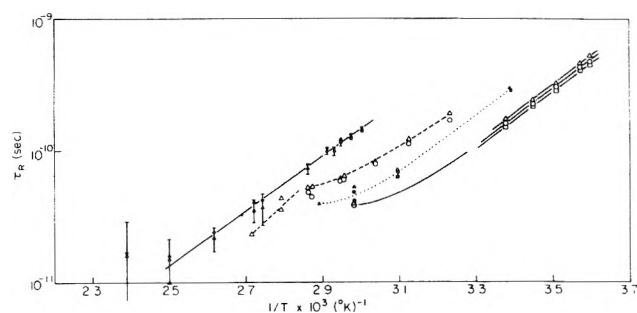


Figure 11. τ_R vs. $1/T$ for PD-Tempone in various nematic solvents. The points \circ , Δ , and \square are for MBBA solvent, but are otherwise defined as in Figure 8. The points \bullet , \blacktriangle , and \blacksquare are equivalently defined, but for OH-MBBA solvent. The dashed line connects the points for BEPC solvent. The small triangles represent the points for BOCP solvent (Δ for $\epsilon = 1$ and ∇ for $\epsilon = 4.6$).

analysis of motional narrowing spectra in the nematic phase, it will be shown that a smaller value of ϵ approximately equal to 2.2 is needed to satisfactorily explain the line width data in the region where nonsecular terms are expected to contribute to the line widths.

(2) *Nematic Phase.* The line width behavior in the

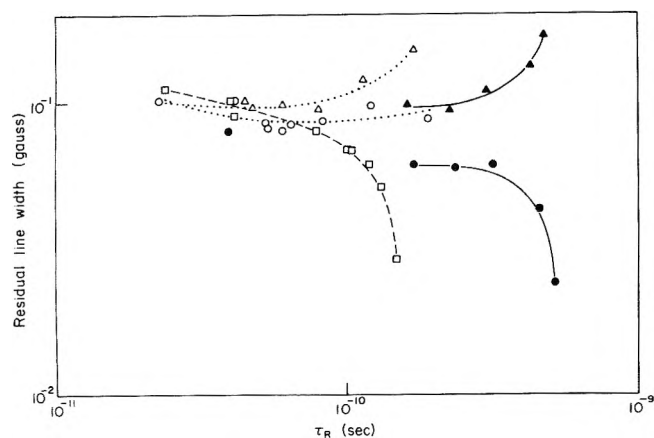


Figure 12. Residual line width A' vs. τ_R for PD-Tempone in a variety of solvents: (—) MBBA, (---) BOCP, and (·····) Tempone in BEPC. The \bullet are MBBA, anisotropic rotation; \blacktriangle are MBBA, anisotropic viscosity; \square are BOCP anisotropic rotation; \circ are BOCP with ϵ' correction; and Δ are Tempone in BEPC.

nematic phase will now be considered. Again we first analyze results for phase V.

The measured A , B , and C for PD-Tempone in the nematic phase of phase V are shown in Figure 8. These results were first analyzed in terms of Brownian rotational diffusion in the presence of an orienting potential. It was first assumed that, except for the orienting potential, the description of the motion should be very similar to that for the isotropic liquid, since the values of τ_R do not change very markedly at the phase transition (cf. Figure 8) nor is the ordering very substantial (cf. Figure 6). Thus we used an $\epsilon \sim 4.6$. When the best single parameter Maier-Saupe potential was used, it was impossible to fit the results, except with a $\tau_R^B \neq \tau_R^C$. However, with the two-parameter potential, one has τ_R^B and τ_R^C more nearly equal. The final adjustment (to the results for $\tau_R \leq 10^{-10}$ sec for $T > 23^\circ\text{C}$) was made by fitting ϵ assuming isotropic rotation under the two-term potential. This yielded $\epsilon = 2.9 \pm 2.4$ (or $\epsilon \sim 2.2 \pm 1.4$ neglecting one result). [Alternatively we could have introduced an anisotropic viscosity factor $\hat{N} = \hat{R}_{\parallel}/\hat{R}_{\perp} = 2.8 \pm 1.3$ to "explain" the C/B ratio with $\epsilon \sim 1$, but with \hat{N} decreasing as the motion slows to $\tau_{R\perp} \sim 10^{-10}$ sec.] Here we let $\tau_R = \tau_{R\perp} = (6\hat{R}_{\perp})^{-1}$ and $\tau_{R\parallel} = (6\hat{R}_{\parallel})^{-1}$. However, for $T < 20^\circ\text{C}$ (or $\tau_R > 2 \times 10^{-10}$ sec) the C/B ratio is increasing suggesting $\tau_R^C > \tau_R^B$. It is possible to "explain" the increase in C/B as due to anisotropic viscosity (which only affects the C term, since (1) only it has pseudosecular contributions and (2) nonsecular terms are already negligible, cf. eq 5 of I). Such an analysis yields the strange result that for $T < 20^\circ\text{C}$, $\tau_{R\perp}$ continues to increase normally (cf. Figure 8) but $\tau_{R\parallel}$ would have to remain virtually constant (i.e., \hat{N} would now be increasing rapidly). An alternative explanation, based on the fact that a similar but weaker effect was observed for PD-Tempone in isotropic glycerol-H₂O solvent (II), is that one must modify the pseudosecular spectral densities to

$$j(\omega_a) = \frac{\tau_R}{1 + \epsilon' \omega_a^2 \tau_R^2}$$

by analogy with the nonsecular corrections; but, in general $\epsilon' > \epsilon$. It was found that $\epsilon' \sim 5$ in glycerol. Our results for PD-Tempone in phase V yield $\epsilon' \sim 20$, provided only the pseudosecular spectral densities are corrected in this fashion and this will be discussed in section VII. [Note that this

TABLE III: Activation Energies and Preexponential Factors for Rotational Relaxation of PD-Tempone Dissolved in Several Liquid Crystal Solvents

Solvent	E_a , kcal/mol	A , sec
Phase V	9.6 ± 0.3	$(1.3 \pm 0.6) \times 10^{-17}$
Phase V (solvent) ^a	8.7	
Phase V (isotropic phase)	8.0 ± 0.6	$(2.2 \pm 1.2) \times 10^{-16}$
Phase IV	8.9 ± 0.2	$(4.4 \pm 1.3) \times 10^{-17}$
Phase IV (solvent) ^a	10.1	
BOCP	9.4 ± 0.3	$(1.5 \pm 0.8) \times 10^{-16}$
MBBA	10.2 ± 0.2	$(7.0 \pm 1.6) \times 10^{-18}$
MBBA (solvent) ^a	11.3, 11.9, 10.5	

^a The result for the twist viscosity coefficient from ref 54.

analysis gives values for τ_R that are very nearly the same as the $\tau_{R\perp}$ obtained from an analysis of anisotropic viscosity.] An alternative explanation in terms of the onset of anisotropic molecular reorientation about the molecular y axis, with N_y increasing from 1 to greater than 2, could also "explain" our observation, but, again, we are loathe to accept such a mechanism which "suddenly appears" as a function of τ_R when there are no phase transitions (cf. I and II). Furthermore, such a prediction ultimately leads to a prediction that the residual line widths A' would tend to become negative at the lower temperatures for this mechanism. Our results for isotropic liquids indicate that A' should be increasing linearly with τ_R for $\tau_R > 10^{-10}$ sec (cf. I and II). These matters are further discussed in section VI, since the anomaly becomes more dramatic as the slow tumbling region is reached.

The activation energy and preexponential factor from the best linear fit (i.e., with the ϵ' correction) of $\log \tau_R$ vs. $1/T$ in Figure 8 are given in Table III. The somewhat different results for the isotropic phase are also given in Table III.

The line width results for B and C for Tempone and PD-Tempone in the other liquid crystalline solvents are shown in Figure 9. One can see that the C/B ratio for PD-Tempone in BOCP is quite different than for the other solvents, and it is slightly changed for BEPC. As noted from the results for the isotropic region, PD-Tempone in BEPC appears to rotate 2.3 ± 0.6 times as rapidly about the molecular y axis than the other two axes (provided the correct magnetic parameters are being used) thus one would expect to see differences in the nematic phase. [No line width data were taken for BOCP in the isotropic phase because PD-Tempone either decayed or distilled out of solvent at the high temperatures $>180^\circ\text{C}$ at which BOCP is isotropic. Note the large errors for B and C in Figure 9 which occur at temperatures $>100^\circ\text{C}$.]

The results for PD-Tempone in phase IV are very similar to those in phase V, and were analyzed in the same manner. One has in Figure 10 graphs of $\log \tau_R$ vs. $1/T$ for the different assumptions of model. One finds isotropic motion within experimental error and $\epsilon' \approx 20$ –25. The activation energy and preexponential factors are given in Table III. They are close to the results for phase V.

As noted, C/B for PD-Tempone in BOCP differs considerably from C/B in all other nematics (cf. Figure 9). The other line width results for this system are given in Figures 11 and 12. We have already noted that the ordering data for PD-Tempone in BOCP could be fit to a Maier-Saupe

potential with the magnetic tensor y axis as the principal axis for orientation. We have used this potential in the line width analysis. All attempts to calculate correlation times using a modified pseudosecular term or an anisotropic viscosity failed. C/B ratios as large as those observed experimentally could not be predicted.⁵⁰ The magnetic parameters used were those given in Table II for PD-Tempone in phase V, but note that a and a_z are equal to within the experimental error for phase V and BOCP. Thus anisotropic rotation (about the molecular y axis) was introduced to analyze the experimental data. The mean value of N_y was 9.4 ± 1.5 . This result is somewhat surprising considering the molecular structure of PD-Tempone. There can be no hydrogen bonding in this system. Other nonbonded interactions between the oxygens in either the nitroxyl groups or carbonyl group in PD-Tempone and the atoms (even the Cl's) in BOCP seem unlikely. However, BOCP is known to form a smectic C state below the nematic phase. Unfortunately, spectra in this smectic phase were indicative of randomization of the director and could not be used to obtain additional information about this system. The observed anisotropic rotation might possibly be due to pretransitional effects; that is, the layered structure characteristic of the smectic mesophase is beginning to form in the nematic phase. One observes the transition to the smectic phase when this layering phenomenon overwhelms the magnetic free energy, and the layers are oriented randomly with respect to the field. In a very strong magnetic field, one might have an ordered smectic, but that was not achieved in the present case. If one is observing pretransitional effects with the PD-Tempone located in the layers, it should be free to reorient about the direction in which it aligns, e.g., the y axis, with diffusion about the other axes more strongly hindered. Note that $\tau_{R\perp} \sim 5.0 \times 10^{-10}$ at 58°C, whereas it is $\sim 4 \times 10^{-11}$ for isotropic rotation in phase V and phase IV at that temperature, which is approximately the value of $\tau_{R\parallel} \sim 4.3 \times 10^{-11}$ observed in BOCP.

Another possibility is that the molecule is rotating slowly enough about the y axis that one must simulate the spectra using the slow-tumbling formalism, but this was ruled out by performing the appropriate simulations. They showed that only slight differences $\sim 3\%$ could be caused between the calculated values of B and C and the experimental values. However these differences can be accounted for by the fact that $\tau_{R\parallel}$ is rapid enough to include some nonsecular contributions to the line widths, and our slow motional program neglects these contributions.

The calculated A' , however, was found to decrease with increasing correlation time, which, as already noted, is not the expected behavior. It was believed that a fully sound analysis of the results should involve fitting an $\epsilon' \neq 1$. Rather than add another adjustable parameter to the analysis of the available data, we have set $\epsilon' \approx 15$, essentially the proper value for phases IV and V. The calculated correlation times are changed by no more than 2%, while $N_y = 9.1 \pm 1.0$ or virtually unchanged. The results are given in Figures 11 and 12. The adjusted A' for $\epsilon' \neq 1$ looks somewhat flatter with τ_R than expected. This may be due to (1) our use of an isotropic spin-rotational formula which may well be inadequate for very anisotropic diffusion in an oriented mesophase and/or (2) the anisotropy in the diffusion has been a little overestimated.

The results on Tempone (and some of PD-Tempone) in BEPC show a slightly larger C/B ratio compared to phases IV and V (cf. Figure 9) as was the case in the isotropic

phases. However, the nematic results fit better to an $N_y = 1.6 \pm 0.2$ vs. 2.3 ± 0.6 for the isotropic phase. We cannot, of course, be certain about such small anisotropies without accurate magnetic parameter measurements in the solvent BEPC. Given, in part, the rather short nematic range for this solvent, no further analysis was made, other than that displayed in Figures 11 and 12.

The liquid-crystal MBBA is one of the most commonly used nematic solvents. Line width results for PD-Tempone in this nematic are given in Figure 9, and are found to be very similar to those in phase IV, cf. Figures 11 and 12 and Table III. The last system studied in the motional narrowing region is PD-Tempone in OH-MBBA. The results in Figure 9 and analysis in Figure 11 indicate it too is rotating isotropically. Not enough data were taken to determine an accurate E_a . In fact this was the only system where the freezing point was not reproducible even for the same sample.

Note that the τ_R vs. $1/T$ behavior shown in Figures 8, 10, and 11 for the different systems differs only slightly if one uses an axially symmetric potential rather than the correct asymmetric potential. However, as we have already noted, the different potentials predict quite different results for the detailed dynamics of asymmetric viscosity about the director. Also, if one has anisotropic rotation about a molecular principal axis, but the molecule is aligned asymmetrically, the axial and asymmetric potentials will give quite different results for the correlation times.

VI. Slow Motional Analysis

In this section the theory developed by PBF for simulating slow tumbling ESR line shapes in an anisotropic solvent is applied to the analysis of ESR spectra in the nematic phase.

One must use a slow motional approach, such as that of the stochastic Liouville method, to explain ESR spectra when the motional narrowing theories break down. For isotropic solvents, this occurs when the lines start to become asymmetric and/or the splitting constants begin to deviate from a constant value. In the liquid crystalline phases, however, splitting constant deviations are also due to change of ordering with temperature. Also, one may have asymmetric lines in the motional narrowing region if there is a static distribution of director orientations in liquid crystals. In the previous section the slow motional region was considered to begin when the ordering parameter curve begins to deviate from a smooth curve (nearly linear) when plotted against the reduced temperature T^* as shown in Figures 4 and 6. This begins to occur when the two "observed" splitting constants for the three line nitroxide spectrum became unequal. The two splitting constants should not be exactly equal because of the nonsecular corrections discussed in section II. However the effects observed are much larger than those predicted for nonsecular shifts and also of the wrong sign. In all the nitroxides studied it was noted that a_{01} became less than a_{-10} as the temperature was decreased. This is shown in Table IV for PD-Tempone. [For PD-Tempone, a_{-10} remains nearly constant whereas for the other systems a_{-10} decreases as the temperature decreases. Some g -value measurements performed on PD-Tempone in phase V in this region showed that observed g values began to decrease with decreasing temperature instead of increasing as they had throughout the motional narrowing region.] Thus one should try to fit these effects plus the line width asymmetry (in the absence of di-

TABLE IV: Dynamic Frequency Shifts and Calculated Residual Line Widths for PD-Tempone in Phase V

T, C	τ_R , nsec	Calcd													
		Exptl. $G^{a,b}$		A^c		B^d		C^e		D^f		A', G			
		$\Delta S_{1,0}$	$\Delta S_{0,-1}$	$\Delta S_{1,0}$	$\Delta S_{0,-1}$	$\Delta S_{1,0}$	$\Delta S_{0,-1}$	$\Delta S_{1,0}$	$\Delta S_{0,-1}$	$\Delta S_{1,0}$	$\Delta S_{0,-1}$	A^c	B^d	C^e	D^f
-6	0.94	-0.03	-0.23	0.00	-0.15	-0.10	-0.33	-0.13	-0.13	-0.03	-0.23	0.60	0.57	0.65	0.5
-14	1.6	+0.07	-0.61	0.09	-0.61	-0.26	-0.66	-0.16	-0.66	-0.16	-0.66	1.0	0.85	-0.15	0.9
-20	2.5	+0.14	-1.35	0.03	-1.27	-0.26	-1.27	-0.07	-1.42	-0.22	-1.47	1.45	1.35	-0.35	1.7
-25	3.6	+0.17	-2.58	-0.21	-2.01	-0.41	-1.51	-0.61	-2.21	-0.51	-2.71	1.75	1.75	-0.4	2.25

^a $\Delta S_{1,0}$ is the difference in shift between the low-field and center lines. $\Delta S_{0,-1}$ is the difference between the center and high-field lines. A positive (negative) ΔS means an apparent increase (decrease) in splitting compared to $\langle a_N \rangle$, which is extrapolated from the higher temperature (a_N), see text. ^b A typical higher temperature result is at +1°C: $\Delta S_{1,0} = -0.01$, $\Delta S_{0,-1} = +0.01$. ^c Calculated with ϵ' (sec) = 1.2, ϵ' (psec) = 19. ^d Calculated with ϵ' (sec) = 4.6, ϵ' (psec) = 15.0. ^e Calculated with ϵ' (sec) = ϵ' (psec) = 1.0. ^f Calculated with anisotropic viscosity model.

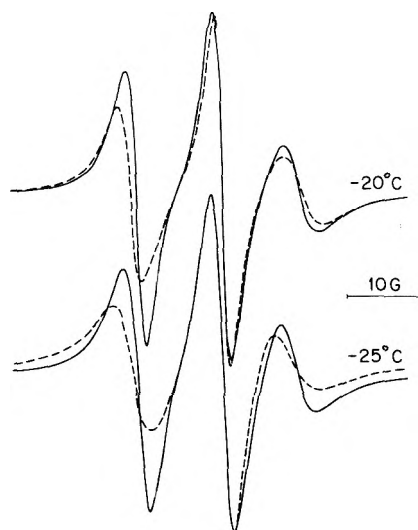


Figure 13. Comparison of experimental and simulated spectra in the incipient slow-tumbling region for PD-Tempone in phase V: (---) experimental result; (—) theoretical result based on isotropic Brownian diffusion with $\tau_R = 2.5 \times 10^{-9}$ sec at -20°C , and $\tau_R = 3.6 \times 10^{-9}$ sec at -25°C ($A' = 0$ G).

rector effects) in the simulation of slow motional spectra in the nematic phase.

The system chosen for a careful slow motional analysis was PD-Tempone in phase V, because it had the largest region of deviation of the splitting constants from near equality, and a thorough study of the motional narrowing region over a long temperature range had been obtained as discussed in the previous section. There, it was shown that PD-Tempone rotates isotropically, but anomalous line width behavior sets in for $\tau_R \geq 2 \times 10^{-10}$ sec. Slow motional type simulations were performed for the spectra taken at 1°C (where $\tau_R = 6 \times 10^{-10}$ sec). The results of this analysis were identical with those from the motional narrowing analysis demonstrating that the anomalous line width behavior is not simply due to the onset of slow tumbling. One finds, from Table IV, that slow-tumbling effects begin to become important for $\tau_R \geq 0.8 \times 10^{-9}$ sec.

We show experimental slow tumbling spectra in Figure 13. The simulated spectra shown in that figure were from the PBF theory using values of λ and ρ extrapolated from Figure 6 to the appropriate temperature with τ_R similarly obtained from Figure 8 for isotropic rotational diffusion. The agreement in Figure 13 is rather poor. This agreement

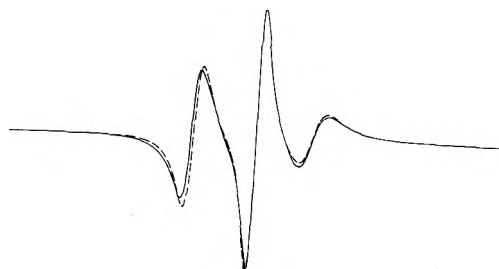


Figure 14. Comparison of experimental (---) and theoretical spectra (—) for PD-Tempone in phase V at -20°C for anisotropic viscosity with $\tau_{R\perp} = 0.05$ nsec is assumed and $\tau_{R\parallel} = 2.5$ nsec ($A' = 1.8$ G).

can be improved by introducing an anisotropic viscosity (cf. section V), but the best fits here suggest that $\tau_{R\parallel}$ must be decreasing with decreasing temperature! (In particular at -20°C one gets $\tau_{R\perp}/\tau_{R\parallel} \approx 50$, cf. Figure 14, while at -25°C one would need a negative $\tau_{R\perp}$.) Such a result appears to be further demonstration of the invalidity of explaining the anomalies in terms of simple anisotropic viscosity. An anisotropic diffusion mechanism is even less successful in "explaining" the anomaly (it requires negative residual widths, N_y increasing with decreasing temperature, e.g., $N_y = 3.5$ at -20°C and the agreement is not satisfactory). In both cases, furthermore, one is postulating the sudden onset of anisotropy at a stage when the spectrum is undergoing drastic changes (incipient slow motion) although the liquid crystal exhibits no phase transitions. Again this is taken as clear evidence for the invalidity of such an analysis. In I and II, it was shown that slow-tumbling spectra are particularly sensitive to the reorientational model, i.e., whether the molecule reorients by small (Brownian) or large angle jumps. We show in Figure 15 model-dependent spectra simulated as described by PBF. It is clear that model dependence has only a small effect compared to the anomalous behavior.⁵¹

It was then decided to introduce the fluctuating torque model discussed in II and in the next section, wherein an $\epsilon' > 1$ is introduced to account for moderately slowly fluctuating torques. Various attempts are shown in Figures 16–18. It is clear that the spectra cannot be fit with a single ϵ' , the best fits being obtained for $\epsilon'_{\text{sec}} \sim 1-2$ and $\epsilon'_{\text{psec}} \sim 15-20$ (cf. Figure 18). The main virtue of this analysis is that one is able to use a single set of parameters for all temperatures to achieve reasonable fits. Summaries of the effects of this analysis on the predictions of C vs. B and A vs. τ_R are given in Figures 19 and 20.

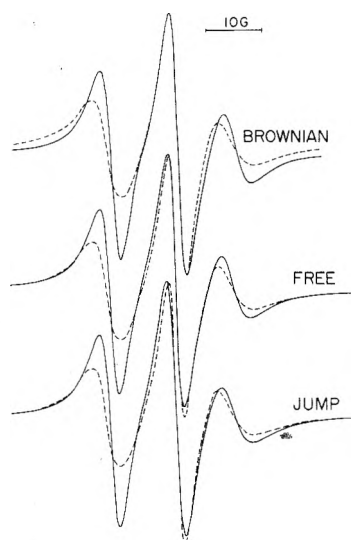


Figure 15. Model dependence and a comparison of experimental (----) and theoretical spectra (—) for PD-Tempone in phase V at -25°C and isotropic rotation with $\tau_R = 3.6 \times 10^{-9}$ sec ($A' = 0$ G). Free diffusion, an approximate inertial model, gives results equivalent to moderate jump diffusion; while the result labeled jump is for strong jump diffusion, cf. ref 2 and 4.

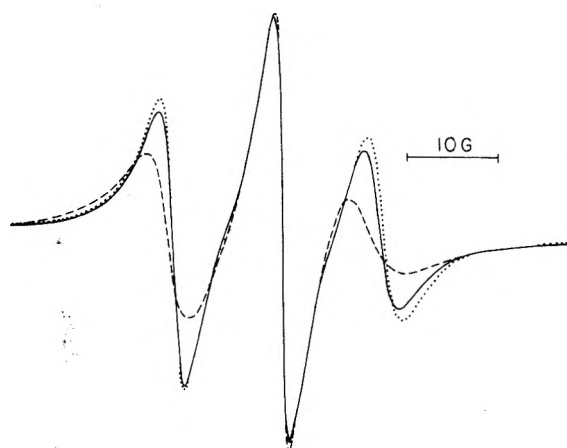


Figure 16. Effects of ϵ' and a comparison of experimental (----) and theoretical spectra for PD-Tempone in phase V at -25°C using a single ϵ' where (—) is for $\epsilon' = 4.6$ ($A' = 1.05$ G) and (----) is for $\epsilon' = 9.4$ ($A' = 1.6$ G). In both cases $\tau_R = 3.8$ nsec.

The implications of these fits are discussed in the next two sections.

VII. Fluctuating Torque Analysis

In II, a detailed discussion was given of a simple dynamic molecular model involving relatively slowly fluctuating torques, and inertial effects only in very lowest order, which appeared to offer a unified explanation to the relaxation anomalies such as the ϵ , $\epsilon' \neq 1$. The existence of $\epsilon' \sim 15\text{--}20 \gg 1$ in this work again requires that one take cognizance of effects from a careful analysis of molecular dynamics in liquids. In the present case, one has the feature of a highly structured liquid in which the nitroxide probe is dissolved. One may give a general statistical mechanical analysis for the rotational motion of the nitroxide probe (labeled B particle), and obtain a generalized Fokker-Planck equation:¹⁶

$$\left[\frac{\partial}{\partial t} + i\omega_B \cdot \mathbf{J}_B + \hat{\mathbf{L}}_B \cdot (\nabla_L)_B + \langle \mathbf{N}_B \rangle \cdot (\nabla_L)_B \right] f_B(t) = (\nabla_L)_B \cdot \int_0^t d\tau \mathbf{G}(t - \tau) \cdot [\omega_B/kT + (\nabla_L)_B] f_B(\tau) \quad (7.1)$$

In eq 7.1, ω_B is the angular velocity of the B particle, \mathbf{L}_B its angular momentum, $\mathbf{J}_B = -i\mathbf{r}_B \times (\nabla_r)_B = -\mathbf{M}$ (cf. eq 2.3–2.4), $\hat{\mathbf{L}}_B \cdot (\nabla_L)_B$ is the precessional term, and $\langle \mathbf{N}_B \rangle$ is the mean-field torque, experienced by the B particle and is equivalent to \mathbf{T} of eq 2.6. The quantity $\mathbf{G}(t)$ is the operator equivalent of the correlation function for the fluctuating or random torques on the B particle. When the assumption is made that angular momentum relaxation occurs very rapidly, then it is possible to introduce a coarse graining in time interval such that the angular momentum is at its

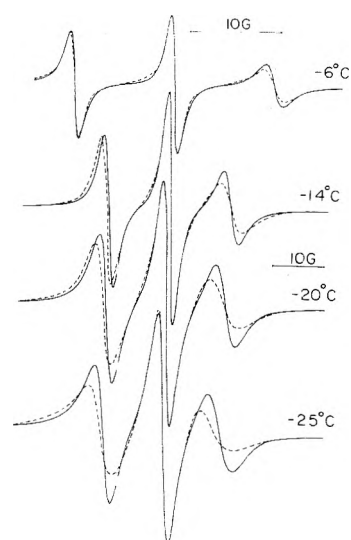


Figure 17. Comparison of experimental (----) and theoretical (—) spectra for PD-Tempone in phase V utilizing $\epsilon'_{\text{sec}} = 4.6$, $\epsilon'_{\text{psec}} = 15$. The values at -6 , -14 , -20 , -25°C are for τ_R 0.9, 1.6, 2.5, 3.6 nsec, respectively, and for A' 0.5, 0.85, 1.25, 1.75 G, respectively.

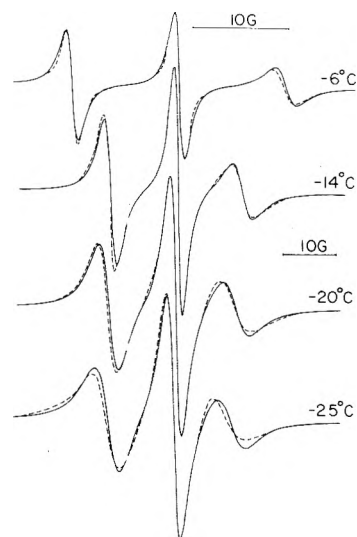


Figure 18. Comparison of experimental (----) and theoretical (—) spectra for PD-Tempone in phase V utilizing $\epsilon'_{\text{sec}} = 1.2$, $\epsilon'_{\text{psec}} = 20$. The values at -6 , -14 , -20 , -25°C are for τ_R 0.9, 1.6, 2.5, 3.6 nsec, respectively, and for A' 0.55, 1.0, 1.45, 1.75 G, respectively.

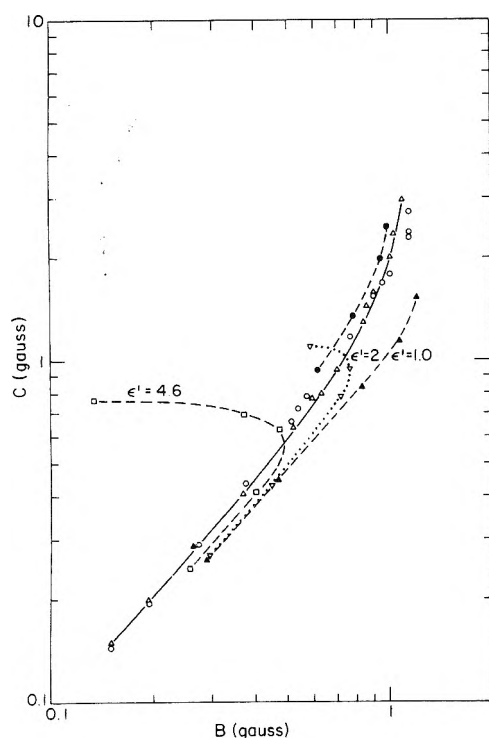


Figure 19. Predictions of C vs. B for PD-Tempone in phase V. The experimental values are given by (O). The predictions for different values of ϵ' are as noted on the figure. The solid curve (and points Δ) correspond to $\epsilon'_{\text{sec}} = 1.2$ and $\epsilon'_{\text{psec}} = 20$.

thermal equilibrium distribution, while the B particle has not appreciably reoriented, nor have the fluctuating components of the torque which are effective in causing the reorientation necessarily relaxed.

In this limit, one may expect to obtain a Smoluchowski-type expression for the reorientational relaxation of the B particle. This limit has been discussed in detail, and one may obtain the result:¹⁶

$$\frac{\partial P(\Omega, t)}{\partial t} = \int_0^t d\tau i\mathbf{J}_B \cdot \mathbf{R}(t - \tau) \cdot \left[i\mathbf{J}_B - \frac{\langle \mathbf{N}_B(t, \Omega) \rangle}{kT} \right] P(\Omega, \tau) \quad (7.2)$$

where the Fourier-Laplace transform of $\mathbf{R}(t)$ is defined by

$$\mathbf{R}[s] = (kT)^2 \mathbf{K}^{-1}[s] \quad (7.3)$$

and $\mathbf{K}(t)$ is a simplified, torque correlation function of only Ω_B and t given by the average:

$$\mathbf{K}(t) \equiv \langle \mathbf{R}_B(t = 0) \mathbf{R}_B(t) \rangle \quad \text{where } \mathbf{R}_B = \mathbf{N}_B - \langle \mathbf{N}_B \rangle \quad (7.4)$$

over a canonical ensemble of solvent molecules (in the presence of the potential field of the B particle). There is, however, a simplifying assumption in obtaining eq 7.2, viz. that $\mathbf{K}(t)$ should be characterized by a relaxation time τ_M (or spectrum of times) such that $\tau_M \lesssim \tau_R$; i.e., the fluctuating torque components relax in times not long compared to the reorientation time of the B particle. It is then still possible to include any slowly relaxing torques into a redefined time dependent $\langle \mathbf{N}_B(t, \Omega_B) \rangle$ in eq 7.2 such that $\mathbf{R}(t) \rightarrow 0$ in times t over which $\langle \mathbf{N}_B(t, \Omega_B) \rangle$ changes negligibly. [However, $\mathbf{N}_B(t, \Omega_B)$ will then still be a function of those local

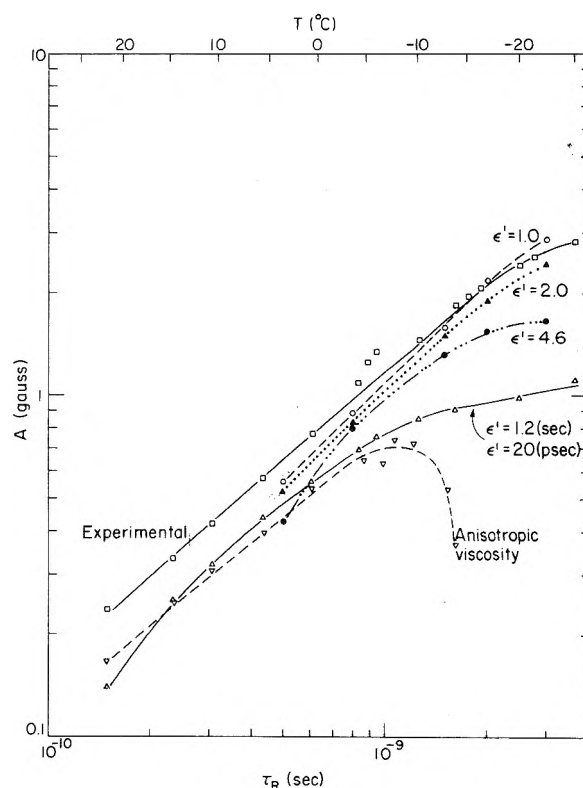


Figure 20. Predictions of A vs. τ_R for PD-Tempone in phase V for different values of ϵ' as noted on the figure. The calculated values are due to \mathbf{g} tensor and dipolar contributions. The experimental values are represented by the points (\square) and the solid line through them.

coordinates and orientations representing the slowly relaxing solvent modes.] Thus the effects of the fluctuating torques are separated into two parts for simplicity: the faster components, which induce the diffusive-type reorientations, and the more persistent components, which represent systematic local torque effects over time scales greater than τ_R , but will average out in times $\tau_X \gg \tau_R, \tau_M$. Fluctuating torque components of order of τ_R will contribute both types of effects, but, because of the greater complexity of their analysis, they are implicitly included in the two limiting types. Our analysis in II for isotropic liquid solvents was based on the model of eq 7.2 where $\langle \mathbf{N}_B(\Omega_B, t) \rangle = 0$. The observation there of $\epsilon, \epsilon' \sim 4$ or 5, corresponds to $\tau_M \sim \tau_R$ and is thus probably at the limit of validity of ascribing the "slowly fluctuating-torques" to $\mathbf{R}_B(t)$. The results in the present work requiring $\epsilon' \sim 15$ –20, as well as the existence of a time-dependent mean-field $\langle \mathbf{N}_B(\Omega_B) \rangle \neq 0$, suggest that this concept of slower fluctuating torque components characterized by a τ_X may well be significant.

Clearly, a complete description of the molecular dynamics is not possible, so we use the above approach to analyze our results. We first discuss the analysis in terms of which the anomalous ϵ' is ascribed to $\mathbf{R}(t)$. Then we discuss a simple limiting model in terms of a τ_X that is suggested by the highly structured properties of liquid crystals. Also, there exists a hydrodynamic model for cooperative fluctuations in the director due to deGennes⁴⁴ and applied to NMR by Pincus.¹⁷ Such long-range hydrodynamic modes are naturally included in an $\langle \mathbf{N}_B(\Omega_B, t) \rangle$ where the time-dependent part of $\langle \mathbf{N}_B \rangle$ is characterized by persistence times $\tau_q \gg \tau_R$. The application of this model to our ESR results is dis-

cussed in the Appendix where it is shown (1) to have negligible predicted effect on our results and (2) to predict spectral anomalies that are qualitatively in the opposite direction to the anomalies observed in the present work.

A. *Fluctuating Torques Inducing Reorientation.* This is the model used in II, but now applied to a liquid crystalline solvent for which

$$\langle N_B \rangle \neq 0 \quad (7.5)$$

We assume an exponentially decaying $\mathbf{K}(t) \equiv IkTV^2e^{-t/\tau_M}$ so that the Fourier-Laplace transform of eq 7.2 becomes (for isotropic rotational diffusion):

$$\{s - R(s)[+J_B^2 + iJ_B\langle N_B \rangle/kT]\}P(\Omega, s) = P(\Omega, t = 0) \quad (7.6)$$

where $s = -i\omega$ and

$$R(\omega) = \frac{kT}{IV^2}(-i\omega + \tau_M^{-1}) \quad (7.7a)$$

so

$$R(0) = kT/IV^2\tau_M \quad (7.7b)$$

One must then diagonalize $\Gamma \equiv J_B^2 - iJ_B\langle N_B \rangle/kT$ as previously discussed (cf. PBF) in order to obtain the normal modes of relaxation for the particle. It is first advantageous to symmetrize this operator to $\bar{\Gamma}$ (cf. eq 2.8a). The normal modes for $\bar{\Gamma}$ will, in general, be linear combinations of the $D_{KM}^L(\Omega) \times [(2L+1)/8\pi^2]^{1/2}$ which we write as $u_{KM}^L(\Omega)$. Since the $u_{KM}^L(\Omega)$ form a complete orthonormal set we may write

$$P(t=0) = \delta(\Omega - \Omega_0) = \sum_{L',K',M'} u_{K'M'}^{L'}(\Omega_0) u_{K'M'}^{L'}(\Omega) \quad (7.8)$$

with the result for the conditional probability of

$$P(\Omega_0, \Omega, s) = \sum_{L',K',M'} u_{K'M'}^{L'}(\Omega_0) u_{K'M'}^{L'}(\Omega) [s + E_{K'M'}^{L'} R_L(s)]^{-1} \quad (7.9)$$

where the $E_{K'M'}^{L'}$ are the eigenvalues of $J_B^2 + iJ_B\langle N_B \rangle/kT$ corresponding to eigenfunctions $u_{K'M'}^L(\Omega)$. These results may be used in the motional narrowing analysis of PBF to give modified spectral density functions, i.e., we now get

$$K_{ab}(s) = \sum_{n \neq 0} \langle u_0(\Omega) | f_a(\Omega) | u_n(\Omega) \rangle \langle u_n(\Omega_0) | f_b(\Omega_0) | u_0(\Omega_0) \rangle / [s + E_{K'M'}^{L'} R_L(s)] \quad (7.10)$$

where $K_{ab}(s)$ is the Fourier Laplace transform of the correlation function of $f_a(t)$ and $f_b(t)$ [cf. section IV of PBF for a more detailed discussion].

One finds that the only change over the motional narrowing theory used in the previous sections is the inclusion of $R(\omega)$ given by eq 7.7. One can also introduce anisotropic diffusion and/or anisotropic viscosity and solve in an analogous manner. In particular, in the latter case, one recovers the old results (cf. eq 2.20) but with

$$\hat{R}_\parallel(\omega) \equiv \hat{R}_\parallel(0)[1 - i\omega\hat{\tau}_{M,\parallel}^{-1}] \quad (7.11a)$$

$$\hat{R}_\perp(\omega) \equiv \hat{R}_\perp(0)[1 - i\omega\hat{\tau}_{M,\perp}^{-1}] \quad (7.11b)$$

i.e., different parallel and perpendicular components of $\hat{R}(0)$ and, in general, different relaxation times for the associated fluctuating torque correlation functions.

The slow tumbling spectra may be analyzed by writing the time-dependent Smoluchowski eq 7.2 in its spin-dependent form,^{4,16} i.e., as a time-dependent SLE. Since this

poses some difficulties in its solution,⁴ we transform to a time-independent augmented SLE in which a specific Markovian model for the fluctuating torques is explicitly included so as to yield results equivalent to the time-dependent SLE, i.e., V and τ_M have the same meaning. The appropriate method is discussed in Appendix D of II, except that here (1) the analysis is based upon the $u_{KM}^L(\Omega)$ rather than the $D_{KM}^L(\Omega)$, (2) $\gamma_L^2 = L(L+1)kT/I$ is then replaced by $E_{K'M'}^{L'}kT/I$, and (3) $\hat{R}_\parallel(0)\hat{\tau}_{M,\parallel} = kT/IV_\parallel$, $\hat{R}_\perp(0)\hat{\tau}_{M,\perp} = kT/IV_\perp$. This is the approach utilized in analyzing the slow-tumbling (and motional narrowing) spectra in sections VI and V. In particular, for $\hat{R}_\parallel(0) = \hat{R}_\perp(0) = R$ and $V_\parallel = V_\perp = V$ one has $\epsilon'_{L'} = [1 + E_{K'M'}^{L'}kT/IV^2]^2$ independent of K' and M' . When $V_\parallel \neq V_\perp$ the precise definitions of $\epsilon'_{L'K'M'}$ become more complex. However, $\epsilon'_{\text{sec}} \equiv \epsilon'_{2,0,0}$ and $\epsilon'_{\text{psec}} \equiv \epsilon'_{2,0,1}$ are given as the actual corrections needed to adjust the spectral densities: i.e., $j_{L'K'M'}(\omega) = \hat{R}_\perp(0)E_{K'M'}^{L'} / \{[\hat{R}_\perp(0)E_{K'M'}^{L'}]^2 + \epsilon'_{L'K'M'}\omega^2\}$ (e.g., for zero ordering but still anisotropic viscosity: $\epsilon'_{\text{sec}} = (1 + 6\hat{\tau}_{M,\perp}\hat{R}_\perp(0))^2$ and $\epsilon'_{\text{psec}} = (1 + 5\hat{\tau}_{M,\perp}\hat{R}_\perp(0) + \hat{\tau}_{M,\parallel}\hat{R}_\parallel(0))^2$ and these expressions are useful, though no longer exact, for low ordering).

The values $\epsilon'_{\text{psec}} \sim 15-20$ and $\epsilon'_{\text{sec}} \sim 1-2$ that were found would then have to imply that $V_\parallel^2 < V_\perp^2$ (with $\hat{\tau}_{M,\parallel} > \hat{\tau}_{M,\perp}$ for $\hat{R}_\parallel \sim \hat{R}_\perp$), i.e., the torques inducing reorientation about the axis parallel to the director are rather weak compared to the more normal torques inducing reorientation perpendicular to the director. This would seem to be a reasonable result for a small probe dissolved in a liquid crystal. However, if this were the case, it would be surprising to have $\hat{R}_\parallel(0) \sim \hat{R}_\perp(0)$ as appears to be the case from the experimental analysis. One would require that $V_\parallel^2\tau_{M,\parallel} \sim V_\perp^2\tau_{M,\perp}$. Lastly, we note that $\epsilon'_{\text{psec}} \sim 15-20$ appears to be too large to justify the frequency-dependent diffusion coefficient analysis.

An analogous analysis can, of course, be made in terms of anisotropic diffusion involving $R_\parallel(0)$, $R_\perp(0)$, $\tau_{M,\parallel}$, and $\tau_{M,\perp}$ (cf. ref 16), and this would have the feature of being independent of the macroscopic ordering with respect to the magnetic field, but it would depend on the molecular symmetry.

B. *Fluctuations in the Local Structure Parameter.* We now consider the case when eq 7.2 may be written as

$$\frac{\partial P(\Omega, t)}{\partial t} = iJ_B \cdot \mathbf{R}(\Omega, t) \cdot [iJ_B - \langle N_B(t, \Omega) \rangle / kT] P(\Omega, t) \quad (7.12)$$

That is, we neglect any "memory" in \mathbf{R} , and we assume that it is possible to diagonalize \mathbf{R} in either a body-fixed or laboratory-fixed basis such that it is time-independent.^{16,24} However, we let

$$\langle N_B(t, \Omega) \rangle = \mathbf{T} + \mathbf{T}'(t, \Omega) \quad (7.13)$$

where \mathbf{T} is the true mean field component and \mathbf{T}' is a slowly fluctuating time-dependent component with relaxation time τ_X such that $\tau_X \gg \tau_R$.

This means that $\langle N_B(t, \Omega) \rangle$ remains essentially constant over time intervals in which the reorientation of the B particle occurs. Thus we may regard \mathbf{T}' as quasistatic, and calculate an ESR line shape due to the combined effects of $\mathbf{T} + \mathbf{T}'$. We shall for the present simple model assume no relation between \mathbf{T} and \mathbf{T}' , so that \mathbf{T}' could also just as well apply to a structured isotropic liquid. Thus $\langle \mathbf{T}' \rangle = 0$ will imply an isotropic distribution of local structure (or order) parameter. This is not an unreasonable model for PD-Tempone which is only weakly ordered in liquid crystals.⁵² [The

other limit, where \mathbf{T}' is due to cooperative fluctuations in the static director is discussed in the Appendix as already noted. A related discussion is given for the local director model when \mathbf{T}' is a small perturbation on \mathbf{T} .]

It is then, in principle, necessary to solve the diffusion equation under the combined torque $\mathbf{T} + \mathbf{T}'$, but we shall assume both $|\mathbf{T}|, |\mathbf{T}'| \leq kT$ and approximate their effects on the spin relaxation as being additive. Thus, we now consider the case $|\mathbf{T}| = 0, |\mathbf{T}'| \neq 0$. We may now speak of a "local director" oriented by Euler angles Ψ relative to the laboratory z axis, and a local order or structure parameter

$$S_1 = \langle \mathcal{D}_{00}^2(\Omega) \rangle \quad (7.14)$$

for the PD-Tempone relative to this local director (we shall assume axial symmetry of the molecular ordering tensor for simplicity). We first calculate the resonant frequencies and line widths in the motional narrowing region for arbitrary Ψ . Then this result is averaged over an isotropic "reorientation" of Ψ with the rather slow relaxation time τ_X .

The first stage of the calculation is equivalent to that of calculating the resonance frequencies and line widths for a "smectic" liquid crystal in which the director is tilted by Ψ from the laboratory z axis.^{8,9} Therefore we have

$$\bar{\mathcal{K}} = \mathcal{K}_0 + \bar{\mathcal{K}}_1(\Psi) \quad (7.15)$$

where $\bar{\mathcal{K}}_1(\Psi)$ is the average over Ω of $\mathcal{K}_1(\Omega, \Psi)$ given by eq 2.1, so

$$\bar{\mathcal{K}}_1(\Psi) = \sum_{\mu, m} S_1 \mathcal{D}_{0m}^2(\Psi) F'_{\mu,1}{}^{(2,0)} A_{\mu,1}{}^{(2,m)} \quad (7.16)$$

Similarly, one may calculate the Ψ -dependent line width $T_2^{-1}(\Psi)$ ^{8,9,12} analogous to eq 2.29–2.31, where, however, the effect of $\Psi \neq 0$ in eq 2.1 is taken into account. In particular, for $\Psi = (0, \theta, \phi)$, and axial symmetry about the director, one obtains the results that eq 2.30–2.31 are again appropriate but with $K = K'$ and the $\mathbf{K}(L, K, M, \omega)$ are replaced by $\hat{\mathbf{K}}(L, K, M, \omega, \theta)$ given by:

$$\hat{K}(2, K, 0, \omega, \theta) = 1/5 D_k + 2/7 P_2(\cos \theta) E_k + 6/35 P_4(\cos \theta) F_k \quad (7.17a)$$

$$\hat{K}(2, K, 1, \omega, \theta) = 1/5 D_k + 1/7 P_2(\cos \theta) E_k - 4/35 P_4(\cos \theta) F_k \quad (7.17b)$$

$$\hat{K}(2, K, 2, \omega, \theta) = 1/5 D_k - 2/7 P_2(\cos \theta) E_k + 1/35 P_4(\cos \theta) F_k \quad (7.17c)$$

with

$$D_k = K(2, K, 0, \omega) + 2K(2, K, 1, \omega) + 2K(2, K, 2, \omega) \quad (7.18a)$$

$$E_k = K(2, K, 0, \omega) + K(2, K, 1, \omega) - 2K(2, K, 2, \omega) \quad (7.18b)$$

$$F_k = 3K(2, K, 0, \omega) - 4K(2, K, 1, \omega) + K(2, K, 2, \omega) \quad (7.18c)$$

Now these results are averaged over the slower motion that averages out Ψ . Thus $\bar{\mathcal{K}} = \mathcal{K}_0$ predicts the isotropic liquid resonance frequencies, while

$$\overline{\hat{K}(2, K, 0, \omega, \theta)} = \overline{\hat{K}(2, K, 1, \omega, \theta)} = \overline{\hat{K}(2, K, 2, \omega, \theta)} = 1/5 D_k \quad (7.19)$$

As long as $S_1 \neq 0$, one finds that $1/5 D_k$ is *unequal* to the isotropic result of eq 2.32. In particular, for $\omega = 0$, one has a simple power series expression for the $\mathbf{K}(2, K, M, 0)$ given by

Polnaszek⁸ that is valid for $S_1 < 0.8$. One then finds that

$$D_0(\omega = 0) \approx [1 + 0.16S_1 - 2.29S_1^2 + 0.934S_1^3] \tau(0)^{-1} \quad (7.20a)$$

and

$$D_2(\omega = 0) [1 + 0.052S_1 + 0.264S_1^2 - 0.177S_1^3] \tau(2)^{-1} \quad (7.20b)$$

Thus the local structure factor $S_1 \neq 0$ tends to lead to differences between the "effective" $\tau(0)^{-1}$ and $\tau(2)^{-1}$. The effect is small for small $S_1 \sim 0.1$ but becomes significant for larger S_1 , where it has the same observable effect as an $R_{\parallel} > R_{\perp}$ for positive S_1 . However, the averaging of the Ψ -dependent parts of $\bar{\mathcal{K}}(\Psi)$ and $T_2^{-1}(\Psi)$ is not very fast. One can then expect residual broadening and frequency shift effects to ensue from this mechanism. In general, this problem can be treated as a slow-tumbling problem by means of the SLE. That is, one may write (cf. eq 2.4 of PBF)

$$\sum_j [\omega \delta_{i,j} + \bar{\mathcal{K}}(\Psi)_{i,j}^x - iT_2^{-1}(\Psi)_{i,j}] Z(\Psi, \omega)_j = (1/2) \omega_1 [S_1^x \rho_0]_i \quad (7.21)$$

where $\text{Im } Z(\Psi, \omega)_j$ refers to the absorption at orientation Ψ for the j th allowed or forbidden transition. Also $\bar{\mathcal{K}}(\Psi)_{i,j}^x$ refers to the matrix element between the i th and j th transitions for the commutator form of $\bar{\mathcal{K}}(\Psi)$. The diagonal $T_2^{-1}(\Psi)_{i,i}$ correspond to the line widths for the i th transition and are given by eq 2.30–2.31 and 7.17 for the three allowed transitions. The other $T_2^{-1}(\Psi)_{i,i}$ as well as the "off-diagonal" components $T_2^{-1}(\Psi)_{i,j}$ ($i \neq j$) may be obtained by the methods already outlined here, in PBF, and by Freed and Fraenkel.⁵³ One then expands the $Z(\Psi, \omega)_j$ in the complete orthonormal set of spherical harmonics $Y_m^0(\theta, \phi)$ and solves for the coefficient of $Y_0^0(\theta, \phi)$.^{14,15}

We now assume for simplicity that (1) motional narrowing theory applies to averaging Ψ as well as to Ω , (2) the local ordering is small, and (3) the relaxation of $Y_m^2(\theta, \phi)$ is governed by relaxation time τ_X . Then we may obtain an approximate result by retaining only the residual width component from the incomplete averaging of $\bar{\mathcal{K}}_1(\Psi)$ and neglect the higher order width components from Ψ -dependent parts of $T_2^{-1}(\Psi)_{i,j}^{-1}$ (we are also neglecting for simplicity the mainly dynamic frequency shift terms that arise from cross terms between $\bar{\mathcal{K}}_1(\Psi)$ and $T_2^{-1}(\Psi)_{i,j}^{-1}$). The final result, which is really for isotropic liquids, but with a dynamical structure, then takes on a simple result. It is, in fact, represented by the basic expression for isotropic liquids given by eq 5 of I except for the simple modifications that

$$j_0(\omega) = \frac{\tau(0)}{1 + \omega^2 \tau(0)^2} \rightarrow \left[D_0(\omega) + \frac{S_1^2 \tau_X}{1 + \omega^2 \tau_X^2} \right] \quad (7.22a)$$

and

$$j_2(\omega) = \frac{\tau(2)}{1 + \omega^2 \tau(2)^2} \rightarrow D_2(\omega) \quad (7.22b)$$

where, when $\omega \tau_R \ll 1$, $D_k(\omega)$ is well represented by $D_k(0)$ given by eq 7.20 (or by eq 4.16 of PBF⁵⁴ and eq 7.18 when the frequency dependence applies). These results are based on a simple exponential relaxation law of the local structure. This is clearly an oversimplification for a liquid crystal where one would expect to have (localized) cooperative modes of rotation yielding more complex frequency dependences (cf. Appendix). The results eq 7.22 still exhibit a more complex ω dependence than the conventional expres-

sions for isotropic liquids. In particular, recognizing that we have $\tau_X \gg \tau_R$, then we may have $\omega^2 \tau_R^2 \ll 1$, while we may have $\omega^2 \tau_X^2 \geq 1$, so that eq 7.22 becomes

$$j_0(\omega) \approx \tau_R(1 + 0.16S_1 - 2.29S_1^2) + S_1^2 \tau_X / [1 + \omega^2 \tau_X^2] \quad (7.23a)$$

and

$$j_2(\omega) \approx \tau_R(1 + 0.052S_1 + 0.264S_1^2) \quad (7.23b)$$

respectively. If we let $S_1 \sim -0.1$ and $\tau_X/\tau_R \sim 10(2)^{1/3}$ then (for $\omega^2 \tau_X^2 \ll 1$) $j_0 \sim 1.12\tau_R$, $j_2 \sim 1.01\tau_R$; however (more generally)

$$j_0(\omega) \approx j_0(0) \left[1 - \frac{S_1^2 \tau_X^3 \omega^2 / \tau_R}{1 + \omega^2 \tau_X^2} \right] \quad (7.24)$$

This may be compared with

$$\frac{\tau_R}{1 + \epsilon' \omega^2 \tau_R^2} \rightarrow \tau_R [1 - \epsilon' \omega^2 \tau_R^2]$$

to yield an

$$\epsilon' \sim \frac{S_1^2 (\tau_X/\tau_R)^3}{1 + \omega^2 \tau_X^2} \sim \frac{20}{1 + \omega^2 \tau_X^2}$$

In the region of $10^{-10} \leq \tau_R \leq 10^{-9}$ when pseudosecular and secular frequencies are important compared to τ_X^{-1} , then eq C2, C3 of II should be used for terms involving $\omega^2 \tau_X^2$. We have performed an analysis analogous to that of Appendix C of II for this local structure mechanism. We have assumed, by analogy to the ordering of the spin probes relative to the main director, that the molecular magnetic z axis orients perpendicular relative to the local ordering. The contributions involving $D_2(\omega)$ of eq 7.22 are then relatively unimportant and we neglect them in the following. One finds that (1) for $\tau_X \leq 3 \times 10^{-9}$ sec this mechanism contributes nearly equally to B and C , and the relative contribution to A (i.e., A/B from this mechanism) is comparable to that from the main reorientational process. (2) for $5 \times 10^{-9} \leq \tau_X \leq 2.5 \times 10^{-8}$ sec, the contribution to B from this mechanism is decreasing (from $3.2S_1^2 G$ to $1.0S_1^2 G$) while that for C first increases before decreasing (i.e., from $4S_1^2 G$ to $5S_1^2 G$ at 10^{-8} sec to $2.7S_1^2 G$). This has the effect of increasing the overall C/B value in this region. Meanwhile, the contribution to A remains large at $4S_1^2 - 5S_1^2 G$.

These results are clearly in the direction of explaining the observed C/B anomaly as well as the residual A' .

Finally, if we assume that the relaxation of the local structure is somewhat related to the mean field (or director) orientation, we may introduce a $\tau_{X_{\parallel}}$ and a $\tau_{X_{\perp}}$ by analogy to anisotropic viscosity (eq 7.11). One might expect that $\tau_{X_{\perp}}/\tau_{X_{\parallel}} \geq 1$ where $\tau_{X_{\parallel}}$ is the relaxation time of the component parallel to the macroscopic director. One then finds that (3) for $\tau_{X_{\perp}} \leq 3 \times 10^{-9}$ sec the effect of $\tau_{X_{\perp}}/\tau_{X_{\parallel}} > 1$ on the contribution to B is negligible, but the contribution to C is enhanced by as much as 50%, while the contribution to A is greatly suppressed; for $5 \times 10^{-9} \leq \tau_X \leq 2.5 \times 10^{-8}$ sec, the contribution to A increases rapidly, and all other observations for (2) are found except that they are enhanced. (4) Lastly we note that one requires $S_1^2 \sim 0.1$ to get effects of the order observed experimentally (assuming $\tau_{X_{\perp}}/\tau_R \sim 10$). [Note, however that one must introduce a more careful slow tumbling analysis for $|S_1 \mathcal{H}_1|^2 \tau_X^2 \geq 1$, i.e., for $\tau_X \geq 2.5 \times 10^{-9}/S_1$. Note $\tau_R \sim 2.5 \times 10^{-9}$ sec is the related value for slow tumbling in the overall reorientation when the modified analysis of Appendix C of II is used.]

These results are thus quite encouraging in indicating that this dynamic local structure mechanism could explain, at least in part, the observed anomalies. The analysis given here, has, for convenience, been highly approximate, but it should indicate the general spectral features of this mechanism.

VIII. Further Discussion

Here we wish to consider some other aspects of the relaxation studies for comparison with the results in I and II. First we note from Table III that the activation energies for PD-Tempone in the various nematics are all quite similar with preexponential factors of about the same order. For several of our liquid crystals the temperature dependence of the twist viscosity coefficient, γ_1 , which characterizes the viscous torque associated with an angular velocity of the director and has no counterpart in isotropic liquids has been measured.⁵⁴ The activation energies compare favorably to our results (cf. Table III). This appears to demonstrate that the same thermal activation processes are the ones affecting the reorientation of the spin probe. This quantity γ_1 is reasonably associated with \hat{R}_{\perp} . If we make this association, and then employ the Stokes-Einstein relation

$$\tau_R = \frac{4}{3} \frac{\pi r_e^3 \eta}{kT} \quad (8.1)$$

with $\eta \approx \gamma_1$ and r_e the effective rotation radius, then it is possible to obtain r_e from Meiboom and Hewitt's measurements of γ_1 ^{54a} and our experimental τ_R 's for MBBA in the nematic phase. We find $r_e \approx 1.13 \text{ \AA}$ (from the range 5–23°C) compared to an estimated hydrodynamic radius r_0 of 3.2 Å (from geometric considerations cf. II), or a value of $\kappa = 0.044$ where $\kappa = (r_e/r_0)^3$. This result for r_e is somewhat smaller than found in isotropic liquids (cf. II), as one would expect for a small solute in a solvent of larger molecules, but it is not very much smaller than the value of 1.46 Å found for glycerol solvent.⁵⁵

One can also estimate the spin-rotational relaxation from the high temperature line width results where $\tau_R \leq 10^{-11}$ sec (cf. I and II). Our most useful data for this was from the isotropic phase of phase V. We obtain $(T_2^{SR})^{-1} = 1.2 \times 10^{-12}/\tau_R$ in gauss (derivative width) compared to the theoretical value of $0.50 \times 10^{-12}/\tau_R$ from simple theoretical considerations (i.e., $\tau_R \tau_J = I/6kT$, cf. II). This experimental result is similar to, but somewhat larger than, the results obtained for isotropic solvents (cf. II where the maximum there was $1 \times 10^{-12}/\tau_R$ in acetone solvent). In terms of a simple jump diffusion model, this result could be interpreted in terms of reorientational jumps of substantial angle (cf. II). However, such information is better obtained from slow tumbling studies as discussed in section VI and in II.

It was shown in II, that a fraction of the low temperature residual width A' is due to intermolecular electron-nuclear spin dipolar interactions, which are modulated by the translational diffusion. There the expression

$$(T_2^{-1})_{\text{di}} = \gamma_I^2 \gamma_e^2 \hbar I(I+1) \frac{8\pi}{45} \frac{N}{dD} \quad (8.2)$$

was used where N is the density of spins, d is the distance of closest approach of the interacting spins, and $D = \frac{1}{2}(D_0 + D_s)$ the mean diffusion coefficient of the solute (D_0) and solvent (D_s). We estimate $N \approx 4.5 \times 10^{22}$ proton/cm³ using a molecular weight of 274 for phase V and 18.6 protons per molecule (the average of the two compounds) and $\rho = 1.1$ g/cm³ (the value for MBBA at room temperature). Thus

$(T_2^{-1})_{\text{dip}} \approx 3.05 \times 10^{-16}/dD$ in gauss. There are no available data on diffusion coefficients in phase V, and recent results on diffusion coefficients in MBBA show widely divergent results.⁵⁶ If, instead, we use the viscosity $\eta \sim \gamma_1$ for phase V at 23°C^{54b} and then extrapolate this η value using the E_a for rotational diffusion found for PD-Tempone in phase V (cf. Table III), we obtain $\eta \approx 20$ P at -25°C which is the temperature for which a maximum experimental value of $A' = 1.75$ G is achieved. If now, the Stokes-Einstein relation

$$D_i = kT/6\pi\eta r_i \quad (8.3)$$

with r_i the effective translational diffusion radius of the i th molecule is used one gets $(T_2^{-1})_{\text{dip}} \approx 6.8 (r_{\text{red.}}/d)$ G where $r_{\text{red.}} = (r_p r_s)/(r_p + r_s) \approx r_p$ for a small probe molecule. Thus, this very crude analysis could "explain" all of A' with $d \approx 4r_p$. However, one might reasonably expect that the use of $\eta \approx \gamma_1$ overestimates the microviscosity for diffusion of the small solute molecule. (A rough lower limit to η might be $\kappa\gamma_1 \approx 1$ P yielding a much smaller dipolar contribution to A' of ca. 0.34 $(r_{\text{red.}}/d)$ G which is small, but not negligible; this latter value is more consistent with results for toluene solvent cf. II.) The main point really is that the intermolecular dipolar mechanism is expected to make a nontrivial contribution to A' for the lower temperature nematics.⁵⁷

IX. Summary and Conclusions

In this work we have demonstrated how the PBF theory for ESR line shapes in both the slow tumbling and motional narrowing regions may be effectively employed in an analysis of experiments on nitroxides dissolved in liquid crystal solvents. The well-resolved spectra obtained from PD-Tempone were of particular aid for accurate results.

In general, we have found that the ordering of the nitroxide spin probes in the liquid crystal solvents requires a two-term potential function. Appropriate symmetry-dependent potential functions were introduced that very conveniently allow for relabeling of molecular axes. It was then shown how the Brownian diffusion (Smoluchowski) equation may be solved for the more general restoring potentials, and this was incorporated into the PBF theory.

The motional narrowing line width analyses in the isotropic and nematic phases were typically best explained in terms of isotropic rotational diffusion of PD-Tempone for most solvents but under the anisotropic ordering potential. The isotropic diffusion is consistent with recent results for PD-Tempone in normal liquids. The activation energies (E_a) for τ_R in several liquid crystal solvents were quite similar (8.9 to 10.2 kcal/mol) and for the cases it could be compared (MBBA and phase IV), it is rather close to E_a for the measured twist viscosity. This appears to demonstrate a close relation between τ_R and the other viscous processes in the liquid crystals. The isotropic values for E_a appear typically to be a little smaller than the nematic values.

It was also demonstrated in this work that slow-tumbling corrections to the spectra from liquid-crystalline solvents can become important even while they consist of three well-resolved lines. In the present case, these corrections are first manifest in the shifts of the line positions. Failure to include the slow tumbling corrections would then necessarily lead to incorrect results for the ordering parameters, which could incorrectly suggest a "phase transition". It appears to be a general feature of the analysis of ESR spectra involving qualitative spectral changes (such as those which

result from slow tumbling) that inappropriate or inadequate analysis can appear to imply discontinuous behavior characteristic of a "phase transition" even while the actual sample being studied does not have discontinuous behavior over the region studied. In the recent isotropic liquid studies, this principle was invoked to provide information on reorientation by jumps of substantial angle.

The slow motional analysis for PD-Tempone in phase V solvent was based on this principle, i.e., all relevant ordering parameters and τ_R values were extrapolated from the results for the motional narrowing region. However, unlike the studies in isotropic liquids, the predicted spectra in the present case were found to be in poor agreement with experiment. No significant improvement could be achieved by introducing jump diffusion models. Partial success in the slow tumbling fits could be obtained by invoking the rather sudden onset of an anisotropic viscosity mechanism, such that while $\tau_{R\perp}$ is behaving normally, $\tau_{R\parallel}$ even begins to speed up as the temperature is lowered! Furthermore, this violates our principle of invoking a discontinuous change in the absence of phase transitions.

In the recent studies on isotropic solvents it was found necessary to introduce the corrections ϵ and ϵ' for non-Debye-like spectral densities. This was again found to be important for the liquid crystals. Typically $\epsilon \sim 4.6$ (for the nonsecular spectral densities) for the isotropic phases in agreement with the results on isotropic liquids. There appears to be a lowering of this value in the nematic phases, but the analysis is not very certain. It was suggested in previous work that this might be explained in terms of relatively slowly fluctuating torques affecting the rotational diffusion, and a theoretical analysis related this to ϵ and ϵ' in terms of frequency-dependent diffusion coefficients. In this work, we applied this analysis to the ordered solvents in an attempt to explain the slow-tumbling spectral anomaly in terms of $\epsilon' \neq 1$. It was indeed possible to obtain rather good agreement in this way, but only by invoking an anisotropic ϵ' analogous to an anisotropic viscosity such that $\epsilon'_{\text{sec}} \sim 1-2$ and $\epsilon'_{\text{psec}} \sim 15-20$.

This latter large value of ϵ' appears on theoretical grounds to be too large; i.e., if there are important components of the fluctuating torque relaxing considerably slower than τ_R , they should more properly be included into a local structure or ordering term which is relaxing on a longer time scale than τ_R . A simple model for this slowly relaxing local structure was then developed to conveniently predict the effects one might expect on the ESR spectra. The simple model, which neglects any correlated effects between the mean field potential (or director) and the slowly relaxing local structure (and may thus be applied to structured isotropic liquids), is shown first of all to predict, in general, non-Debye-like spectral densities for the rotational reorientation. It is further found that this effect can lead to spectral densities which would appear to imply anisotropic rotational diffusion coefficients, whereas, in effect, the anisotropy is in the local structure. Our analysis of this model shows that it has the potential of explaining, at least in part, the observed slow-tumbling spectral anomalies. The absence of such an anomaly in the higher temperature region where nonsecular terms are important would have to imply important temperature dependence of the local structure, or else a spectral density lacking in high frequency components.

The model of hydrodynamic fluctuations in the director due to deGennes and Pincus is found both qualitatively

and quantitatively to be inconsistent with the observed spectral anomalies. In general, we could find no evidence for this mechanism in our experimental results, but this is consistent with the weak ordering (i.e., $\langle D_{00}^2 \rangle \approx -0.1$) of the PD-Tempone spin probe.

However, our slowly relaxing local structure model would definitely be consistent with (nonhydrodynamic) cooperative reorientational modes of relaxation of the liquid crystal molecules on a time scale faster than director fluctuation, a mechanism which should be associated with a frequency dependence more typical of hydrodynamic modes than with a localized mode.

It is pointed out that a more rigorous (albeit a more complicated) analysis of both the slowly relaxing local structure mechanism and the director fluctuations may be obtained from a solution based upon more general Smoluchowski equations explicitly including the slowly fluctuating torques (as well as the mean-field torques) and introduced into an augmented stochastic Liouville equation, which includes the spin degrees of freedom.

Further experimental and theoretical work on these interesting phenomena is clearly warranted.⁵⁸

Acknowledgments. We wish to acknowledge many helpful discussions with Drs. G. V. Bruno, S. A. Goldman, J. S. Hwang, L. P. Hwang, R. P. Mason, and K. V. S. Rao.

Appendix. Director Relaxation and ESR Line Widths

In this case, the motion which causes modulation of the magnetic tensors can be thought of as arising from two processes: (1) motion of the molecule with respect to the director, and (2) motion of the director axis with respect to the preferred axis of director orientation (fluctuations of the direction of the ordering axis).

The perturbation hamiltonian required to describe the relaxation effects in this case can be written as follows

$$\mathcal{H}_1'(\Omega, \Psi) = \mathcal{H}_1(\Omega, \Psi) - \langle \mathcal{H}_1(\Omega, \Psi) \rangle \quad (A1)$$

with $\mathcal{H}_1(\Omega, \Psi)$ given by eq 2.1.

The orientation-dependent part of the spectral density is required for relaxation and is given by

$$\begin{aligned} \bar{K}_{KMK'M'}(\omega) = & \sum_{N,N'} \int_0^\infty \langle [D_{-KN}^{(2)}(\Omega) D_{NM}^{(2)}(\Psi) - \\ & \langle D_{-KN}^{(2)}(\Omega) D_{NM}^{(2)}(\Psi) \rangle] [D_{-K'N'}^{(2)}(\Omega_0) * D_{N'M'}^{(2)}(\Psi_0) * - \\ & \langle D_{-K'N'}^{(2)}(\Omega_0) * D_{N'M'}^{(2)}(\Psi_0) * \rangle] e^{-i\omega t} dt = \\ & \int_0^\infty \bar{C}_{KMK'M'}(t) e^{-i\omega t} dt \quad (A2) \end{aligned}$$

where the $\bar{C}(t)$ is the correlation function. If one assumes that the motion of Ω and of Ψ are independent processes (but see below), then $\bar{C}(t)$ can be written as

$$\begin{aligned} \bar{C}_{KMK'M'}(t) = & \sum_{N,N'} \{ \langle D_{NM}^{(2)}(\Psi) D_{N'M'}^{(2)}(\Psi_0) * \rangle [\langle D_{-KN}^{(2)}(\Omega) D_{-K'N'}^{(2)}(\Omega_0) * \rangle - \\ & \langle D_{-KN}^{(2)}(\Omega) \rangle \langle D_{-K'N'}^{(2)}(\Omega_0) * \rangle] + \langle D_{-KN}^{(2)}(\Omega) \rangle \langle D_{-K'N'}^{(2)}(\Omega_0) * \rangle \times \\ & [\langle D_{NM}^{(2)}(\Psi) D_{N'M'}^{(2)}(\Psi_0) * \rangle - \langle D_{NM}^{(2)}(\Psi) \rangle \langle D_{N'M'}^{(2)}(\Psi_0) * \rangle] \} \quad (A3) \end{aligned}$$

The quantity in square brackets in the first term on the right-hand side of eq A3 is $C_{KNKN'}(t)$, the correlation function when there is no motion of the director; the evaluation of this quantity is given in section II. The quantity in

brackets in the second term is an analogous expression for the correlation function for motion of the director only. Note that this quantity is multiplied by a product of order parameters for the molecular orientation. In the limit of no director motion $\Psi = \Psi_0 = (0,0,0)$ and $D_{NM}^{(2)}(\Psi) = \delta_{NM}$ and the ensemble average over Ψ in the first term becomes $\delta_{NM} \delta_{N'M'}$ and the bracketed quantity in the second term is zero. Thus $\bar{C}_{KMK'M'}(t) = C_{KMK'M'}(t)$ in this limit. In the limit of $\langle D_{KN}^{(2)}(\Omega) \rangle = 0$, i.e., no ordering of the molecule by the director, the second term of eq A3 again disappears, but the first term can still be modified by the motion of the director. This latter is a physically unreal result in this limit of no ordering. It arises because the form of eq 2.1 refers the molecular motion relative to a moving (or fluctuating) reference frame, i.e., that of the director. A more rigorous, but more difficult to analyze model, would involve solving for the molecular diffusive motion by means of an equation such as eq 7.2, but with the restoring potential including the director fluctuations.⁶⁵ In such a treatment, the motion of Ω is, in general, dependent upon Ψ . We hereafter neglect any unrealistic effects of director fluctuation on the first term of eq A3 and consider only the effects in the second term of eq A3 which are physically more realistic. This is, in effect, the approach used by several authors,¹⁷⁻²⁰ although they have not discussed these matters.

In order to simplify the evaluation of eq A3, the following assumptions are made. (1) The distribution of director and molecular orientations are axially symmetric with respect to the preferred axis of director orientations. This results in $N = N'$, $K = K'$, and $M = M'$ and the $\langle D_{KN}^{(2)}(\Omega) \rangle$ are zero unless $K = N = 0$.¹⁴ (2) The magnetic tensors have axial symmetry. Thus $K = 0$ in all terms. (3) The fluctuations in the director are small in amplitude so that the $D_{KN}^{(2)}(\Psi)$ can be approximated by their forms for small θ given in Appendix B of PBF. Thus the correlation function of eq A3 becomes

$$\begin{aligned} \bar{C}_{0M}(t) = & \sum_N \langle D_{NM}^{(2)}(\Psi) D_{NM}^{(2)}(\Psi_0) * \rangle C_{0N}(t) + \\ & \langle D_{00}^{(2)}(\Omega) \rangle^2 [\langle D_{0M}^{(2)}(\Psi) D_{0M}^{(2)}(\Psi_0) * \rangle - \langle D_{00}^{(2)}(\Psi) \rangle^2 \delta_{M0}] \delta_{N0} \quad (A4) \end{aligned}$$

Equation A4 will be evaluated by using two different approaches: (1) considering the thermal fluctuations of the director as done by several authors for NMR relaxation,¹⁷⁻²⁰ and (2) considering the motion of the director to be a diffusion process in the presence of a very strong orienting potential. The latter is more appropriate for a localized mode (e.g., the local structure model of section VIIB).

For the thermal fluctuations, one must first expand the $D_{NM}^{(2)}$ for small θ . Thus eq A4 becomes

$$\begin{aligned} \bar{C}_{0M}(t) = & \sum_N \{ \langle \delta_{NM} + \frac{\theta \theta_0}{4} (-1)^{N+M+1} [\delta_{M,N+1} f_+(2, M - \\ & 1) f_-(2, M - 1) + \delta_{M,N-1} f_+(2, M + 1) f_-(2, M + \\ & 1)] \} e^{iM(\phi-\phi_0)} \rangle C_{0N}(t) + \langle D_{00}^2(\Omega) \rangle^2 \langle e^{iM(\phi-\phi_0)} \theta \theta_0 \rangle^2 \times \\ & [\delta_{M,-1} + \delta_{M,+1}] \delta_{N,0} \quad (A5) \end{aligned}$$

where the $f_{\pm}(L,M)$ are defined as in PBF. The quantity

$$\langle \theta \theta_0 e^{i(\phi-\phi_0)} \rangle \approx \langle \delta \hat{n}(\mathbf{r}) \delta \hat{n}(\mathbf{r}_0) * \rangle \quad (A6)$$

where

$$\delta \hat{n}(\mathbf{r}) = \hat{n}(\mathbf{r}) - \hat{n}_0 \quad (A7)$$

is the fluctuating component of the director orientation with the unit vector \hat{n}_0 , the preferred director orienta-

tion.²¹ The quantity $\langle \delta \hat{n}(\mathbf{r}) \delta \hat{n}(\mathbf{r}_0)^* \rangle$ can be evaluated by considering the fluctuation $\delta \hat{n}(\mathbf{r})$ to be a superposition of plane-wave disturbances given by Fourier components:

$$\delta \hat{n}(\mathbf{r}) = V^{-1/2} \delta \hat{n}_q e^{i\mathbf{q} \cdot \mathbf{r}} \quad (\text{A8})$$

where V is the volume. The correlation function for fluctuations of the director becomes²⁰

$$\langle \delta \hat{n}(\mathbf{r}) \delta \hat{n}(\mathbf{r}_0)^* \rangle = \frac{V}{(2\pi)^3} \int_0^{q_c} \frac{kT}{Kq^2 V} \exp\left\{-\frac{Kq^2 t}{\eta}\right\} 4\pi q^2 dq \quad (\text{A9})$$

where $kT/Kq^2 V$ is the thermal amplitude of the modes, Kq^2/η is the damping constant of the slow mode, τ_q^{-1} , and $[V/(2\pi)^3]4\pi q^2$ is the number of states in a volume element $4\pi q^2 dq$, with K the average elastic constant of the liquid crystal. Also, η is the viscosity, and q_c is the wave vector which corresponds to a cutoff in the modes near the molecular length.²⁰ In the true hydrodynamic limit, $q_c \rightarrow \infty$ and the integration in eq A9 is readily performed. For q_c finite, one has

$$\langle \delta \hat{n}(\mathbf{r}) \delta \hat{n}(\mathbf{r}_0)^* \rangle = \frac{kT\eta^{1/2}}{4\pi^{3/2}K^{3/2}t^{1/2}} \Phi[(\omega_c t)^{1/2}] \quad (\text{A10})$$

where $\omega_c = Kq_c^2/\eta$ is the cutoff frequency and $\Phi(\chi)$ is the error or probability function.⁵⁹ Note for $\omega_c \rightarrow \infty$, $\Phi[(\omega_c t)^{1/2}] \rightarrow 1$. Thus the contribution to the correlation function needed for relaxation due to fluctuations of the director is

$$\bar{C}_{01}(t) = \bar{C}_{0-1}(t) = \frac{3kT\eta^{1/2} \langle D_{00}^{(2)}(\Omega) \rangle^2}{8\pi^{3/2}K^{3/2}t^{1/2}} \Phi[(\omega_c t)^{1/2}] \quad (\text{A11})$$

The spectral density then has the form²⁰

$$\bar{K}_{01}(\omega) = \frac{3kT\eta^{1/2} \langle D_{00}^{(2)}(\Omega) \rangle^2}{8\sqrt{2}\pi K^{3/2}\omega^{1/2}} \left\{ 1 - \frac{1}{2\pi} \ln \left| \frac{1 + \sqrt{2\omega/\omega_c} + \omega/\omega_c}{1 - \sqrt{2\omega/\omega_c} + \omega/\omega_c} \right| - \frac{1}{\pi} \arctan(\sqrt{2\omega/\omega_c} + 1) - \frac{1}{\pi} \arctan(\sqrt{2\omega/\omega_c} - 1) \right\} \quad (\text{A12})$$

which is valid for $\omega > 0$. [The discontinuity at $\omega = 0$ would undoubtedly be removed by an analysis recognizing the coupled dependence of Ω upon ψ as discussed above.]

In this case, the ESR line width contribution in gauss due to fluctuations in the director orientation is

$$T_2^{-1} = \frac{|\gamma_e|}{3\sqrt{3}} \{ (a_n - a_1)^2 [I(I+1) - m_I^2] \bar{K}_{01}(\omega_\pm) + [1/2(g_n - g_1)^2 B_0^2 - 2(a_1 - a_n)(g_n - g_1) B_0 m_I + 2(a_n - a_1)^2 m_I^2] \bar{K}_{01}(\omega_0) \} \quad (\text{A13})$$

For typical molecular lengths, i.e., 40 Å for MBBA, one finds $\omega_c \approx 1.9 \times 10^8$. Thus, the nonsecular terms in eq A13 can be neglected as the quantity in brackets $\{ \}$ in eq A12 approaches zero for $\omega_0 \gg \omega_c$. For the pseudosecular terms $\omega_\pm \lesssim \omega_c$, and the quantity in brackets is somewhat less than unity (ca. 0.32). Using the values $\eta = \gamma_1$, K_{11} ²¹ and the order parameter for PD-Temponone in MBBA at 23°C, one predicts that the contributions to the A and C line width coefficients to be 0.01 and -0.005 G, respectively, which are too small to be of importance. Also, relaxation due to thermal fluctuations of the director predicts that the C/B ratio should be decreased by this process. Furthermore, these contributions are expected to have little temperature dependence.¹⁸ It is observed in our experiments that the C/B ratio increases substantially with decreasing tempera-

ture. Thus this process cannot account either qualitatively or quantitatively for this behavior.

Note that the average over the director fluctuations in the first term of eq A5 reduces to δ_{NM} as the leading term, and the line width contribution calculated from this term is just that predicted from the rotation of the molecule.

Alternatively one can evaluate the quantity in brackets in the second term of eq A4 by using a formalism which corresponds to the diffusion of a "localized" \hat{n} in the presence of a very strong restoring potential of the form

$$V(\Psi)/kT = \alpha \cos^2 \theta \quad (\text{A14})$$

where the distribution parameter $\alpha \gg 1$. As the potential is a function of θ only, the diffusion equation can be separated into its components by letting¹⁴

$$Y_N^M(\Psi) = y_N^M(\theta) \exp(iM\phi) (2\pi)^{-1/2} \quad (\text{A15})$$

and to lowest order in θ and α^{-1} , one has

$$-D^{-1} \bar{\Gamma}_\Psi = \partial^2/\partial \theta^2 + \theta^{-1}(\partial/\partial \theta) - (M/\theta)^2 - \alpha^2 \theta^2 + 2\alpha \quad (\text{A16})$$

where D is the diffusion constant for director motion.¹⁴

The eigenfunctions for this differential equation are given by

$$y_N^{M1}(\theta) = [2\alpha N!/(N + |M|)!]^{1/2} e^{-\alpha \theta^2/2} (\alpha^{1/2} \theta)^{|M|} L_N^{|M|}(\alpha \theta^2) \quad (\text{A17})$$

where the $L_N^{|M|}(z)$ are the generalized Laguerre polynomials.⁶⁰ The eigenvalues of this equation are

$$W_N^{M1} = 2\alpha D(2N + |M|) \quad (\text{A18})$$

These eigenfunctions and eigenvalues can be used for the evaluation of the correlation functions for director motion in eq A3 or A4. The quantity in brackets in eq A4 can be rewritten as

$$\hat{C}_{0M}(t) = \langle [D_{0M}^{(2)}(\Psi) - \langle D_{0M}^{(2)}(\Psi) \rangle] [D_{0M}^{(2)}(\Psi_0)^* - \langle D_{0M}^{(2)}(\Psi_0)^* \rangle] \rangle \quad (\text{A19})$$

The evaluation of this integral over all angles Ψ and Ψ_0 requires the conditional probability

$$P(\Psi, \Psi_0, t) = \sum_{N,M} \exp(-W_N^{M1}(\Psi) t) |Y_N^M(\Psi)\rangle \langle Y_N^M(\Psi_0)| \times \left[\frac{P_0(\Psi)}{P_0(\Psi_0)} \right]^{1/2} \quad (\text{A20})$$

Thus we can proceed as in PBF for molecular rotation and finally obtain

$$\hat{C}_{0M}(t) = \sum_{p,q} \langle Y_0^0(\Psi) | D_{0M}^{(2)}(\Psi) | Y_p^q(\Psi) \rangle e^{-W_p^q t} \langle Y_p^q(\Psi_0) | D_{0M}^{(2)}(\Psi_0)^* | Y_0^0(\Psi_0) \rangle \quad (\text{A21})$$

where Σ' means that the term $p = q = 0$ has been omitted. Keeping the leading terms in the $D_{0M}^{(2)}(\Psi)$,¹⁴ one has

$$\hat{C}_{01}(t) = \hat{C}_{0-1}(t) = \sum_{q,p} \langle Y_0^0(\Psi) | e^{i\phi} d_{01}^{2}(\theta) | Y_p^q(\Psi) \rangle^2 e^{-W_p^q t} \quad (\text{A22})$$

Substituting for the Y_p^q from eq A15 and A17 and for $d_{01}^2(\theta)$ from eq A5, the integral over Ψ in eq A22 becomes

$$\int_0^\infty \theta d\theta \int_0^{2\pi} d\phi (2\alpha)^{1/2} \exp(-\alpha\theta^2) \frac{e^{i\phi}}{\sqrt{2\pi}} \frac{3}{2} \theta \times \left[\frac{2\alpha p!}{(p+|q|)!} \right]^{1/2} \frac{e^{i\alpha\theta}}{\sqrt{2\pi}} (\alpha^{1/2}\theta) L_p^{1/2}(\alpha\theta^2) \quad (\text{A23})$$

The integration over ϕ requires that $q = \mp 1$. Substituting $u = \alpha\theta^2$, the integral over θ now has the form⁵⁹

$$\frac{3}{2} \left[\frac{p!}{\alpha(p+1)!} \right]^{1/2} \int_0^\infty e^{-u} u L_p^1(u) du = \frac{3}{2} \left[\frac{p!}{\alpha(p+1)!} \right]^{1/2} \frac{\Gamma(p)}{p! \Gamma(0)} = \frac{3}{2\alpha^{1/2}} \delta_{p,0} \quad (\text{A24})$$

The correlation function for localized director motion then is⁶¹

$$\hat{C}_{01}(t) = \left(\frac{9}{4\alpha} \right) e^{-2\alpha D t} \quad (\text{A25})$$

Thus we can define a single correlation time for localized director motion as

$$\tau_D^{-1} = 2\alpha D \quad (\text{A26})$$

and the spectral density for this case is

$$\bar{K}_{01}(\omega_\pm) = \frac{9}{4\alpha} \frac{\tau_D}{1 + (\omega_\pm \tau_D)^2} \langle D_{00}^{(2)}(\Omega) \rangle^2 \quad (\text{A27})$$

and the line width contribution becomes

$$T_2^{-1} = \frac{1}{3\sqrt{3}} (a_{11} - a_{\perp})^2 [I(I+1) - m_I^2] \frac{9}{8\alpha^2 D} \langle D_{00}^{(2)}(\Omega) \rangle^2 [1 + (\omega_\pm \tau_D)^2]^{-1} \quad (\text{A28})$$

Again the prediction is that the C line width coefficient resulting from director motion is negative. It has been estimated that $R/D \sim 1000$ ⁶² where R is the rotational rate of the molecule. The values of $\langle D_{00}^{(2)}(\Omega) \rangle^2$ observed experimentally were ~ 0.01 . Thus for $\alpha > 10$ – 100 the line width contribution from this model for director motion is calculated to be negligible compared to that resulting from molecular motion.⁶³

References and Notes

- (1) A preliminary account of this work was given at the Varian Workshop, Vanderbilt University, June 1973. Supported in part by grants from the National Science Foundation, the Donors of the Petroleum Research Fund, administered by the American Chemical Society, and by the Cornell University Materials Science Center.
- (2) S. A. Goldman, G. V. Bruno, C. F. Polnaszek, and J. H. Freed, *J. Chem. Phys.*, **56**, 716 (1972); hereafter referred to as I.
- (3) S. A. Goldman, G. V. Bruno, and J. H. Freed, *J. Chem. Phys.*, **59**, 3071 (1973).
- (4) J. S. Hwang, R. P. Mason, L. P. Hwang, and J. H. Freed, *J. Phys. Chem.*, **79**, 489 (1975); hereafter referred to as II.
- (5) J. H. Freed, *Ann. Rev. Phys. Chem.*, **23**, 265 (1972).
- (6) G. R. Luckhurst in (a) "ESR Relaxation in Liquids", L. T. Muus and P. W. Atkins, Ed., Plenum Press, New York, N.Y., 1972, Chapter XV; (b) "Liquid Crystalline Systems", Vol. 2, G. W. Gray and P. A. Winsor, Ed., Ellis Horwood, New York, N.Y., 1974, Chapter 7.
- (7) L. J. Berliner, Ed., "Spin Labeling Theory and Applications", Academic Press, New York, N.Y., in press.
- (8) C. F. Polnaszek, *Quart. Rev. Biophys.*, submitted for publication.
- (9) (a) G. R. Luckhurst and A. Sanson, *Mol. Phys.*, **24**, 1297 (1972); (b) G. R. Luckhurst, M. Setaka, and C. Zannoni, *ibid.*, **28**, 49 (1974).
- (10) W. E. Shutt, E. Gelerinter, G. C. Fryburg, and C. F. Sheley, *J. Chem. Phys.*, **59**, 143 (1973).
- (11) G. R. Luckhurst and R. Poupko, *Chem. Phys. Lett.*, **29**, 191 (1974).
- (12) H. Schindler and J. Seelig, *J. Chem. Phys.*, **59**, 1841 (1973); **61**, 2946 (1974); *Ber. Bunsenges Phys. Chem.*, **78**, 941 (1974).
- (13) (a) P. L. Nordio and P. Busolin, *J. Chem. Phys.*, **55**, 5485 (1971); (b) P. L. Nordio, G. Rigatti, and V. Segre, *ibid.*, **56**, 2117 (1972).
- (14) C. F. Polnaszek, G. V. Bruno, and J. H. Freed, *J. Chem. Phys.*, **58**, 3185 (1973). Referred to as PBF.
- (15) J. H. Freed, G. V. Bruno, and C. F. Polnaszek, *J. Phys. Chem.*, **75**, 3385 (1971).
- (16) L. P. Hwang and J. H. Freed, *J. Chem. Phys.*, **63**, 118 (1975).
- (17) P. Pincus, *Solid State Commun.*, **7**, 415 (1969).
- (18) J. W. Doane and D. L. Johnson, *Chem. Phys. Lett.*, **6**, 291 (1970).
- (19) T. C. Lubensky, *Phys. Rev. A.*, **6**, 2497 (1970).
- (20) J. W. Doane, C. E. Tarr, and M. A. Nickerson, *Phys. Rev. Lett.*, **33**, 620 (1974).
- (21) (a) M. J. Stephen and J. S. Straley, *Rev. Mod. Phys.*, **46**, 617 (1974). (b) P. G. deGennes, "The Physics of Liquid Crystals", Oxford University Press, New York, N.Y., 1974.
- (22) G. Heppke and F. Schneider, *Ber. Bunsenges Phys. Chem.*, **75**, 61 (1971).
- (23) P. Ferruti, D. Gill, M. A. Harpold, and M. P. Klein, *J. Chem. Phys.*, **50**, 4545 (1969); G. Havach, P. Ferruti, D. Gill, and M. P. Klein, *J. Am. Chem. Soc.*, **91**, 7526 (1969).
- (24) L. D. Favro in "Fluctuation Phenomena in Solids", R. E. Burgess, Ed., Academic Press, New York, N.Y., 1965, p 79.
- (25) J. H. Freed in "Electron-Spin Relaxation in Liquids", L. T. Muus and P. W. Atkins, Ed., Plenum Press, New York, N.Y., 1972, Chapters VIII and XIV.
- (26) E. C. Kemble "The Fundamental Principles of Quantum Mechanics", Dover Publications, New York, N.Y., 1958, pp 230–234.
- (27) In PBF, $\mathcal{M} = -\nabla_{ij}^2$. Note that eq 2.5 of PBF should have been written as
$$\tilde{Z} \equiv P_0^{-1/2} [Z P_0]$$
 and eq 2.9 should have $P_0^{1/2}$ instead of $P_0^{-1/2}$.
- (28) S. H. Glarum and J. H. Marshall, *J. Chem. Phys.*, **44**, 2884 (1966); **46**, 55 (1967).
- (29) W. Maier and A. Saupe, *Z. Naturforsch. A*, **13**, 564 (1958); **14**, 882 (1959); **15**, 287 (1960).
- (30) L. C. Snyder, *J. Chem. Phys.*, **43**, 4041 (1965).
- (31) C. F. Polnaszek, Ph.D. Thesis, Cornell University, 1975.
- (32) Dinsie et al. [*Chem. Phys. Lett.*, **14**, 196 (1972)] have observed the effects of quadrupole splittings in the ¹⁴N ENDOR of tempo: in phase IV. If the ¹⁴N quadrupole tensor were known, one could determine a third parameter.
- (33) The perturbation eq 4.16 of PBF require some modification. The terms quadratic in λ_2^2 are respectively for eq 4.16a–f: $-(0.0777R_{00} + 0.0434)$; $-(0.1283R_{01} + 0.0262)$; $+(0.0311R_{02} - 0.0149)$; $-(0.2061R_{11} + 0.0481)$; $-(0.0376R_{12} + 0.0066)$; $+(0.0764R_{22} + 0.0062)$. Also the quantity $(\lambda_2^2/48)[s + E_{11}^{(0)}]^{-1}$ must be added to eq 4.16d. Other, more general expansions, based upon the complete computer solutions, may be found in ref 8 and 31.
- (34) If the principal axis of the magnetic tensors and the principal axes of the molecular orientation do not coincide, one must transform between them. It is usually easier to work with the magnetic tensors in the (x' , y' , z') system than the orientation tensor in the (x , y , z) system.
- (35) E. G. Rozantsev, "Free Nitroxyl Radicals", Plenum Press, New York, N.Y., 1970.
- (36) A. K. Hoffmann and A. T. Henderson, *J. Am. Chem. Soc.*, **83**, 4671 (1961).
- (37) D. Jones, *Appl. Phys. Lett.*, **16**, 61 (1970).
- (38) J. G. Koch, Ph.D. Thesis, Cornell University, 1972.
- (39) I. Teucher, C. M. Paleos, and M. M. Labes, *Mol. Cryst. Liq. Cryst.*, **11**, 187 (1970).
- (40) G. Zemplén, L. Farkas, and T. Sattler, *Acta Chim. Hung.*, **22**, 449 (1960).
- (41) (a) R. Steinstrasser and L. Pohl, *Z. Naturforsch. B*, **26** 577 (1971); (b) *Tetrahedron Lett.*, 1921 (1971).
- (42) J. R. Bolton and G. K. Fraenkel, *J. Chem. Phys.*, **40**, 3307 (1964).
- (43) R. W. Kreilick, *J. Chem. Phys.*, **46**, 4260 (1967).
- (44) P. G. deGennes, *Mol. Cryst. Liq. Cryst.*, **7**, 325 (1969).
- (45) S. A. Brooks, G. R. Luckhurst, and G. F. Pedulli, *Chem. Phys. Lett.*, **11**, 159 (1971).
- (46) Luckhurst and Poupko¹¹ have made similar observations on the cholesteric spin label in phase IV.
- (47) A. Abragam and B. Bleaney, "Electron Paramagnetic Resonance of Transition Ions", Oxford University Press, New York, N.Y., 1970.
- (48) L. J. Libertini and O. H. Griffith, *J. Chem. Phys.*, **53**, 3185 (1973), note that the coordinate axes for the g and A tensors of DTBN do not exactly coincide and that there is a 6° difference in the x - y plane. Most nitroxides including PD-Tempone have nearly axially symmetric A tensors about the z axis. Therefore, any large differences in the x - y plane would not be expected to have a large effect.
- (49) As noted above, PD-Tempone may not have its principal axes of orientation coincident with the principal axes of the magnetic tensors for several of the nematics studied. If the orienting potential were cylindrically symmetric about a particular molecular axis, then, as shown in section II, it should be possible to relate that axis to one of the principal axes of the magnetic tensor. If this is the case, then the experimentally observed g and A values can be used to determine an ordering parameter and one tilt angle. From eq 2.27 one finds for the tilt angle relative to the z magnetic principal axis, $\beta' = 33 \pm 1^\circ$, and with the x axis as the principal axis one has $\beta' = 53 \pm 1^\circ$. However neither of these look reasonable from the point of view of the known structure of Tempone. With the y axis as the principal axis, there is no real solution of eq 2.27 for β' . Therefore, we shall not consider the effect of the tilt angle any further.
- (50) For anisotropic viscosity in the presence of a weak ordering potential, one can show that this calculated $(C/B)_{\beta_1 \sim 100 \beta_1} = 1.8(C/B)_{\beta = \beta_1}$ for

the λ_y values used for BOCF.

- (51) For ordered liquid solvents it is true that even in the motional narrowing region where the lines are lorentzian, the widths are somewhat dependent on rotational model. This is because the larger the size of the elementary jump angle, the less the reorientational process is affected by the orienting potential. Our τ_R 's in the motional narrowing region were also estimated by means of a strong jump model (cf. PBF) and this typically yielded values of τ_R that were 5–10% shorter than the analysis based on a Brownian model. This difference was not deemed very significant. All other aspects of the analysis remained essentially unchanged.
- (52) The effect of the weak ordering is to reduce the PD-Tempone line width coefficients by about 30% below what they would be if the ordering potential were zero but τ_R were the same.
- (53) J. H. Freed and G. K. Fraenkel, *J. Chem. Phys.*, **39**, 326 (1963).
- (54) (a) S. Meiboom and R. C. Hewitt, *Chem. Phys. Lett.*, **30**, 261 (1973); (b) P. J. Flanders, *Mol. Cryst. Liq. Cryst.*, **29**, 19 (1974).
- (55) If we estimate κ from the relation used by J. S. Hwang, D. Kivelson, and W. Z. Plachy [*J. Chem. Phys.*, **58**, 1753 (1973)]

$$\kappa = [6(r_s/r_0) + (1 + r_s/r_0)^{-3}]^{-1}$$

where r_s is the solvent radius ($r_s \approx 14 \text{ \AA}$ for MBBA), then we get $\kappa = 0.038$.

- (56) Thus Zupancic et al. [*Solid State Commun.*, **15**, 227 (1974)] obtained an activation energy E_a for D_{\perp} of 5.4 kcal/mol using an NMR pulse technique, while H. Hake-mi and M. M. Labes [*J. Chem. Phys.*, **61**, 4020 (1974)] found $E_a = 17 \pm 2.5$ kcal/mol using an optical method. These results extrapolate to D_{\perp} of 1.4×10^{-7} and $4.4 \times 10^{-10} \text{ cm}^2/\text{sec}$, respectively, at -25°C .
- (57) Hoel and Kivelson [*J. Chem. Phys.*, **62**, 4535 (1975)] have recently suggested that the residual A' in VOAA studies is to be attributed to spin-rotational relaxation in the absence of any other known mechanism. This requires that the spin-rotational relaxation component about the symmetry axis begins to slow down when η/T becomes large enough (instead of typical decrease with η/T). (They do not see the effects of reorientational relaxation about the symmetry axis, because of the symmetry of the magnetic parameters.) We have implicitly argued against such mechanisms in our recent work on nitroxides (ref 3 and II), where R_{\parallel} and R_{\perp} were both observed and varying magnitudes of A' were found. In particular, we summarize for isotropic liquids: (1) $N = R_{\parallel}/R_{\perp}$ was typically found to be constant with temperature, and for PD-Tempone $N \approx 1$, and in all cases $R_{\parallel} \propto R_{\perp} \propto T/\eta$. (2) It is possible for small rotational asymmetry relative to the molecular z axis to significantly affect A' , and there is usually a small contribution from intermolecular electron-nuclear dipolar interactions. (3) The observed A' are typically simply linear in η/T for large enough viscosity. (4) In II they were found to be significantly dependent upon magnetic field, which should not be true for a spin-rotation mechanism, although this observation is dependent upon the rotational model such as implied in (2). Also most important (5) the measurements of W_0 in ref 3 and II from saturation studies show that precisely when A' becomes anomalous (increasing with η/T), the W_0 are decreasing (cf. Figure 12 of II). Since, at the higher temperatures, $W_0 \propto T/\eta$ is found to be virtually equal to $A'/2$ as predicted for a

spin-rotational mechanism [i.e., $T_1(\text{SR}) = T_2(\text{SR})$], then, if A' at the lower temperatures (where $A' \propto \eta/T$) were due to a spin-rotational mechanism, one would still expect $W_0 \approx A'/2$, which it decidedly is not. It appears that A' is due essentially to a purely secular mechanism. Furthermore (6) we have consistently argued against any physical explanations of spectral anomalies which appear to be "turned on", although the sample exhibits no phase transitions. We believe a likely possibility for explaining an anomalous A' could be in terms of modulation of the dipolar and g -tensor terms by rotational reorientation, but where the reorientation is complicated by a slowly relaxing local structure and/or related considerations. (Cf. section VII.) In II it was suggested that (2) above might help to explain the anomalous A' , but more careful considerations show that A'/C is not very significantly affected by such small rotational asymmetry, so it would not be a very satisfactory explanation. (We wish to thank Dr. B. Kowert for a helpful discussion on this point.)

- (58) Recent pressure-dependent studies on the PD-Tempone system will be reported on elsewhere: J. S. Hwang, K. V. S. Rao, and J. H. Freed, to be submitted for publication.
- (59) I. S. Gradshteyn and I. M. Ryzhik, "Table of Integrals, Series, and Products", Academic Press, New York, N.Y., 1965.
- (60) M. Abramowitz and I. A. Stegun, "Handbook of Mathematical Functions", Dover Publications, New York, N.Y., 1965.
- (61) We can establish a formal equivalence between eq A25 and eq A9 with eq A5 by regarding the result eq A25 as the result for the q th mode and letting $2\alpha D \rightarrow Kq^2/\eta$ while letting $9/4\alpha \rightarrow 3kT/2Kq^2V$ or $D \rightarrow kT/3\eta V$ and $\alpha \rightarrow 3Kq^2V/2kT$.
- (62) G. R. Luckhurst, *Phys. Bull.*, **23**, 279 (1972).
- (63) It should be noted that we have avoided the question as to whether a motional-narrowing theory actually applied for the slow director fluctuations. First we should note that the criterion for validity is given by $|\mathcal{J}C_{11}^2| \tau_D^2 \ll 1$ where $|\mathcal{J}C_{11}^2|^{1/2}$ measures the root mean square value of modulation of $\mathcal{J}C_{11}(\psi)$ by the small amplitude director motion. Thus for example, for the diffusion model we require

$$\left[\frac{9}{4\alpha} \langle D_{00}^{(2)}(\Omega) \rangle^2 \frac{|\gamma_e|^2}{3\sqrt{3}} (a_{11} - a_{12})^2 \right] [\tau_D^{-2} + \omega_z^2]^{-1} \ll 1$$

These conditions should be obeyed in the present case. When they are not obeyed, a slow tumbling theory analogous to PBF for the diffusion model or analogous to that of J. B. Pedersen and J. H. Freed [*J. Chem. Phys.*, **58**, 2746 (1973); **59**, 2869 (1973)], for the hydrodynamic model, should be employed.

- (64) Similar results have been observed in ^2H NMR studies on deuterated stearic acids in the liquid crystalline phase of egg lecithin [G. W. Stockton, C. F. Polnaszek, A. P. Tulloch, F. Hasan, and I. C. P. Smith, *Biochemistry*, submitted for publication]. The ordering parameters for the totally deuterated acids are also reduced compared to those of partially deuterated (at one position) acids.
- (65) NOTE ADDED IN PROOF: Actually by using eq 7.12 and the method outlined in section VIIB, but applied to director fluctuations, it is easy to demonstrate that (1) the analysis involving the second term of eq A3 as given below is indeed appropriate; and (2) the first term of eq A3 is to be replaced by $C_{\text{KMK}'}(f)$, so the physically unreal feature is indeed removed.

Spin-Lattice Relaxation and Hydrogen Bonding in Methanol-Solvent Mixtures

Rush O. Inlow,¹ Melvin D. Joesten,* and John R. Van Wazer*

Department of Chemistry, Vanderbilt University, Nashville, Tennessee 37235 (Received March 21, 1975)

Nuclear spin-lattice relaxation times, T_1 , of the hydrogen nuclei in CD_3OH and CH_3OH have been measured as a function of concentration in solvents of varying hydrogen bonding ability. $\text{CD}_3\text{OH}-\text{CCl}_4$, $\text{CD}_3\text{OH}-(\text{CD}_3)_2\text{CO}$, $\text{CD}_3\text{OH}-\text{CD}_3\text{OD}$, $\text{CD}_3\text{OH}-(\text{CD}_3)_2\text{SO}$, $\text{CH}_3\text{OH}-\text{CCl}_4$, and $\text{CH}_3\text{OH}-(\text{CD}_3)_2\text{CO}$ mixtures were studied over the entire range of concentration at 31° . The results show that T_1 reaches a minimum in all solvents at ~ 0.9 mole fraction alcohol. This is interpreted in terms of the structure of pure liquid methanol being disrupted by insertion of small amounts of solvent. Extrapolation of the spin-lattice relaxation time to infinite dilution, T_1° , gives an indication of the strength of the alcohol-solvent hydrogen bond. T_1° is shortest in CCl_4 and increases in the order: $(\text{CD}_3)_2\text{CO} < \text{CD}_3\text{OD} < (\text{CD}_3)_2\text{SO}$. This behavior is explained by the hindrance of rotation of the alcohol as a result of the formation of hydrogen bonds of increasing strength with the solvent. At large mole fractions of methanol, relaxation is interpreted to be a mixture of dipole-dipole and spin-rotation interaction; while in dilute solutions the spin-rotation mechanism seems to predominate.

Introduction

The spin-lattice relaxation time, T_1 , has been extensively used to describe molecular motion in liquids. The theoretical basis of the method is well developed.^{2a} Many studies in this area describe the analysis of T_1 values for a molecule in terms of specific relaxation mechanisms and compare experimental results with the predictions of a theoretical model for the motion of the molecule in a liquid.

NMR chemical-shift studies have been used to examine hydrogen-bonding effects in alcohols.^{2b} Relaxation-time studies of water-alcohol mixtures,^{3,4} ROD-perdeuterio-ROD mixtures,⁵ and acetone-water mixtures⁶ have been reported; but, to our knowledge, no systematic examination for the effect of hydrogen bonding on the relaxation time of hydroxylic protons in alcohols has been published.

In this paper, relaxation measurements on hydrogen in the following binary systems are reported: (1) methyl- d_3 alcohol with carbon tetrachloride, acetone- d_6 , methanol- d_4 , or dimethyl- d_6 sulfoxide, and (2) methanol with carbon tetrachloride or acetone- d_6 .

Experimental Section

NMR Spectrometer System. A Varian XL-100-15 multi-nuclear spectrometer was employed with an external heteronuclear lock on ^2H . This system includes a Transform Technology, Inc. (TT-100) Fourier-transform unit. Sample temperature in the probe was 31° .

T_1 Measurements. Measurements of ^1H spin-lattice relaxation times, T_1 , were accomplished by the inversion-recovery pulse method.^{7,8} For the systems examined here $P(180^\circ)$ was found to be $150 \mu\text{sec}$ and $P(90^\circ)$ $75 \mu\text{sec}$. The delay times between the pulses, τ , were chosen to bracket the inversion point at which $T_1 = \tau/\ln 2$. The computer permits automated accumulation of the $180^\circ-\tau-90^\circ$ sequences and then rapid processing, storage, and presentation of data. T_1 values were computed automatically and by hand from a plot of $\ln(I_\infty - I\tau)$ vs. τ , where I is the intensity of the peak. Results obtained by both methods were in close agreement. However, the hand-plotted T_1 values were used in subsequent calculations because they exhibited somewhat less scatter. The T_1 values obtained were

found to be reproducible to within a few percent; but the usual error assumed in measurements of this type is $\pm 10\%$.

Chemicals. Methanol and carbon tetrachloride were Fisher reagent grade. These were carefully distilled before use with the middle one-third fraction being collected and dried over molecular sieves. Methyl- d_3 alcohol (99.5% D) was purchased from IC & N Chemicals and used without further purification. Methanol- d_4 (99.5% D), acetone- d_6 (99.5% D), and dimethyl- d_6 sulfoxide (99.5% D) were purchased from Wilmad Glass Co. and were dried over molecular sieves. Deuterium oxide (99.8% D) was purchased from Stohler Isotope Chemicals.

Sample Preparation. The components of each mixture were deoxygenated by bubbling high-purity nitrogen through the liquid for 10 min. The components were then weighed into a nitrogen-filled 5-mm NMR tube. This tube was placed inside a 12-mm tube containing the reference lock material, D_2O . The concentration of the sample was varied by adding more of the appropriate component to the original mixture. Samples prepared in this manner gave reproducible T_1 values, and the plots of $(T_1)^{-1}$ vs. concentration obtained from dilutions of several different samples could be joined without disconcerting discontinuities. For each pair of components, at least four separate samples were prepared and then diluted to obtain T_1 data over the entire concentration range. In addition, several samples were prepared without deoxygenating the components, and the resulting T_1 values were found to be 10–20% shorter than those of the corresponding deoxygenated samples. Deoxygenation by the freeze-pump-thaw method did not increase T_1 values.

Results and Discussion

Interpretation in Terms of Liquid Structure. Figures 1 and 2 show the ^1H spin-lattice relaxation rate, $(T_1)^{-1}$, in mixtures plotted against the mole fraction of alcohol monomer for CD_3OH and CH_3OH , respectively. The relaxation rates at infinite dilution, $(T_1^\circ)^{-1}$, were obtained by extrapolation of the linear portion of each plot to zero mole fraction of alcohol.

A perturbed nuclear-spin system relaxes to its equilibri-

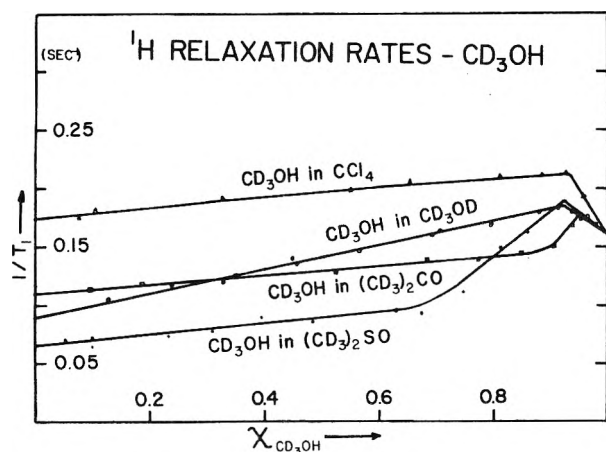


Figure 1. Relaxation rate, $1/T_1$, for the hydrogen nucleus in CD_3OH plotted against the mole fraction of CD_3OH monomer, $\chi_{\text{CD}_3\text{OH}}$, in CCl_4 , CD_3OD , $(\text{CD}_3)_2\text{CO}$, and $(\text{CD}_3)_2\text{SO}$.

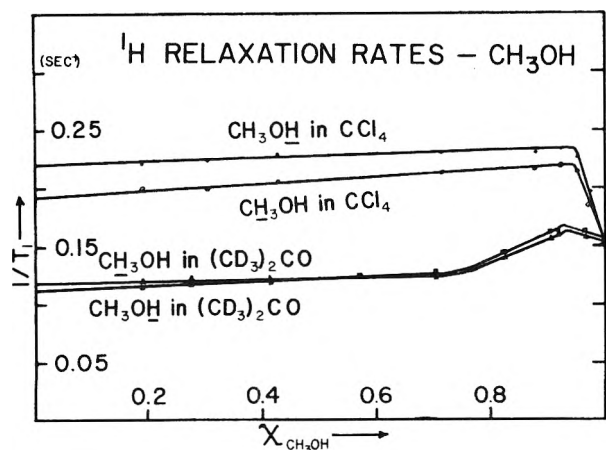


Figure 2. Relaxation rate, $1/T_1$, for the hydrogen nuclei in CH_3OH plotted against the mole fraction of CH_3OH monomer, $\chi_{\text{CH}_3\text{OH}}$, in CCl_4 and $(\text{CD}_3)_2\text{CO}$. The underlining of CH_3OH denotes that the curve represents the behavior of the methyl hydrogens; whereas CH_3OH is underlined to denote that the curve refers to the behavior of the hydroxyl hydrogen.

um state by coupling between the spin system and the surrounding environment. The principal processes that lead to spin-lattice relaxation in liquids involve some type of molecular motion. For hydrogen nuclei these processes are:⁹ (1) magnetic dipole-dipole interaction, (2) spin-rotation interaction, (3) scalar-coupling interaction, (4) chemical-shift anisotropy interaction, and (5) interaction due to the presence of paramagnetic materials in the sample.

Mechanism 5 is eliminated by the use of glassware and chemicals not contaminated by paramagnetic materials and by careful deoxygenation of the test samples. Mechanism 4 is relaxation due to the tumbling of structures exhibiting large chemical-shift anisotropy. For nonviscous liquids it has been shown that this relaxation rate is proportional to $H_0^2(\sigma_{\parallel} - \sigma_{\perp})^2$, where H_0 is the magnetic field strength and σ_{\parallel} and σ_{\perp} are the values of the shielding factor parallel to and perpendicular to the axis of symmetry of the molecule.⁹ Studies have shown that the ^1H relaxation rates in ethanol¹⁰ and HF¹¹ do not vary with H_0 . We esti-

mate the $(T_1)^{-1}$ contribution due to chemical-shift anisotropy is $<10^{-5} \text{ sec}^{-1}$.

Scalar coupling, mechanism 3, can contribute importantly to relaxation in methanol under certain conditions.^{12,13} When methanol is carefully acidified, the ^1H relaxation rate varies with acid concentration, passing through a sharp peak at $\text{pH} \sim 3$. The magnitude of the scalar relaxation rate depends on the proton-exchange rate and is important only at proton-exchange rates intermediate between that of pure methanol and highly acidified methanol.

For pure methanol at 31° the following contributions from scalar coupling relaxation are estimated: $[T_1(\text{CH}_3)]_{\text{sc}}^{-1} = 0.004 \text{ sec}^{-1}$ and $[T_1(\text{OH})]_{\text{sc}}^{-1} = 0.012 \text{ sec}^{-1}$. This is about 8% of the total experimental relaxation rate for the hydroxyl proton and 3% of the experimental relaxation rate for the methyl protons. As methanol is diluted, the correlation time for proton exchange increases, and the scalar mechanism rapidly becomes less important. For CD_3OH the scalar relaxation rate will be smaller due to the small hydrogen-deuterium coupling constant.

The total relaxation rate is given by $(T_1)^{-1} = (T_{1\text{DD}})^{-1} + (T_{1\text{SR}})^{-1} + (T_{1\bullet})^{-1}$, where $(T_{1\bullet})^{-1}$ represents the sum of the remaining relaxation rates which, to a good approximation, should contribute 10% or less to $(T_1)^{-1}$. Most ^1H relaxation has been shown to be of the dipole-dipole type, although spin-rotation may be important in some instances.¹⁴⁻¹⁶ The magnitude of the ^1H - ^1H dipole-dipole relaxation rate is directly proportional to the number of hydrogen nuclei per unit volume of solution and inversely proportional to the sixth power of the distance between these nuclei. ^1H - ^2H dipole-dipole relaxation is an interaction that, for the same situation, is weaker by a factor of 24 than the ^1H - ^1H relaxation.

In Figure 3, the ^1H relaxation rate for CD_3OH - CD_3OD mixtures is plotted against the mole fraction of CD_3OH monomer. The ^1H - ^1H dipole-dipole contribution must essentially vanish at zero mole fraction alcohol (excluding a negligible contribution from intramolecular ^1H - ^2H interaction in the CD_3OH monomer) since the hydrogen nuclei are isolated from one another in a deuterated lattice. Therefore the entire ^1H relaxation rate at infinite dilution ought to arise from the spin-rotation mechanism. Because substitution of H for D in the hydroxyl group of methanol should not affect the liquid structure of the alcohol, it is assumed that $(T_{1\text{SR}})^{-1}$ remains fairly constant over the entire CD_3OH mole fraction range. The difference between the experimental relaxation rate and the spin-rotation contribution is attributed to dipole-dipole relaxation, the rate of which therefore should rise linearly with increasing ^1H concentration, as it does for $0 < \chi_{\text{CD}_3\text{OH}} < 0.92$. The dotted portion of the dipole-dipole relaxation rate line in Figure 3 is an extension of this linear increase to $\chi_{\text{CD}_3\text{OH}} = 1.0$, while the solid line in this region represents the observed behavior. The difference between the experimental relaxation rate and the sum of $(T_{1\text{SR}})^{-1} + (T_{1\text{DD}})^{-1}_{\text{linear}}$ may be designated the excess relaxation rate, $(T_{1\text{xs}})^{-1}$. Using the same method, values of $(T_{1\text{xs}})^{-1}$ can be determined for CD_3OH in the other solvents. Then, relaxation rate ratios can be converted into distance ratios using the relation $r'/r = \{(T_{1\text{DD}})^{-1} / [(T_{1\text{DD}})^{-1} + (T_{1\text{xs}})^{-1}]\}^{1/6}$, where r' is the ^1H - ^1H distance indicated by the experimental relaxation rate minus the spin-rotation relaxation rate, and r is the ^1H - ^1H distance indicated by the linear dipole-dipole relaxation rate. Figure 4 shows r'/r for CD_3OH in the various solvents plotted against mole fraction of alcohol monomer. At

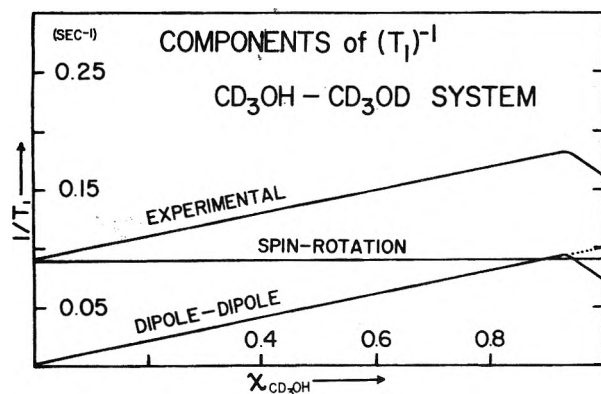


Figure 3. Components of $1/T_1$ for the $\text{CD}_3\text{OH}-\text{CD}_3\text{OD}$ system. Relaxation rate, $1/T_1$, plotted against the mole fraction of CD_3OH monomer, $\chi_{\text{CD}_3\text{OH}}$. The upper curve represents the experimentally determined values. The spin-rotation contribution was determined by assuming that as $\chi_{\text{CD}_3\text{OH}} \rightarrow 0$ essentially all of the relaxation is of the spin-rotation type. The dipole-dipole contribution is the difference between the experimental and spin-rotation curves. When $0.93 < \chi_{\text{CD}_3\text{OH}} < 1.00$, the dotted portion of the dipole-dipole curve represents the expected behavior, while the solid portion of this curve represents the observed behavior.

$\chi_{\text{CD}_3\text{OH}} < 0.2$, $(T_{1x})^{-1}$ becomes difficult to determine graphically, and at $\chi_{\text{CD}_3\text{OH}} = 0$ the ratio r'/r is indeterminate.

A great deal of discussion on the nature and relative amounts of the species present in liquid methanol is available.¹⁷ The data on which these studies are based are derived from a variety of physical methods, including NMR, ir, and dielectric-moment measurements. There is general agreement that the liquid is composed of a mixture of polymeric chains and rings, although no consensus on the size or relative amounts of the rings and chains exists.

Scaled models of methanol chain and ring structures were used to obtain H-H distances, $r_{\text{H-H}}$. In chain structures $r_{\text{H-H}}$ is ~ 2.30 Å between nearest neighbors. With the next set of hydrogens being at $r_{\text{H-H}} \sim 4.20$ Å, and the H-H interaction falling off with $r_{\text{H-H}}^{-6}$, this gives an effective $r_{\text{H-H}}$ of ~ 2.29 Å [$r_{\text{eff}} = (r_1^{-6} + r_2^{-6})^{-1/6}$]. The cyclic dimer and trimer are highly strained structures which should be present only in low concentration, if they exist at all. The cyclic tetramer is an interesting structure in several respects. A nearly planar ring of four linear O-H...O bonds has an effective $r_{\text{H-H}}$ of ~ 1.93 Å. Pauling noted that the cyclic tetramer should be especially stable for methanol and that it has been observed in methanol vapor and in the crystal structures of other alcohols.¹⁸ As ring size is increased to the pentamer, hexamer, or larger rings, the effective $r_{\text{H-H}}$ becomes nearly the same as in the chain structures. In terms of H-H distance these are not significantly distinguishable from chains. Therefore, liquid methanol may be viewed as a mixture of chains and cyclic tetramers, where "chains" refers to both the linear polymers of varying size and the large ring polymers.

As seen in Figure 4, the substitution of D for H in CD_3OH causes $r_{\text{H-H}}$ to decrease sharply until a break occurs at 0.92 mole fraction of CD_3OH in CD_3OD . Further dilution by CD_3OD results in a constant $r_{\text{H-H}}$ over the observed concentration range. If the deuterium nuclei are placed at random in one of the chain structures, they have the effect of gradually spacing out the hydrogen nuclei and reducing the interaction between them. The trend is accounted for by the decreasing magnitude of the dipole-di-

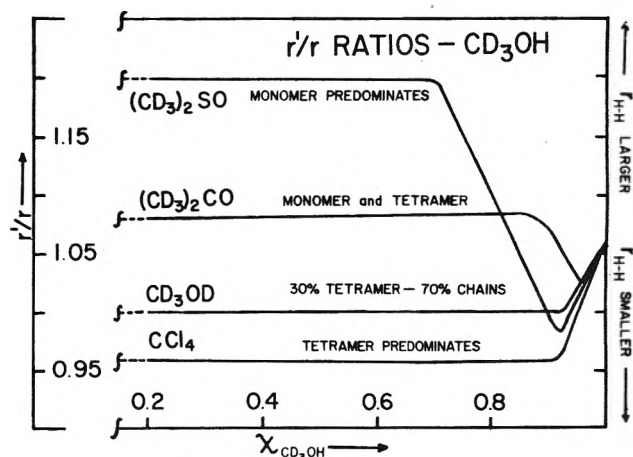


Figure 4. The ratio of the calculated hydrogen-hydrogen distance (r') for CD_3OH in $(\text{CD}_3)_2\text{SO}$, $(\text{CD}_3)_2\text{CO}$, and CCl_4 to the calculated hydrogen-hydrogen distance (r) for CD_3OH in CD_3OD plotted against the mole fraction of CD_3OH monomer, $\chi_{\text{CD}_3\text{OH}}$. The species of CD_3OH assumed to predominate in each solvent is indicated on the curve for that solvent.

pole relaxation rate observed in Figure 3. There should be no abrupt breaks in this behavior. However, when one of the hydrogens in the hydrogen-bonded tetramer ring is replaced by a deuterium, the effective $r_{\text{H-H}}$ (including a correction for the H-D interaction) decreases from 1.93 to 1.73 Å. The insertion of a second deuterium into the tetramer ring gives an effective $r_{\text{H-H}}$ value of 1.71 Å, which is approximately equal to the previous distance and, therefore, not distinguishable as a different $r_{\text{H-H}}$. The break in the $\text{CD}_3\text{OH}-\text{CD}_3\text{OD}$ curve of Figure 4 must correspond to the composition at which each cyclic tetramer structure has one deuterium in the ring. The location of the break at $\chi_{\text{CD}_3\text{OH}} \sim 0.92$ implies that in the alcohol there are approximately 2.2 hydrogens in the chain structures for each hydrogen in the cyclic tetramer structure, so that the pure alcohol is $\sim 30\%$ cyclic tetramer. The observed $r_{\text{H-H}}$ decrease from $\chi_{\text{CD}_3\text{OH}} = 1.0$ to $\chi_{\text{CD}_3\text{OH}} = 0.92$ in Figure 4 is 6% as compared to the calculated decrease of 7% (effective $r_{\text{H-H}}$ decreases from 2.13 to 1.99 Å). In terms of relaxation rate, the maximum experimental relaxation rate in Figure 3 corresponds to the point at which the average distance between hydrogen nuclei in CD_3OH is at a minimum.

Carbon tetrachloride acts as an inert solvent toward methanol with respect to hydrogen bonding. Any methanol- CCl_4 hydrogen-bonded adduct must be of negligible stability in comparison to the stability of self-associated methanol clusters ($\Delta H_{\text{H-bond}} \sim -3$ kcal/mol^{17f}). It seems reasonable to assume that as methanol is diluted by CCl_4 the larger polymeric species are successively broken up until the stable methanol cyclic tetramer becomes the predominant species. The position of the $\text{CD}_3\text{OH}-\text{CCl}_4$ curve in Figure 4 at the smallest $r_{\text{H-H}}$ value supports this assumption. Presumably the break in this curve represents the point at which an essentially constant fraction of the alcohol is in the cyclic tetramer form and no further decrease in $r_{\text{H-H}}$ occurs. At this point $r_{\text{H-H}}$ is 10% smaller than in the pure alcohol. This may be compared with a calculated decrease of 12% (pure alcohol effective $r_{\text{H-H}} = 2.13$ Å; cyclic tetramer, effective $r_{\text{H-H}} = 1.93$ Å). The discrepancy between these two values is probably due to the presence of other species, such as the dimer, in the methanol- CCl_4 mixtures. The postulation here of the cyclic tetramer

as the predominant species is in good agreement with the conclusions of other authors on the structure of methanol in dilute methanol- CCl_4 mixtures.^{17b,e,h}

As dimethyl sulfoxide is a moderately strong hydrogen-bonding solvent, the predominant species in dilute methanol-DMSO solutions would be expected to be a 1:1 adduct. A model of this adduct has a diameter of $\sim 5.8 \text{ \AA}$. Assuming that $r_{\text{H-H}}$ in a lattice of these monomer adducts is about one-half the diameter ($\sim 2.9 \text{ \AA}$), then the change in $r_{\text{H-H}}$ in going from the pure alcohol to the 1:1 $\text{CD}_3\text{OH-DMSO-}d_6$ adduct would be an increase of 36% (2.90/2.13). The increase indicated by Figure 4 is 13%. For the methanol-dimethyl sulfoxide adduct ΔH is $\sim -6.3 \text{ kcal/mol}$.^{2b} A model of the $\text{CD}_3\text{OH-acetone-}d_6$ 1:1 adduct has a diameter of $\sim 5.5 \text{ \AA}$. Again using $r_{\text{H-H}}$ in a lattice of monomer adducts as one-half the diameter (2.75 \AA), the change in $r_{\text{H-H}}$ from the pure alcohol to the 1:1 adduct would be an increase of 29% (2.75/2.13). The increase indicated by Figure 4 is 3%. For the methanol-acetone adduct ΔH is $\sim -2.5 \text{ kcal/mol}$.² The indicated increases in $r_{\text{H-H}}$ are less than the calculated increases because the methanol cyclic tetramer competes with the methanol-solvent adduct. The indicated changes in $r_{\text{H-H}}$ from Figure 4 imply that the methanol-dimethyl sulfoxide system at $\chi_{\text{CD}_3\text{OH}} < 0.7$ is 82% 1:1 adduct and 18% cyclic tetramer (effective $r_{\text{H-H}} = 2.43 \text{ \AA}$), while the methanol-acetone system at $\chi_{\text{CD}_3\text{OH}} < 0.7$ is 62% 1:1 adduct and 38% cyclic tetramer (effective $r_{\text{H-H}} = 2.20 \text{ \AA}$). This is consistent with the values of ΔH for self-association and adduct formation. The decreasing portion of the curves for these solvents in Figure 4 represents the breakup of the pure alcohol into smaller fragments, with the minimum $r_{\text{H-H}}$ representing the point of maximum cyclic tetramer concentration. As significant amounts of 1:1 alcohol-solvent adduct are formed, $r_{\text{H-H}}$ begins to increase. The flat portion of the curve represents an equilibrium between the adduct and the cyclic tetramer.

From Figure 2 it is apparent that similar trends are present for CH_3OH in CCl_4 and acetone- d_6 . The presence of the methyl hydrogens in CH_3OH complicates the analysis, since the monomer intramolecular relaxation rate becomes significant.

Estimation of Relaxation Rates. The dipole-dipole mechanism has been discussed extensively for systems similar to these. It is composed of two contributions: $(T_{1\text{DD}})^{-1} = (T_{1\text{intra}})^{-1} + (T_{1\text{inter}})^{-1}$. The contributions can be separated, yielding for hydrogen-hydrogen relaxation³

$$(T_{1\text{intra}})^{-1} = F\tau_r = (\hbar^2\gamma^4\alpha/n) \left(\sum_{i=1}^n \sum_{j=1, j \neq i}^n \tau_r/r_{ij}^6 \right) \quad (1)$$

$$(T_{1\text{inter}})^{-1} = (\Pi\hbar^2\gamma^4N_H\tau_t/d^3)(1 + 2d^2/5D\tau_t) \quad (2)$$

where γ = gyromagnetic ratio of ^1H ; n = number of ^1H per molecule; $\alpha = 4I(I+1)/3$, except that $\alpha = 4/3$ when $i = j$; r_{ij} = distance between hydrogens i and j ; τ_r = correlation time for reorientation; N_H = number of hydrogens/cm³; d = distance of closest approach between hydrogens; D = self-diffusion constant; and τ_t = diffusion jump time. The same expressions may be used to calculate hydrogen-deuterium relaxation, although the weaker interaction must be corrected by a factor of 24 ($\alpha_{\text{HH}}\gamma_{\text{H}}^2/\alpha_{\text{HD}}\gamma_{\text{D}}^2 = 24$). The reorientation time, τ_r , may be estimated from the Debye relation for a spherical molecule $\tau_r \sim 4\pi f_r\eta a^3/kT$, where a is the effective molecular radius, which may be obtained from the molar volume for the cubic closest-packing case: $4\pi N_0 a^3/3 = 0.74V_m$; η is the macroscopic viscosity; and f_r is

the Gierer-Wirtz rotational correction¹⁹ factor, which equals 0.17 for methanol. The self-diffusion constant may be estimated from the relation $D \sim kT/6\pi f_t\eta a$ where f_t is the Gierer-Wirtz translational correction factor, which equals 0.79 for methanol.

The spin-rotation interaction arises from the coupling of a nuclear magnetic moment to the magnetic field set up at the nuclear site by the rotational motion of the surrounding molecular charge distribution.²⁰ Excellent papers by Gillen²¹ and Hubbard²² discuss the assumptions required and difficulties involved in quantitative evaluation of the spin-rotation relaxation rate. For spherical molecules of moment of inertia I , at absolute temperature T , Hubbard obtained

$$(T_{1\text{SR}})^{-1} = (8\pi^2IkT/h^2)C_{\text{eff}}^2\tau_{\text{SR}} \quad (3)$$

where C is the spin-rotation coupling constant and τ_{SR} is the spin-rotation correlation time. When the spin-rotation coupling constant is not available from the literature, an alternate method of evaluating τ_{SR} comes from the theoretical expression derived by Hubbard relating τ_{SR} to the reorientational correlation time, τ_r , for a spherical molecule undergoing isotropic Brownian rotational diffusion, $\tau_{\text{SR}} \sim I/6kT\tau_r$. Substituting for τ_{SR} in eq 3 yields

$$(T_{1\text{SR}})^{-1} = \frac{4\pi^2I^2}{3h^2\tau_r} C_{\text{eff}}^2 \quad (4)$$

In theory, C should be evaluated for each of the principal axes of the molecule in question using the moment of inertia about that axis. In practice, I is often taken as $I_{\parallel}/3 + 2I_{\perp}/3$, I_{\parallel} and I_{\perp} referring to the moments of inertia about and perpendicular to the major symmetry axis. The value of C obtained in this manner is then the effective spin-rotation coupling constant, C_{eff} .

For the pure alcohols the partitioning of the dipole-dipole relaxation rate between the intramolecular and intermolecular contributions may be envisioned in two ways. The intramolecular rate may be considered as arising from interactions within the monomer unit only and the intermolecular rate as arising from interactions between monomers in the different polymeric species. Alternately, the intramolecular rate may take into account all the internal interactions in the various polymeric species and the intermolecular rate only the external interactions. The two methods are actually roughly equivalent as eq 2 is derived from eq 1 by integration over distance. Since there is no detailed knowledge of the composition of liquid methanol, the first method is more easily applied. In dilute methanol the species postulated in the previous discussion may be used to calculate the intramolecular and intermolecular dipole-dipole relaxation rates.

The spin-rotation relaxation rate is, likewise, difficult to predict for the pure alcohols, as C_{eff} is not available from the literature and it is not possible to calculate a meaningful value of the moment of inertia for the complex mixture of species present. In the diluted solutions, the moment of inertia can be estimated for each major species and a value for C_{eff} extracted from eq 4.

Results of the estimation of theoretical contributions to the total relaxation rate and comparison of the total estimated relaxation rates with the experimental relaxation rates are presented in Table I. Contributions to $(T_{1\text{intra}})^{-1}$ from $^1\text{H-}^{13}\text{C}$ and $^1\text{H-}^{17}\text{O}$ interactions and to $(T_{1\text{inter}})^{-1}$ from $^1\text{H-}^2\text{H}$ interactions are calculated to be negligible ($< 10^{-3} \text{ sec}^{-1}$). The distance of closest approach, d , is usually taken to be twice the effective molecular radius, a .

TABLE I: Relaxation Rates for CD₃OH and CH₃OH (in sec⁻¹)

	$(T_{1\text{ intra}})^{-1}$	$(T_{1\text{ inter}})^{-1}$	$(T_{1\text{ SR}})^{-1}$	$(T_{1\text{ tot}})^{-1}$	$(T_{1\text{ expt}})^{-1}$
CD ₃ OH	0.001	0.066	0.089	0.156	0.161
CH ₃ OH	0.010	0.086	0.056	0.152	0.156
CH ₃ OH	0.027	0.068	0.056	0.151	0.151

TABLE II: Relaxation Rates (sec⁻¹) and Spin-Rotation Coupling Constants (kHz) for CD₃OH and CH₃OH at Infinite Dilution

Identity of H	Solvent	$(T_{1\text{ DD}})^{-1}$	$(T_{1\text{ SR}})^{-1}$	C_{eff}	$(T_{1\text{ expt}})^{-1}$
CD ₃ OH	CCl ₄	0.063	0.110	7.0	0.173
CD ₃ OH	Acetone- <i>d</i> ₆	0.016	0.093	8.5	0.109
CD ₃ OH	DMSO- <i>d</i> ₆	0.052	0.014	10.8	0.067
CH ₃ OH	CCl ₄	0.098	0.123	8.4	0.221
CH ₃ OH	Acetone- <i>d</i> ₆	0.026	0.087	9.9	0.113
CH ₃ OH	CCl ₄	0.046	0.146	9.1	0.192
CH ₃ OH	Acetone- <i>d</i> ₆	0.021	0.097	10.4	0.118

However, this "hard-sphere" model is deficient in several respects: it does not distinguish between the intermolecular interaction of two methyl groups and the markedly different type of interaction between hydroxyl groups in a hydrogen-bonding system. Adjustments to the model should logically follow some scheme of considering d between hydroxyl groups to be less than $2a$, while d for the hydroxyl-methyl interaction should be increased to greater than $2a$. At the same time, for methyl-methyl interaction, satisfactory results should be obtained using $d = 2a$. The results in Table I were obtained using $d = 1.2a$ for the hydroxyl-hydroxyl distance, $d = 4a$ for the hydroxyl-methyl distance, and $d = 2a$ for the methyl-methyl distance. This choice of parameters yields good agreement with experimental results. Radius a is estimated to be 2.30 Å for CD₃OH and 2.29 Å for CH₃OH. The experimentally determined τ_t for methanol is 41×10^{-12} sec.²³ For comparison, the τ_t obtained from dielectric-relaxation studies is 69×10^{-12} sec.^{24,25} $(T_{1\text{ SR}})^{-1}$ for CD₃OH was estimated by subtracting $(T_{1\text{ intra}})^{-1}$ from $(T_{1\text{ expt}})^{-1}$. $(T_{1\text{ SR}})^{-1}$ for CH₃OH was roughly estimated by assuming that C_{eff} is the same for CD₃OH and CH₃OH, and setting the ratio of the moments of inertia equal to that calculated for the monomers ($I_{\text{CD}_3\text{OH}}/I_{\text{CH}_3\text{OH}} = 3.16 \times 10^{-39}/2.48 \times 10^{-39} = 1.27$). $(T_{1\text{ SR}})^{-1}$ was then calculated from eq 4. The validity of these assumptions is questionable, but the results they give are consistent with the experimental relaxation rates. These results indicate that spin-rotation represents 55% of the total relaxation rate in CD₃OH and 36% of the total in CH₃OH. For comparison, in acetonitrile at 31° spin-rotation has been estimated to account for 45% of the total relaxation rate.¹⁵

At infinite dilution $(T_{1\text{ inter}})^{-1}$ vanishes. $(T_{1\text{ intra}})^{-1}$ may be estimated for methanol in each solvent using $r_{\text{H-H}}$ obtained from models of the species presumed to be present in each case. Again, $(T_{1\text{ SR}})^{-1}$ is taken as $(T_{1\text{ expt}})^{-1} - (T_{1\text{ intra}})^{-1}$. C_{eff} may be calculated from eq 4 by estimating a value of I for each species. The results of these calculations are presented in Table II. The values of $(T_{1\text{ SR}})^{-1}$ show a dependence on the hydrogen-bonding ability of the solvent. This may be visualized as increasingly hindered rotation when the strength of the methanol-solvent hydro-

gen bond increases. The somewhat arbitrary partitioning of the total relaxation rate between $(T_{1\text{ intra}})^{-1}$ and $(T_{1\text{ SR}})^{-1}$ is not a crucial factor if one bears in mind that they are both forms of intramolecular relaxation.

The variation of $(T_{1\text{ expt}})^{-1}$ with χ_{MeOH} can be explained quite consistently by taking in account the different species present at each concentration and the effect of methanol-solvent hydrogen bonding on the structure of the alcohol.

Acknowledgments. We wish to thank Dr. P. J. Wang, working under NSF Grant No. GP-28698X, for assistance in the operation of the NMR spectrometer. The Varian XL-100 spectrometer was purchased through Vanderbilt's Center of Excellence Award under the National Science Development Program sponsored by the National Science Foundation and Vanderbilt University.

References and Notes

- (1) Tennessee Eastman Fellow, 1974-1975.
- (2) (a) A. Abragam, "The Principles of Nuclear Magnetism", Clarendon Press, Oxford, 1961. (b) M. D. Joesten and L. J. Schaad, "Hydrogen Bonding", Marcel Dekker, New York, N.Y., 1974, Chapter 4 and references therein.
- (3) E. von Goldammer and M. D. Zeidler, *Ber. Bunsenges Phys. Chem.*, **73**, 4 (1969).
- (4) J. Oakes, *J. Chem. Soc., Faraday Trans. 2*, **69**, 1311 (1973).
- (5) M. D. Zeidler, *Ber. Bunsenges Phys. Chem.*, **69**, 659 (1965).
- (6) L. W. Reeves and C. P. Yue, *Can. J. Chem.*, **48**, 3307 (1970).
- (7) R. L. Vold, J. S. Waugh, M. P. Klein, and D. E. Phelps, *J. Chem. Phys.*, **48**, 3831 (1968).
- (8) A. Allerhand, D. Doddrell, V. Glushko, D. W. Cochran, E. Wenkert, P. J. Lawson, and F. R. N. Gurd, *J. Am. Chem. Soc.*, **93**, 544 (1971).
- (9) T. C. Farrar and E. D. Becker, "Pulse and Fourier Transform NMR", Academic Press, New York, N.Y., 1971.
- (10) N. Bloembergen, E. M. Purcell, and R. V. Pound, *Phys. Rev.*, **79**, 679 (1948).
- (11) H. S. Gutowsky and D. E. Woessner, *Phys. Rev.*, **104**, 843 (1956).
- (12) M. Cocivera, *J. Chem. Phys.*, **47**, 1112 (1967).
- (13) T. Fukcumi, Y. Arata, and S. Fujiwara, *J. Chem. Phys.*, **49**, 4198 (1968).
- (14) C. Deverell, *Mol. Phys.*, **18**, 319 (1970).
- (15) D. E. Woessner, B. S. Snowden, Jr., and E. T. Strom, *Mol. Phys.*, **14**, 265 (1968).
- (16) K. T. Gillen, M. Schwartz, and J. H. Noggle, *Mol. Phys.*, **20**, 899 (1971).
- (17) (a) W. Weltner, Jr., and K. S. Pitzer, *J. Am. Chem. Soc.*, **73**, 2006 (1951); (b) M. Saunders and J. B. Hyne, *J. Chem. Phys.*, **29**, 1319 (1958); (c) J. C. Davis, Jr., K. S. Pitzer, and C. N. R. Rao, *J. Phys. Chem.*, **64**, 1774 (1960); (d) E. Grunwald, C. F. Jumper, and S. Meiboom, *J. Am. Chem. Soc.*, **84**, 4664 (1962); (e) P. I. Gold and R. L. Perrine, *J. Phys. Chem.*, **71**, 4218 (1967); (f) R. M. Hammaker, R. M. Clegg, L. K. Patterson, P. E. Rider, and S. L. Rock, *ibid.*, **72**, 1837 (1968); (g) E. E. Tucker, S. B. Farnham, and S. D. Christian, *ibid.*, **73**, 3820 (1970); (h) W. B. Dixon, *ibid.*, **74**, 1396 (1970).

- (18) L. Pauling, "The Nature of the Chemical Bond", 3rd ed, Cornell University Press, Ithaca, N.Y., 1960.
 (19) A. Gierer and K. Wirtz, *Z. Naturforsch. A*, **8**, 532 (1953).
 (20) R. L. Armstrong and J. A. Courtney, *Can. J. Phys.*, **50**, 1262 (1972).
 (21) K. T. Gillen, *J. Chem. Phys.*, **56**, 1573 (1972).
 (22) P. S. Hubbard, *Phys. Rev.*, **131**, 1155 (1963).
 (23) H. G. Hertz and M. D. Zeidler, *Ber. Bunsenges. Phys. Chem.*, **67**, 774 (1963).
 (24) R. W. Rampolla, R. C. Miller, and C. P. Smyth, *J. Chem. Phys.*, **30**, 566 (1959).
 (25) J. A. Saxton, R. A. Bond, G. T. Coats, and R. M. Dickinson, *J. Chem. Phys.*, **37**, 2132 (1962).

Electrochemical and Transport Properties of Lithium Chloride Solutions in Dimethyl Sulfoxide–Water and Dimethyl Sulfoxide–Methanol Mixtures

Melvin H. Miles,* L. Wayne McMahon, and Susan M. Nelson

Department of Chemistry, Middle Tennessee State University, Murfreesboro, Tennessee 37130 (Received April 9, 1975)

Publication costs assisted by Middle Tennessee State University

Solutions of 1.00 M LiCl in DMSO–water and in DMSO–methanol mixtures were investigated to determine the effect of solvent composition on viscosity, electrolytic conductance, and electrochemical reactions of the solution. Addition of LiCl shifts the composition of the viscosity maxima observed in DMSO–water systems. Activation energies for ionic motion and viscous flow seem to give consistent information regarding solvent compositions at which molecular interactions are greatest. Cyclic voltammetric measurements on platinum electrodes indicate that the electrochemical reduction of lithium ions is hindered in DMSO–water mixtures. Possible explanations include the existence of adjacent layers of DMSO and water at the electrode surface which hinder the penetration of the solvated lithium ion.

Introduction

Dimethyl sulfoxide (DMSO) is a versatile solvent characterized by a broad liquid range, good dissolving power, and electrochemical stability over a wide potential range. When mixed with water, strong intermolecular interactions between water and DMSO molecules are suggested by physical properties such as viscosities and heats of mixing,^{1–4} as well as by phase diagrams,⁵ sound propagation,⁶ and spectroscopic studies.^{7,8} Most of these studies indicate that the strongest interactions occur at about 0.35 mole fraction DMSO suggesting the existence of a thermolabile DMSO·2H₂O association complex. For electrochemical applications, mixed solvents containing a strong electrolyte are desired. Fundamental properties could not be located in the literature for such three-component systems, hence studies were made of the electrochemical and transport properties of 1.00 M LiCl solutions in DMSO–water mixtures and in DMSO–methanol mixtures. A previous study reported properties of electrolyte solutions in water–methanol mixtures.⁹

Experimental Section

Electrolytic conductivity measurements were made with a Beckman conductivity bridge (Model RC-18A) having a specified accuracy of $\pm 0.05\%$. Resistance measurements were made at a frequency of 1000 Hz using cells of the conventional Jones design with platinized platinum electrodes. Cell constants were determined using 0.1000 M KCl and the specific conductivity values of 0.012889 $\text{ohm}^{-1} \text{cm}^{-1}$ at 25°C and 0.019457 $\text{ohm}^{-1} \text{cm}^{-1}$ at 50°C reported by DeWane and Hamer.¹⁰ Cell constants determined at 25 and 50°C differed by less than 1%. Due to difficulties in remov-

ing water from the salt,¹¹ the lithium chloride (Fisher) was dried for at least 1 week at 160°C prior to use. Conductivity measurements at 25°C on two separate aqueous solutions of 1.00 M LiCl prepared using the dried salt gave an average specific conductivity of $0.0735 \pm 0.0005 \text{ ohm}^{-1} \text{cm}^{-1}$ which agrees favorably with the value of 0.0731 $\text{ohm}^{-1} \text{cm}^{-1}$ from the International Critical Tables.

Viscosity measurements were made as previously described,⁹ except for the application of kinetic-energy corrections in calculating the viscosities. This correction was usually less than 1% of the actual viscosity. The Ostwald viscosimeter was calibrated with water using handbook values of 8.904 mP at 25°C and 5.468 mP at 50°C for the viscosity of water. For both conductivity and viscosity measurements, the temperature was controlled to $\pm 0.01^\circ\text{C}$ of the stated temperature.

Electrode stability limits were determined by cyclic voltammetric measurements made with a PAR electrochemistry system (Model 170) using a potential sweep rate of 100 mV/sec. The experimental details of such studies are given elsewhere.⁹

Solution preparations were made using Baker reagent grade dimethyl sulfoxide with spectrophotometric reagent grade methanol or deionized distilled water. The reported water content was 0.02% for both the DMSO and methanol.

Results

The experimental viscosities of 1.00 M LiCl in DMSO–water and DMSO–methanol mixtures are displayed in Figure 1 for the temperatures of 25 and 50°C. For the DMSO–water salt solutions, maxima on the viscosity–composition curves occur at about 0.5 mole fraction DMSO. This differs from the reported viscosity maxima at a composition of

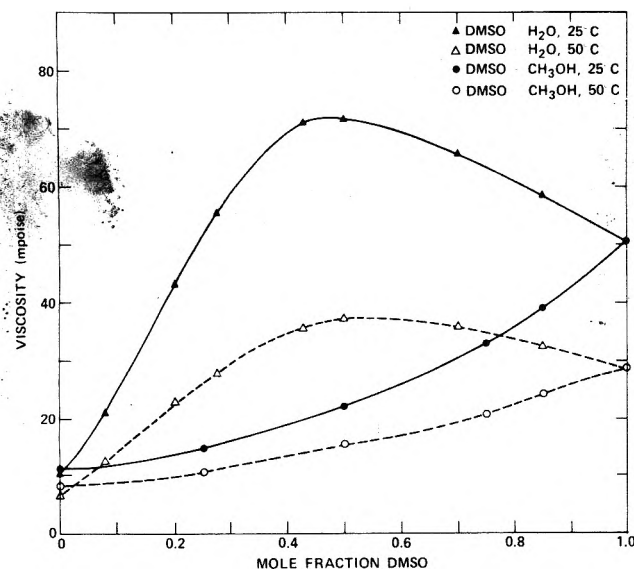


Figure 1. Variation of viscosity with mole fraction DMSO for 1.00 M LiCl solutions in DMSO-water and DMSO-methanol mixtures at 25.0 and 50.0°C.

about 0.35 mole fraction DMSO in the absence of any added salt.¹⁻⁴ The addition of lithium chloride greatly increases the viscosity as well as causing a shift in the composition at which viscosity maxima occur. As found in the studies involving the solvents only,^{1,2} a sharper viscosity maximum is found at the lower temperature.

No viscosity maxima are found for the DMSO-methanol solutions. The viscosity-composition curve for DMSO-methanol solutions is similar to that found in the absence of added electrolyte,³ except that the viscosity values are again greatly increased by the addition of lithium chloride.

Specific conductivity-composition curves shown in Figure 2 again display the contrasting behavior of the DMSO-water and DMSO-methanol mixtures containing 1.00 M LiCl. In the DMSO-water system, the specific conductivity decreases sharply with increasing DMSO concentration up to about 0.5 mole fraction DMSO. In the DMSO-methanol system, the specific conductivity shows a gradual, linear decrease with increasing mole fraction of DMSO over the entire composition range.

Typical cyclic voltammetry curves for the DMSO-water system containing 1.00 M LiCl are shown in Figure 3 for three different solvent compositions. Each experiment was performed at room temperature ($25 \pm 1^\circ\text{C}$) using a platinum electrode. The shape of the cathodic sweep trace was found to depend greatly on the solvent composition. The reduction of water dominates in the water-rich systems while the reduction of lithium ions is the dominating cathodic reaction in the DMSO solution. At the intermediate composition, there is neither significant reduction of water nor of lithium ions even at extremely negative potentials of -5.0 V vs. SCE. Similar results were observed for the DMSO-methanol system with the exception that significant methanol reduction was observed in solutions containing up to 0.75 mole fraction DMSO.

The horizontal line segments in Figure 3 represent an arbitrary limit where the current density exceeds 10 mA/cm^2 (geometrical area). The potential region within these anodic and cathodic limits defines the electrostability region for the selected solvent-electrolyte-electrode system.^{9,12} Figure 4 presents the electrostability limits for 1.00 M LiCl in

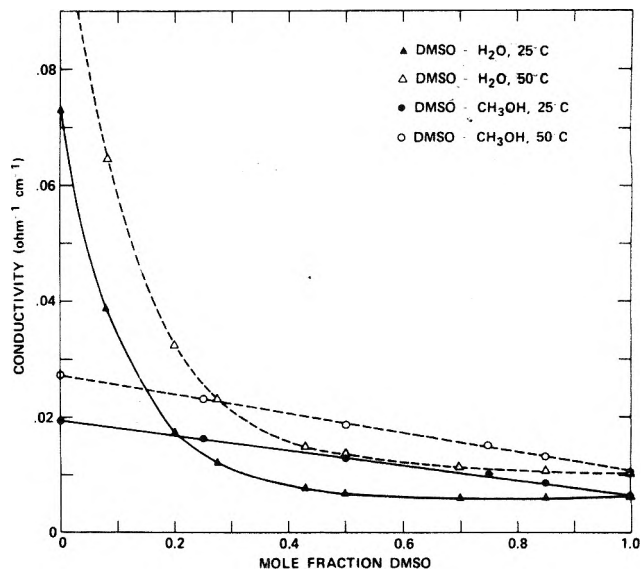


Figure 2. Variation of the specific conductivity with mole fraction DMSO for 1.00 M LiCl solutions in DMSO-water and DMSO-methanol mixtures at 25.0 and 50.0°C.

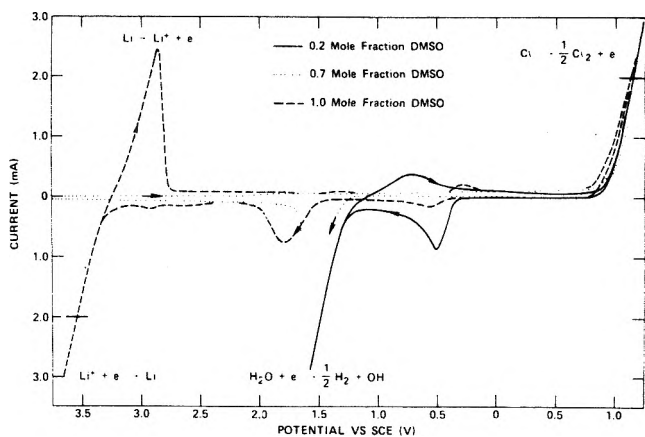


Figure 3. Cyclic voltammograms for 1.00 M LiCl solutions in DMSO-water mixtures at 25°C on a platinum wire electrode with geometrical area equal to 0.2 cm^2 . The potential sweep rate used was 100 mV/sec .

DMSO-water and in DMSO-methanol mixtures as observed using a platinum electrode. While the anodic limits undergo little change with solvent composition, the cathodic limits show sharp changes at compositions where neither the reduction of the solvent nor the reduction of lithium ions can yield a current of 10 mA/cm^2 at a sweep rate of 100 mV/sec . Significant reduction of lithium ions becomes possible only at very high DMSO concentrations.

Discussion

The energy barriers for both ionic motion and viscous flow are determined largely by solvent molecules jumping from one equilibrium position to another. Since the activated state requires formation of holes for the molecules to move into,¹³ it is logical that the activation energies for such processes will be highest where solvent interactions are greatest. Arrhenius-type activation energies for viscous flow (E_η) and for specific conductivity (E_κ) calculated from the experimental data at 25 and 50°C are displayed in Figure 5. Both types of activation energies show maxima in the

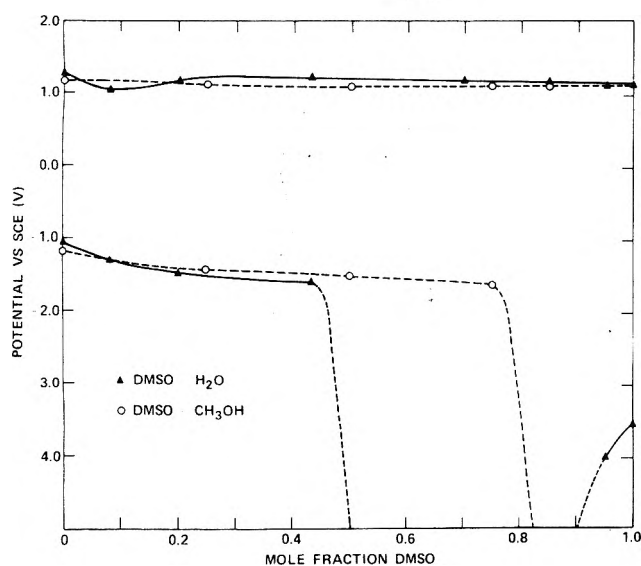


Figure 4. Variation of the anodic and cathodic electrostability limits with mole fraction DMSO at 25°C on a platinum electrode in DMSO-water and DMSO-methanol mixtures containing 1.00 M LiCl.

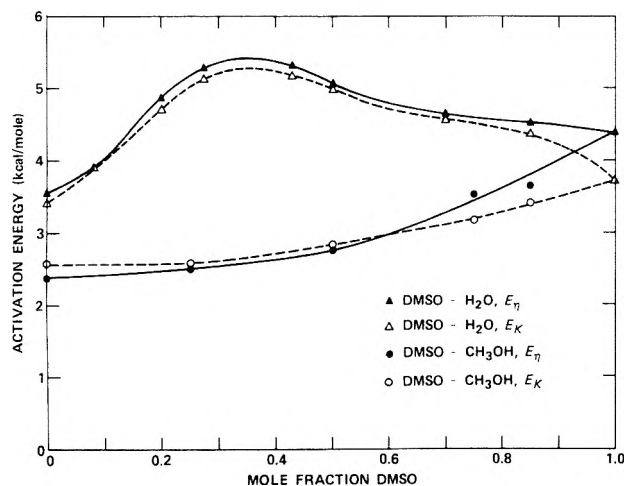


Figure 5. Activation energies for viscosity and specific conductivity as a function of the solvent composition for 1.00 M LiCl solutions in DMSO-water and DMSO-methanol mixtures.

DMSO-water-LiCl system at about 0.35 mole fraction DMSO rather than at the composition of the maxima in viscosities. In the absence of added electrolyte in the DMSO-water system, maxima in both viscosities and activation energies occur at about the same composition.^{1,2} Viscosity measurements on various mixed solvent systems by Ebert and Wendorff⁴ also indicate shifts in the composition at the viscosity maxima with the addition of various salts whereas the compositions at maxima in activation energies seem to be scarcely affected. Changes in temperature also tend to shift the composition of the viscosity maxima,^{2,4} hence activation energies for ionic motion and viscous flow seem to give more consistent information regarding compositions at which molecular interactions are greatest in mixed solvent systems. Results in Figure 5 for the DMSO-methanol system show increasing activation energies with increasing mole fraction DMSO, indicating that interactions between DMSO molecules are the strongest type present in this system.

TABLE I: Calculated Parameters for the DMSO-Water Mixtures

X_{DMSO} , mole fraction	LiCl:DMSO: H ₂ O, mole ratios	E_{η} , kcal mol ⁻¹	$\Delta S_{\eta}^{\ddagger}$, cal deg ⁻¹ mol ⁻¹	Δ
0.00	1:0:55	3.53	4.3	
0.08	1:3.5:40	3.92	3.8	0.56
0.20	1:7:27	4.86	5.0	1.11
0.28	1:8:21	5.31	5.7	1.23
0.35	1:9:17	5.32	5.2	1.31
0.43	1:10:14	5.31	4.9	1.25
0.50	1:11:11	5.08	3.8	1.14
0.70	1:12:5	4.64	2.1	0.74
0.85	1:13:2	4.53	1.7	0.38
1.00	1:14:0	4.38	1.2	

By use of the Eyring rate equation for viscous flow¹³

$$\eta = \frac{Nh}{V} e^{-\Delta S_{\eta}^{\ddagger}/R} e^{\Delta H_{\eta}^{\ddagger}/RT} \quad (1)$$

the entropy of activation, $\Delta S_{\eta}^{\ddagger}$, can be calculated for each mole fraction if E_{η} is identified with $\Delta H_{\eta}^{\ddagger}$. The calculated values for $\Delta S_{\eta}^{\ddagger}$ can be found in Table I. A maximum value of about 6 cal deg⁻¹ mol⁻¹ is found near the composition of 0.3 mole fraction DMSO. This positive, maximum value reflects that the disordering process in forming holes is greatest where solvent structure is most extensive. From the data of Cowie and Toporowski,¹ maxima values of 5.1 kcal mol⁻¹ for E_{η} and 6 cal deg⁻¹ mol⁻¹ for $\Delta S_{\eta}^{\ddagger}$ are also observed in pure DMSO-water systems at about 0.3 mole fraction DMSO. (Values given by ref 2 covering a lower temperature region are in error due to neglect of the factor 2.303 in calculating E_{η} .) It appears that addition of LiCl increases the viscosity by making it energetically more difficult to create the necessary holes. The small lithium and sodium ions are well known for their strong interactions with DMSO and water producing an increase in solvent structure.¹⁴⁻¹⁶

Viscosities of mixtures of similar liquids often tend to obey the Kendall equation

$$\log \eta = x_1 \log \eta_1 + x_2 \log \eta_2 \quad (2)$$

where x_1 and x_2 represent mole fractions of the two mixed solvents. This equation can be derived from the Eyring equation for the viscosity of mixtures of similar liquids.¹³ The DMSO-methanol mixtures give reasonable agreement as calculated values range only 3-7% higher than the experimental values. For the DMSO-water system; the difference, Δ , given by

$$\Delta = \log \eta_{\text{expt}} - x_1 \log \eta_1 - x_2 \log \eta_2 \quad (3)$$

seems to reflect the extent of interactions between the molecules. As shown in Table I, Δ shows the expected maximum at about 0.35 mole fraction DMSO. Theoretically, the excess free energy of activation for viscous flow in associated mixtures is related to Δ by the expression $\Delta G_{\text{excess}}^{\ddagger} = 2.303RT\Delta$. Fort and Moore³ have proposed the use of the parameter d where $d = \Delta/x_1x_2$ as a measure of the strength of interaction between solvent components in liquid mixtures. However, for DMSO-water, the value of d shows only a steady decrease as the mole fraction of DMSO increases.

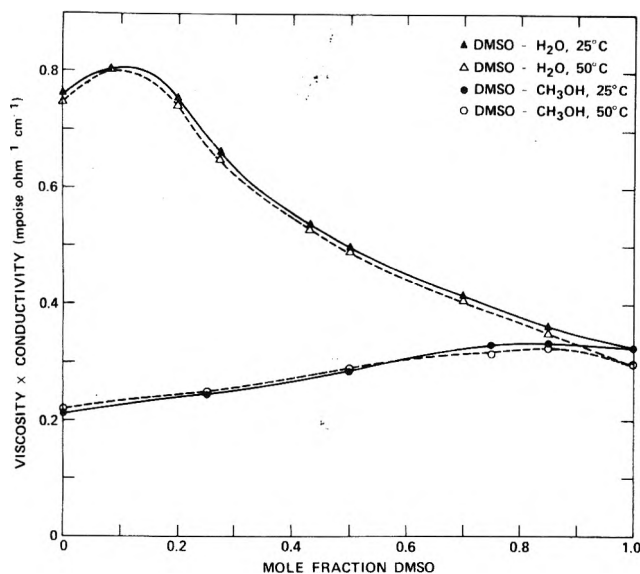


Figure 6. Variation of the specific conductivity-viscosity product with mole fraction DMSO for 1.00 M LiCl solutions in DMSO-water and DMSO-methanol mixtures at 25.0 and 50.0°C.

Conflicting conclusions exist concerning ion association of salts dissolved in DMSO.¹⁷⁻¹⁹ The product of specific conductivity and viscosity shown in Figure 6 is usually considered to be approximately proportional to the ionic concentration. Judging from this $k\eta$ product, 1.00 M lithium chloride is about 40% ionized in DMSO and about 30% ionized in methanol. However, theoretical calculations indicate that chemical equilibria between the ions and components of the solvent may also cause the $k\eta$ product to vary with solvent composition.²⁰ It is interesting to note from Figure 6 that the $k\eta$ product is relatively insensitive to changes in temperature.

The influence of the solvent on the electrochemical reduction of lithium ions is complex and involves ion-solvent-electrode interactions within the double layer. Considering Figure 4 and Table I, lithium ion reduction on platinum electrodes becomes possible in DMSO-water mixtures at about the solvent composition where there are fewer water molecules than lithium ions. Blocking of the electrode surface by a substance such as LiOH would hinder the electrochemical reactions,^{21,22} however, no obvious blocking effects were observed for the subsequent chlorine-evolution reaction (Figure 3). The study by Dey²³ has shown that water bound to the dissolved salt is much more difficult to reduce than the free water.

From Gibbs isotherm

$$\Gamma_2 = -\frac{1}{RT} \frac{\partial \gamma}{\partial \ln a_2} \quad (4)$$

the decreasing surface tensions with increasing DMSO content reported for DMSO-water mixtures²⁴ indicate that DMSO molecules will tend to accumulate at any surface. Since the potential for lithium ion reduction is negative to the zero-charge potential for platinum electrodes, the DMSO molecules will probably be attached to the electrode through the positive sulfur atoms while the negative oxygen atoms likely extend outward toward the solution. Due to the strong interaction between DMSO and water, an adjacent water layer would be formed by hydrogen bonding with the negative oxygen atoms of DMSO. Thus,

in becoming reduced, a lithium ion will have to penetrate both solvent layers. Extra solvation exchange processes which hinder the reaction would explain the experimental difficulty observed in the reduction of lithium ions in DMSO-water mixtures. Ion-solvent forces seem to be the major factor controlling the rate constants for the reduction of alkali metal ions in various solvents^{14,16} as well as for the reduction of cadmium ions in DMSO.²⁵ Solvation exchange steps also appear to control the rate of discharge of zinc ions in mixtures of water and 1-propanol where, as in the DMSO-water system, there is specific adsorption of the organic component on the electrode surface.²⁶ It is interesting to note that large currents could not be obtained for the anodic oxidation of chloride ions in DMSO-water mixtures where the reduction reactions were hindered. This is likely due to the lack of a reduction process required to complete the cell which can sustain large currents at the platinum screen counter electrode.

Acknowledgment. The financial support of this work by the Faculty Research Committee at Middle Tennessee State University is gratefully acknowledged.

Supplementary Material Available. A listing of experimental values for viscosities, specific conductivities, and solution densities at 25.0 and 50.0°C will appear following these pages in the microfilm edition of this volume of the journal. Photocopies of the supplementary material from this paper only or microfiche (105 × 148 mm, 24× reduction, negatives) containing all of the supplementary material for the papers in this issue may be obtained from the Business Office, Books and Journals Division, American Chemical Society, 1155 16th St., N.W., Washington, D.C. 20036. Remit check or money order for \$4.00 for photocopy or \$2.50 for microfiche, referring to code number JPC-75-2312.

References and Notes

- (1) J. M. G. Cowie and P. M. Toporowski, *Can. J. Chem.*, **39**, 2240 (1961).
- (2) S. A. Schichman and R. L. Amey, *J. Phys. Chem.*, **75**, 98 (1971).
- (3) R. J. Fort and W. R. Moore, *Trans. Faraday Soc.*, **62**, 1112 (1966).
- (4) G. Ebert and J. Wendorff, *Ber. Bunsenges. Phys. Chem.*, **74**, 1071 (1970).
- (5) D. J. Rasmussen and A. P. MacKenzie, *Nature (London)*, **220**, 1315 (1968).
- (6) D. E. Bowen, M. A. Priesand, and M. P. Eastman, *J. Phys. Chem.*, **78**, 2611 (1974).
- (7) O. D. Bonner and Y. S. Choi, *J. Phys. Chem.*, **78**, 1727 (1974).
- (8) T. Tokuhira, L. Menafra, and H. H. Szmant, *J. Chem. Phys.*, **61**, 2275 (1974).
- (9) M. H. Miles and V. Jiamsakul, *J. Electrochem. Soc.*, **120**, 709 (1973).
- (10) H. J. DeWane and W. J. Hamer, *Natl. Bur. Stand. Rep.*, No. 10076 (1969).
- (11) H. J. Gardner, C. T. Brown, and G. J. Janz, *J. Phys. Chem.*, **60**, 1458 (1956).
- (12) M. H. Miles and P. M. Kellett, *J. Electrochem. Soc.*, **115**, 1225 (1968).
- (13) S. Glasstone, K. J. Laidler, and H. Eyring, "The Theory of Rate Processes", McGraw-Hill, New York, N.Y., 1941.
- (14) J. Broadhead and P. J. Elving, *J. Electrochem. Soc.*, **118**, 63 (1971).
- (15) N. Yao and D. N. Bennion, *J. Phys. Chem.*, **75**, 1727 (1971).
- (16) G. J. Hills and L. M. Peter, *J. Electroanal. Chem. Interfacial Electrochem.*, **50**, 175 (1974).
- (17) P. G. Sears, G. R. Lester, and L. R. Dawson, *J. Phys. Chem.*, **60**, 1433 (1956).
- (18) J. S. Dunnitt and R. P. H. Gasser, *Trans. Faraday Soc.*, **61**, 922 (1965).
- (19) B. W. Maxey and A. I. Popov, *J. Am. Chem. Soc.*, **91**, 20 (1969).
- (20) P. Hemmes, *J. Phys. Chem.*, **78**, 907 (1974).
- (21) B. Burrows and S. Kirkland, *J. Electrochem. Soc.*, **115**, 1164 (1968).
- (22) B. K. Makarenko, Y. M. Povarov, P. A. Sereda, and N. Y. Bobrova, *Elektrokhimiya*, **9**, 705 (1973).
- (23) A. N. Dey, *J. Electrochem. Soc.*, **114**, 823 (1967).
- (24) E. Tommila and A. Pajunen, *Suom. Kemistil. B*, **41**, 172 (1968).
- (25) G. J. Hills and L. M. Peter, *J. Electroanal. Chem. Interfacial Electrochem.*, **50**, 187 (1974).
- (26) M. H. Miles and H. Gerischer, *J. Electrochem. Soc.*, **118**, 837 (1971).

Influence of the Formation of Ions on the Viscosity of Phenol–Amine Mixtures

Noël G. Felix and Pierre L. Huyskens*

Department of Chemistry, University of Leuven, Celestijnenlaan 200-F, B-3030 Heverlee, Belgium (Received June 3, 1975)

Publication costs assisted by KUL and FCFO, Belgium

Mixing of aliphatic amines with phenols brings about a spectacular increase of the viscosity η which in some cases becomes more than a hundred times greater than that of the pure liquid compounds. These mixtures are also characterized by a great volume contraction, the maximum of which occurs in the vicinity of a mole fraction $x_A = 0.67$ in phenol. The maximal viscosity does not correspond with the maximum in the volume contraction but is shifted toward higher values of x_A . The electric conductivity κ as a function of x_A shows in some cases two maxima but this is no longer the case for the product $\kappa\eta$, the single maximum of which lies in the vicinity of that of the viscosity. $\kappa\eta$ is proportional to $\langle w_i \rangle \Sigma C_i$ where $\langle w_i \rangle$ is the mean Walden product of the ions and ΣC_i their total concentration. It appears that the enhancement of the viscosity occurs in the range of mole fractions where $\kappa\eta$, and thus the ion concentration, becomes nonnegligible. The high value of the viscosity of this mixture is thus related to the presence of ions which are also responsible for the conductivity. These ions are not directly derived from the ab complexes although these are characterized by important volume contractions which extend to parts of the molecules outside the hydrogen bond and which depend on the acid strength of the phenol. The addition of a second phenol molecule to the ab complex causes a marked increase in the volume contraction but the a_2b complexes are not yet principally responsible for ion formation and for the increase of the viscosity. This is realized by $a_n b$ complexes of still higher stoichiometry. The comparison of the η and $\kappa\eta$ curves shows that cations of several types participate to a significant extent in the conductivity in the region of high viscosity, namely, the homoconjugated ions $R_3NH^+NR_3$ and the cations where R_3NH^+ form a hydrogen bond with a lone pair of electrons of the oxygen atom of the phenol. An important role seems to be devoted to the anions where the phenolate ion is bonded with three phenol molecules. The viscosity depends not only on the concentration of the ions which are responsible for the conductivity but also to an important extent on the size of these ions.

Introduction

Mixing of aliphatic amines with phenols brings about a spectacular increase in the viscosity of the liquid phase. For instance, if the viscosity of pure 2-chlorophenol is 3.4 cP and that of triethylamine only 0.35 cP at 298 K, a mixture of both compounds shows a maximum of viscosity as high as 594 cP at a mole fraction of the phenol $x_A = 0.72$.

The phenol–amine mixtures are also characterized by an important volume contraction. This volume contraction shows a single maximum which in the 2-chlorophenol–triethylamine mixtures represents 10% of the molar volume of the phenol.

A third property which varies in a spectacular way as a function of the mole fraction is the electric conductivity κ . Whereas the conductivities of pure 2-chlorophenol and pure triethylamine are very small, of the order respectively of 5×10^{-9} and 5×10^{-13} ohm $^{-1}$ cm $^{-1}$, two maxima appear in the mixtures of these compounds; these maxima amount to 2×10^{-4} and 4×10^{-4} ohm $^{-1}$ cm $^{-1}$.

It is the aim of this work to try to correlate these various phenomena on the basis of a molecular model, considering the hydrogen bonds which are broken and which are formed when the phenol and the amine are mixed together.

The work is based on the measurement of the viscosities η , the densities ρ , and the electric conductivities κ of seven phenol–amine systems at 298 K.

Experimental Section

Viscosity measurements were performed by means of viscosimeters of the Ostwald type and with the MGM Lauda

viscosimeter with an accuracy of 0.1%. Densities were measured within 0.001 g cm $^{-3}$ with a hydrostatic balance. For conductivities above 10^{-7} ohm $^{-1}$ cm $^{-1}$ the Wayne-Kerr universal bridge B 221 A, operating at 1592 Hz, was used, whereas lower conductivities were measured with a Keitley electrometer. The cells were Philips DW 9512 calibrated following the method of Lind, Zwolenik, and Fuoss¹ or Balsbaugh 100 T₃.

Phenol, 4-methylphenol (Merck pro analysis), and 2-chlorophenol (Fluka purissimum) were further purified by vacuum distillation. Triethylamine and diethylamine (Fluka purissimum) were distilled in the presence of KOH.

Results

For each system, the dynamic viscosities η , the densities ρ , and the electric conductivities κ of some 16 binary mixtures were determined. As an example the data for the system triethylamine–2-chlorophenol are tabulated in Table I. (The experimental data for the other systems are included in an extended Table available on microfilm; see paragraph at end of text regarding supplementary material.)

When the viscosities of the mixtures are plotted vs. the mole fraction (Figures 1 and 2) all the curves show a single maximum. The mole fraction x_A , where this maximum appears, and its value are given in Table II. The maximum in the viscosity curve does not appear at the same fraction x_A for all the systems. There is a systematic shift toward the lower mole fraction when the phenol becomes more acidic. Furthermore, for a given phenol the height of the viscosity peak is greater with triethylamine which, although less

TABLE I: Viscosities, Densities, Conductivities, Molar Volumes, and Molar Volume of Mixing of the System Triethylamine–2-Chlorophenol at 298 K

x_A	η , cP	ρ , g cm ⁻³	κ , ohm ⁻¹ cm ⁻¹	\bar{V} , cm ³ mol ⁻¹	$\Delta\bar{V}_M$, cm ³ mol ⁻¹
0.000	3.50×10^{-1}	0.724	5.00×10^{-13}	139.8	0.0
0.074	4.47×10^{-1}	0.762	5.63×10^{-11}	135.5	-1.5
0.305	1.41	0.891	5.07×10^{-5}	122.9	-5.4
0.408	3.58	0.958	1.50×10^{-4}	117.3	-7.2
0.473	7.81	1.001	1.93×10^{-4}	113.7	-8.3
0.552	2.62×10^1	1.059	1.74×10^{-4}	109.8	-9.2
0.616	1.09×10^2	1.107	1.02×10^{-4}	106.6	-10.0
0.650	2.55×10^2	1.132	7.29×10^{-5}	105.1	-10.2
0.703	5.29×10^2	1.165	6.75×10^{-5}	103.4	-10.0
0.720	5.94×10^2	1.175	6.94×10^{-5}	102.9	-9.8
0.751	4.51×10^2	1.189	1.09×10^{-4}	102.4	-9.8
0.769	3.43×10^2	1.196	1.29×10^{-4}	102.2	-8.7
0.797	2.13×10^2	1.207	2.02×10^{-4}	101.9	-7.9
0.843	6.89×10^1	1.222	3.33×10^{-4}	101.8	-6.4
0.870	3.43×10^1	1.228	3.94×10^{-4}	101.8	-5.3
0.901	1.83×10^1	1.230	3.67×10^{-4}	102.3	-3.6
0.956	5.91	1.244	1.11×10^{-4}	102.4	-1.5
1.000	3.36	1.258	5.40×10^{-9}	102.2	0.0

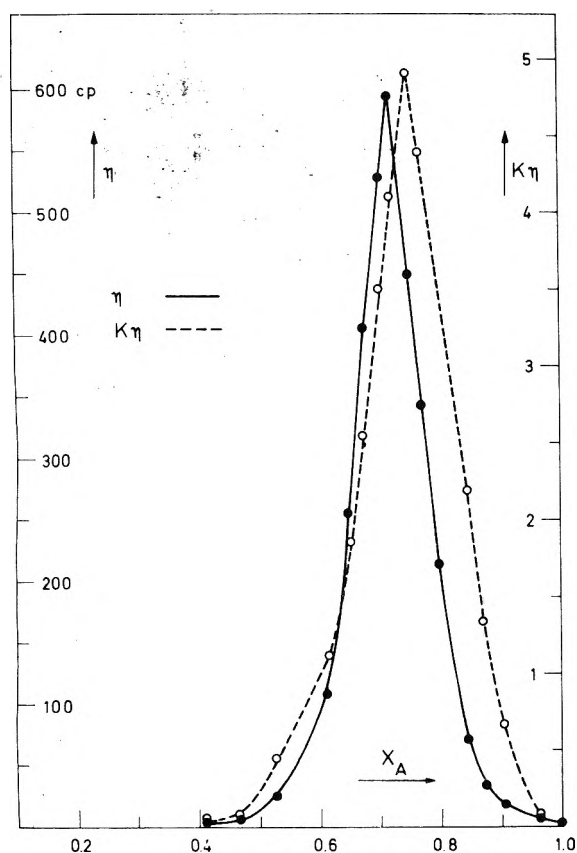
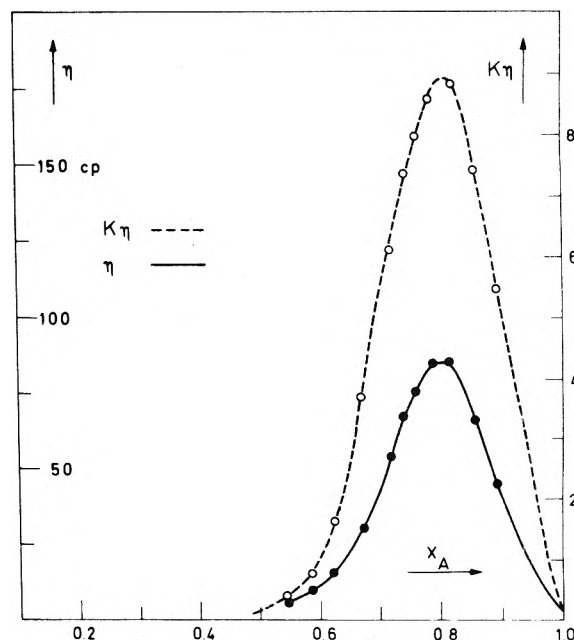

Figure 1. Triethylamine–2-chlorophenol. Viscosity η (in cp) (●) and product $\kappa\eta$ (in 10^{-2} ohm⁻¹ cm⁻¹ cp) (○) as a function of the mole fraction x_A of the phenol at 298 K.

TABLE II: Maximal Viscosities of the Mixtures, Mole Fraction of the Phenol at the Maximum, and pK_a of the Phenol

System	η_{max} , cP	x_A	pK_a
TEA–2-chlorophenol	594	0.72	8.49
TEA–4-chlorophenol	396	0.76	9.39
TEA–phenol	128	0.80	9.98
TEA–4-methylphenol	129	0.84	10.18
DEA–4-chlorophenol	263	0.75	9.39
DEA–phenol	87	0.80	9.98
DEA–4-methylphenol	88	0.83	10.18


Figure 2. Diethylamine–phenol Viscosity η (in cp) (●) and product $\kappa\eta$ (in 10^{-2} ohm⁻¹ cm⁻¹ cp) (○) as a function of the mole fraction x_A of the phenol at 298 K.

$$\Delta\bar{V}_M = \bar{V} - x_A\bar{V}_A^0 - x_B\bar{V}_B^0 = \frac{x_A M_A + x_B M_B}{\rho} - x_A\bar{V}_A^0 - x_B\bar{V}_B^0 \quad (1)$$

where \bar{V} , \bar{V}_A^0 , and \bar{V}_B^0 are the molar volume of the mixture and of the pure compounds, was computed from the densities (for the phenols which are solid at room temperature \bar{V}_A^0 was determined by extrapolation of the densities of the mixtures).

In the seven cases, $-\Delta\bar{V}_M$ show a single maximum at a mole fraction between 0.65 and 0.72 (Figure 3). It appears thus that the maximum in the viscosity does not occur at the mole fraction where the contraction is maximal, but is shifted toward higher values of x_A . Furthermore, the volume contraction is already important at mole fractions beneath 0.5 where the viscosity does not yet reach 10 cP.

At 298 K some conductivity curves are characterized by the appearance of two maxima which lie between $x_A = 0.5$ and $x_A = 0.9$ (Figure 4).

Discussion

(1) *Viscosity and Concentration of the Ions.* When instead of the conductivity, the product of the conductivity

basic in water than diethylamine, has an higher molar volume. The molar volume of mixing $\Delta\bar{V}_M$, defined as

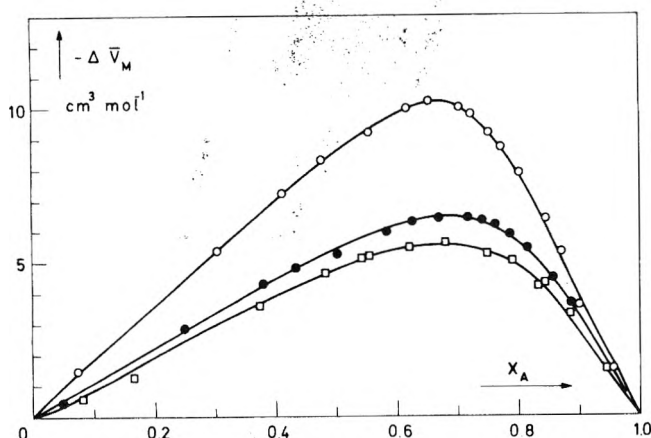


Figure 3. Volume contraction $-\Delta \bar{V}_M$ vs. the mole fraction x_A of the phenol at 298 K: (O) triethylamine-2-chlorophenol; (●) diethylamine-phenol; (□) diethylamine-4-methylphenol. The other curves lie between the two extremes.

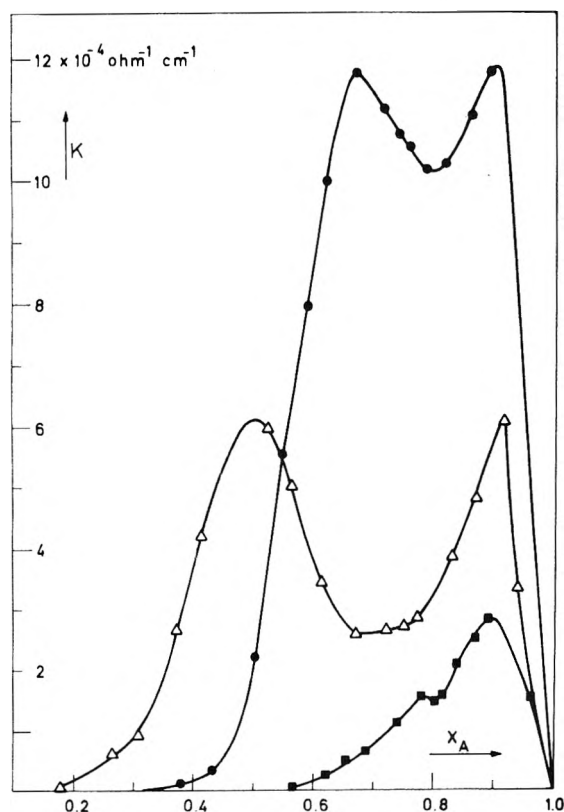


Figure 4. Electric conductivities κ of the mixtures vs. the mole fraction of the phenol at 298 K: (Δ) diethylamine-4-methylphenol; (●) diethylamine-phenol; (□) triethylamine-4-methylphenol. In the last case and for diethylamine-4-methylphenol and triethylamine-phenol only a shoulder is observed in the curves.

times the viscosity is plotted against the mole fraction, one no longer observes two maxima, but the curves show a single maximum the position of which is given in Table III. When only ions with a single charge appear, as it is the case here, the conductivity is related to the concentrations of the ions C_i by the relation

$$\kappa = \sum \lambda_i C_i / 1000 \quad (2)$$

where λ_i is the ionic equivalent conductance of the ion. λ_i

TABLE III: Maximal Value of the Product Conductivity-Viscosity and Mole Fraction x_A at the Maximum

System	$\kappa\eta$, $\text{ohm}^{-1} \text{cm}^{-1} \text{cP}$	x_A
TEA-2-chlorophenol	4.8×10^{-2}	0.75
TEA-4-chlorophenol	6.3×10^{-2}	0.83
TEA-phenol	7.2×10^{-2}	0.83
TEA-4-methylphenol	3.0×10^{-2}	0.85
DEA-4-chlorophenol	7.0×10^{-2}	0.77
DEA-phenol	9.0×10^{-2}	0.80
DEA-4-methylphenol	4.4×10^{-2}	0.83

depends upon the viscosity of the medium and, as a first approximation, this dependence is given by Walden's rule²

$$\lambda_i = w_i / \eta \quad (3)$$

where w_i is the "Walden product" of the ion. This leads to the expression

$$\kappa\eta = \sum w_i C_i / 1000 \quad (4)$$

which can also be written

$$\kappa\eta = \frac{\langle w_i \rangle}{1000} \sum C_i \quad (5)$$

where $\langle w_i \rangle$ is the mean Walden product of the ions.

The Walden product w_i depends upon the molar volume of the conducting species, but as shown in Figure 5³ where the data are taken from the literature, increasing this molar volume from 100 to 200 $\text{cm}^3 \text{mol}^{-1}$ only brings about a decrease of w_i ⁰ from 31.5 to 25.5 $\text{ohm}^{-1} \text{cm}^2 \text{equiv}^{-1} \text{cP}$, thus 19% of the original value.

The appearance of a sharp maximum in the $\kappa\eta$ curves, owing to the fact that in the vicinity of this maximum $\langle w_i \rangle$ can only vary to a limited extent, indicates a sharp maximum in the global ion concentration $\sum C_i$. The maximum of $\sum C_i$ must lie in the immediate vicinity of the maximum of $\kappa\eta$. When we consider the whole range of mole fraction, $\kappa\eta$ varies in several orders of magnitude. This is certainly not the case for $\langle w_i \rangle$. The value of $\kappa\eta$ reflects thus the order of magnitude of the total ion concentration $\sum C_i$.

It appears then that for the seven systems studied here, the range of the mole fractions x_A where the viscosities of the mixtures show a marked enhancement exactly corresponds with the range where $\kappa\eta$, and thus the total concentration of ions $\sum C_i$ becomes nonnegligible. Two examples are given in Figures 1 and 2. More precisely the viscosity exceeds that of the pure phenol when $\kappa\eta$ becomes greater than $10^{-3} \text{ohm}^{-1} \text{cm}^{-1} \text{cP}$. Furthermore for the systems with diethylamine the maxima in the viscosity and in $\sum C_i$ nearly correspond with each other. On the other hand, for the systems with triethylamine, although the maxima in $\kappa\eta$ are slightly shifted toward higher values of x_A , they are, at any rate not far removed from the maxima in the viscosity curves.

We can therefore conclude that the strong enhancement of the viscosity of given phenol-amine mixtures is related to the formation of ions which are able to contribute to the electric conductivity of the solution.

(2) Volume Contraction. (a) Contraction at Low Mole Fractions of Phenol. At low mole fractions of the phenol the volume contraction is due to the replacement of the hydrogen bonds of the autoassociated phenol by the stronger and more polar hydrogen bonds between the phenol and

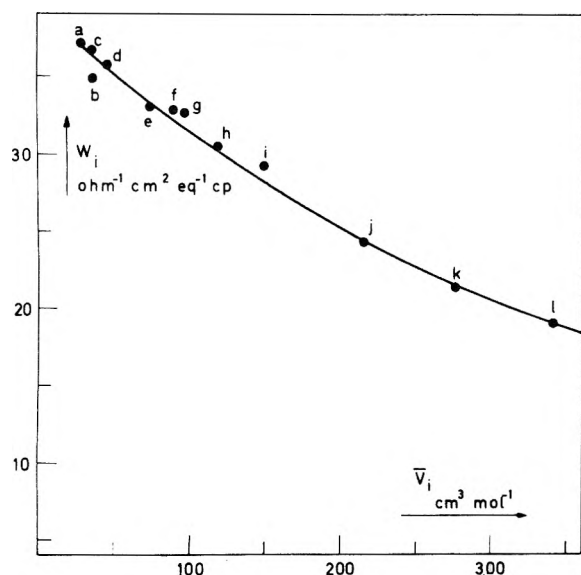


Figure 5. Walden product w_i as a function of the molar volume, \bar{V}_i , of the ion (a) NO_3^- , ref 3a; (b) CH_3COO^- , ref 3b; (c) I^- , ref 3c; (d) ClO_4^- , ref 3d; (e) $\text{C}_6\text{H}_5\text{O}^-$, ref 3e; (f) Et_2NH_2^+ , ref 3f; (g) Me_4N^+ , ref 3g; (h) Et_3NH^+ , ref 3h; (i) Et_4N^+ , ref 3i; (j) Prop_4N^+ , ref 3j; (k) Bu_4N^+ , ref 3k; (l) Am_4N^+ , ref 3l.

the amine. Owing to the high values of the complexation constant k_{ab} ³ it can be assumed that at low concentrations of the phenol in the amine, most of the phenol molecules appear as ab complexes. If $-\Delta\bar{V}_{ab}$ is the volume contraction accompanying the formation of 1 mol of this complex starting from the pure acid and from the pure base, the molar volume of mixing in this range of mole fractions must then obey the relation

$$\Delta\bar{V}_M = x_A \Delta\bar{V}_{ab} \quad (\text{low } x_A) \quad (6)$$

$\Delta\bar{V}_{ab}$ corresponds thus to the initial slope of the curves of $\Delta\bar{V}_M$ vs. x_A . The values of $\Delta\bar{V}_{ab}$ computed from the slopes are tabulated in Table IV. For a given base, $-\Delta\bar{V}_{ab}$ follows the sequence of the $\text{p}K_a$'s of the phenols. This is also the case for the complexation constant k_{ab} of the phenols without ortho substituents, determined in CCl_4 by Zeegers-Huyskens.⁴ Furthermore, it appears from the work of Ratajczak and Sobczyk⁵ and Jadzyn and Malecki,⁶ that the polarity of the ab complexes, described by the dipole increment $\Delta\mu$ brought about by the complexation, increases in the complexes with triethylamine when the phenol becomes more acidic. The contraction $-\Delta\bar{V}_{ab}$ will thus increase when the polarity of the hydrogen bond between the phenol and the amine is higher.

In such a hydrogen bond a reduction of the $\text{O}\cdots\text{H}$ distance of 1 Å in a region corresponding to the van der Waals radii of both atoms would only give a contraction of the order of 4 $\text{cm}^3 \text{mol}^{-1}$. The experimental values of $-\Delta\bar{V}_{ab}$ are much higher than this value, thus it can be concluded that the contraction is not restricted to the hydrogen bond itself but involves more removed regions of the molecules of the partners.

This important contraction accompanying the formation of the ab complex seems, however, to have rather limited influence on the viscosity of the solutions.

(b) *Volume Contraction in the Intermediate Range of Mole Fractions.* If the addition of more phenol molecules to an ab complex would not cause a supplementary volume contraction (this means if these bonds would maintain the

TABLE IV: Volume Contraction $-\Delta\bar{V}_{ab}$ of the ab Complex (Eq 6), Estimation of the Volume Contraction of the a_2b Complex

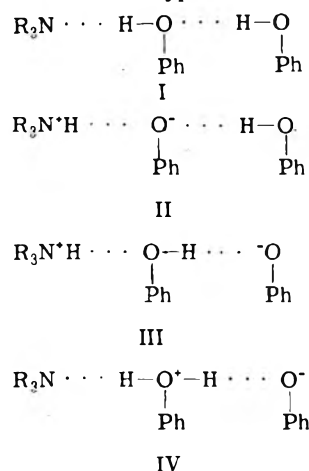
System	$-\Delta\bar{V}_{ab}$, cm^3 mol^{-1}	$-3\Delta\bar{V}_M$ (0.67)
TEA-2-chlorophenol	18	30.5
TEA-4-chlorophenol	16	22.5
TEA-phenol	12.5	20.7
TEA-4-methylphenol	11	18.8
DEA-4-chlorophenol	15	20.4
DEA-phenol	12	19.2
DEA-4-methylphenol	9	16.5

same volume characteristics as those of the autoassociation bonds in the pure phenol), $-\Delta\bar{V}_M$ would have a maximum at $x_A = 0.5$. As a matter of fact in all the systems studied here $-\Delta\bar{V}_M$ continues to increase above $x_A = 0.5$. From this it can be inferred that the addition of a second phenol molecule to the ab complex is accompanied with a marked volume contraction. If $-\Delta\bar{V}_{a_2b}$ represents the contraction corresponding to the formation of 1 mol of the a_2b complex starting from the pure phenol and the pure amine, this means that $-\Delta\bar{V}_{a_2b}$ is significantly greater than $-\Delta\bar{V}_{ab}$. This effect can be related to the fact that the addition constant k_{a_2b} is much greater than the autoassociation constant k as shown by Zeegers-Huyskens.⁴

At $x_A = 0.667$ the solutions contain, in addition to a_2b complexes, ab complexes and higher complexes a_3b , a_4b , ... as well as small concentrations of uncomplexed molecules. As a rough approximation, however, one can take for $-\Delta\bar{V}_{a_2b}$ three times the experimental value of $-\Delta\bar{V}_M$ at this mole fraction. These values are also tabulated in Table IV.

It must be noted that in some cases (4-chlorophenol-DEA, phenol-DEA, phenol-TEA) this estimation can be perturbed by the presence of a marked concentration of ions. However, in the other cases the values of $\kappa\eta$ are rather small at $x_A = 0.67$; thus it can be concluded that in the systems studied here the addition of a second molecule of acid to the ab complex causes a supplemental volume contraction of several centimeters³ mole⁻¹ compared with the complex ab and the pure phenol.

When one assumes that the potential curves of the proton in both cases present a double minimum, four configurations can be considered for the a_2b complex, namely I-IV. Of course these are hypothetical structures and in



practice some of them, as, for example, IV, may not be present to a significant extent.

(c) *Volume Contraction at High Values of x_A* . In a previous work⁷ we showed that in the pure liquid state, and at high concentrations in cyclohexane, the phenols studied which do not bear ortho substituents are highly associated, the mean number of molecules per associate \bar{n}_N exceeding seven at the concentration of 10 mol dm⁻³. When the amine is dissolved in a medium of high concentration of phenol, most of the molecules are bonded to phenol chains, the mean length of which is certainly not smaller than the value of \bar{n}_N which corresponds to the concentration of phenol. As a matter of fact one can only expect that the N...HO hydrogen bond will reinforce the adjacent O...HO bonds and this effect can only make the chain longer. This would result in a larger average degree of association.

Under these circumstances the molar volume of mixing $\Delta\bar{V}_M$ at high values of x_A obeys the relation

$$\Delta\bar{V}_M = x_A \Delta\bar{V}_{a_n b} (x_A - 1) \quad (7)$$

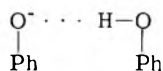
where n represents the average number of a molecules with which one base molecule is bonded ($n \geq \bar{n}_N$).

From the foregoing equation a value of $-\Delta\bar{V}_{a_n b}$ of 43 cm³ mol⁻¹ is deduced at high values of x_A for the system 2-chlorophenol-triethylamine. For the other systems the determination is less accurate, due to the uncertainty about the density of the pure phenols in the liquid phase, but, at any rate, the values of $\Delta\bar{V}_{a_n b}$ lie between 25 and 45 cm³ mol⁻¹ showing that $\Delta\bar{V}_{a_n b}$ is two or three times greater than $\Delta\bar{V}_{ab}$.

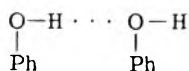
If now the mole fraction x_b becomes appreciable there is of course an upper limit of average chain length when all the phenol chains are terminated by amine, namely, x_a/x_b .

It must be borne in mind that an $a_n b$ complex can show several configurations which differ with the position of the proton.

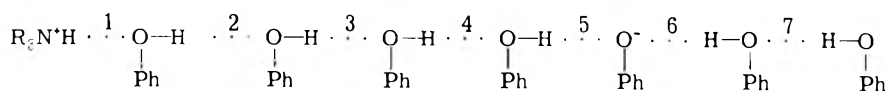
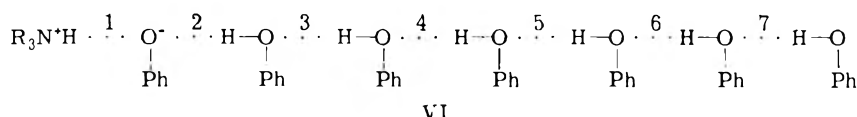
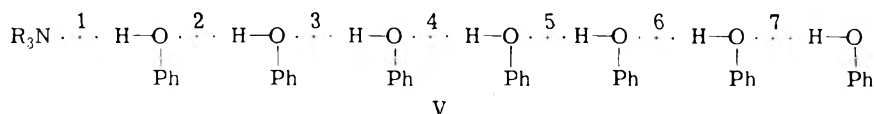
Let us consider for instance configurations V-VII of the $a_7 b$ complex. It can be expected that, owing to the symmetric character of the homoconjugated ion



the hydrogen bond in that ion will be much stronger than the hydrogen bond between two adjacent phenol molecules:



In configuration V, hydrogen bond 2 is somewhat strengthened by the effect of hydrogen bond 1. In a recent paper⁸ we showed that the perturbation of the electron acceptor



VII

ability of the other specific sites of a molecule brought about by a first hydrogen bond is as great in a given sequence as the vertical difference between the two minima in the potential curve of the proton of the first bond is small. One can assume that this also holds for the electron donor ability. Under these circumstances, as in bond 2 of configuration V, the vertical difference between the two minima must be important and the effect on bond 3 must be rather weak and nearly completely vanish in the following bonds. In configuration VI bond 3 undergoes the influence of bond 2 where the levels of the two maxima are not far removed from each other. Bond 4 is much less influenced. In configuration VII, bonds 7 and 4 must be strengthened by the two strong bonds 5 and 6. The vertical difference between the minima in bond 1 is fairly large, so that no great strengthening of bond 2 is expected. Bond 3 must be also weakly influenced. The presence of the two strong bonds and the strengthening of the others must bring about a more important volume contraction in this configuration than for configuration V. The effect must be still greater when the last molecule becomes bonded directly to the lone pair of electrons of the phenolate ion. This explains why $\Delta V_{a_n b}$ is significantly larger than $\Delta V_{a_2 b}$.

In connection with the conductivity it can be pointed out that, if in a given configuration the formal charges are separated by hydrogen bonds which are all much stronger than the normal hydrogen bonds of the medium, such an entity will behave as an ion pair and will not contribute to the electrical conductivity. This is the case, for instance, for configuration VI. However, when one or more hydrogen bonds which separate the formal charges are of similar strength as those of the medium, the ions of such a complex become able to contribute to the conductivity of the solution. This is the case for configuration VI.

(3) *Influence of the Size of the Complexed Ions on the Viscosity*. The concentration of a given ion will thus depend on the concentration of the mother complexes in which such an ion appears and of the weight of the favorable configurations. As discussed before, the enhancement of the viscosity is due to an important formation of these ions.

However, it appears that from the point of view of the viscosity factors other than the concentration of the ions must play a determining role. For instance, the maximal values of the viscosity for the systems with 4-chlorophenol are three times higher than those of the systems with unsubstituted phenol while the maximal values of $\kappa\eta$ are greater in the last systems. On the other hand, the viscosity maxima are nearly the same for the systems with 4-methylphenol and with phenol, while the values of $\kappa\eta$ are two times higher in the last case. This can hardly be explained

TABLE V: Values of $\kappa\eta$ which Correspond to a Given Value of the Viscosity (the First Value Corresponds to the Lowest Value of x_A)

System	Viscosity, $\kappa\eta$, ohm ⁻¹ cP			System	Viscosity, $\kappa\eta$, ohm ⁻¹ cP		
TEA-2-chloro-phenol	500	35	47	TEA-2-chloro-phenol	300	21	41
TEA-4-chloro-phenol	400	25	47	TEA-2-phenol	200	16	35
TEA-4-chloro-phenol	350	24	44	TEA-4-phenol	100	10	26
TEA-4-chloro-phenol	250	25	64	DEA-4-chloro-phenol	250	67.5	69
TEA-4-chloro-phenol	200	21	62.5	DEA-4-phenol	200	57.5	65
TEA-4-chloro-phenol	150	17	55	DEA-4-phenol	150	47	57
TEA-4-chloro-phenol	100	12.5	41	DEA-4-phenol	100	35	45
TEA-4-chloro-phenol	50	7.5	27	DEA-4-phenol	50	21	30
TEA-phenol	100	32	70	DEA-phenol	75	80	83
TEA-phenol	75	24	62	DEA-phenol	75	56	60
TEA-phenol	50	15	46	DEA-phenol	50	33	35
TEA-phenol	25	8	27	DEA-phenol	25	15	8
TEA-4-methyl-phenol	100	13.5	25	DEA-4-methyl-phenol	75	38	30
TEA-4-methyl-phenol	75	10	20.5	DEA-4-methyl-phenol	50	25	18
TEA-4-methyl-phenol	50	6	14	DEA-4-methyl-phenol	50	25	18
TEA-4-methyl-phenol	25	2	4	DEA-4-methyl-phenol	25	15	8

on the basis of differences in $\langle w_i \rangle$ alone so that it can be concluded that for the same value of the concentration of the ions ΣC_i , the viscosity is significantly greater for the systems with 4-chlorophenol and with 4-methylphenol than for the systems with phenol. Obviously, the differences between the systems lie here in the size of the ions. We can therefore conclude that a factor which, in addition to the total concentration of the ions, plays an important role in the viscosity of the studied mixtures is the size of the ions.

In that connection it can be pointed out that the viscosity of molten salts also strongly depends on the dimensions of the ions. For instance, at 393 K the viscosity of molten tetrapropylammonium picrate is 18.75 cP according to the measurements of Walden,⁹ whereas that of molten tetraiso-pentylammonium picrate reaches 37.67 cP under the same conditions. At 435 K the viscosity of Bu_4NBF_4 determined by Lind is 9.95 cP whereas that of Hex_4NBF_4 is 14.6 cP.¹⁰

Outside the maximum, a given value of η appears at two different mole fractions x_A of the phenol. One can determine for these two conjugated values of x_A the corresponding values of the product $\kappa\eta$. The results are given in Table V. With the exception of the system 4-methylphenol-diethylamine, the same viscosity is realized with a lower value of $\kappa\eta$ at the lowest x_A . In many cases the ratio between the two values of $\kappa\eta$ and that of $\langle w_i \rangle \Sigma C_i$ which realizes the same viscosity of the mixture is greater than two. Differences in $\langle w_i \rangle$ cannot account for such discrepancies and one can therefore conclude that, at the lowest value of x_A , the same viscosity is obtained by a much lower concentration of ions and that the size of the ions is significantly greater than at the upper value of x_A .

This demonstrates that the nature of the ions which are responsible for the high viscosities varies with the composition of the mixture.

In the case of the diethylamine systems the differences between the two paired values of $\kappa\eta$ is less pronounced, and, in the case of 4-methylphenol, there is even an inversion of the situation. This difference in behavior between diethylamine and triethylamine cannot be ascribed to the anions, which in absence of a marked solvation by the bases

TABLE VI: Approximate Molar Volumes of the Cations (cm³ mol⁻¹)

Cation	Molar Volume (cm ³ mol ⁻¹)	Cation	Molar Volume (cm ³ mol ⁻¹)
I Et_3NH^+	117	E_2NH_2^+	85
II $\text{Et}_3\text{N}-\text{H}\cdots\text{NEt}_3$	257	$\text{Et}_2\text{NH}_2^+\cdots\text{NHEt}_2$	190
III $\text{Et}_3\text{N}-\text{H}\cdots\text{O}-\text{H}$	205	$\text{Et}_2\text{NH}_2^+\cdots\text{O}-\text{H}$	173
III' $\text{Et}_3\text{N}-\text{H}\cdots\text{O}-\text{H}$	217	$\text{Et}_2\text{N}-\text{H}_2^+\cdots\text{O}-\text{H}$	185
III'' $\text{Et}_2\text{NH}^+\cdots\text{O}-\text{H}$	222	$\text{Et}_2\text{NH}_2^+\cdots\text{O}-\text{H}$	190

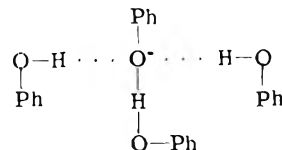
must be of similar nature for a given phenol. Let us then consider the various cations which can be formed in the systems. In Table VI we give an estimation of the molar volume of the cations computed from crystallographic data for the ion and from the molar volume of the ligand.

As the mole fraction x_A increases, the percentages of the two first cations must decrease to the benefit of the third one. In the case of triethylamine, the molar volume of the homoconjugated cation II is fairly greater than that of cations III. For diethylamine the differences are less important. The significantly higher viscosity obtained by the same concentration of ions at the left side of the maximum can perhaps be ascribed to a greater proportion of homoconjugated cations. This effect disappears in the case of the system 4-methylphenol-DEA where the molar volumes of II and III are very similar.

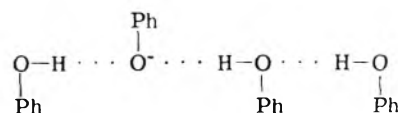
The presence of an important percentage of homoconjugated cations in excess of phenol where the concentration of free base is obviously small can be ascribed to stronger hydrogen bond in this symmetrical entity compared with the bond between R_3NH^+ and a lone pair of electrons of the oxygen of the phenol molecule the basicity of which must be rather weak.

However, it must be noted that the ion $(\text{Et}_3\text{NH}^+\cdots\text{NEt}_3)$ is sterically hindered and this will limit to some extent its concentration.

At $x_A = 0.83$, in the vicinity of which the maximum of $\kappa\eta$ appears for many systems studied here, the ratio of the number of amine molecules to the number of phenol molecules is one to five. The a_5b complex can furnish in addition to the cation III the anion



or anions with the same stoichiometry but with a linear structure as



Our results suggest thus that these anions plays an important role both in the conductivity and in the viscosity of the solutions. However, the intervention of still higher solvated anions cannot be excluded.

Acknowledgments. This research had been supported by F.C.F.O. and KUL (Belgium).

Supplementary Material Available. The data for the other systems studied, included in an expanded form of Table I, will appear following these pages in the microfilm edition of this volume of the journal. Photocopies of the supplementary material from this paper only or microfiche (105 × 148 mm, 24× reduction, negatives) containing all of the supplementary material for the papers in this issue may be obtained from the Business Office, Books and Journal Division, American Chemical Society, 1155 16th St., N.W., Washington, D.C. 20036. Remit check or money order for \$4.00 for photocopy or \$2.50 for microfiche, referring to code number JPC-75-2316.

References and Notes

- (1) J. E. Lind, J. Z. Zwolenik, and R. M. Fuoss, *J. Am. Chem. Soc.*, **81**, 1557 (1959).
- (2) P. Walden, *Z. Phys. Chem.*, **55**, 207 (1906).
- (3) (a) T. Shedlovsky, *J. Am. Chem. Soc.*, **63**, 2811 (1941); (b) D. A. McInnes and T. Shedlovsky, *ibid.*, **54**, 1429 (1932); (c) B. B. Owen and H. Zeldes, *J. Chem. Phys.*, **18**, 1083 (1959); (d) S. H. Jones, *J. Am. Chem. Soc.*, **67**, 85 (1945); (e) R. Mecke and H. Zeiniger, *Z. Elektrochem. Angew. Phys. Chem.*, **47**, 49 (1948); (f) D. L. Flower and C. A. Kraus, *J. Am. Chem. Soc.*, **62**, 2237 (1940); (g) P. Walden and J. Birr, *Z. Phys. Chem.*, **153**, 1 (1931); (h) H. Daggett, E. Bair, and C. A. Kraus, *J. Am. Chem. Soc.*, **69**, 1731 (1947); (i) D. F. Evans and P. Gardam, *J. Phys. Chem.*, **73**, 161 (1969); (j) E. Horsch and R. M. Fuoss, *J. Am. Chem. Soc.*, **82**, 1018 (1960); (k) E. G. Taylor and C. A. Kraus, *J. Am. Chem. Soc.*, **69**, 1731 (1947).
- (4) D. Clotman, D. Van Lerberghe, and Th. Zeegers-Huyskens, *Spectrochim. Acta, Part A*, **23**, 1627 (1967).
- (5) H. Ratajczak and L. Sobczyk, *J. Chem. Phys.*, **50**, 556 (1969); *Zh. Struk. Khim.*, **6**, 262 (1965).
- (6) J. Jadzyn and J. Malecki, *Acta Phys. Polon.*, **A41**, 599 (1972).
- (7) J. Tack and P. Huyskens, *J. Chim. Phys.*, **71**, 1231 (1974).
- (8) M. C. Haulait and P. Huyskens, *J. Phys. Chem.*, **79**, 1812 (1975).
- (9) P. Walden, H. Ulich, and E. J. Birr, *Z. Phys. Chem.*, **131**, 21 (1928).
- (10) J. E. Lind, H. Abdel-Rehin, and S. W. Rudich, *J. Phys. Chem.*, **70**, 3610 (1966). See also V. C. Reinsborough, *Rev. Pure Appl. Chem.*, **18**, (1968).

COMMUNICATIONS TO THE EDITOR

Copper Catalysis in the Hexacyanoferrate(III) Oxidation of Mercaptoacetate

Publication costs assisted by the University of Wyoming

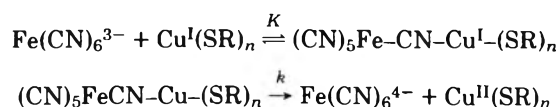
Sir: The reactions of a number of mercaptans, including mercaptoacetate,¹ have been studied kinetically in which hexacyanoferrate(III) was used as oxidant.¹⁻⁶ In most cases, rather strange effects were noted, such as an increase in rate upon adding $\text{Fe}(\text{CN})_6^{4-}$ or a retarding of the reaction by the addition of CN^- .³ These effects become explainable when it is recognized that copper, a ubiquitous impurity, is a very pronounced catalyst for mercaptan oxidations by hexacyanoferrate(III) in alkaline solution. Bridg- art and coworkers⁶ have shown that copper is a catalyst for the oxidation of some mercaptans in acid solution.

Experimental Section. Solutions prepared from ACS reagent grade chemicals and redistilled water were as follows: 0.04 M $\text{Fe}(\text{CN})_6^{3-}$, 1.00 M KOH standardized and adjusted against standard HCl, 1.00 M $\text{HSCH}_2\text{COONa}$ standardized and adjusted against standard I_2 , 0.10 M $\text{K}_4\text{Fe}(\text{CN})_6$, 0.001 M CuSO_4 , and 1.00 M KNO_3 . The solutions not otherwise standardized were made up by weight.

Appropriate mixtures of $\text{HSCH}_2\text{COONa}$, KOH, KNO_3 , and CuSO_4 solutions were prepared by transferring these solutions to 50.0-ml volumetric flasks with pipets. Another solution 0.0004 M in $\text{Fe}(\text{CN})_6^{3-}$ and 0.02 M in KOH was prepared; ionic strength was 0.1, maintained by adding KNO_3 solution. These solutions were used in a Gibson-Durum stopped-flow device to obtain the kinetic data. The copper could not be mixed with the $\text{Fe}(\text{CN})_6^{3-}$ be-

cause even at very low copper concentrations (10^{-5} M), colloidal suspensions of $\text{CuKFe}(\text{CN})_6$ formed.

Results and Discussion. The reaction proved to be first order in $\text{Fe}(\text{CN})_6^{3-}$, first order in copper, and close to zero order in both OH^- and mercaptoacetate. First-order plots in $\text{Fe}(\text{CN})_6^{3-}$ were good straight lines over at least 90% of the reaction. (All slopes of first-order plots had least-squares standard deviations of less than 1%, with correlation coefficients greater than 0.9995). Although the addition of $\text{Fe}(\text{CN})_6^{4-}$ at constant ionic strength appeared to increase the rate of the reaction, this increase could be attributed quantitatively to a copper impurity in the potassium hexacyanoferrate(II) reagent. Analysis of a 0.1 M stock solution of this reagent spectrophotometrically using diethyldithiocarbamate and CHCl_3 extraction showed a Cu^{2+} concentration of 4×10^{-6} M. The increased rates observed agreed with those predicted from the copper content of the $\text{Fe}(\text{CN})_6^{4-}$ reagent. The very small temperature effect indicates that some exothermic equilibrium precedes the slow step. A mechanism which fits these facts is



followed by the Cu(II) oxidation of the mercaptan to the disulfide in a non-rate-determining step. This leads to the expression

$$\frac{-d[\text{Fe}(\text{CN})_6^{3-}]}{dt} = kK[\text{Fe}(\text{CN})_6^{3-}][\text{Cu}]$$

TABLE I: Carbon-13 Spin-Lattice Relaxation Data

Solution	Compound ^a	Visc, cP	¹³ C T ₁ 's of carbon number, ^c sec						CCl ₄ ^d
			1	2	3	4	5	6	
1	3,5-Dichlorophenol ^e	0.97		3.15		2.94			
2	2,5-Dichlorophenol ^e	0.88			5.75	5.17		5.94	
3	2,6-Dichlorophenol ^e	0.93			6.08	6.70			
4 ^b	3,5-Dichlorophenol	1.05	0.050	0.060	0.161	0.236	0.161	0.060	1.02
5 ^b	Phenol	1.05	0.065	0.100	0.187	0.300	0.187	0.100	0.87
6 ^b	2,5-Dichlorophenol	0.92	0.096	0.266	0.361	0.400	0.290	0.086	0.93
7 ^b	2,6-Dichlorophenol	0.95	0.192	0.306	0.370	0.346	0.370	0.306	0.79
8 ^b	3,5-Dichlorophenol	1.49	0.049	0.080	0.182	0.237	0.182	0.080	0.71
	Phenol		0.103	0.150	0.279	0.327	0.279	0.150	
9 ^b	2,5-Dichlorophenol	1.23	0.146	0.260		0.323	0.296	0.113	
	Phenol		0.077	0.083		0.288		0.083	0.78
10 ^b	2,6-Dichlorophenol	1.30	0.183	0.263	0.314	0.285	0.314	0.263	0.55
	2,6-Dimethylphenol		0.153	0.208	0.342	0.351	0.342	0.208	

^a 2M solutions of chlorinated phenols in CCl_4 . Molarity of the mixed phenol solution: 1.7M chlorinated phenol, 1.7M phenol, or 2,6-dimethylphenol in CCl_4 . ^b 5.0×10^{-2} M $\text{Cr}(\text{acac})_3$ added. ^c Measured at 67.9 MHz by inversion-recovery (IRFT) method; accuracy $\pm 4-10\%$; internal accuracy and reproducibility generally $\pm 2-5\%$ (between solutions, $\pm 10\%$); temperature $38 \pm 3^\circ\text{C}$. ^d In the absence of $\text{Cr}(\text{acac})_3$ $T_1(\text{CCl}_4)$ is ca. 80 sec (without degassing). ^e T_1 's for phenol: ca. 4.1 sec (C-2, C-3) and ca. 2.4 sec (C-4) (from G. C. Levy, J. D. Cargioli, and F. A. L. Anet, *J. Am. Chem. Soc.*, 95, 1527 (1973)).

The binuclear complex involving $\text{Fe}(\text{CN})_6^{3-}$ and $\text{Cu}^1(\text{SR})_n$ is not surprising in view of the propensity of Cu^1 to coordinate with either S- or N-containing ligands. The oxidation of mercaptans by Cu^{II} is well known.⁷

Attempts to separate K and k by increasing the $\text{Fe}(\text{CN})_6^{3-}$ concentration to the point where deviation from first order in this substance could be detected failed. $[\text{Cu}^{2+}]$ could not be varied substantially because $\text{Cu}^1(\text{SR})$ is quite insoluble at higher Cu^1 concentrations.

The slight variation in rate caused by variation in mercaptan concentration very likely results from variation in n in the above intermediate formula. This could in turn cause variation in k or K .

The results are listed in Table I.

References and Notes

- (1) R. C. Kapoor, O. P. Kachwaha, and B. P. Sinha, *J. Phys. Chem.*, **73**, 1627-1631 (1969).
- (2) O. P. Kachwaha, B. P. Sinha, and R. C. Kapoor, *Indian J. Chem.*, **8**, 806-808 (1970).
- (3) I. M. Kolthoff, E. J. Meehan, M. S. Tsao, and Q. W. Choi, *J. Phys. Chem.*, **66**, 1233 (1962).
- (4) E. J. Meehan, I. M. Kolthoff, and H. Kakinchi, *J. Phys. Chem.*, **66**, 1238 (1962).
- (5) K. Wiberg, H. Maltz, and M. Okano, *Inorg. Chem.*, **7**, 830 (1968).
- (6) G. J. Bridgman, M. W. Fuller, and I. R. Wilson, *J. Chem. Soc., Dalton Trans.*, 1274-1280 (1973).
- (7) P. F. Warner and J. A. McBride, U.S. Patent 2503644 (1940); *Chem. Abstr.*, **44**, 5896 (1950).

Department of Chemistry
University of Wyoming
Laramie, Wyoming 82071

Frederick R. Duke*
Vernon C. Bulgrin

Received June 11, 1975

Electron Spin Resonance Study of the Intermetallic Molecules AgZn , AgCd , and AgHg

Publication costs assisted by the Union Carbide Corporation

Sir: The nature of metal-metal bonds found between pairs of metal atoms in complex compounds¹ as well as those existing between ligand free metal atoms² has been the subject of many recent investigations. We wish to report here the generations in rare-gas matrices, and observation by electron spin resonance (ESR) spectroscopy of three intermetallic diatomic molecules, AgZn , AgCd , and AgHg .

The cryostat-spectrometer assembly that would permit trapping of high-temperature vapor phase species in a rare-gas matrix at ~ 4 K, and observation of the resulting matrix by ESR has been detailed earlier.³ In the present series of experiments the Ag atoms were vaporized from a resistively heated tantalum cell, and were trapped in argon matrices together with the atoms of other metal independently vaporized from the second cell. The frequency of the spectrometer locked to the sample cavity was 9.410 GHz and all the spectra were obtained while the matrices were maintained at ~ 4 K.

The molecular symmetry of AgM ($M = \text{Zn}, \text{Cd}, \text{Hg}$) dictates that their ESR spectra be compatible with the spin hamiltonian of the form

$$\mathcal{H}_{\text{spin}} = g_{\parallel} \beta H_z S_z + g_{\perp} \beta (H_x S_x + H_y S_y) + A_{\parallel} I_z S_z + A_{\perp} (I_x S_x + I_y S_y) + A_{\parallel}' I_z' S_z + A_{\perp}' (I_x' S_x + I_y' S_y) \quad (1)$$

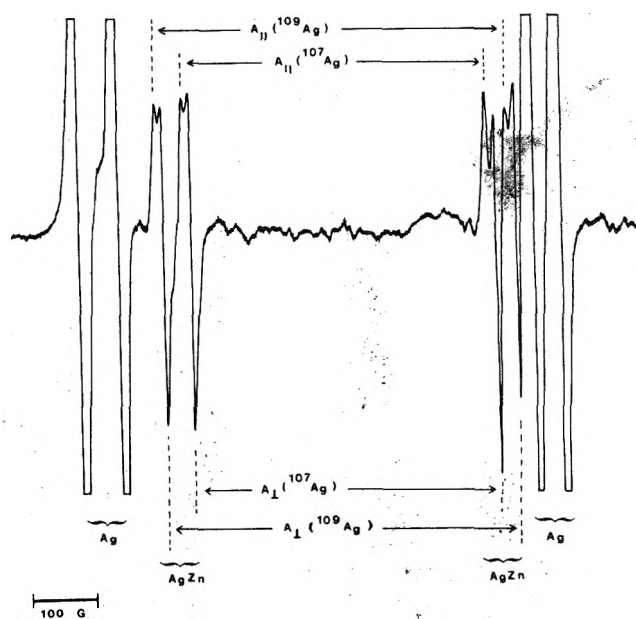


Figure 1. ESR spectrum of AgZn generated in an argon matrix. The sharp, off-scale doublets are due to Ag atoms.

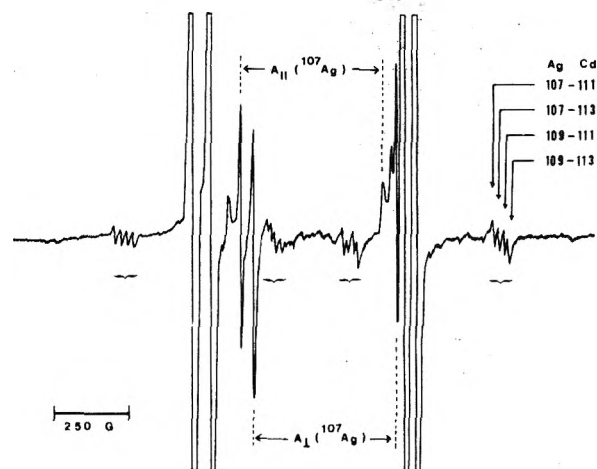


Figure 2. ESR spectrum of AgCd generated in an argon matrix. The brackets indicate the groups of satellites due to ^{111}Cd and ^{113}Cd nuclei.

where A_{\parallel} and A_{\perp} represent the hyperfine coupling tensor to the Ag nucleus, and the last two terms involving A_{\parallel}' and A_{\perp}' are to be added when the atom M possesses a magnetic nucleus.

The ESR spectrum of Ag atoms ($4d^{10} 5s^1$) isolated in an argon matrix is known.⁴ It consists of two sets of sharp isotropic doublets with the spacings of ~ 620 and ~ 720 G attributed to the couplings to ^{107}Ag (natural abundance = 51%, $I = 1/2$, $\mu = -0.1130 \beta_N$) and ^{109}Ag (natural abundance = 49%, $I = 1/2$, $\mu = -0.1299 \beta_N$).

The ESR spectra obtained from an argon matrix containing Ag and Zn atoms, and that containing Ag and Cd atoms, are shown in Figures 1 and 2. In addition to the sharp doublets due to Ag atoms described above, one notes the presence of additional doublets with the spacings slightly less than those of Ag atoms, and with the patterns expected from an ensemble of randomly oriented radicals possessing an axially symmetric spin hamiltonian. We propose to assign these doublets to AgZn and AgCd , respec-

TABLE I: Spin Hamiltonian Parameters of AgM
(M = Zn, Cd, Hg)

AgM	g_{\parallel}^a	g_{\perp}^a	$A_{\parallel}(=A_{\perp}),^b$ GHz	$A_{\parallel}',^c$ GHz	$A_{\perp}',^c$ GHz
AgZn	2.0025	1.9905	1.324 (± 0.003)		
AgCd	2.0014	1.9711	1.327 (± 0.003)	2.18 (± 0.25)	1.99 (± 0.03)
AgHg	1.9958	1.9136	1.562 (± 0.003)	3.13 (± 0.20)	2.52 (± 0.03)

^a Accuracy ± 0.0002 . ^b Coupling to ^{107}Ag . ^c Coupling to ^{111}Cd or ^{199}Hg .

tively. The assignments of the parallel and perpendicular components for the case of AgZn are indicated in Figure 1.

The major pattern of the AgCd spectrum is quite similar to that of AgZn, although one of the high-field perpendicular components is masked by the strong Ag signals. A closer inspection of the AgCd spectrum revealed, however, the presence of four groups of satellites (see Figure 2). They were recognized as the perpendicular components of the spectra due to AgCd possessing ^{111}Cd (natural abundance = 13%, $I = 1/2$, $\mu = -0.5922 \beta_N$) or ^{113}Cd (natural abundance = 12%, $I = 1/2$, $\mu = -0.6195 \beta_N$) nucleus. The corresponding parallel components of these species were too weak to be observed.

The major pattern of the spectrum assigned to AgHg is also similar to that of AgZn. In this case, however, the satellite signals attributable to the perpendicular components of AgHg possessing ^{199}Hg (natural abundance = 17%, $I = 1/2$, $\mu = 0.4993 \beta_N$) or ^{201}Hg (natural abundance = 13%, $I = 3/2$, $\mu = -0.607 \beta_N$) were observed providing a further support to the assignment.

In each case of AgM discussed above, the large hyperfine coupling interactions with the magnetic nuclei prevented the accurate evaluation of the spin hamiltonian parameters using the usual second-order solutions. The g and the hyperfine coupling tensors of the AgM were, therefore, determined from the observed signal positions resorting to the exact diagonalization of the hamiltonian (1). Table I shows the results. The A_{\parallel}' 's of the magnetic Cd and Hg nuclei were evaluated from the observed perpendicular components of the relevant species. This is possible because, when the magnetic field is perpendicular to the symmetry axis, the off-diagonal elements of the hamiltonian (1) are related to $A_{\parallel}' + A_{\perp}'$ and $A_{\parallel}' - A_{\perp}'$.⁵ The large uncertainties indicated for the A_{\parallel}' 's are due to this indirect approach.

In spite of the different separations of the parallel and the perpendicular components, the coupling tensor to the Ag nucleus was found to be completely isotropic ($A_{\parallel} = A_{\perp} = A_{\text{iso}}$) in each case. The coupling tensors to the ^{111}Cd and ^{199}Hg nuclei are also essentially isotropic. For Ag atoms isolated in an argon matrix the coupling constant to ^{107}Ag has been measured to be 1.806 GHz.⁴ Using the Goudsmit's relation⁶ and the known coupling constants of Ag and Au atoms,⁴ the isotropic coupling constants of unpaired electrons localized, respectively, in the valence s orbitals of ^{111}Cd and ^{199}Hg are estimated to be 12.5 and 40.0 GHz. In the present series of AgM the unpaired electron should occupy the orbital given essentially by an antibonding combination of the valence s orbitals of Ag and M. The ionization potentials of these orbitals are 7.6, 9.4, 9.0, and 10.4 eV for

Ag, Zn, Cd, and Hg atoms, respectively. The dominance of the Ag 5s orbital in the semifilled, antibonding orbital of the present series of AgM is thus expected. The small but clearly observed anisotropies of the coupling tensors to the ^{111}Cd and ^{199}Hg nuclei indicate admixture of the valence p_z orbital of the atom M, however. Such admixture would also account for the observed anisotropies of the g tensors with the increasing trend of $A_{\parallel}' \text{Zn} < \text{AgCd} < \text{AgHg}$.

We have also succeeded in generating and observing the ESR spectra of Ag-alkaline earth intermetallic molecules. The results obtained from these species together with more detailed accounts of the AgM spectra communicated here will be reported soon.

References and Notes

- (1) F. A. Cotton, *Acc. Chem. Res.*, **2**, 240 (1969).
- (2) K. A. Gingerich, *J. Cryst. Growth*, **9**, 31 (1971).
- (3) P. H. Kasai, E. B. Whipple, and W. Weltner, Jr., *J. Chem. Phys.*, **44**, 2581 (1966).
- (4) P. H. Kasai and D. McLeod, Jr., *J. Chem. Phys.*, **55**, 1566 (1971).
- (5) See, for example, ref 4.
- (6) S. Goudsmit, *Phys. Rev.*, **43**, 336 (1933).

Union Carbide Corporation
Tarrytown Technical Center
Tarrytown, New York 10591

Paul H. Kasai*
D. McLeod, Jr.

Received July 21, 1975

Intra- and Intermolecular Hydrogen Bonding in Chlorinated Phenols and Related Compounds

Publication costs assisted by the U.S. Environmental Protection Agency

Sir: Paramagnetic relaxation reagents such as trisacetylacetonatochromium [$\text{Cr}(\text{acac})_3$] are good proton acceptors, hydrogen bonding to molecules with both strongly and weakly acidic hydrogens.^{1,2} We wish to show that the combination of *intermolecular* ^{13}C T_1 's (T_1^e in solutions containing paramagnetic reagents) along with T_1 measurements in diamagnetic solutions (*intramolecular* ^{13}C - ^1H dipolar T_1 's) gives a significant increase of information in studies of solution dynamics for liquids where hydrogen bonding occurs. This is the first report to our knowledge of the use of *both* techniques to probe chemical dynamics.

The ^{13}C T_1 's for the diamagnetic solution of 3,5-dichlorophenol (solution 1 in Table I) monitor the presence of intermolecular hydrogen bonding in this phenol. The T_1 's are half as long as those of the other two dichlorophenols (solutions 2 and 3). Formation of hydrogen bonded molecular aggregates causes the averaged molecular correlation time (τ_c) to be approximately twice as long and thus the T_1 's are shortened. For 2,5- and 2,6-dichlorophenol the data indicate less extensive aggregation in solution. This may be explained by a combination of *intramolecular* hydrogen bonding between the phenolic OH and ortho chlorine atoms and by steric inhibition of intermolecular hydrogen bonding. Interestingly the molecular motion as probed by ^{13}C T_1 data is *not* indicated by the solution macroscopic viscosities (Table I).

The ^{13}C T_1 's for 2,5-dichlorophenol are somewhat shorter than those of the 2,6-disubstituted phenol. If one as-

TABLE I: Variation in Rate with Copper, HSCH₂COO⁻, and OH⁻ Concentrations and Temperature^a

$10^4[\text{Fe}(\text{CN})_6^{3-}]$	$10^3[\text{RSH}^-]$	$10^2[\text{OH}^-]$	$10^5[\text{Cu}^{2+}]$	$T, ^\circ\text{C}$	k', sec^{-1}	$10^5 kK, M^{-1} \text{sec}^{-1}$
2.0	10.0	3.0	0.78	20	2.00	2.56
2.0	10.0	3.0	1.53	20	4.44	2.90
2.0	10.0	3.0	2.03	20	5.50	2.71
2.0	10.0	3.0	2.53	20	6.46	2.55
2.0	10.0	3.0	0.78	30	2.03	2.60
2.0	10.0	3.0	1.53	30	4.51	2.95
2.0	10.0	3.0	2.03	30	5.45	2.68
2.0	10.0	3.0	2.53	30	6.35	2.51
2.0	1.0	3.0	1.03	30	2.45	2.38
2.0	2.0	3.0	1.03	30	2.61	2.53
2.0	3.0	3.0	1.03	30	2.69	2.61
2.0	4.0	3.0	1.03	30	2.77	2.69
2.0	2.0	1.50	1.03	30	2.39	2.32
2.0	2.0	1.75	1.03	30	2.43	2.36
2.0	2.0	2.5	1.03	30	2.42	2.35
4.0	8.0	1.5	1.03	10	2.69	2.61
6.0	8.0	1.5	1.03	10	2.69	2.61
8.0	8.0	1.5	1.03	10	2.78	2.70
10.0	8.0	1.5	1.03	10	2.71	2.63
12.0	8.0	1.5	1.03	10	2.88	2.80
14.0	8.0	1.5	1.03	10	2.81	2.73
16.0	8.0	1.5	1.03	10	2.90	2.81
18.0	8.0	1.5	1.03	10	2.94	2.85
20.0	8.0	1.5	1.03	10	2.92	2.83
4.0	8.0	1.5	1.03	0	2.51	2.44
20.0	8.0	1.5	1.03	0	2.76	2.68
20.0	2.0	2.0	None added	30	0.082	2.73 ^b

^a k' is the slope of $-\ln [\text{Fe}(\text{CN})_6^{3-}]$ vs. time plots. All concentrations are in moles per liter. ^b Taking the Cu^{2+} impurity to be $0.03 \times 10^{-5} M$, found by analysis of reagent mixtures using diethyldithiocarbamate and extraction with CHCl_3 .

sumes that the (averaged) correlation time for 2,6-dichlorophenol represents largely monomer and τ_c for 3,5-dichlorophenol represents an oligomer aggregate, then the mole fraction of dimer may be estimated for the 2,5-dichlorophenol solution, to be under 25%. This is in agreement with an ir^3 and $^1\text{H}^4$ NMR study on ortho-substituted halogenated phenols which showed the existence of "cis-trans dimers" in equilibrium with the monomeric molecules. For *o*-chlorophenol the molar fraction of the dimer was estimated from cryoscopic measurement to be 10% (0.5 *m* solution in benzene).⁵

In solutions containing $\text{Cr}(\text{acac})_3$ the ^{13}C T_1 's are much shorter than in the diamagnetic solutions; electron-nuclear dipole-dipole interactions dominate the ^{13}C nuclear spin-lattice relaxation.^{2a,6} With this technique an exact evaluation of solvation shell and outer-sphere effects remains elusive because of several complications.⁷ Nevertheless, qualitative conclusions may be drawn concerning intermolecular hydrogen bonding with $\text{Cr}(\text{acac})_3$ as well as about other weak solvation effects. When there is intermolecular association between the paramagnetic chelate and phenol molecules due to hydrogen bonding from the OH proton to the ligands of the metal chelate this can be observed in two ways: (1) the phenol T_1 's are significantly shorter than T_1 for the "inert" standard, CCl_4 ; (2) T_1 for the C-1 and ortho carbons of the phenol (close to the site of complexation) are

shorter than the meta and para carbon T_1 's.⁸ Several trends can be observed from the data in Table I.

In all of the phenols listed in Table I intermolecular hydrogen bonding with the $\text{Cr}(\text{acac})_3$ molecules is evidenced. In 3,5-dichlorophenol (solution 4) the C-1 carbon T_1 is ca. 20 times shorter than the CCl_4 ^{13}C T_1 whereas in phenol (solution 5) the same ratio is approximately 13. This difference results from an increase in acidity for the phenolic proton in the dichloro compound.

By contrast, the T_1 for C-1 in 2,6-dichlorophenol (solution 7) is only four times shorter than the CCl_4 T_1 . In this case intramolecular hydrogen bonding between the phenolic OH and the ortho chlorines and/or steric effects lessen intermolecular association with the chelate.

It is possible to study these effects by doing competition experiments. In solutions 8 and 9, 3,5-dichlorophenol and 2,5-dichlorophenol were run against the unsubstituted phenol. In the 3,5-disubstituted compound the greater acidity of the phenolic OH is indicated by shorter T_1 's for the C-1 and ortho carbons (by a factor of 2). In the 2,5 compound intramolecular H bonding to the 2-chlorine reverses the competition between the chlorinated and unsubstituted phenols.

In an attempt to partially separate the steric and intramolecular hydrogen bonding effects, 2,6-dimethylphenol was used as a steric model for the 2,6-dichlorophenol. Solution 10 contained both compounds. In spite of its greater acidity the 2,6-dichlorophenol shows less tendency to H bond to the $\text{Cr}(\text{acac})_3$ as evidenced by the longer T_1 for C-1 and also by the relative lack of polarization of the ring carbon T_1 's (comparing the T_1 's for all ring positions in both compounds of solution 10).

In another experiment designed to help differentiate between the steric effect and intramolecular hydrogen bonding, *o*-chlorophenol and *o*-bromophenol solutions containing $\text{Cr}(\text{acac})_3$ were examined. The bromine substituent is sterically larger and thus steric inhibition of intermolecular H bonding would be more effective than with ortho chlorine atoms. By contrast, bromine is less favorable as an intramolecular H-bond acceptor. To the extent that the model is correct if this intramolecular association is the major cause of reduced intermolecular association then the *o*-bromophenol T_1 's should be shorter than those observed for *o*-chlorophenol.⁸ This was in fact observed. T_1 's for C-1 and C-6 in *o*-bromophenol were ca. 20% shorter than the analogous T_1 's in *o*-chlorophenol [C-1: 0.159(Br), 0.185(C-1); C-6: 0.139(Br), 0.170(Cl); and for the internal "standard," cresol; C-1, 0.104 sec; C-6, 0.074 sec].

We are currently studying these systems in more detail in an attempt to quantify steric and electronic effects and to better determine the nature of the intermolecular interaction between $\text{Cr}(\text{acac})_3$ and self-associated phenols.

Acknowledgments. We gratefully acknowledge the financial support of the U.S. Environmental Protection Agency and the National Science Foundation.

References and Notes

- (1) (a) J. P. Fackler, Jr., T. S. Davis, and I. D. Chawla, *Inorg. Chem.*, **4**, 130 (1965); (b) T. S. Davis and J. P. Fackler, Jr., *ibid.*, **5**, 242 (1966); (c) M.-F. Rettig and R. S. Drago, *J. Am. Chem. Soc.*, **88**, 2966 (1966).
- (2) (a) G. C. Levy and J. D. Cargioli, *J. Magn. Reson.*, **10**, 231 (1973); (b) G. C. Levy and R. A. Komoroski, *J. Am. Chem. Soc.*, **96**, 678 (1974).
- (3) (a) I. S. Pereygin and T. F. Akunov, *Opt. Spektrosk.*, **33**, 246 (1972), and literature cited therein; (b) D. A. K. Jones and J. G. Watkinson, *Chem. Ind. (London)*, 661 (1961); (c) A. W. Baker and W. W. Kaeoling, *J. Am. Chem. Soc.*, **81**, 5904 (1959).

- (4) (a) C. M. Huggins, G. C. Pimentel, and J. N. Shoolery, *J. Phys. Chem.*, **60**, 1311 (1956); (b) E. A. Allan and L. W. Reeves, *ibid.*, **67**, 591 (1963).
 (5) N. E. Vanderborgh, N. R. Armstrong, and W. D. Spell, *J. Phys. Chem.*, **74**, 1734 (1970).
 (6) (a) R. Freeman, K. G. Pachler, and G. N. LaMar, *J. Chem. Phys.*, **55**, 4586 (1972); (b) O. A. Gansow, A. R. Burke, and G. N. LaMar, *Chem. Commun.*, 456 (1972); (c) S. Barcza and N. Engstrom, *J. Am. Chem. Soc.*, **94**, 1762 (1972).
 (7) G. C. Levy, U. Edlund, and J. G. Hexem, *J. Magn. Reson.*, in press.
 (8) Viewing these effects only as association between the phenols and the $\text{Cr}(\text{acac})_3$ may be somewhat simplistic since there is obviously a competition between phenol-phenol and phenol-chelate association. In spite of a significantly greater steric hindrance the carbonyl ligands of $\text{Cr}(\text{acac})_3$ can compete favorably as hydrogen bond receptors.
 (9) (a) Alfred P. Sloan Fellow, 1975-1977. (b) On leave of absence from Jagiellonian University, Krakow, Poland. (c) Universitat Dusseldorf, Dusseldorf, West Germany.

Department of Chemistry
 The Florida State University
 Tallahassee, Florida 32306

George C. Levy^a
 Tadeusz Holak^b
 Alois Steigel^c

Received March 24, 1975

On the Micellar Properties of Bolaform Electrolytes in Aqueous Solution

Sir: Last year Menger and Wrenn¹ reported surface tension and kinetic measurements on aqueous solutions of bolaform electrolytes of general formula $\text{R}_3\text{N}(\text{CH}_2)_n\text{NR}_3\text{Br}_2$ (abbreviated C_nR_6 ; $\text{R} = \text{Me}, n\text{-Bu}; n = 4, 8, 12$). Micellization of the C_{12}Me_6 and C_{12}Bu_6 compounds was inferred from the sigmoidal surface tension vs. log concentration curves for these compounds, and it was suggested that, up to the highest concentration investigated (0.1 M), a minimum chain length of 12 methylene groups was required before micellization occurs for C_nMe_6 bolaforms.

Our measurements of the apparent molal volumes (ϕ_v) of

C_{10}Me_6 and C_6Me_6 in water at 25° extend to near saturation (1.8 and 2.1 M, respectively, according to Pearson²), and they support the low concentration results of Menger and Wrenn, and also those of Pearson² obtained from dye uptake and bromide ion activity measurements. Our results for the behavior of ϕ_v with $c^{1/2}$ for C_{10}Me_6 and C_6Me_6 are shown in Figures 1 and 2, respectively.

Density measurements for the determination of ϕ_v were made below 0.4 M with 34-cm³ capacity pycnometers to an accuracy of $\pm 4 \times 10^{-6} \text{ g cm}^{-3}$, and above this concentration with an automatic precision digital densimeter Model DMA 02C manufactured by Anton Paar KG, the accuracy in this case being $\pm 5 \times 10^{-6} \text{ g cm}^{-3}$. The calculated error in ϕ_v at various concentrations is shown by the vertical barred lines on the graphs. The Debye-Hückel theoretical limiting slope (DHLL) is also shown on the graphs. This is given by S_v where

$$S_v = kw^{3/2}$$

in which

$$w = 0.5 \sum v_i z_i^2$$

and k has a value of $1.668 \text{ cm}^3 \text{ mol}^{-3/2} \text{ l}^{1/2}$ for water at 25°. The number of i ions of valence z_i formed from dissociation of 1 molecule of electrolyte is given by v_i , and thus S_v for these compounds is $9.706 \text{ cm}^3 \text{ mol}^{-3/2} \text{ l}^{1/2}$.

Micellization is usually indicated in a $\phi_v(c^{1/2})$ graph by a rapid increase in ϕ_v with concentration.⁴ There is no evidence of this for the C_{10}Me_6 and C_6Me_6 bolaforms and so the micellization conditions of Menger and Wrenn are confirmed for $n \geq 10$. However the $\phi_v(c^{1/2})$ behavior of our compounds is quite different from that of C_8Bu_6 studied by Broadwater and Evans.⁵ This shows a pronounced minimum at about 0.6 M which suggests aggregate formation above this concentration. The exact concentration at which the $\phi_v(c^{1/2})$ graph for C_8Bu_6 deviates from the DHLL was not determined by Broadwater and Evans, but, as would be expected from the molecular structure, C_8Bu_6 shows greater deviations from DHLL than C_6Me_6 or C_{10}Me_6 over the entire concentration range.

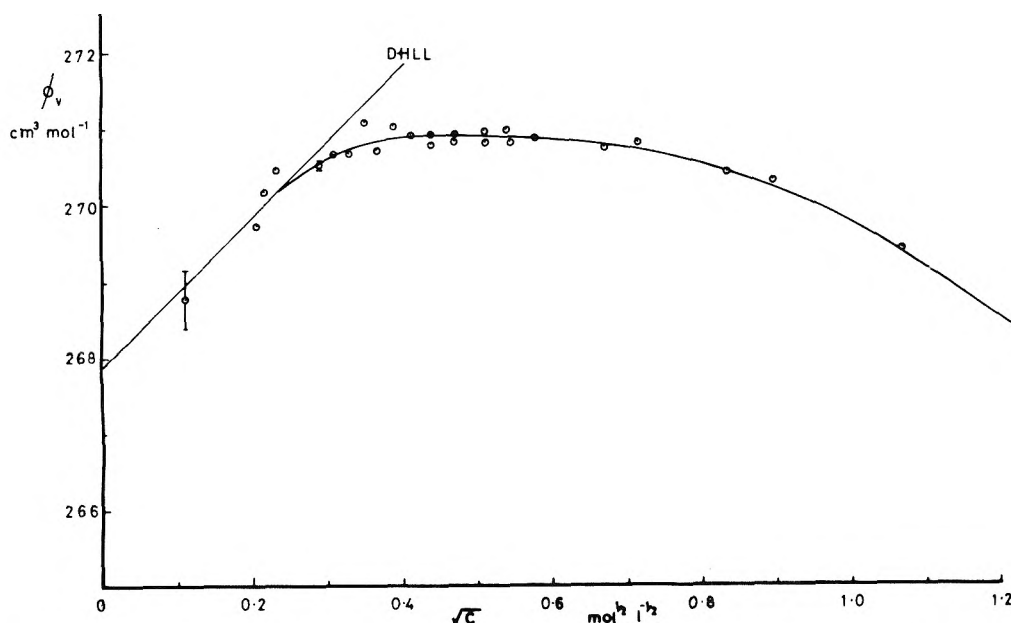


Figure 1. Variation of apparent molal volume with $c^{1/2}$ at 25° for hexamethonium bromide $[(\text{CH}_3)_3\text{N}(\text{CH}_2)_6\text{N}(\text{CH}_3)_3\text{Br}_2]$.

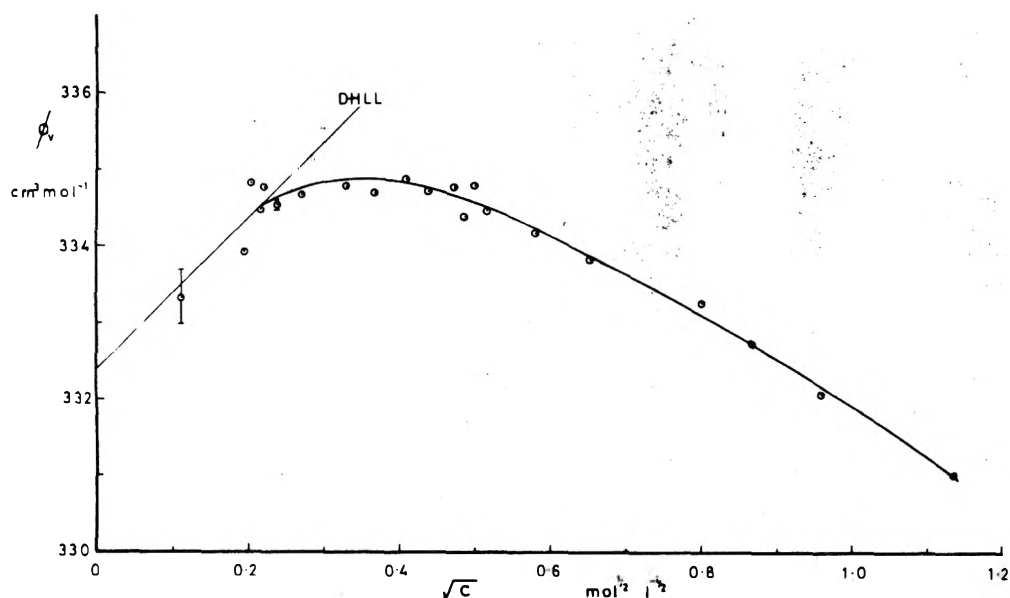


Figure 2. Variation of apparent molal volume with $c^{1/2}$ at 25° for decamethonium bromide $[(\text{CH}_3)_3\text{N}(\text{CH}_2)_{10}\text{N}(\text{CH}_3)_3\text{Br}_2]$.

It is interesting to note that significant deviations from DHLL occur at about the same concentration ($0.045 M$) for both C_6Me_6 and C_{10}Me_6 . This observation recalls the report by Fuoss and Chu⁶ of the conductance of the $\text{C}_n\text{Me}_3\text{I}_2$ ($n = 3, 4, 5$) bolaform electrolytes for which cation-anion association was indicated. The extent of association was found to be practically independent of methylene chain length. Thus it was postulated that one of the cationic sites became associated with an anion and the other site would be attracted to this anion and cause the methylene chain to bend into a loop (cf. "wickets" of Menger and Wrenn¹). This phenomenon could account for the similarity in $\phi_v(c^{1/2})$ behavior at low concentrations for C_6Me_6 and C_{10}Me_6 .

At concentrations above ca. $0.16 M$, C_{10}Me_6 shows greater deviations from DHLL than C_6Me_6 , but neither compound shows evidence of micellization.⁴ Evidently some effect associated with the longer methylene chain for the C_{10}Me_6 compound is responsible for this difference; it is possible that a hydrophobic interaction between the methylene chains, exposed by the curved configuration suggested above, could result in the observed reduction in ϕ_v .

It appears that bolaform quaternary ammonium electrolytes exhibit considerable bending of the methylene chain in aqueous solution as well as at the air-water interface. However, clarification of the exact nature of any higher aggregates requires further experimental data.

References and Notes

- (1) F. M. Menger and S. Wrenn, *J. Phys. Chem.*, **78**, 1387 (1974).
- (2) J. T. Pearson, *J. Colloid Interface Sci.*, **37**, 509 (1971).
- (3) F. J. Millero, *Chem. Rev.*, **71**, 147 (1971).
- (4) J. E. Desnoyers and M. Arel, *Can. J. Chem.*, **45**, 359 (1967).
- (5) T. L. Broadwater and D. F. Evans, *J. Phys. Chem.*, **73**, 164 (1969).
- (6) R. M. Fuoss and V. F. H. Chu, *J. Am. Chem. Soc.*, **73**, 949 (1957).

Pharmaceutical Chemistry Department
University of Strathclyde
Glasgow, G1 1XW, Scotland

J. R. Johnson*

The School of Pharmacy
University of London
London, WC1N 2AX, England

R. Fleming

Received March 20, 1975

PHYSICAL PHENOMENA

spectroscopy,
thermodynamics,
reaction kinetics,
and other areas
of experimental
and theoretical
physical chemistry
are covered
completely in

THE JOURNAL OF PHYSICAL CHEMISTRY

The biweekly JOURNAL OF PHYSICAL CHEMISTRY includes over 25 papers an issue of original research by many of the world's leading physical chemists. Articles, communications, and symposia cover new concepts, techniques, and interpretations. A "must" for those working in the field or interested in it, the JOURNAL OF PHYSICAL CHEMISTRY is essential for keeping current on this fast moving discipline. Complete and mail the coupon now to start your subscription to this important publication.

The Journal of Physical Chemistry American Chemical Society

1155 Sixteenth Street, N.W.
Washington, D.C. 20036

1975

Yes, I would like to receive the JOURNAL OF PHYSICAL CHEMISTRY at the one-year rate checked below:

	U.S.	Canada**	Latin America**	Other Nations**
ACS Member One-Year Rate*	<input type="checkbox"/> \$20.00	<input type="checkbox"/> \$24.50	<input type="checkbox"/> \$24.50	<input type="checkbox"/> \$25.00
Nonmember	<input type="checkbox"/> \$80.00	<input type="checkbox"/> \$84.50	<input type="checkbox"/> \$84.50	<input type="checkbox"/> \$85.00

Bill me Bill company Payment enclosed

Air freight rates available on request

Name _____

Street _____

Home
Business

City _____

State _____

Zip _____

Journal subscriptions start on January '75

*NOTE: Subscriptions at ACS member rates are for personal use only. **Payment must be made in U.S. currency, by international money order, UNESCO coupons, U.S. bank draft, or order through your book dealer.

A New Serial Publication . . .

THEORETICAL CHEMISTRY

Advances and Perspectives

VOLUME 1

edited by DOUGLAS HENDERSON and HENRY EYRING

Theoretical Chemistry: Advances and Perspectives will fill the need for a serial publication covering all aspects of the field. Each volume will consist of articles at the research level written by outstanding scientists in theoretical chemistry or other fields. The series will occasionally feature articles concerning experimental chemistry which pose or answer questions of theoretical interest, and from time to time monographs will also be published as supplements.

CONTENTS OF VOLUME 1: *W. G. Hoover and W. T. Ashurst, Nonequilibrium Molecular Dynamics. D. J. Caldwell and H. Eyring, Models in Optical Activity. P. J. Leonard and J. A. Barker, Dipole Oscillator Strengths and Related Quantities for Inert Gases. P. J. Leonard, Conformal Solution Theory: First-Order Generalized Theory for Mixtures. F. E. Harris, Hartree-Fock Studies of Electronic Structures of Crystalline Solids. 1975, 240 pp., \$19.50/£9.75*

ELECTRON DENSITIES IN MOLECULES AND MOLECULAR ORBITALS

by JOHN R. VAN WAZER and ILYAS ABSAR

A Volume in the PHYSICAL CHEMISTRY Series

This book is unique because it features pictures of how electrons are distributed in molecular orbitals. Unlike the conventional, heavily math-oriented presentation, it makes no use of mathematical equations at all. With this book, therefore, even those with no great aptitude in mathematics can gain a better understanding of molecular-orbital theory as applied to specific molecules, while obtaining a "spatial" concept of electronic behavior. The pictures are computer-produced, three-dimensional plots of electron densities in molecular cross sections. These plots, obtained from self-consistent field (SCF) calculations, offer considerable insight into the

electronic structure of matter. The accompanying text relates them to conventional chemical and electronic theory.

The first two chapters discuss the significance of SCF plots. Chapter three contains the main thrust of the work—cross sectional electron-density plots of a variety of organic and inorganic molecules. In each individual orbital, the book discusses the electron distribution in terms of classical chemical concepts of electronic structure, and elucidates esoteric features of chemical bonding.

1975, 112 pp., \$14.50/£7.25

THE EXCIPLEX

Proceedings of a meeting held under the auspices of the Photochemistry Unit, University of Western Ontario, May 28/31, 1974

edited by M. GORDON, W. R. WARE, P. DE MAYO, and D. R. ARNOLD

CONTENTS: *The Late Th. Förster, Excimers and Exciplexes. A. Weller, Singlet- and Triplet-State Exciplexes. J. Birks, The Photophysics of Aromatic Excimers. N. Orbach and M. Ottolenghi, Intersystem Crossing and Ionic Recombination Processes Studied by Pulsed Laser Excitation of Charge-Transfer Systems. N. Mataga, Electronic Structures and Dynamical Behavior of Some Exciplex Systems. J. Michl and R. D. Poshusta, Hydrogen Excimer—A Bound State of H₄. N. J. Turro, The Acetone Excimer. A Case for the Concept of "Masked" or "Crypto" Electronically Excited States. E. A. Chandross, Complexes of Dipolar Excited States and Small Polar Molecules. A. Ledwith, Cation Radical Intermediates, Exciplexes and Encounter Complexes in Photochemically-Induced Polymerization and Cyclodimerization of Olefins. D. G. Whitten, J.*

K. Roy, and F. A. Carroll, Spectroscopic Studies of Nonluminescent Exciplexes. Electron Transfer and Exciplex Formation from Triplet States of Anthracene and Metalloporphyrins. K. Zachariasse, Exciplexes in Chemiluminescent Radical Ion Recombination. A. J. Bard and S. M. Park, Exciplexes in Electrogenerated Chemiluminescence. S. Farid, S. E. Hartman, and T. R. Evans, Electron-Transfer Reactions in Multicomponent Systems. T. R. Evans, R. W. Wake, and O. Jaenicke, Singlet Quenching Mechanisms—Sensitized Dimerization of Phenyl Vinyl Ether. P. J. Wagner, D. A. Ersfield, and B. J. Scheve, Intramolecular Triplet-State Charge-Transfer Interactions in Aminoketone.

1975, 388 pp., \$17.50/£8.75

ADVANCES IN QUANTUM CHEMISTRY, Volume 9

edited by PER-OLOV LÖWDIN

CONTENTS: *B. O'Leary, B. J. Duke, and J. E. Eilers, Utilization of Transferability in Molecular Orbital Theory. S. D. Peyserimhoff and R. J. Buenker, A Series of Electronic Spectral Calculations Using Non-Empirical CI Techniques. J. Paldus and J. Cizek, Time-Independent Diagrammatic Approach to*

Perturbation Theory of Fermion Systems. W. A. Lester, Jr., Coupled-Channel Studies of Rotational and Vibrational Energy Transfer by Collision. R. K. Nesbet, Theory of Low Energy Electron Scattering by Complex Atoms.

1975, 320 pp., \$42.00/£21.00

ADVANCES IN PHYSICAL ORGANIC CHEMISTRY, Vol. 11

edited by V. GOLD, Associate Editor: D. BETHELL

CONTENTS: *T. H. Fife, Physical Organic Model Systems and the Problem of Enzymatic Catalysis. D. G. Farnum, Charge Density-NMR Chemical Shift Correlations in Organic Ions. G. M. Kramer, The Norbornyl Cation: A Reappraisal of Its Structure under Stable Ion Conditions. J. Cornilisse, G. P. de*

Gunst, and E. Havinga, Nucleophilic Aromatic Photosubstitution. M. Liber, Alternative Protonation Sites in Ambident Conjugated Systems

1975, in preparation

N.B.: Postage plus 50¢ handling charge on all orders not accompanied by payment.

Prices subject to change without notice.

ACADEMIC PRESS, INC.

A Subsidiary of Harcourt Brace Jovanovich, Publishers

111 FIFTH AVENUE, NEW YORK, N. Y. 10003

24-28 OVAL ROAD, LONDON NW1 7DX

17 2510